NASA SP-381

(NASA-SP-381) AERONAUTICAL PROPULSION   N75-31068
(NASA) 476 p HC $12.00   CSCL 21E   THRU
                                                        N75-31082
C18   Unclas
                                               F1/07   35538

AERONAUTICAL PROPULSION

A conference held at

LEWIS RESEARCH CENTER

Cleveland, Ohio

May 13-14, 1975

NATIONAL AERONAUTICS AND SPACE ADMINISTRATION

AERONAUTICAL PROPULSION

*The proceedings of a conference held at
Lewis Research Center in Cleveland, Ohio,
on May 13 and 14, 1975*

Prepared at Lewis Research Center

FOREWORD

During the more than three decades of its life, this Center has
been privileged to have been a participant in the development of our
Nation's truly great aeronautical posture. We are keenly aware of
the great importance of aviation, both civil and military, to our well
being and of the key role that advanced technology has in assuring
our future economic strength and security.

Today the Country calls for continued technological advancement
in aircraft propulsion as the key ingredient for future aircraft of ever
better performance and economy with socially acceptable levels of
noise and emissions. We hope that this Conference will be of value
in aiding government, industry, and the universities to meet these
challenges.

We invite your comments and questions on any aspect of this
Conference in the continuing spirit of "technical excellence in service
to others."

Bruce T. Lundin
Director

CONTENTS

v

I. PROPULSION SYSTEM NOISE REDUCTION

Charles E. Feiler, Laurence J. Heidelberg, Allan M. Karchmer,
Donald L. Lansing*, Brent A. Miller, and Edward J. Rice

This paper reviews some of the progress in propulsion system noise reduction since the Aircraft Engine Noise Reduction Conference held at NASA Lewis Research Center 3 years ago and reported in NASA SP-311. That conference centered on the early results from the NASA/GE Quiet Engine Program. Today our technology programs are concerned with the noise from a variety of aircraft and engine types as illustrated in figure I-1. These are conventional aircraft using high-bypass ratio turbofan engines; over-the-wing (OTW) and under-the-wing (UTW) powered lift systems using high- or very-high-bypass ratio turbofans; supersonic cruise aircraft using turbojets or low-bypass ratio turbofans; and general aviation aircraft using, perhaps, geared turbofans. The turbofan engine is common to these aircraft. Its noise sources are reviewed in figure I-2. Internal sources are the fan stage, compressor, and the engine core including the combustor, turbine, and struts. External sources are the fan and core jets. An additional external source for powered lift systems, not illustrated, is the noise of the exhaust jets scrubbing over the lifting surfaces or flaps.

The allowable noise levels for new aircraft are specified by the FAA noise rule known as FAR 36. The rule applies to the noise an observer would hear from an aircraft flyover at each of the three ground locations shown in figure I-3. These are the approach point under the aircraft flight path 1 nautical mile prior to touchdown, the takeoff point under the aircraft flight path 3.5 nautical miles from brake release, and the sideline point on a line parallel to the runway at a distance of 0.35 nautical mile for four-engined aircraft. The sideline point is at a distance of 0.25 nautical mile for aircraft with less than four engines.

---

*NASA Langley Research Center.

From the NASA/GE Quiet Engine Program there evolved two 22 000-pound thrust engines of about 5.5 bypass ratio, each incorporating noise reduction features and acoustic suppression into its basic design. Figure I-4 shows engine A with the acoustic nacelle designed by Boeing-Wichita as a part of the Quiet Engine Program, while figure I-5 shows this engine with the hardwall nacelle with bellmouth inlet. A major difference between these engines was in the fan designs. Engine A had a tip-shrouded single-stage fan with a tip speed of 1160 feet per second. Engine C also had a single-stage fan but with a supersonic design tip speed of 1550 feet per second.

The measured noise data from static tests of these engines were projected to yield estimates of the flyover noise a four-engined narrowbodied aircraft would make, if it used these engines. The estimates are shown in figure I-6 relative to the FAR 36 noise rules. The allowable flyover noise level, given in EPNdB, is shown as a fraction of aircraft takeoff gross weight. The upper curve is for the takeoff point and the lower for approach or sideline. Figure I-6 shows that with the hardwalled nacelle, engine A was about 7 to 8 EPNdB quieter than the rule at both takeoff and approach, while the suppressed engine was 14 to 17 EPNdB quieter. On the other hand, engine C with its high-tip-speed fan was noisier. In the hardwalled configuration, it was near the rule at both takeoff and approach. In the fully suppressed configuration, engine C was about 12 to 15 EPNdB less at both measuring points.

The noise levels demonstrated with these engines were quite low. Efforts have continued to reduce the noise output from the various sources described earlier and to obtain these reductions in efficient ways. The need for efficiency is particularly important today in view of the energy situation.

The noise technology areas addressed in this paper are formed around the different noise sources described earlier. These areas in the order discussed are: fan noise; advances in suppression including conventional acoustic treatment, high Mach number inlets, and wing shielding; engine core noise; flap noise from both OTW and UTW powered-lift systems; supersonic jet noise suppression; and finally the NASA program in noise prediction.

FAN NOISE

On a high bypass ratio turbofan engine such as engine A or C, the jet noise is reduced because of the reduced jet velocity, and the dominant noise source is the fan stage. Fan noise has two different characteristic sounds that depend on whether the fan tip speed is subsonic or supersonic. The spectral differences between these two kinds of fan sound are shown in figure I-7. The subsonic tip speed fan has a spectrum composed of tones at the blade passing frequency and its harmonics superimposed on a broadband spectrum. Much effort has gone into identifying the sources and mechanisms for this noise. Briefly, the blade passing tone arises, in the simplest sense, from the periodicity involved when the repetitive wakes from an upstream blade row interact with a downstream blade row to produce rotor-stator interaction noise. The broadband noise arises from the random unsteadiness inherent in the flow field over the blade rows.

The supersonic fan spectrum shows a multiplicity of tones that occur at multiples of the shaft rotational frequency. These tones, called multiple pure tones or "buzz-saw" noise, are associated with shock waves on the rotor blade leading edges due to the supersonic relative velocity over the blades.

A significant portion of the in-house fan noise research at NASA Lewis has been devoted to determining the far-field noise behavior of a number of 6-foot-diameter fan stages. Summary correlations of these and other data for different fan classes are shown in figure I-8, where the maximum perceived noise level from a 1000-foot flyover is plotted against fan pressure ratio for takeoff conditions. The data are normalized to a total of 90 000 pounds of thrust.

The bands for the different fan classes are those presented at the conference 3 years ago and reported in NASA SP-311. The upper band represents two-stage fans of the type used on narrow-bodied aircraft. They have only limited noise reduction features. The middle band represents single-stage high-tip-speed fans having low noise features typified by fan C. The lower band represents single-stage low-tip-speed fans having the low noise features typified by fan A. Some of these low noise features, common to most of the single-stage fans in the correlation, are wide separation between the rotor and stator; selection of proper number of rotor blades and

stator vanes; and elimination of inlet-guide vanes.

In the range of fan pressure ratios between about 1.5 and 1.9, figure I-8 raises the question whether or not a two-stage fan, designed with known noise reduction features, would be less noisy than a similarly designed high-tip-speed single-stage fan. Two such fan stages were designed and tested under contract to NASA Lewis. The GE high-tip-speed single-stage fan is shown in figure I-9. This fan stage incorporated the earlier experience gained with fan C of the Quiet Engine Program. It has a design tip speed of 1650 feet per second and uses a tip-shrouded fan. The two-stage fan, designed and tested by Pratt & Whitney Aircraft, incorporated low noise features such as wide axial spacing between blade rows and selection of the proper number of blades and vanes in each stage. It has a design tip speed of 1200 feet per second.

Data for these two fan stages are shown in the summary plot of figure I-10 to indicate their noise level relative to earlier experience. It can be seen that the high-tip-speed fan was about 2 PNdB quieter than earlier experience. An interesting behavior was observed with this fan; when it was tested at overspeed, the noise decreased another 1 or 2 PNdB. The two-stage fan was about 6 PNdB quieter than earlier two-stage fans and was also a little quieter than the earlier high-tip-speed single-stage fan experience. The data indicate that the two approaches to a low noise fan design produced fan stages that were about equal in noise output. The aerodynamic performance of both these fan stages is described in paper IX.

Several concepts for reducing fan source noise have been explored, four of which are illustrated in figure I-11. Most of these concepts are related to rotor-stator interaction noise. The first concept is the rotor with serrated blade leading edge. Then there are the leaned stator and long-chord stator. These latter two concepts are intended to reduce the response of the stator to the rotor wake fluctuations. This would reduce the fluctuating stator lift and also the noise. The last concept shown is wide spacing between the rotor and stator which is intended to allow the rotor wakes to dissipate before they intercept the stator. As has been mentioned, large rotor-stator spacing has been used in several of the low noise fan stages discussed.

Experimental tests of these concepts in ground static test facilities have shown somewhat limited noise reduction benefits. The reason for this

result is thought to be that the rotor-stator source noise is masked by rotor noise due to inflow disturbances and turbulence. The recent appearance of actual flight noise data, brought about by FAA noise certification requirements, has supported this viewpoint. Figure I-12 compares flyover and static inlet sound pressure spectra for CF 6-6 engines on a DC-10 aircraft. The data were for aircraft approach, and the engines were throttled back to approach thrust. For this engine, at this speed, the fundamental blade passing tone should not be present in the spectra, at least according to the theory of rotor-stator interaction noise. The flight spectrum shows no sign of this tone as expected, while it is clearly present in the static spectrum.

Results similar to these have been recorded by different observers for other aircraft/engine combinations. The result, as indicated earlier, seems clearly to be related to the differences in inflow conditions prevailing between static and flight tests. The sketches in figure I-13 attempt to illustrate what the differences are. In static tests, atmospheric turbulence drawn from a large area around the inlet and the ground vortex are candidate sources. Large-scale turbulent eddies are elongated in passing through the inlet and are ideal for generating fan tone noise. In flight, these disturbances are either absent or substantially minimized, resulting in lower fan noise.

These effects point to the need for further research on the sources of fan noise, particularly for ground static testing, with a view to obtaining cleaner inflows. Future research on fan source noise and reduction concepts at NASA Lewis will be conducted with 20-inch-diameter fan stages. For this purpose, a new indoor facility was constructed for both model fan and jet noise experiments. This facility is shown in figure I-14. In figure I-14, the view is from the location of the jet noise rig toward the fan rig. The walls of the room are acoustically treated with the wedge-shaped structures to achieve a free-field acoustic environment over a wide frequency range.

To summarize, significant source noise reductions have been demonstrated for a high-tip-speed single-stage fan and for a two-stage fan relative to earlier experience with these fan classes. While source noise reduction concepts relating to rotor-stator noise have shown limited success, the explanation advanced seems reasonable. Research on fan noise sources

with careful attention paid to inflow disturbances is needed to completely resolve these effects.

Finally, it is observed that even though fan source noise has been reduced, there is still need for further reduction. This leads to the next topics which discuss advances in acoustic suppression such as conventional acoustic treatment, high Mach number inlets, and wing shielding.

CONVENTIONAL SUPPRESSORS

Figure I-4 showed quiet engine A with a fully suppressed nacelle. Three years ago it was thought that this type of nacelle configuration was needed to reach the desired low noise goals. Note that there are several splitter rings: three are visible in the inlet and there is also one in the exhaust duct. The effectiveness of such highly suppressed configurations has been thoroughly demonstrated in the Quiet Engine Program. A desirable goal is now to maintain this high noise suppression while reducing the cost and losses involved with the suppressors. These losses could be substantially reduced by eliminating the splitter rings.

Two subjects are considered here: (1) increased information about the noise source can lead to better suppressor designs; (2) the wall acoustic impedance can be used in a more effective way than in the past. These two items may provide enough improvement in suppression to allow elimination of the splitter rings.

Noise Source Effect on Suppressor Performance

Three sets of noise suppression data are shown in figure I-15. The upper curve is for the baseline configuration with no splitter rings and a hard outer wall. The bottom curve shows results for the fully suppressed configuration with three treated splitter rings and outer wall treatment. When the splitter rings are removed and only wall treatment remains, the results shown by the middle curve are obtained. The main point of this figure is that the outer wall treatment is very effective - almost as good as the fully suppressed case.

6

Several data points obtained from inlet suppressors with wall treatment only are presented in figure I-16. The solid line represents the old axisymmetric propagation theory results. Note that the experimental data with wall treatment only are far above this theoretical limit. These suppressors are working much better than anticipated from the old theory, and in fact, better than anticipated from flow duct tests. Suppressors with splitter rings fall somewhat below this type of axisymmetric theory. Use of the old theory would predict that without splitter rings extremely long treated inlets would be needed.

An inlet suppressor and fan noise source are illustrated in figure I-17. The noise output of the fan is considered as the input to the acoustic liner in the theoretical calculations. As previously mentioned, the noise source was considered to be axisymmetric and in some instances even to produce a plane wave. This source description in the propagation theory will now be changed to be nonaxisymmetric or in general to be a spinning mode.

A rotating pressure pattern standing in front of the rotor is illustrated in figure I-18. The plus signs represent pressures above ambient and the minus signs those below ambient. Four high and low pressure regions are pictured representing a four-lobe pattern with $m = 4$. The presence of these spinning modes has been known for years. They may be produced by rotor-stator interactions, turbulence-rotor interactions, or the rotating potential field around the rotors. With splitter rings these rotating pressure patterns did not seem to produce a significant effect, and axisymmetric theory seemed to be sufficient to account for the suppressor data. However, suppressors with wall treatment only cannot be described by this earlier theory. Therefore, the sound propagation theory was reevaluated with spinning modes as the noise source input.

Calculated results for several lobe numbers are shown in figure I-19 with $m = 0$ to 50. These results represent the least attenuated mode for a given lobe number. The lobe number is seen to have a powerful effect on the attenuation. The experimental data are now seen to be in the attenuation range which might be expected for spinning modes, and the presence of these modes may be the reason for the high attenuation observed. It should be noted here that this is merely an order of magnitude type of comparison between theory and experiment, and no correlation should be implied. The modal content of the noise for these fans and engines is unknown at this time.

The determination and prediction of the actual modes of a fan will require more study in the future.

The results shown in figure I-19 may be summarized as follows. The presence of spinning modes have a large effect on the suppression obtained from circular liners with wall treatment only. With splitter rings the spinning modes can usually be ignored. These conclusions can be supported both experimentally and theoretically. Use of the true fan source properties should enable the building of much more effective inlet suppressors.

Wall Impedance Effects

A suppressor wall construction with nonuniform properties is shown in figure I-20. Such a structure can be used in two different ways. The first way, called series treatment, is used to broaden the attenuation bandwidth. In this approach, the thicker section may be tuned for the blade passage frequency, while the thinner section is tuned for a higher harmonic. The combined attenuation spectrum is simply the sum of the two attenuation spectra. Another approach, called phased or segmented treatment, is to tune both sections for the same frequency, but with different resistances. The resulting thickness difference then compensates for the large porosity difference required between the two panels to maintain the same tuning. If properly designed, a large increase in sound attenuation may occur which is much more than just the sum of the two attenuation spectra.

Some preliminary suppressor calculations for both phased treatment and uniform treatment (same construction throughout) are shown in figure I-21. These are considered as preliminary or illustrative since they were calculated using a finite difference technique with fairly large grid spacing. Both configurations were optimized for a plane wave input, that is, the wall impedances were selected to give maximum attenuation for a plane wave input. Starting with the uniform liner, a fairly uniform increase in attenuation with duct length is seen. Each unit length is operating about the same as all others.

With the phased treatment, the first half of the duct length attenuates the sound only slightly. This section appears to condition the plane wave and to set it up for the second section. In the second half of the duct the

attenuation is seen to increase dramatically to over double that of the uniform liner.

An explanation of why the phased treatment is working so well can be obtained from figure I-22. The two wall treatment sections shown here might be called the conditioning section on the left and the attenuation section on the right. Relative acoustic pressure amplitudes are shown at the beginning and end of each section. A plane wave enters the conditioning section at $X/L = 0$. At the end of this section $(X/L = 1/2)$, the sound is seen to be redistributed toward the outer wall where the acoustic treatment is located and where the power extraction must take place. With this skewed pressure profile, the second or attenuation section has an increased effectiveness and can quickly attenuate the sound before it reaches the duct end. This figure is intended to explain the effectiveness of phased treatment for low frequency plane wave input without a steady flow. It should be noted that, for other conditions, the controlling mechanism may be different than illustrated here.

Data on phased treatment liners were obtained using the 12-inch-diameter research compressor located in the Langley Anechoic Test Facility, which is shown in figure I-23. By placing various combinations of acoustical inserts in the inlet, a parametric study of 21 phased liner configurations was conducted. Figure I-24 shows example spectra obtained from these tests. The spectra are for a hardwall inlet, a uniform liner, and a phased liner having three sections with different backing depths. It can be seen that the phased liner produces greater noise reduction than the uniform liner in the low and mid-frequency range, which might be expected because of the two thicker treatment sections. However, the high frequency attenuation is maintained with the phased treatment even though only a small amount of high frequency treatment is present. One of the main directions of current research is to obtain a better understanding of how phased liners operate and to improve their effectiveness. In particular, work is continuing to broaden the range of frequencies over which significant additional noise reduction can be realized.

As pointed out earlier, the attenuation characteristics of liners depend strongly on the type of noise field to which the liner is exposed. Consequently, there is a definite need for a liner test apparatus which provides careful control of the incident sound field. Figure I-25 shows a schematic

of the test and source sections for such an apparatus which is being developed for the Acoustics and Noise Reduction Laboratory at Langley Research Center. A cylindrical test duct containing airflow represents a fan engine inlet. The test section will accommodate a wide selection of phased treatment configurations. The probe can be moved throughout the test section to obtain detailed data on flow profiles and acoustic pressure distributions. The source section, which is a central feature of the device, consists of an array of acoustic drivers and microphones located around the periphery of the duct. These drivers and sensors are linked together through a computer to generate and maintain prescribed spinning mode patterns of the type discussed earlier. This apparatus promises to be a major new tool for studying the ability of liners to suppress individual components of fan noise, such as the tones and broadband noise, and for obtaining a more precise comparison of theory and experiment than is possible using an actual fan.

Flow Visualization in a Resonator

Up to this point in the discussion, wall impedance concepts have been used rather abstractly as a boundary condition for sound propagation theories. In order to design a liner, these abstract numbers must be converted into actual wall constructions. To do this we must know the physics of the flow processes occurring in a typical liner structure such as that shown in figure I-26. The wall is constructed from a perforated plate bonded to a honeycomb back cavity. Both steady flow and oscillatory pressures are impressed upon the liner surface.

A flow visualization facility, shown schematically in figure I-27, was developed at Lewis to provide insight into the physics of the impedance phenomenon. This is a water flow device with dye injection used to visualize the flow. At the right is the main channel with grazing flow moving vertically. The back cavity is shown on the left with an oscillating flow input. This causes the orifice flow to oscillate and thus simulates an acoustic input. The field of view observed by the camera is also indicated.

Sketches of four frames taken from a high-speed motion picture are shown in figure I-28. These point out some of the interesting phases of the flow cycle. The grazing flow is again vertically upward. The first frame

shows a small amplitude inflow. Note that, because of the upward momentum of the grazing flow, not much fluid is diverted into the orifice. Inflow is confined to the small channel on the top of the orifice. If inflow amplitude is increased, the flow channel size increases. This partial channel flow makes the holes appear smaller and increases the flow resistance.

At the start of outflow the high velocity fluid at the orifice top cannot be immediately stopped, and the dead region at the bottom is first accelerated outward. The net flow may be zero but a counterflow exists in the orifice for a brief instant. This phenomenon is unique to the oscillatory visualization apparatus and would be expected to occur in an actual suppressor. As the flow exits outward from the orifice, it is turned by the steady grazing flow and is again restricted in cross-sectional area.

The flow in the near vicinity of the orifice may be considered as nearly incompressible even when a gaseous system is used. Thus the water system seen here should be a good approximation to the orifice flow in an actual suppressor.

In summary, the objective in recent research has been to maintain the high noise attenuation obtainable with splitter ring suppressors while reducing the losses, cost, and other problems associated with the rings. It appears to be possible that the rings can be removed without much loss in attenuation. Two promising techniques have been shown which should lead to this goal. Effective use of the noise source properties, such as the spinning mode phenomenon, and of wall impedance change benefits, such as phased treatment should provide enhanced noise suppression in engines of the future. To properly implement either approach, a thorough understanding of the wall impedance phenomenon with steady flow must be obtained.

HIGH-MACH-NUMBER INLET

Another way to reduce the noise emanating from the engine inlet is to use a sonic or high-throat-Mach-number inlet. The operating principle of the sonic inlet is illustrated in figure I-29. Engine noise suppression is achieved by accelerating the inlet flow to near-sonic velocity in the inlet throat. This high inflow velocity does not allow the forward propagating sound waves to escape from the inlet. Also, the flow velocity gradient

generated within the inlet, shown by the arrows, bends the sound waves onto the wall and further reduces engine noise.

A basic characteristic of the noise reduction obtained with a sonic inlet is shown by figure I-30. The noise reduction is defined as the change in noise level measured when the sonic inlet is substituted for a conventional inlet having a lower inflow velocity for the same design flow rate. The figure indicates how this noise reduction typically varies with inlet airflow and average throat Mach number. Airflow is shown as a percent of the choking, or limiting value, that occurs at an average throat Mach number of one.

The figure indicates that large noise reductions are possible near choking airflow. However, noise reduction is a strong function of inlet flow and is not obtained until the inlet average throat Mach number is increased above approximately 0.6. If reduced noise is desired at low airflows, for example at approach to landing where engine thrust is reduced, the inlet flow area must be made smaller in order to maintain the necessary high inflow velocity.

Many sonic inlet configurations have been identified that can yield noise reductions of 20 decibels or more. Several of the configurations that have been tested are illustrated in figure I-31. The simplest inlet is the fixed geometry type. However, this inlet reduces noise only at maximum inlet flow (e.g., takeoff condition). The other inlets shown in the figure have a variable flow area so that noise reductions can be maintained over a range of inlet airflows (e.g., takeoff and approach). The flow area can be varied by translating the centerbody, contracting the cowl wall, or by retracting or translating vanes and rings within the inlet.

Model Tests

A question of major importance with all types of sonic inlets is their ability to perform well at forward velocity and angle of attack. In order to obtain inlet performance under these conditions, a number of model sonic inlets were tested in the Lewis Research Center 9- by 15-Foot Wind Tunnel. Figure I-32 shows a model inlet installed in the wind tunnel. During these wind tunnel tests, simultaneous measurements were made of inlet aerodynamic and acoustic performance.

Figure I-33 shows some typical results obtained from these tests. Here inlet total pressure recovery is plotted as a function of sound attenuation. Increased attenuation was obtained by increasing inlet flow. These data are from tests of a fixed-geometry inlet at a tunnel airflow velocity of 80 knots. Data are shown for flow angles of 0°, 30°, and 50°.

The data indicate a progressive drop in pressure recovery with increased sound attenuation. For all flow angles the maximum attenuation obtained was limited by the tunnel background noise level, not by the ability of the inlet to suppress noise. The data indicate that increasing flow angle also results in a loss in pressure recovery. However, at all operating conditions, the general level of aerodynamic performance is quite good. For example, a total pressure recovery approaching 99 percent can be obtained with a sound attenuation of 20 decibels while being subjected to the severe 50° flow angle condition.

The results of these tests, as well as tests conducted by Boeing under contract to Lewis, have demonstrated that sonic inlets can be designed to give good aerodynamic and acoustic performance while subjected to simulated takeoff and landing conditions.

While the results obtained from small scale model tests are useful, the question can be raised as to how well these results may apply for large or full-sized inlets. In addition, any effects the inlet might have on the engine fan or compressor are difficult to determine from small scale tests. For these reasons two of the most promising variable-area sonic inlet configurations were tested at large model size.

Tests With Fans

Figure I-34 shows the translating centerbody sonic inlet that was designed and tested by Pratt & Whitney under contract to Lewis. This inlet was tested with an advanced-design two-stage fan. General Electric, also under contract to Lewis, designed and tested the contracting cowl wall sonic inlet shown in figure I-35. This inlet was tested with an advanced-design single-stage fan.

Some acoustic results obtained with the contracting cowl wall inlet are presented in figure I-36. Noise reduction is plotted against percent of take-

off airflow. Data obtained with hard inlet walls are shown by the open symbols, while solid symbols show data obtained with acoustically treated walls. As the sketch indicates, data were obtained for two values of inlet flow area.

The data on the right side of figure I-36 were obtained with the inlet in the takeoff configuration where maximum engine thrust and airflow are required. Here the inlet flow passage, shown by the solid contour in the sketch, was sized to yield near choking conditions at takeoff airflow. As indicated in figure I-30, this can result in a large noise reduction. The data in figure I-36 show a maximum noise reduction of approximately 20 PNdB. Noise reductions larger than this could not be detected due to the background noise level, or noise floor, of the test facility.

The data on the left side of figure I-36 were obtained with the inlet flow area reduced, shown by the dashed contour in the sketch, so that choking would occur at approach airflow. For this inlet, the approach flow was approximately 75 percent of the takeoff flow. Again, a maximum noise reduction of approximately 20 PNdB was obtained. Large noise reductions could be obtained at any other airflow by making the appropriate change in inlet flow area.

The solid symbols in figure I-36 indicate that the addition of wall treatment to the inlet with the takeoff flow area allowed some noise reduction to be maintained at reduced airflow where the suppression due to sonic inlet effects was approaching zero. For some applications, a sonic inlet with wall acoustic treatment, sometimes referred to as a hybrid inlet, may yield sufficient noise reduction at reduced flows to eliminate the need for variable inlet geometry.

The contracting cowl wall inlet discussed in figure I-36 performed well aerodynamically with total pressure recovery ranging between 97 and 99 percent. Results similar to these were obtained from the Pratt & Whitney tests of the translating centerbody inlet.

Full-Scale Engine Tests

In order to determine the effect of a sonic inlet on overall engine performance, full-scale tests are being conducted here at Lewis using engine C. Figure I-37 shows the engine installed on a thrust stand where tests are be-

ing conducted with a contracting cowl wall inlet. This inlet is similar to the one tested by General Electric with the model fan stage.

Some results obtained from these engine tests are shown in figure I-38. Noise reduction and percent takeoff thrust are shown as a function of engine airflow. The data for the sonic inlet were obtained with the inlet in the take-off mode with acoustically treated inlet walls. The noise data indicate that at low weight flows a noise reduction of approximately 6 PNdB was obtained due to wall treatment. As inlet flow was increased, the noise reduction obtained also increased. However, while model tests indicated that a maximum noise reduction of 20 PNdB or greater could be expected, these engine test data show a maximum noise reduction of approximately 15 PNdB. An examination of the data indicated that the noise reduction that could be measured in front of the engine was limited by exhaust jet noise coming forward from the rear, and not by the ability of the sonic inlet to suppress noise. This result indicates the need for looking at all potential sources of engine noise to achieve maximum noise reduction.

The open symbols in the bottom half of figure I-38 show engine thrust measured with the sonic inlet, while the thrust obtained with a high performance bellmouth calibration inlet is shown by the solid symbols. The curve indicates that the presence of the sonic inlet did not measurably affect engine thrust when compared to the calibration inlet. This indicates that the sonic inlet is yielding good aerodynamic performance.

In summary, it is apparent from the available data that the sonic inlet can be very effective in reducing engine noise. However, in order to fully evaluate this method of achieving engine noise reduction, more effort is required to define what penalties may be associated with using a sonic inlet in terms of increased cost, weight, and complexity.

WING SHIELDING

Another approach to reducing the noise that an aircraft radiates to the ground is to use a barrier to shield that noise. The wing can be used as such a barrier if the engines are placed above it. Two possible engine positions where the wing shields propulsion-related noise are illustrated in figure I-39. Aft noise shielding can be obtained with the engine located in a

forward position. Here both internal engine noise and jet noise can be shielded. With the engine in the aft position, fan inlet noise can be shielded.

A TF34 engine was used to investigate inlet shielding. The engine is shown on the test stand with the wing in position in figure I-40. The large muffler on the rear of the engine removes most of the jet noise along with all other aft-radiated noise. This test was run at a relatively new facility here at Lewis. This facility is used primarily for powered lift tests and will be described briefly later in the section POWERED LIFT.

The results of these tests are shown in figure I-41 where the directivity for a 500-foot flyover is plotted in terms of perceived noise level. The engine-alone noise peaks between 50° and 60°, typical of inlet noise. The presence of the wing greatly reduces the noise as shown by the lower curve. The shielding begins at an angle of 30°. This corresponds to the angle at which the inlet would no longer be visible to an observer under the wing. The maximum shielding demonstrated here is 19 PNdB. For this case, where inlet noise is the only source, the maximum perceived noise level for a flyover was reduced 15 PNdB. However, for any practical case the jet noise would limit the overall noise reduction obtainable to a much lower value.

The effect of the shielding on the spectrum can be seen in figure I-42. The engine-alone spectrum is typical of a supersonic tip speed fan, with multiple pure tones and blade passage tones. While little or no shielding is evident at the lowest frequencies, the shielding increases with frequency until over 30 decibels is shown at 20 000 hertz. This behavior is predicted by theory. The shielding effectiveness can be shown to increase as the ratio of the barrier height to wave length increases.

Aft shielding tests were conducted using quiet engine C. A photograph of the engine on the test stand next to the wing is shown in figure I-43. The wing is mounted on a flat-bed trailer so that its position can be changed quickly. These tests were run with both an unsuppressed and a fully suppressed version of the engine.

The results of the aft shielding tests on the unsuppressed engine are shown in figure I-44, where the directivity for a 1000-foot flyover is plotted. Noise reductions of 5 PNdB in the aft quadrant were obtained. The noise shielded here is a combination of aft fan and jet noise.

The results of aft shielding on a fully suppressed engine are shown in

16

figure I-45. Here a sonic inlet with both aft fan and core treatment is used to suppress the engine noise to the jet noise floor. The maximum jet noise shielding shown here is just over 4 PNdB, although the peak noise is reduced only 2 PNdB. The reason for the limited effectiveness is twofold. First, jet noise is a low frequency source and, as indicated before, less shielding can be obtained at low frequencies. Second, jet noise is a source that extends for many diameters downstream of the nozzle. This puts a portion of the source in a position too far aft for the wing to shield.

Jet noise shielding has been investigated extensively with small scale models. One of the results of this work was to show that forward velocity does not have any detrimental effect on shielding. In fact, since jet noise is reduced with forward velocity the shielded noise is also reduced.

In summary, inlet shielding was shown to be very effective, and might be considered as a low-loss alternative to acoustic treatment or a sonic inlet. Possible aerodynamic and installation problems may occur with an engine mounted in an aft OTW position. Although jet noise shielding was less effective, few low-loss alternatives currently exist in reducing noise from this source.

COMPARISON OF SUPPRESSOR METHODS

It has been shown that all three methods discussed offer promise for effectively suppressing fan noise. Which method is chosen perhaps will be determined by nonacoustic considerations as well as by how much suppression is needed. For not too large a suppression requirement, conventional acoustic treatment offers the simplicity of fixed geometry and, in the case of an inlet, it appears that wall treatment alone could do the job. For very large inlet suppression requirements, the high-Mach-number or sonic inlet would be indicated. However, if the high-Mach-number inlet is to be effective at both takeoff and approach, it must have the complexity of variable geometry. The high-Mach-number inlet with acoustic treatment, called a hybrid inlet, offers a possible compromise between the variable-area sonic inlet and conventional acoustic treatment. Suppression by wing shielding, while posing no acoustic problems, may have associated aerodynamic and

structural problems as well as the problem of exposing the aircraft passenger cabin to more noise.

As is well known and as was illustrated by the data in the presentation, the effectiveness of these methods when used on an inlet is often limited by aft-radiated jet noise. This result would also limit the flyover noise reduction obtainable, which points to the need to address both aft-radiated and inlet noises. In this regard, the phased treatment concept discussed relative to conventional acoustic treatment is expected to benefit noise reduction from aft fan ducts.

ENGINE CORE NOISE

The previous discussion has indicated that considerable progress has been made in developing and improving techniques to reduce and suppress fan noise. As higher bypass ratio engines are utilized, the jet velocity and therefore the jet noise is considerably reduced. As these two sources of noise are brought down, additional internal noise sources from the engine core are heard: combustor noise; turbine broadband noise and tones; and possibly internal strut noise. Figure I-46 is a schematic plot of overall engine sound power level against jet velocity. At high jet velocities the jet noise is high and, assuming the fan noise has been successfully suppressed, the total sound power from an engine is jet-noise dominated. With decreasing jet velocity, the total engine noise decreases, and the core noise begins to emerge as a new noise floor.

The spectral distribution of engine noise sources, again assuming the fan noise has been successfully suppressed, is shown in figure I-47 for an engine operating at approach power. The sound pressure level of each of the noise sources is plotted against frequency, along with the total engine noise. The plot of figure I-47 is for the noise sources determined from a static ground test. For this test condition, the jet noise and combustor noise are approximately the same, and the total noise is not dominated by either of the two. However, when the relative jet velocity is lessened as a result of the forward motion of the aircraft, the jet level is substantially reduced, as shown in figure I-48. The combustion noise, being an internal noise source is not subject to the effects of forward velocity and its level

remains the same. The total noise, therefore, remains essentially unchanged and is now dominated by the internal noise sources.

These internal noise sources, therefore, represent a possible new noise floor which requires attention. Consequently, NASA has been conducting and sponsoring research to determine the fundamental parameters governing their generation and transmission. Since other government agencies, particulary the FAA, have programs investigating turbine noise, NASA is concentrating on combustion noise.

The general approach to these initial investigations into combustion noise contains three basic steps. First, through direct in-duct measurements, establish the combustor noise generation level and the relevant governing parameters. Second, also through direct in-duct measurements, determine combustion noise transmission across the turbine, and finally, determine its efficiency in radiating to the far-field. In other words, how much of the noise generated in the combustion region actually reaches the far field?

Figure I-49 shows the results of some preliminary experiments designed to establish both the level of noise in the combustion region and the effects of two parameters: temperature rise across the combustor and combustor design. Both plots show the sound pressure level plotted against 1/3 octave center frequency as measured in the duct of a combustor development rig. In figure I-49(a), the dashed curve shows the sound pressure level spectrum for a purely cold flow through this test rig. The solid curve shows the effect of a 1500° F temperature rise due to combustion. The important point is that combustion noise, at least as measured in duct, is not merely flow noise but is associated with the elevated temperatures and possibly the increased duct velocities, and combustion itself. What is not clear yet is how much of the increased noise level is due merely to the elevated temperature level independent of actual combustion, and how much is due to the actual combustion process.

Figure I-49(b) shows representative in-duct spectra from a similar combustor development rig, but different combustor can designs from the experimental clean combustor program, which is discussed in a later section of this document. Here, the temperature rise due to combustion is approximately the same in both cases, around 1200° F. The dashed upper curve is a Pratt & Whitney version called a vorbix can, and the solid curve

is a NASA swirl can design. Clearly, there are at least two relevant parameters in determining combustor noise generation level: temperature rise across the combustor and the specific geometric can configuration.

As mentioned earlier, the second step in the study of combustion noise is determining the transmissability of combustor-generated noise across the turbine; that is, how much of the noise actually gets through the turbine? Figure I-50 illustrates this. The figure shows sound power level plotted against frequency as measured in duct in an actual engine. These data are for approximately 40 percent engine speed. The uppermost curve represents the sound power level as measured at the combustor igniter, and the middle curve represents the sound power level downstream of the turbine in the tailpipe. It can be seen, therefore, that at least in terms of the total fluctuating pressure field, there is significant attenuation across the turbine. There is some theoretical work indicating that the attenuation of combustor noise across an entire set of turbine stages is much greater even than indicated in this figure. Some theories, in fact, indicate that virtually none of the combustor-generated noise gets through the turbine, but the core noise downstream of the turbine consists of broadband turbine noise generated as the entropy or temperature spotiness of the combustor flow passes through the turbine.

The third step in the process of examining combustor generated noise, and obviously the most important, is determining how much of this noise, if any, reaches the far field. As a first approximation a direct comparison between internal engine measurements and far-field engine noise data can be made. This type of comparison is also shown in figure I-50. The bottom curve represents the sound power level as measured in the far field, and it can be seen that there is a further attenuation from the noise measured in the tailpipe. If the far field data contained an additional large contribution from a source downstream of the turbine or tailpipe, for example the jet noise, this attenuation might not be observed. A preliminary conclusion can be made that the far-field noise for this low operating speed is internal core noise, therefore.

In summary, the continuing improvements in fan and jet noise reduction have revealed that engine core noise emerges as a possible new noise floor. Whether or not the absolute levels of this noise pose a significant problem has yet to be determined. Some of the preliminary NASA efforts in investi-

gating the nature of this noise have been shown. These efforts are a neces-
sary first step before suppression techniques can be developed and imple-
mented.

POWERED LIFT

The two powered lift concepts that are receiving the most attention are
the engine-under-the-wing (UTW) and engine-over-the-wing (OTW) configu-
rations. These two concepts are illustrated in figure I-51. In the under-
the-wing case the engine exhaust is directed into the flaps where it is de-
flected downward. Both the deflected jet and the increased circulation over
the wing and flap system result in added lift. In the engine-over-the-wing
case, the jet is blown over the upper surface of the wing and flap. By taking
advantage of the Coanda effect, the jet follows the surface and is deflected
downward. Here again, the result is added lift. In addition to the engine
internal noise and jet noise, both powered lift systems generate noise caused
by the interaction of the jet with the wing and flaps. This jet-flap noise is
generally the dominant source in powered lift systems. The over-the-wing
system has an advantage in that the wing provides some shielding of noise
sources above it. The under-the-wing system has the advantages of a sim-
pler more conventional engine installation and nozzle, as opposed to a slot
or D-shaped nozzle or deflector as required in the over-the-wing case.

The engine-under-the-wing concept was investigated in full scale using
a suppressed TF34 engine. The engine is shown on test in an under-the-
wing configuration in figure I-52. It was necessary to heavily suppress the
engine to prevent contamination of flap noise measurement with fan and core
noise. Inlet noise is suppressed with a treated three splitter ring inlet.
Both the aft fan duct and the core duct are also heavily treated. The core
and fan streams are mixed internally with a 12-lobe forced mixer nozzle.
For the configuration shown here, the nozzle exit is located 1 foot behind
the leading edge of the wing. These tests were run at a relatively new facil-
ity here at Lewis. This facility is capable of both noise and performance
testing of an engine and wing. The engine is hung from an overhead thrust
frame which in turn is supported by a cantilevered structure. The wing is
mounted vertically on a movable table.

An over-the-wing configuation on test at the same facility is shown in figure I-53. Here a slot nozzle with an aspect ratio of 4 to 1 was fitted to the TF34 engine. Tests were also run using a circular nozzle and deflector.

The results of some of the powered lift tests can be seen in the comparison plot of both the under- and over-the-wing systems shown in figure I-54. Here the maximum perceived noise level for a 500-foot flyover is plotted against exhaust velocity. For reference, the suppressed engine-alone data are included in this plot. The strong influence of velocity can be seen here. The slope of all three lines on this plot indicate a seventh to eighth power dependence on velocity. Comparison of the different systems at the same velocity corresponds to a comparison at the same thrust since the nozzle exit area is a constant. The under-the-wing system is shown to be around 5 PNdB higher than the over-the-wing system. Both systems are noisier than the engine alone. The under-the-wing system is the noisier of the two by only 3 PNdB when compared on a 500-foot sideline and an altitude of 250 feet. This is due to differences in directivity between the two systems.

A spectral comparison of flap noise for both powered lift systems and the engine alone is shown in figure I-55. The flap noise is characterized by the large increases in low frequency noise above the engine-alone noise. The under-the-wing noise generally has a spectral peak at a higher frequency and a higher level than the over-the-wing case. In figure I-55, the peaks are at around 200 hertz for the under-the-wing case and at 50 hertz for the over-the-wing case. These high levels of low frequency noise may prove to be more of a problem with cabin interior noise than with community noise. It is very difficult to attenuate low frequency noise with aircraft cabin walls.

Much work has been done with small-scale models on the under-the-wing concept in an effort to reduce the noise. Many novel ideas were tried such as porous flaps, compliant flap surfaces, trailing edge blowing, trailing edge geometry variations, flap gap spacing, and wing nozzle spacing. Most of these approaches had little or no effect on the maximum flyover noise. However, work is continuing in the area of noise source identification and reduction. One approach that was effective in lowering the noise involves a velocity decayer nozzle with a treated ejector shroud. Unfortunately, this system has serious problems with high cruise drag and weight.

The over-the-wing concept has been investigated to a lesser degree. One of the important noise variables for this system is flap length. The results of changing the flap length with slot nozzle are shown in figure I-56. The short flaps are 4 PNdB noisier than the long flaps. The velocities at the flap trailing edge were surveyed for both flaps. The long flap had a velocity decay of 17 percent based on the peak trailing edge velocity. The decay for the short flap was essentially zero. It seems likely that the lower velocity at the trailing edge is the prime reason for the reduced noise. The greater shielding effectiveness of the long flap may also play a part in the noise reduction. Further investigation into novel approaches in the over-the-wing system, especially in the area of velocity decaying nozzles or deflectors, may prove fruitful.

The effect of forward velocity on flap noise has been investigated with small-scale models and to a limited extent in large-scale. For both the over- and under-the-wing systems, forward velocity reduces the noise by about 2 decibels.

The aerodynamic effectiveness of these powered lift systems has been investigated extensively at Langley in small-scale and more recently in large scale. A modified Aero Commander airplane equipped with two JT15D engines in an over-the-wing configuration is shown in figures I-57 and I-58, in a wind tunnel test. Both static and forward velocity effects were investigated. The results of these tests are in general agreement with the small-scale results. A four-engine over-the-wing configuration is shown in figure I-59 in the Ames 40- by 80-Foot Wind Tunnel. Large models such as this one are used as a final step in investigating the aerodynamics of powered lift systems. In this test an upswept wing was used to gain stall margin.

In summary, both the under- and over-the-wing systems are still competitors with the over-the-wing having the noise advantage. The over-the-wing system may yield further noise reductions as more work is done in this area. Noise reductions in the under-the-wing case appear less likely. Both systems have noise that is strongly velocity dependent and can be reduced by using engines with higher bypass ratios and correspondingly lower exhaust velocities.

SUPERSONIC JET NOISE SUPPRESSION

A supersonic cruise aircraft would require relatively high jet velocities, and exhaust jet noise once again would become a problem. Some of the candidate engine types for a supersonic cruise aircraft are a straight turbojet, a low bypass turbofan, a variable cycle engine, or a duct-burning turbofan. The present discussion will concentrate on jet noise suppression for a duct-burning turbofan engine.

Figure I-60 is a schematic representation of a duct-burning turbofan engine. This type of engine is discussed in considerably more detail in papers XIV and XV. Essentially, the fan flow is increased in temperature and velocity by the use of a relatively high pressure ratio fan and direct burning of fuel in the fan stream. The fan stream, which now has a greater exit velocity than the core stream, thus provides the bulk of the thrust, with a corresponding extraction of energy from the core turbine and jet. One of the advantages of this approach is that a jet noise suppressor would only have to be applied to the fan stream and would, therefore, be presumably smaller and lighter in weight. General Electric and Pratt & Whitney, under contract to NASA Lewis, have been testing various nozzle configurations for a duct-burning turbofan engine.

Figures I-61 and I-62 illustrate the General Electric configurations. Figure I-61 shows the basic unsuppressed nozzle with a plug in the primary nozzle, and figure I-62 shows the nozzle with a multitube secondary supressor, and the nozzle with a multichute secondary suppressor.

Figures I-63 and I-64 show the Pratt & Whitney configurations. The unsuppressed nozzle and the nozzle with a multitube secondary suppressor are shown in figure I-63. Figure I-64 shows the nozzle with a convoluted secondary suppressor, and an acoustically lined ejector which could be used with any of the nozzle configurations shown.

Figure I-65 illustrates the noise characteristics of the Pratt & Whitney configurations. Plotted here is the sound pressure level against frequency. The data are scaled up from model tests to a 40 000-pound thrust engine at takeoff conditions. The upper curve is for a reference conical nozzle with the equivalent fan flow of the duct-burning nozzle. In configuration sequence are the unsuppressed duct-burning nozzle, the nozzle with a convoluted secondary suppressor, then a multitube secondary suppressor, and

finally a multitube secondary suppressor with lined ejector. Noise reductions are achieved by each of the various suppressor types, but the major reduction is for the basic unsuppressed duct-burning nozzle compared to the convergent nozzle. This coannular suppression effect, which results from a velocity profile inversion from that of a conventional turbofan engine is especially promising because it is achieved without the addition of suppression hardware.

Thrust performance is also important. Figure I-66 shows a plot of noise reduction against thrust loss. The reference is for the same conical nozzle in figure I-65. The largest reduction, about 8 PNdB at sideline, comes from the unsuppressed duct-burning turbofan nozzle compared to a conical nozzle with about 2 to 3 percent loss in thrust. The convoluted secondary gives an additional small reduction in noise with no additional thrust lost, and the addition of a lined ejector gives further suppression and actually improves thrust somewhat, at least on a static basis. The acoustic advantages of the multitube suppressor on the secondary are similar, but with greater penalties. It is felt though, that with a more properly matched ejector, the thrust penalty can be considerably reduced for this configuration.

It is emphasized that the acoustic and thrust performance shown in figures I-65 and I-66 are for static tests. Experience has shown, from a variety of flight and flight simulation techniques for other types of suppressors, that forward velocity effects alter the acoustic and thrust characteristics. The general trend in these types of tests indicate that forward velocity tends to reduce the amount of suppression and increase the thrust loss compared to static observations. It is possible that similar effects would also show up in these configurations, particularly for the suppressed and ejector versions. On the other hand, it is felt, as mentioned previously, that improved designs, especially for the ejector, can substantially reduce the thrust penalty.

In summary, data from nozzle and suppressor tests for just one of several candidate engine types for a supersonic cruise aircraft have been presented and the preliminary results appear promising.

NOISE PREDICTION

There is a recognized need for the capability to calculate aircraft flyover noise from the individual component sources that have been discussed herein. Aircraft flyover noise calculations are necessary in order to determine the true benefits to be gained from any individual source noise reduction, since such individual reductions may not show up in the total system noise signature. Such a capability is also necessary to do propulsion system trade studies and to assess community noise impact.

It has long been recognized that the results of flyover noise calculations, such as effective perceived noise levels (EPNL) or footprint areas, for example, depend upon the method for doing the calculations and hence may differ, in spite of starting with the same data base. This is because the problem is quite complex, involving the source, the propagation path, and the receiver as shown in figure I-67. For each of these inputs, certain key technology areas, also shown in figure I-67, need to be properly understood in order to make reliable predictions.

In response to the need to develop the capability to make accurate flyover noise calculations, the Aircraft Noise Prediction (ANOP) Office was established at Langley Research Center to coordinate an agency-wide effort. The development of this capability follows a dual path. The first path involves the acquisition of existing computer programs from which is established what is called an "interim" prediction capability. The long-term effort is devoted to developing an original NASA prediction program. This proceeds by identifying the critical research areas which must be understood in order to make successful calculations, preparing key technology documents in these areas to establish the state-of-the-art particularly as regards prediction, and then integrating the best available methodology into an overall computer program.

The creation of the ANOP computer program is illustrated in figure I-68. The two fundamental elements of the computer program are the prediction methodology as specified in the key technology documents and the computer software. The documents are being prepared by NASA with industry participation. The development of the software is a major effort of the ANOP office at Langley which will draw on the assistance of consultants in programming and systems analysis.

The structure of the resulting computer program is shown schematically in figure I-69. A major element of the program is the executive system which will manage the calculation of individual noise sources and combine them into a complete overall noise signature. The output can be selected to suit the user's needs and might consist of time histories of flyover noise or plots of footprints, for example. It will be possible to compute the noise of a single aircraft flyover or the community impact of a mix of aircraft. The prediction method may be selected to have a completely empirical basis or to proceed from purely analytical models or have some mix of these methodologies.

The status of the ANOP effort at present is as follows. An interim computer program capability based on currently available computer programs is in existence. For the long-term effort, first versions of many of the key technology documents have been prepared and are being issued as NASA publications. (The preparation of the documents will be an on-going process, and they will be updated as new information becomes available.) Finally, a contract to do the computer programming, including development of the executive system, is in the procurement stage.

SUMMARY

Progress in the various noise technology areas may be summarized as follows:

Fan Noise. - Advanced quiet conventional fans, particularly the two-stage fan, show significantly reduced noise levels relative to prior experience. A better understanding of the nature of fan source noise has been attained that shows why rotor-stator noise reduction concepts have been of only limited success and points to the need for obtaining cleaner inflow in static tests.

Suppression. - Conventional acoustic treatment shows considerable promise with the demonstrated large suppression by no-ring inlets. Theoretical advances accounting for spinning modes and quantifying the phased treatment concept could lead to elimination of inlet splitter rings and the penalties they cause. A number of attractive high-Mach-number inlet configurations have been identified. Good acoustic and aerodynamic perfor-

mance have been demonstrated statically on full-scale inlets and over a wide range of angle of attack under simulated model flight conditions. Wing shielding has been shown to be effective for both inlet and exhaust noise. Shielding can provide reduction in jet noise without penalty and it remains effective in forward flight.

Core Noise. - This is a recently recognized source that is not yet well understood and quantified.

Flap Noise. - Noise from both over- and under-the-wing (OTW and UTW) powered lift systems can be reduced by reducing the jet velocity over the flaps. OTW systems appear to be somewhat quieter than UTW systems. Increasing flap length shows promise as a method for reducing OTW flap noise.

Supersonic Jet Noise. - The duct-burning turbofan nozzle configuration, because of the coannular suppression effect, is quieter than a comparable convergent nozzle, which is an encouraging result.

Noise Prediction. - This effort is serving to bring all these technology areas together to address the total airplane noise problem and to point out voids in the existing technology.

The technology discussed herein will certainly find application in any low-noise propulsion systems of the future. In fact, some of this technology will be evident in papers II and III. It appears safe to say that aircraft using engines having these technological advances would be several EPNdB quieter than the FAA rule which was discussed at the beginning of this paper. In addition, as was mentioned, the acoustic suppression techniques now being considered promise significant reductions in the penalties formerly paid for fan quieting.

CONVENTIONAL (CTOL)			HIGH-BYPASS TURBOFAN
POWERED LIFT	OVER-THE-WING (OTW)		HIGH-BYPASS TURBOFAN
	UNDER-THE-WING (UTW)		VERY HIGH-BYPASS TURBOFAN
SUPERSONIC CRUISE AIRCRAFT			TURBOJET LOW-BYPASS TURBOFAN
GENERAL AVIATION			GEARED TURBOFAN

CS-73243

Figure I-1. - Types of aircraft and engines for noise reduction technology.

FAN INLET NOISE

FAN EXIT NOISE

FAN JET NOISE

CORE JET NOISE

COMPRESSOR NOISE

ENGINE CORE NOISE
COMBUSTOR
TURBINE
STRUTS
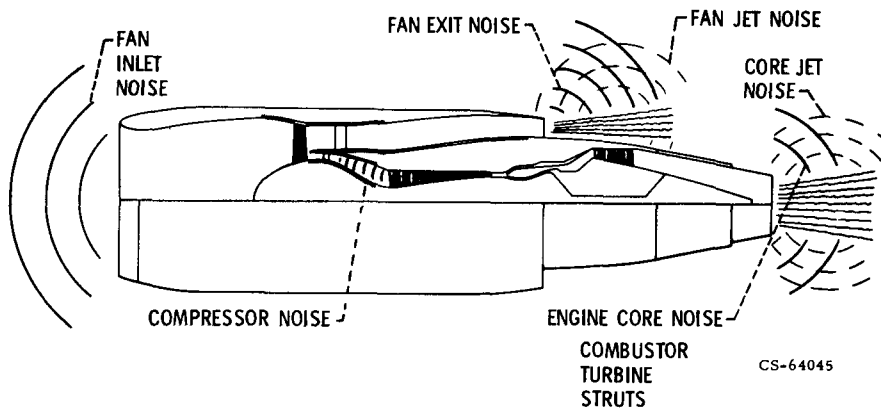
CS-64045

Figure I-2. - Turbofan engine noise sources.
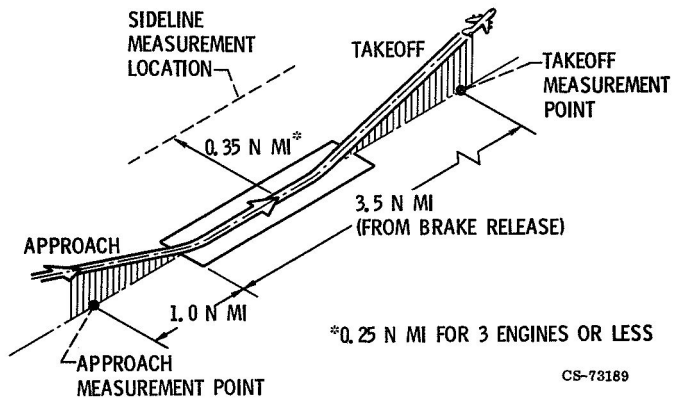
Figure I-3. - FAA noise measurement locations.

SIDELINE MEASUREMENT LOCATION
TAKEOFF
TAKEOFF MEASUREMENT POINT
0.35 N MI*
3.5 N MI (FROM BRAKE RELEASE)
APPROACH
1.0 N MI
*0.25 N MI FOR 3 ENGINES OR LESS
APPROACH MEASUREMENT POINT
CS-73189
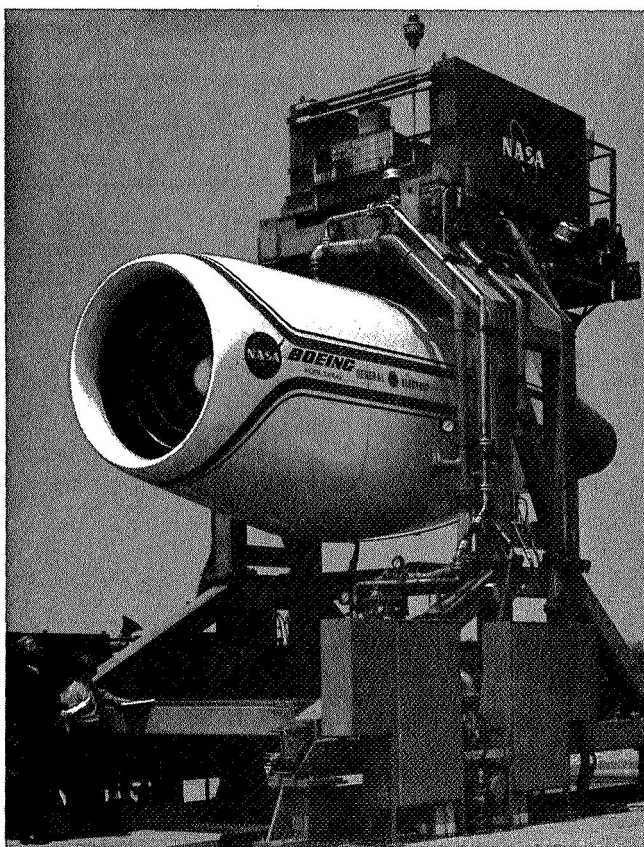
CS-73280

Figure I-4. - Quiet engine in Boeing nacelle.
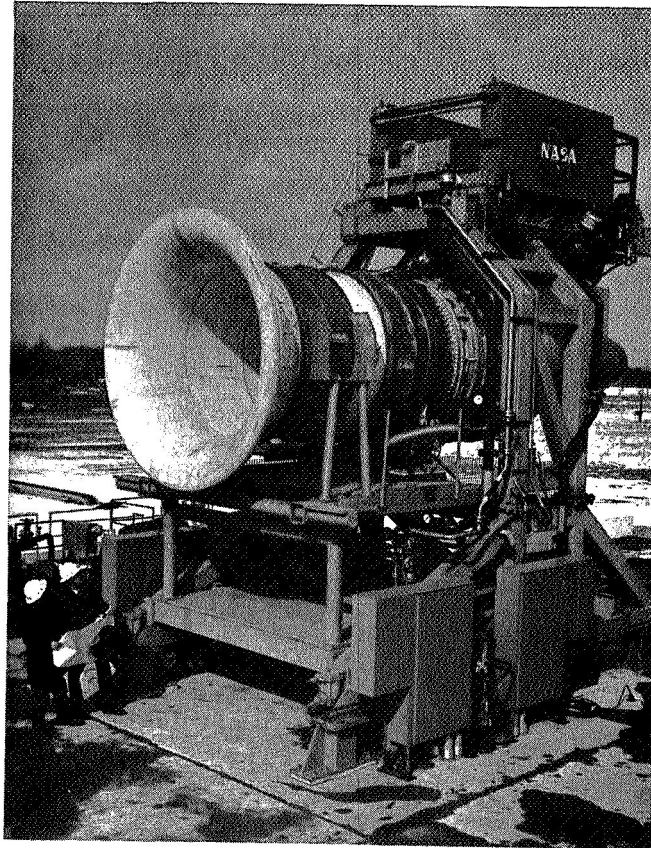
CS-73279

Figure I-5. - Quiet engine in baseline configuration.
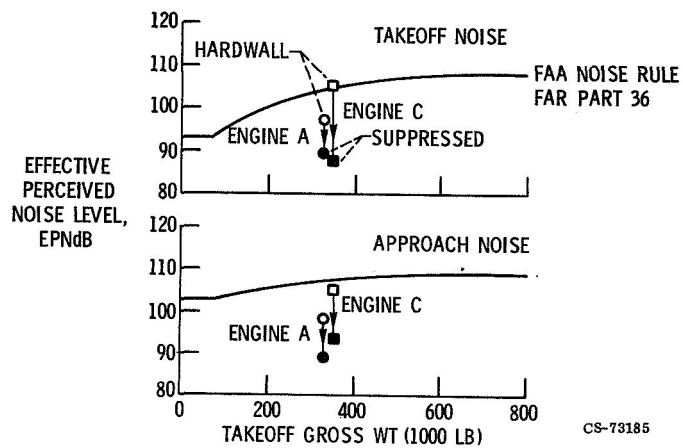
CS-73185

Figure I-6. - Quiet engine noise performance.
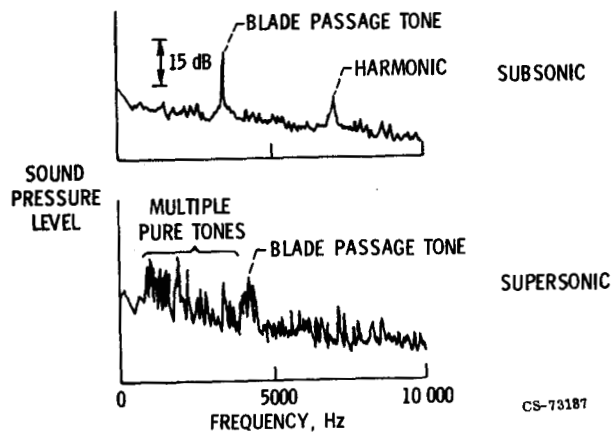
Figure I-7. - Fan noise spectra at low and high tip speeds.
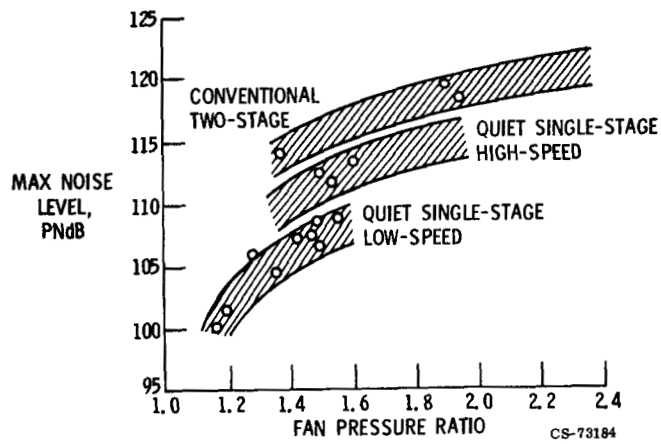
Figure I-8. - Fan noise (90 000-lb takeoff thrust; 1000-ft flyover).
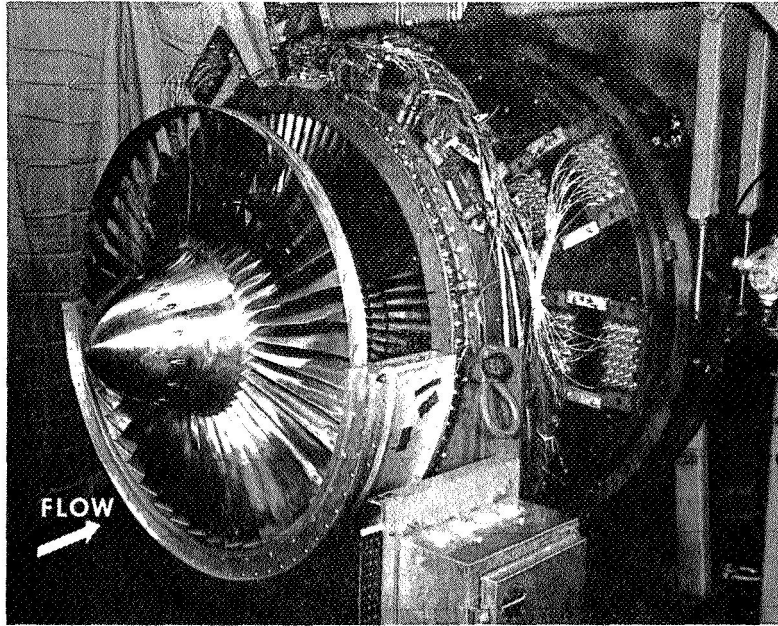
Figure I-9. - Single-stage fan.
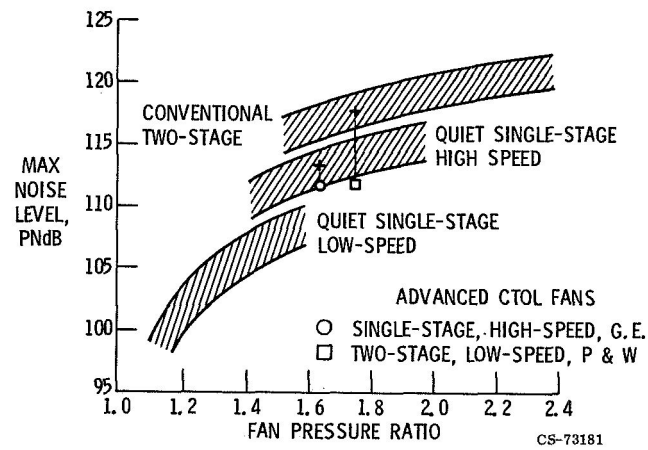
Figure I-10. - Noise of advanced CTOL fans (90 000-lb takeoff thrust; 1000-ft flyover).

SERRATED ROTOR BLADES

LEANED STATOR VANES

LONG CHORD STATOR VANES

ROTOR-STATOR SPACING

CS-73744
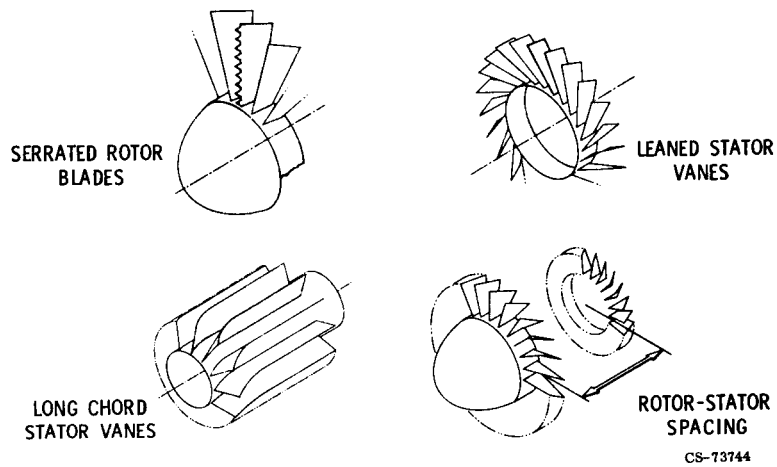
Figure I-11. - Fan noise reduction concepts.

10 dB

BLADE PASSAGE TONE

PROJECTED FROM STATIC DATA

SOUND PRESSURE LEVEL

DC-10 FLIGHT DATA

400   1000   10 000

FREQUENCY, Hz   CS-73182
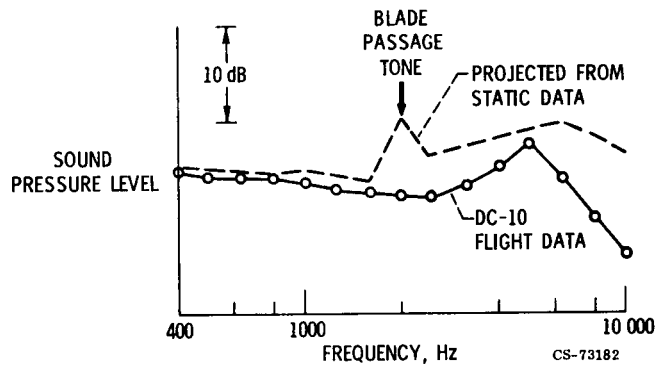
Figure I-12. - Comparison of flight and projected static inlet sound pressure spectra (CF 6-6 engine at approach condition).
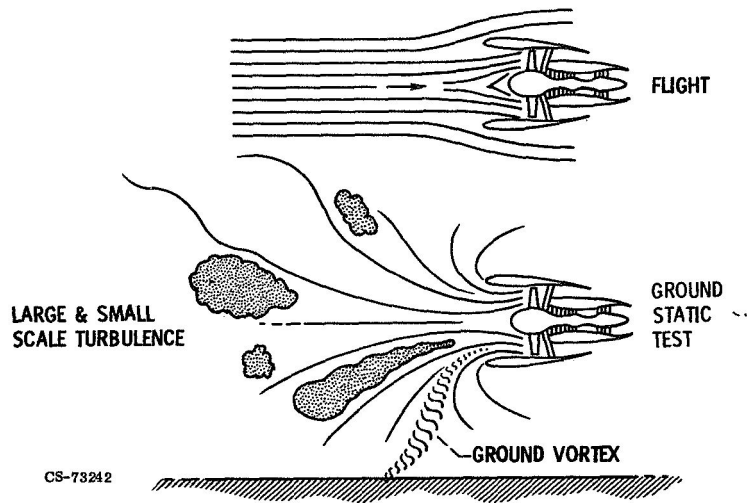
Figure I-13. - Effect of flight on inlet flow.

FLIGHT

LARGE & SMALL
SCALE TURBULENCE

GROUND
STATIC
TEST

GROUND VORTEX

CS-73242
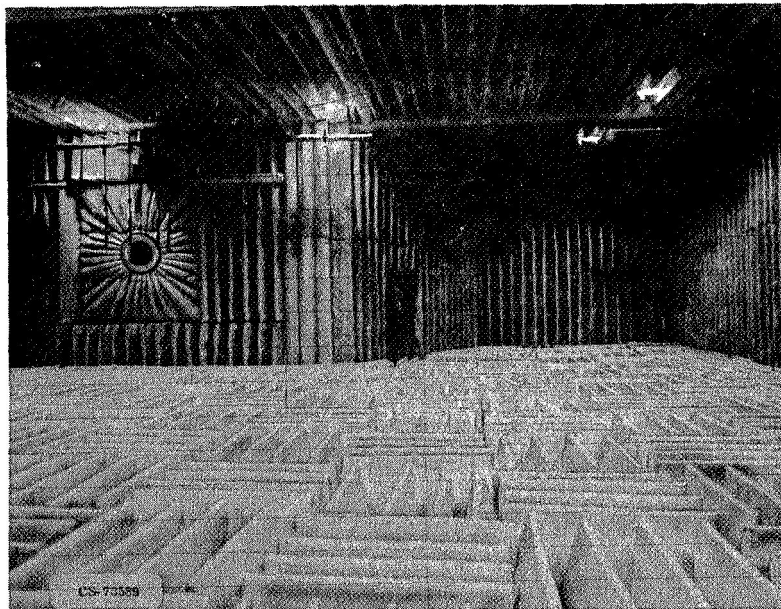
Figure I-14. - Engine fan and jet noise facility.
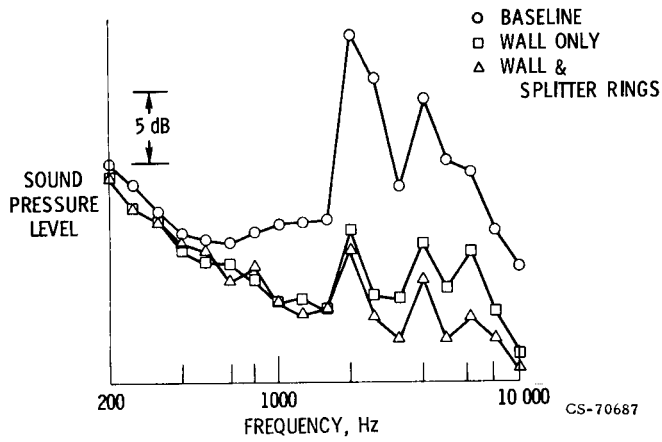
Figure I-15. – Effect of inlet configuration on sound pressure level spectrum (engine A, takeoff power).
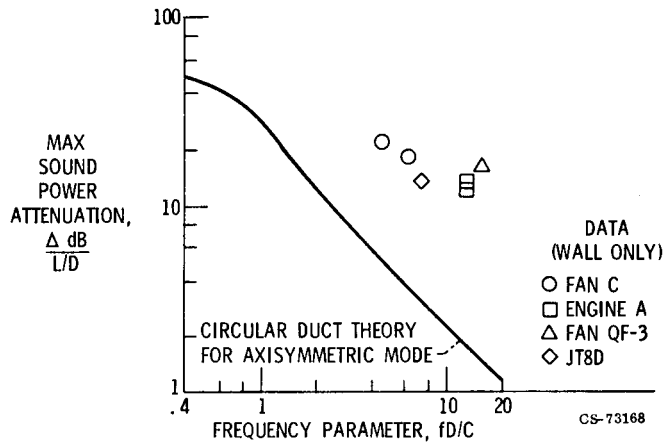
Figure I-16. – Comparison of suppressor theory with data.

36
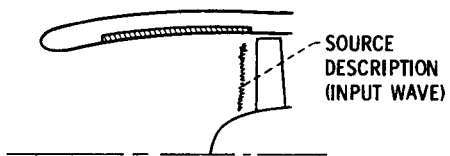
CS-73099

Figure I-17. - Noise source description.

ACOUSTIC PRESSURE

BELOW AMBIENT   ABOVE AMBIENT

ROTATION
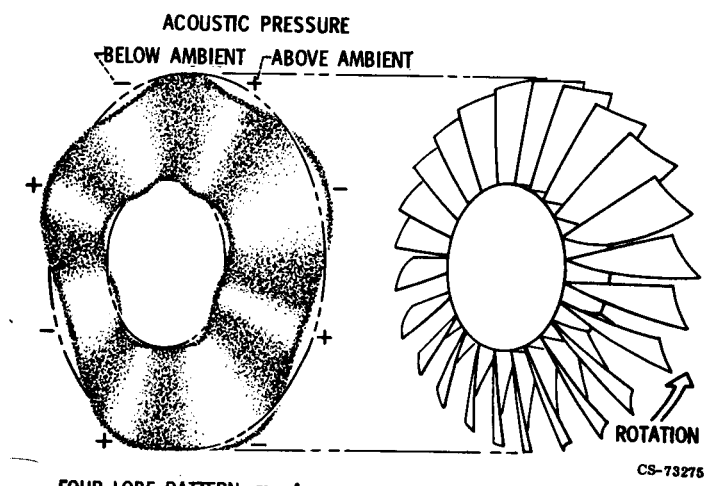
CS-73275

FOUR LOBE PATTERN, m = 4

Figure I-18. - Spinning lobe or mode pattern.
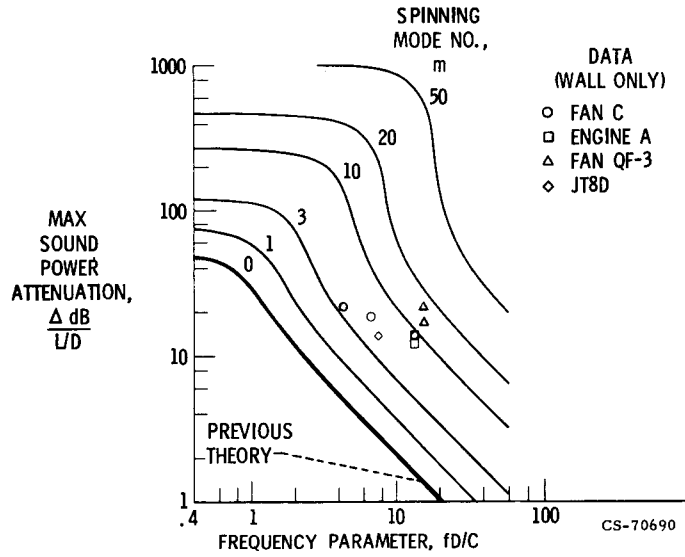
Figure I-19. - Effect of spinning mode number on theoretical maximum sound attenuation.
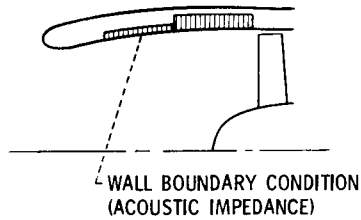
Figure I-20. - Increased attenuation by wall impedance variation.
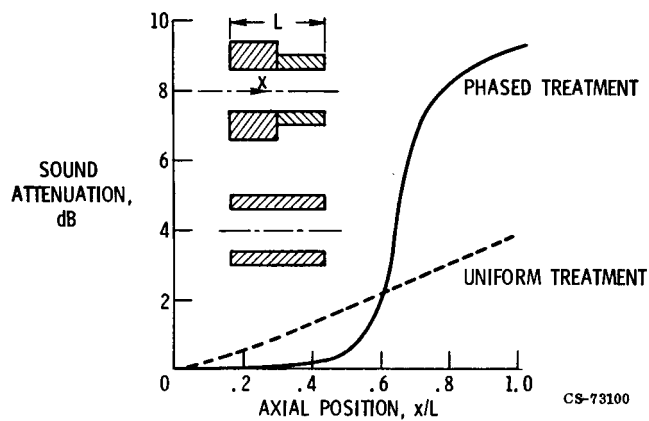
Figure I-21. - Theoretical attenuation for optimized phased and uniform acoustic treatments.
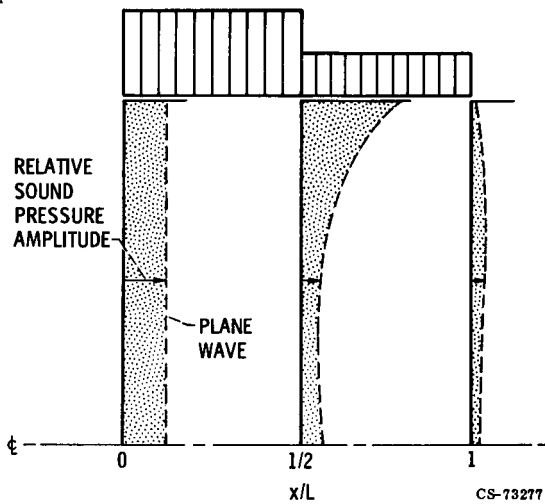
Figure I-22. - Sound pressure profiles in duct with optimum phased treatment.

Figure I-23. - Model fan in Langley anechoic chamber.
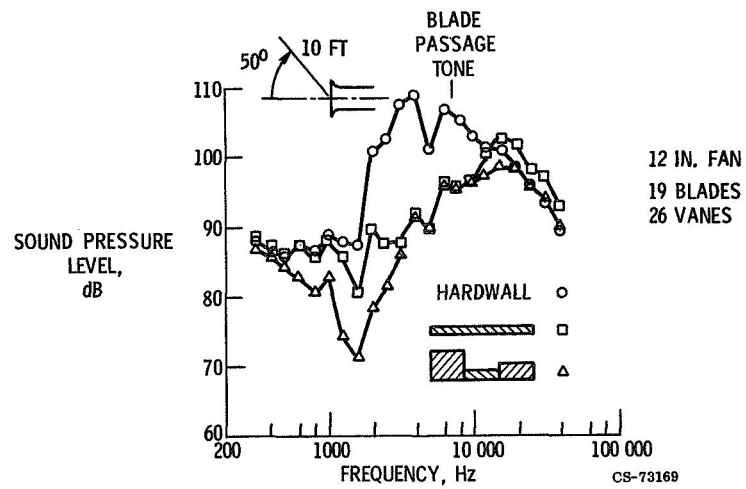
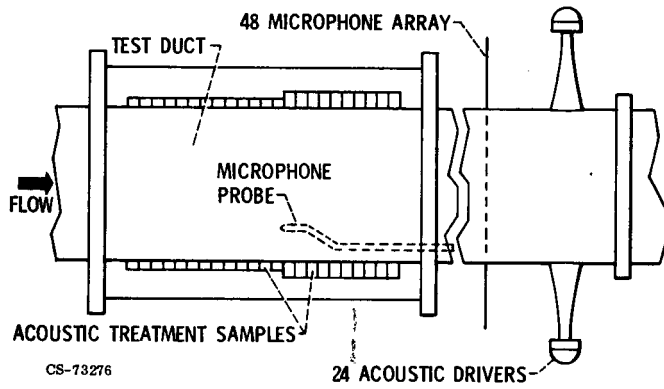Figure I-24. - Comparison of noise spectra for sample uniform and phased treatments.

48 MICROPHONE ARRAY

TEST DUCT

MICROPHONE PROBE

FLOW

ACOUSTIC TREATMENT SAMPLES

CS-73276

24 ACOUSTIC DRIVERS

Figure I-25. - Test and source sections.

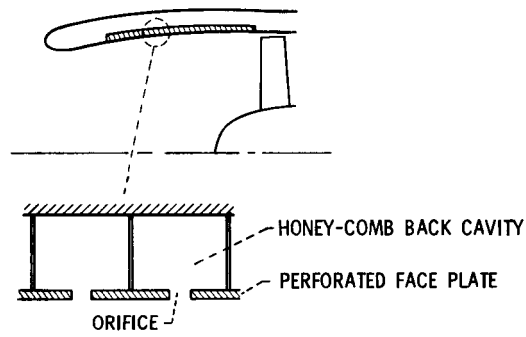HONEY-COMB BACK CAVITY

PERFORATED FACE PLATE

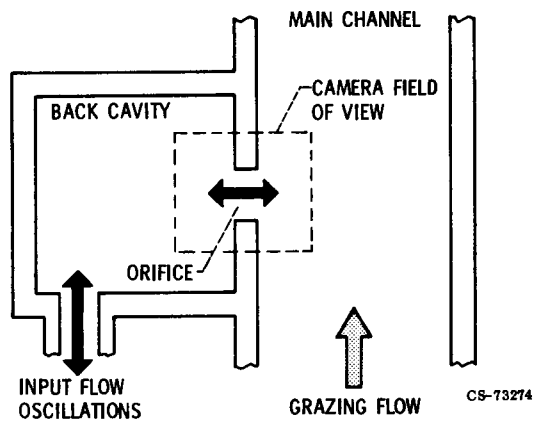ORIFICE

CS-73098

Figure I-26. - Study of acoustic impedance.
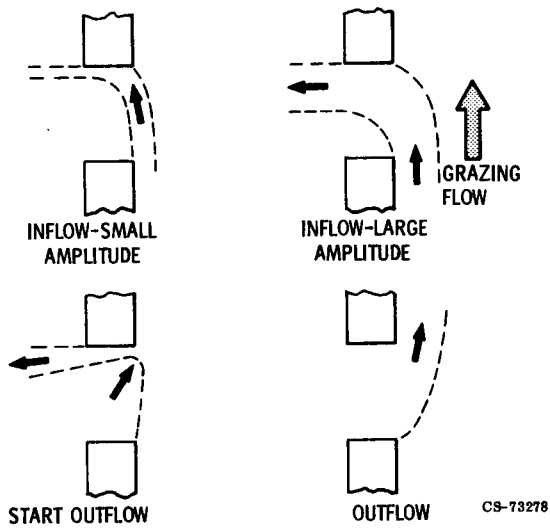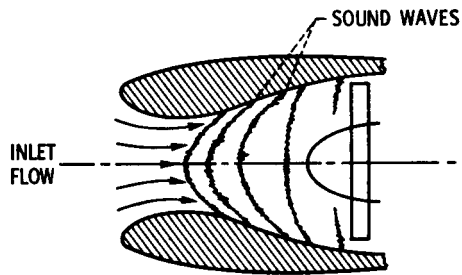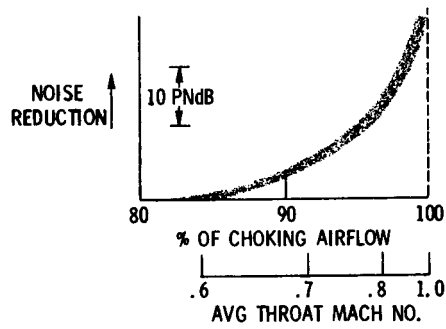
Figure I-27. - Oscillatory flow visualization apparatus.

Figure I-28. - Oscillatory orifice flow with grazing flow.

Figure I-29. - Sonic inlet principle.

Figure I-30. - Sonic inlet noise reduction.

43

FIXED
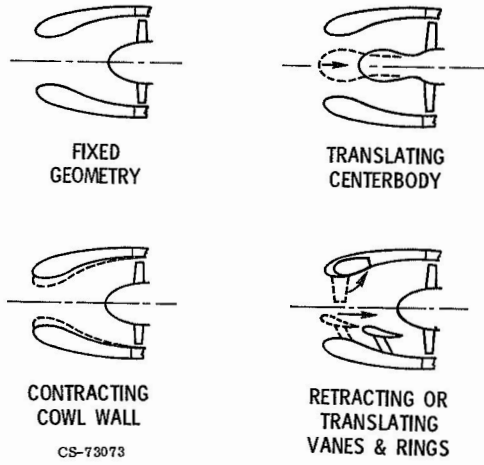GEOMETRY

TRANSLATING
CENTERBODY

CONTRACTING
COWL WALL

CS-73073

RETRACTING OR
TRANSLATING
VANES & RINGS

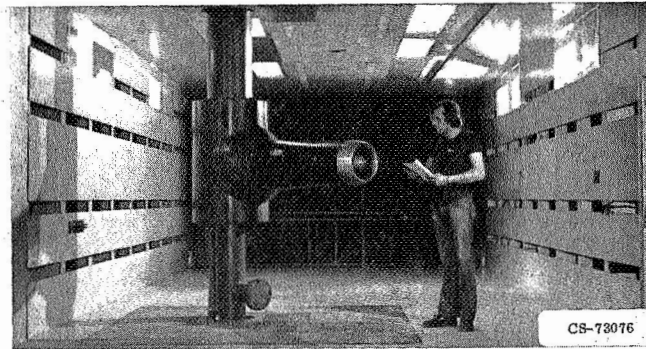Figure I-31. - Sonic inlet configurations tested.

CS-73076

Figure I-32. - Sonic inlet wind tunnel test.
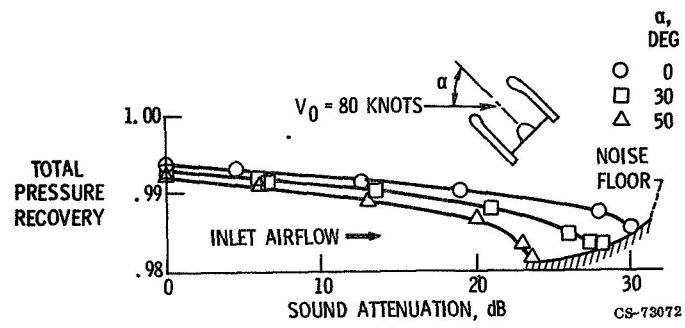
Figure I-33. - Sonic inlet performance (wind tunnel tests).
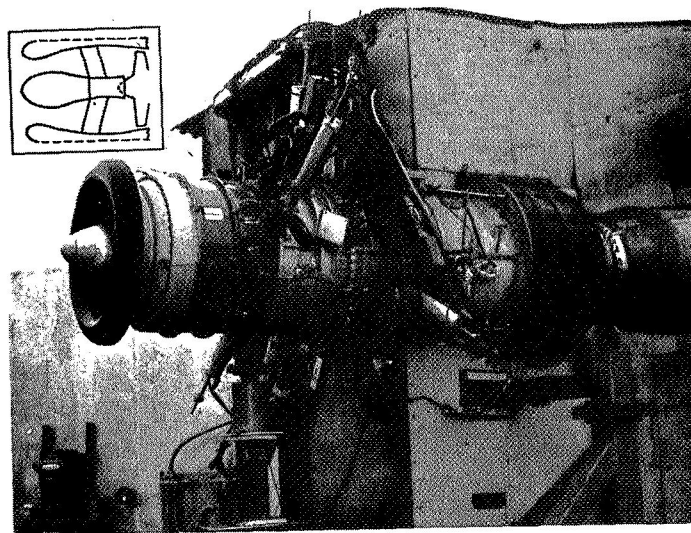
Figure I-34. - Translating centerbody sonic inlet (Pratt & Whitney Aircraft advanced CTOL two-stage fan).
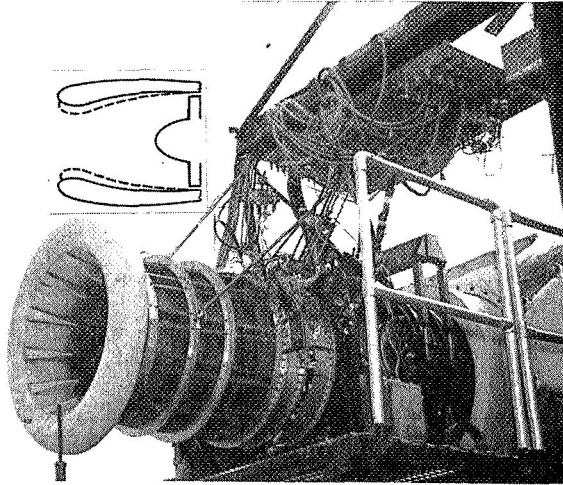
CS-73069

Figure I-35. - Contracting cowl wall sonic inlet (General Electric advanced CTOL single-stage fan).
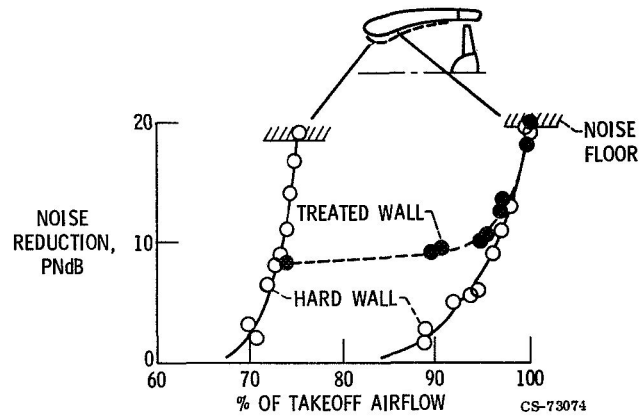
Figure I-36. - Performance of contracting cowl wall inlet.
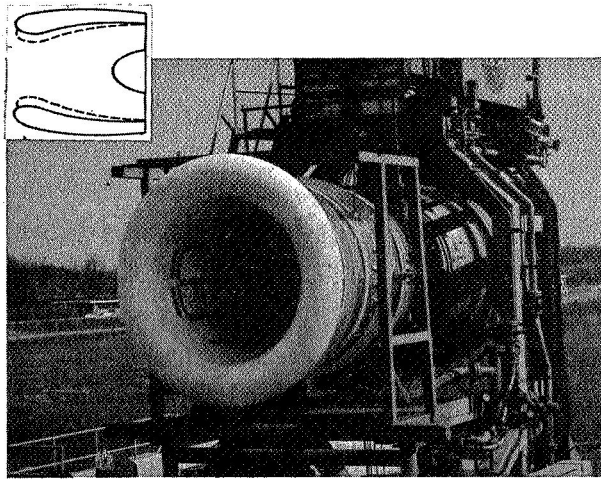
Figure I-37. - Engine C with sonic inlet.
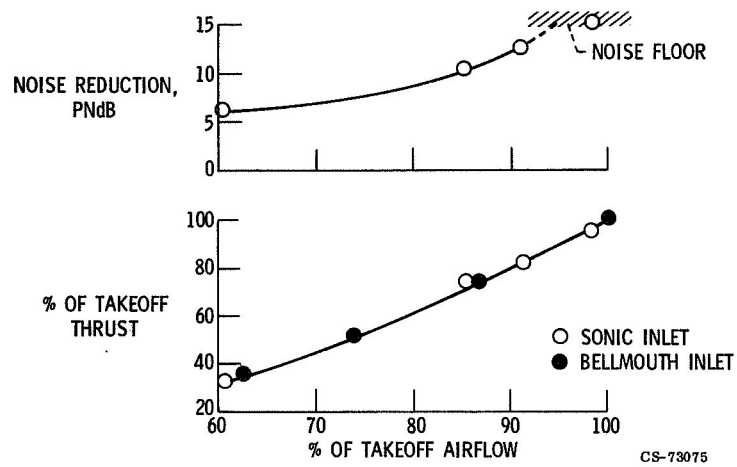
Figure I-38. - Turbofan engine performance (contracting cowl wall inlet).

47
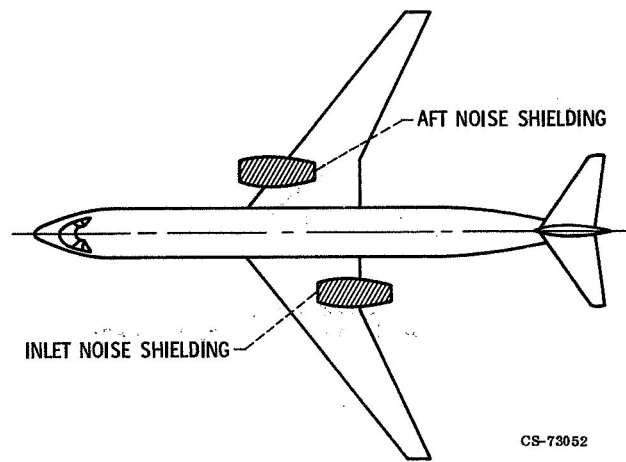
Figure I-39. - Wing shielding concepts.
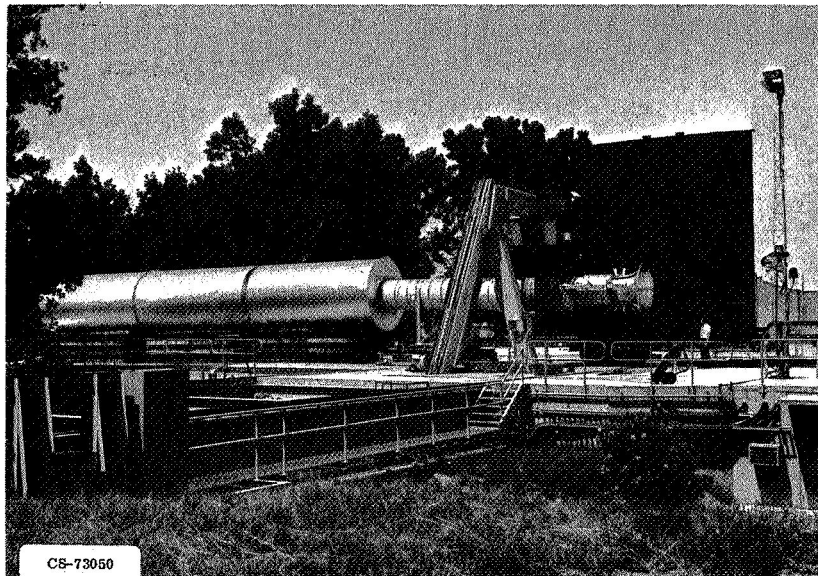
Figure I-40. - Inlet noise shielding tests using TF34 engine and muffler.
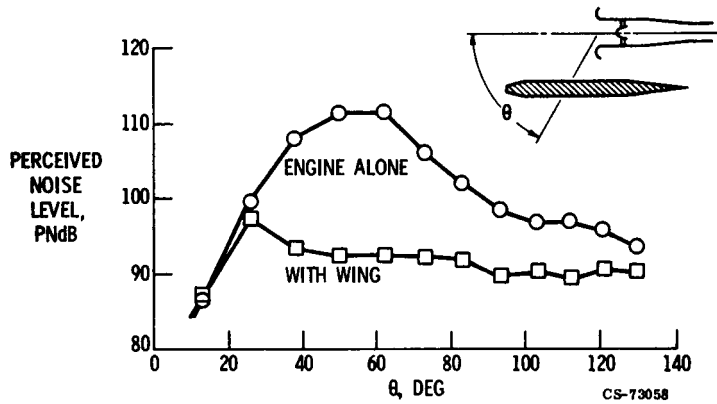
Figure I-41. - Effect of inlet shielding on noise directivity (500-ft flyover).
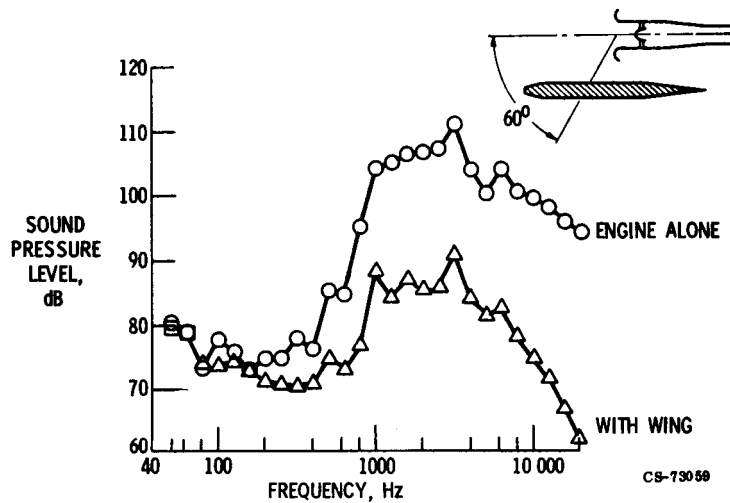
Figure I-42. - Effect of inlet shielding on noise spectra (100-ft radius).

49
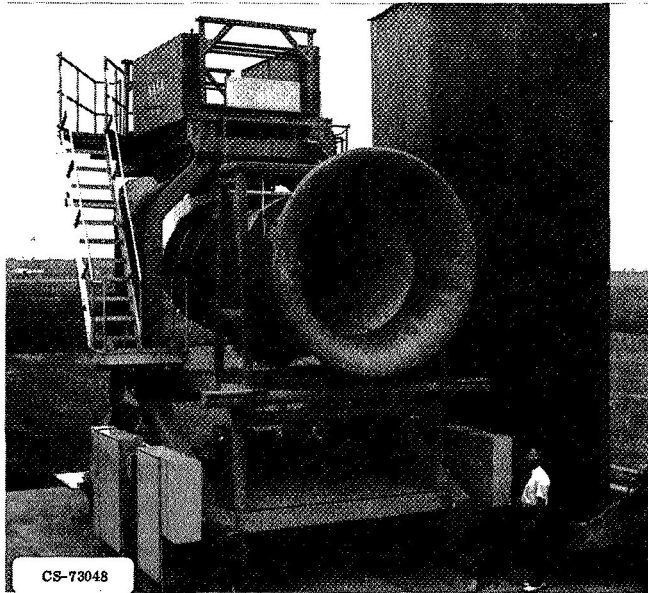
Figure I-43. - Aft noise shielding tests with quiet engine C.
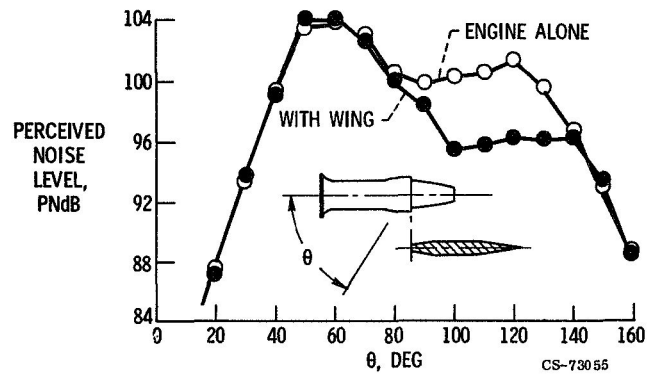
Figure I-44. - Effect of aft shielding on noise directivity (unsuppressed engine, 1000-ft flyover).
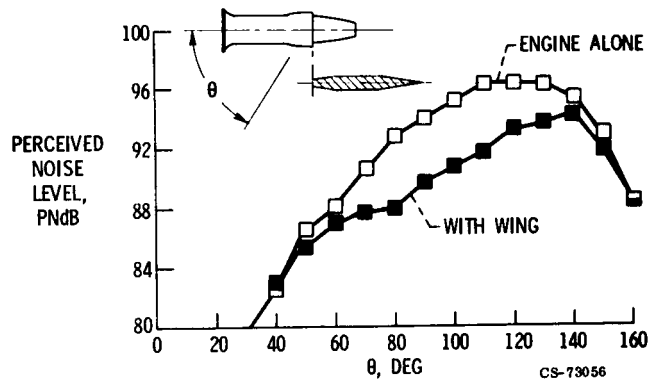
Figure I-45. - Effect of aft shielding on noise directivity (suppressed engine, 1000-ft flyover).
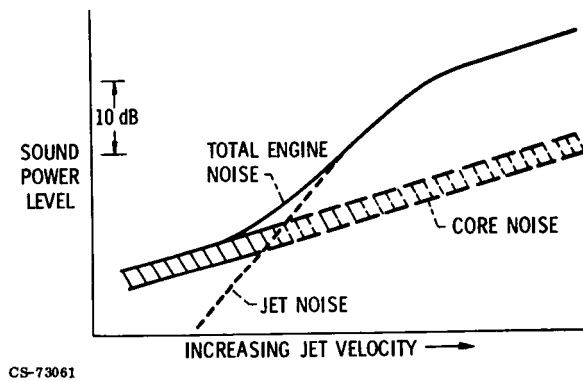
Figure I-46. - Engine noise (fan noise suppressed).
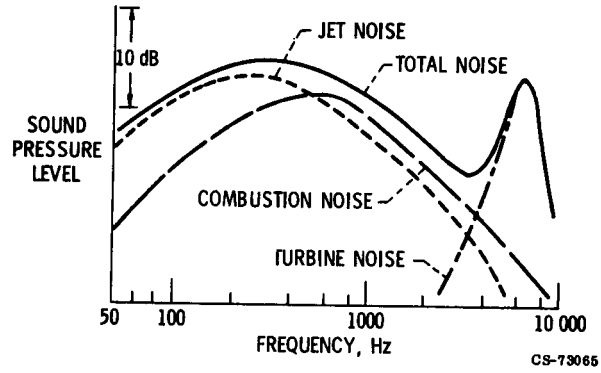
Figure I-47. - Static engine spectrum (approach power).
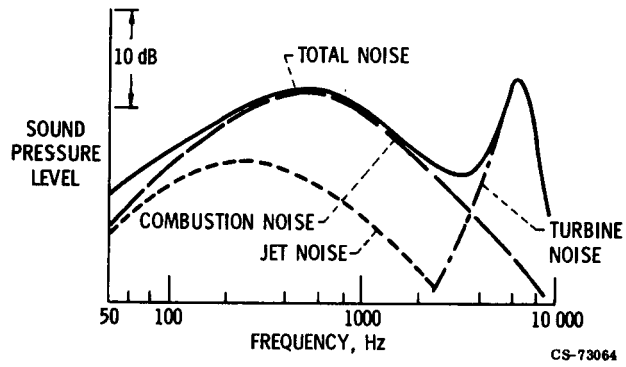
Figure I-48. - "In-flight" engine spectrum (approach conditions).
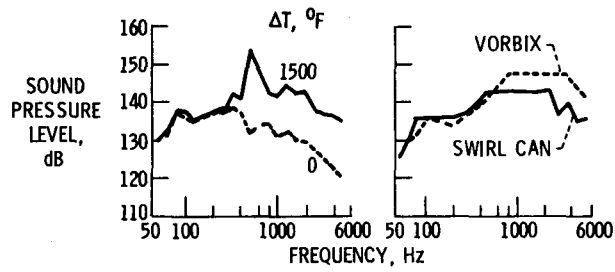
(a) Effect of combustion.   (b) Effect of design
                             ($\Delta T \sim 1200^\circ$ F).

Figure I-49. - In-duct combustor noise data.   CS-73066
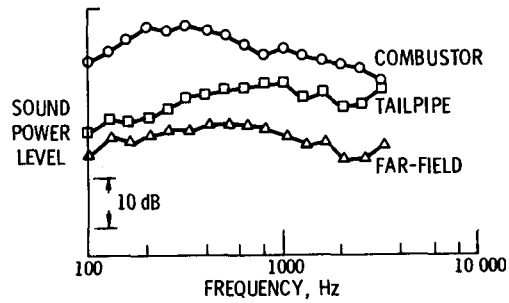
CS-73063

Figure I-50. - Comparison of internal and far-field data
for core noise studies.
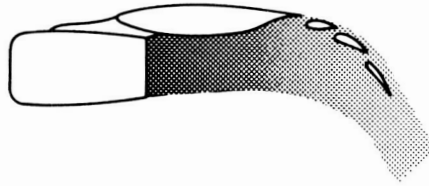
(a) Engine under the wing (UTW).
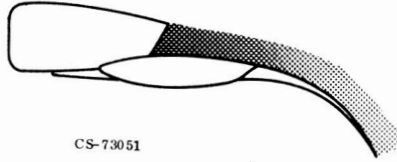
(b) Engine over the wing (OTW).

CS-73051

Figure I-51. - Powered lift concepts.
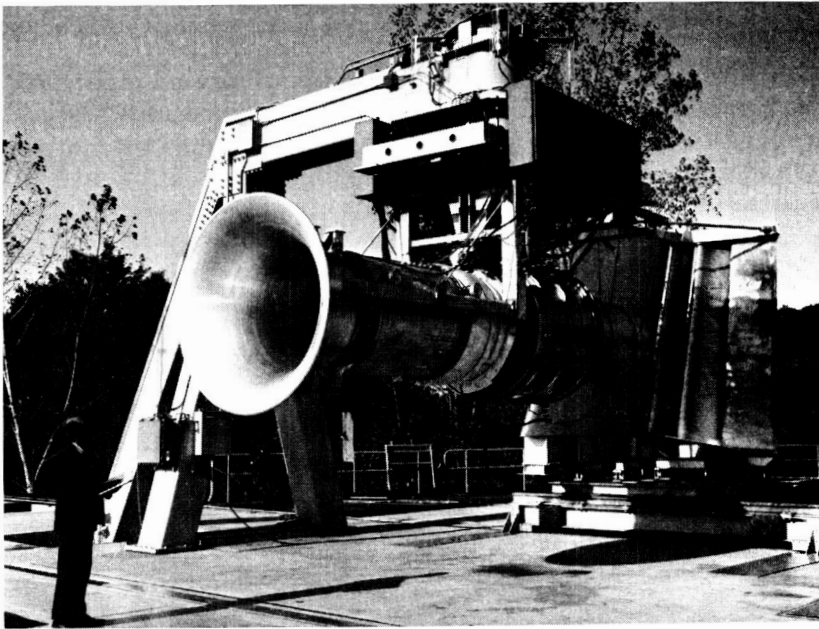
CS-73068

Figure I-52. - Suppressed TF34 in UTW test configuration.
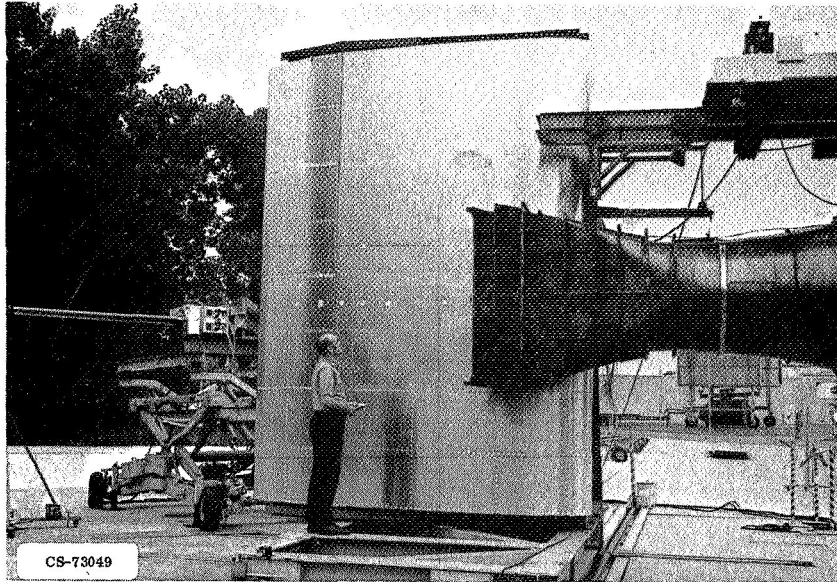
Figure I-53. - OTW test configuration with slot nozzle.
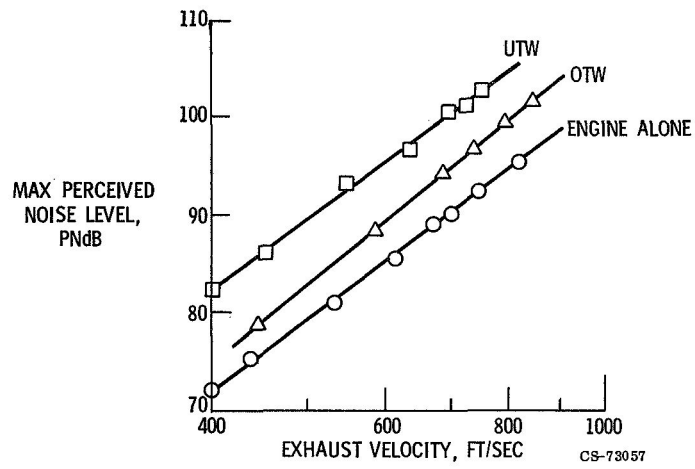
Figure I-54. - Noise comparison of OTW and UTW concepts (500-ft flyover).

55
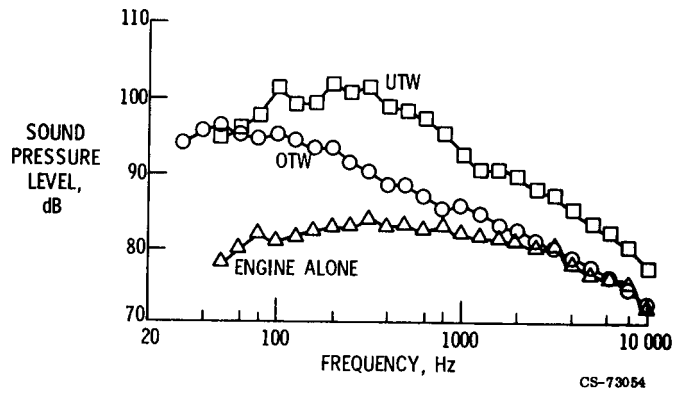
Figure I-55. - Spectral comparison of OTW and UTW noise (90° from inlet; 100-ft radius).
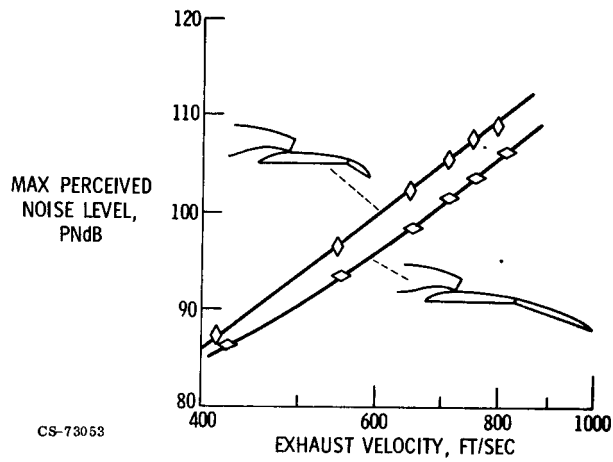
Figure I-56. - Effect of flap length on OTW noise (slot nozzle; 500-ft flyover).
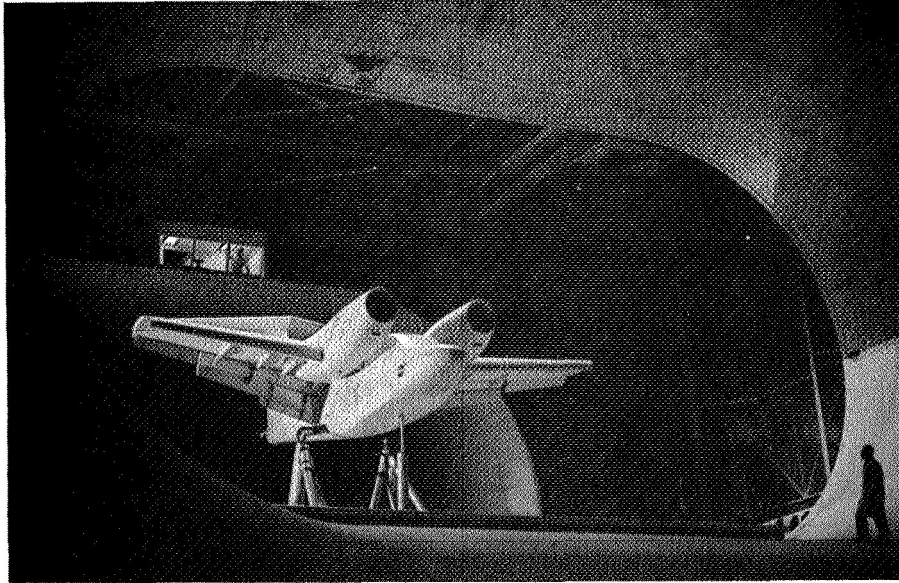
CS-73046

Figure I-57. - Front view of large scale OTW configuration at Langley.
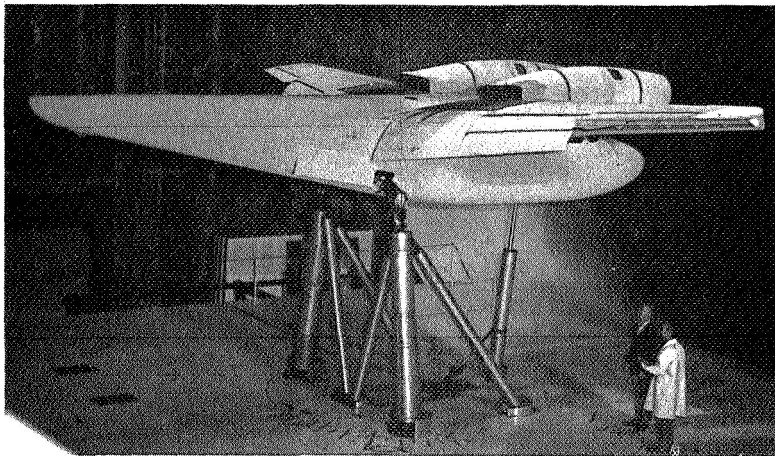
CS-73047

Figure I-58. - Side view of large scale OTW configuration at Langley.
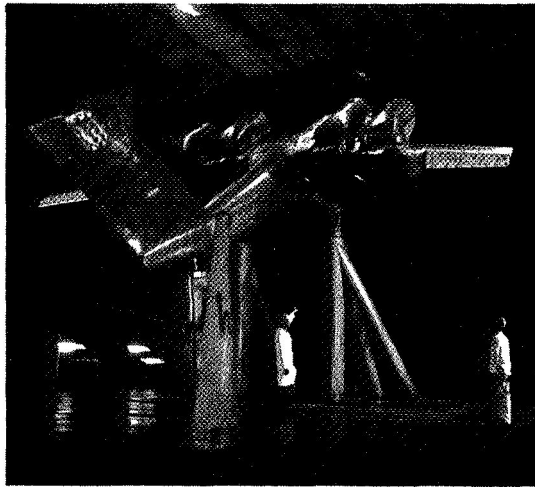
CS-73045

Figure I-59. - Four-engine OTW configuration at Ames.

SECONDARY COMBUSTOR

EJECTOR

PRIMARY COMBUSTOR

CS-73271
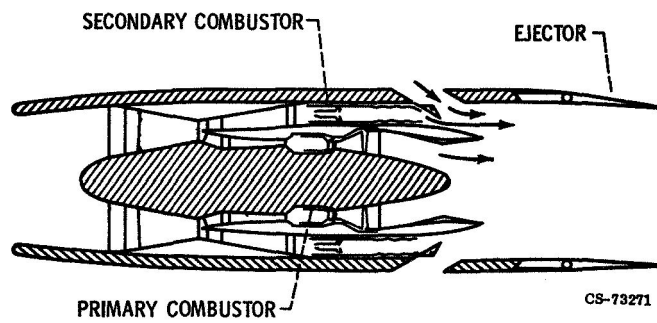
Figure I-60. - Duct-burning turbofan (DBTF) engine for supersonic cruise aircraft.

58
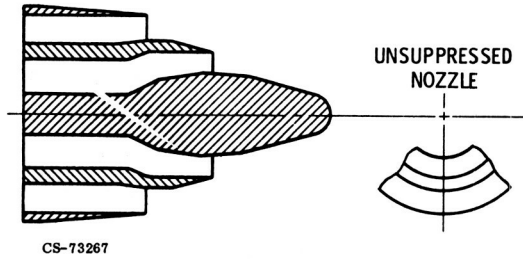
Figure I-61. – General Electric duct-burning turbofan unsuppressed nozzle configuration.
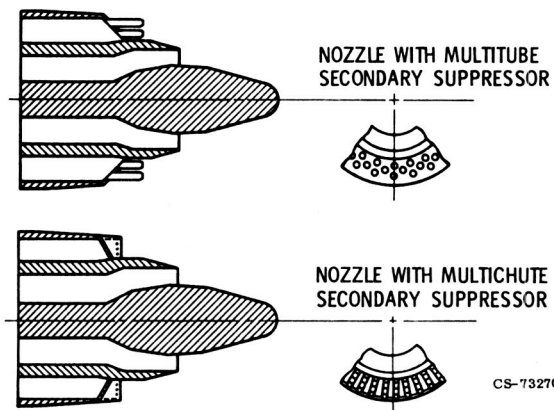
Figure I-62. – General Electric duct-burning turbofan suppressed nozzle configurations.
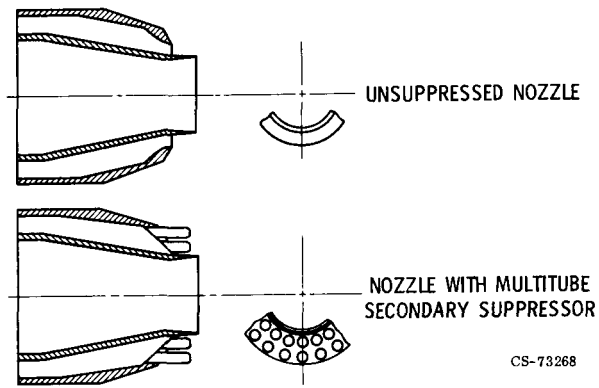
Figure I-63. - Pratt & Whitney duct-burning turbofan nozzle configurations.

UNSUPPRESSED NOZZLE

NOZZLE WITH MULTITUBE SECONDARY SUPPRESSOR

CS-73268
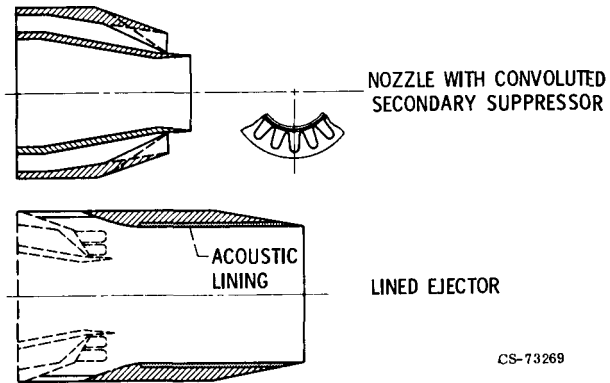
Figure I-64. - Pratt & Whitney duct-burning turbofan nozzle configuration and lined ejector.

NOZZLE WITH CONVOLUTED SECONDARY SUPPRESSOR

ACOUSTIC LINING

LINED EJECTOR

CS-73269

60

REFERENCE: FAN FLOW
THROUGH CONICAL NOZZLE

DBTF NOZZLE

WITH CONVOLUTED
SECONDARY

SOUND
PRESSURE
LEVEL

10 dB

WITH
MULTITUBE
SECONDARY

WITH MULTITUBE
SECONDARY & LINED EJECTOR

40   100   1000   10 000
              FREQUENCY, Hz   CS-73067
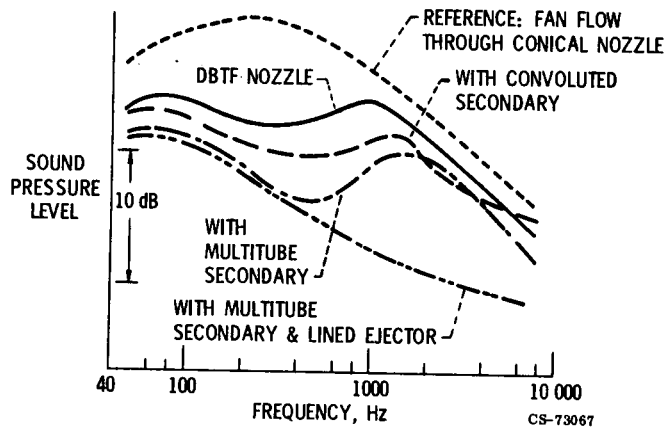
Figure I-65. – Spectra for DBTF configurations (peak sideline noise).

20

+LINED
EJECTOR

15

+LINED
EJECTOR

NOISE REDUCTION,
PNdB

+MULTITUBE

10   +CONVOLUTE

DBTF

5

REFERENCE:
CONICAL NOZZLE

0
-5   0   5   10
        THRUST LOSS, %   CS-73062
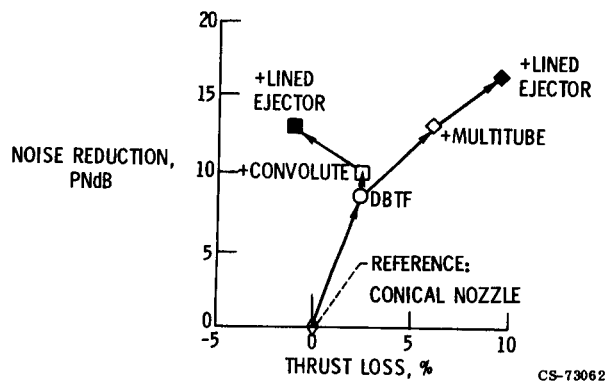
Figure I-66. – Static performance of DBTF nozzles (scaled to
  40 000-lb thrust engine at takeoff).

61

KEY TECHNOLOGY AREAS

SOURCE NOISE
{
TURBOMACHINERY
JET
COMBUSTION
FLAP
DUCT ACOUSTICS
AIRFRAME
SHIELDING/REFLECTION
}

PATH
{
ATMOSPHERIC ATTENUATION
EXTRA GROUND ATTENUATION
}

RECEIVER
{
HUMAN FACTORS
COMMUNITY EXPOSURE
}

CS-73043
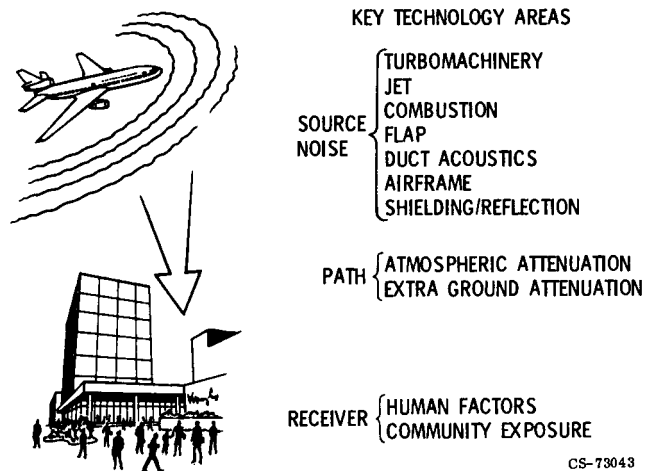
Figure I-67. - Aircraft noise prediction (ANOP).
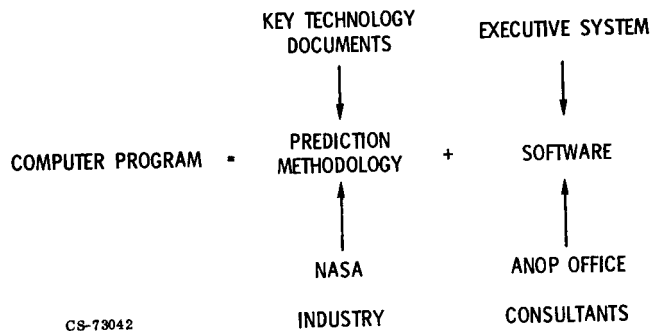
Figure I-68. - ANOP computer program.

INPUT ───▶ EXECUTIVE SYSTEM ───▶ OUTPUT

PREDICTION METHODOLOGY

| EMPIRICAL DATA BASE | ANALYTICAL MODULES |
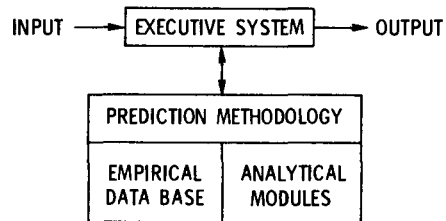
CS–73039

Figure I-69. – ANOP computer program structure.

Page intentionally left blank

II. QCSEE PROGRAM

Carl C. Ciepluch

This paper reviews the objectives, scope, and status of the NASA QCSEE (Quiet, Clean, Short-Haul Experimental Engine) program. This program has been very active for almost a year and a half. During this period, the designs of the two engines in the program have just about been completed, and fabrication of one of the engines has been initiated. The progress reported herein is concerned primarily with the engine design characteristics.

The interest in short-haul aircraft propulsion in this program results from studies which suggest that there is a potential market for this type of aircraft in the 1980's. Short-haul aircraft, in addition to operating out of major airports, will have to operate out of small local airports as well as close-in urban airports. Consequently, operation on short runways is necessary. Such operation suggests using the engines to provide some of the aircraft lift. This propulsion concept where part of the engine thrust is used to help lift the aircraft is usually referred to as powered-lift.

As indicated in paper I, the two currently preferred methods of obtaining powered lift are the under-the-wing (UTW) and the over-the-wing (OTW) concepts. The choice between these two approaches for commercial applications is complicated by the competing requirements of good aircraft economics and design and of low noise. An example of a short-haul aircraft using the UTW concept is shown in figure II-1 with the wing flaps stored in a cruise configuration. This configuration offers the advantage of being a more conventional and simpler engine installation from both mechanical and aerodynamic standpoints. The OTW concept, which is shown conceptually in figure II-2, is an alternate less conventional approach where the engines are cantilevered from the upper wing surface. The advantage to this approach is the shielding of the engine exhaust noise from ground observers provided by the large wing surface. Both acoustic and propulsive performance data are needed for both concepts to provide a firm basis for selecting either concept for future com-

mercial aircraft applications.

The following are some of the characteristics of a conceptual, commercial short-haul aircraft similar to those shown in figures II-1 and II-2:

PASSENGERS	150
AIRCRAFT TAKEOFF WEIGHT, LB	150,000
RANGE, N. MI.	500
FIELD LENGTH, FT	3000
CRUISE MACH NUMBER	0.7

Of most significance are the relatively short range (500 n. mi.), the field length of 3000 feet, and the 0.7 cruise Mach number. The relatively low cruise Mach number is chosen to improve aircraft economy. Because of the short aircraft range, the lower cruise speed has a negligible effect on total trip time.

OVERALL PROGRAM

The first objective of the QCSEE program is to develop short-haul aircraft propulsion technology which is environmentally acceptable and economically feasible (so it is the commercial value) and is also suitable for powered-lift applications. The technology will be developed and demonstrated using full-scale engines. The second objective is to provide the government with data on the environmental acceptability of the concepts investigated which could then serve as the basis for future government rule making. The final objective is to provide industry with data so that the new technology can be incorporated into future engine development programs with a reduced amount of risk.

The primary technical requirements established for the QCSEE engines are given in table II-1. The noise requirement for the engines is quite low. An aircraft noise limit of 95 EPNdB at a 500-foot sideline distance was set for both takeoff and approach conditions. The reverse thrust noise was limited to 100 PNdB. In terms of footprint area, a 0.5-square-mile limit was

66

set for the 95 EPNdB noise contour. From a pollution standpoint, the requirement is to meet the EPA 1979 emission levels. Because of the large effort in combustor emissions reduction technology in other programs, the QCSEE program, for the most part, is relying on these other programs to provide the technology needed to meet the required emission levels. The installed thrust requirements of the UTW and OTW engines are 17 400 and 20 300 pounds, respectively. For short-haul aircraft, a 35 percent reverse thrust capability appears adequate, and this level was established as the QCSEE requirement.

A challenging requirement of the QCSEE engines is the relatively high installed thrust to weight ratios. The installed thrust to weight ratio is used here because this parameter not only includes engine performance but it recognizes the installation effects on thrust and weight. It is intended to improve these installation factors in the QCSEE program. For the UTW and OTW propulsion systems the thrust to weight ratio requirements are 4.3 and 4.7, respectively. For comparison, the installed thrust to weight ratio of a modern engine such as the CF-6 used in the DC-10 aircraft is about 3.5. Finally, short-haul, powered-lift aircraft will require improved engine dynamic response because of operating from short runways and using engines for providing lift. Accordingly, an approach to takeoff thrust transient capability of 1.0 second and a reverse thrust capability of 1.5 seconds were established as requirements.

The QCSEE engines contain a wide range of advanced technologies:
High bypass ratios engines
Variable pitch fan
Variable area fan nozzle
Advanced acoustic suppression
    High Mach inlet
    Acoustic linings
Digital electronic controls
Reduction gearing
Composite components
    Fan blades
    Fan frame
    Nacelle
These new technologies contribute to either reduced engine noise or im-

proved performance, and in some cases they help in both areas. Although the QCSEE program is directed toward short-haul, powered-lift aircraft, most of the new technology items shown here would also be beneficial if applied to more conventional aircraft. Furthermore, studies of advanced engine concepts for reducing energy consumption suggest the possible use of engines with very high bypass ratios similar to those in the QCSEE engines (see paper VI). It is believed that the technology being developed in the QCSEE program has the potential for benefiting a wide range of future aircraft developments. These new technology items are discussed in some depth in a later section of this paper.

An overall QCSEE program schedule is shown in figure II-3. The major part of the program is being done under contract. A contract was awarded to the General Electric Company on January 1, 1974, to design, fabricate, and test two QCSEE engines. At this time, General Electric has completed the UTW engine design and the OTW engine design is nearly complete. Fabricating the UTW and OTW engines and the boiler plate and composite nacelles will be completed in 1976. Following the engine and nacelle tests at General Electric, both propulsion systems will be delivered to NASA late in 1977. NASA tests will include acoustic evaluation of the engines with wing and flap sections installed to simulate the powered-lift condition. This testing will be followed by altitude performance tests in one of the altitude test chambers at the Lewis Research Center.

UTW PROPULSION SYSTEM DESIGN

As indicated previously, the design phase of the program is nearly completed. Some of the significant design details of the UTW propulsion system are now presented. Figure II-4 shows a cross section of the UTW engine and nacelle with the advanced technology components identified. The UTW engine employs the F101 engine core. The F101 engine is being developed by the General Electric Company for use in the Air Force B-1 bomber. It is an advanced technology core which fits into the QCSEE engine designs. One of the major technical advances in the UTW engine is the composite nacelle. It consists of the inlet duct, the fan duct outer wall, the acoustic splitter, and the core cowl. The acoustic treatment in the nacelle is built-

in or integral with the structure, and it therefore serves the dual functions of acoustic suppression and structural load-carrying. This construction contributes to the lightweight and low-cost characteristics of the design. The digital control system is located along with the accessories at the top of the engine. This location makes the engine accessories connections to the aircraft more convenient.

The composite fan frame is the primary structural element in the engine. It supports the fan, the nacelle components, and the front portion of the core. Also, the engine thrust loads are carried through it to the aircraft. The frame is made of graphite fibers and an epoxy resin system. This type of construction is expected to save considerable frame weight and reduce fabrication costs. Composite materials are also used in the fan blades for the same reasons. The engine has a variable area fan nozzle, which consists of four hinged flaps which are moved by hydraulic actuators.

The reduction gears and fan variable-pitch mechanism are located inside the fan spinner. Another of the major new technologies being investigated in the engine is the ability to reverse fan blade pitch to obtain reverse thrust. This is accomplished much like it has been done with reverse-pitch propellers. However, this principle is quite new to turbofan engines. This reverse thrust concept results in a significant weight advantage over conventional thrust reversers, particularly if the design pressure ratio of the fan is below about 1.35. Another advantage of the fan variable-pitch feature is the improved engine thrust response. In a variable-pitch fan engine, thrust can be controlled by changing the fan pitch instead of the engine rotational speed as is usually done. The improved thrust response results from the greater rate at which blade pitch can be changed compared to engine rotational speed.

For low pressure ratio fans which require lower rotational speeds, the use of reduction gears can significantly reduce the number of turbine stages required to drive the fan. Thus, for low pressure ratio fans, reduction gears offer the advantage of lower overall engine weight.

In view of the research findings that high-Mach-number inlets can effectively reduce the propagation of fan inlet noise, this principle was adopted in the QCSEE inlet in order to avoid the use of splitter rings or excessively long acoustically treated inlets. Both of these approaches add to the weight and performance losses of the propulsion system and are, therefore, less

desirable. The inlet is a fixed area inlet which was designed for a 0.79 throat Mach number at the takeoff condition. For the approach thrust condition the inlet Mach number is lower, and for the reverse thrust case the flow is in the opposite direction; as a result, acoustic suppression is obtained by the use of acoustic treatment in the inlet walls. This combined suppression approach is often referred to as a hybrid inlet.

The major acoustic considerations in the UTW propulsion system design are given in table II-2. Since the most difficult acoustic requirement is for the takeoff noise condition, this becomes the design point. The two major noise sources for the takeoff condition are jet/flap interaction noise and fan noise. However, core noise becomes a noise source to control when the two primary noise sources are reduced. Jet/flap interaction noise is caused by the engine exhaust impinging on the wing flaps. At this time, the only known method of its control is to reduce the velocity at which the exhaust impinges on the wing flaps, or in effect, to reduce the fan pressure ratio. Accordingly, the UTW fan pressure ratio is limited to 1.27 at takeoff. Thus, the reduction of jet/flap interaction noise has a major affect on the overall engine cycle, requiring a low fan pressure ratio and a corresponding high engine bypass ratio.

Unlike jet/flap interaction noise, there are several techniques available for reducing fan noise. The techniques incorporated into the UTW design include low fan tip speed, large spacing between rotor and stator, optimum blade/vane ratio, and, finally, the addition of acoustic suppression or linings. The high-Mach-number inlet and wall acoustic treatment are used to suppress fan inlet noise. Acoustic treatment on the fan exhaust duct walls and a splitter ring are used to suppress fan aft noise. Wall acoustic treatment is contained in the core nozzle for core noise suppression.

Projections of aircraft noise levels using the UTW propulsion system characteristics indicate that all the noise requirements described earlier can be met. Estimates of aircraft footprint area for 95 EPNdB noise contours show that footprint area will approach one-quarter square mile, which is well within the one-half square mile requirement. This footprint area is significantly lower than that of the quietest commercial aircraft in service today - by about a factor of ten - and, therefore, represents a significant noise improvement.

The major engine characteristics that were found necessary to meet the

acoustic and performance requirements of the engine are presented in table II-3. At takeoff, the engine has a relatively high bypass ratio of around 1½. This is due to the relatively low (1.27) fan pressure ratio, which as previously indicated, is a result of acoustic considerations. Because of the low fan pressure ratio, the fan tip speed is reduced in order to reduce fan source noise. At takeoff, the fan tip speed in 950 feet per second. The engine overall pressure ratio is 14.3. Commercial engines usually employ higher overall cycle pressure ratios to improve propulsive performance. This could be accomplished in the UTW engine as well as in the OTW engine by adding booster stages. However, this was not done because it would not contribute significantly to the technology being developed and it can be expensive. The thrust capability of the engine is 17 400 pounds.

In order to achieve maximum cruise thrust with the engine with airflow limited by the near-sonic inlet, the fan pressure ratio can be raised to greater than 1.35 for the cruise condition. This is done by reducing the fan nozzle area in conjunction with a 3° opening of the fan blade pitch.

OTW PROPULSION SYSTEM DESIGN

Having reviewed the design of the UTW propulsion system, the next subject is a similar look at the OTW propulsion system. A cutaway view of the OTW engine and nacelle is shown in figure II-5. Again an F101 engine core is being used. Because of the noise shielding benefits of the OTW type of installation, particularly in regard to jet/flap interaction noise, the design fan pressure ratio can be raised and the noise goal can still be met. The higher fan pressure ratio is advantageous because it results in better engine propulsive performance and consequently improves aircraft operating economy. Although the fan rotor was aerodynamically designed to accept composite blades, metal ones are being used to reduce program costs. The design of the composite frame is similar to that used in the UTW engine. The OTW engine is a mixed core and fan flow type of design. This is the preferred arrangement for OTW type installations because a single exhaust nozzle produces better powered-lift aerodynamics. The unique variable area nozzle has the dual function of improving powered-lift and propulsive performance.

A target-type thrust reverser is employed in the OTW design, and the fan does not have variable pitch capability. For the OTW type of installation, the combination of higher fan pressure ratio, the mixed core and fan flows, and the OTW reverse flow discharge capability make the target-type thrust reverser more attractive. The OTW propulsion system also employs reduction gears, a digital control system, and the high-Mach- number inlet, much the same as the UTW propulsion system. It is interesting to note that the type of installation has a major effect on the engine fan design. The UTW installation results in a variable pitch, lower pressure ratio fan, whereas the OTW installation results in a fixed pitch, higher pressure ratio fan.

The characteristics for the OTW propulsion system are presented in table II-4. For comparison, those of the UTW propulsion system are also included. The OTW propulsion system has a lower bypass ratio, which is near 10. This is a result of the higher pressure ratio (1.34) selected for the engine. The higher fan pressure ratio requires a higher fan tip speed. At takeoff the fan tip speed is 1162 feet per second. The overall pressure ratio of the engine is about 17. Finally, the engine thrust capability is 20 300 pounds. The relatively higher thrust of the OTW engine is not significant but is simply a result of the higher fan pressure ratio and the desire to have similar airflow capability for both engines. A common engine airflow was desired to permit using nearly identical fan frames and engine inlets and thereby to reduce program costs. During operation at cruise conditions, the fan pressure ratio can be raised to about 1.4 to increase the cruise thrust of this engine. The variable fan nozzle area capability is used to produce the increase in fan pressure ratio. Projections of the acoustic and aerodynamic performance of the OTW engine indicate that it will also meet all the requirements established for it.

QCSEE SUPPORTING TECHNOLOGY

In the previous discussion, the design status of the two QCSEE propulsion systems was presented. Now a review of some of the QCSEE supporting technology programs is presented. The discussion will be limited to the nacelle aerodynamics area.

The forward and reverse thrust flow paths are illustrated for the UTW

engine in figure II-6. In the forward thrust condition, the important consideration is providing acceptable inlet airflow profiles during the high inlet upwash angles encountered by powered-lift aircraft. A second consideration is providing acceptable airflow to the fan during reverse thrust operation. Here the variable area fan nozzle can be opened to assist in obtaining acceptable airflow which must now flow in the opposite direction.

In order to arrive at a nacelle inlet design that could provide the desired good inlet flow characteristics, aerodynamic tests of model inlets were run. The results of these tests, which were conducted in the Lewis 9 by 15 foot wind tunnel are shown in figure II-7. Here the maximum inlet airflow angle for nonseparated flow is plotted against the percent of maximum inlet airflow. Data are presented for range of contraction ratios from 1.37 to 1.56. Contraction ratio is defined as the ratio of the highlite to throat areas. The highlite and throat diameters (D_{HL} and D_T) are identified in the figure. As shown in the figure, a contraction ratio of 1.46 will successfully meet the 50° inlet airflow angle requirement. As a result of these tests, the QCSEE inlet was designed with a 1.46 contraction ratio.

Aerodynamic tests of QCSEE model reverse-thrust inlet configurations were also run to help design this part of the nacelle, which is called an "exlet". (An exlet is a combination of exit and inlet to indicate the required dual function.) In order to obtain high pressure recovery and low airflow distortion, the most important parameter was found to be the exlet flare angle. The results of model exlet aerodynamic tests are shown in figure II-8. As can be seen, the QCSEE goal of 0.97 pressure recovery can be attained at both 0 and 80 knots forward speed with a 30° flare angle. The 80-knot condition is a typical takeoff and landing speed for powered-lift aircraft and is, therefore, the maximum forward speed at which reverse thrust will be required. This 30° flare angle capability was designed into the QCSEE fan exhaust nozzle.

CONCLUDING REMARKS

The QCSEE program has progressed to the point where the engine design phase effort is nearly completed. In about a year the fabrication phase is scheduled for completion on the first engine, which is the UTW engine.

First engine tests will be initiated shortly thereafter. The wide range of advanced technologies being incorporated into the QCSEE propulsion systems offer the potential for significant advancement in the acoustic and propulsive performance of future, short-range, powered-lift types of aircraft. In addition, many of the individual QCSEE technology elements have the potential for being beneficial to a much broader spectrum of future aircraft developments.

TABLE II-1. - QCSEE TECHNICAL REQUIREMENTS

NOISE, 500 FT SIDELINE:	
TAKEOFF & APPROACH, EPNdB	95
REVERSE, PNdB	100
FOOTPRINT, 95 EPNdB CONTOUR, SQ MI	<0.5
POLLUTION	EPA 1979 EMISSION LEVELS
INSTALLED THRUST:	
FORWARD {UTW, LB	17 400
{OTW, LB	20 300
REVERSE	35% OF FORWARD THRUST
INSTALLED THRUST/WEIGHT:	
UTW	4.3
OTW	4.7
DYNAMIC RESPONSE:	
APPROACH TO TAKEOFF THRUST, SEC	1.0
REVERSE THRUST, SEC	1.5

CS-73086

TABLE II-2. - UTW PROPULSION SYSTEM ACOUSTIC DESIGN

[DESIGN POINT, TAKEOFF.]

NOISE SOURCES	METHOD OF REDUCTION
JET/FLAP INTERACTION	REDUCED FAN PRESSURE RATIO, 1.27
FAN NOISE	LOW FAN TIP SPEED LARGE ROTOR/STATOR SPACING BLADE/VANE RATIO ACOUSTIC SUPPRESSION
CORE NOISE	ACOUSTIC SUPPRESSION

CS-73079

TABLE II-3. - UTW ENGINE CHARACTERISTICS AT TAKEOFF

BYPASS RATIO	12.1
FAN PRESSURE RATIO	1.27
FAN TIP SPEED, FT/SEC	950
OVERALL PRESSURE RATIO	14.3
THRUST, LB	17 400

CS-73080

75

TABLE II-4. - ENGINE CHARACTERISTICS
AT TAKEOFF

	UTW	OTW
BYPASS RATIO	12.1	10.1
FAN PRESSURE RATIO	1.27	1.34
FAN TIP SPEED, FT/SEC	950	1162
OVERALL PRESSURE RATIO	14.3	17.3
THRUST, LB	17 400	20 300

CS-73078

CS-73093
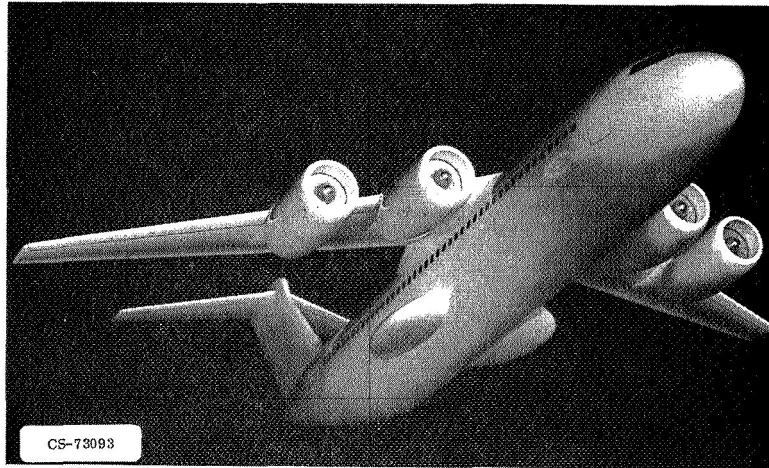
Figure II-1. - UTW short-haul aircraft.
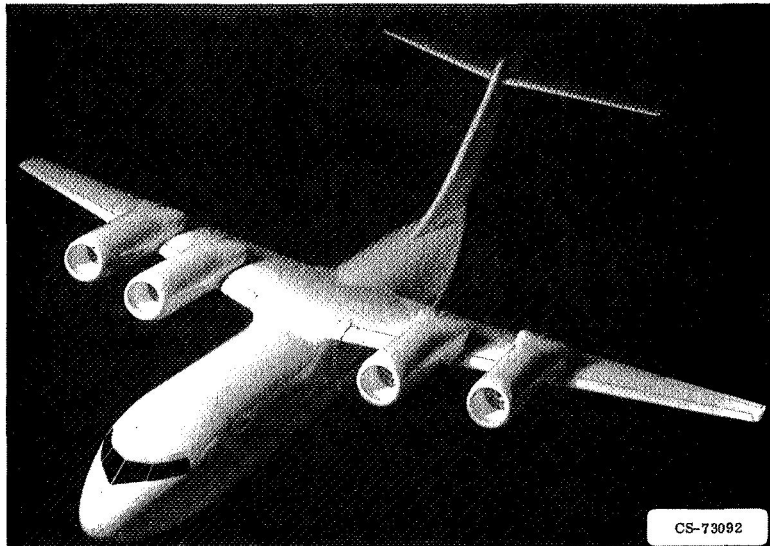
Figure II-2. - OTW short-haul aircraft.

MILESTONES	CY 74	CY 75	CY 76	CY 77	CY 78
GENERAL ELECTRIC CO.					
DESIGN UTW/OTW					
COMPONENT TECHNOLOGY					
FABRICATION					
UTW BOILERPLATE					
OTW BOILERPLATE					
UTW COMPOSITE					
TEST					
UTW BOILERPLATE					
UTW COMPOSITE					
OTW BOILERPLATE					
DELIVER UTW/OTW					
NASA LEWIS TEST					
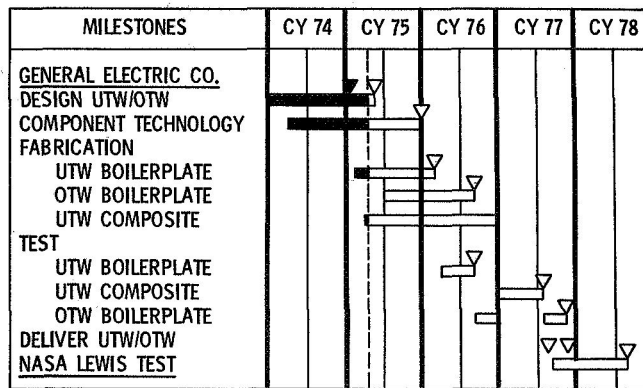
CS-73087

Figure II-3. - QCSEE project schedule.

COMPOSITE FRAME

DIGITAL CONTROL

VARIABLE FLARE
NOZZLE

COMPOSITE
NACELLE

VARIABLE
PITCH FAN

HIGH MACH INLET

REDUCTION GEARS

COMPOSITE FAN BLADES

CS-73091
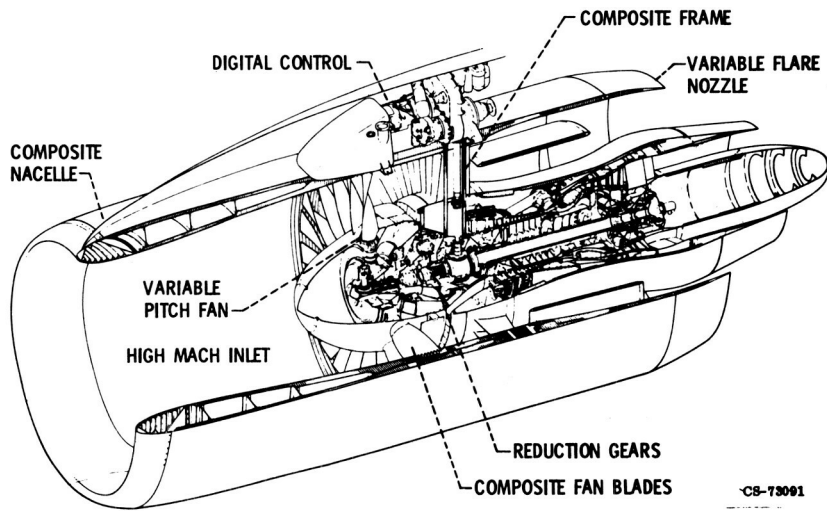
Figure II-4. - QCSEE UTW engine.

TARGET-TYPE
THRUST REVERSER

COMPOSITE FRAME

FIXED-PITCH
TITANIUM BLADES

VARIABLE-
AREA "D"
NOZZLE

REDUCTION GEARS

HIGH MACH INLET

DIGITAL CONTROL

CS-73090
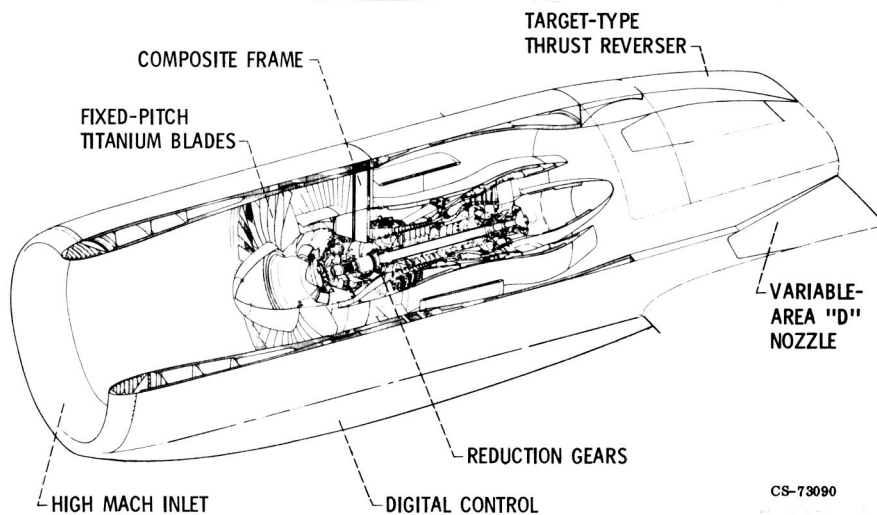
Figure II-5. - QCSEE OTW engine.

FORWARD THRUST

UPWASH
AIRFLOW

REVERSE THRUST

AIRFLOW

CS-73089
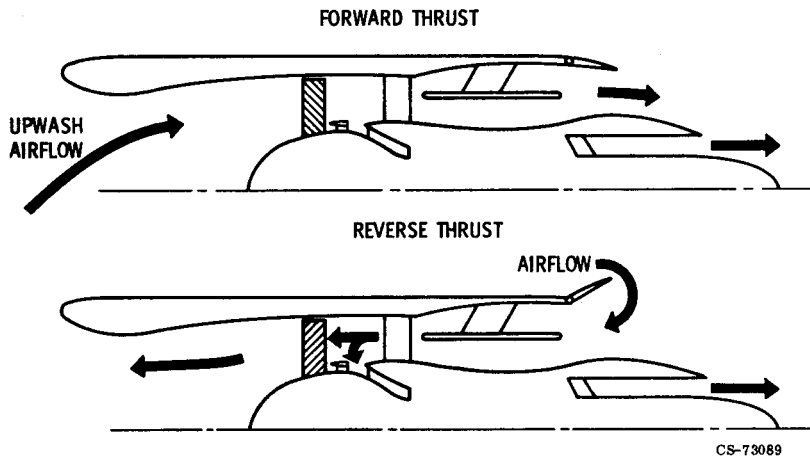
Figure II-6. - QCSEE UTW nacelle aerodynamic flowpath.

V = 80 KNOTS

α

D_T

D_{HL}

CONTRACTION
RATIO,
$(D_{HL})^2/(D_T)^2$

1.56

1.46

MAX FLOW
ANGLE,
α,
DEG

REQUIREMENT

1.37

% MAX AIRFLOW

CS-73085
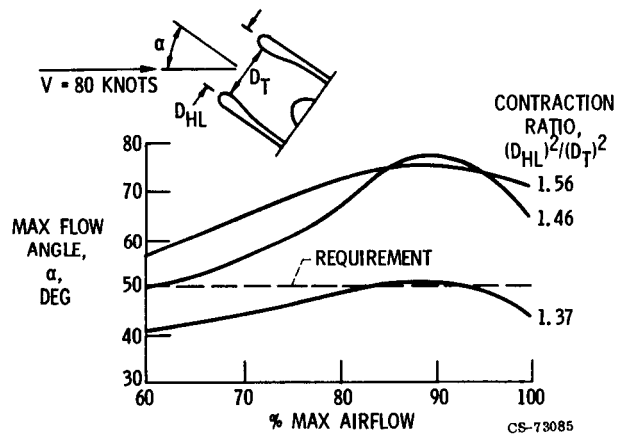
Figure II-7. - QCSEE model inlet test results.

79
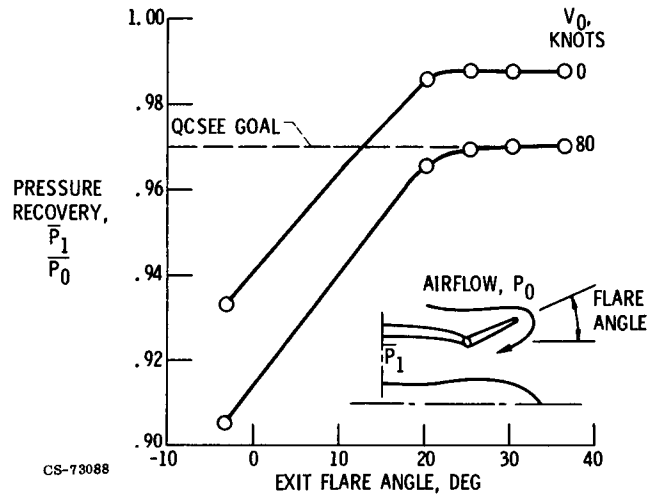
Figure II-8. - QCSEE exlet aerodynamic performance.

III. REFAN PROGRAM

Robert W. Schroeder

The most recently designed commercial aircraft in this country (the wide-body aircraft) satisfy federal noise regulations (FAR Part 36). These aircraft include the DC-10, the 747, and the L-1011. However, several thousand narrow-body aircraft including the 707, DC-8, 727, 737, and DC-9 were certified prior to the formulation of the current noise regulations, and many of these will continue to fly for at least another 15 years. These airplanes are quite noisy and, because of the frequency of their operations, dominate the noise pattern at most airports. The NASA Refan Program is a demonstration of the use of current noise abatement technology to quiet the narrow-body fleet. The program initially embraced both the JT3D and the JT8D powered aircraft, but budgetary limitations later restricted the program to demonstrations with the JT8D engine, which powers the 727, 737, and DC-9 aircraft.

This paper reviews the JT8D Refan Program and outlines the overall objectives and program status, some test results, and current noise level predictions.

PROGRAM APPROACH

The means by which current noise abatement technology can be applied to the JT8D engine are illustrated in figure III-1. Jet noise tends to dominate at takeoff thrust. This is reduced in the refan configuration by decreasing the core jet velocity through increased turbine work and by decreasing the fan duct jet velocity by employing a lower fan pressure ratio and a higher bypass ratio. Fan noise, which tends to dominate during approach, is reduced in the refan configuration by substituting a single-stage fan for the baseline two-stage fan and by using acoustic treatment in the engine and nacelle. The

cross sections in figure III-1 indicate the larger single-stage fan and the application of acoustic treatment in the refan configuration, which will be discussed in more detail later.

The overall aircraft noise reduction goals for the refan are indicated in figure III-2. They include a significant reduction in noise exposure contour area (the so-called footprint bounded by a line of any specified EPNL) and a reduction in the noise measured at the FAR Part 36 measuring stations of the order of 6 to 10 EPNdB. The sketch indicates the rather major reduction in contour area expected under the takeoff flightpath as well as the improvement expected under the approach flightpath.

The major JT8D Refan Program elements are indicated in figure III-3. Phase I included preliminary studies, and phase II includes detailed design, fabrication, and testing. The program participants include Pratt & Whitney Aircraft for engine development, the Boeing Commercial Airplane Company for 727 nacelle development, and the Douglas Aircraft Company for DC-9 nacelle development. Boeing is also responsible for 727 configuration ground tests and Douglas for DC-9 flight tests. Other program participants included American Airlines and United Airlines to ensure that airline viewpoints are included and accorded proper weight.

As of May 1975 (dashed line in fig. III-3) all program testing has been completed. Remaining activities include final data analyses and correlation, completion of reports, and restoration of the DC-9 airplane and the test engines to their original configuration.

ENGINE CHARACTERISTICS

The changes to the baseline JT8D-9 engine are illustrated in figure III-4. The original two-stage fan has been replaced by a larger single-stage fan. The reduction in fan pressure ratio is compensated for by two additional low compressor stages in order to maintain the overall cycle pressure ratio. The high pressure spool is unchanged. The low pressure turbine is not changed other than for new fourth-stage blading. Acoustic treatment is placed in the fan duct and in the nacelle inlet upstream of the fan to attenuate fan noise.

Table III-1 compares some of the major performance parameters of the

baseline JT8D-9 engine with the refan JT8D-109 engine. Note that the higher bypass ratio permits an increase of almost 15 percent in static takeoff thrust. Fan and inlet diameters are increased, as noted previously. The overall length is increased somewhat as is the engine weight. Total airflow has been increased with a reduction in fan pressure ratio. The fan tip speed has also been increased, but the fan noise is reduced because a quieter single-stage fan is used. The bypass ratio is approximately doubled. Turbine inlet temperature is retained at the original value so that engine life expectancy will be unimpaired. Significant reductions in primary jet velocity and in mixed jet velocity result in reduced jet noise.

FNGINE TESTS

As indicated in figure III-5, a significant amount of engine testing was completed by both Pratt & Whitney and Lewis Research Center to establish engine performance characteristics, to measure noise levels and validate acoustic treatment design, and to ensure that the engines are structurally adequate for the DC-9 flight test program. Three development engines were used in these programs. The first engine evaluated stress, low cycle fatigue, core noise, and accomplished FAA endurance testing. The second test engine evaluated stress and performance, alternate turbine strut configurations, and measured overall noise; it was then used for Douglas nacelle and thrust reverser compatibility testing. The third engine was tested by the Lewis Research Center in an altitude test facility. Altitude performance tests measuring thrust and fuel consumption were conducted together with transients, altitude relight tests, etc. These three test engines accumulated approximately 1200 hours of test stand time.

Figure III-6 is a photograph of test engine 1 installed on an outdoor noise measurement stand at the Pratt & Whitney facility in Hartford, Connecticut. As illustrated, the engine is equipped with a modified bellmouth inlet and an untreated tailpipe with a reference nozzle. Figure III-7 shows test engine 3 installed in the Lewis Research Center Altitude Test Facility. In this facility, the engine was tested at simulated altitudes to 40,000 feet and simulated airspeeds to Mach 0.85.

BOEING 727 PROGRAM

Figure III-8 illustrates the 727 side-engine nacelle with the baseline engine above the centerline and the refanned engine below the centerline. The length of the inlet ducting is constrained by the location of the 727 galley access door. Two alternate refan acoustic treatment configurations are shown. The first configuration has lining on the nacelle wall and on the centerbody; the second configuration retains this but adds a treated inlet splitter and a treated tailpipe flow divider. A new target-type thrust reverser was applied to the refan configuration. Acoustic treatment is required in the exit duct to attenuate turbomachinery noise. In the past, this often was fabricated from stainless steel honeycomb with significant weight penalties. The Boeing refan nacelle uses aluminum-brazed titanium honeycomb panels, developed under the Refan Program, for weight saving. An enlarged view of these panels is shown in figure III-9. Note that the panels include the inner and outer skin and the honeycomb core bonded together using aluminum as the brazing material. To safeguard against gravitational effects during the brazing process, the assembly was brazed on a specially developed rotating mandrel.

The 727 center-engine installation posed special problems as it was necessary to accommodate increased airflow without changing the major 727 structural components. As indicated in figure III-10, the refan S-duct includes five different types of acoustic treatment in order to attenuate over a broad frequency range. The fan duct and the exhaust duct treatment are the same as for the side engines.

The newly designed S-duct with the higher refan airflows required an evaluation of engine performance and stall margins with varying amounts of inlet crossflow. This testing was performed with a special 20-inch fan and scaled-down S-duct at the Lewis Research Center (fig. III-11). Crossflow inlet distortion was simulated by the use of screens. These tests verified the adequacy of the fan stall margins under the simulated distortion patterns.

Figure III-12 illustrates the testing performed on the 727 side-engine nacelle at the Boeing facility in Boardman, Oregon. This facility was used to test the side-engine nacelle in the hardwall baseline configuration and in both of the refan treatment configurations previously discussed. The test article was modified later to permit testing (including crosswind effects) the

727 center-engine installation with the S-duct.

A comparison of the 727 baseline performance and the refan performance is shown in table III-2. The refan estimates are based on Pratt & Whitney ground testing. Boeing test results are not yet fully correlated, but preliminary indications tend to confirm the expectations based on the Pratt & Whitney testing. Data are presented for each of the FAR Part 36 measuring stations and with two different approach flap settings. The expected improvement ranges from 7 EPNdB at approach to 8.5 EPNdB at takeoff. The refan noise levels are lower than the FAR Part 36 requirements in all instances. The 95-EPNdB contour area is reduced from about 9 square miles to 3 square miles for a reduction of 67 percent. The 90-EPNdB contour areas are also tabulated, and a refan area reduction of 74 percent is indicated. If the airport area is subtracted from these contour areas, the populated area impacted would be reduced by about 80 percent or more, depending on airport size, for both levels.

Figure III-13 illustrates the baseline and refan 95-EPNdB noise contours for a 727 aircraft superimposed on a map of the Chicago O'Hare airport. The airport boundaries are shown. The major reduction in populated area subjected to noise levels of 95 EPNdB or higher, as alluded to previously, is shown more vividly on this figure.

DOUGLAS DC-9 PROGRAM

As indicated previously, the Douglas phase of the program includes flight testing a DC-9 aircraft with refanned engines. These flight tests have been completed. Figure III-14 is a photograph of the refanned DC-9 airplane taken during flight testing in February 1975. After the refan flight testing started, side-by-side flight testing with a baseline DC-9 airplane was added to the program to permit an assessment of the noise differences. This testing program was completed almost 2 months ahead of the established schedule.

Figure III-15 compares the DC-9 baseline nacelle, above the centerline, with the refan nacelle, below the centerline. Note that Douglas elected to extend the forward treated portion of the nacelle significantly, which gives good noise attenuation and obviates the need for treatment on the centerbody.

Table III-3 compares the DC-9 refan performance with the DC-9 baseline performance on the basis of Pratt & Whitney engine test data (flight test data are still being correlated). Refan noise reductions range from 5 EPNdB at approach, with a 35° flap setting, to 10 EPNdB at takeoff. In all cases, the refan noise levels are comfortably below the FAR Part 36 requirements. The 90-EPNdB noise exposure contour area is reduced by about 61 percent. If the airport area is subtracted from these contour areas, the reduction in exposed populated area might be 80 percent or more, depending on the size of the airport.

Figure III-16 illustrates the baseline and refan 90-EPNdB contour areas that were just discussed. It is noted that the takeoff portion of the refan profile is only about 3 nautical miles in length compared to about 6 nautical miles for the baseline airplane.

It was mentioned earlier that refanning increases the takeoff thrust by about 15 percent. This affects the takeoff gross weight and attainable payload if field length is constraining. Figure III-17 illustrates the takeoff gross weight as a function of the field length for the DC-9 baseline airplane and the DC-9 refan airplane. It is noted that, for field lengths ranging from approximately 3500 feet to approximately 6000 feet, the refanned airplane has higher permissible takeoff gross weights and payload increases of about 2500 pounds for any given field length.

CONCLUDING REMARKS

The preceding discussion presented a condensed summary of the Refan Program status and emphasized the achieving of acoustical improvements as the primary goal of the program. However, there are several other topics that are of general interest, and these will be mentioned very briefly.

Because of energy conservation needs, there is, of course, interest in specific fuel consumption, especially at altitude cruise. The refan engine was tested at Lewis under simulated altitude conditions, but testing of the same engine in the baseline configuration was confined to sea level only. Therefore, to compare this engine in the baseline configuration and in the refan configuration, it was necessary to construct altitude performance predictions from the baseline sea level data. In so doing, it was found that the

refan engine has a fuel consumption lower than the baseline by about 1 percent at a 5000-pound cruise thrust at an altitude of 30,000 feet and airspeed of Mach 0.8. The difference diminishes to zero at a cruise thrust of about 4250 pounds, which probably is the lower limit of the thrust range of interest.

There is also general interest in the prospects of using refan technology. The program initially was intended to evaluate a retrofit option. However, the economic situation has changed somewhat since the program started, and the FAA currently believes that the retrofit costs are not warranted. The estimated cost of retrofitting the JT8D-powered fleet ranges from about $2 billion to about $4 billion, depending on assumptions regarding the number of airplanes involved and on how certain operating cost differences are treated. Although there currently appears to be little prospect of regulatory action requiring refan, the use of refan technology in new production JT8D engines and new production DC-9 and 727 airplanes is being considered by the manufacturers.

TABLE III-1. - COMPARISON OF BASELINE JT8D-9 AND

REFAN JT8D-109 ENGINES

	BASELINE	REFAN
THRUST, SLS, LB	14 500	16 600
FAN	2-STAGE	1-STAGE
INLET GUIDE VANES	YES	YES
FAN DIAM, IN.	40.5	49.2
INLET DIAM, IN.	42.5	54.5
LENGTH, IN.	120	134
ENGINE WEIGHT (DRY), LB	3218	3780
TOTAL AIRFLOW, SLS, LB/SEC	319	467
FAN PRESSURE RATIO	1.97	1.67
FAN TIP SPEED AT TO, FT/SEC	1420	1600
BYPASS RATIO	1.05	2.03
TURBINE INLET TEMP, °F	1766	1766
PRIMARY JET VELOCITY, FT/SEC	1766	1445
MIXED JET VELOCITY, FT/SEC	1470	1140

CS-73027

TABLE III-2. - 727-200 ACOUSTIC PERFORMANCE COMPARISON

[GROSS WEIGHT, 172 500 LB.]

POSITION	FAR 36, EPNdB	BASELINE, EPNdB	REFAN #1, EPNdB	BASELINE -REFAN, ΔEPNdB
SIDELINE	104.4	99.9	92.8	7.1
TAKEOFF/5° FLAPS	99.0	107.4	98.9	8.5
CUTBACK	99.0	100.0	92.4	7.6
APPROACH/40° FLAPS	104.4	109.5	102.5	7.0
APPROACH/30° FLAPS	104.4	108.2	100.9	7.3

NOISE LEVEL, EPNdB	NOISE EXPOSURE CONTOUR AREA*, SQ MI		
	BASELINE	REFAN	AREA REDUCTION, %
95	9.1	3.0	67
90	27.6	7.2	74

*40° APPROACH FLAPS.

CS-73031

TABLE III-3. - DC-9 ACOUSTIC PERFORMANCE COMPARISON

[GROSS WEIGHT, 108 000 LB.]

POSITION	FAR 36, EPNdB	BASELINE, EPNdB	REFAN, EPNdB	BASELINE -REFAN, ΔEPNdB
SIDELINE	103.1	100	93	7
TAKEOFF	95.6	103	93	10
TAKEOFF/CUTBACK	95.6	97	87	10
APPROACH/50° FLAPS	103.1	103	97	6
APPROACH/35° FLAPS	103.1	101	96	5

90 EPNdB NOISE EXPOSURE CONTOUR AREA*, SQ MI		
BASELINE	REFAN	AREA REDUCTION, %
7.7	3.0	61

*50° APPROACH FLAPS.

CS-73030

88

REDUCE JET NOISE (TAKEOFF)

    DECREASE CORE JET VELOCITY (INCREASED TURBINE WORK)

    DECREASE FAN DUCT JET VELOCITY (REDUCED FAN PRESSURE RATIO)

BASELINE ENGINE
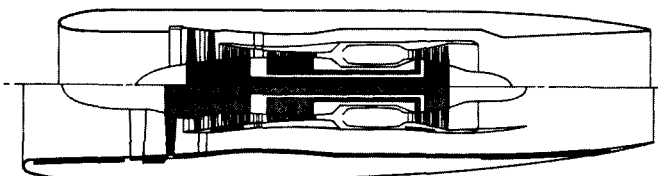
REFAN ENGINE

CS-72961

REDUCE FAN NOISE (LANDING APPROACH)

    USE SINGLE-STAGE FAN (REPLACES TWO-STAGE)

    ACOUSTICALLY-TREAT ENGINE & NACELLE

Figure III-1. - Refan concept for aircraft noise reduction.

RUNWAY THRESHOLD — BASELINE AIRCRAFT

REFAN AIRCRAFT
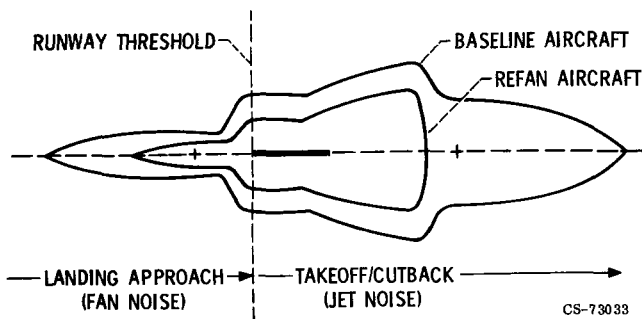
— LANDING APPROACH → — TAKEOFF/CUTBACK —————→
(FAN NOISE)   (JET NOISE)   CS-73033

Figure III-2. - Aircraft noise reduction goals: significant reduction in
noise exposure contour area; reduction in landing approach and take-
off noise at FAR Part 36 measuring stations by about 6 to 10 EPNdB.

	CY 1972	CY 1973	CY 1974	CY 1975
	JASOND	JFMAMJJASOND	JFMAMJJASOND	JFMAMJJASOND
PHASE I	▬▬▬▬			
PHASE II		▬▬▬▬		▭
P & WA ENGINE DEV	▬▬▬▬▬▬▬▬▬▬▬▬▬▬▬▬▬▬▬▬▬▬▬▬▬			
BOEING 727 NACELLE DEV	▬▬▬▬▬▬▬▬▬▬▬▬▬▬▬▬▬▬▬▬▬▬			
DOUGLAS DC-9 NACELLE DEV	▬▬▬▬▬▬▬			
BOEING 727 GROUND TESTS			▪	▬
DOUGLAS DC-9 FLIGHT TESTS				▬
AMERICAN AIRLINES	▬▬▬▬▬▬▬▬▬▬▬▬▬▬▬▬▬▬▬▬▬▬▬			
UNITED AIRLINES	▬▬▬▬▬▬▬▬▬▬▬▬▬▬▬▬▬▬▬▬▬▬▬▬			▭

CS-73038

Figure III-3. - JT8D Refan program elements.

PRODUCTION JT8D-9

TWO FAN STAGES

FOUR LOW COMPRESSOR STAGES

℄ ENGINE

SINGLE STAGE FAN

ENGINE CORE COMMON AFT OF THIS LINE EXCEPT AS STATED

NEW 4TH STAGE BLADE

TWO ADDITIONAL LOW COMPRESSOR STAGES

REVISED FLANGE "M"

REFAN JT8D-109
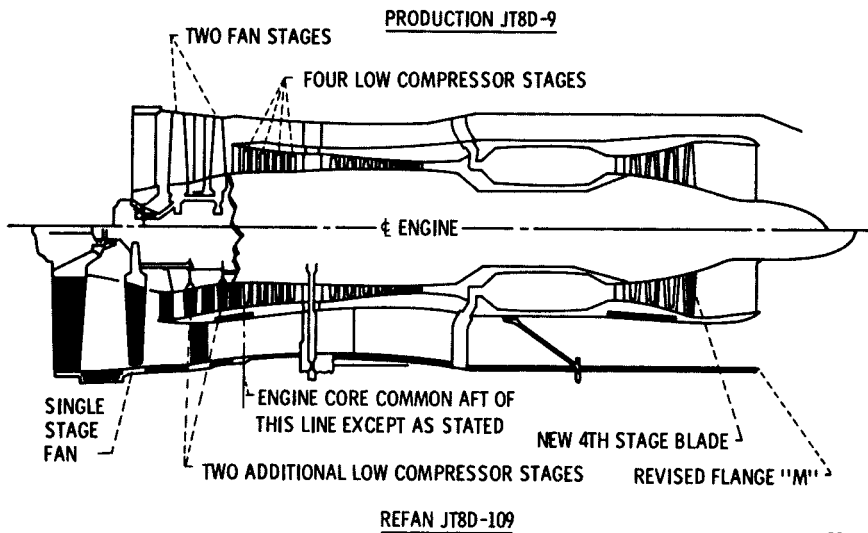
CD-11670
CS-69528

Figure III-4. - Production and refan engine comparison.

	CY 1972	CY 1973	CY 1974	CY 1975
	JASOND	JFMAMJJASOND	JFMAMJJASOND	JFMAMJJASOND

TEST ENGINE NO. 1 (655 HR)
  STRESS, PERFORMANCE
  ENDURANCE, LOW CYC FAT.
  CORE NOISE
  FAA ENDURANCE				

TEST ENGINE NO. 2 (325 HR)
  STRESS, PERFORMANCE
  TURBINE STRUT EVALUATION
  NOISE
  NACELLE & THRUST REV (DAC)				

TEST ENGINE NO. 3 (220 HR)
  SLS CALIBRATION (P & WA)
  ALTITUDE TESTS (LeRC)				

CS-73037

Figure III-5. - Engine test programs (Pratt & Whitney Aircraft and Lewis Research Center).
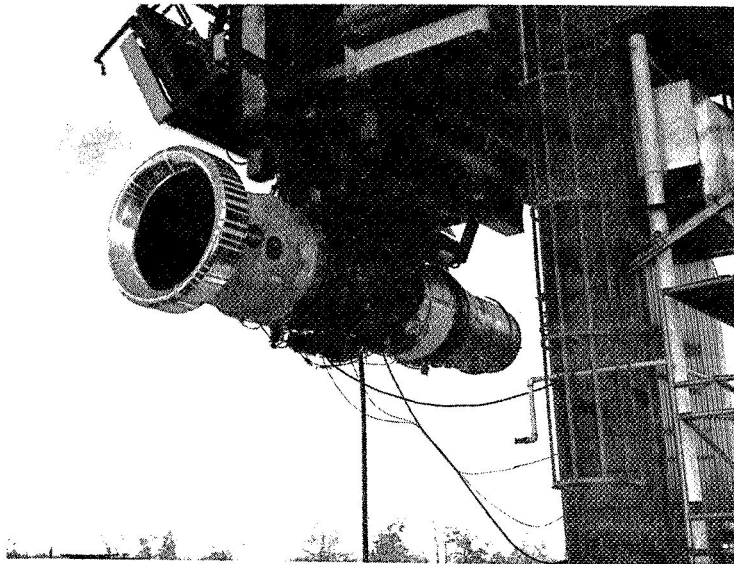
CS-73026

Figure III-6. - Refan engine 1 at Pratt & Whitney Aircraft.
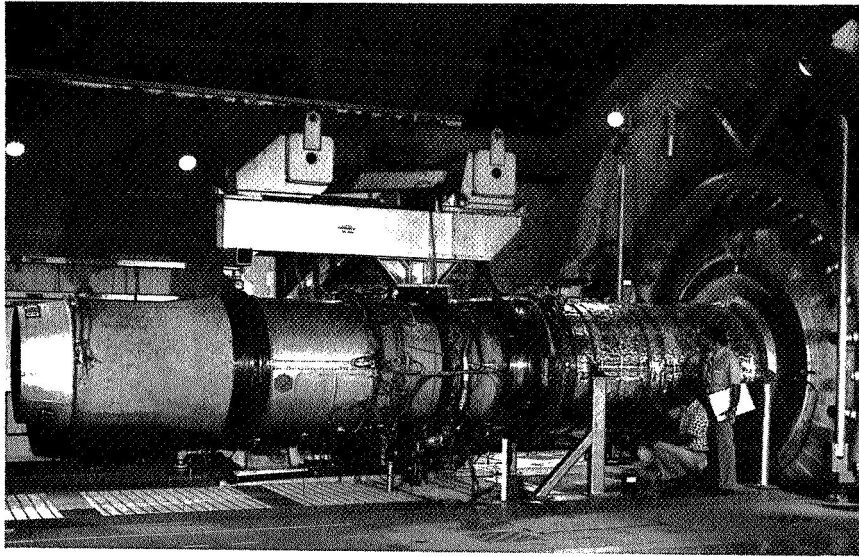
C-74-3152
CS-73025

Figure III-7. - Refan engine 3 in Altitude Test Facility at Lewis Research Center.

BASELINE JT8D-9 (HARDWALL)   ⌐CLAMSHELL T/R

▬▬▬ REFAN JT8D-109 (CONFIG 1)

▬▬▬ REFAN JT8D-109 (CONFIG 2)*   ⌐TARGET-TYPE T/R
                                              ⌐ALUMINUM-BRAZED
                                               TITANIUM ACOUSTIC
*ALSO CONFIG 1 TREATMENT   HONEYCOMB PANELS

                                                      CS-72960
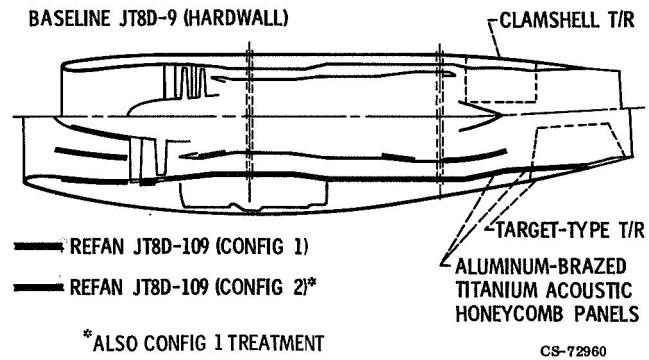
Figure III-8. - 727 Side-engine nacelle comparison.
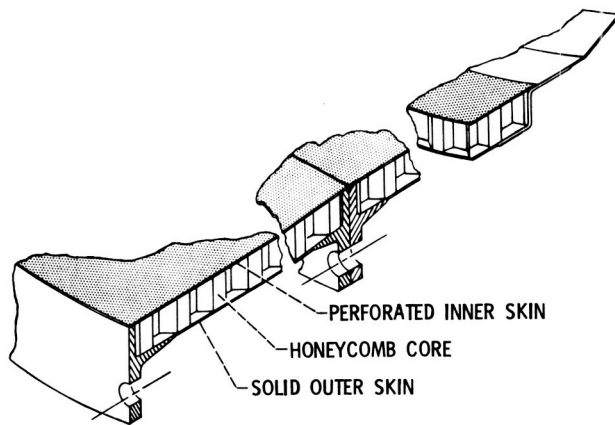
CS-73036

Figure III-9. - 727 Exhaust duct acoustic treatment (aluminum-brazed titanium honeycomb panels).
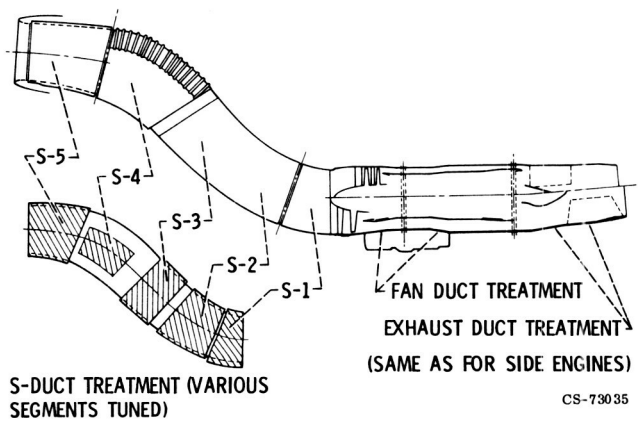
S-DUCT TREATMENT (VARIOUS SEGMENTS TUNED)

S-5
S-4
S-3
S-2
S-1

FAN DUCT TREATMENT

EXHAUST DUCT TREATMENT

(SAME AS FOR SIDE ENGINES)

CS-73035

Figure III-10. - 727 Center engine and S-duct inlet (refan acoustic treatment configuration).

93
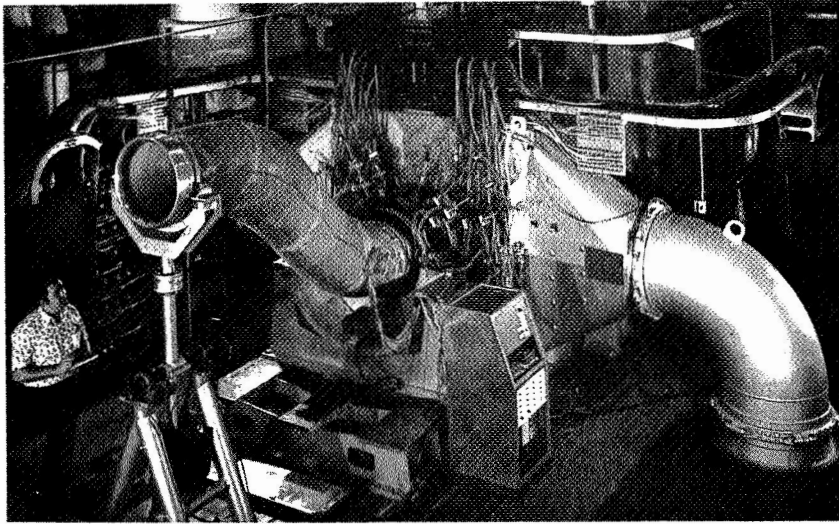
C-74-2270
CS-73022

Figure III-11. - S-duct model in 20-inch fan rig at Lewis Research Center
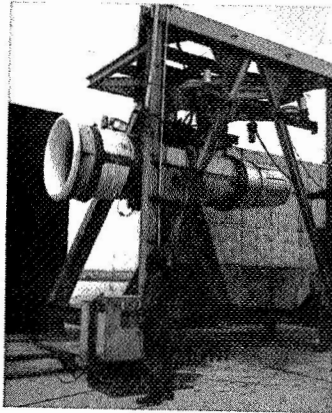
CS-73023

Figure III-12. - Refan 727 side-engine
nacelle at Boardman test site.
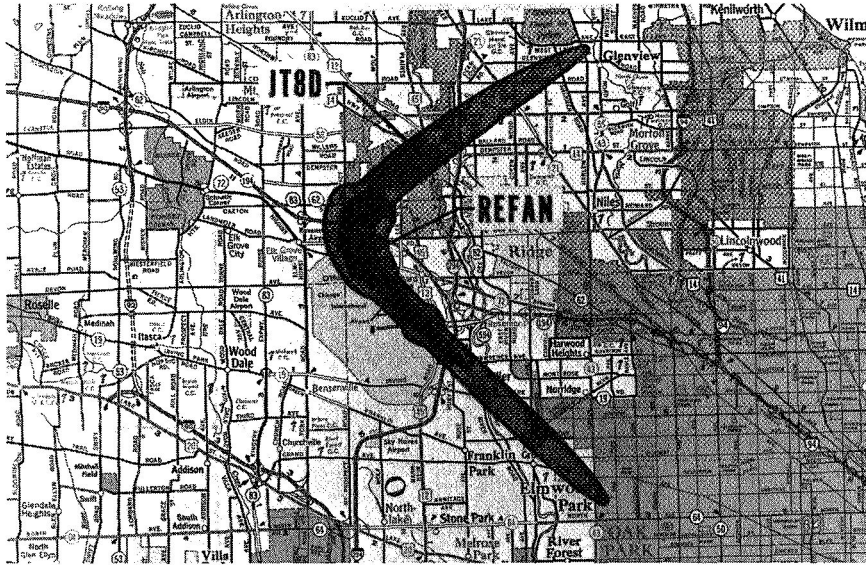
Figure III-13. - Noise contour comparison.

C-75-993
CS-730-24

Figure III-14. - DC-9 refan airplane.

BASELINE NACELLE - JT8D-9

202 IN.

D_{max} = 53 IN.

D_{max} = 64 IN.

261 IN.

REFAN NACELLE - JT8D-109
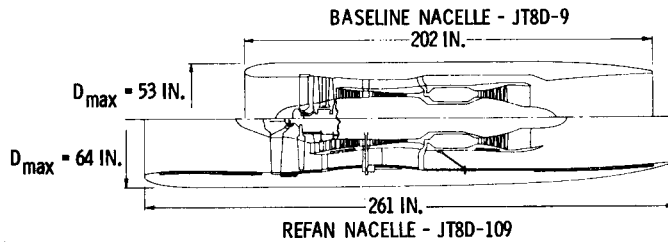
CS-73032

Figure III-15. - DC-9 nacelle comparison.

BASELINE 7.7 SQ MI

REFAN 3.0 SQ MI

.5

N MI   0

.5

LANDING WITH
3° APPROACH

TAKEOFF WITH
CUTBACK

-4   -2   0   2   4   6
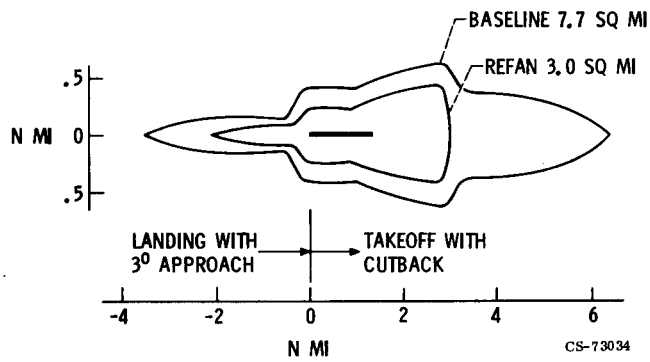
N MI   CS-73034

Figure III-16. - 90-EPNdB noise exposure contours for DC-9 with 50°
approach flaps.
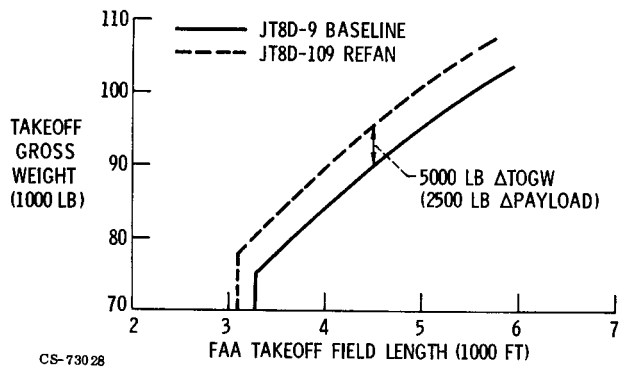
Figure III-17. - FAA takeoff field length comparison for DC-9 baseline and refan airplanes.

CS-73028

Page intentionally left blank

IV. COMBUSTION AND EMISSIONS TECHNOLOGY

Jack Grobman, David N. Anderson, Larry A. Diehl,
and Richard W. Niedzwiecki

At the aeronautical propulsion conference held at NASA Lewis Research Center in 1970 (ref. 1), an area of emphasis was the research that was being performed to evolve short-length combustors for advanced engines that would operate at elevated temperatures and pressures. This type of combustor research is still being pursued. However, over the last several years there has been an increasing emphasis on the evolution of low-pollutant combustor technology. Our research programs in this area include the development of combustors for higher compressor pressure ratio engines, the testing of advanced combustor components, and the evaluation of alternate jet fuels derived from oil shale and coal. This conference paper discusses combustor development as it relates to emissions reduction. Another paper entitled FUEL-CONSERVATIVE ENGINE TECHNOLOGY, briefly describes our alternate fuels program.

The scope of this paper is as follows: First, by way of introduction, the nature of the aircraft pollution problem is examined. Second, the aircraft pollution standards that have been established by the Environmental Protection Agency (EPA) are described. NASA is not directly involved in establishing these standards but is actively conducting the emissions reduction research that is necessary to achieve them. Next, the effect of engine operating conditions on pollutant formation levels is shown, as well as how close present-day engines are to meeting the established standards. The magnitude of the emissions reductions required to meet these standards is indicated. The progress that has been made to date in evolving the needed emissions reduction technology is the main topic of this paper.

NATURE OF AIRCRAFT POLLUTION PROBLEM

Aircraft engine pollution is of primary concern at very high and very low altitudes. At low altitudes, below 3000 feet, jet aircraft emissions may affect urban air quality in the vicinity of airport terminals. During high-altitude cruise, these emissions may affect the global environment.

The main emission products formed at low altitudes and their effects on the urban environment are given in table IV-1. Carbon monoxide (CO) and total hydrocarbons (THC) are formed as a result of incomplete combustion when the engines are idling at low power. Total hydrocarbons are defined as including both unburned and partially oxidized hydrocarbons. Oxides of nitrogen (NO_x) are mainly composed of nitric oxide and lesser amounts of nitrogen dioxide. Nitric oxide in the exhaust eventually combines with the oxygen in the atmosphere to form nitrogen dioxide. All these products are undesirable because they are either toxic or form photochemical smog.

Jet aircraft smoke is mainly undesirable from asthetic considerations. The presence of smoke in the engine's exhaust plume is generally not indicative of a low combustion efficiency. The engine manufacturers have made considerable progress in eliminating the smoke nuisance from more recent engines designs. These smoke reductions have been accomplished mainly by improving fuel injectors and by improving fuel-air mixing in the primary zone of the combustion chamber. Because of the considerable progress already achieved by the industry in reducing smoke, this paper concentrates on the invisible gaseous pollutants - carbon monoxide, total hydrocarbons, and NO_x.

Paper V discusses the effect of cruise emissions on the upper atmosphere. Our discussion of cruise emissions is limited to the possible effects of nitric oxide produced in the stratosphere and to reviewing the approaches that may be taken to reduce these emissions during cruise.

AIRCRAFT ENGINE EMISSION STANDARDS

For regulation purposes the EPA has divided aircraft engines into various classes. These classes, along with some typical applications, are listed in

100

Table IV-2. A major division in the classes is on the basis of thrust. The T1 class represents general aviation engines of less than 8000-pound thrust. The T2 class includes engines of over 8000-pound thrust, essentially all jet engines in the commercial fleet. The JT3D and JT8D are special classes of T2 engines which were set aside at an earlier date for purposes of smoke retrofit. A separate class has been established for turboprop engines because of their different mode of operation. Standards have also been established for piston engines, the P1 class, but are not discussed herein. All these standards are for engines manufactured after January 1, 1979. Standards for supersonic cruise engines have been proposed but have not been finalized into law.

The EPA regulations governing carbon monoxide, total unburned hydrocarbons, and NO_x are expressed in terms of an integrated number. This number relates mass of pollutant, time, power level, and fuel flow for a simulated takeoff-landing cycle. A diagrammatic representation of this cycle is shown in figure IV-1. Several points are worthy of note. The times shown were based on peak traffic conditions at a large metropolitan airport and as such represent a typical adverse case. The cycle includes 19 minutes of taxi-idle (out) at approximately 5 percent engine power, 0.5 to 0.7 minute for takeoff at 100 percent engine power, 2.2 to 2.5 minutes for climbout to 3000 ft at 85 percent engine power, 4 to 4.5 minutes for approach at 30 percent engine power, and 7 minutes for taxi-idle (in) at 5 percent engine power. Only altitudes below 3000 feet are of concern since the main goal of aircraft emission standards is to protect the environment in the vicinity of large metropolitan areas. Even though no standards have been formulated for altitudes above 3000 feet, there is, of course, great concern over the effects of aircraft cruise emissions on the global environment. Separate studies such as the Department of Transportation's Climatic Impact Assessment Program (CIAP) are examining this problem.

Although the total time for taxi-idle is high (fig. IV-1), the power level is low. The total fuel burned by a typical T2-class engine in a wide-body jet transport at taxi-idle is about equal to the total fuel consumed during high-power operation at takeoff and climbout to 3000 feet. Consideration of the amount of fuel burned has given rise to the relatively convenient pollutant rating criterion known as the emission index: the ratio of pollutant formed to

the amount of fuel burned. Figure IV-2 shows typical emission index values of carbon monoxide, unburned hydrocarbons, and NO_x for a wide-body-transport engine for each of the operating modes in the takeoff-landing cycle. Compared with the other operating modes, the low-power, taxi-idle mode produces the greatest amount of carbon monoxide and total unburned hydrocarbons. Both products represent a loss in combustion efficiency. Conversely, at high-power operation, such as takeoff, negligible amounts of carbon monoxide and hydrocarbons are formed. Combustion efficiency is high, and combustor conditions are conducive to the formation of oxides of nitrogen. Shown for comparison are the levels required by the 1979 EPA standards at these modes of operation. Each pollutant must be reduced by a factor of 3 to 4. For combustor evaluation purposes, the study of emissions can be conveniently limited to taxi-idle and takeoff. If the required emission levels at taxi-idle and takeoff are far from being met, the additional trouble and expense of testing a combustor at climbout and approach is not warranted. In addition, it is generally true that any NO_x reduction achieved at takeoff will manifest itself as a proportionate decrease at climbout. The remainder of this paper focuses on the problem of reducing carbon monoxide and hydrocarbons at taxi-idle and on the problem of reducing NO_x at takeoff.

OPERATION OF A TYPICAL COMBUSTOR

A typical combustor for a turbojet engine, which contains features common in current aircraft, is shown in figure IV-3. The view is a cross-sectional slice of an annular combustor. Airflow from the compressor exit enters the combustor through a diffusing section. Often, as shown, combustor hardware is extended into the diffuser to aid in dividing the air properly. Approximately one-fourth of the airflow enters the combustor primary zone, through either swirlers or holes. Fuel is also injected into the primary zone, where it mixes with the air. In the primary zone, combustion is initiated and stabilized. The remaining three-fourths of the airflow bypasses the primary zone and is injected into the secondary zone. There it mixes with exhaust gases to complete combustion and to produce the desired exit temperature profile.

A term frequently used in describing the relative amounts of fuel and air is the equivalence ratio. An equivalence ratio of 1 means that exactly the right amounts of fuel and air are present for complete combustion. Equivalence ratios less than 1 indicate an excess of air. Ratios greater than 1 indicate an excess of fuel. Current aircraft normally operate with primary-zone equivalence ratios greater than 1 at high-power conditions.

The principal products of combustion are also shown in figure IV-3. Water vapor and carbon dioxide are normal products of combustion and occur whenever hydrocarbon fuels are burned. The remaining constituents shown are pollutants. Total unburned hydrocarbons and carbon monoxide are measures of combustion efficiency loss. Gas turbine combustors operate at very nearly 100 percent combustion efficiency at all operating conditions except at low power, such as engine idle. Thus, it can be assumed that unburned hydrocarbons and carbon monoxide pollutants are emitted primarily at idle. Oxides of nitrogen and smoke are emitted primarily during full-power operation and are not due to combustion efficiency loss. Rather, levels of these pollutants are controlled by combustor design and inlet conditions.

EMISSIONS AT IDLE CONDITIONS

The mechanisms of pollutant formation at idle operating conditions together with corrective approaches for their elimination are shown in table IV-3. Aircraft combustors represent compromise designs geared primarily for optimum performance at takeoff and cruise conditions. Thus, when they are operated at low-power conditions, such as engine idle, low combustion efficiencies result from design compromises and poor burning conditions. Typical combustion efficiencies at engine idle, for current aircraft, vary between 88 and 98 percent. The actual values depend on engine size, type, age and operational procedures. Poor burning conditions at idle are caused by low fuel flow rates, low fuel-air ratios in the primary zone, and low inlet air temperature and pressure.

Low fuel flow rates produce low fuel-nozzle pressure drops, causing poor atomization and distribution as illustrated in figure IV-4. At high power and high fuel flow rates, fuel nozzles produce an atomized, conical spray of

well-distributed, small-diameter fuel droplets, which burn quickly. At idle fuel rates, a coarse, tulip-shaped spray pattern occurs. Fuel distribution is poor, and droplet size is large. Two techniques for improving idle fuel-nozzle performance are shown in figure IV-4. The first technique, an air-assist nozzle, combines a conventional fuel nozzle and externally supplied, high-pressure air injected through a secondary passage to atomize and better distribute fuel. The second technique, the air-blast nozzle, accomplishes the same purpose by using the kinetic energy of the compressor air to atomize the fuel.

Low idle fuel flow rates also result in low primary-zone fuel-air ratios. The result is poor combustion stability, since primary-zone equivalence ratios approach the lean flammability limit of the fuel. In order to correct this problem, the primary-zone equivalence ratio should be increased to a value near 1.

Low inlet air temperatures and pressures at idle reduce burning intensity and cause the combustion reaction to be quenched before completion. Extending the residence time of the hot gases in the primary zone, either by reducing air velocity or by delaying mixing of the combustion gases with the secondary air, corrects this problem.

A technique for overcoming low fuel-air ratios, as well as low idle inlet air temperatures and pressures, is to use combustor designs which incorporate multiple burners. One of these designs, a double-annular combustor, is shown in figure IV-4. With multiple burners, one burner can be designed specifically for the idle condition. When fuel is supplied to only the idle burner, localized burning intensity can be increased, since each nozzle is supplied with twice as much fuel as formerly. Also, airflow to the idle burner can be reduced, thus increasing equivalence ratio and reducing air velocity. Mixing of secondary air with combustion gases can be delayed or eliminated.

IDLE EMISSION REDUCTION TESTS
Air-Assist Fuel Injection

An air-assist fuel nozzle was tested at NASA Lewis Research Center in an experimental can-type combustor operating at idle conditions. The results

of these tests are shown in figure IV-5. The measured carbon monoxide (CO) and total unburned hydrocarbon (THC) emissions are given as a function of the nozzle differential pressure; that is, the difference between atomizing air pressure inside the nozzle and combustor pressure. As the atomizing air pressure was increased, fuel atomization improved. The improved atomization resulted in a decrease in carbon monoxide emissions from 75 g per kg of fuel without air assist to 20 g per kg of fuel with 30-psi differential pressure. Similarly, unburned hydrocarbons were reduced from 35 g/kg to 5 g/kg. It should be emphasized that these results are for one particular can-type combustor; this technique may give different degrees of improvement for other combustors.

Fuel Flow and Airflow Scheduling

Another approach to the reduction of idle emissions is the use of fuel scheduling and air scheduling. In the schematic shown in figure IV-4, each of two annular rows of fuel nozzles incorporates an independently controllable fuel feed. Thus, radial fuel staging can be obtained by turning off the fuel to one annular row. Fuel scheduling in this manner provides a greater idle fuel flow through each nozzle. The result is better atomization and a higher local equivalence ratio. By scheduling airflow as well as fuel flow, increases in burning-zone residence times can also be achieved. Results for an experimental combustor using these concepts are presented in figure IV-6. The measured idle emissions are compared with a baseline configuration in which both annular rows of fuel nozzles were used. With fuel supplied to only one annular row of nozzles, total unburned hydrocarbons were reduced to 25 percent of the baseline value, and carbon monoxide to 80 percent. When changes were also made to the airflow pattern to increase the burning-zone residence time, the hydrocarbon emissions were reduced to 13 percent of the baseline levels, and carbon monoxide to 57 percent.

EMISSIONS AT FULL-POWER CONDITIONS

The mechanisms of pollutant formation at full-power operating conditions, together with corrective approaches for their reduction, are shown in table IV-4. The principal gaseous pollutant formed at full power is NO_x. At full-power conditions, combustors operate with high inlet temperatures, high inlet pressures, and high fuel-air ratios - all of which contribute to the formation of NO_x. The NO_x formation rate increases with increasing flame temperature, and flame temperature increases proportionately with increases in combustor inlet temperature. Higher combustor inlet temperatures result from higher engine compression ratios or from higher aircraft flight speeds, particularly during supersonic cruise. Nonuniform fuel distributions in the primary zone also cause local peak flame temperatures.

The effect of flame temperature on the formation of NO_x is illustrated in figure IV-7. These results were calculated for a combustor inlet temperature of about 1000° F, a pressure of 5 atmospheres, and a residence time of 2 milliseconds. The formation of NO_x increases exponentially with increasing flame temperature. Conventional combustors have flame temperatures of the order of 3600° to 4000° F in the primary zone since they are designed to operate near an equivalence ratio of unity, where near-maximum flame temperatures occur. Injecting water into the primary zone or burning a leaner fuel-air mixture lowers the flame temperature. If flame temperatures below 3000° F could be achieved, the formation of NO_x would be significantly reduced. Local peak flame temperatures in the primary zone could also be eliminated by improving fuel atomization, by premixing fuel and air prior to combustion, or by prevaporizing the fuel.

Another cause of high NO_x formation levels is excessive residence time of combustion gases in the primary zone. Figure IV-8 shows the effect of residence time on NO_x formation calculated for a primary-zone equivalence ratio near unity. The formation of NO_x was somewhat linear with residence time over a limited time span for this primary-zone equivalence ratio. Later in this paper, we show that this effect tends to be less significant as the equivalence ratio is reduced. The residence time in a combustion chamber is typically of the order of 2 to 4 milliseconds. However, the equilibrium value of NO_x is not reached until after several minutes and is much higher

than the quantity of NO_x which is actually formed within a typical combustion chamber. Residence time may be reduced either by increasing velocities in the primary zone or by providing more rapid quenching of the combustion products.

FULL-POWER EMISSION REDUCTION TESTS

Water Injection

One technique for lowering flame temperature, and hence reducing the formation of NO_x, is water injection. The combustor modifications required to implement this technique are relatively simple. Water injection is currently used on some wide-body transports for thrust augmentation. Depending on the engine model, various locations upstream of the combustor, such as the diffuser, are used as injection sites. In order to be most effective for reducing NO_x, however, water must be injected directly into the combustor primary zone. Figure IV-9 shows that, when water is injected at a rate equal to the fuel flow rate, a reduction in NO_x of approximately 75 percent can be achieved. This level is close to that required by the 1979 EPA standards. If the water injection is done properly, this 75 percent reduction can be achieved without loss in combustion efficiency. While it is seemingly an ideal solution, several problems are involved with water injection. First, the water used must be demineralized to prevent deposits from forming in the engine; second, antifreeze is needed to prevent freezing of the water either at the airport or aboard the aircraft. In addition, there are logistics problems involved at the airport in handling the water. Finally, water injection, which would be employed mainly at takeoff and climbout, is not as promising as combustor design improvements which would reduce NO_x formation at altitude cruise operation as well as during takeoff and climbout.

Premixing-Prevaporizing Combustor

Another approach for reducing average flame temperature is to burn leaner mixtures. Lean burning is most effective when local high-temperature

zones are eliminated by the use of a homogeneous fuel-air mixture. This mixture can be obtained by premixing a prevaporized fuel upstream of the combustor. A series of experiments were performed to determine what minimum levels of NO_x could be achieved in an idealized premixing-prevaporizing combustor. A test section of this type is shown in figure IV-10. A long inlet section was provided to ensure thorough mixing between fuel and air. Gaseous propane was used in initial tests to avoid vaporization problems. A single-point probe located at the combustor centerline permitted the sampling of exhaust gases which were free from wall cooling effects. A simple perforated-plate flameholder stabilized the flame.

The NO_x emissions for this combustor, measured at an inlet temperature of 1000° F and a pressure of 5 atmospheres are shown in figure IV-11 as a function of equivalence ratio. These 2-msec-residence-time data are compared with a well-stirred-reactor theoretical model. Later, liquid fuels and a slightly modified fuel introduction system were also tested. The liquid-fuel test results, also shown in figure IV-11, agree well with the gaseous-fuel data. Minimum emissions of less than 1 g NO_2 per kg of fuel were obtained at primary-zone equivalence ratios less than 0.5. All data shown were taken with combustion efficiencies greater than 99 percent.

The formation of NO_x can be reduced by decreasing residence time, as well as by lowering the local and average flame temperatures. By moving the gas sampling probe axially, it is possible to determine the effect of residence time on NO_x emissions. The results (fig. IV-12) show that, at 0.6 equivalence ratio φ, a reduction in residence time from 3 msec to 1 msec gives a 43 percent decrease in NO_x. At 0.4 equivalence ratio, however, the same reduction in residence time gives only a very small drop in NO_x. Thus, residence time becomes less and less important to NO_x formation as equivalence ratio is decreased to very lean values; that is, rates of NO_x formation are lower at lean conditions.

In considering residence time reduction for NO_x control, it is important to determine what minimum residence time is required for good combustion efficiency. Bands of constant combustion efficiency are shown in figure IV-12. The shaded area represents combustion efficiencies of 99 to 99.7 percent. The crosshatched area represents combustion efficiencies less than 99 percent. Data in the unshaded portion of the graph denote combustion efficiencies

greater than 99.7 percent. The results of these experiments show that, for good combustion efficiency, less NO_x was produced with very lean equivalence ratios and long residence times than at somewhat higher equivalence ratios and short times. These data were taken in a flame tube at idealized conditions and do not include effects of wall quenching or imperfect fuel-air mixing. Practical combustors may not be able to achieve these same results.

Another premixing-prevaporizing study using liquid JP-5 fuel is being conducted under contract to NASA Lewis by General Applied Sciences Laboratories. Results from this study are similar to those obtained in the in-house program.

Catalytic Combustion

In the premixing-prevaporizing combustor experiments, it was not possible to sustain combustion when flame temperature dropped below 2600° F. At this temperature, NO_x emissions were near 0.3 g per kg of fuel. One way to obtain lower flame temperatures by burning even leaner mixtures, and thereby to form still less NO_x, is to employ catalytic combustion. In order to determine the feasibility of such an approach, catalytic reactors have been evaluated at a number of laboratories, including the Air Force Aero Propulsion Laboratory and the Lewis Research Center. Potential applications being investigated include stationary power, ground transportation, and aircraft gas turbine engines.

A schematic of one possible catalytic combustor configuration is shown in figure IV-13. A premixed, prevaporized fuel-air feed is required. The inset illustrates the use of a monolithic substrate similar in appearance to those used in some 1975 model cars for exhaust pollution control. It might be necessary to use several different catalysts, stacked lengthwise, to take full advantage of the different operating temperature limits of each catalyst. Depending on the application, inlet temperature to the reactor could be as little as 400° F or as great as 1400° F, and exit temperature would fall in the range of 1900° to 2500° F.

Shown in figure IV-14 are typical catalytic reactor test results that were obtained by the Air Force Aero Propulsion Laboratory using an Engelhard reactor. The inlet temperature was 700° F and the pressure was 10 atmo-

spheres. Catalytic combustion reactions were initiated without an external source of ignition with nearly zero fuel flow. However, poor efficiency was obtained for equivalence ratios below 0.25. This equivalence ratio corresponds to a flame temperature of about 1900° F. Higher equivalence ratios produced higher exit temperatures and virtually 100 percent combustion efficiency. For the test reactor, 2400° F was considered a safe maximum reactor exit temperature for continuous operation. The upper temperature limit is defined partly by the maximum allowable use temperature of the ceramic substrate. Thus, the reactor had a very limited operating range of 1900° to 2400° F. Within this temperature range, combustion efficiency was high and NO_x emissions were below the minimum accurate measuring limit of the analyzer, which corresponds to about 0.25 g per kg of fuel.

Although catalytic reactor tests have shown encouraging results, a great deal of research and development is required before the feasibility of catalytic combustion for aircraft applications can be demonstrated. Additional catalyst and substrate development must be directed to broadening the practical operating range. The physical and chemical durability of catalysts and substrates at high temperatures remain to be proved. Removal of known catalyst poisons from the fuel would be necessary. The possibility of foreign object damage to the ceramic substrate or damage to the turbine from breakdown of the ceramic bed is of concern. Also a cold-start ignition system is needed, as well as a low-power unit for idle operation. Finally, fuel vaporization and fuel-air premixing are required.

Modular Combustors

Another experimental combustor concept which has demonstrated significant NO_x reduction is the NASA swirl-can combustor. This combustor has been studied at Lewis for several years. Compared with the premixing-prevaporizing and catalytic combustor concepts, this combustor is in a more advanced state of real combustor development. Shown in figure IV-15 is a cross-sectional view of a 40-inch-diameter experimental full-annular modular combustor and a component sketch of one of the 120 individual fuel modules, a design feature that produces more uniform fuel distribution. Each individual module consists of a carburetor, in which some degree of premixing is

achieved, a swirler and a flame stabilizer. Unlike conventional combustor designs, all air except that required for liner cooling passes through the primary combustion zone. The result is leaner operation. The small localized recirculation zones promote rapid mixing and thus quench the formation of NO_x. A swirl-can combustor is shown in figure IV-16. This upstream view shows how the individual modules are arranged to form the array. The inner transition liner has been removed so that the modules can be seen more clearly.

The quantitative NO_x reductions achievable with the swirl-can combustor are shown in figure IV-17. Since these combustors were tested at 6-atmosphere pressure, the NO_x levels are lower than those that would be generated by operation at true engine takeoff condition. The NO_x formation depends strongly on the combustor inlet air temperature. Compared with a conventional combustor, twofold reductions in NO_x are achievable with the swirl can. The double-annular combustor data also presented are from an advanced experimental design which contains 64 fuel nozzles arranged on two annuli. This is slightly greater than twice the number of fuel nozzles contained in a conventional large annular combustor. The superior fuel and air management resulting from this arrangement produced levels of NO_x intermediate between those of a conventional combustor and those of a swirl-can combustor.

EMISSIONS CONTROL FOR THE OVERALL ENGINE CYCLE

The various approaches that may be used to reduce either idle (CO and THC) or full-power (NO_x) pollutants are summarized in table IV-5. In general, techniques that improve fuel atomization and fuel distribution are useful in lowering all pollutants. Unfortunately, a technique useful in reducing one pollutant may increase the formation of another. Burning a stoichiometric fuel-air mixture (which is the same as an equivalence ratio of unity) tends to reduce the formation of CO and total hydrocarbons; however, burning a lean mixture is necessary to minimize NO_x formation. Maximizing residence time reduces CO and THC formation at idle conditions; however, minimizing residence time reduces NO_x formation at full-power conditions.

Thus, we are faced with a dilemma in deciding on design settings for the equivalence ratio and the residence time in the primary zone that would minimize all pollutants formed over the entire engine operating cycle. There are several possible approaches to solving this dilemma. One of these approaches is to use a multizone burning concept consisting of two or more separate combustion stages. One stage acts as a pilot combustor, is used for idle operation, and is designed to burn a stoichiometric fuel-air mixture with a relatively long residence time. The other stage acts as the main combustor, is used during full power, and is designed to burn a lean mixture with a relatively short residence time.

A more extreme approach is to introduce variable geometry into the design of the combustion chamber to enable the continuous control of both fuel flow and airflow distribution in the reaction zone. Combustor airflow distribution could be varied by using variable-area air entry ports controlled by mechanical linkages. Another method for varying combustor airflow distribution involves the pneumatic control of the combustor inlet velocity profile by means of boundary-layer bleed within the diffuser.

EMISSIONS REDUCTION TECHNOLOGY PROGRAMS

The preceding sections of this paper describe some of the fundamental and applied research that has been performed to evolve concepts for reducing emissions from jet aircraft combustors. This section describes several NASA contract efforts that have been organized to implement and evaluate these concepts in actual engine environments. Each of these contract efforts is being conducted in three separate phases. The first phase consists of screening out various candidate low-pollutant combustor concepts. The second phase consists of refining the more promising concepts identified during the first phase. And the third phase consists of an actual demonstration of the more promising low-pollutant combustors in a state-of-the-art engine.

The four different engine classes listed in table IV-6 are currently being investigated. The T2-class engine program, designated the "Experimental Clean Combustor Program," which started about $1\frac{1}{2}$ years earlier than the others, is furthest along. This program consists of two contracted efforts.

One is being conducted by General Electric Company on the CF6-50 engine and the other by Pratt & Whitney Aircraft Company on the JT9D-7 engine. Both contractors have completed the screening effort (phase I), and both are presently working on concept refinement (phase II). The other three engine programs, designated the "Pollution Reduction Technology Programs," are all in the early stages of the screening effort.

Experimental Clean Combustor Program

The engines of concern for the Experimental Clean Combustor Program are in the EPA T2 class and are shown in figure IV-18. The T2-class engines are large, high-bypass-ratio engines with thrust greater than 8000 pounds and are used to power the wide-body jets. The two engines selected for this program are the Pratt & Whitney JT9D-7 and the General Electric CF6-50.

Program pollution goals are listed in table IV-7. These goals are consistent with published 1979 EPA standards. Listed are the pollutants of interest, the engine mode at which each goal is specified, and the 1979 EPA standards, in terms of emission index. Also listed for comparison are current pollution levels for the JT9D-7 and CF6-50 engines. These goals are ambitious in that they require substantial reductions of all gaseous pollutants. The NO_x goal, specified at the takeoff condition, requires a threefold reduction in current values. Carbon monoxide and THC goals, specified at engine idle, require reductions of four- to sixfold. Smoke is not a problem for this engine class, since both engines currently produce levels below the 1979 standard.

In addition to the pollution goals, the program also specifies performance goals. These include combustion efficiencies of at least 99 percent at all conditions, reasonable pressure loss, good exit temperature distribution, and adequate altitude relight and durability.

Figure IV-19 presents schematic drawings of the Pratt & Whitney combustors being evaluated in phase II. Tests are being conducted on 90° sectors of these combustors, designed to fit within the JT9D envelope. In order to reduce pollution at both low- and high-power conditions, these designs incorporate multiple burners and fuel scheduling. In operation, only the pilot stage is fueled at the idle condition. Both stages are fueled at higher power points, with the majority of air and fuel passing through the main stage.

The first design, the hybrid combustor, uses a parallel fuel staging approach. This design evolved from the phase I screening tests. It is an attempt to mate the pilot premix combustor, which produced the lowest idle pollutants obtained under both programs, with a swirl-can design, which produced the lowest Pratt & Whitney NO_x levels at takeoff.

The second combustor shown in figure IV-19, designated the Vorbix Combustor, incorporates a series staging concept. A Vorbix Combustor sector is shown in figure IV-20. The view is downstream through the combustor inlet. The pilot-stage nozzle assembly is shown at the bottom of the figure. The design uses pressure-atomizing fuel nozzles in both the pilot and main stages. Main-stage fuel is injected into the hot gases issuing from the pilot stage. The main stage has high-intensity swirlers (shown at the top of fig. IV-20) immediately downstream of the fuel injection point. These swirlers promote very intense, rapid mixing of fuel and air. The combination of intense mixing and hot pilot gases permits lean main-stage combustion. Also, residence time is reduced by the quick quenching of the hot gases.

The two General Electric phase II combustor designs for the CF6-50 engine are shown in figure IV-21. Full-annulus designs of these combustors are being evaluated. As with the JT9D combustors, both designs use multiple burning zones and fuel scheduling as the principal pollution controlling approaches. The radial/axial combustor incorporates a series-type orientation for the two burning stages. A three-dimensional sketch of this combustor is shown in figure IV-22. A section of the annulus has been removed to better show the burning stages. The main combustor stage incorporates a premixed fuel-air passage. Fuel is injected upstream of the burning zone, and combustion is stabilized by V-gutter-type flameholders and pilot-stage hot gases. The combination of hot pilot gases and main-stage premixing permits very lean main-stage burning. This design has produced the lowest NO_x levels at takeoff that have been obtained from either of the two experimental clean combustor efforts.

The double-annular combustor shown in figure IV-21 incorporates two parallel burning zones. Air-blast-type fuel nozzles are used in both stages. In operation, only the outer annulus is fueled at low power. Both annuli are fueled at high power.

The best pollution results obtained for combustor concepts tested in

phase I are summarized in figure IV-23. Current pollution levels for the CF6-50 and JT9D-7 engines, component test results obtained in the Experimental Clean Combustor Program, and the requirements to meet the 1979 EPA standards are compared on an emission index basis. Both carbon monoxide and THC have been substantially reduced at the engine idle condition. The best configurations produced values for both pollutants that approach one-half the 1979 EPA requirements. Shown are idle data for a Pratt & Whitney staged/premix combustor concept. It appears that all combustor designs investigated in phase I appear capable of achieving the 1979 EPA required idle values with sufficient additional effort.

NO_x measurements obtained at lower than takeoff pressure have been extrapolated to takeoff conditions. Reductions in NO_x of over 50 percent have thus been obtained and the 1979 required values have been approached. Phase I test results at simulated takeoff for the General Electric radial/axial combustor are shown in figure IV-23. Larger NO_x reductions than shown in figure IV-23 have been obtained but at the expense of combustion efficiency falloff at both low- and high-power conditions.

Although these results are quite encouraging, it must be kept in mind that these are the results of component tests and represent the best composite results obtained to date for two different combustors. No single combustor that either Pratt & Whitney or General Electric has investigated has produced as good results. Also, only performance at idle and takeoff have been described since phase I program goals were specified only at these power settings. A practical engine combustor has to perform well and must produce low pollution concentrations at the intermediate-power conditions of approach, cruise, and climbout as well. So, much additional work must still be done. In phase II, which is currently in progress, the combustors are being further developed. Although additional idle and takeoff pollution reductions are being sought, the principal effort is in investigating the part-power points of approach and climbout and in obtaining EPA cycle data. Pollution data are also being obtained at simulated altitude cruise conditions.

Performance areas of emphasis are exit temperature control, altitude relight, and combustor durability. In order to use multiple-burning-zone combustors, a new, more complex, engine fuel control system is required to stage fuel at the various engine power points. Thus, design efforts are in

progress to devise fuel control systems of this type.

In phase III, which is to be initiated in mid-1975, the best combustor design from each contractor will be evaluated as part of a complete engine. Thus, the first phase III efforts will be to solve interface problems involved in installing the combustors in the CF6-50 and the JT9D-7 engines. The intent of phase III is to authenticate the pollution reductions obtained in the phase I and phase II component tests. Several engine pollution sampling techniques involving sample density will be investigated for both stationary and rotating instrumentation. Performance investigations will include acceleration/deceleration engine tests, as well as any thrust transients caused by fuel staging.

The Experimental Clean Combustor Program will be terminated upon completion of phase III. At that time, it is anticipated that a technology base for low-emissions combustor concepts will have been provided, and that low-emissions combustors will have been demonstrated in full-scale engines. However, additional efforts will be required by industry to ready the low-emissions combustors for installation in the commercial fleet. Long cyclic endurance testing is not part of the Experimental Clean Combustor Program, even though the engine hardware was designed to withstand long-duration cyclic tests. Thus, engine durability testing will remain to be undertaken. The effects of the combustors on related engine components will also require investigation. The breadboard engine fuel control system currently being developed will have to be refined further, with the incorporation of additional functions, such as control of engine bleeds. Finally, the normal sequence of demonstration flight tests for Federal Aviation Agency (FAA) certification will be required.

Pollution Reduction Technology Programs

Shown in table IV-8 are the goals for the Pollution Reduction Technology Programs. For each engine, the CO and THC emissions at idle and the NO_x and smoke emissions at takeoff are compared to the 1979 EPA requirements. The T4 class is comprised solely of the JT8D. The TFE731 and 501D22, which represent the T1 and P2 classes, respectively, are selected from a wide class of engines. Thus, the particular problems shown may not be indicative

of all other engines within these classes. The emission levels required of the JT8D are particularly severe, being a factor of 2 lower than those of many other engines in a similar thrust category. Smoke is more significant here than in the case of the T2-class engines. While both the JT8D and TFE731 are able to meet present smoke standards, a design change causing even a slight increase in smoke would not be acceptable. Smoke reduction for the 501D22 is one of its predominant problems, while NO_x and CO seem to be well in hand. Each of the three Pollution Reduction Technology Programs is structured in a similar manner.

The AirResearch TFE731 program structure is typical. Figure IV-24 is a cutaway view of this engine showing the location of the combustor. This T1-class engine has a maximum thrust of 3500 pounds. The airflow exits the high-pressure centrifugal compressor, flows around the combustor, flows through the combustor in the reverse direction, and turns again in exiting the combustor. Because of its small size and reverse-flow design, this combustor has a very high surface-to-volume ratio. Such combustor designs typically exhibit problems in reducing idle pollutants because of quenching of the combustion reaction at the wall.

The test hardware concepts that will be evaluated in the TFE731 program are outlined in figure IV-25. In initial tests, modifications to the baseline combustor will be evaluated. Such modifications are typified by the use of standard nozzles in an air-assist mode or by changes to the dilution air pattern. The intent here is to determine how much pollution reduction can be achieved without serious combustor redesign. Following this, more sophisticated combustor designs will be studied. The second combustor shown incorporates a redesigned front end and a piloted air-blast or air-assist fuel nozzle. The third concept represents premixing-prevaporizing-type configurations consisting of multiple stages. Each succeeding configuration carries with it an increased potential for achieving the 1979 EPA standards. At the same time, there is an associated increase in complexity and/or difficulty in adapting the design to an engine configuration. At the end of this program, as in each of the other two Pollution Reduction Technology Programs, the amount of combustor redesign required for a given reduction of pollutant achieved will be evaluated.

REDUCTION OF OXIDES OF NITROGEN EMISSIONS AT CRUISE

Preceding discussions have concentrated on emissions during the EPA takeoff-landing cycle, which affect pollution levels only near ground level. Nitrogen oxides emitted during altitude cruise are also of concern, however, particularly for aircraft flying in the stratosphere. The Climatic Impact Assessment Program (CIAP) has investigated altitude pollution and concluded that, in order to prevent depletion of the ozone layer, reductions in current NO_x emissions of six- to sixtyfold may be necessary, depending on the size of the aircraft fleet and the cruise altitude.

Many of the techniques discussed for NO_x reduction at takeoff are also applicable for NO_x reduction during cruise. Figure IV-26 shows the current status of altitude-cruise NO_x emissions. These data are for typical supersonic-cruise operating conditions, including combustor inlet temperatures of about 1000° F and pressures of 4 to 6 atmospheres. Current supersonic transport (SST) combustors, such as those used on the Concorde or the TU-144, emit 18 to 20 g of NO_2 per kg of fuel during cruise conditions. The best experimental combustors from the screening phase of the T2 class in the Emission Reduction Technology Program produce about 8 g/kg. However, some practical problems remain to be solved before production can proceed with these concepts. Premixing flame tubes operating under ideal conditions have, as previously stated, displayed levels of 0.5 to 1.5 g/kg. Premixing combustors are a long way from production. However, they are already receiving some developmental attention in the industry and Lewis has a contract with Solar Division of International Harvester which includes work on premixing-type combustors. Finally, tests of catalytic reactors have exhibited NO_x emissions of less than 0.25 g/kg. However, the catalytic reactor approach poses the greatest practical problems and will require the most developmental effort before its feasibility can be determined.

It is apparent that although techniques exist to demonstrate combustion with low NO_x levels, a great deal of research and development will be required to produce a practical combustor with six- to sixtyfold reductions in NO_x emissions.

CONCLUDING REMARKS

Each emissions reduction concept must be judged by comparing its potential for reducing emissions against both development difficulties and its effects on engine performance and durability. We should learn more regarding the practicality of using these various concepts in the engine demonstration phases of the various Emissions Reduction Technology Programs. In summary, techniques listed in table IV-9 that may be used to reduce total hydrocarbons and carbon monoxide at low power include air-assist and air-blast fuel injection and fuel scheduling. The use of any of these techniques requires a relatively moderate change in the engine's fuel system.

Among the techniques that may be used at full power, the concept of water injection provides an acceptable means of eliminating oxides of nitrogen at takeoff conditions but, of course, could not be used for cruise operation. There are other disadvantages to water injection related to the need for demineralization and antifreeze protection. Thus, the use of a "dry" corrective approach is more desirable. Using modular combustor designs that burn leaner fuel-air mixtures involves a major modification to the engine. Perfecting a lean premixing-prevaporizing combustor design will require a very major research and development effort. Much research is still required to apply the fundamental data on premixing-prevaporizing combustors that have been generated with laboratory combustors to a practical aircraft combustor design. Catalytic reactors have not yet been fully investigated in small-scale burner facilities. A great deal of research remains to be done to determine whether it is feasible to use a catalytic reactor as a gas turbine combustor.

Finally, since the dilemma of reducing pollutants at both low-power and full-power levels exists, it will probably be necessary to design combustion systems that combine low- and full-power concepts by using either multiple burning zones or variable geometry. The use of multiple burning zones will require a major modification to the combustion chamber. If it becomes necessary to use variable geometry to control fuel flow and airflow distribution, a very major modification to the design of the combustion system will be required. In conclusion, we believe that good progress has been made in defining the pollution problem and in reducing pollutants. However, a considerable amount of research and development remains to be done to determine

the minimum level to which emissions may be reduced by using practical engine hardware.

REFERENCE

1. Aircraft Propulsion. NASA SP-259, 1970.

TABLE IV-1. - AIRCRAFT ENGINE POLLUTION
[LOW ALTITUDE, <3000 FT.]

ENGINE EMISSION	ENVIRONMENTAL EFFECT
CO	TOXIC GAS
THC (TOTAL HYDROCARBONS)	ODORS PHOTOCHEMICAL SMOG
NO_x	TOXIC GAS PHOTOCHEMICAL SMOG
SMOKE	VISIBLE PARTICLE DEPOSITION

CS-73135

120

TABLE IV-2. - EPA ENGINE CLASSES

ENGINE CLASS	DEFINITION	APPLICATION
T1	TURBOFAN/TURBOJET < 8000-LB THRUST	GENERAL AVIATION
T2	TURBOFAN/TURBOJET > 8000-LB THRUST	WIDE-BODY TRANSPORTS
T3	JT3D MODELS	B707, DC-8
T4	JT8D MODELS	B727, B737, DC-9
T5	SUPERSONIC CRUISE ENGINE	SUPERSONIC TRANSPORTS
P2	TURBOPROPS	GENERAL AVIATION

CS-73146

TABLE IV-3. - IDLE POLLUTION MECHANISMS

AND CORRECTIONS

[PRINCIPAL IDLE POLLUTANTS: CO AND THC;
PRINCIPAL CAUSES: LOW VALUES OF FUEL-NOZZLE
PRESSURE DROP, FUEL-AIR RATIO COMBUSTOR
INLET TEMPERATURE AND PRESSURE.]

POLLUTION MECHANISM	CORRECTION
POOR ATOMIZATION & DISTRIBUTION	IMPROVE ATOMIZATION & DISTRIBUTION
POOR COMBUSTION STABILITY	INCREASE EQUIVALENCE RATIO TO 1
QUENCHING	INCREASE RESIDENCE TIME REDUCE VELOCITY DELAY MIXING

CS-73148

121

TABLE IV-4. - FULL-POWER POLLUTION MECHANISMS AND CORRECTIONS

[PRINCIPAL POLLUTANT: NO_x;
PRINCIPAL CAUSES: HIGH VALUES OF COMBUSTOR INLET TEM-
PERATURE, PRESSURE, AND FUEL-AIR RATIO.]

POLLUTION MECHANISM	CORRECTION
HIGH FLAME TEMP	LOWER FLAME TEMP BY ADDING DILUENTS (WATER) BURNING LEANER MIXTURES PREMIXING FUEL & AIR PREVAPORIZING FUEL
EXCESSIVE RESIDENCE TIME	REDUCE RESIDENCE TIME BY INCREASING VELOCITY RAPID QUENCHING

CS-73149

TABLE IV-5. - OVERALL POLLUTION REDUCTION APPROACHES

POLLUTANT REDUCTION APPROACH	
CO & THC	NO_x
BURN STOICHIOMETRIC MIXTURE	BURN LEAN MIXTURE
MAXIMIZE RESIDENCE TIME	MINIMIZE RESIDENCE TIME
IMPROVE FUEL ATOMIZATION & DISTRIBUTION	

CS-73138

TABLE IV-6. - EMISSIONS REDUCTION TECHNOLOGY PROGRAMS

ENGINE CLASS	ENGINE DEMONSTRATION	STATUS
T1	AIRESEARCH TFE731	PHASE I INITIATED
T2	GENERAL ELECTRIC CF6-50 ⎫ PRATT & WHITNEY JT9D-7 ⎭	PHASE I COMPLETE, PHASE II INITIATED
T4	PRATT & WHITNEY JT8D-17	PHASE I INITIATED
P2	ALLISON 501D22	PHASE I INITIATED

CS-73145

TABLE IV-7. - GOALS FOR T2-CLASS ENGINES IN EXPERIMENTAL

CLEAN COMBUSTOR PROGRAM

POLLUTANT	ENGINE MODE	1979 REQD VALUE	JT9D-7 ENGINE CURRENT VALUE	CF6-50 ENGINE CURRENT VALUE
NO_x, g/kg	TAKEOFF	13	32	36
CO, g/kg	IDLE	22.5	75	67
THC, g/kg	IDLE	4.5	27	27
SMOKE, SAE NO.	TAKEOFF	<25	12	15

CS-73147

123

TABLE IV-8. - GOALS FOR T4-, T1-, AND P2-CLASS ENGINES IN POLLUTION REDUCTION TECHNOLOGY PROGRAMS

PHASE III ENGINE	THC, g/kg (IDLE)		CO, g/kg (IDLE)		NO$_x$, g/kg (TAKEOFF)		SMOKE, SAE NO. (TAKEOFF)	
	PRES.	1979 REQD	PRES.	1979 REQD	PRES.	1979 REQD	PRES.	1979 REQD
JT8D-17	8	2.1	35	12.2	27	5	25-30	<25
TFE731	23	5	62	25	21	12	32-44	40
501D22	13	6	27	33	10	16	55	29

CS-73164

TABLE IV-9. - ASSESSMENT OF EMISSIONS REDUCTION TECHNOLOGY

POWER LEVEL	TECHNIQUE	REQUIRED ENGINE MODIFICATION
LOW	FUEL PREPARATION: AIR-ASSIST FUEL INJECTION AIR-BLAST FUEL INJECTION FUEL SCHEDULING	MODERATE
FULL	WATER INJECTION	
	LEANER FUEL-AIR MIXTURES: MODULAR PREMIX-PREVAPORIZATION CATALYTIC REACTOR	MAJOR VERY MAJOR EXTREME
ALL	MULTIPLE COMBUSTION ZONES	MAJOR
	VARIABLE GEOMETRY	VERY MAJOR
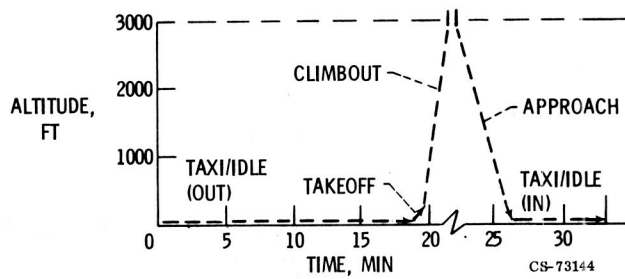
Figure IV-1. - EPA takeoff-landing cycle.
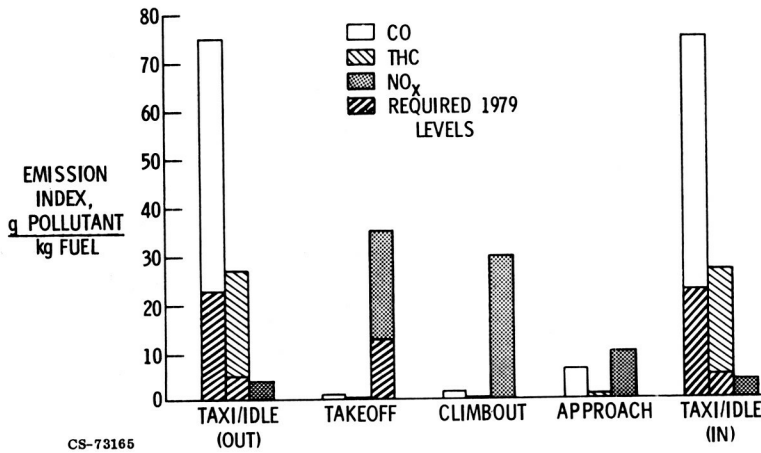
Figure IV-2. - Typical T2-class engine emissions.

125
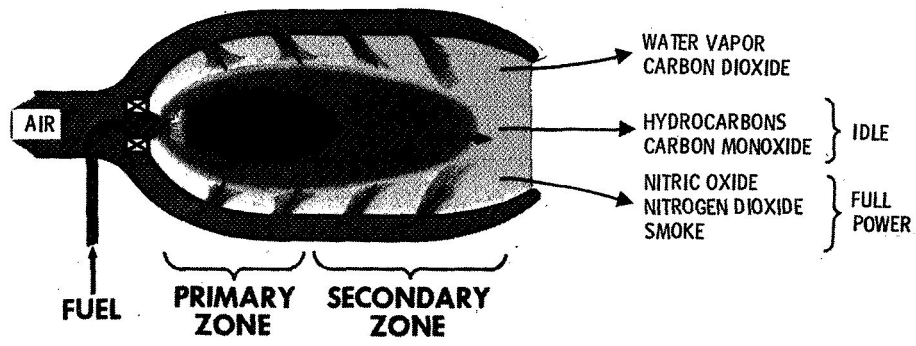
Figure IV-3. - Typical combustor showing emissions.
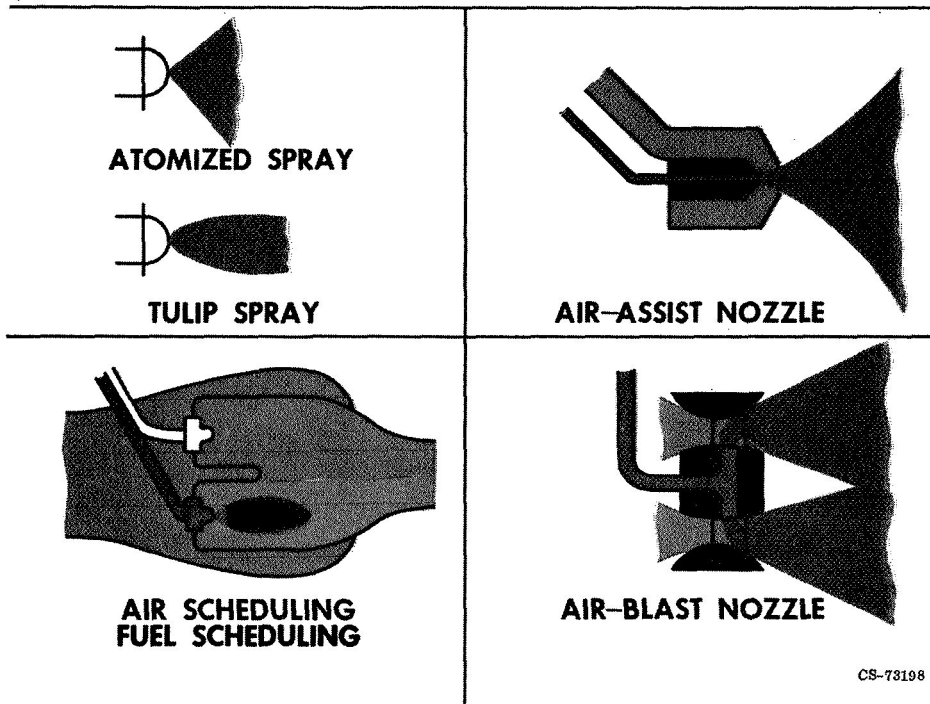
Figure IV-4. - Emissions reduction at idle.
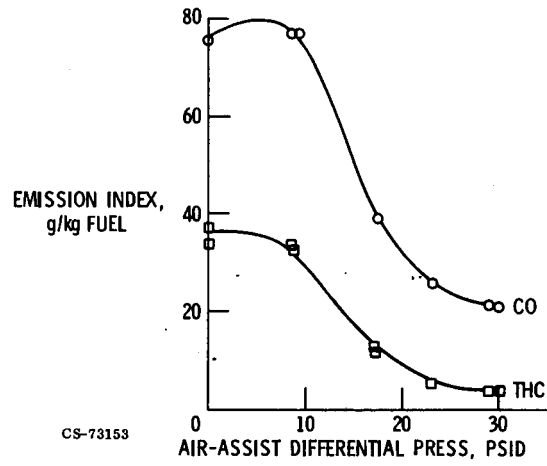
Figure IV-5. - Effect of improving fuel atomization on idle emissions.
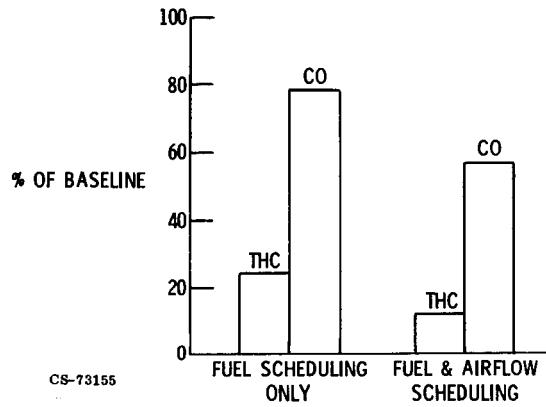
Figure IV-6. - Effect of fuel flow and airflow scheduling on idle emissions.
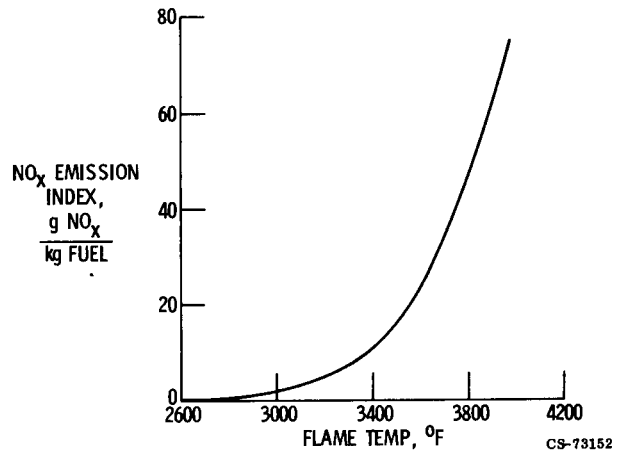
Figure IV-7. – Effect of flame temperature on NO_x emissions.
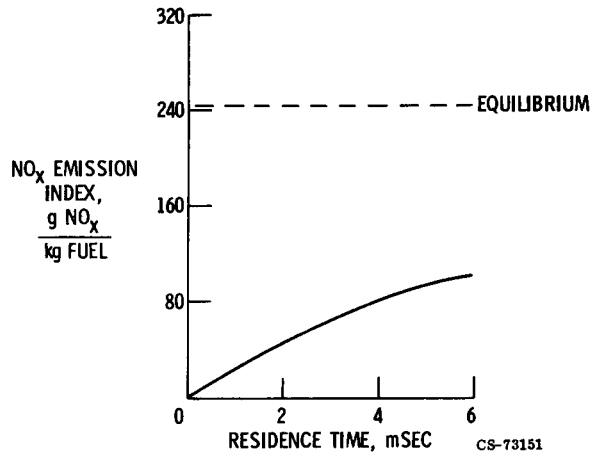
Figure IV-8. – Effect of residence time on NO_x emissions.

128
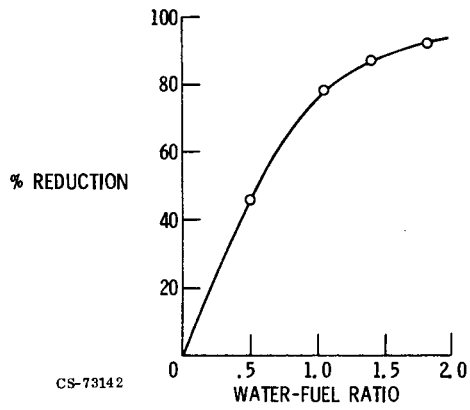
Figure IV-9. - Effect of water injection on NO_x emissions.

CS-73142
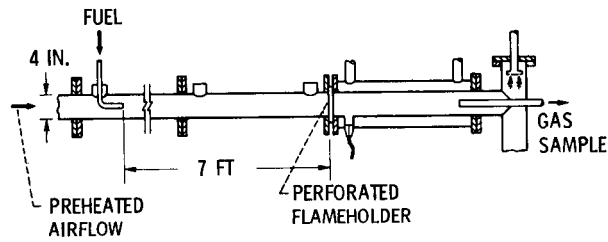
Figure IV-10. - Premixed-primary-zone test section.

CS-73137

129
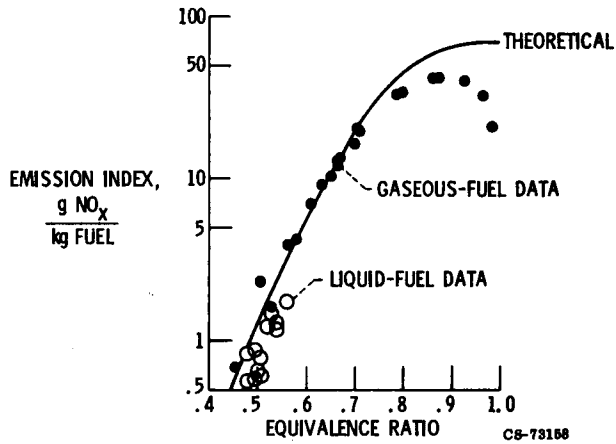
Figure IV-11. - Nitrogen oxides emissions from premixing-prevaporizing test section.
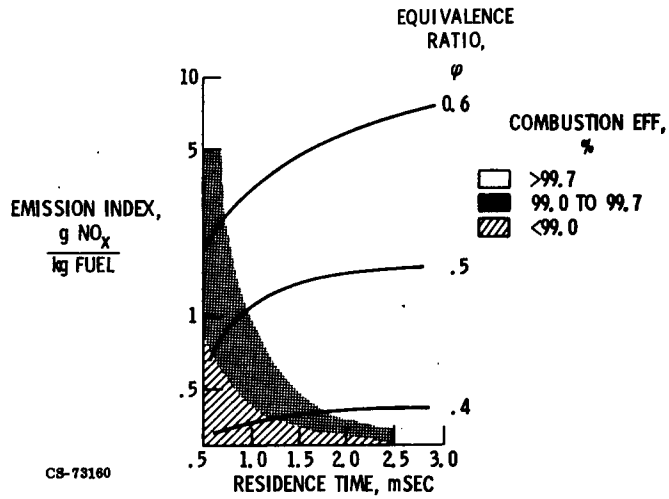
Figure IV-12. - Effect of residence time on NO_x emissions for various combustion efficiencies and equivalence ratios.
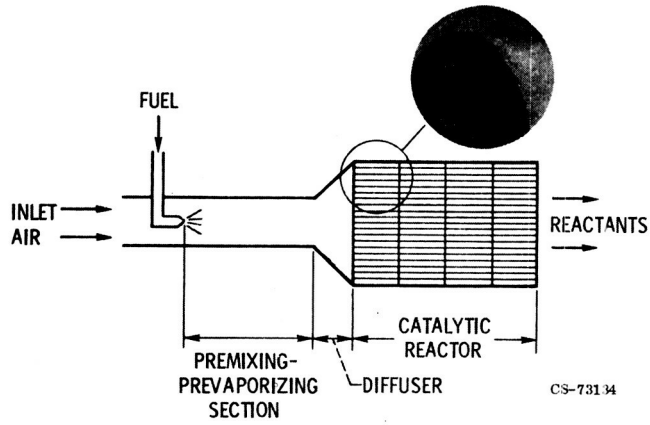
Figure IV-13. - Schematic of catalytic combustor.

INLET AIR

FUEL

PREMIXING-
PREVAPORIZING
SECTION

DIFFUSER

CATALYTIC
REACTOR

REACTANTS

CS-731 34
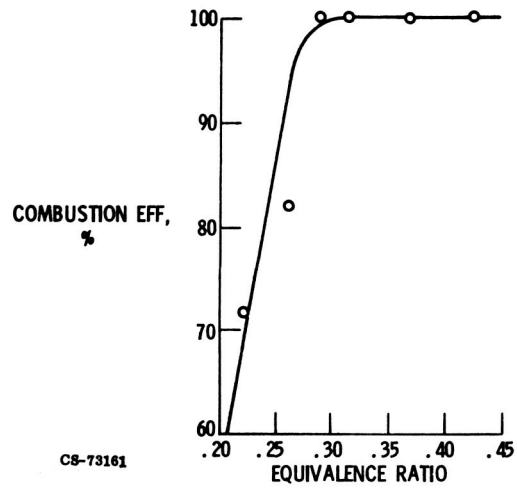
Figure IV-14. - Combustion efficiency with catalytic reactor.

COMBUSTION EFF,
%

EQUIVALENCE RATIO

CS-73161

CROSS-SECTIONAL VIEW

FUEL

PREMIX

120 FUEL INLETS

LOCALIZED
RECIRCULATION
ZONES

AIRFLOW

MODULE COMPONENTS

FUEL

AIRFLOW

CS-64851

CARBURETOR   SWIRLER   FLAME
STABILIZER
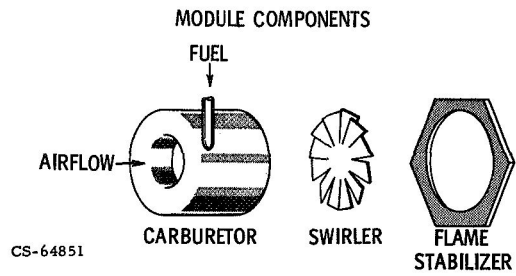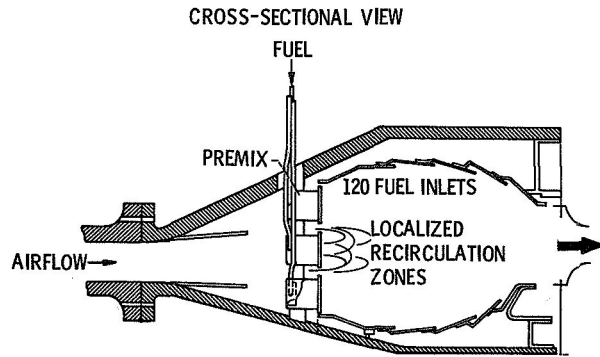
Figure IV-15. - Experimental modular combustor.

C-70-869
CS-53891
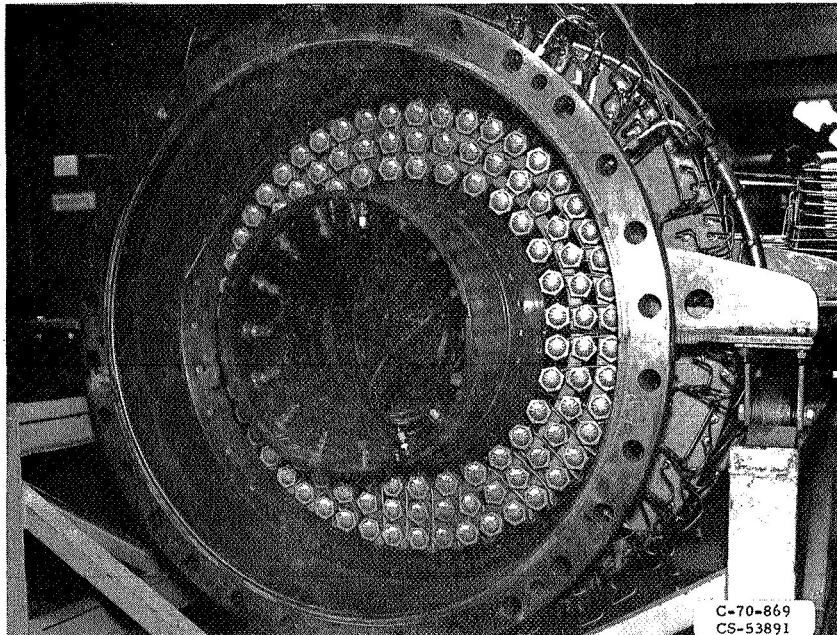
Figure IV-16. - High-temperature swirl-can combustor.
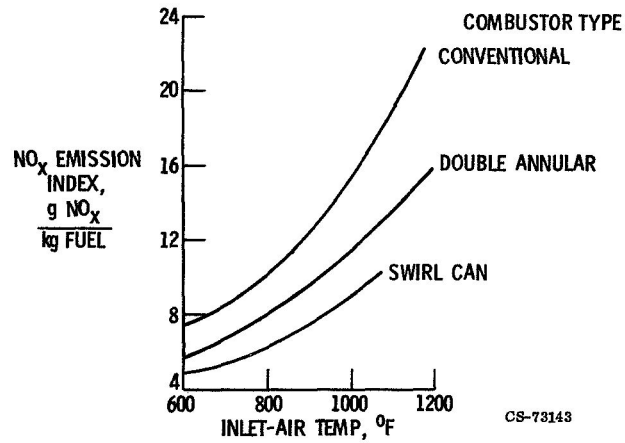
Figure IV-17. - Effect of combustor inlet temperature on NO_x emissions. Combustor pressure, 6 atm.

THRUST - 43 500 LB MAX
PRESSURE RATIO - 22:1

JT9D P&W

THRUST - 50 000 LB MAX
PRESSURE RATIO - 30:1

CF6-50 G.E.
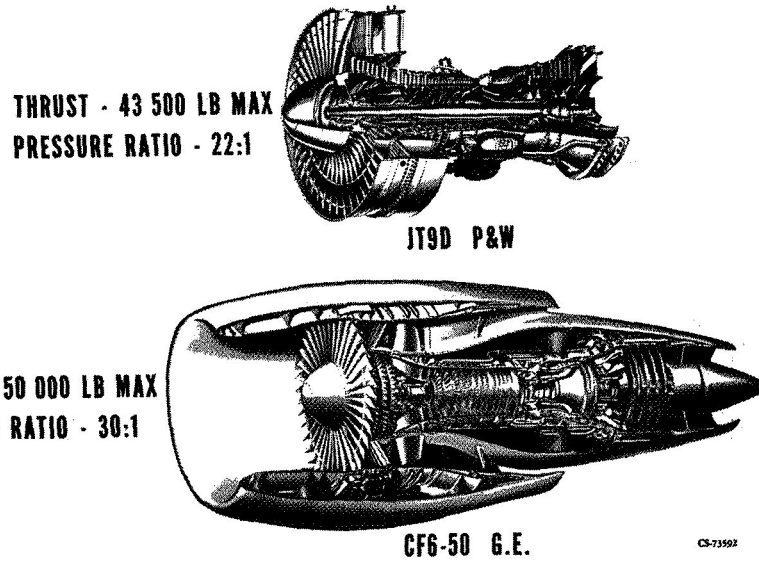
Figure IV-18. - T2-class engines evaluated in Experimental Clean Combustor Program.

PILOT STAGE

MAIN STAGE

HYBRID COMBUSTOR

FUEL

PILOT STAGE

MAIN STAGE

VORBIX COMBUSTOR

FUEL

CS-73150
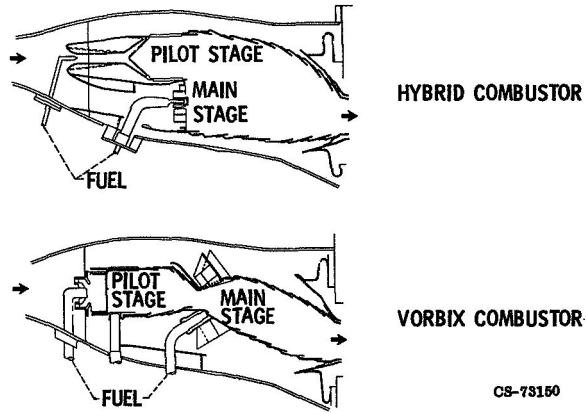
Figure IV-19. – Schematic drawings of JT9D combustors evaluated in phase II of Experimental Clean Combustor Program.
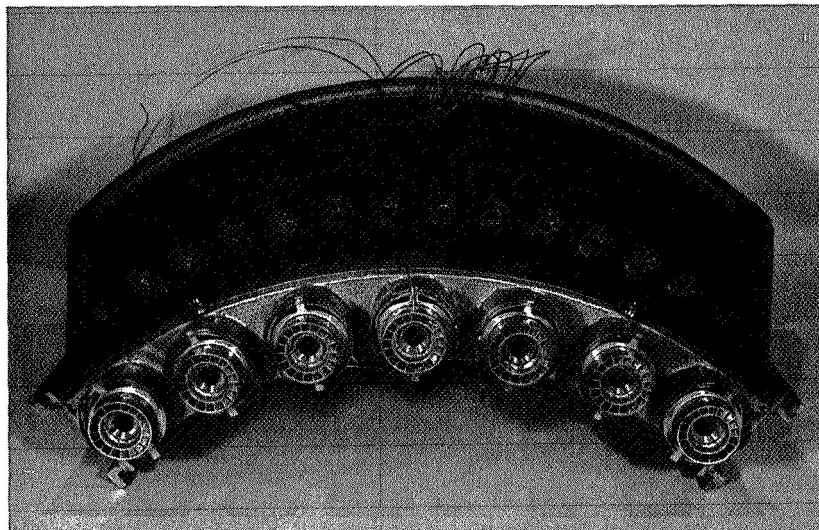
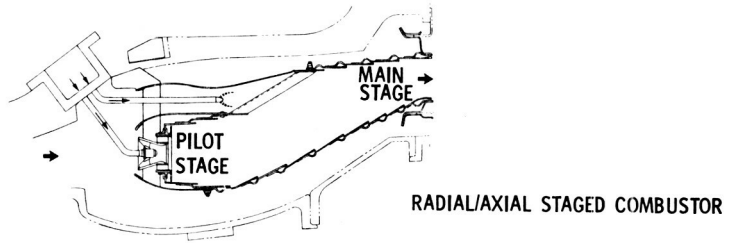

CS-73117

Figure IV-20. – Sector of Vorbix Combustor.

RADIAL/AXIAL STAGED COMBUSTOR

DOUBLE-ANNULAR COMBUSTOR

CS-73157
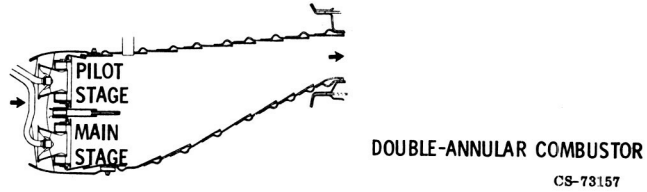
Figure IV-21. - Schematic drawings of CF6-50 combustors evaluated in phase II of Experimental Clean Combustor Program.
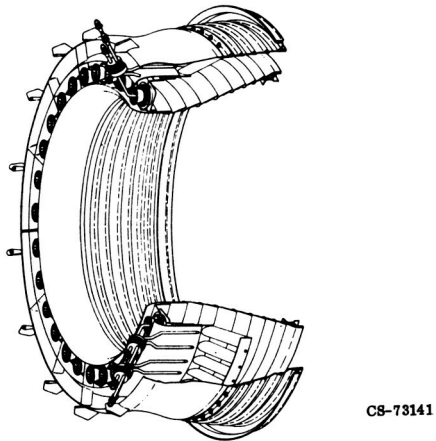

CS-73141

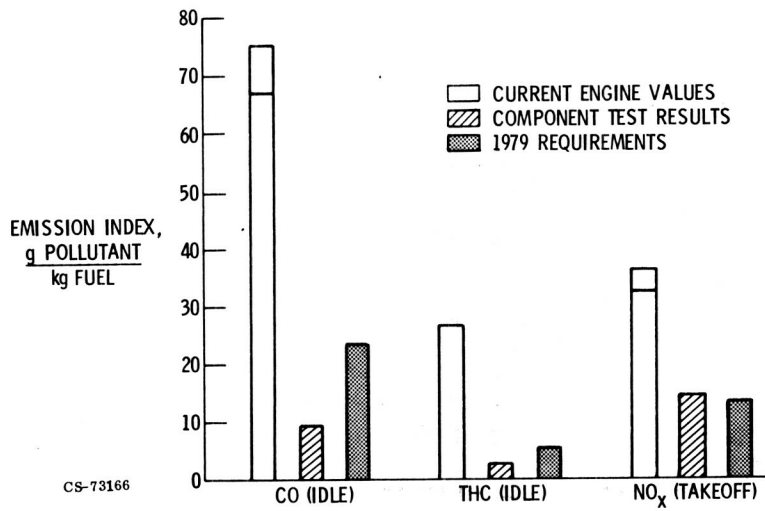Figure IV-22. - Radial/axial staged combustor.

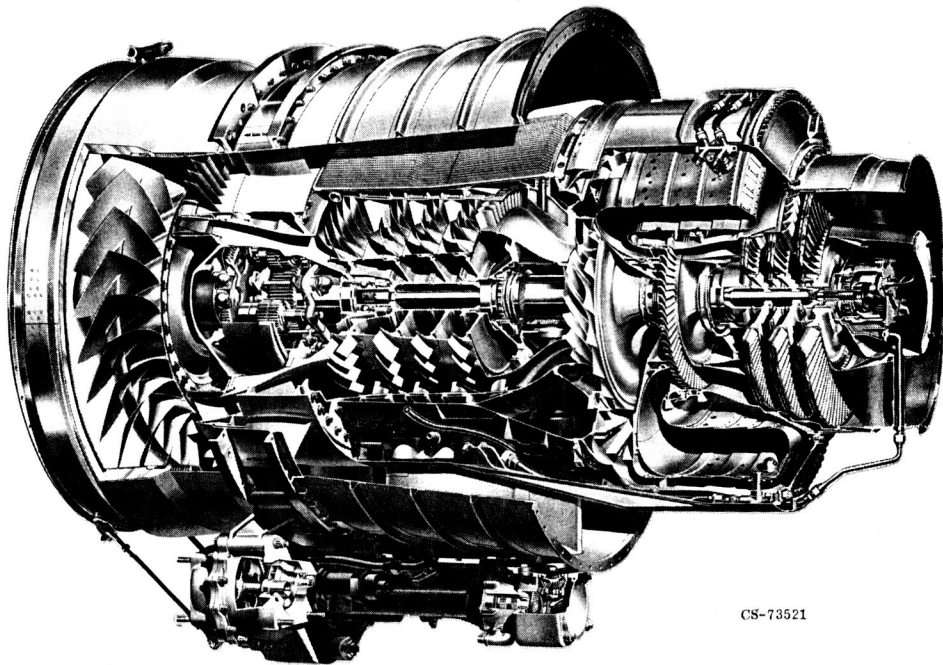Figure IV-23. - Pollution reduction achieved in Experimental Clean Combustor Program for T2-class engines.

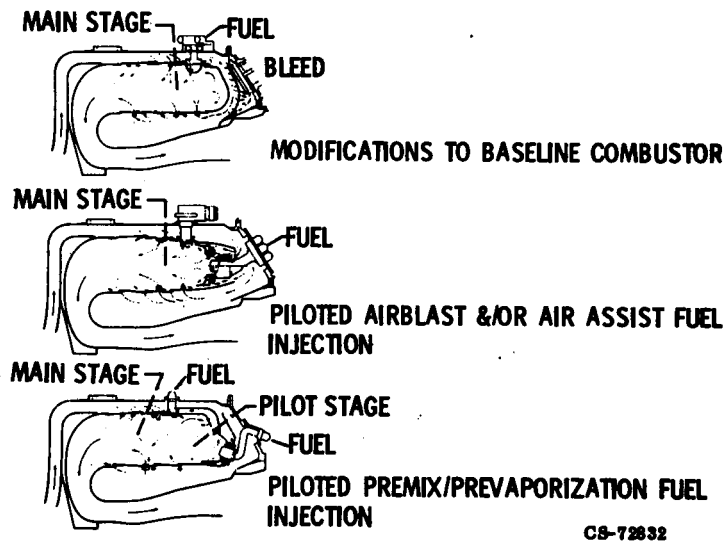Figure IV-24. - Cutaway view of TFE731 engine.

MAIN STAGE ┐ ┌FUEL

BLEED

MODIFICATIONS TO BASELINE COMBUSTOR

MAIN STAGE ┐

FUEL

PILOTED AIRBLAST &/OR AIR ASSIST FUEL INJECTION

MAIN STAGE ┐ ┌FUEL

PILOT STAGE

FUEL

PILOTED PREMIX/PREVAPORIZATION FUEL INJECTION

CS-72832

Figure IV-25. - Schematic drawings of possible combutor modifications to TFE731 engine.

EMISSION INDEX, g NO_x / kg FUEL

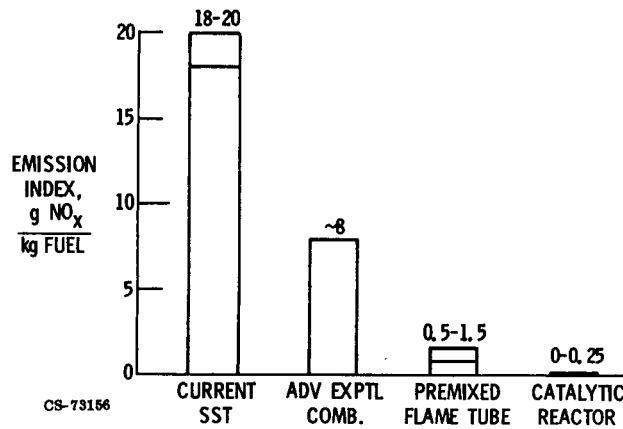|			
18-20	~8	0.5-1.5	0-0.25
CURRENT SST	ADV EXPTL COMB.	PREMIXED FLAME TUBE	CATALYTIC REACTOR

CS-73156

Figure IV-26. - Current status of NO_x emissions at altitude cruise and possible reductions.

Page intentionally left blank

V. UPPER ATMOSPHERE POLLUTION

MEASUREMENTS (GASP)

Richard A. Rudey and James D. Holdeman

The past 5 years have seen an increasing awareness of the potential problems that may occur due to the discharging of certain pollutants into our atmosphere. The EPA has taken regulatory action to control the level of certain emissions from industrial sources and transportation vehicles in the United States. In the case of air transportation, paper IV describes the principal aircraft engine pollutants, their related effects on both the low and high altitude environment, and the EPA regulations for low altitude emissions.

For the high altitude environment (or the upper atmosphere) no such regulations exist. The potential upper atmosphere problem is complex and worldwide, and the data needed for its assessment are difficult to obtain and to evaluate. Because of this, both national and international environmental impact programs will be needed in the future. An example of a national program is the NASA Stratospheric Research Program that is now being organized. The Lewis program described in this paper is an important part of this NASA effort.

THE POTENTIAL UPPER ATMOSPHERE PROBLEM

Two recent climatic impact studies, the Climatic Impact Assessment Program (CIAP) and a study conducted by the National Research Council (NRC), arrived at the conclusion that, if future large fleets of aircraft were to cruise in the upper atmosphere (stratosphere), certain engine effluents could have an adverse effect on our environment. This conclusion was based on several factors that are related to the chemical composition of the engine exhaust and to certain atmospheric properties.

Atmospheric Properties

One important atmospheric property, the static air temperature, is illustrated in figure V-1. That portion of the atmosphere where the temperature decreases with altitude is the troposphere, which can extend to an altitude varying from approximately 25 000 to 50 000 feet. This variation is both seasonal and geographical. The troposphere can be generally characterized as a turbulent region with a large amount of both vertical and horizontal mixing. This turbulence, along with associated rainfall, allows the troposphere to rapidly cleanse itself of most impurities. Pollutants injected into it normally have short residence times - on the order of days or weeks. The region of the atmosphere where the temperature-altitude relationship changes from decreasing to increasing is known as the tropopause. It is generally characterized by an altitude band rather than a discrete point. Above the tropopause is the stratosphere where the temperature increases with altitude. This increasing temperature characteristic is similar to the temperature inversions that contribute to our urban smog problem when they occur over large cities. In the stratosphere, the increasing temperature inhibits vertical mixing, thus the region is quite stable and any pollutants injected into it have long residence times - on the order of months and possibly years. However, horizontal dispersion around the globe is quite rapid - on the order of weeks. Thus, the effect of a pollutant injected into the atmosphere at one geographical location can be worldwide.

Two other important properties of the upper atmosphere, ozone and particulates, are illustrated in figure V-2. The ozone layer, which has its peak concentration at approximately 70 000 feet, absorbs short wave ultraviolet solar radiation. This absorption capability allows life to exist on Earth in its present form; hence, any change in the concentration level of the ozone layer could produce biological effects on the Earth's surface.

The particulate (aerosol) layer, which is composed of both solid and liquid particles, has a significant effect on the heating of the atmosphere and influences the radiation balance of heat at the Earth's surface. Any change in the thickness, composition or extent of this layer could produce climatic changes. There is a natural variability in both of these layers which is not clearly understood and which contributes to much uncertainty in climatic impact studies.

Aircraft Engine Effluents

Those aircraft engine effluents of most concern in the upper atmosphere and their associated potential environmental effects are listed in table V-1. Oxides of nitrogen (NO_x) are highly reactive with ozone (O_3) and may cause a reduction in the ozone layer. This reduction could result in an increase of short wave ultraviolet radiation on the Earth's surface, thus producing possible biological effects. The other three effluents, sulphur dioxide (SO_2), water vapor, and particulates, could contribute to a change in the density and composition of the atmospheric particles. The result could be a change in the Earth's radiation balance and, potentially, the climate. Of these engine effluents, the amount of NO_x emissions are considered the most important from an environmental viewpoint. This is the principal reason for the concentrated effort to reduce cruise NO_x that is discussed in paper IV.

If these potential environmental effects are of concern, the question arises as to why there are no regulations governing the injection of these effluents into the upper atmosphere. One reason is that the potential effect was only recently recognized (about 1971). Another reason is the high degree of uncertainty involved in assessing the effects of these aircraft effluents as distinguished from the natural variability of atmospheric properties and the effects of other man made pollutants injected at ground level. (One of these ground level pollutants will be discussed later.) A principal contributor to the uncertainty is the lack of comprehensive, long term upper atmosphere data.

UPPER ATMOSPHERE MEASUREMENTS

There are several programs currently underway to obtain the necessary data, and they include a variety of measurement techniques. The ultimate future system will probably utilize remote sensing devices aboard satellites to provide continuous global monitoring. Even though an operational satellite system is not likely within this decade, an experimental system is scheduled for launch on the Nimbus G satellite in the late 1970's. Until the time when a satellite system becomes operational, most upper atmosphere data will be obtained by using airplane, balloon, and rocket instrument carriers. Of

these three techniques only airplanes have both independent altitude and location flexibility.

One airplane currently in use for making atmosphere measurements is the U2 (fig. V-3). This aircraft is being flown out of the NASA Ames Research Center to measure NO_x, water vapor, carbon monoxide (CO), ozone and chlorofluoromethane concentrations in the atmosphere from altitudes of 20 000 to 70 000 feet. The air sampling instruments and an inlet probe are located in the lower part of the fuselage. Another aircraft currently in use for making atmospheric measurements is the WB-57F aircraft being flown out of the NASA Johnson Space Center in cooperation with the Department of Transportation (fig. V-4). Measurements of NO_x, particulates, ozone, and water vapor are being made with this aircraft up to altitudes of 60 000 feet. Air sampling instruments are located in the fuselage, and inlet probes are located in the nose. Both aircraft have large, lightly loaded wings and can easily penetrate the stratosphere. However, they are dedicated research vehicles and are used on an as-required and relatively local basis. As such, they do not provide a continuous, global data gathering capability.

Global Air Sampling Program

About 3 years ago the use of commercial airliners as instrument carriers on a continuous global basis was considered. A study was initiated by Lewis with commercial airlines and aircraft manufacturers to determine the feasibility of this approach. The feasibility question was answered in the affirmative and out of this study came the now operational Lewis Global Air Sampling Program (GASP). The objectives of GASP are to provide baseline data of selected atmospheric constituents in the upper troposphere and lower stratosphere (from 20 000 to 40 000 ft) and to assess potential adverse effects between aircraft exhaust emissions and the natural atmosphere. The approach being used is to install and operate automated instrument systems on commercial Boeing 747 aircraft, to acquire global air quality data during routine airline operation, and to document and analyze these data for 5 to 10 years. The 747 aircraft was selected because it has the space available for locating a measurement system, it has an inertial navigation system for determining geographical location, and it operates on a global route structure.

Atmospheric constituents of concern. - The upper atmosphere constituents to be measured and related information needed for data analysis were also determined during the feasibility study and are shown in table V-2. The constituents are divided into two major groups - particulates and gases. In the particulate group the number density and the size distribution will be measured on a continuous basis. Mass concentration and chemical composition will be obtained by periodically collecting a filter sample. Laboratory analysis techniques will then be used to determine the presence of sulfates, nitrates, and carbon. The gases will be measured continuously using a dedicated instrument for each constituent except for the chlorofluoromethanes, which will be determined from laboratory analysis of air samples periodically collected in cylindrical containers. Chlorofluoromethanes are one form of inert gas used as a propellant in many aerosol spray cans. Recently, these species have been the subject of a controversy regarding stratospheric ozone destruction. This has led to the inclusion of this measurement in GASP even though it is not related to aircraft emissions. The list of measurements contains most of the constituents that are known to be important for determining the potential effect of aircraft emissions on the upper atmosphere plus others, such as chlorofluoromethanes, which are pollutants injected at ground level.

In addition to the air sample measurements, geographical information (such as latitude and longitude), meteorological information (such as temperature, pressure, wind direction, and velocity), and aircraft operational information (such as altitude, flight Mach number, and time) are obtained from aircraft systems. These data will be recorded along with the air sample data to precisely describe conditions when a data point is recorded.

The 747 measurement system. - The design, fabrication, and installation of the 747 air sampling systems have been contracted to United Airlines. The constituent measuring part of the system is shown in figure V-5. The instruments for measuring CO, O_3, water vapor, and particles were developed by Lewis from commercially available units. The flow control unit was also developed by Lewis and was provided along with the instruments as government furnished equipment (GFE) to United. United integrated the GFE with a data management and control unit (DMCU), a flight data acquisition unit (FDAU), a cassette tape recorder, and all the supporting wiring and aircraft interconnects. The equipment is packaged to fit on standard ARINC (Aeronautical Radio, Inc.) approved racks and has been certified by the FAA

for flight operation. A small, portable system development panel (SDP) is used to periodically check the operation of the system between flights. It can also be used in-flight on properly equipped aircraft.

The entire air sampling system is installed directly below the first class compartment of the aircraft (fig. V-6). The constituent measuring system is located adjacent the nose gear wheel well. (See fig. V-6 insert.) Air samples are collected by probes located under the nose of the aircraft and delivered to the gas measuring instruments through a 1-inch line and to a particulate collecting filter located on the opposite side of the aircraft through a 3-inch line.

A photograph of the probe installations on the United Airlines 747 is shown in figure V-7. The main probe has two inlets. The top inlet collects the air sample for the gaseous and filter measurement systems. The lower inlet is designed for isokinetic sampling at aircraft cruise speeds and collects the air sample for the particle size and distribution measuring system. Isokinetic sampling is obtained when sample velocity inside the probe inlet matches the free-stream velocity. This provides optimum collection of all particle sizes. The main probe cap automatically opens by rotating into the slot when the aircraft exceeds an altitude of 20 000 feet, at which time the system begins to take data. The separate probe located at the top right of the insert contains the water vapor measuring sensor. The entire system operates automatically without attention by the flight crew and in no way interferes with the normal operation of the aircraft. Data can be recorded for up to 24 days under normal operation. The GASP equipped 747 shown in figure V-7 has now been taking data for approximately 6 months.

The 747 route structure. - Current plans call for installing four systems in 747 aircraft from the three airlines shown in figure V-8 plus one additional aircraft yet to be selected. In addition to the United aircraft, a GASP equipped Pan American World Airways aircraft has been in operation on a global basis for about $2\frac{1}{2}$ months. With the addition of a Qantas Airways aircraft in late 1975, global data acquisition will be available over the routes illustrated in figure V-9. A desired route structure for atmospheric analysis as proposed by the National Oceanic and Atmospheric Administration (NOAA) is also shown in this figure. NOAA and NASA will be collaborating on data analysis throughout this program. The route structure of the participating airlines provides data acquisition around the globe in the northern hemisphere

144

and into portions of the southern hemisphere. The lack of acceptable 747 routes is the reason for the missing coverage of some of the desired routes. The bulk of the data will be obtained in the heavily traveled routes of the northern hemisphere where aircraft emission effects are likely to be the greatest.

The near polar route of Pan Am is of special interest because much of the data will be obtained in the stratosphere, which is extremely important in terms of potential environmental problems. The southern hemisphere routes of Qantas are important because the air there is generally much cleaner than in the northern hemisphere. This is because atmospheric flow circulation patterns near the equator act as a barrier to prevent the pollutants discharged into the northern hemisphere from being transported to the southern hemisphere. The Qantas routes will provide data to compare the air qualities of the two hemispheres. The frequency of the United flights over the continental United States and Hawaii will provide a good statistical data base for this region.

Examples of GASP data. - An example of one type of data obtained during a United Airlines flight from Chicago to Honolulu is shown in figure V-10. The upper plot shows the aircraft's geographical location. An outline of the continental United States is shown for reference purposes. The lower plot shows the ozone readings that were obtained during the flight as a function of longitude. The ozone levels were very low at the beginning of the flight which was at a cruise altitude of 31 000 feet. This is a normal ozone level for the troposphere. When the aircraft climbed to a 35 000-foot cruise altitude, the ozone readings rose sharply to a level which is characteristic of readings in the lower stratosphere. An extremely rapid rise and high level of ozone was encountered at 124° W longitude even though the aircraft cruise altitude was constant. Ozone concentrations this high are normally associated with flight operation well into the stratosphere. The data shown in figure V-11 can be used to determine the cause of this ozone level change. At the point where the high ozone concentration began (indicated by the arrows in fig. V-11), a rise in static temperature occurred along with significant changes in both wind direction and wind velocity, indicating that the aircraft encountered significantly different meteorological conditions at this geographical location. A plausible explanation for the ozone rise would be the existence of a polar air mass which normally has higher ozone concentra-

tions at a given altitude (lower tropopause altitude). Regardless of the cause, the data in figure V-10 clearly illustrate some of the natural variability in ozone that was previously mentioned.

Another type of data being obtained is shown in figure V-12. The plot shows a correlation between the number density and size distribution of particles measured during a flight between San Francisco and Honolulu at an average altitude of 39 000 feet. The slope of the distribution curve is similar to that observed at ground level but the density of particles of a given size range is much lower, showing the increased cleanliness of the air at high altitudes. Similar data in less and more heavily traveled air traffic routes will be compared to determine if a correlation exists between air traffic density and particle density and size.

Off-Route Data Acquisition

In addition to the on-route GASP data that will be obtained from the four commercial 747's, two NASA aircraft are being used to help develop measurement and analysis techniques and to obtain off-route and supplemental data. The Ames Research Center CV-990 (fig. V-13) has been used extensively to flight test all of the instruments currently used on the 747's. A typical instrument installation used for flight testing is shown in the lower photograph. This aircraft will continue to be used for development of improved instruments when they become available. An automated GASP system will be built and installed on this aircraft on a semipermanent basis. This will allow off-route data to be obtained during normal aircraft flight experiments and during dedicated flights to specific localities. The aircraft shown in figure V-14 is one of the two Lewis F-106's which are primarily used for propulsion research flight testing. For supporting the GASP work, the aircraft is equipped with two particle sampling filter systems located in removable pods that are attached to the lower surface of the wings as shown in the lower left photograph. The current configuration carries a single filter cartridge in each pod as shown in the lower right photograph. With these pods installed, particulate samples are being obtained up to altitudes of 45 000 feet. This F-106 aircraft is also being equipped to carry a cylindrical container system for obtaining high altitude "grab" samples which will be analyzed for chlorofluoromethanes.

DATA REDUCTION AND ANALYSIS

With all of these measuring systems in operation, a considerable quantity of data will be obtained. Under normal conditions, each 747 operates an average of 10 hours per day, and the GASP system takes a data point every 5 minutes above 20 000 feet. The 747 data and the off-route and supplemental data obtained by the NASA aircraft will be processed as illustrated in figure V-15. The Lewis computer center will compact the data and format it to provide a consistent basis for subsequent analysis. Then, the data will be distributed to three places (see fig. V-15). NASA/NOAA will analyze the data to assess potential pollutant emission effects on a case-by-case basis. (A case may be defined as a particular flight or a group of flights.) NOAA will also perform studies related to meteorology, climatology, and atmospheric chemistry. An independent procedure will be established at Lewis to maintain a complete documentation of all data obtained as a function of time, altitude, and geographical location. Specialized analyses will be performed on particulate mass concentration and composition and on selected gaseous constituent variations. Another flow path for the data will be to a NOAA data storage center at Asheville, North Carolina (National Climatic Center) where it will be available to other atmospheric research programs and to independent researchers on request. NASA Lewis will periodically publish reports describing the type of data available and how it can be obtained from this source.

CONCLUDING REMARKS

Data such as that being obtained in the NASA Global Air Sampling Program will help provide a basis for understanding the complex potential pollution problems in the upper atmosphere. With respect to the work described in this paper, the current status in this quest for understanding can be summarized as follows:

1. The effect of aircraft emissions on the upper atmosphere is presently uncertain. However, the potential reaction of certain species in a jet engine exhaust with ambient atmospheric constituents, such as the $NO-O_3$ reaction, is factual, and is reason for concern. Also, because of certain properties

of the atmosphere, the possibility of environmental impact will likely increase when cruise altitudes go higher into the stratosphere and that the effect, if it occurs, will be worldwide.

2. A comprehensive global air quality data bank must be established on a long term basis. This will be necessary to ferret out the effect of aircraft emissions from the natural variability of the atmosphere and from other man made pollutant sources. For the next decade the bulk of the data will come from aircraft, rocket, and balloon systems. Eventually, satellites using remote sensors should provide a global atmospheric monitoring system.

3. The Lewis Global Air Sampling Program will provide an important continuous input to this global data bank for at least the next 5 to 10 years. These data will be valuable for general atmospheric studies as well as for aircraft emission impact studies.

4. The interest and assistance of United and other airlines and of aircraft manufacturing companies, such as Boeing, has been invaluable. Allowing NASA to install and operate GASP systems on in-service 747 aircraft demonstrates the interest and concern of the airlines in defining the effects of air transportation on our environment. In addition, the interest and participation of the aircraft engine manufacturers in the emission reduction programs (described in paper IV) indicates their concern for reducing engine emissions and minimizing the potential adverse effect of aircraft on our environment.

TABLE V-1. - UPPER ATMOSPHERE EMISSIONS

ENGINE EFFLUENT	POTENTIAL ENVIRONMENTAL EFFECT
OXIDES OF NITROGEN SULFUR DIOXIDE WATER VAPOR PARTICULATES	REDUCTION IN OZONE INCREASE IN SULFATES INCREASE IN CLOUDS INCREASE IN PARTICLES

TABLE V-2. - GASP MEASUREMENTS

PARTICULATES	GASES	RELATED INFORMATION

DENSITY
SIZE DISTRIBUTION
MASS CONCENTRATION
CHEMICAL COMPOSITION
   SULFATES
   NITRATES
   CARBON
	OZONE
	WATER VAPOR
	OXIDES OF NITROGEN
	CARBON MONOXIDE
	CARBON DIOXIDE
	CHLOROFLUOROMETHANES
		GEOGRAPHICAL LOCATION
		METEOROLOGICAL CONDITIONS
		AIRCRAFT OPERATING
		   CONDITIONS
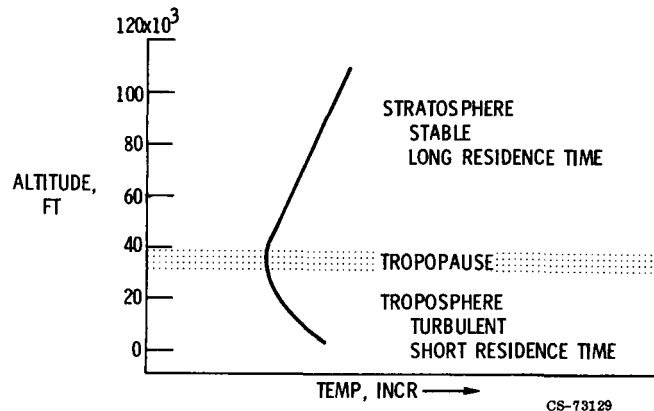
Figure V-1. - Variation of static air temperature with altitude.
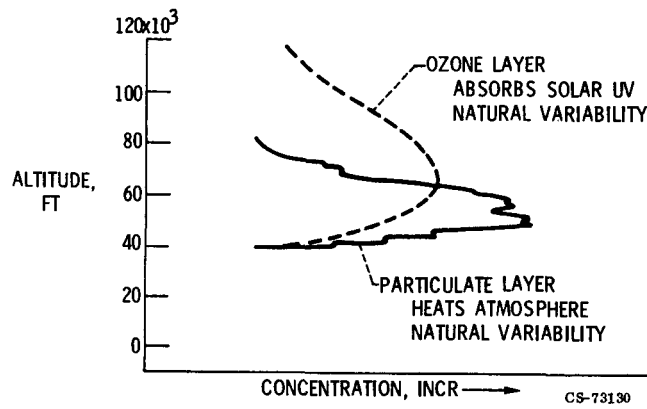
Figure V-2. - Variation of ozone and particulates with altitude.

150

Figure V-3. - U2 aircraft used for atmospheric air quality measurements.
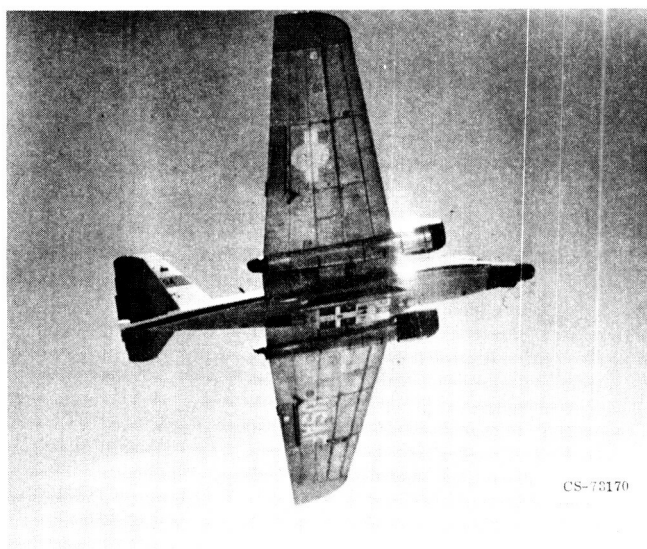
Figure V-4. - WB-57F aircraft used for atmospheric air quality measurements.
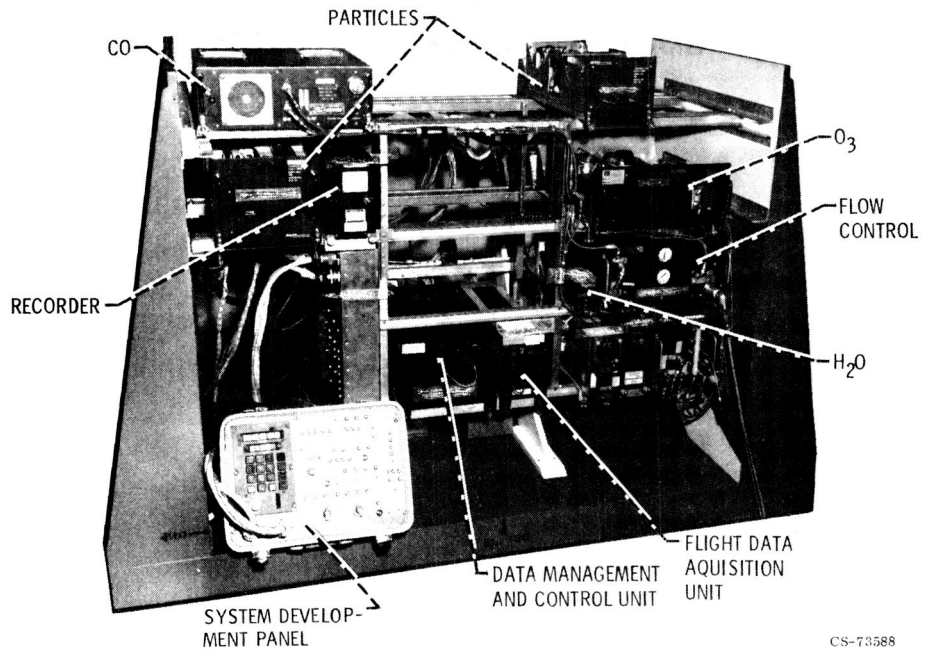
Figure V-5. - GASP constituent measuring system.
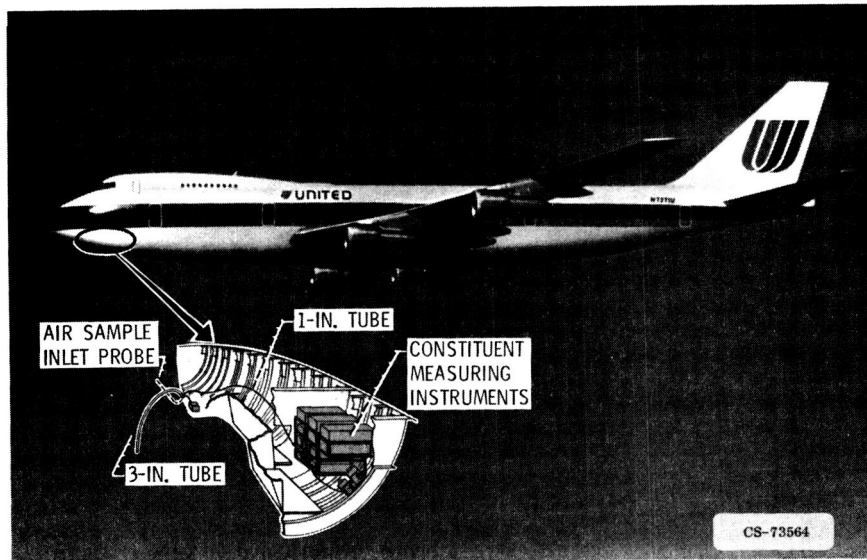
Figure V-6. - GASP system installation.
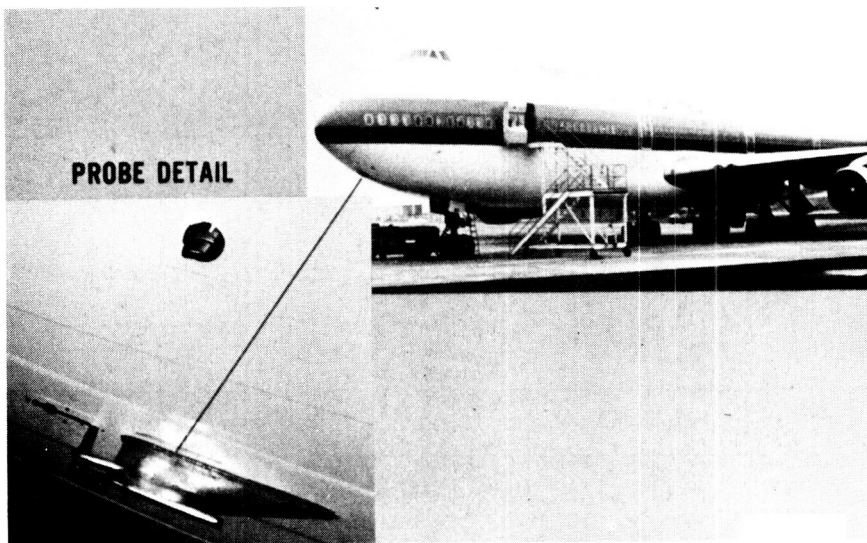
Figure V-7. - First operational GASP aircraft rollout at United Airlines (Dec. 10, 1974).
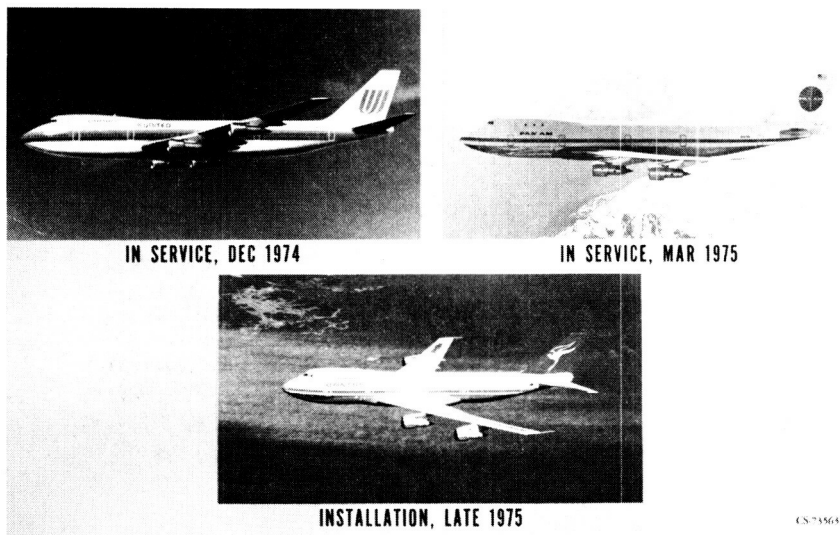
Figure V-8. - Airlines currently participating in GASP.
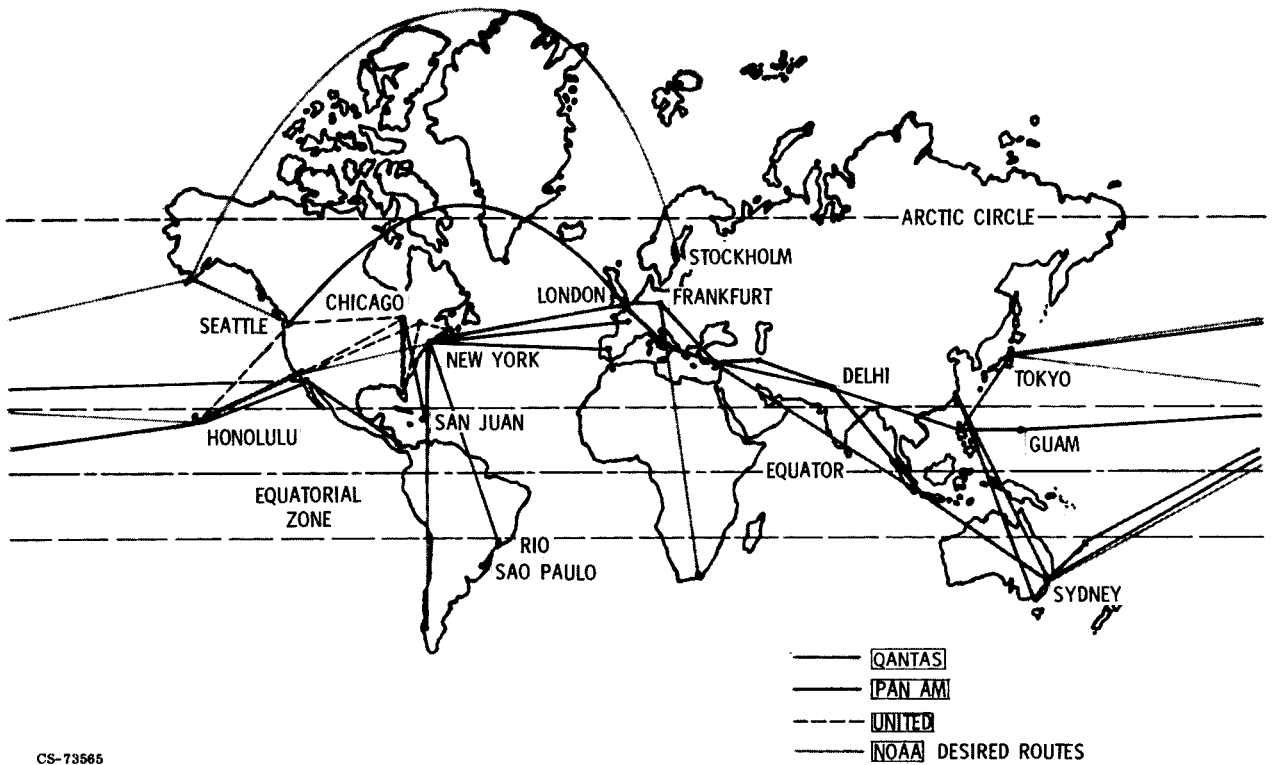
Figure V-9. - GASP route structure.

CS-73565
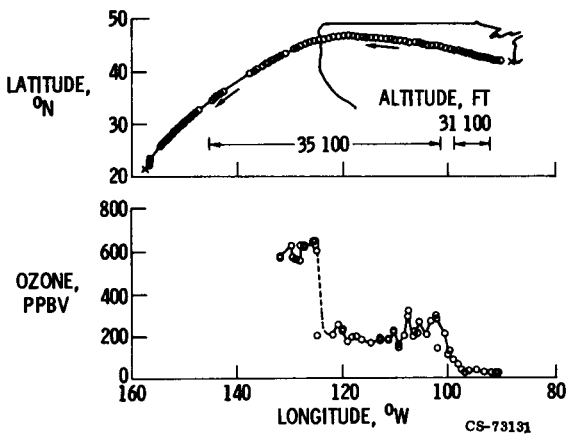
Figure V-10. - Aircraft location and ozone data for Chicago to Honolulu flight on United 747.

CS-73131
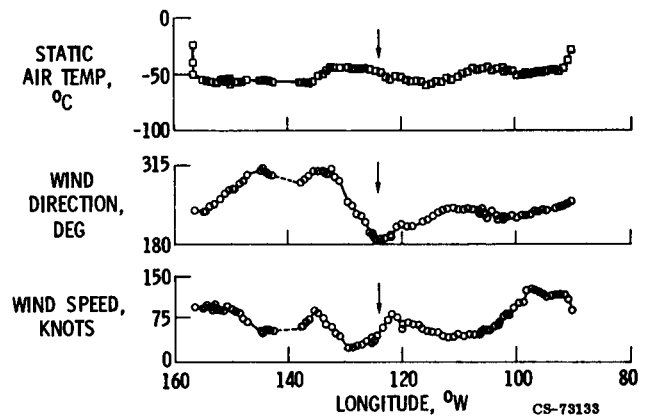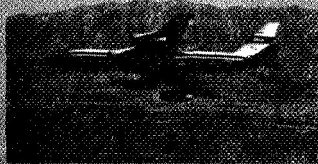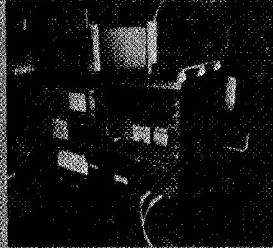

Figure V-11. - Meterological data for the flight in figure V-10.

CS-73133

154
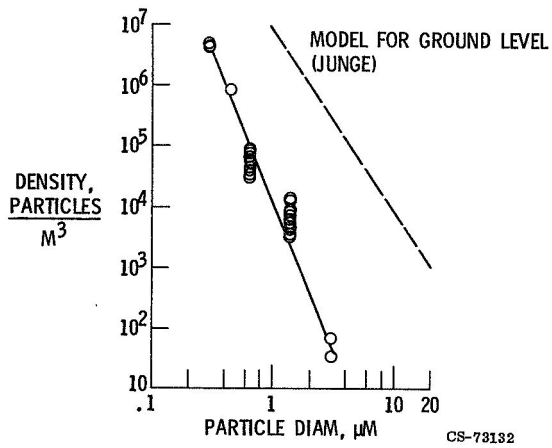
Figure V-12. - Particle size distribution on flight from
San Francisco to Honolulu at 39 000 feet.
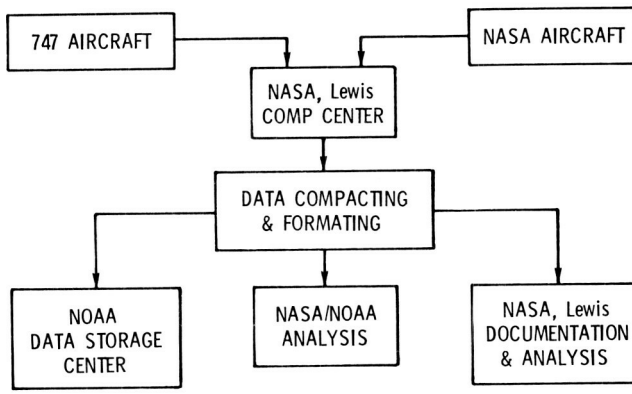

Figure V-13. - GASP instrument evaluation on Ames CV-990.

PURPOSE

FLIGHT EVALUATION OF PARTICLE MEASUREMENT EQUIPMENT, OPERATIONAL PROCEDURES AND SAMPLE ANALYSIS TECHNIQUES, AND SUPPLEMENTAL FLIGHT DATA ACQUISITION FOR THE GLOBAL AIR SAMPLING PROGRAM

LEWIS F-106 AIRCRAFT

PARTICLE SAMPLER POD

FILTER CARTRIDGE

FLOWMETER

INLET CAP

PARTICULATE FILTER INSTALLATION

Figure V-14. - Upper atmosphere particle sampling with F-106.

Figure V-15. - GASP data flow chart.

CS-73125

VI. FUEL-CONSERVATIVE ENGINE TECHNOLOGY

James F. Dugan, Jr., John E. McAulay, Thaine W. Reynolds, and William C. Strack

Fuel conservation is especially important to the aircraft industry be-
cause it depends completely on oil for its fuel. This is unfortunate because
our oil supply is dwindling, and, perhaps as a consequence, the price of fuel is
rising. If nothing is done about the problem, the consequences will be most
unpleasant - more and more dependence on foreign oil, an outflow of cash to
pay for the foreign oil, higher air fares to compensate for rising fuel costs,
a curtailment of air traffic growth, and eventually total depletion of the
world oil supply, conceivably within 100 years.

Fortunately, there are solutions. There are ways to increase our fuel
supply, and it is possible to use fuel more efficiently. With regard to fuel
supply, one attractive long-term solution would be for our country to go to a
hydrogen economy. In this case, our aircraft would be fueled with liquid
hydrogen. A second nearer-term solution is to obtain oil from coal and
oil shale. We have the technology to make synthetic jet fuel from our large
reserves of coal and oil shale.

With regard to the efficient use of aircraft fuel, aircraft operation can
be improved, new aircraft can be built that have lower drag and hence re-
quire less fuel, and more efficient engines can be built. It is this last ap-
proach that will be elaborated on in this paper.

Results are from in-house studies and early contract studies that are
still going on. A comprehensive experimental program aimed at aircraft
fuel conservation is being developed by NASA, but it has not yet been final-
ized and approved.

The major oil users are shown in figure VI-1. Currently, surface
transportation requires about 50 percent of our annual oil requirement, in-
dustry about 20 percent, residential and commercial needs about 20 per-
cent, and the aircraft industry about 10 percent. Certainly, all segments of

our society must strive to use fuel more efficiently. Our concern here is with the aircraft segment. Even now the jet fuel bill is large, about $4 billion a year. By 1985 aircraft are forecast to require a somewhat larger fraction of our total oil requirement, about 15 percent.

Figure VI-2 shows how our oil demand is being supplied. Currently, about 35 percent of our oil must be imported. Unless something is done to increase our supply, the projection is that by 1985 almost half of our oil will be imported. This increasing dependence on foreign oil is a major national concern.

In figure VI-3 aircraft efficiency is considered. Revenue passenger miles per gallon of fuel are shown for a 2000-mile trip using a bus, auto, train, and airplane. Currently, the airplane is competitive with the auto and train but far less efficient than the bus. Much of the discussion in this paper centers on ways to increase the efficiency of the airplane by improving its engine. The emphasis is on transport engines, and figure VI-4 shows why.

In 1970, general aviation used 5 percent of the fuel, commercial transports 66 percent, and military aviation 29 percent. About half the military fuel was used by long-range aircraft, so 80 percent of the fuel was used by aircraft powered by transport-type engines. A significant impact can be made on the aircraft fuel crisis if we can implement ways of making these engines more efficient.

The recent trends in airline fuel prices are shown in figure VI-5. For many years, fuel was sold for 10 and 11 cents per gallon. Then, in late 1973 fuel prices rose sharply. Within a year the price of fuel doubled for the domestic operators and tripled for the transatlantic operators. The difference in price results from the difference in source. The domestic airlines get most of their fuel from U.S. oil that is price controlled at about $6 a barrel. The transatlantic airlines buy bonded fuel that is not price controlled but which comes from oil costing about $11 a barrel. As domestic oil becomes more scarce, or perhaps when price controls are removed, all airlines may have to pay the same high price for their fuel. Prior to the fuel crisis in 1973, the fuel cost represented about 25 percent of the direct operating cost. For those operators now paying three times the old fuel price, fuel cost is 50 percent of the direct operating cost. This has led to fewer flights and higher fares for airline passengers. In spite of the higher

income resulting from higher load factors and higher fares in 1974, the net profit of U.S. airlines was $250 million, which is equivalent to only a $2\frac{1}{2}$ cents per gallon increase in fuel price.

The picture for 1975 is much worse according to preliminary Air Transport Association (ATA) figures. The U.S. scheduled airlines lost more than $190 million during the first quarter of 1975. ATA attributed the record loss to a $1 billion fuel cost increase in 1974 which is resulting in about $75 million more a month in fuel costs for 1975.

FUEL FROM COAL AND OIL SHALE

Comparative Magnitudes of Energy Resources

When one considers the projected future energy demands in the United States, there is as much concern about the types of fuel that will be required as there is about the types of users. While some users may be able to convert to alternative forms of energy, others may not. Within the next 25 years or so, aircraft are going to be primarily dependent on petroleum-derived fuels or similar fuels derived from alternate sources. So, it is important to look at the energy problem in aeronautics in terms of the available sources from which we can get jet fuels as we now know them.

There are two major sources of energy other than petroleum in the United States from which we can get petroleum-like fuels. Figure VI-6 shows some comparisons of the amounts of these materials with domestic oil resources. The alternate sources are oil shale, located primarily in Colorado, Utah, and Wyoming, and coal, which is more widespread throughout the United States.

The numbers given in figure VI-6 are derived from Department of Interior estimates. It is difficult to establish parallel categories for comparison, but the interest here is primarily in showing some relative magnitudes of these alternate sources compared to our oil supply. The oil category includes Alaskan oil and off-shore oil as well as in-land resources. The "proven" reserves here account for known deposits recoverable with present techniques; the "estimated total" includes yet undiscovered oil as well as the assumption of advanced recovery methods to get it. The shale

is all listed as known resources; what is labeled "recoverable" corresponds to shales with oil content greater than 10 gallons per ton, and the "estimated total" includes leaner shales with oil contents down to 5 gallons per ton. The coal resources were listed as "identified by mapping and exploration" with the "estimated total" being about twice this amount. For the purposes of this figure, coal tonnage estimates were converted to barrels of oil equivalent assuming one could get 3 barrels of oil (126 gallons) per ton of coal, which is a conservative conversion as far as the energy equivalents are concerned. The energy equivalence is about $4\frac{1}{2}$ barrels (approximately 190 gallons) per ton.

The time scale on figure VI-6 may give a better perspective of the magnitude of these resources. The years of supply correspond to using these resources at our present total energy use rate in the United States, approximately 34 million barrels per day oil equivalent. At these rates oil would run out shortly after the turn of the century. The alternate sources are large enough to supply our total energy needs for several hundred years at our present rate of use. If one assumes some higher projected use rate than this, then the time scale will be correspondingly shortened - but the comparisons of amounts remain the same.

Hydrogen Deficiency of Alternate Sources

Oil shale and coal represent substantial resources of energy, and petroleum-like fuels can be obtained from them. There are, of course, a number of problems in getting fuels from these alternate sources, but only one, which is a major technical consideration for the aircraft fuels situation, is discussed here.

This consideration involves the hydrogen requirements for processing synthetic crudes (fig. VI-7). Coal contains about 3 to 6 weight percent hydrogen; the organic material in oil shale has around 11 percent. Jet fuel, the desired end product, contains about 14 percent hydrogen. The coal and shale are hydrogen deficient. To process these materials to jet fuels involves adding hydrogen chemically. Although hydrogenation is a common petroleum-processing operation, it is a relatively expensive one since it involves high-pressure, high-temperature, catalytic processing equipment.

This hydrogen deficiency is also important as it relates to the nature of the hydrocarbons obtained from the synthetic sources. The synthetic crudes are higher in aromatic hydrocarbon content - the coals more so than the shale oils. Aromatics are the unsaturated ring structure compounds that have low hydrogen-carbon ratios. The aromatics are desirable components in automotive gasolines for their anti-knock property. In fact, reforming petroleum stocks is presently done just to obtain a higher aromatic content for this purpose. But, in jet engines the aromatics tend to smoky burning, they cause increased combustor liner temperatures, and they are somewhat incompatible with the elastomers used in fuel systems.

Figure VI-8 illustrates the effect of burning fuels with different hydrogen contents, in a JT8D combustor at simulated cruise conditions. The Jet A fuel, at around 14 percent hydrogen, had a maximum liner temperature under these conditions of a little over 1200° F. The trend of increased liner temperature with decreasing hydrogen content of the fuel is quite apparent. So it appears it may take more processing of some synthetic crude oils to get suitable jet fuels than to get suitable automotive gasolines. On the other hand, with some petroleum crudes the reverse may be true.

While the emphasis in this discussion is on the jet fuel problem, one naturally should consider the overall product-distribution requirements, such as when both petroleum crudes and synthetic crudes will be supplying our refineries. We would like to take the most energy-efficient path to get the total distribution of products that will be needed.

Alternate Fuels Evaluation Program

Figure VI-9 illustrates the distribution of a barrel of finished products out of a current refinery. The numbers indicate the percentage distribution of products according to present U.S. use. The products are arranged in a barrel essentially according to their boiling-range distribution, with the more volatile materials at the top and the higher boiling fractions at the bottom of the barrel. The kerosene boiling-range fraction from which most of the jet fuel is obtained represents about 10 percent of the total. The jet fuel itself is only about 7 percent. The largest portions go to the more volatile gasolines and to the higher boiling diesel and heating oils.

Considering this distribution of products and recalling the discussion on the processing of the synthetic crudes, one can see essentially two approaches that can be taken toward meeting the demand for future aircraft fuels:

(1) Investigate the effects of relaxing or broadening the specifications currently applied to jet fuels so that future engines and fuel systems might have more flexibility in the range of fuels they can use.

(2) Investigate the additional processing of alternate (or synthetic) crude oil sources that will be required to get fuels meeting either present jet fuel specifications or broadened fuel specifications.

Looking toward these two approaches, NASA, in cooperation with other government agencies and private industry, is currently beginning an Alternate Fuels Evaluation Program which has three main goals.

First is to evaluate the performance in aircraft engine components and fuel systems of broadened specification jet fuels from petroleum stocks and of synthetic jet fuels meeting both current and broadened specifications. Typical of some of the broadened specifications to be looked at are ones that appear to have the most significant effect on yield or processing severity: wider volatility (extending both ends of the boiling range), higher aromatics (or equivalently, lower hydrogen-carbon ratio), higher freezing point fuels (which generally accompany the higher boiling range fractions). The Navy sponsored a project involving Applied Systems Inc., Standard Oil of Ohio, and Development Engineering Inc. that produced 10 000 barrels of shale oil and hydroprocessed it into a number of fuel products, one of which corresponded to Jet A specifications. About 1500 gallons of this Jet A fuel was received at Lewis, and some of it has been run in the JT8D combustor used for the liner temperature measurements shown in figure VI-8. Since this processed fuel met Jet A specifications it, not surprisingly, did not show any differences in performance from the petroleum-based fuel. Some of this same fuel has also been run in a standard CF6-50 combustor by the General Electric Company as part of the clean combustor program discussed elsewhere in this report. There, also, these preliminary runs showed no differences in performance or emissions from regular Jet A fuel.

A second goal of the program is to develop any necessary component technology that may become evident in the evaluation program so that future aircraft engines and fuel systems will be ready to use the available future

fuels. If we could be assured of continuing to meet future aircraft fuel needs with fuels processed according to present jet fuel specifications, there would be little incentive to consider some of the development areas to be discussed. Should broadened specifications be needed, however, it may be necessary to develop vaporizing combustors to handle higher boiling fuels, pressurized tankage for higher volatility fuels, and fuel system heating to handle higher freezing point fuels. It may also be necessary to perform materials investigations to assure compatibility with the new fuels.

The third major element of the program is to determine the characteristics of fuels obtainable from shale and coal syncrudes and the processing necessary to get fuels to meet either current or broadened jet fuel specifications. This will involve the usual physical property and hydrocarbon type analyses and being on the lookout for any unusual properties or constituents that might affect thermal stability, emissions, or corrosion of the new fuels. In the processing area, the Air Force and NASA are jointly sponsoring a contract with Exxon Research and Engineering to evaluate the methods of producing aviation turbine fuels from synthetic crude oils. As part of this effort Exxon is processing two coal syncrudes and three shale syncrudes to jet fuels and providing analyses of the products.

EFFICIENT USE OF FUEL

The syncrude approach to increasing our jet fuel supply appears very promising. It may be some time, however, before large supplies of syncrude will be available. In the meantime, there are things that can be done to use fuel more efficiently. For the present, the work will be with current engines. Since the engines in service are not performing as well as when first installed, the first thing to do is to find ways of restoring lost performance. A second approach is to use advanced technology in derivative engines to make them more efficient than the older models.

For the longer term, much more efficient engines can be anticipated. Low fuel consumption has always been the goal, but a third generation turbofan truly optimized for low fuel consumption might offer an appreciable gain over our best turbofans flying today. Also, there are some unconventional engines that offer great potential for using fuel efficiently.

Existing Engines and Their Derivatives

There appears to be potential for reduced fuel usage with existing engines and their derivatives. To better understand what this potential is, the fuel consumed by U.S. airlines in recent years (1970-1974) and the predicted usage from 1975 to 1990 is presented in figure VI-10. Currently, a total of about 10 billion gallons are being used. About 85 percent is being consumed by current low bypass ratio engines (JT3D and JT8D). By 1990 the consumption is expected to grow to about 16 billion gallons per year. By this time, a sizable part of the total will be used by current high bypass ratio engines, the JT9D, CF6, and RB211. In addition, it is expected that new high bypass ratio engines, the CMF56 and the JT10D, will become fuel users in the 1980's, but through this 10-year period these engines will only use about 13 percent of the total fuel consumed.

The significant fact to draw from this figure is that current engines and their derivatives are going to use at least 90 percent of the fuel consumed during the next 15 years - about 200 billion gallons. Whether the total predicted fuel usage or the fuel split among the engine types is precise is not particularly important. What is of significance is that if the air transport industry is going to reduce the amount of fuel it will use during the next 15 years it will be accomplished with today's engines. New engines will not have much of an impact before the 1990's.

Two approaches offer practical ways of reducing the fuel consumption of current engines. The first approach is to regain a substantial part of the performance lost through engine deterioration as engine time is accumulated. The second approach is to incorporate low risk, new technology concepts in these engines, concepts that do not require large amounts of money or time to develop.

Performance retention. - The first approach, performance retention, is discussed with the aid of figures VI-11 to VI-14. Figure VI-11 shows the loss in engine performance as engine time is accumulated. A broad band is used to illustrate this trend because there are fairly wide variations from engine to engine, even those of the same model. The loss in performance is quite rapid at first and then tends to level off as the engine becomes older. Fuel consumption eventually increases from 4 to 10 percent above new engine performance, an average deterioration of 7 percent. If it were

164

assumed that deterioration could be limited to an average of 4 percent, instead of the 7 percent that is being experienced, then 400 million gallons per year or 6 billion gallons of fuel could be saved. With fuel at 30 cents per gallon, the corresponding dollar savings would be 130 million per year or a total of 1.8 billion.

To obtain greater insight into how engine performance might be retained, the causes of deterioration and some of the economic consideration involved need to be examined. Deterioration comes about because the engine components operate less efficiently and the engine flow-handling capacity changes as engine time is accumulated. Foreign objects such as stones or nuts and bolts enter the engine inlet and damage the fan or compressor. In addition, smaller particles in the air cause blade and vane erosion, particularly at the blade tips and blade and vane trailing edges. These same particles cause the blade and vane surfaces to become rougher. In the combustor, liners become warped or cracked and fuel nozzles may become partially clogged because of excessive local temperatures and fuel coking. The turbine is particularly vulnerable because of its high temperature environment. Turbine vanes bow and crack and deformation of the case and other parts of the turbine assembly change clearances and increase leakages. There are numerous seals throughout the engine that are affected and do not perform as well as designed.

It might be expected that the periodic overhauls that an engine goes through might restore its original performance. However, this is not the case. The trends shown in figure VI-12 illustrate the effect of engine overhauls. As shown on the previous figure, as engine time is accumulated, the fuel consumption rises. Typically, after 2500 to 4000 hours of engine time an overhaul is performed. These overhauls, as shown by the discontinuous reductions in fuel consumption, generally regain some of the performance lost through deterioration. Nevertheless, the net long term trend is still toward increased fuel consumption as shown by the dashed line. Engine overhauls have not regained the original performance because they have been aimed primarily at the very necessary goals of making engines operate safely and insuring that the engines produce the required thrust. Neither of these goals, however, necessarily promotes low fuel consumption. The pre-1974 fuel prices, and apparent endless supply, along with the lack of hard data on how selective part replacement might reduce fuel consumption

produced maintenance procedures which did not emphasize long-term fuel consumption. It is important to also point out that the information required for selective engine part replacement is at best difficult to obtain. Even if these data are technically achievable, it still might lead to a conclusion which is not economically viable - that is, the replacement of a large number of gas path parts or those that are most costly.

Nevertheless, now that fuel prices are two to three times higher and there is a need to be conscious of fuel consumption, the engine deterioration problem needs to be re-evaluated. This re-evaluation is being done by industry and NASA. Just recently American Airlines and Pratt & Whitney conducted a study sponsored by NASA on performance deterioration of JT3D and JT8D engines. The purposes of the study were to document the deterioration problem and try to obtain a better idea of what parts of the engine need greater attention.

One of the conclusions reached during this study is shown by the bar on the right side of figure VI-12. The total length of the bar represents 100 percent of the repaired engine performance deterioration. As is noted on the bar, 15 percent of the total deterioration is associated with the turbine. Such things as turbine nozzle area changes, tip seal wear, and vane platform leakage were judged to be responsible. These losses are over and above the losses that are typically corrected during overhaul.

Another 20 percent of the losses are attributed to seal leakages. The combination of a large number of seals and their relative inaccessability precludes seal repair or replacement except in the more obvious cases. Finally, about 65 percent of the performance deterioration is charged to the fan-compressor gas-path parts. As indicated in the figure, these parts suffered because of erosion, foreign object damage, or increased surface roughness. Of these categories, foreign object damage is the only one consistently dealt with, primarily because it is the only one affecting structural integrity. The cure generally consists of smoothing out the rough edges, or in the more severe cases, welding on additional metal. Neither of these contributes greatly to restoring performance.

The results of this study were not expected to produce all the answers needed to solve the deterioration problem. But the study did provide some direction as to where effort is required.

Another aspect to the previous problem is the economic considerations.

Economic trade-off possibilities have been examined as part of a recent study conducted by American Airlines, Boeing, and Pratt & Whitney. Figure VI-13 shows cost as a function of increased maintenance effort. As the maintenance effort is increased above the current level, maintenance cost, as would be expected, rises. Hoepfully, fuel costs would decrease at least with the initial increment of maintenance effort. The net result would be a total cost that would minimize at some point above the current level of maintenance effort. If fuel costs increase and shift the fuel curve upward, then the minimum point on the total cost curve will shift to the right. Thus, increased fuel prices make it economically sound to increase the maintenance effort in the search for lower fuel consumption.

These trends are quantified in figure VI-14 which shows the percent increase in maintenance costs as a function of fuel cost. In this case, a specific fuel consumption reduction of 3 percent is assumed to result from the increased maintenance effort. The line represents a break-even point insofar as airline direct operating cost is concerned. At fuel costs prior to 1974 (10 to 12 cents/gallon) the airlines could only tolerate about a $2\frac{1}{2}$ percent increase in maintenance effort. At today's prices (1975) the maintenance costs could be increased about 8 percent and still keep the direct operating costs the same. In addition, a rather small but important benefit to our national balance of payments results if we spend our money domestically on engine parts instead of fuel.

There is another aspect of maintaining the original fuel consumption that merits some discussion. It has possible application to engine maintenance, but it is probably more relative to the next subject which will be discussed, namely, the application of new technology to current and derivative engines and future engines. Simply stated, it is research directed at designing and fabricating components which would have less long-term deterioration than the components currently being used. The goal of this research would be, for example, to develop materials and blade shapes which would be less susceptible to performance deterioration. The satisfactory outcome of such research as applied to future engines is quite obvious. In the case of current engines, the results could lead to revised guidelines for component rework or replacement.

Modifications for derivative engines. - In addition to research of this kind, the application of new technology to current engines is presently being

studied by Pratt & Whitney and General Electric under contract to NASA. A great many modifications for reducing fuel consumption have been examined. Table VI-1 shows a partial list of these changes and their estimated effects on fuel usage and direct operating costs. This itemized list of modifications illustrates that both fuel saving potential and direct operating cost were considered when selecting the modifications for more detailed study. Items such as hydrodynamic seals and advanced high pressure turbine blade material which exhibited a direct operating cost increase were automatically omitted. In addition, some items which showed only a very small potential fuel reduction, such as advanced shroud material, or items that required major modifications or development risks, such as the use of composites, were also dropped from further consideration for current or derivative engines. Figure VI-15 summarizes the items that remained from this selection process and were considered suitable for current or derivative engines. The engine schematic in this figure has been numbered to give the approximate location where modifications can produce lower fuel consumption. At the bottom of the figure are the estimated maximum fuel savings that could be realized if these modifications were made on new engines coming off the production lines. Modification 1 refers to an improved fan blade shape to produce higher efficiency. The second modification would be combining the function of the fan exit guide vanes with that of the fan case struts and thereby reducing the pressure loss. Modification 3 is a more effective shaft bearing seal that blocks high pressure air from escaping the main flow path, and modification 4 refers to the use of fan duct air to cool the high pressure turbine case. The cooling air shrinks the case in a controlled manner and allows very tight running tolerances. Another seal improvement, this one in the low pressure turbine and identified by the number 5, permits closer running tolerances. All of these improvements could produce about a 4-percent reduction in fuel consumption.

Two other improvements which can be used, but not in conjunction with each other, are a forced mixed flow exhaust, modification 6, or a combination nozzle redesign and removal of the primary thrust reverser, modification 7. The forced mixer means a new piece of hardware in the exhaust section that forces the fan and gas generator or core flow to mix. This can produce up to a 3-percent reduction in fuel consumption. Using the other route, an improved nozzle design without a primary thrust reverser can gain us

about 2 percent. Using the best of all of these modifications can produce up to a 7-percent reduction in fuel usage. A realistic assessment would be to expect a 5-percent improvement. These gains are on new engines coming off the production lines. Because of the economics involved, the retrofitting of existing engines with the types of modifications just discussed would be expected to produce only about half ot these gains.

It is well to remember that these improvements in current engines could be implemented in the next several years. If they improve the fuel consumption of our current and derivative engines by 5 percent, then by 1990 we will have saved an estimated 10 billion gallons of fuel worth about $4 billion. In the longer term, much greater fuel savings can be achieved with new engines for 1990 and beyond.

Future Engines

There are a number of different ways to reduce aircraft fuel consumption. The most important ways to reduce fuel consumption for transport airplanes are to increase the airplane lift/drag ratio and the engine efficiency. The airplane lift/drag ratio is primarily an airframe parameter and is not considered here. Therefore, only a single parameter - engine efficiency - remains the focal point from a propulsion standpoint. Engine efficiency is normally quoted in terms of specific fuel consumption (SFC) and figure VI-16 shows the historical trend of SFC. All of the SFC values are given relative to the 1960 turbojet performance.

Turboprops were in commercial service a few years before the turbojets and they were much more efficient (40 percent). However, the faster speed of the turbojets plus the low cost of fuel in those days made the turbojets more attractive economically. When the first turbofans were introduced in the early 1960's they reduced fuel consumption by about 15 percent. And when the second generation, high bypass ratio engines were introduced in the early 1970's, they further reduced fuel consumption an additional 20 percent. If the proposed modifications to the existing engines (as discussed in the previous section) were actually implemented, the gain would be a few more percent as indicated by the shaded bars. There is little doubt that these existing engines, and any derivative versions of them, will be

used for quite some time yet. Thus, any hoped for major reductions in SFC must await the introduction of future engines that are many years away. The historical trend does indicate, though, that when such engines do become available they may indeed provide substantial improvement.

Engine efficiency. - Perhaps it would be helpful to review the basic concept of engine efficiency in order to see where some of the anticipated gains might come from. Figure VI-17 helps illustrate how engine efficiency is defined. A turboprop is shown here to make the explanation simple. In essence, the chemical energy of the fuel is converted by the engine into "available power" and in this case the "available power" is in the form of shaft horsepower (the small portion remaining in the jet exhaust is ignored here for simplicity). Once the engine creates the "available power", it can then be used to drive either a fan or a propeller (as shown in the figure) which in turn provides thrust. Useful power is defined as that power which actually does work on the airplane. It is calculated simply as the product of thrust times the aircraft flight velocity. Thus, the whole process of converting fuel power into useful power can be separated into two logical steps. The efficiency of the first step is called thermal efficiency and that of the second step is called propulsive efficiency:

$$\text{Thermal efficiency} \equiv \frac{\text{Available power}}{\text{Fuel power}}$$

$$\text{Propulsive efficiency} \equiv \frac{\text{Useful power}}{\text{Available power}}$$

The overall powerplant efficiency is simply the product of thermal and propulsive efficiencies:

$$\eta_{\text{overall}} = \eta_{\text{thermal}} \times \eta_{\text{propulsive}}$$

Some methods to increase thermal efficiency are discussed next and then the following section discusses propulsive efficiency.

The traditional methods of increasing thermal efficiency are raising component efficiencies, raising cycle temperature, and raising cycle pres-

sure ratio. The individual components in an engine are upgraded continually as better designs and manufacturing methods are introduced. Cycle temperatures and pressures have also been increasing in a historical trend as a result of technology advances in high-temperature materials and turbine cooling. Bypass ratio has been rising too, and although it affects propulsive rather than thermal efficiency, its rise is mostly due to higher temperature levels so it becomes another incentive for raising temperatures.

Advanced turbofans. - At some future time advanced turbofan designs of still higher levels of temperature, pressure, bypass ratio, and component efficiencies can be expected. NASA has both an in-house effort and several engine companies under contract to estimate the advantage of such turbofans. Some early results are shown in figure VI-18 which is a plot of the change in SFC as a function of cycle pressure ratio where the reference point is a modern high bypass ratio engine. The top band represents current technology with maximum temperature levels of 2400° to 2500° F and bypass ratios around 5. The lower two bands represent a very advanced design - one that is based on a technology level estimated to be available in the late 1980's. The middle band shows that the gains expected from internal aerodynamic improvements are 5 to 10 percent and that there is not much incentive to raise the cycle pressure ratio. The lower band represents advances in high-temperature materials technology and turbine cooling. These advances permit higher turbine-inlet temperatures (e. g., 2600° to 3200° F) and shift the optimum pressure ratio to 40 or beyond and raise the optimum bypass ratio to at least 8. The overall effect is to produce a potential reduction in SFC of 15 percent or better. It should be mentioned that these results (and those that follow) are preliminary and have not been subjected to a detailed analysis. Also, it should be emphasized that these engines are quite advanced and present a real challenge. The problems associated with very high-pressure and high-temperature engines are important enough that a separate discussion of this subject is presented in another section in this volume.

Regenerative turbofan. - Figure VI-19 illustrates the similarity and difference between a conventional turbofan cycle at the top and a regenerative turbofan cycle at the bottom. The conventional cycle requires a large compressor to produce the high pressure ratio that gives low fuel consumption. It also requires a large turbine to drive the high pressure ratio compressor. In the bottom diagram, showing a regenerative turbofan cycle,

the same components plus a regenerator downstream of the tubine are shown. The lower dashed line represents a duct that carries air from the compressor back to the regenerator where the compressor air is heated by the turbine exhaust. Another duct carries the heated compressor air forward to the burner. Since heat has been added to the compressor air, less fuel is required in the burner to reach the desired turbine temperature. In this way, then, a lower fuel consumption is achieved. Notice that a smaller compressor and turbine are shown for the regenerative cycle. Figure VI-20 shows why. Some of the turbofan story, relating SFC to cycle pressure ratio, is repeated. The middle band, representing 1985 turbofan technology, indicates the SFC can be improved about 15 percent, relative to current turbofans, by increasing the cycle pressure ratio to very high values - 40 to 60. The band at the lower left is for advanced regenerative turbofans. A comparable reduction in SFC is achieved at a cycle pressure ratio of only 15 to 20. In a regenerative engine, the job of heating the air for the burner is split between the compressor and the regenerator. This explains why a regenerative turbofan requires a much smaller compressor and turbine than a conventional turbofan. Since both engines offer about the same potential for reducing SFC, it is likely that the preferred engine for low fuel usage depends on other factors such as development risk, engine price, and maintenance and reliability features. Thus, a SFC improvement of the order of 15 percent can be expected using an advanced turbofan of the late 1980's with either high pressure ratio or a regenerator. There are other methods (e.g., intercooling, compounding, constant-volume burning) that theoretically could also improve thermal efficiency. These are usually shown to have small gains and relatively large "costs" (weight, complexity, cost, etc.). So rather than discuss them here, our attention is directed toward other improvements - those that produce a better propulsive efficiency.

Short cowl turbofan. - One way to increase propulsive efficiency is to raise the bypass ratio of a conventional turbofan. This is, in fact, one of the usual byproducts of raising cycle temperature, and part of the 15-percent SFC reduction just discussed is due to raising the bypass ratio. Raising the bypass ratio is normally accompanied by a reduction in fan pressure ratio, which in turn reduces the fan exhaust stream jet velocity. Thus, less energy is wasted in the form of exhaust stream kinetic energy.

172

The key, then, to better propulsive efficiency really lies in lowering the fan pressure ratio. This is illustrated in figure VI-21. The top dashed curve represents an ideal situation of zero losses. The ideal propulsive efficiency gradually drops from 100 percent at a fan pressure ratio of 1.0 to about 80 percent at pressure ratios near 1.6, which is a typical value for modern engines. However, if a realistic fan efficiency and also a drag penalty for the engine nacelle are accounted for, a lower propulsive efficiency is obtained. This is illustrated by the solid curve which is representative of traditional nacelles as in the sketch on the right in the figure. The ideal curve indicates that lower fan pressure ratios are desirable, but in practice the efficiency flattens out and eventually drops rapidly. This effect is caused by the increasing nacelle drag that occurs as a result of increasing the airflow and fan diameter to maintain a fixed thrust level. Furthermore, the nacelle weight also increases so we are penalized in two ways.

Still, there have been efforts to move in this direction. In particular, figure VI-22 shows one of the QCSEE engines that was discussed earlier. It has a fan pressure ratio of about 1.4 at cruise, and it illustrates some of the new features required at low pressure ratios. For example, it has speed reduction gearing and also variable pitch fan blades. The variable pitch feature helps off-design performance and provides thrust reversing. This eliminates the large separate thrust reverser that would otherwise be housed inside the aft cowling.

Figure VI-21 shows that propulsive efficiency will not be improved unless the nacelle drag is reduced. Obviously, this QCSEE type nacelle is large and would not meet our needs at very low pressure ratios. Let us examine it from the viewpoint of trying to shorten it and see what problems might be encountered. First, the inlet is long; traditionally, this is to prevent flow separation problems at all flight conditions and to provide a large surface area for noise suppression material. This is especially true of the QCSEE, which was designed for an application that requires a lot of suppression. Even the aft end of the QCSEE cowl is long for this reason. But for a conventional transport engine application much of this suppression is not needed - especially if an even lower fan pressure ratio is used and the source noise is reduced. Thus, it might be possible to use a short cowl, such as the one shown in figure VI-23. This appears to achieve the goal of

minimizing the high nacelle drag. If it really could be used, we estimate the favorable performance shown by the shaded region in figure VI-21 (perhaps as high as the upper solid line).

But short cowls present problems of their own. Their surface area for noise suppression may be too small. This is a question of how much suppression is needed. The main problem, however, is that a short inlet like the one shown in figure VI-23 has a relatively sharp lip instead of a well-rounded one. This would cause flow separation at a low speed and high angle of attack or in crosswinds. This could reduce takeoff thrust and induce high aero-elastic stress in the fan blades, which become longer and more flexible as the pressure ratio is reduced. So more variable geometry features in the cowling may be needed to reduce flow separation. Or perhaps, since low pressure fans tend to have excess takeoff thrust anyway, it might be possible to operate with some separation instead of avoiding it. As a result of factors like these, an increasingly large area of uncertainty exists as attempts for lower pressure ratios are made, and we do not know how far we can go in this direction before the problems become insurmountable.

Turboprops. - Instead of trying to solve all these problems, a turboprop might be chosen. Turboprops perform quite well at very low pressure ratios and low flight speeds. But, at high speeds the propeller efficiency tends to drop rapidly and thus to offset the theoretical advantage shown in figure VI-21. Figure VI-24 is a plot of propeller efficiency as a function of flight Mach number for several levels of propeller technology. It is obvious that the thick-bladed World War II propellers and even the thin-bladed Electra propellers have poor performance at the high speeds we are interested in. It is estimated that the 1960 era Russian technology was considerably better. Two points are shown that represent two of their long range airplanes designed for speeds up to Mach 0.75. These airplanes use counter-rotation propellers that operate at high power loading.

Beyond the Russian data, a number of circled points are shown that represent some old 1950's test data for high-speed models. While these thin-bladed models performed very well, they were run at such low power loadings that a full-size application would be impractical because the propeller diameter would be enormous. To overcome this problem, more blades (8, for example) would be needed as well as a high blade loading, which tends to lower efficiency. On the other hand, technological advances in

airfoil aerodynamics and blade structures could improve the picture. The shaded band represents the estimated 1985 technology. The upper curve of this band is based on the excellent performance of the models and is viewed as a potential goal. It assumes the full application of supercritical aerodynamics, improved design techniques, and improved materials such as composites. The lower curve represents a very conservative performance estimate. Rather than trying to predict which of these two curves is closer to the truth, suppose that first one and then the other is valid. We can also make a corresponding set of optimistic and pessimistic component assumptions for advanced engines as follows (for all three engines - turbine inlet temperature, 2960° R; overall pressure ratio, 40):

COMPONENT PROPERTIES	TURBOFAN[a]	TURBOPROP	
		PESSIMISTIC	OPTIMISTIC
FAN (PROPELLER) EFFICIENCY	0.88	FIGURE 24 (BOTTOM CURVE)	FIGURE 24 (TOP CURVE)
POD DRAG (PERCENT OF CLEAN AIRCRAFT)	8.8	10.2	4.8
INLET RECOVERY	0.993	0.98	1.0
LOW PRESSURE TURBINE EFFICIENCY	0.90	0.89	0.90
GEAR BOX EFFICIENCY	-----	0.983	0.994
PROPELLER AND GEARBOX WEIGHT	-----	1975 TECHNOLOGY	ONE-HALF OF 1975 TECHNOLOGY
FAN DUCT $\Delta P/P$ LOSS	0.017	------	-----

[a]BYPASS RATIO, 8; FAN PRESSURE RATIO, 1.6.

Both an optimistic and pessimistic evaluation of turboprop performance can now be determined as displayed in figure VI-25. This figure shows the relative trip fuel consumed by a hypothetical, 200-passenger airliner with a 3000-mile design range and flying at 36 000 feet. Since the whole plot is drawn for "rubberized" 1985 technology airframes, the differences in trip fuel are due solely to different propulsion systems. The reference point is in the top line and represents a Mach 0.8 design with modern high bypass ratio engines. The middle line represents a late 1980's advanced turbofan with an estimated 20-percent savings in trip fuel. This is higher than the 15 percent better SFC number quoted earlier because the airplane is resized

for a smaller fuel load and a lighter engine. The bottom band represents advanced turboprops that have the same core technology as the advanced turbofans. The top of the band corresponds to the pessimistic set of assumptions and the bottom to the optimistic set. The band gets wider at higher speeds because of the greater uncertainty there. The fuel savings for the optimistic case are quite impressive even at high speeds - showing a total of about 40 percent less trip fuel than current engines at Mach 0.8.

The pessimistic turboprop is considerably less attractive at Mach 0.8 with about an 8 percent margin over the advanced turbofan. Backing off in speed allows the pessimistic turboprop to quickly recover its advantage. At Mach 0.75, for example, it uses 13 percent less fuel than the advanced turbofan at the same speed.

This question of speed is an interesting one. The importance of speed to the passenger varies with total distance traveled. Slowing down by 0.05 Mach number on a 3000-mile trip would increase trip time by about 1/2 hour, which is not at all desirable. But most airline trips are considerably shorter than that as indicated in figure VI-26. Sixty percent of the fuel is used for trips of 1500 miles or less. And for these shorter distances, the difference in travel time becomes less important. So maybe turboprops could be designed for these shorter trips. Or perhaps they could be designed to go to Mach 0.8 to handle the long trips and then slow up a bit on the shorter legs in order to capture these fuel savings, even with the pessimistic performance.

Of course, real life is not as simple as the previous situation. There are questions involving productivity, direct operating costs, air traffic control, and so on that should be examined. And there are certainly other difficulties associated with turboprops, such as gear box weight and reliability, cabin noise and vibration, and maintenance. But many of the problems of turboprops are associated with older technology. Perhaps advanced technology may be able to minimize these problems.

CONCLUDING REMARKS

Although the world's oil supply could be depleted within 100 years, the supply of synthetic fuel from U.S. coal and oil shale reserves is estimated

to be sufficient for many centuries. Here at Lewis, a program has been started with other government agencies and industry that will enable our aircraft engines to use this synthetic fuel.

Since large quantities of syncrude will not be available for some years, our allotted fuel must be used more efficiently. With current engines, fuel usage can probably be improved about 3 percent by revising engine maintenance procedures to restore some of the lost performance. With derivative engines that incorporate some presently available advanced technology, about a 5 percent improvement can be expected.

Much larger gains appear to be possible with future engines truly optimized for low energy consumption. With a third generation turbofan, fuel usage can be improved 10 to 20 percent. The potential gain is doubled for at least one of the unconventional engines. Undoubtedly the effort to make these large gains possible will be expensive and difficult. NASA has recently developed several comprehensive aircraft fuel conservation programs requiring different fundings levels. Hopefully, one of these programs will be approved, funded, and implemented in the very near future.

TABLE VI-1. - DERIVATIVE ENGINES - MODERN HIGH BPR TURBOFAN

DESIGN CHANGE	ΔFUEL, %	ΔDOC, %
IMPROVED FAN AERO	-0.28	-0.11
COMPOSITE BLADES	-.60	-.53
COMPOSITE FRAME	-.17	-.19
HYDRODYNAMIC SEALS	-.50	+.10
ADV HPT BLADE MATERIAL	-.62	+.13
ADV SHROUD MATERIAL	-.19	-.08
HPT CLEARANCE CONTROL	-.45	-.16
MIXED FLOW COMPOSITE NACELLE	-3.9	-1.47

CS-73718

20x10⁶

15

BARRELS/
DAY   10

5

0
1970   1975   1980   1985
YEAR

AIRCRAFT

SURFACE TRANSPORTATION

RESIDENTIAL & COMMERCIAL

INDUSTRIAL

CS-73011

Figure VI-1. - Oil usage.

100

80

60

%

40

20

0
1970   1975   1980   1985
YEAR

DOMESTIC

IMPORTED

CS-73004
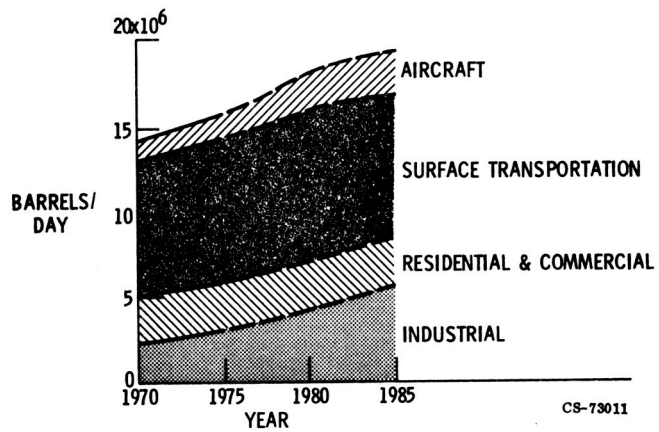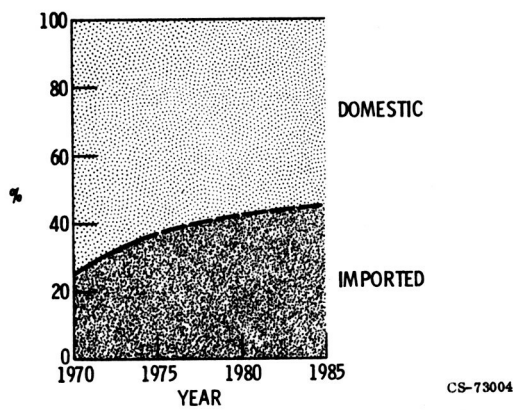
Figure VI-2. - Oil supply.
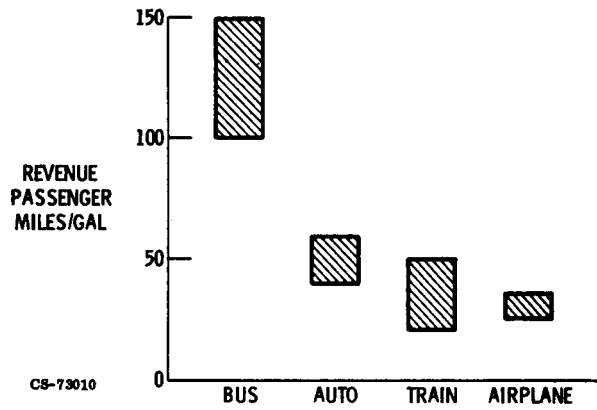
Figure VI-3. - Comparison of vehicle efficiency for a trip of 2000 miles.
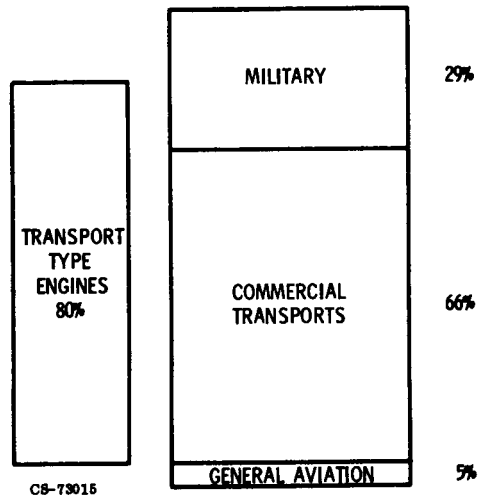
Figure VI-4. - Aircraft fuel use (1970 data).
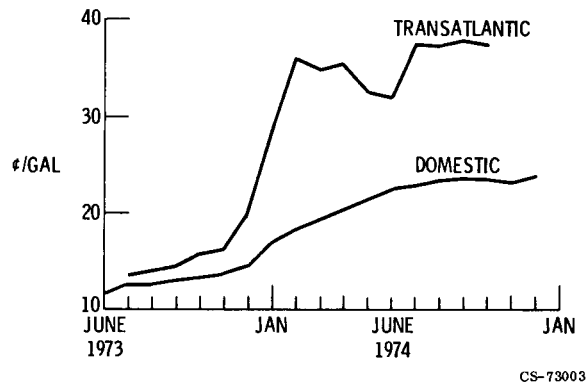
Figure VI-5. - U. S. airline average fuel prices.
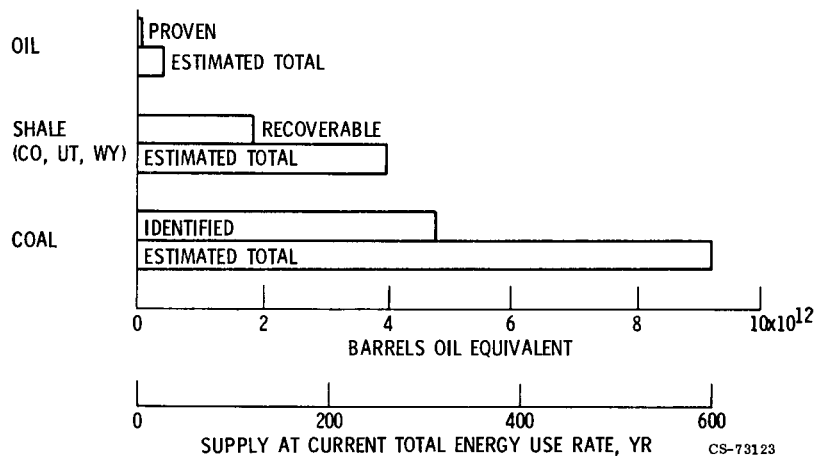
Figure VI-6. - Comparison of U. S. resources.
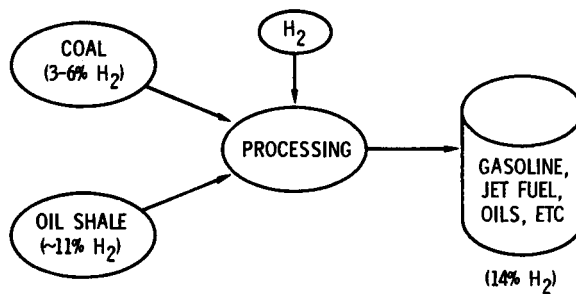
Figure VI-7. - Hydrogen requirement for processing. High aromatics (low H/C) - good in cars, bad in jets.

CS-73120
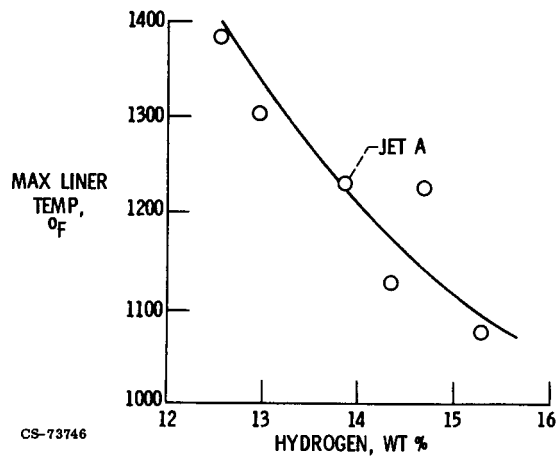
Figure VI-8. - Effect of hydrogen content of fuel for JT8D combustor at simulated cruise conditions.

181

	% OF TOTAL
LPG, PETROCHEMICALS	7
GASOLINE	45
JET FUEL (7) + KEROSENE (3)	10
DIESEL, HOME HEATING, INDUSTRIAL FUEL OILS	32
LUBE OILS, ASPHALT, COKE	6

CS-73122
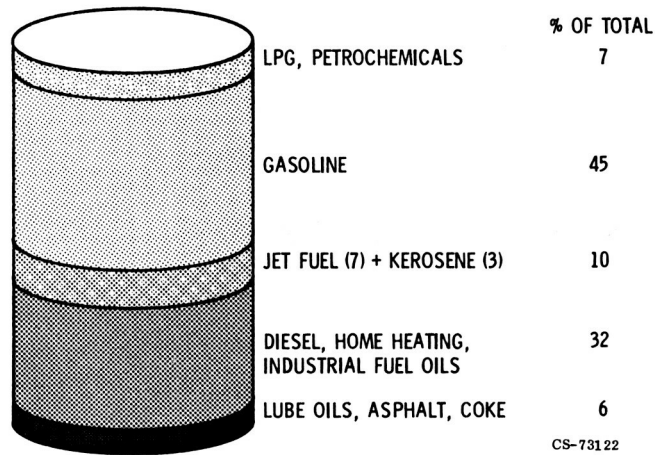
Figure VI-9. – Distribution of petroleum to finished products.
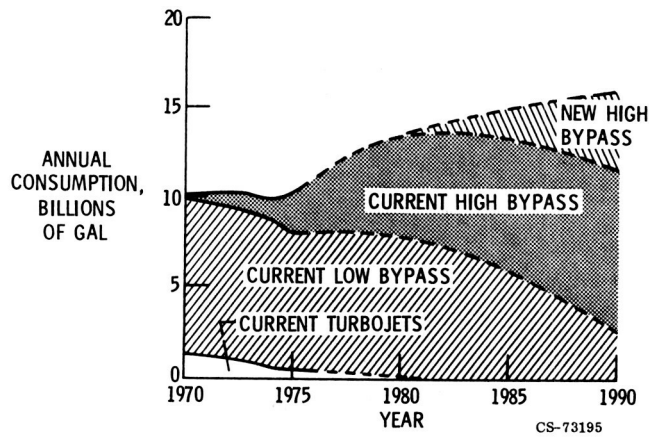
Figure VI-10. – U. S. airline fuel consumption by engine type.
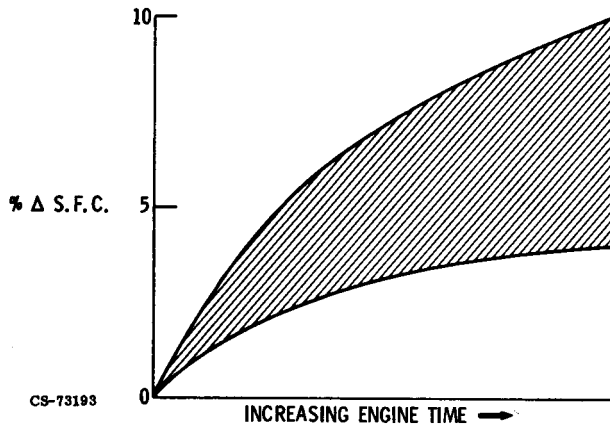
Figure VI-11. - Engine performance deterioration.
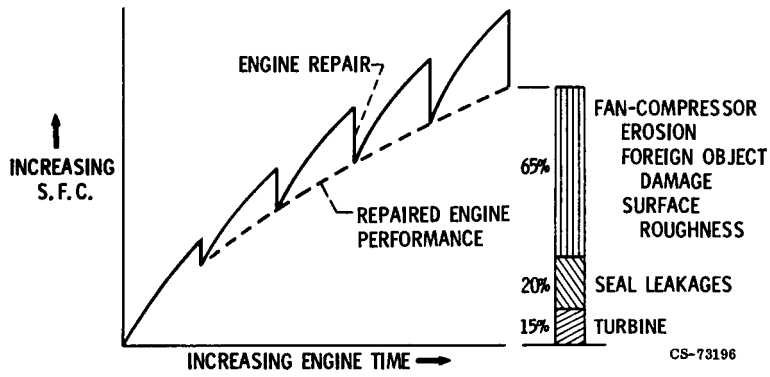
Figure VI-12. - Performance deterioration causes.

183
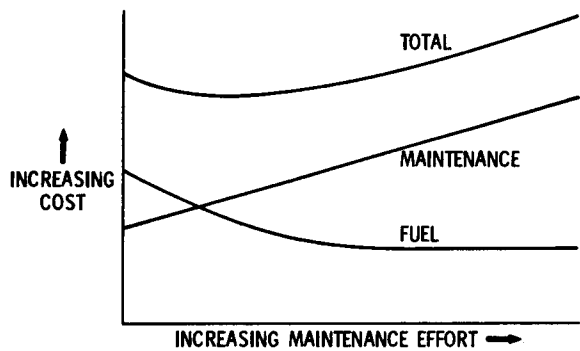
CS-73191

Figure VI-13. - Fuel-maintenance trade-off.
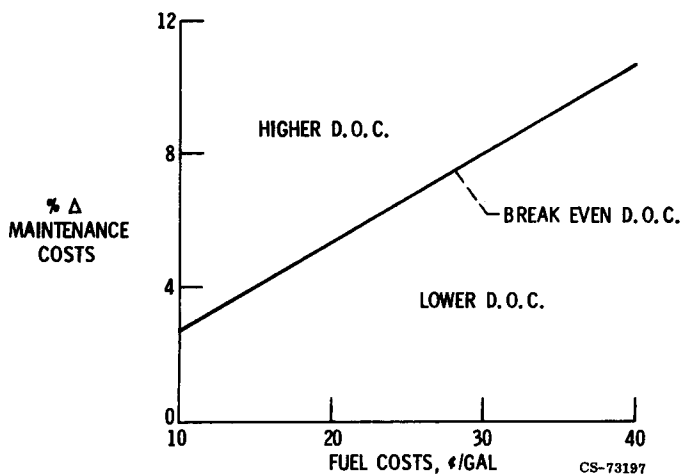
CS-73197

Figure VI-14. - Fuel-maintenance trade-off with specific fuel
consumption reduced 3 percent.
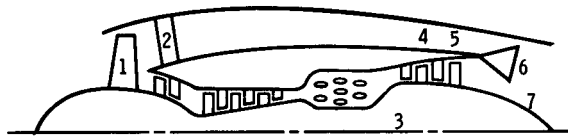
MODIFICATION	MAX ΔSFC, %
1-5 AERODYNAMICS, SEALS, CLEARANCES	4
6 MIXED EXHAUST OR	3
7 NOZZLE REDESIGN & REMOVE PRIMARY REVERSER	2

CS-73008

Figure VI-15. – Fuel savings of derivative engines.
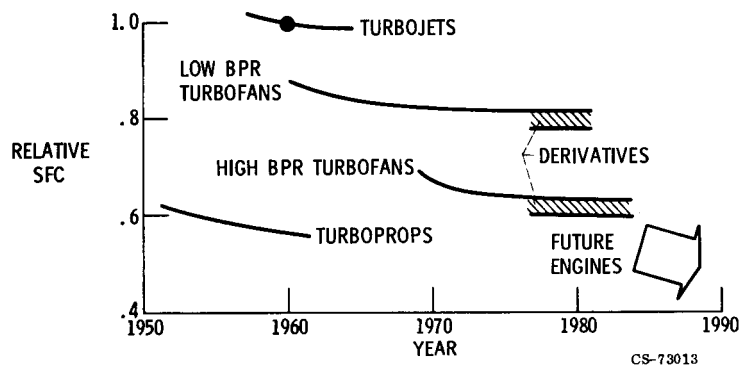
Figure VI-16. – Trends in aircraft engine fuel consumption.
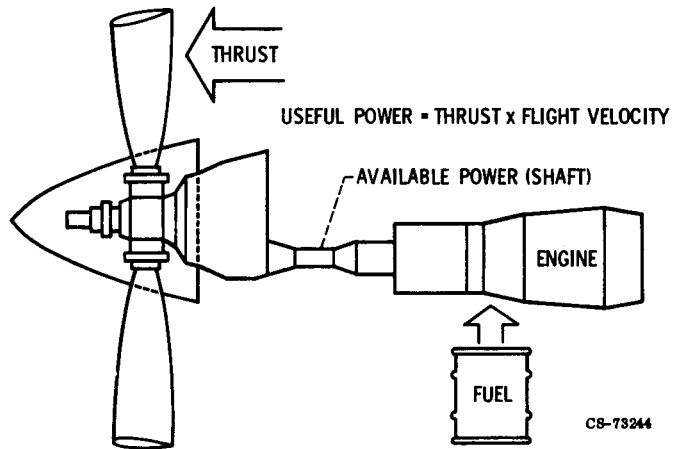
Figure VI-17. - Conversion of fuel to useful power.
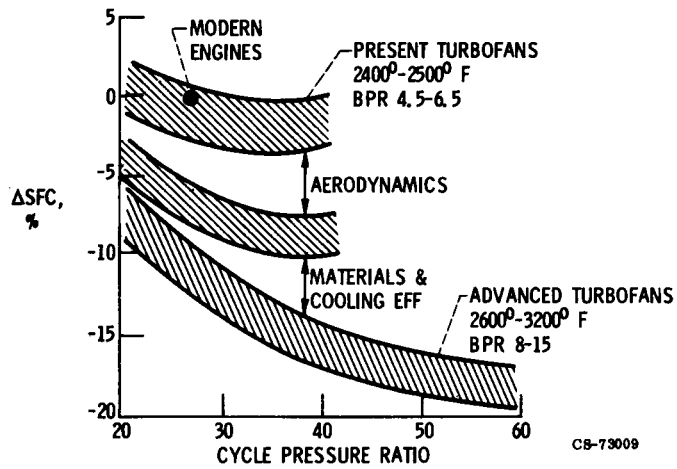
Figure VI-18. - Advanced technology benefits for turbofans.
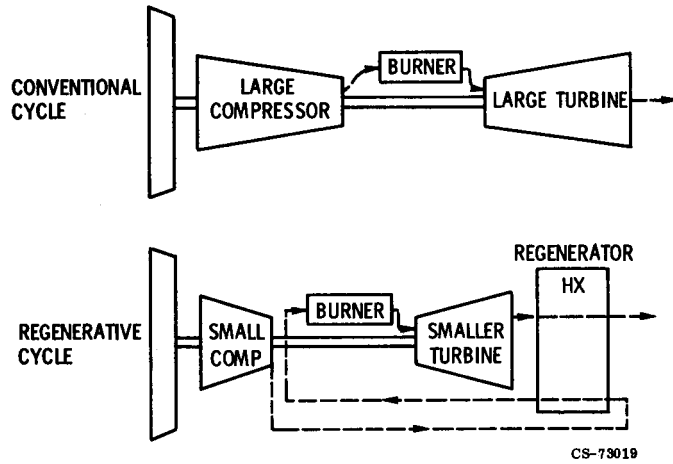
Figure VI-19. – Comparison of conventional and regenerative cycle compressors and turbines.
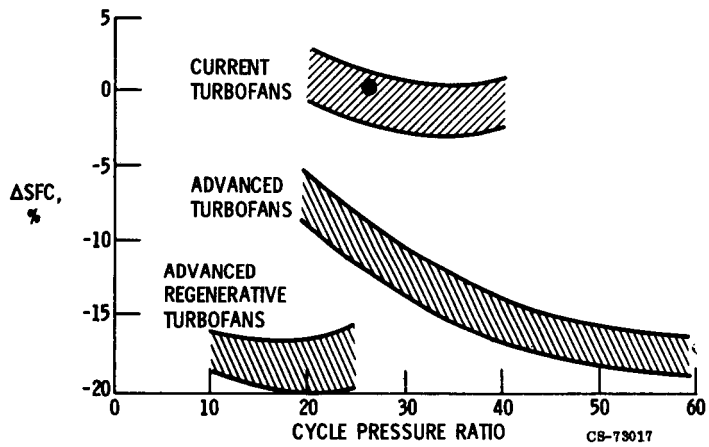
Figure VI-20. – Lower cycle pressure ratio for regenerative turbofans.

187
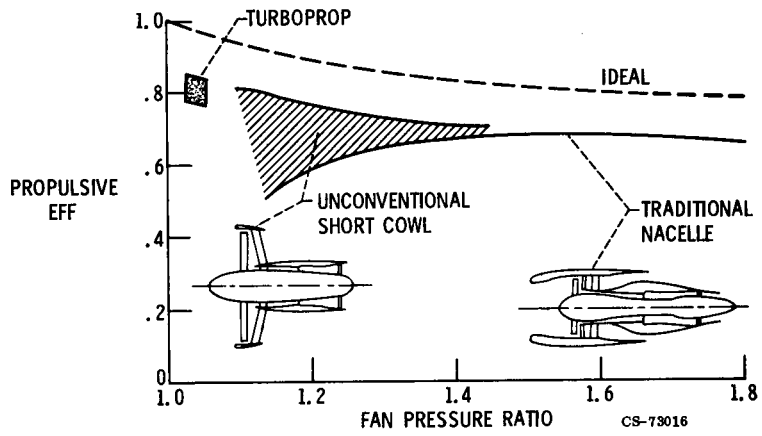
Figure VI-21. - Potential of low fan pressure ratios. Flight Mach number, 0.8.
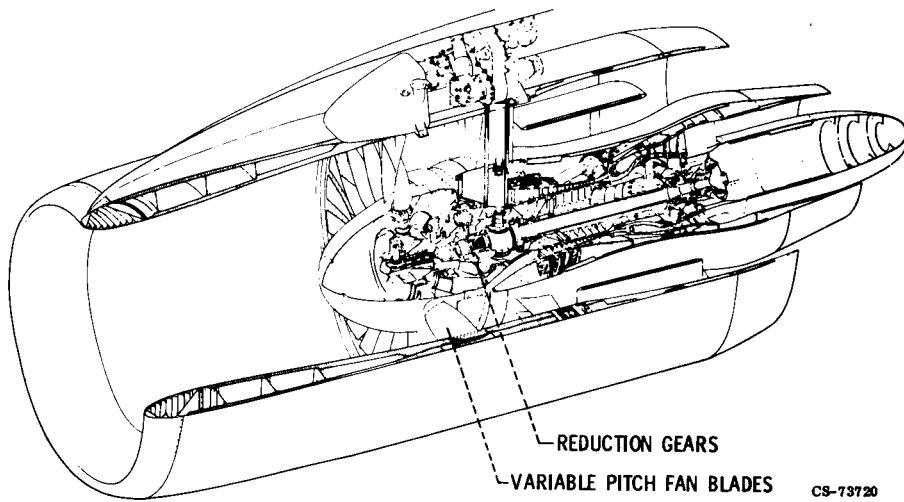
Figure VI-22. - QCSEE under-the-wing engine.

SMALL NOISE
SUPPRESSION AREA

FLOW
SEPARATION
AT INLET LIP

AEROELASTIC
STRESSES IN BLADES

CS-73716
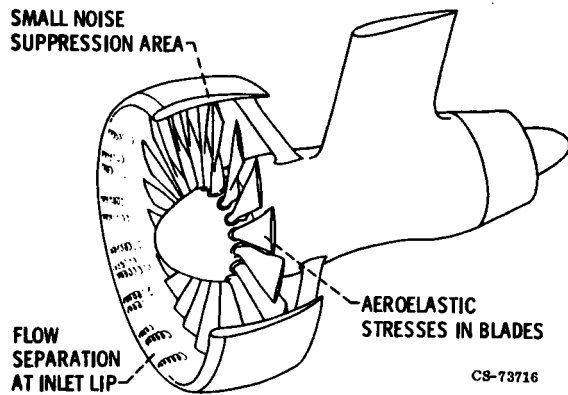
Figure VI-23. - Short cowl turbofan.

LOW POWER LOADING MODELS (1950'S)
HIGH POWER LOADING EST (1985)

EST 1960 RUSSIAN TECH

PROPELLER
EFF

CIRCA WWII   ELECTRA

FLIGHT MACH NO.   CS-73014
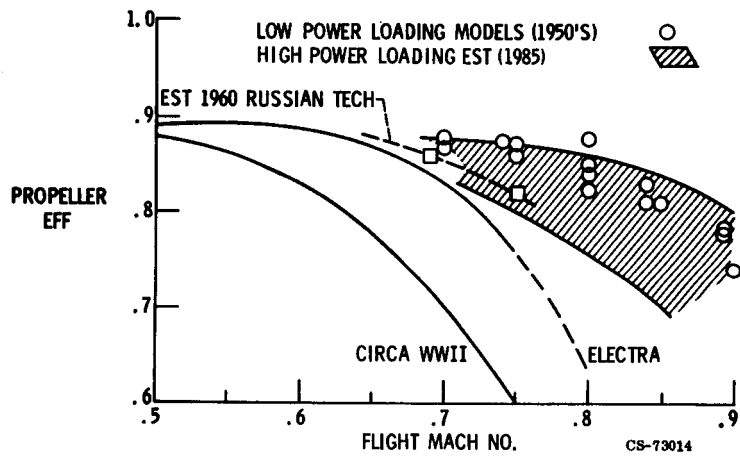
Figure VI-24. - Propeller efficiency trends.

189
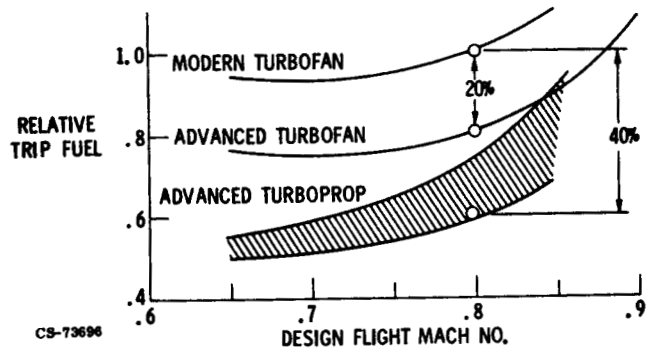
Figure VI-25. - Potential fuel savings of future aircraft powerplants. Airliner capacity, 200 passengers; range, 3000 nautical miles; altitude, 36 000 feet.
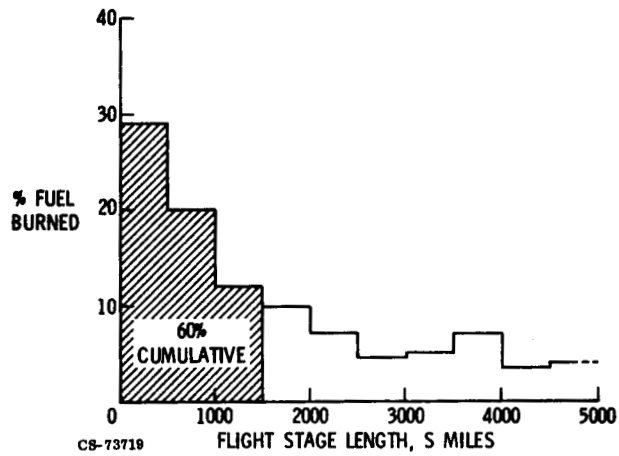
Figure VI-26. - World jet fuel consumption.

190

VII. COMPOSITES FOR FANS AND COMPRESSORS

Tito T. Serafini

Recent studies (refs. 1 and 2) have shown that the use of advanced fiber composites in the low temperature section of turbofan engines can result in significant improvements in overall engine performance. Figure VII-1 shows a schematic diagram of a turbofan engine. The low temperature engine components which have been considered in these studies include fan blades, the fan frame, nacelle, and early stage compressor blades. The use of composite materials for these components can result in reductions in the engine weight, specific fuel consumption, and direct operating costs leading to an increased return on investment. The benefits from using polymer matrix materials in high bypass turbofan engines are summarized in table VII-1. The data used in preparing the table were taken from reference 1. The bases for the cost and benefit analysis studies were a commercial fleet of 100 subsonic aircraft with engine certifications in the years 1980 and 1985. The data shown in the table for gallons of fuel saved per year and reduced operating costs per year are for a fleet of 500 aircraft. It can be seen that significant weight, fuel, and cost savings can be obtained by the use of composite materials.

This paper reviews the composites research being conducted at Lewis for the application of composite materials to fan and compressor blades. The major areas to be discussed include the development of improved materials and fabrication methods, recent progress in providing composite fan and compressor blades with improved resistance to foreign object damage, and the development of advanced design and analysis procedures for composite blades.

CHARACTERISITICS OF COMPOSITE MATERIALS

The benefits that result from the use of composite materials can be attributed to their unique characteristics. Therefore, before proceeding

with the discussion of our composites studies, it is appropriate to briefly review two of the most important characteristics of composite materials. Figure VII-2 shows the specific strength and modulus of several polymer matrix composite materials and conventional metallic alloys. Consideration of the specific properties (property divided by density) of various materials permits a comparison of their properties on an equal weight basis. It can be seen in the figure that the specific properties of metals are quite low and limited to a rather narrow range of values. In contrast, the specific properties of a selected composite material can vary over a broad range. The upper limit for a particular composite system represents the case in which all of the fibers are parallel to the applied load. A composite with this type of construction is referred to as a single ply. The lower limit of the range for each composite represents the case where the fibers are oriented in several directions within the plane, resulting in a material whose elastic properties (within the plane) are uniform. Composites with this kind of construction are not used in actual designs. The important point to be noted is that the broad range of properties which can be obtained from each of the composite materials makes it possible to "tailor-make" materials to meet specific design requirements. This cannot be done with conventional metallic alloys.

The use temperature of a material is another important property which needs to be considered when selecting a material for a particular application. Figure VII-3 shows the use temperatures of various composite materials being considered for use in turbofan engines. The shaded region of each bar represents an increase in use temperature which can be expected in the near future. The use temperature of graphite/epoxy and boron/epoxy composites is about 275° F. High temperature resin/fiber composites have potential for considerably higher use temperatures. As can be seen in the figure, the use temperature of polyimide composites is about 550° F. Because of processing difficulties, the use of polyimide composites has been limited. Studies being conducted here at Lewis to develop processable polyimide composites will be reviewed in the next section of this paper. The figure also shows the use temperature for boron/aluminum composites to be about 600° F.

PROCESSABLE POLYIMIDE COMPOSITES

Studies conducted in our laboratory have led to the development of an improved process for fabricating polyimide composites (refs. 3 and 4). The steps involved in a conventional process and the NASA PMR (polymerization of monomer reactants) process are compared in table VII-2. It can be seen in the table that the PMR process involves a smaller number of steps. The major reason for the smaller number of steps in the PMR process is that the PMR process eliminates the need for the separate polymerization step. Significant cost savings result by eliminating the polymerization and subsequent materials handling steps.

Figure VII-4 schematically illustrates the steps in the PMR process for fabrication of polyimide composites. The upper half of the figure shows the key steps in the PMR process. Fiber is drawn through the solution of monomer reactants. The use of monomer reactants eliminates the need for using highly toxic solvents such as those employed in the conventional process. The use of less toxic solvents provides greater safety to fabricators of polyimide composites. Following impregnation of the fiber, in situ polymerization of the monomer reactants is caused by mild heating. The single layer of impregnated fiber, called the prepreg, is then removed from the drum by cutting it into sections, referred to as broad goods. The lower half of the figure shows the remaining steps needed to fabricate a composite blade. The piece of broad goods is then cut into shapes having the fiber orientation specified by the designer. These layers, or plies, are then placed in a matched metal die and laminated under heat and pressure to form the finished part.

In addition to providing greater safety to fabricators of composites and lower costs, polyimide composites fabricated with the PMR process exhibit improved performance. Figure VII-5 compares the properties of PMR polyimide composites with composites fabricated from a commercial polyimide. The figure shows that after 600 hours of exposure in air at 600° F, the flexural strength of the PMR composites at 600° F was 50 percent higher than the flexural strength of the composite made with the commercial polyimide.

The excellent processing characteristics of PMR polyimide composites have made it possible to fabricate high performance structural components. Figure VII-6 illustrates a polyimide/graphite fiber composite fan blade that

was fabricated using the PMR process (ref. 5).

COMPOSITE BLADES WITH IMPROVED RESISTANCE TO

FOREIGN OBJECT DAMAGE

Polymer Matrix Composite Fan Blades

Polymer matrix composite materials have not, as yet, been introduced into the fan rotor assembly of commercial turbofan engines. The primary reason for this is that polymer matrix composites are quite brittle and have been unable to withstand impact from large objects, such as birds. Before describing our studies to develop polymer matrix composite fan blades with improved impact resistance, the foreign object ingestion requirements established by the FAA and two basic fan blade design concepts currently being investigated will be reviewed.

The FAA foreign object ingestion requirements are summarized in table VII-3. The Group I objects contain large objects including birds weighing up to 4 pounds. In the event the engine ingests one of these objects, the requirement is that the engine must be capable of being safely shut down. The Group II objects are smaller and the requirement is that the engine power recovery must be at least 75 percent.

Figure VII-7 schematically illustrates the two fan blade design concepts currently being studied. The upper schematic is the so-called solid hybrid composite design. The term solid hybrid is used to denote that two or more kinds of fibers are used to construct the blade. The design concept shown in the lower schematic is known as the spar shell composite blade design. Spar shell blades are constructed by encasing a solid or hollow spar (metallic or composite) in foam or honeycomb around which there is placed a composite shell airfoil shape. Studies to evaluate the impact properties of blades fabricated using both design concepts have been conducted.

The results from impact tests conducted in a whirling arm facility on TF39 fan blades are shown in figure VII-8. The tip speed of the rotating blades was 800 feet per second. The all graphite/epoxy blade (shown on the left) failed catastrophically when impacted with a 12-ounce slice of a $1\frac{3}{4}$-pound simulated (RTV silicone foam) bird. The solid hybrid blade (shown on

the right) was impacted with a 24-ounce slice of a $2\frac{1}{2}$-pound bird. It can be seen in the figure that this blade underwent only localized tip damage. These test results (ref. 6) and results being obtained by others lead us to believe that polymer matrix composite fan blades capable of meeting FAA requirements can be developed.

Metal Matrix Compressor Blades

Fiber reinforced metal matrix composites have also been found to possess limited impact resistance. The most highly developed metal matrix composite system is based on boron fibers in an aluminum alloy matrix (B/Al). Recent studies performed with this particular system have shown considerable promise for meeting FAA foreign object ingestion requirements.

The approaches currently being investigated to develop B/Al composites with improved foreign object damage (FOD) resistance are listed in table VII-4. The use of larger diameter fibers in more ductile or in hybrid matrices, together with improved processing and design, has resulted in B/Al composites with significantly improved impact resistance (ref. 7). The use of larger diameter fibers results in increased interfiber separation. This is illustrated schematically in figure VII-9 for composites using 4-mil B fibers (shown on the left) and for composites using 8-mil B fibers. The larger interfiber separation permits the strain capability of the matrix to be more effectively utilized (i. e., greater strain can occur upon impact).

The improved impact strengths obtained with B/Al composite impact specimens by using these approaches are illustrated in figure VII-10. The use of a more ductile matrix, with no change in fiber diameter, led to nearly a fourfold increase in impact strength. Note the cleavage type of failure exhibited by the specimen made with the brittle matrix (specimen illustrated in upper left of the figure) and the ductile failure of the specimen made with the ductile Al matrix (specimen illustrated in upper right of figure). An even more marked improvement in impact strength was obtained by using larger diameter fibers in the ductile matrix. This specimen had an impact strength of 68 foot-pounds and did not fracture upon impact (specimen illustrated in lower half of figure).

These approaches are being used in a joint NASA/AFML program to fab-

ricate B/Al compressor blades for the J79 engine. Figure VII-11 illustrates
the impact resistance of two J79 B/Al compressor blades. Both blades shown
in the figure were impacted in a whirling arm test with birds weighing $2\frac{1}{2}$
ounces. The failed blade did not utilize the advanced techniques described
whereas the blade on the right which showed no visible damage after impact
did. The ultimate objective of this jointly sponsored program is to demon-
strate the viability of B/Al J79 compressor blades in flight tests using an
F4 airplane.

COMPOSITE BLADE DESIGN AND ANALYSIS

Figure VII-12 shows a schematic diagram of a typical composite. Vari-
ous layers, or plies, are oriented at different angles, shown in the figure as
0°, $+\theta^{o}$, $-\theta^{o}$, and 90°, to meet specific strength and stiffness design require-
ments. To characterize the mechanical properties of even a simple unidi-
rectional fiber composite with all fibers alined parallel to the X-axis in the
figure requires working with nine different strength and stiffness properties.
In contrast, to characterize a homogeneous material, such as steel or al-
uminum, requires only three strength and stiffness properties. Because of
the inherent complexity in designing components with fiber composite mate-
rials, a computerized capability for the structural analysis and design of
composite blades has been developed (refs. 8 and 9).

The "flow sheet" for the computerized approach is shown in figure
VII-13. The approach couples composite mechanics and laminate analysis
with the NASTRAN computer program (managed by NASA Langley) by means
of preprocessor and postprocessor computer programs developed at Lewis.
The computerized approach for design and analysis of composite blades is
referred to as NASTRAN-CB (NASA structural analysis - composite blades).
NASTRAN is a general purpose structural/stress analysis digital computer
program based on the use of finite elements. NASTRAN can be used to solve
several different classes of problems including static structural, elastic
stability, dynamic structural, and general matrix.

Using input data, that is, fiber and matrix properties, airfoil geometry
and ply configuration, the preprocessor performs composite mechanics and
then introduces the results into NASTRAN. The postprocessor uses the out-

196

put data from NASTRAN to establish the ply margin-of-safety in terms of limit stresses and strains. To achieve an optimized blade design the program is used in an iterative manner.

Establishing the margin-of-safety of plies subjected to complex stress states requires composite mechanical properties data from well controlled tests and a proven combined-stress failure criterion.

Figure VII-14 illustrates the composite specimens being used to generate data for the NASTRAN-CB program. These tubular specimens have a length of 12 inches, an inside diameter of 2 inches, and a wall thickness of 60 mils. The specimens are tested in a multiaxial testing machine which can apply axial, torsion, or pressure (internal or external) loads. These loads can be applied individually, sequentially, or simultaneously and can be either static or cyclical (up to 10 cps). Figure VII-15 shows a comparison of data obtained from multiaxial tests of high modulus graphite fiber/epoxy composites with failure envelopes that were calculated using a combined-stress failure criterion developed here at Lewis. The arrows on the schematic diagram in each quadrant represent the directions of the applied tensile and compressive loads. The addition of a shear stress (represented by the schematic with head-to-head arrows) causes the failure envelopes to decrease in size. Although only limited experimental data have been obtained thus far, there is excellent agreement between theory (failure envelopes) and experimental data.

Analytical and experimental studies are also in progress to extend the computerized blade design approach for the design of blades with improved impact resistance. Data are being generated for composites tested at strain rates comparable to those resulting from high velocity impact. These data will be incorporated into the computer data bank and used to design blades having improved impact resistance.

SUMMARY

The use of composite materials for components in turbofan engines can result in significant weight and cost savings. Significant progress has been made in the following areas: (1) development of processable polyimide matrix resins, (2) development of polymer and metal matrix composites with improved impact resistance, and (3) establishment of a computerized facility

for the design and analysis of composite blades.

REFERENCES

1. Steinhagen, C. A.; Stotler, C. L.; and Neitzel, R. E.: Study of the Costs and Benefits of Composite Materials in Advanced Turbofan Engines. (R74AEG418, General Electric Co.; NAS3-17775), NASA CR-134696, 1974.

2. Metal Matrix Composites: Status and Prospects. (NMAB-313, National Materials Advisory Board), NASA CR-142191, 1974.

3. Serafini, Tito T.: Processable High Temperature Resistant Polymer Matrix Materials. Presented at International Conf. on Composite Materials, Geneva, Switzerland, Apr. 7-11, 1975.

4. Serafini, Tito T.; Delvigs, Peter; and Lightsey, George R.: Preparation of Polyimides from Mixtures of Monomeric Diamines and Esters of Polycarboxylic Acids. U.S. Patent 3, 745, 149. July 10, 1973.

5. Cavano, P. J.: Resin/Graphite Fiber Composites. (TRW-ER-7677F, TRW Equipment; NAS3-1777), NASA CR-134727, 1974.

6. Impact Resistance of Composite Fan Blades. (R74AEG320, General Electric Co.; NAS3-16777), NASA CR-134707, 1974.

7. Signorelli, Robert A.: Metal Matrix Composites for Aircraft Propulsion Systems. Presented at International Conf. on Composite Materials, Geneva, Switzerland, Apr. 7-11, 1975.

8. Chamis, C. C. and Lynch, J. E.: High-Tip-Speed Fiber Composite Compressor Blades - Vibration and Strength Analysis. Presented at 2nd. Conf. on Fibrous Composites in Flight Vehicle Design, Dayton, Ohio, May 22-24, 1974.

9. Chamis, C. C. and Minich, M. D.: Structural Response of a Fiber Composite Compressor Fan Blade Airfoil. Presented at Gas Turbine Conf. and Prod. Show, Houston, Tex., Mar. 2-6, 1975.

TABLE VII-1. - BENEFITS FROM COMPOSITE MATERIALS

WEIGHT SAVINGS
  24 TO 30% (FAN ROTOR ASSEMBLY)
  24 TO 46% (FAN FRAME)

FUEL SAVINGS
  1.91 TO 3.53%
  (80 TO 120 MILLION GAL/YR)

REDUCED OPERATING COSTS
  2.82 TO 4.64%
  (55 TO 95 MILLION $/YR)

CS-73459

TABLE VII-2. - COMPARISON OF CONVENTIONAL AND IN SITU
PMR FABRICATION PROCESSES

CONVENTIONAL FABRICATION PROCESS	IN SITU PMR PROCESS
MONOMERS	
POLYMERIZATION	MONOMERS
PACKAGING	
SHIPMENT	MIXING VESSEL
STORAGE	
PREPREG FAB	PREPREG FAB
PACKAGING	
SHIPMENT	ASSEMBLY
STORAGE	
ASSEMBLY	MOLD
MOLD	

CS-69020

199

TABLE VII-3. - FAA FOREIGN OBJECT INGESTION REQUIREMENTS

GROUP	OBJECTS	REQUIREMENT
I	TOOLS TIRE TREAD CLEANING CLOTH BIRDS 4 LB	SAFE SHUTDOWN OF ENGINE
II	GRAVEL SAND ICE BIRDS UP TO 2 LB	POWER RECOVERY TO 75% LEVEL

CS-73466

TABLE VII-4. - METHODS TO IMPROVE FOD RESISTANCE OF B/Al COMPOSITES

LARGER DIAMETER FIBERS

MORE DUCTILE MATRIX

HYBRID MATRIX

LOWER TEMPERATURE PROCESSING

OPTIMIZED PLY CONFIGURATION

LOW TEMP   INTERMEDIATE TEMP   HIGH TEMP

FAN BLADES   EARLY COMPRESSOR BLADES   STATOR VANES   TURBINE BLADES

DISK

CS-73101
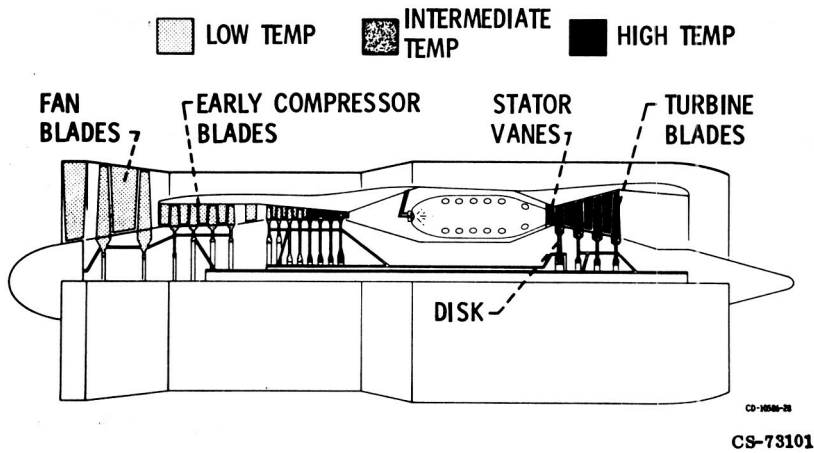
Figure VII-1. - Schematic diagram of turbofan engine.
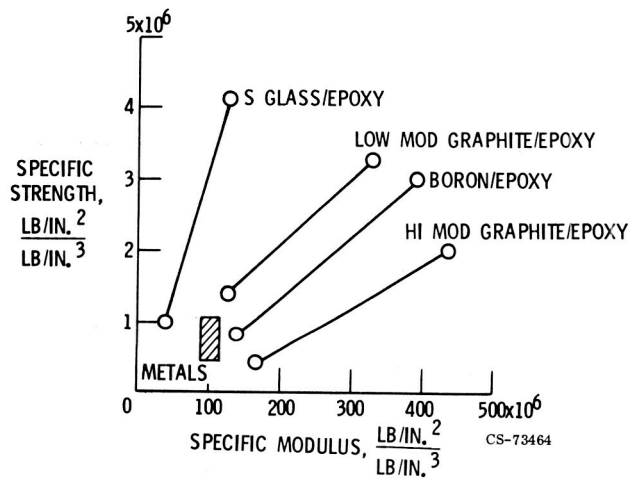
Figure VII-2. - Advantages of composites over metals (room temperature data).
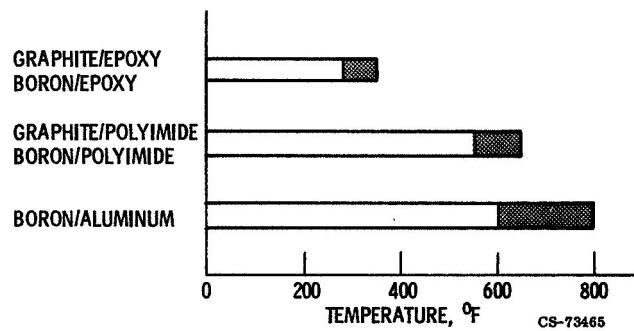
Figure VII-3. - Use temperatures of composite systems under investigation.
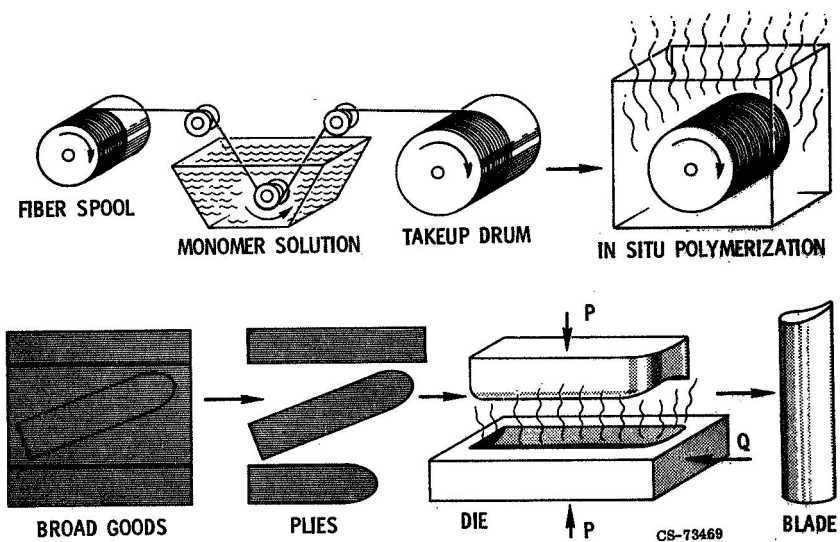
Figure VII-4. - PMR polyimide fabrication process.

600 HR DATA FOR HTS GRAPHITE
FIBER COMPOSITES EXPOSED &
TESTED IN AIR AT 600° F

FLEXURAL
STRENGTH,
KSI

CS-73460
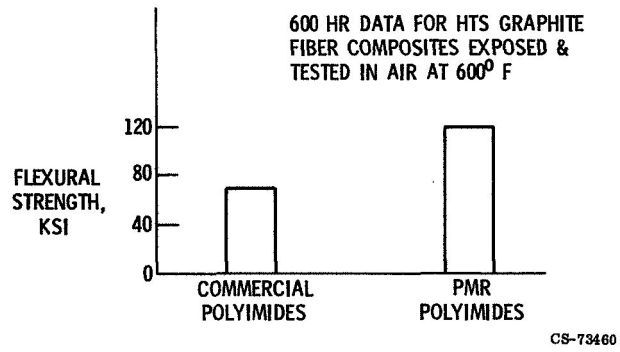
Figure VII-5. - Improved strength of PMR polyimide/graphite fiber
composites.

CS-73471

Figure VII-6. - PMR polyimide/graphite fiber fan blade.
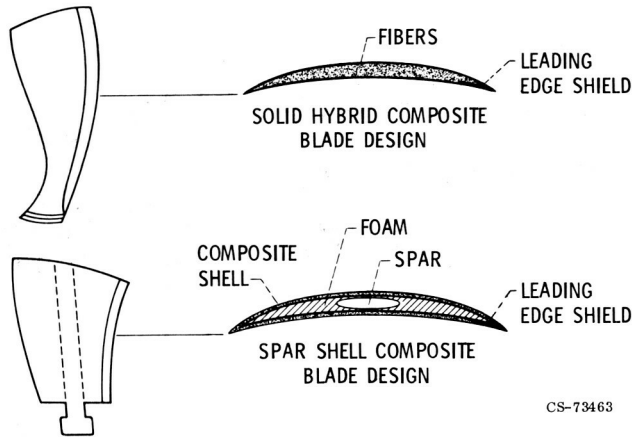
Figure VII-7. - Composite fan blade design concepts.
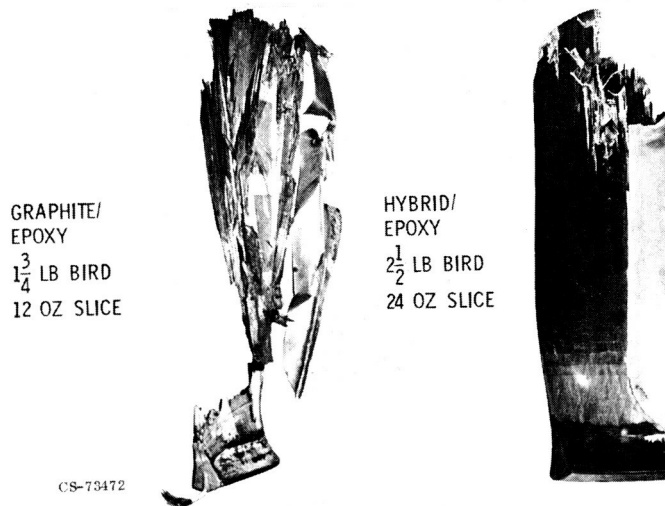
Figure VII-8. - Improved impact resistance of hybrid fiber/epoxy TF39 fan blades.

4 MIL FIBERS

8 MIL FIBERS
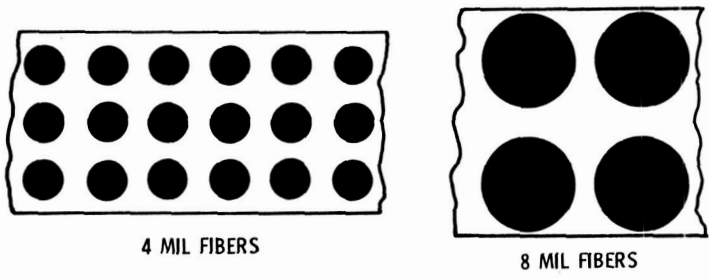
CS-73468

Figure VII-9. - Larger diameter fibers increase interfiber separation (50 volume percent fibers).

13 FT-LB
5.6 MIL B IN BRITTLE MATRIX

47 FT-LB
5.6 MIL B IN DUCTILE MATRIX

68 FT-LB
8 MIL B IN DUCTILE MATRIX
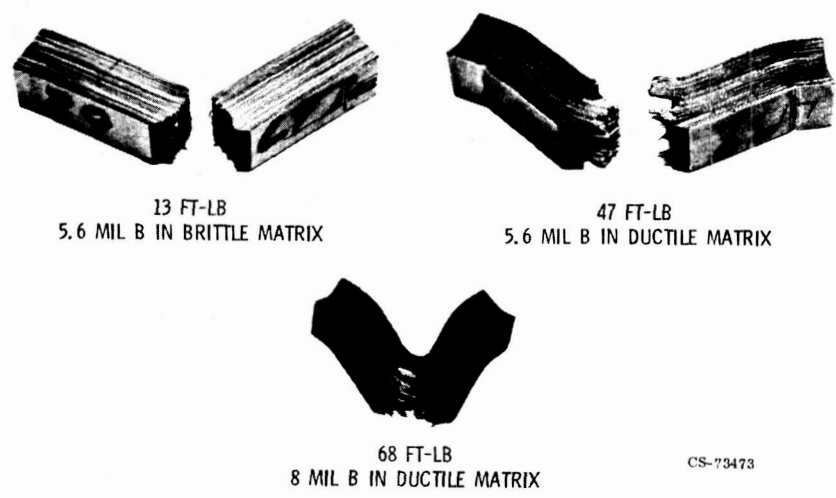
CS-73473

Figure VII-10. - Improved B/Al impact resistance (50 volume percent fibers).
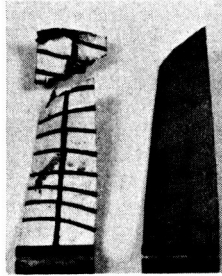
205

Figure VII-11. - Improved impact resistance of J79 B/Al compressor blades.
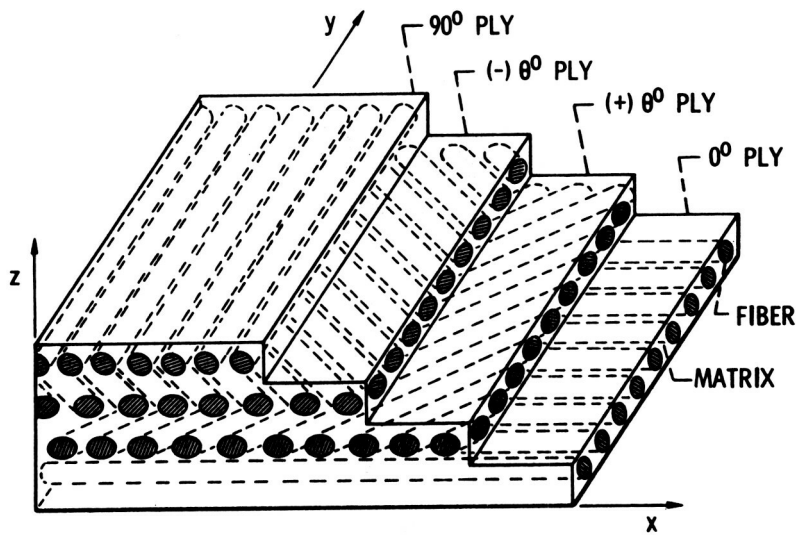
CS-52405

Figure VII-12. - Schematic diagram of construction used in typical fiber composites.
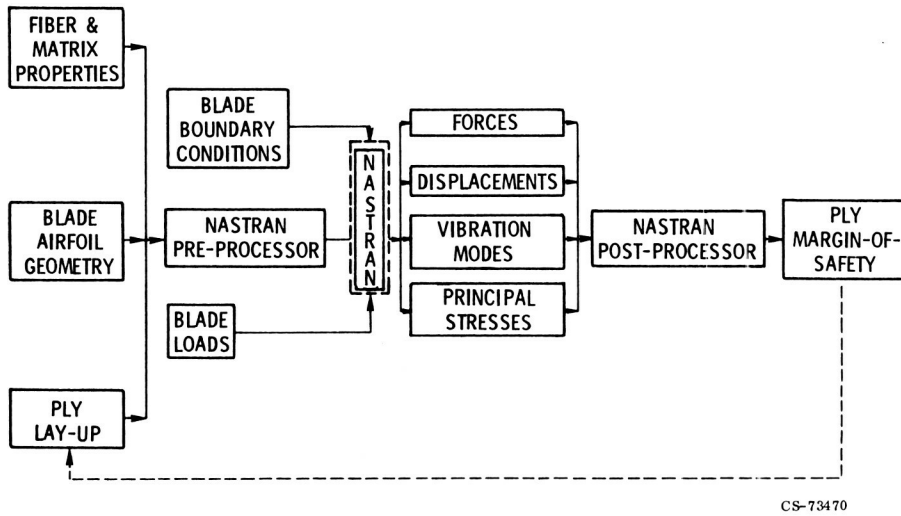
Figure VII-13. - NASTRAN-CB computerized approach for analysis and design of composite blades.

ORIGINAL PAGE
BLACK AND WHITE PHOTOGRAPH
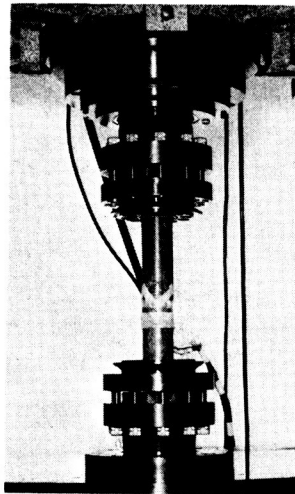
Figure VII-14. - Combined loading specimen.

207
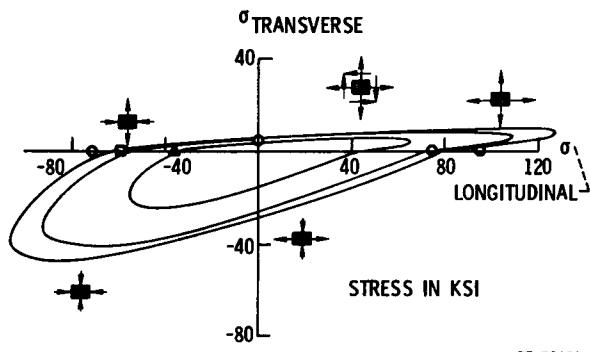
Figure VII-15. – Combined stress failure envelopes.

VIII. TURBINE MATERIALS AND LIFE PREDICTION

Hugh R. Gray

A key to advanced turbine engine performance lies in the development of advanced materials. Paper VII describes recent progress and future directions of our research programs in the fields of composite materials for fan and compressor components. This paper describes the recent developments and future potential of advanced materials for turbine components. The components discussed in detail are disks, blades, and vanes (see fig. VIII-1).

The major goals of turbine materials research and development are to (1) increase material use temperature, (2) increase material strength, and (3) increase component life. Materials with higher use temperatures can permit higher turbine inlet temperatures and reduced cooling. The resultant benefits or payoffs are decreased fuel consumption and increased engine thrust A detailed discussion of fuel conservation is presented in paper VI. Higher strength materials permit increases in rotor speed (discussed in detail in paper IX) and decreases in component weight. Hence, engine payoffs may include fewer stages and reduced weight and cost. An increase in life obviously permits an increase in time between overhauls and thereby decreases engine maintenance costs and increases reliability.

We recently conducted cost-benefit studies which quantified the economic benefits of these material improvements (refs. 1 and 2). These studies were performed for a fleet of 500 subsonic commercial transport aircraft utilizing advanced technology representative of the mid-1980's. The basic characteristics of these studies were a 3000-nautical-mile-range aircraft and a load factor of 55 percent of the total passenger capacity of 180.

Some of the major results of these cost-benefit studies are summarized in figure VIII-2. The economic benefits of four advanced turbine components are illustrated in terms of both increase in return on investment (ΔROI) and decrease in direct operating costs (ΔDOC). The resultant economic benefits

over the life of the aircraft are $45 million for prealloyed powder metallurgy disks, $90 million for eutectic blades, and $200 million for ceramic vanes. The remaining turbine component shown in figure VIII-2 is ceramic shrouds. The fuel savings from these advanced high-temperature wear-resistant shrouds are shown not only for the baseline case of a 3000-nautical-mile range but also for an aircraft capable of a 5000-nautical-mile range. The fuel savings of 20 and 56 million gallons per year are worth approximately $6 and $17 million, respectively, at current fuel costs of $0.30 per gallon.

DISK ALLOYS

Strengths of early, current, and future alloys for latter stage compressor and turbine disks are shown in figure VIII-3, which indicates the 1200° F yield strength and year of introduction of the alloys. Data for three of the more common conventionally cast disk alloys are shown in this figure. Initially casting was done in air and more recently in vacuum. A promising approach for achieving higher strength disk alloys involves a new processing technique, prealloyed powder processing.

The NASA IIB-7 prealloyed powder alloy (ref. 3) has excellent strength at 1200° F and has potential for use as a disk alloy within a few years. The reason for the potentially higher strength of alloys made by the prealloyed powder process may be seen from the microstructures of such alloys. Figure VIII-4 illustrates the microstructure of a typical nickel-base superalloy, NASA-TRW VIA, in both the cast and prealloyed powder forms (ref. 4). It is immediately evident that the cast version of the alloy contains massive γ' particles as well as a large grain size. In contrast, the same alloy in the prealloyed powder form exhibits a homogeneous distribution of strengthening phases and a fine grain size.

A prealloyed powder process is schematically illustrated in figure VIII-5 and compared with the conventional forging process. In the former process an alloy is inductively melted and then atomized by an inert gas jet. The droplets solidify rapidly into homogeneous fine powder particles, which are then compacted and extruded into a blank. This blank is then superplastically formed into a shape that closely resembles the machined disk. In contrast, the conventional forging process requires induction melting,

remelting of the ingot, and then several forging steps to obtain the rough oversize forging, from which a large amount of material must be machined away to produce the finished disk. Hence, it is apparent that the prealloyed powder process saves not only raw material but also processing and machining steps.

A specific example of these savings is shown in figure VIII-6. A commercial turbine disk, currently produced in large volumes by forging, requires a starting billet of 360 pounds. This billet is forged and machined to a preform weighing 198 pounds. This rectilinear preform is required for current ultrasonic flaw inspection techniques. The prealloyed powder process could enable the preform to be produced directly and thus save 162 pounds or 45 percent of the raw material required for conventional forging. In both processes the preform is machined to the finished disk weighing 145 pounds. However, the powder disk would require only 53 pounds of material to be machined away, compared with 215 pounds for the current forged disk. These savings in both raw material and machining could result in a turbine disk costing only $8000 rather than the current price of $10 000.

Another example of the benefits of prealloyed powder alloys is shown in figure VIII-7. Because alloy segregation is avoided in powder alloys, higher strength alloys can be developed by increasing the amount of strengthening phases. Figure VIII-7 illustrates how this increased strength can result in thinner lighter weight disks. A disk made from a widely used forged alloy with a tensile strength of 170 ksi at 1200° F would be 3 inches thick at the disk rim. A thinner and 20 percent lighter disk could be made from a forged alloy with a tensile strength of 195 ksi. A still more significant weight saving of 40 percent could be realized if the NASA IIB-7 prealloyed powder alloy, with a strength level of 240 ksi, were to be used as the disk alloy.

TURBINE BLADE ALLOYS

The historical and projected use-temperature capabilities of blade alloys are shown in figure VIII-8. The use temperatures are based on 5000 hours of life at a blade stress level of 30 ksi. As for disk alloys, future projected advances in blade alloys rely on radical changes in processing technology. Most current blade alloys are conventionally cast with a controlled grain size,

but with random grain orientations. Significant advances in use temperatures are being achieved with directional structures. For example, MAR M-200 with hafnium (Hf) is currently being used at about 1600° F in its conventionally cast form, while the directionally solidified (DS) version of the same alloy is being used at significantly higher temperatures. Directionally solidified eutectic alloys and tungsten-fiber-reinforced superalloy composites offer still greater potential in terms of use temperature. Tungsten-fiber-reinforced superalloys are in the very early stages of development and hence are not discussed in this paper. However, the directionally solidified eutectics are farther along in their development cycle, and our current efforts toward qualifying one of these alloys for use as a turbine blade alloy at 1900° F are described.

Conventionally cast and directionally solidified turbine blades are shown in figure VIII-9. Enlargements of portions of the blades illustrate the differences between the equiaxed randomly oriented grains typical of cast blades and the elongated unidirectional grains that are produced by directionally solidifying a blade from the root toward the tip. Directional structures have optimum properties along the length of the blade, parallel to the main stress axis of the blade. Hence, the creep strength and use-temperature capability of such directional structures are markedly increased as a result of this unique processing technique.

The directionally solidified eutectic alloy that we are currently investigating is intended for use as a 1900° F hollow turbine blade; its microstructure is shown in figure VIII-10. The alloy, called the γ/γ'-δ eutectic alloy, has been successfully cast into advanced turbine blades. It consists of a matrix of γ phase strengthened by a precipitate of small particles of γ', Ni_3Al, and reinforced by lamellae of the δ phase, Ni_3Cb (ref. 5). The alinement of these phases along the principal blade stress axis contributes to the excellent high-temperature creep strength of the eutectic alloy.

Metallic turbine blades, whether they are eutectics or fiber-reinforced superalloys, will require protective coatings to extend their useful life in engines. Some preliminary results of work on protective coatings for the γ/γ'-δ eutectic alloy are shown in figure VIII-11. Laboratory tests were conducted up to 2200° F in a cyclic mode. This condition was a severe test since the eutectic blade is designed for operation at 1900° F. The uncoated γ/γ'-δ eutectic alloy exhibited a very rapid weight loss (approx. 8 mg/cm^2

within the initial 20 hr of testing). A conventional nickel-chromium-aluminum (NiCrAl) coating provided a substantial improvement with respect to oxidation weight loss. A recently developed coating, a nickel-chromium-aluminum-yttrium-plus-platinum (NiCrAlY+Pt) coating, provided excellent protection of the γ/γ'-δ eutectic alloy (ref. 6). Only a very slight weight increase was measured for this coating system. Further research on protective coatings to provide reliable and extended operational lifetimes for advanced turbine blade alloys is under way at this Center.

A major challenge posed by all directional structures is their inherent anisotropy. Because mechanical properties of directional structures are optimum along the blade stress axis, shear strength and transverse properties may not be adequate for advanced turbine blade applications. For example, the root teeth of turbine blades are subject to shear stresses. The shear strength and temperature conditions encountered by current root designs are indicated in figure VIII-12, together with root design conditions anticipated for future advanced turbine blades. The shear rupture strength of the γ/γ'-δ eutectic alloy is only marginally acceptable for current root design conditions. We are conducting research in an attempt to increase the shear strength of this eutectic alloy so that its full potential may be realized in advanced turbine blade applications.

TURBINE VANE MATERIALS

Recent progress and the future potential of turbine vane materials are shown in terms of use temperatures in figure VIII-13. These use temperatures are based on a vane stress of 2.5 ksi, 0.2 percent creep, and a melting point margin of safety extending to at least 250° F below the material melting temperature. Conventionally cast alloys (e.g., X-40) have been used for vanes since the mid-1950's. The most advanced of the recent cast alloys is NASA WAZ-16, which has a potential use temperature of approximately 2000° F.

Additional increases in use temperature once again are dependent on new types of processes or materials. A recently developed alloy, thoria-dispersed nickel-chromium alloy (TD-NiCr), is representative of a class of alloys called oxide-dispersion-strengthened (ODS) superalloys. For this type

of alloy, extremely small particles of an inert high-melting-point oxide, such as thoria or yttria, are mixed into a superalloy matrix to provide strengthening to temperatures of 2200° to 2300° F (ref. 7). Current efforts are focused on ODS-NiCrAl.

The most promising class of vane materials currently receiving substantial attention is ceramics. As indicated in figure VIII-13, ceramics have potential use temperatures in the range 2400° to 2600° F. The two leading candidates, silicon nitride (Si_3N_4) and silicon carbide (SiC), have the most potential of the many ceramics screened in laboratory investigations during recent years.

The oxidation resistance of dense ceramics is outstanding, as is evidenced in figure VIII-14. The results of cyclic laboratory tests in a Mach 1, 2200° F airstream are shown for a commercially coated TD-NiCr alloy and for hot-pressed SiC. The coated alloy specimen exhibited a substantial weight loss rate, while the ceramic specimen exhibited almost negligible weight change. The photographs of the test specimens dramatically illustrate the superior resistance of the ceramic to both oxidation-erosion weight loss and thermal fatigue cracking at the specimen leading edge.

The biggest challenge facing the materials engineer with respect to ceramic vanes is to increase the impact resistance of ceramics. Ceramics are relatively brittle, but significant progress has been made within the past few years (see fig. VIII-15). In 1970 the best impact strength obtainable for unmodified silicon carbide at either room temperature or 2400° F was less than 1 inch-pound. Slight improvements in impact strength were obtained by adding either 25 volume percent silicon carbide whiskers or 10 volume percent carbon fibers. Fairly substantial increases, to about 5 inch-pounds, were obtained by improving the hot-pressing technique or by introducing residual compressive stresses in the surface layers of the test specimen. (An analogy to this latter technique is found in the window glass manufacturing industry, where the surface layers of glass sheets are placed in residual compression because they cool at a faster rate from the high processing temperatures than do the central portions of the glass sheet.) The highest impact strength obtained for silicon carbide was almost 12 inch-pounds - approximately a factor of 10 greater than the baseline impact strength. This best value was obtained during testing at 2400° F with an energy absorbing surface layer on the ceramic test specimen. The material used as a surface

214

layer was lithium aluminum silicate (ref. 8). This concept is particularly effective at 2400° F, where the surface layer is viscous and thus can absorb a large amount of impact energy. We are continuing extensive efforts to increase the impact strengths of ceramics to still higher levels over the entire temperature range expected to be encountered in turbine engine operation. We are confident that ceramics will eventually realize their full potential in vanes, as well as in other components, in advanced turbine aircraft engines.

LIFE PREDICTION

The third major goal of turbine materials research is to increase component life and reliability. Inherent in meeting this challenge is the ability to predict component lives accurately. To accomplish this we have a coordinated life prediction program that involves material property determinations, rig tests, and actual component performance (see fig. VIII-16). The material property determinations consist of typical laboratory tensile, creep, fatigue, and oxidation tests. The properties generated are incorporated into life prediction theories to determine the cyclic thermal fatigue characteristics of materials. Rig tests are conducted in high-velocity airstreams, in cyclic temperature modes, and under stress to simulate more closely the actual operating conditions encountered in turbine engines. The results of these tests are also incorporated into our life prediction theories to improve their accuracy. The validity of the prediction techniques evolved is finally determined in ground engine tests with actual components.

Several life prediction theories have been developed at the Lewis Research Center. About a decade ago the method of universal slopes was introduced to predict the fatigue lives of turbine components at low and intermediate temperatures. This theory utilizes only simple tensile properties (strength, ductility, and modulus) of materials and is widely used today by designers. However, at elevated temperatures creep interacts with fatigue. Hence, the 10-percent rule was developed to account for the detrimental influence of creep at elevated temperatures. This rule states that the cyclic lives of components operating in a creep-fatigue regime are only 10 percent of the lives which would be predicted if only fatigue effects were acting.

In order to achieve additional accuracy for high-temperature creep-

fatigue life predictions, the method of strainrange partitioning (ref. 9) was introduced. This method is extremely accurate and promises to become a very useful technique for aerospace and industrial designers. This section describes the method of strainrange partitioning.

During fatigue testing of a metal specimen, the structure of the metal can deform in two distinctly different ways. Figure VIII-17 schematically illustrates these deformation models for a microscopic portion of the metal specimen. The enlarged view of the specimen shows two metal grains separated by a grain boundary. Within one of the grains, a slip plane is shown. Deformation occurs along either grain boundaries or slip planes, as shown in the sketches in the lower portion of figure VIII-17. The sketch at the lower left corner illustrates the situation when fatigue cycling occurs at a rapid rate (e.g., 1 cycle/sec). Upon the application of a tensile stress, deformation occurs along a slip plane across a grain (i.e., transgranularly). When the stress is reversed by compression, deformation occurs back along the same slip plane and essentially reverses the transgranular deformation. For this type of rapid cycling, no creep occurs - only pure fatigue.

The sketch at the lower right corner of figure VIII-17 illustrates the case of very slow cycling (e.g., 1 cycle/engine start). The applied tensile stress forces grain boundaries to slide across each other, which results in the formation of small holes or voids in the grain boundaries. This process is termed intergranular deformation. Reversal of the stress by compression causes reversed sliding along the grain boundaries and, theoretically, a closing up of the voids previously created. For this type of slow cycling, either tensile or compressive creep deformation is dominant rather than fatigue.

There are only four basic types of cyclic deformation, and they are illustrated schematically in figure VIII-18. For a given cyclic range of strain, the longest possible life (greatest number of cycles to failure) occurs when no creep (pure fatigue) takes place. This pure fatigue is the upper bound of cyclic life. As discussed previously, when creep occurs at elevated temperatures, cyclic life is shortened. This effect is evident from the three lower lines in figure VIII-18, which represent the three types of creep deformation. The shortest life (fewest number of cycles to failure) occurs when creep in tension is involved. This is the lower bound of cyclic life. The remaining

two types of cyclic deformation, compressive creep and tensile plus compressive creep, result in cyclic lives intermediate to the two extremes.

Figure VIII-19 shows micrographs of fractured specimens of 316 stainless steel tested at 1300° F under two types of cyclic straining. The specimen shown at the left was subjected to a cyclic tensile creep strain of 0.015 percent. This specimen failed after only 15 cycles, and as is evident from the micrograph, failure occurred along grain boundaries (was intergranular). Many voids occurred along grain boundaries away from the fracture surface. In contrast, the specimen at the right was subjected to a similar amount of cyclic creep strain, but in compression rather than in tension. This compressively strained specimen did not fail until 264 cycles were applied. As is evident from the micrograph, the fracture plane crossed the grain boundaries (was transgranular).

The ability of the strainrange partitioning theory to predict cyclic lives is dramatically illustrated in figure VIII-20, which shows data for 12 different alloys (iron-, nickel-, cobalt-, tantalum-, and copper-base) over a wide range of test temperatures. The actual cycles to failure are compared with the calculated cycles to failure. If the agreement of actual lives with predicted lives were perfect, all the data points would fall on the solid 45° line. Not all the data agree perfectly with the theory, but the data are all within a factor of 2. This capability to predict cyclic lives to within a factor of 2 is a substantial improvement over the capabilities of previous life prediction theories, which typically were not accurate to less than a factor of 10.

The tremendous potential of the theory of strainrange partitioning has already been widely recognized by aerospace and industrial designers, and the theory is continuing to be refined not only at the Lewis Research Center but also at several universities. We are confident that the theory of strainrange partitioning will become a powerful and widely used design technique.

SUMMARY

Some of our recent developments and the future potential of advanced materials for turbine components are described in this paper. Prealloyed powder disks, directionally solidified eutectic turbine blades, and ceramic turbine vanes offer substantial economic benefits in advanced commercial

aircraft. Their increased strength and/or use-temperature capability, together with improved life prediction methods, will result in substantial improvements in advanced turbine engine performance.

REFERENCES

1. Bisset, J. W.: Cost/Benefit Study of Advanced Materials Technologies for Aircraft Turbine Engines. (PWA-5073, Pratt & Whitney Aircraft; NAS3-17804.) NASA CR-134701, 1974.

2. Ross, E. W.; Johnston, R. P.; and Neitzel, R. E.: Cost Benefit Study of Advanced Materials Technology for Aircraft Turbine Engines. (General Electric Co.; NAS3-17805.) NASA CR-134702, 1974.

3. Kent, William B.: Development Study of Compositions for Advanced Wrought Nickel-Base Superalloys. (U-C-R-1055, Cyclops Corp.; NAS3-14309.) NASA CR-120934, 1972.

4. Freche, John C.; Ashbrook, Richard L.; and Waters, William J.: Application of Powder Metallurgy to an Advanced-Temperature Nickel-Base Alloy, NASA-TRW VI-A. NASA TN D-6560, 1971.

5. Lemkey, F. D.: Eutectic Superalloys Strengthened by δ, Ni_3Cb Lamellae and γ', Ni_3Al Precipitates. NASA CR-2278, 1973.

6. Felton, F. J.; Strangman, T. E.; and Ulion, N. E.: Coatings for Directional Eutectics. (PWA-5091, Pratt & Whitney Aircraft; NAS3-16792.) NASA CR-134735, 1974.

7. Probst, H. B.: Powder Metallurgy Approaches to High Temperature Components for Gas Turbine Engines. Presented at Eighth Plansee Seminar, Reutte, Austria, vol. I, May 27-30, 1974.

8. Kirchner, H. P.; and Sevetsky, J.: Improving Impact Resistance of Ceramic Materials by Energy Absorbing Surface Layers. (Ceramic Finishing Co.; NAS3-17765.) NASA CR-134644, 1974.

9. Manson, S. S.; Halford, G. R.; and Hirschberg, M. H.: Creep-Fatigue Analysis by Strain-Range Partitioning. In Design for Elevated Temperature Environment, New York, American Society of Mechanical Engineers, 1971, pp. 12-24.

LOW TEMP   INTERMEDIATE TEMP   HIGH TEMP

FAN BLADES   EARLY COMPRESSOR BLADES   STATOR VANES   TURBINE BLADES
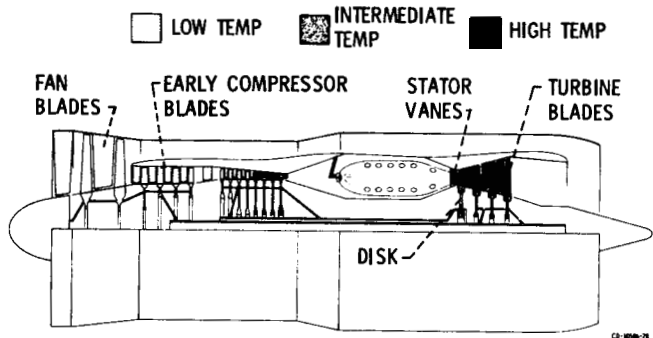
DISK

CS-73101

Figure VIII-1. - Schematic diagram of turbofan engine.

ΔROI, POINTS

ΔDOC, %

FUEL SAVINGS, GAL

$45 MILLION
POWDER METALLURGY DISKS

$90 MIL.
DIRECTIONALLY SOLIDIFIED EUTECTIC BLADES

$200 MIL.
CERAMIC VANES

5000 MI 56×10^6 ($17 MIL)
3000 MI 20×10^6 ($6 MIL)
CERAMIC SHROUDS
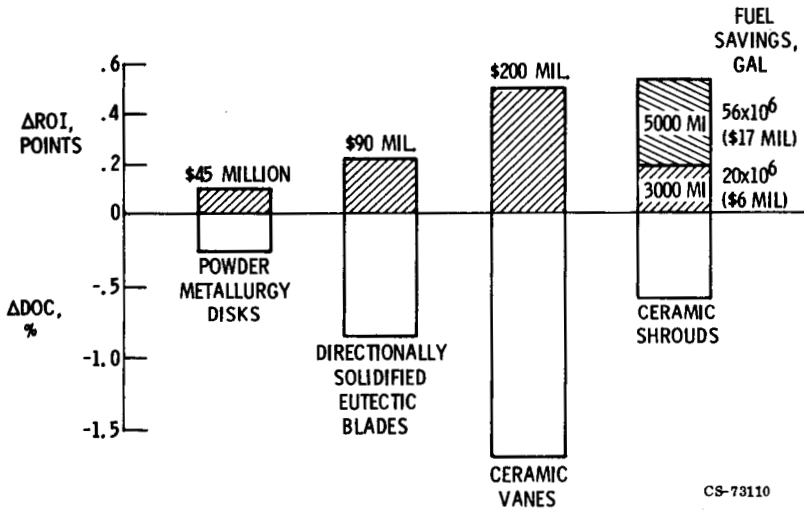
CS-73110

Figure VIII-2. - Potential economic benefits from advanced turbine components.
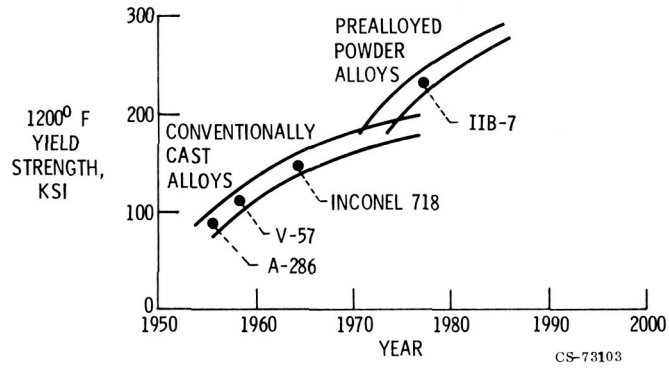
Figure VIII-3. - Strengths of turbine disk alloys.

AS CAST

PREALLOYED POWDER PRODUCT

CS-66862
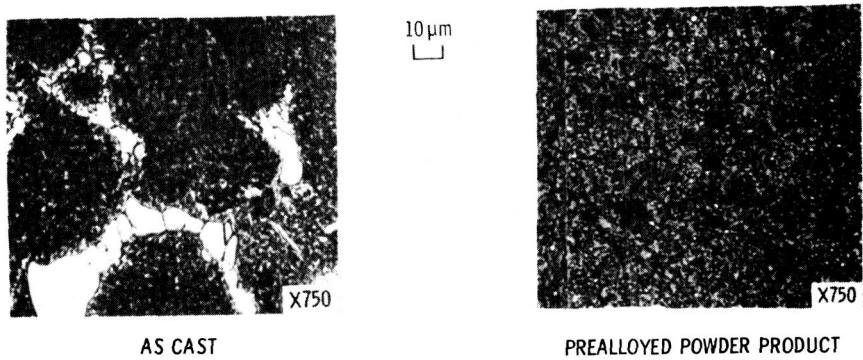
Figure VIII-4. - Microstructures of NASA-TRW VIA alloy.

PREALLOYED POWDER PROCESS

INDUCTION MELT

POWDER

EXTRUDED BLANK

SUPERPLASTICALLY FORMED SHAPE

FORGING PROCESS

INDUCTION MELT

ARC REMELT INGOT

BLANK

PREFORM

FINAL

FORGED

FINISH MACHINED DISK

CS-73112
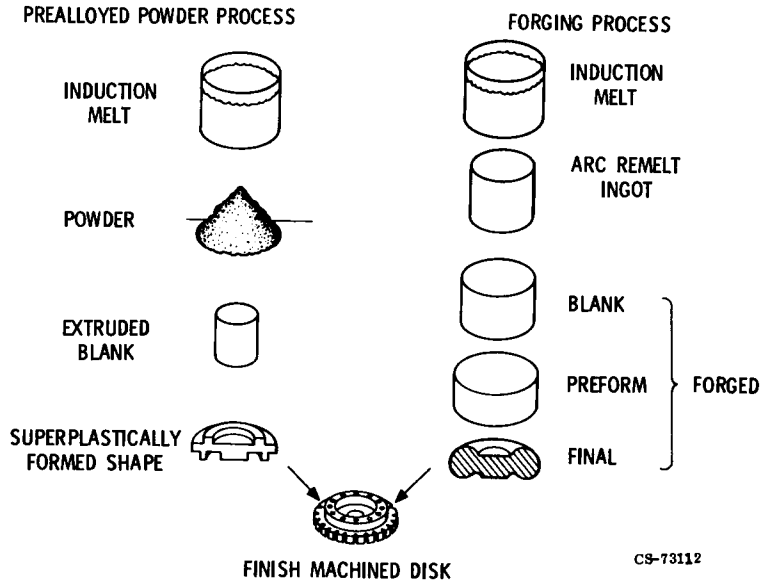
Figure VIII-5. - Comparison of processing steps needed to produce powdered and forged turbine disks.

BILLET - 360 LB (REQUIRED IN FORG-ING PROCESS ONLY)

PREFORM - 198 LB

FINISHED DISK - 145 LB

MATERIAL SAVED BY POWDER PROCESS   162 LB OR 45%
TOTAL MACHINING REQUIRED
    BY POWDER PROCESS   53 LB OR 27%
    BY FORGING PROCESS   215 LB OR 60%

CS-72316
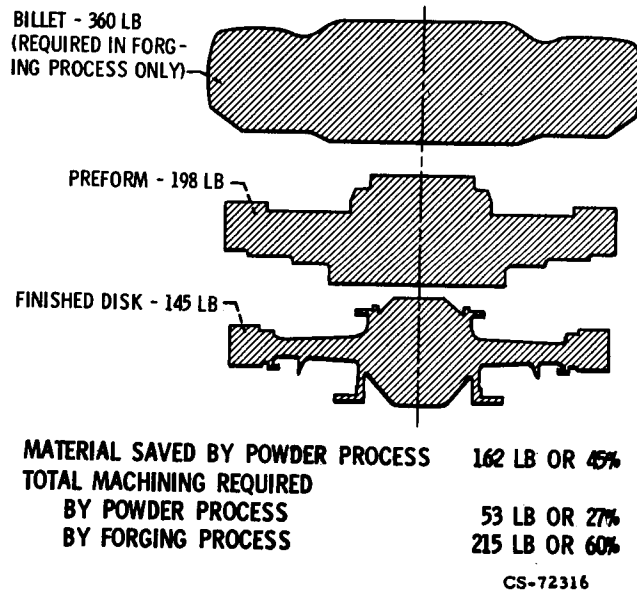
Figure VIII-6. - Material and machining saved by using prealloyed powder process.

221

WIDELY USED
FORGED DISK ALLOY

RECENTLY DEVELOPED
FORGED DISK ALLOY

IIB-7
PREALLOYED POWDER
DISK ALLOY

1200° F
TENSILE
STRENGTH,
KSI

170

195

240

3.0 IN. THICK

2.3 IN. THICK
20% LIGHTER

1.6 IN. THICK
40% LIGHTER
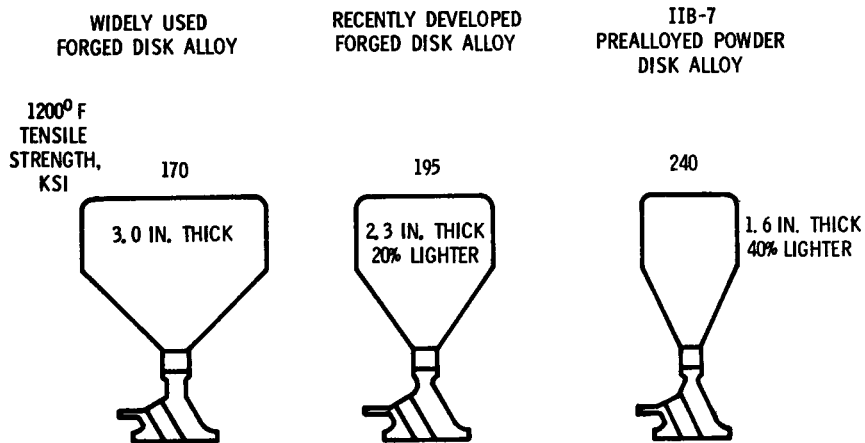
CS-73111

Figure VIII-7. - Advances in disk technology made possible by new stronger alloys.
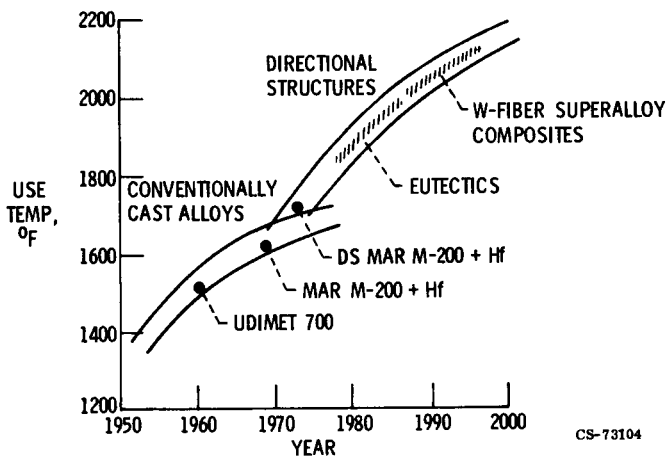
Figure VIII-8. - Use temperatures of turbine blade alloys.

CS-73104

222
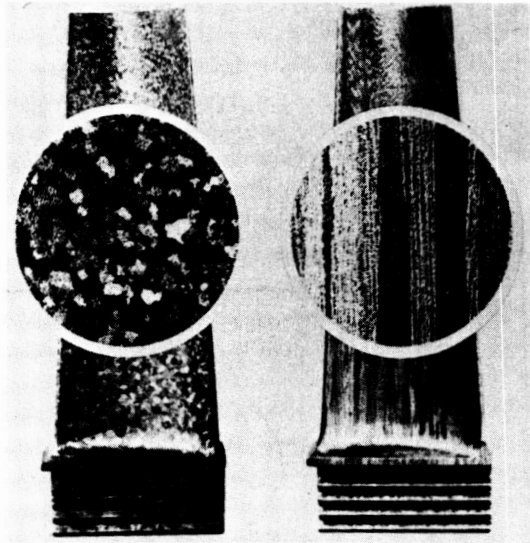
CONVENTIONALLY CAST   DIRECTIONALLY SOLIDIFIED

CS-73114

Figure VIII-9. - Random and controlled grain structures in
cast blades. (Courtesy of Pratt & Whitney Aircraft.)
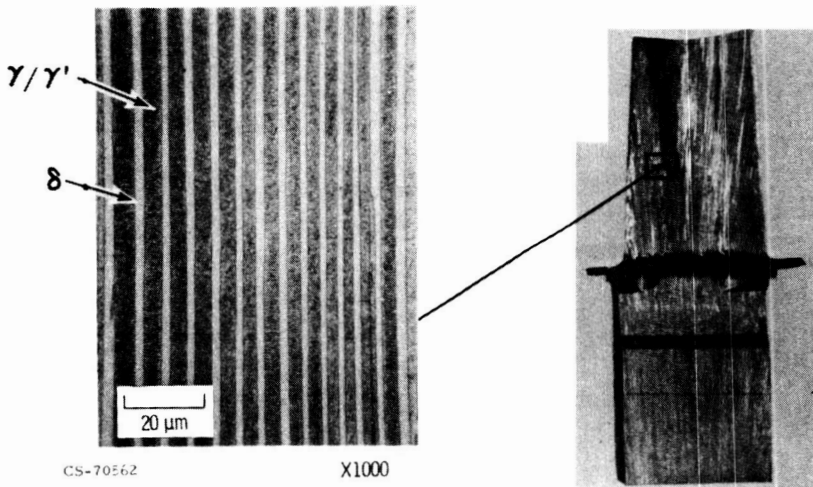
Figure VIII-10. - Turbine blade of γ/γ'-δ directionally solidified eutectic.
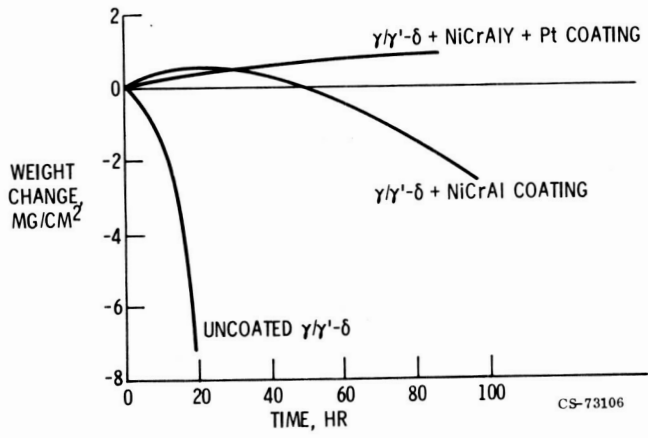
Figure VIII-11. - Effect of protective coatings on $\gamma/\gamma'-\delta$ eutectic. Temperature, 2200° F; static air.
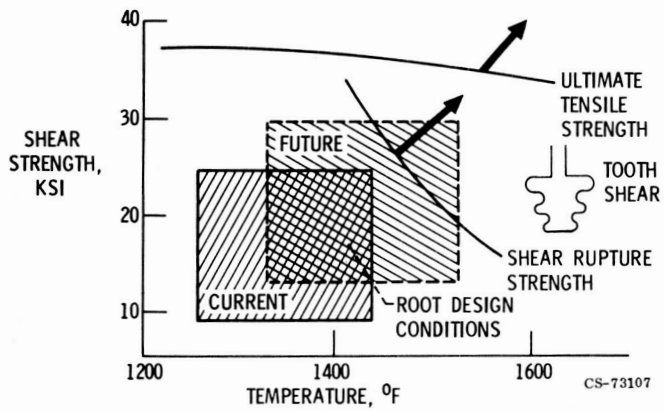
Figure VIII-12. - Comparison of current and future shear strength requirements for $\gamma/\gamma'-\delta$ eutectics.
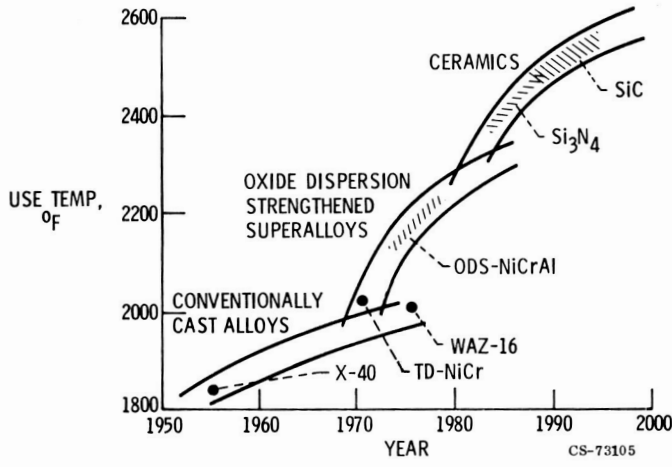
Figure VIII-13. - Use temperatures of turbine vane materials.
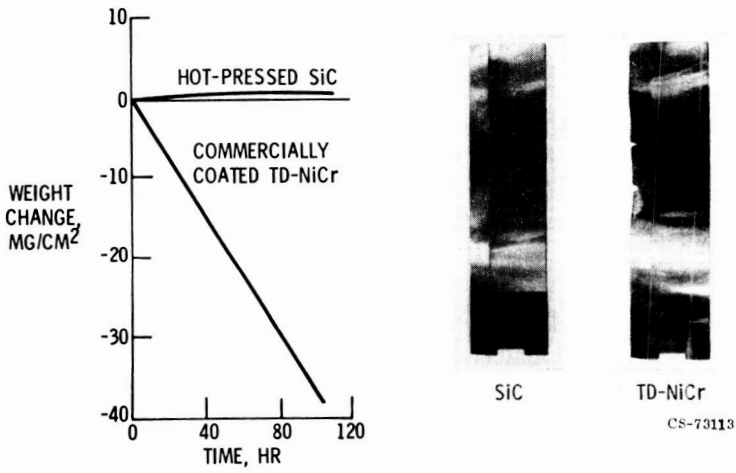
Figure VIII-14. - Oxidation resistance of ceramics. Mach 1; 2200° F; 1-hour cycles.
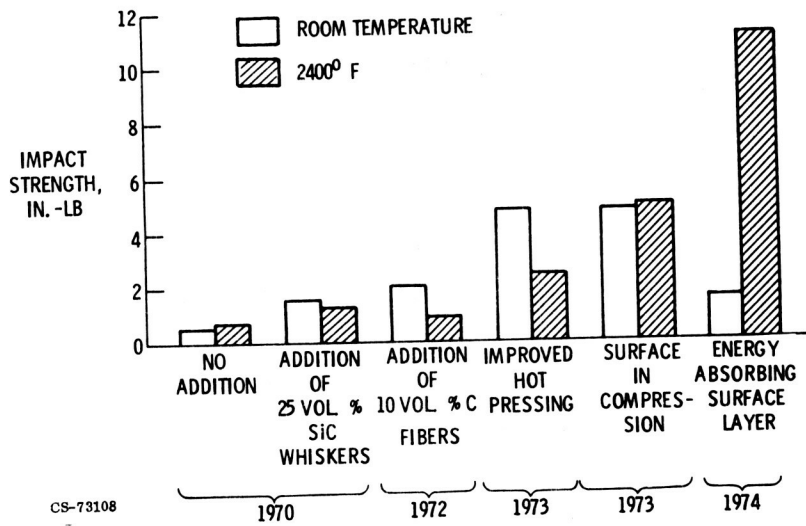
Figure VIII-15. - Best impact strength values for silicon carbide. Unnotched Charpy specimen (0.25 by 0.25 by 1.5 in.).
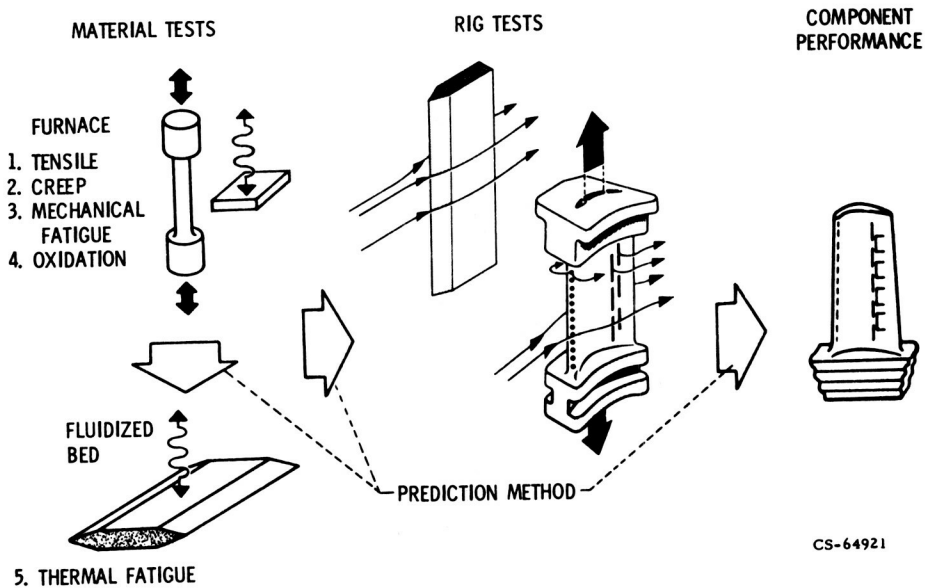
Figure VIII-16. - Turbine component life prediction program.

226
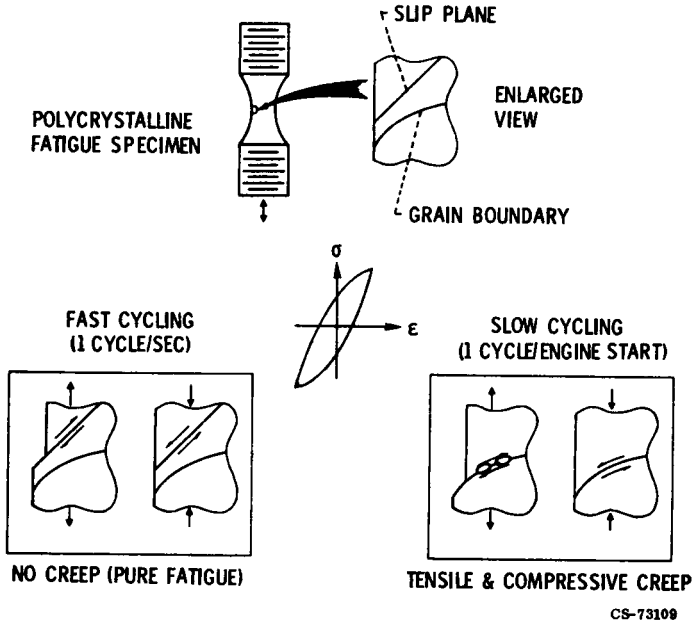
Figure VIII-17. – Simple cyclic deformation models for strainrange partitioning.
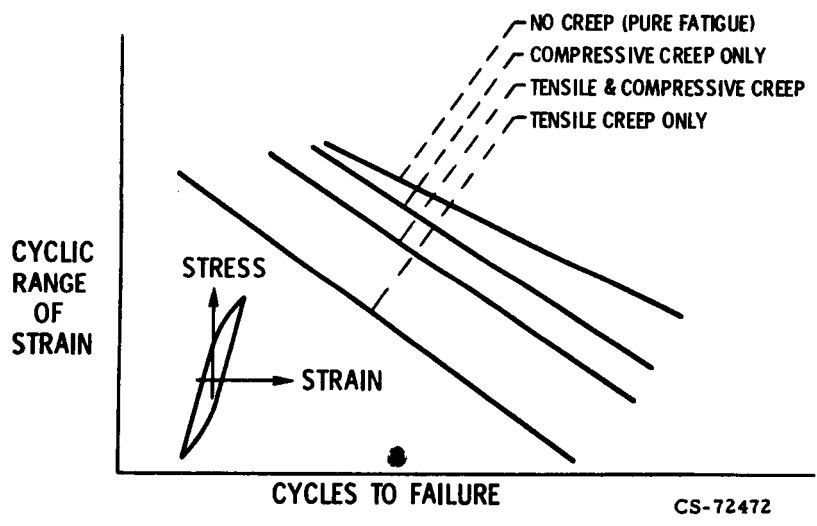
Figure VIII-18. – Characterization of material behavior by strainrange partitioning.

TENSILE CREEP = 0.015%   COMPRESSIVE CREEP = 0.016%

0.5 mm

$N_F = 15$
(INTERGRANULAR)

$N_F = 264$
(TRANSGRANULAR)

CS-73115
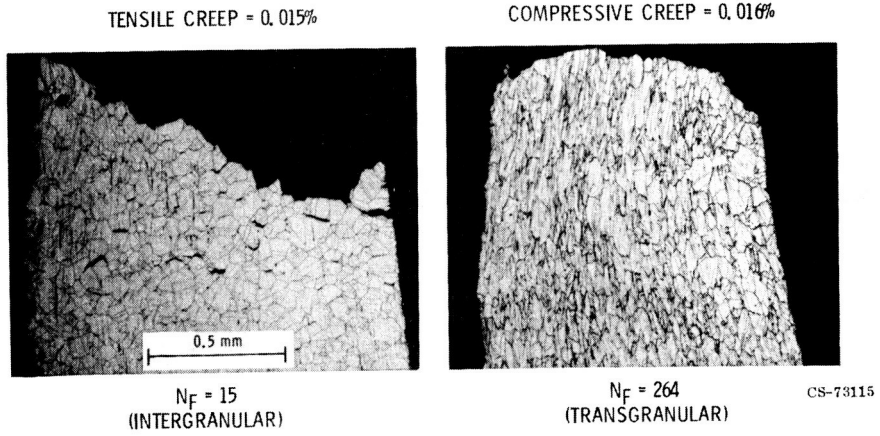
Figure VIII-19. - Fatigue fractures of 316 stainless steel at 1300° F.

OBSERVED
CYCLES TO
FAILURE

FACTORS OF 2 ON LIFE

CYCLES TO FAILURE CALCULATED BY
STRAINRANGE PARTITIONING

CS-72382
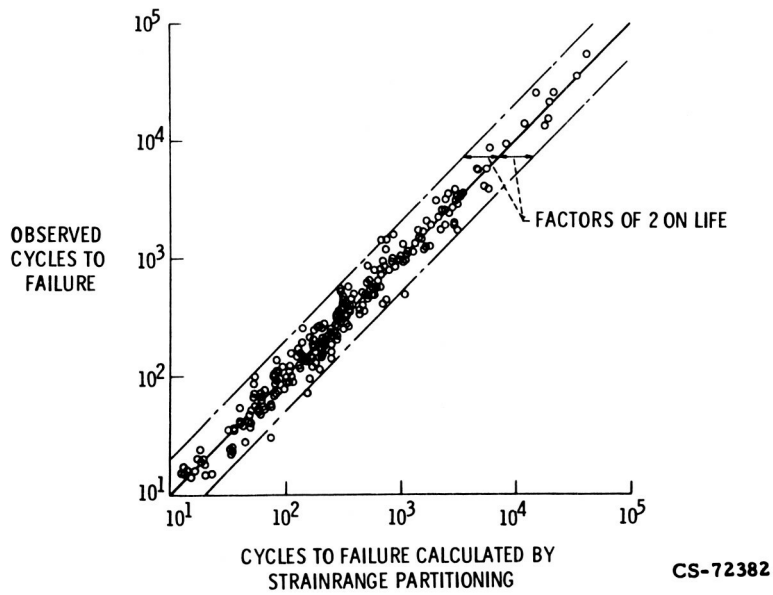
Figure VIII-20. - Prediction of cyclic lives by strainrange partitioning. Twleve alloys (iron-,
nickel-, cobalt-, tantalum-, and copper-base).

IX. COMPRESSOR AND TURBINE TECHNOLOGY

Cavour H. Hauser, Calvin L. Ball, Raymond S. Colladay, William D. McNally, and Thomas P. Moffitt

The advanced turbofan engine should have a low specific fuel consumption, low weight, low cost, and should be quiet. Each of these desired characteristics is related to the performance of the engine turbomachinery components (fig. IX-1).

With a high bypass ratio fan, engine noise is reduced; propulsive efficiency of the engine is increased, giving reduced specific fuel consumption. The use of near-sonic velocity in the inlet duct attenuates the forward transmission of fan noise. Increased core pressure ratio together with a higher turbine inlet temperature gives a higher thermodynamic cycle efficiency and, therefore, low specific fuel consumption. Good core component efficiencies must be maintained, however. One of the goals of compressor research is higher pressure ratio per stage with good efficiency, allowing a higher overall pressure ratio with a minimum number of stages and therefore a lower weight. Compressor blades are expensive; if there are fewer blades per stage and a reduced number of stages, fewer blades are needed, resulting in a significant cost saving. In the high temperature core turbine, film-cooled blades are required for the temperature levels of advanced engines. Cooling air must be bled through small holes distributed over the blade surfaces. Experimental studies are used to derive the most effective means of placing these film cooling holes in order to keep the required coolant flow to a minimum. The effect of mixing this coolant flow with the mainstream on the blade surfaces on the efficiency of the turbine must be considered. The fan turbine must run at low speed if it is coupled directly to the fan. The use of high turbine stage work factors can reduce engine cost and weight by reducing the number of stages required.

FANS AND COMPRESSORS

Stage Performance Trends

A major objective of fan and compressor research is to obtain high pressure ratio per stage with high efficiency. There are two factors which affect stage pressure ratio: rotor speed and blade loading (fig. IX-2). The blade loading parameter is a measure of the static pressure rise through the blade passage and is similar to the lift coefficient for an airfoil. As speed is increased, the flow velocities relative to the blades become supersonic and flow shocks form within the blade passage resulting in increased losses. As blade loading is increased, the tendency is for the flow to become unstable and separate from the blade suction surface resulting in higher losses. To attain high efficiency, it is necessary to evolve improved blade profiles and flow path geometries that will minimize shock losses and flow separation.

Some of the results of NASA's program to obtain high efficiency in high pressure ratio single stages are presented in figure IX-3. The lower plot in this figure shows data obtained from stages ranging in tip speed from 700 to 1800 feet per second and in stage pressure ratios from 1.2 to 2.2. The blade loading parameter for these stages ranged from about 0.3 to 0.6 and accounts for the spread in pressure ratio at a given speed. The adiabatic efficiencies for these stages are presented in the upper plot. The cross-hatched band represents the best efficiencies achieved to date. Very high efficiencies have been demonstrated for tip speeds up to about 1500 feet per second. The point shown as a solid symbol is for an efficiency of 87.5 percent. The stage achieved a pressure ratio of 1.7. Above 1500 feet-per-second tip speed, the maximum efficiencies that have been obtained are somewhat lower. At 1800-feet-per-second tip speed, a stage pressure ratio of 2.2 was obtained with an acceptable efficiency of 82 percent (ref. 1). We are confident that a higher level of efficiency in this high-speed range can be achieved by further improvement in blade design.

Combining High Pressure Ratio Stages

In order to determine the effect of stage interaction on the performance of high pressure ratio stages, a study of a two-stage fan was conducted under contract with Pratt & Whitney Aircraft (ref. 2). An overall view of the fan test rig with casing installed is shown in figure IX-4 together with a model of the bladed flow path. A tip speed of 1450 feet per second was selected for the fan and the overall pressure ratio set at 2.8. The individual stage pressure ratios were 1.74 and 1.61. Dampers were incorporated on both rotors to control blade vibration.

The performance of the fan is presented in figure IX-5 with efficiency and pressure ratio displayed as a function of weight flow for a range of constant speeds (ref. 3). The fan met its design weight flow and pressure ratio at design speed, and it exceeded its design efficiency. Peak efficiency at design speed was 85.5 percent. The results obtained from this fan show that high pressure ratio stages can be combined without stage interaction effects appreciably derating the overall performance. The performance of this two-stage fan is remarkable when it is compared to fans in engines currently under development. The pressure ratio of 2.8 was obtained in two stages where current fans require three stages. Because of the excellent performance of this fan, it has generated considerable interest in the industry and is now being evaluated for a specific application.

Analytical and Experimental Methods

The detailed understanding of the flow in blade rows needed for further improvements in performance is obtained in the following ways: first, by the use of analytical computer codes, and second, by using advanced experimental techniques.

The use of analytical codes and advanced experiments are needed to get a better understanding of the complicated flow situation depicted in figure IX-6. This figure shows a portion of a rotor blade row with three adjacent blades rotating to the right. Many of the flow phenomena which contribute to low performance in any blade row are schematically represented on these three blades.

One important flow phenomenon which affects performance is the development of the boundary layer flow on each blade surface. Large viscous losses exist due to the friction between this flow and the blades. As the boundary layers on the suction and pressure surfaces join at the blade trailing edge and pass downstream, they mix together in the wake region, causing additional losses.

Other boundary layers exist on the end walls or casings, which form the inner and outer boundaries of the flow path. Only the hub boundary layer is shown in the figure. These wall boundary layers are often thicker than those on the blades. Losses are particularly severe in the corner regions where the blade surface and end wall boundary layers exist together.

The passage of fluid through the clearance space at the tips of the blades also reduces performance. This flow meets an adverse pressure gradient from the next blade, which curls it into a corner vortex, forming another region of high loss. Other vortices are also shed from some of the other blade corners. These have different causes, but they still add to the overall loss.

Because low velocity flow in the boundary layer regions cannot withstand the centrifugal forces due to blade rotation, secondary or outward flows are set up in the boundary layers. These flows add to the losses in the tip and corner regions of the blades.

The cross-hatched area in figure IX-6 represents a shock surface in the flow passage, which is an additional source of loss. Shocks exist there because the rotative speeds of both fan and core stages cause a good portion of these blade rows to be operating in the transonic flow range.

Finally, the flow through a blade row is generally unsteady in time. Unsteadiness is due to the alternating rotation and nonrotation of adjacent blade rows; and also to flow distortions and flow oscillations in the inlet region of the engine. Unsteadiness complicates all of the other flow problems mentioned previously. All of these flow problems have to be kept under control to maintain high pressure ratio and efficiency in transonic blade rows.

To understand this flow two things are needed: first, the ability to predict the performance of a given rotor or stator blade row for both design and off-design conditions. This involves the use of analytical computer codes which model in various ways the flow through the blade passages. Second, the ability to experimentally measure complicated flow effects in already

existing hardware is required. Experimentally measured data provide an understanding of the flow, and are also used in the design of future blade rows. Such measurements also provide data to verify the analytical computer models.

In the design of analytical codes, several key choices have to be made. Will the code analyze an entire three-dimensional flow passage, including all of the flow between two blades? Or will it just analyze some two-dimensional surface within that region? Will it include viscous effects such as the boundary layers and wakes, or not? Will it analyze transonic flow so that it can predict the shocks? And finally, are the unsteady effects dominant enough that they have to be included in the analysis? A wide variety of computer codes can result depending upon how these effects are combined. Furthermore, as more and more important flow effects are included, the complexity of the code, its running time, and the amount of information it produces, all go up dramatically.

On the other side of the design control picture are the advanced measurement systems. Dynamic pressure sensors make use of high-response transducers to measure pressure fluctuations in regions where pressure is changing very rapidly. They are generally used externally to the blades, either upstream or downstream, or mounted in the shroud above the blade tip.

The hot wire probe is another high-response device which is used to obtain a map of all the velocity components - axial, radial, and tangential - in the high-loss regions behind blade rows.

Two other measurement systems - both laser devices - are used to study the flow within the blade passages. The laser velocimeter can obtain a map of the internal velocities between blades. In that way, shock surfaces, secondary flows, and boundary layers can be studied. Laser holography obtains a three-dimensional picture of the shocks within the passage. The complex nature of these three-dimensional shocks can be studied using special viewing techniques on a hologram.

The following examples present some results of applying analytical codes and measurement systems to some modern high-speed blade rows. These are some of the initial applications of transonic computer codes to NASA's blade rows. In the first example, a program to analyze two-dimensional, inviscid, transonic steady flow is used to check dynamic

pressure measurements taken in the shroud over the tip section of a transonic rotor (ref. 4). Two blades from this rotor are shown schematically at the top right of figure IX-7. These blades have a tip speed of 1500 feet per second and a pressure ratio of 1.66. The experimentally determined shock pattern is also shown. At the bottom right of the figure are the locations of the transducers mounted in the shroud above the blade tip. At the left are shown the blade surface pressures obtained both analytically and experimentally. The square symbols are data from the eleven transducers. These data include the influence of viscous effects in the tip flow, including shock interaction with the shroud boundary layer. The circular symbols, on the other hand, are analysis results from computer solution mesh points along the blade surfaces. The nine points along each surface represent a very coarse mesh, and the program does not include viscous effects. Considering these differences, the results are remarkably close. On the upper or suction surface, the shock is located at the trailing edge of the blade. The two techniques agreed on the location and magnitude of this trailing edge shock. On the pressure side of the blade there are two shocks, one at the leading edge, and one further back on the surface. The analysis did not predict as strong a leading edge shock as the transducers measured. Likewise, the shock further back on the blade was displaced somewhat from what was measured by the shroud transducers. Further work with these two systems, principally through refinement of the computer solution mesh, should provide even better agreement, and thus a more precise study and control of transonic flow in blade tip regions.

The next example again shows a comparison between analysis and experiment. The same program for two-dimensional, transonic flow is used, but here experimental results are obtained from laser holography. Holograms have been obtained under contract with AiResearch on a 1600-feet-per-second transonic rotor, designed for a pressure ratio of 1.5 (ref. 5). A schematic picture of the tip sections of these fan blades is shown at the upper left of figure IX-8. These blades were designed to contain weak oblique shocks off the leading and trailing edges in order to minimize losses. This figure also shows three two-dimensional photographs taken of actual holograms. These three photographs show the tip region of the blade row, operating at 90, 95, and 100 percent of design speed. The orientation of the blades is the same as in the upper left diagram, with only the leading

234

edge regions shown. The full holograms show a great deal more detail than can be seen here, of course. The lower right photograph for the design speed condition shows an oblique shock off the leading edge extending back into the passage. At 95 percent speed the blade row is still started, but the leading oblique shock has begun to move forward a bit. And at 90 percent speed, at the upper right, the shock system within the blade passage has moved out in front of the leading edge and has become detached. Although it is not clear in this figure, the actual holograms show that this detached shock crosses the passage as a normal shock. This unstarted condition causes higher loss and a drop in efficiency, and would contribute to buzz-saw noise for this blade row.

Figure IX-9 shows the performance of this rotor (ref. 6). At the bottom of the figure total pressure ratio is given over a range of weight flows and wheel speeds. There is a dip in the stall line near 90 percent speed, indicating that stall occurred sooner there. The efficiency is quite high, except for the 90 percent curve. The difference in efficiency between 90 and 100 percent is explained by the structure of the shocks within the blade passages, as shown in the two circles above the curves. At 90 percent speed, the holograms showed a normal shock, and at 95 and 100 percent speed where efficiency was high, the shock was oblique.

Figure IX-10 shows the results of using a code for two-dimensional transonic flow to verify this result. Both the hologram and the analysis results are shown at 90 percent speed at the left and at full design speed at the right. In both photographs the observed hologram shocks are represented by solid lines, and the calculated analysis shocks by dashed lines. At the right, in the design case, analysis and experiment agreed very well, although the hologram shocks could only be clearly observed in the front portion of the blade passage. At the rear of the passage, the predicted analysis shock was located where the design trailing edge shock should be for this flow condition.

At the 90 percent speed condition the analytical shock at the trailing edge, which was oblique at design speed, has become normal to the passage, and is located behind the minimum area point, or throat. At this same back pressure, the holograms showed a bow shock at the blade leading edge; that is, the normal passage shock has moved forward to the passage throat, and then joined with the leading edge oblique shock, and jumped out in front of

the blade. If the analytical solution was obtained at increased back pressure, that calculated shock would also move up to the throat and then jump to the blade leading edge. However, for the back pressure of the hologram photographs, this did not occur using a computer code for two-dimensional, inviscid flow. Blade surface and end-wall boundary layers, along with other real three-dimensional flow effects, are probably controlling the placement of the shock that was observed in the hologram. This example points to the need for analytical programs that account for three-dimensional and, eventually, viscous effects to calculate three-dimensional flow in the complete passage from hub to shroud. A program for inviscid three-dimensional flow analysis is under development, and its calculated results are currently being compared to experimentally measured flow conditions within blade rows.

Of course, analysis and experiment have both been used for a long time; but because of recent progress in electronics, lasers, numerical analysis, and computer speed, analysis and experiment bring us much closer to describing the real flow within turbomachinery blade passages. Proper use of these new techniques should enable us to consistently derive better designs for high-speed blade rows.

Fans for Low Noise

Recently, experimental studies have been made to evaluate both the acoustic characteristics and the aerodynamic performance of a high tip speed single-stage fan and a low tip speed two-stage fan. It was found that with the application of noise-suppression inlets these fans did achieve low noise. Because of the effects of compromises in the aerodynamic design of the fans to reduce noise, some reduction in efficiency is expected.

Flow paths for the two fans are shown in figure IX-11. The single-stage fan was designed and investigated under contract with General Electric. It has a design pressure ratio of 1.8 and a tip speed of 1650 feet per second. The design specific flow is high, 44 pounds per second per square foot of annulus area. A tip shroud is utilized to control blade vibration. The two-stage fan was studied in a contract with Pratt & Whitney (ref. 7). It has a design overall pressure ratio of 1.9 and a tip speed of

1200 feet per second. The design specific flow of 42.9 pounds per second per square foot is also relatively high.

The compromises to reduce noise are the following:

(1) High specific flow

(2) Blade rows spaced

(3) Stator/rotor blade number ratio

(4) Staging

(5) Large rotor blade throat area

The purpose of the first of these items, high specific flow, is to allow the fan to produce acceptable performance when matched with a noise-suppression near-sonic inlet. Both of the low noise fans were designed for a high specific flow. The resulting high axial velocity at the fan face minimizes the deceleration of the flow downstream of the throat of the inlet. The other listed compromises are designed to reduce the generation of noise within the fan. For both the single-stage and the two-stage fans the blade rows were spaced apart to reduce blade interaction noise. The ratio of the number of stator vanes to rotor blades should be somewhat greater than two, according to fan noise theory, to eliminate the transmission of fundamental blade passing frequency noise. This results in stator vanes having relatively short chord; that is, they have high aspect ratio. The resulting vanes are not necessarily optimum for good aerodynamic performance. The photograph of the single-stage fan (fig. IX-12) shows the large number of stator vanes as compared to the rotor blades. The wide blade spacing is also apparent.

The use of two stages in the low speed two-stage fan is in itself a low noise compromise. The lower speed is inherently quieter, but this advantage must be balanced against the greater blade interaction noise with two stages.

The single-stage fan is designed with the throat area in the rotor blade passage larger than would be optimum for best aerodynamic performance. The function of the large rotor blade throat area is illustrated in figure IX-13. For a high bypass ratio fan, the 0.9 design speed curve typically corresponds to the engine takeoff condition and design speed to the cruise condition. The purpose of the large blade throat area is to reduce noise at the 0.9 speed takeoff condition. With the large throat area the desirable flow condition shown in the lower inset is obtained. A weak oblique shock is

attached to the blade leading edge. This is similar to attached shock in the hologram photograph of figure IX-8. If the throat section had been smaller, as would normally have been used, strong detached bow waves would stand out ahead of each rotor blade, generating multiple pure tone noise or buzz-saw noise during takeoff. However, there is a price for this large throat compromise. The potential penalty of this approach is the difficulty of maintaining high fan efficiency at the design speed cruise condition. As shown in the upper inset of figure IX-13, with the oversized throat the leading edge shock is pulled back into the passage and separation of the flow from the blade suction surface in the subsonic diffusion region downstream of the throat may become severe. Alternatively, supersonic reacceleration downstream of the throat can give rise to secondary shocks, which add to the loss. High fan efficiency at cruise is important for low specific fuel consumption.

The question is how much the various compromises in the aerodynamic design of these two fans to obtain low noise will penalize their performance.

The aerodynamic performance for both the single-stage and the two-stage fans was first evaluated with a bellmouth inlet to establish baseline performance. Then each of these fans was tested with a noise suppression inlet so that the effect of these inlets on fan performance was determined. The flow paths for both fans with the bellmouth inlets are shown in figure IX-14. The corresponding performance of the single-stage fan is shown in figure IX-15. The speeds of 0.7, 0.9, and 1.0 N_D correspond to those for approach, takeoff, and cruise, respectively. At the design speed the fan did not quite achieve its design flow and pressure ratio. The maximum efficiency at design speed was 82 percent, about two points lower than design. The fan was designed for high specific flow and had a large rotor blade throat area to reduce shock noise during takeoff. While the level of efficiency is not the ultimate for a low noise fan, some penalty in performance with these aerodynamic design compromises was expected.

The performance of the two-stage fan with the bellmouth inlet with speeds of 0.63, 0.94, and 1.0 N_D, corresponding to those for approach, takeoff, and cruise, respectively, is shown in figure IX-16. The efficiency was high but the fan performance was limited by the stall line to values below the design pressure ratio. This premature stalling has been attributed

primarily to the compromise of increased blade spacing to minimize blade row interaction noise.

The diagram of figure IX-17 illustrates the aerodynamic problem that arises when the blade rows are spaced apart from one another. The flow paths for a typical fan with a close-coupled stator and for the spaced stator are compared. It is recognized that spacing the blade rows apart from one another requires special care in the design of the inner flow path. The point of concern is the possibility of separation of the flow from the inner wall. The increased blade spacing causes a greater curvature in the critical region just downstream of the rotor. The greater flow path length between the blade rows increases the losses. Surveys of the flow downstream of the rotor indicated high losses along the inner wall. The premature stall was apparently initiated by the thick boundary layer on this inner wall indicating imminent flow separation.

The two low noise fans were tested with near-sonic inlets as in figure IX-18. The single-stage fan has a variable throat to give near-sonic velocities in the inlet ducting for the takeoff and approach condition. The translating centerbody for the inlet of the two-stage fan would allow the throat area for the approach and takeoff conditions to be sized to achieve a Mach number of about 0.9. At these high Mach numbers the noise is sufficiently suppressed without the higher inlet losses associated with sonic velocity in the throat.

The performance of the single-stage fan with separate inlet ducts simulating both the takeoff and the approach contours is shown in figure IX-19. The inlet shape for cruise is essentially like that of the bellmouth so a separate performance evaluation was not made. For the takeoff condition, there is only a small difference between the bellmouth baseline performance and that obtained with the near-sonic inlet. For the approach configuration some reduction in stable operating range resulted. Overall, the inlet had little effect on the fan performance.

The performance of the two-stage fan with the inlet positioned for approach and cruise is shown in figure IX-20 in comparison with that obtained with the bellmouth. The near-sonic inlet had essentially no effect on fan performance. It was found that the pressure recovery of this type of inlet is very high, approaching that of a bellmouth.

To summarize, it was found that, in these static tests, the near-sonic

inlet ducts designed for noise suppression did not adversely affect the fan performance. However, when the aerodynamic design of the fan is compromised to reduce noise there is some penalty in the performance. If the fan itself is relatively quiet, less noise suppression in the inlet and outlet ducts is required. The performance decrement caused by the fan design compromises may well be offset by weight savings and decreased flow losses in noise suppressing inlet and exit ducts. It could well be that the best overall design will tolerate a small loss in fan performance in order to reduce the degree of suppression required.

Application of High Pressure Ratio Stages to Core Compressors

Application of current technology to meet the higher core pressure ratios desired in advanced engines would result in a large number of stages and blades. Of course, this would increase the weight and cost of advanced engines. To minimize engine weight and cost, NASA has embarked on a major multistage compressor program effort to reduce the number of stages and blades. Our goal is to reduce the required number of stages to that shown in figure IX-21. The number of core compressor stages is presented as a function of overall pressure ratio. The upper shaded area covers the range of pressure ratios and number of stages of present core compressors. The lower shaded area represents NASA's goal - 6 to 12 stages for a core pressure ratio range from 15 to 20.

Reducing the number of stages in advanced core compressors to about one-half of that in present cores will in itself reduce the number of blades to about one-half. However, it is desirable to further decrease the total number of blades by reducing the number of blades in each stage. In figure IX-22 the number of blades is presented as a function of overall pressure ratio. The upper shaded area indicates the number of blades used in current core compressors. The lower shaded area represents NASA's goal which is to reduce the number of blades to about one-third of that required in present engines.

It is recognized that these goals impose new and more demanding requirements of advanced core compressors. First, high stage pressure ratio which requires high tip speed and high blade loading is needed to reduce the

240

number of stages. To meet the goal of reduced number of blades requires high stage pressure ratio to reduce the number of stages and lower blade aspect ratios to reduce the number of blades in each stage. The high overall pressure ratio of advanced core compressors and the resulting low outlet volume flow requires high hub tip ratios in the rear stages. It is required that the stages be matched over the speed range. Historically, the matching of stages in multistage compressors has been a problem; and, as overall pressure ratio, tip speed, and blade loading are increased, the matching becomes increasingly difficult. Also advanced materials will be required in the higher pressure ratio high tip speed core compressor because of the increased temperature and because of the higher stresses.

To illustrate these requirements, an example core compressor that fits within the goal of reduced number of stages and blades is presented in figure IX-23. This example compressor was designed for an overall pressure ratio of 20 to 1 and has eight stages. To achieve the 20-to-1 overall pressure ratio requires a pressure ratio in the first stage of about 1.8; this decreases to 1.25 in the last stage because of the increasing temperature. The first stage rotor has a design tip speed of 1500 feet per second. The average blade loading parameter of the rotors is relatively high, about 0.5. The hub tip ratio ranges from 0.7 at the inlet to 0.95 at the outlet.

In addition to the features illustrated in this example, the advanced core compressor must have high efficiency and a wide stable flow range. To attain high efficiencies in the front stages will require the use of blade shapes similar to those developed for transonic single stages. For the higher hub tip ratios of the middle and rear stages, the end-wall boundary layers extend over a large portion of the blade span. The interaction of these boundary layers with the blades results in high losses, particularly for highly loaded stages. Conventionally these boundary layers are treated only in terms of an area blockage. However, reshaping the rotor and stator blades in the end-wall regions to accommodate the low velocity incoming flow should result in improved performance. A study was conducted under contract with Pratt & Whitney to assess the benefits to be realized by so shaping the blades (refs. 8 and 9). The stator blades show the greatest effect. A comparison of the reshaped blade to a conventional blade is made in figure IX-24. Appreciable differences in the blade shape in the end-wall regions can be noted.

The performance of the stage (refs. 10 and 11) designed for the end-wall effect is compared with that of the conventional stage of similar design in figure IX-25. Although the stages are not directly comparable, a part of the large improvement in efficiency is attributed to the blade end-wall corrections. These data indicate that to attain high efficiency in highly loaded, high hub-tip ratio stages of advanced core compressors, design approaches which accommodate the end-wall boundary layers should be used.

There is evidence that further improvements in efficiency and improvements in flow range can be achieved in the advanced core compressor stages through the use of low aspect ratio blading. In addition to performance benefits, low aspect blading will reduce the number of blades in each stage as shown in figure IX-26. A comparison is made between moderate and low aspect ratio stages. The lower aspect ratio stage has fewer blades with longer chords and thicker profiles. Such blades should prove more resistant to erosion and retain their performance over a longer period of time.

Combining of low aspect ratio with the blade end-wall design approach appeared to be a promising concept for the stages of highly loaded core compressors. A stage incorporating these features was fabricated and tested. The performance obtained from this stage is presented in figure IX-27. The design tip speed is 933 feet per second, which is representative of the middle stages of an advanced core compressor. The average blade loading parameter for the rotor is very high, about 0.60. At design tip speed the stage achieved a pressure ratio of 1.56 and an efficiency of 87 percent. This is considered excellent for the low speed and high loading. The flow range between peak efficiency and stall is very wide. From these results it is concluded that a high efficiency and a wide stable flow range can be achieved from a low aspect ratio highly loaded stage designed to account for end-wall boundary layer effects.

The higher overall pressure ratio desired of advanced core compressors makes the matching problem more difficult. This can be offset, at least partially, by the use of low aspect ratio stages which have wide stable flow ranges. But in addition to this, more extensive use of variable geometry will probably be needed. Possibly more interstage bleed will be required. One concern is the effectiveness of variable geometry in providing the desired flow adjustments as design tip speed is increased. Figure IX-28 shows the effect of tip speed on required inlet guide vane reset to obtain an outlet

volume flow reduction of 10 percent. The data were obtained from three experimental stages ranging in design tip speed from 1140 to 1500 feet per second and is presented for 70 percent speed - representative of a part speed condition. For the higher design tip speeds the required reset increases. For the stage designed for 1140 feet per second (ref. 12) a reset of approximately 15° was required, whereas to obtain the outlet flow reduction of 10 percent for the 1500-feet-per-second stage (ref. 13) required over 25° of reset. The problem in the use of large reset angles is that losses increase, as shown in figure IX-29 where the loss coefficient for an inlet guide vane (IGV) is given as a function of reset angle (ref. 13). As the reset angle is increased above about 20°, the losses increase very rapidly. This general trend of a larger required reset angle with increased speed has been substantiated in analytical studies. The tendency for variable geometry to become less effective in matching high tip speed stages must be taken into account in the design of advanced core machines.

To attain the goals of the advanced core compressor will require a considerable amount of research activity. The need for precise design control is paramount when considering the staging of high tip speed, highly loaded stages to achieve an overall pressure ratio of 15 to 20 with high efficiency.

TURBINES

The trend towards higher core compressor pressure ratios for advanced fan engines has been discussed in the previous section. Similarly, a higher core turbine inlet temperature is required for increased cycle efficiency. These elevated temperatures and pressures require sophisticated cooling schemes to protect the blades, vanes, and end walls from the hot gas stream. But cooling leads to added costs and losses in turbine efficiency. If potential cycle benefits are to be realized, turbine cooling must be accomplished minimizing the penalty in aerodynamic performance.

Turbine Cooling Heat Transfer

There are three basic methods that can be considered for cooling air-

craft turbines. They are convection, film, and transpiration cooling. The quantity of cooling air needed to maintain a given blade temperature for each of these three methods is indicated in figure IX-30. Coolant requirements are given as a percentage of compressor exit flow in terms of increasing turbine inlet temperature and pressure. The temperature and pressure level typical of current engines is located on the abscissa for reference. It can be seen by the shape of the upper curve that cooling by convection becomes increasingly more difficult as the temperature increases. At the high temperature levels of advanced core turbines, it becomes impossible to maintain a reasonable wall temperature using convection cooling alone. At the very high temperatures, film and transpiration cooling are clearly superior because they provide a thermal barrier of cool air along the surface of the blade to shield it from the hot gas stream. Transpiration is the most effective scheme, but it has structural limitations, and there are also potential problems associated with clogging of small pores. For these reasons, it is not currently being considered as a practical method of cooling blades and vanes. Full-coverage film cooling from an array of closely spaced holes is the most practical method currently under consideration for attaining the temperature levels of advanced core turbines. It is the heat transfer characteristics of this type of cooling that will be discussed in the following section.

Discrete hole film cooling. - The insert in figure IX-30 shows a photograph of a film cooled blade with holes spaced about 8 diameters apart. There are many variables which influence the effectiveness of discrete hole film cooling. The shape of the holes, their diameter, their angle with respect to the mainstream and surface, their location around the airfoil, the mass flow from a given hole; all of these affect heat transfer and aerodynamic performance of the turbine. The design engineer must adjust these variables to achieve a reasonable compromise between thermal and aerodynamic constraints. Poor designs can lead to severe losses and, in some instances, even increase heat transfer to the surface.

There are two qualities that a film injected from discrete holes should have. One, it should provide a good blanket of coverage to protect the surface from the hot gas stream, and two, it should remain attached to the surface rather than separating and mixing with the mainstream. These two film characteristics have been evaluated in a flow visualization test rig

which has an array of four film injection holes in the floor of the test section as shown in figure IX-31. Photographs of film streamlines were taken both from the top looking down on the test surface and from the side looking through the boundary layer. The two viewing angles are illustrated in figure IX-31 with two cameras mounted in the positions used when taking photographs. The top view photographs show the spreading characteristics of the film as it leaves the holes and the side view photographs show the degree of penetration of the film into the mainstream relative to the boundary layer thickness and the surface. The test section is made of clear plastic on the top and front face. The floor where the holes are located and the back side are painted black. The mainstream flow is from right to left, and the boundary layer thickness over the test surface is scaled relative to the hole diameter to simulate core turbine applications. The film air passes from the plenum through the array of film cooling holes. The film air is made visible by seeding it with small neutrally buoyant bubbles which, when illuminated, appear as bright streaks against the black background. The bubbles follow the flow field and map out individual streaklines which can be photographed.

A top view of the film streaklines from the four-hole staggered array is shown in figure IX-32. Here the mainstream flow is from left to right. The holes are spaced 5 diameters apart and angled 30° to the surface inline with the mainstream. Notice that there is very little spreading of the film even when passing over the downstream injection location. The side view in figure IX-33 shows the path of the film relative to the boundary layer thickness and the surface. The boundary layer thickness just upstream of the holes is indicated by the tick mark on the left. The two outer holes in the four-hole array were plugged in the side view in order to give a clear plane view of the two holes directly in line. As expected for this low blowing rate case, the film velocity out of the hole is low compared to the mainstream velocity and the film is bent over on the surface giving good protection.

For comparison, a high blowing rate case is shown in figure IX-34 from the top and in figure IX-35 from the side. Notice the increase in the turbulent mixing between the film and mainstream. Also, the side view shows how the film jets separate from the surface and penetrate the boundary layer, allowing the mainstream to wrap around under the jets. A close-up view of the downstream hole in figure IX-36 shows the jet passing right

through the upstream film rather than lying underneath it. This penetration and high turbulence increases the heat flux to the wall as can be seen from the quantitative data for discrete hole film cooling given in figure IX-37.

The data of figure IX-37 are from a film cooling study conducted under contract with Stanford University to experimentally investigate and predict the performance of full-coverage film cooling for core turbine applications. Details of the experimental test facility are given in reference 14. The test rig is similar to the flow visualization rig just described, but there are copper heater strips along the surface to measure the heat flux to the wall. In the figure, the heat flux is given as a function of blowing rate, or mass velocity ratio, relative to the non-film cooled case. Reducing the heat flux lowers the wall temperature for a given quantity of cooling air. The main-stream and wall temperatures were fixed, while the temperature of the in-jected film air was varied. Consider the upper curve where the tempera-ture of the film air is equal to the mainstream gas temperature. This con-dition isolates the hydrodynamic effect that blowing has on the boundary layer when no cooling is provided by the film. The flow visualization pic-tures showed how the injected film air mixed up the boundary layer. This turbulent mixing increases the heat flux to the wall relative to the unblown case. As the film air temperature is reduced, the cooler film next to the wall generally reduces the heat flux as can be seen in the two lower curves in the figure. So there are two counteracting effects - a cool film layer tending to reduce the heat flux and the high turbulence due to injection tend-ing to increase it. But once the film separates from the surface as shown in the flow visualization photographs (figs. IX-35 and IX-36), it can no longer provide any protection and the heat flux increases from its minimum value. This minimum occurs on each curve at a mass velocity ratio of about 0.4; about the blowing rate at which separation is first observed to occur in the flow visualization studies. The particular blowing rate which minimizes the heat flux is a function of such design parameters as hole spacing, angle, and diameter. It is important for the designer to be aware of operating condi-tions which could lead to a significant departure from the optimum point. For example, suppose the mass velocity ratio was increased from 0.4 to 1.2 for the condition $T_{film} < T_{wall}$. For a fixed geometry, that means three times more cooling air would be used, while at the same time the heat flux to the surface would increase to more than twice its minumum value.

To illustrate what such an increase in heat flux means in terms of higher wall temperatures, figure IX-38 repeats the middle curve but with the heat flux ratio expressed in terms of wall temperature for a scaled engine condition of a 3000° F gas temperature and a 1000° F coolant supply temperature. For comparison, a transpiration curve has also been included. It gives the minimum wall temperature that could be achieved if the same quantity of film air were injected uniformly over the entire surface. In that case, there is no turbulent mixing caused by discrete jets and the film always remains adjacent to the surface.

With just convection cooling and no film, the wall temperature would reach 2300° F; well above metal temperature limits. Optimum blowing for 30° injection reduces the wall temperature 425° F. But even at this condition, the temperature is 740° F above the minimum attainable. The difference in the two curves illustrates the importance of improving injection methods to reduce turbulent mixing and prevent the film from separating from the surface.

It has been observed that one way of keeping the film attached to the surface is to orient the holes at a compound angle to the surface and the mainstream. If the film remains attached, it should be possible to extend this minimum to higher blowing rates. To illustrate the effectiveness of this injection method, consider once again the flow visualization photographs. A four-hole staggered array with holes spaced 5 diameters apart angled 30° to the surface is shown in figure IX-39. Now the hole axes are rotated 45° laterally to the mainstream. A closeup top view of the upstream hole is shown in figure IX-40. At high blowing rates, the oblique angle that the film makes with the mainstream generates a vortex immediately downstream of the holes. This vortex keeps the film attached to the surface at high blowing rates. This can be seen by comparing the side view of the compound angle injection shown in figure IX-41 with the high blowing rate inline photograph of figure IX-35. The blowing rate is the same in both cases. The film separated from the surface with inline injection. In the case of compound angle injection, the downstream film stays near the wall and lies underneath the film from the upstream hole. In areas on the turbine blade where high blowing cannot be avoided or for injection in adverse pressure gradient regions where the boundary layer may have a tendency to separate, compound angle injection offers significant advantages by keeping

the film and the boundary layer attached to the surface.

The previous discussion has shown what happens to a film layer once it is injected into the stream. To visualize the temperature distribution on an actual film cooled wall, figure IX-42 shows an infrared photograph taken of a full coverage film cooled surface tested in a hot gas tunnel. The mainstream flow is from right to left. Radiation emitted from the surface is recorded on infrared film which is then processed through a precision densitometer to give quantitative temperature contours. The hot regions on the surface appear dark because they radiate more energy. Conversely, the light regions are cool. In this experiment, the wall was cooled using a combination of film and convection cooling. Light streaks caused by the cool film are visible extending downstream from each hole. Also, alternate light and dark vertical bands caused by the impingement of cooling air on the back side of the wall can be seen. However, the primary interest here is in the wall temperature distribution in the immediate vicinity of the film cooling holes. The isotherm pattern around three holes has been enlarged to show the temperature gradients that exist at conditions scaled to 3000° F gas temperature. The surface temperature varies by as much as 150° F within a short distance just upstream of the 0.020-inch hole. Thermal stresses caused by such large gradients become an important factor affecting the life of turbine blades.

Thermal barrier ceramic coatings. - The thermal protection that a layer of film cooling air on the surface of a blade can provide has been discussed. Another kind of thermal barrier which is currently being evaluated is a thin coating of ceramic plasma sprayed on the surface of the blade. Such coatings have the advantage of reducing the heat flux without the use of film cooling. The potential benefits of ceramic coated blades can be seen in figure IX-43 which compares the cooling air requirements for the three active methods of cooling discussed earlier, with the ceramic coated blade cooled internally by convection. The cooling air required for the coated blade is less than half of that needed for plain convection, and only slightly more than that needed for film cooled blades in current engines; and, of course, there are none of the aerodynamic penalties associated with film cooling. There is some question whether these coatings will stay on. The initial phase of a test program has just been completed to evaluate the durability of a plasma sprayed coating of zirconia by running coated blades in an

engine undergoing transient cycles between full power and flame out. The gas temperature dropped from 2500° to 100° F in 10 seconds and then returned to the full power condition in 15 seconds. The test results have been very encouraging. The rotor assembly of coated blades after 500 transient cycles is shown in figure IX-44. Two blades were left uncoated for reference. There has been no coating deterioration. Except for some minor foreign object damage, the blades look as good as when they were first installed. More tests will be run to further study the feasibility of ceramic coatings for turbine applications.

The two blades that were left uncoated were used during the test as reference blades for a new radiation pyrometer system recently designed and built at Lewis. A very sensitive radiation detector permits high resolution temperature profile scans to be made across the blades as they rotated past the optical probe at speeds in excess of 1200 feet per second. To illustrate the resolution of the instrument, a V-shaped target was placed on one of the uncoated blades. The target is visible on the right uncoated darker blade in the figure. During operation, multiple scans were made along the blade span. A three-dimensional isometric view of the blade temperature distribution is shown in figure IX-45. The target has a lower emissivity than the metal, so its outline emerges as an apparent lower surface temperature in that region. Each time the targeted blade passed the detector, 200 discrete measurements were made to generate one scan line. The spot size detected on the surface is 0.020 inch in diameter. The system can also be operated in a mode which would distribute the 200 measurements over more than one blade.

NASA high pressure turbine rig. - Some of the basic research needed to build analytical prediction models of film cooling as well as test results in the moderate temperature and pressure range of a J75 engine have been discussed. A new high pressure, high temperature turbine facility illustrated in figure IX-46 is currently under construction at Lewis which will permit vane, blade, and end-wall cooling studies to be done in an actual core turbine environment at temperatures up to 4000° F and pressures up to 40 atmospheres. The turbine rig has its own combustor immediately upstream of the turbine and there is also a parallel combustor test rig. Auxiliary compressors and an air/natural gas heat exchanger provide a wide range of combustion air temperatures and pressures.

Turbine Cooling Aerodynamics

The ejection of cooling air into the vane or blade boundary layer will result in a decrease in turbine efficiency. If the associated penalty approaches or exceeds the cycle benefits in going to the higher temperatures, a serious problem would exist. Therefore, it is important to know the factors that influence loss and study means to reduce their harmful effects. Considerable work is being done in this area. Two phases of the work being conducted at, or contracted by, Lewis Research Center, will be described. The first will cover some of the cascade work done to study the basic factors that influence cooling loss. The second will cover rotating tests of a single-stage 20-inch-diameter core turbine.

Two-dimensional cascade program. - Figure IX-47 is a photograph of a 12-vane two-dimensional cascade used at Lewis. Flow is from left to right, through the cascade of vanes, and down through the exhaust. Data are taken with a survey probe (actuator shown in fig. IX-47) that travels across the plane of the trailing edges. The data were used to calculate efficiency as a function of the amount of coolant used. About 100 different coolant configurations have been tested to study the effect of such factors as the amount of coolant, the angle the coolant holes make with the local surface, the hole size, and the location of the coolant holes on vane performance. Typical efficiency results will be presented for amount of coolant, hole angle, and hole location.

The effect of inline ejection angle on vane efficiency as a function of coolant flow is shown in figure IX-48. This coolant flow is the ratio of the total coolant to the inlet mainstream flow, and is different than the individual hole blowing rate described in the previous section used for heat transfer. Three vanes were used, each having 44 rows of cooling holes around the surface. Angle orientations of 35°, 45°, and 55° were used. For all of the vanes tested, figure IX-48 shows a large decrease in efficiency as coolant flow was increased. For the range of coolant flows shown by the data points, there was about a 1 to 2 point difference in efficiency for the three vanes tested. For example, at 6 percent coolant, the penalty of the 35° ejection vane compared to the solid vane is about 4 points. This penalty increases to about 5 points for the 55° ejection vane.

In addition to inline holes, compound angle holes were also tested and

the results are shown in figure IX-49. All of the holes for the inline and compound angles were inclined 35° to the local surface. Up to about 7 percent coolant, the penalty in going from inline to 45° compound holes is small. Because they help to keep the coolant on the surface as described in the previous section, 45° compound holes show promise. However, there is a larger penalty for the 90° radial holes. At 6 percent coolant, the efficiency of the radial-hole vane is only 91 percent or 3 percent less than the inline holes. This is primarily because there is no component of coolant flow from the radial holes in the direction of the mainstream. In effect, the energy of the coolant is lost. However, most of the penalty with radial holes occurs on the vane suction surface where the mainstream Mach number is high. The penalty for the radial holes is very small near the leading edge region of the vane where the mainstream velocity is low. The conclusion from these figures, then, is to eject coolant at an angle as close to the local mainstream flow as feasible, particularly when the mainstream velocity is high.

Figure IX-50 shows the effect of hole location on vane efficiency. Each vane shown had only one row of coolant holes to isolate the effect of location. As a result, the amount of coolant is small as compared to that for the vanes previously considered. The row for the upper vane in the figure was located in the forward, or accelerating region of the suction surface. The row for the lower vane was located in the diffusing, or decelerating, portion of the suction surface. Both vanes ejected coolant through the same number and size of holes inclined 35° to the local surface. Figure IX-50 shows a significantly higher penalty when coolant is ejected in the diffusing region of the vane. From an aerodynamic standpoint, then, coolant ejection from the diffusing region should be minimized. For related reasons, this is also the most difficult area to cool, so it is sensitive for both heat transfer and aerodynamics.

Although not shown in figure IX-50, data are available that show the effect of hole size on efficiency. The tests indicate that, from an aerodynamic viewpoint, fewer larger holes are slightly preferable. However, this is in conflict with the heat transfer requirements where good film coverage favors a greater number of smaller holes. This difference, then, should be considered for a given vane design.

Single-stage core turbine performance. - Figure IX-51 is a photograph

of the turbine test facility used under contract by General Electric in Evendale, Ohio. Flow is from right to left. A 20-inch single-stage core turbine is located in the housing as indicated in the figure. A photograph of a rotor blade of the first turbine tested is shown as figure IX-52. The hole pattern is the same as the basic vane used in our inhouse two-dimensional cascade program. They are inline holes inclined 35° to the local surface. The holes are about 0.012 inch in diameter, with a spacing to hole diameter ratio of about 8. Some of the holes used to cool the blade platform can be seen in figure IX-52. The vane used for this turbine had the same hole pattern as this blade. The schematic of figure IX-53 shows the five cooling circuits involved - the vane, the vane outer wall, the vane inner wall, the blade (which includes the platform), and the static shroud. In addition to overall tests, the rotor blades were removed and surveys were made downstream of the vanes.

Figure IX-54 is a bar graph which shows the performance of the core turbine relative to that of the solid turbine with no coolant holes. As indicated by the figure, about a 3 percent penalty in performance was predicted because of the coolant. However, experimental tests indicated a penalty $2\frac{1}{2}$ percent greater than design. The data were analyzed in an effort to determine whether the cause of this deficiency was in the vane, the blade, or both.

Consider first the vanes. Contour plots of pressure loss taken at the exit plane of the vanes with a survey probe are shown as figure IX-55. Exit survey results are shown for the solid vane on the left and the cooled vane on the right. The dashed line shows the projection of the vane trailing edge. The cooled vane shows a much larger area of high pressure loss both in the wake and near the hub wall region. Flow angle measurements made near the hub area, where the wake has moved away from the vane surface, indicated more underturning of the flow compared to the solid vanes. The reduced efficiency of the vane due to the coolant was the same as that predicted. However, the underturning near the hub area, the thicker wakes, and the large buildup of secondary flow in the hub region probably compounded the losses in the following blade row. Consequently, rotor blade exit surveys were used to calculate the condition of the flow as it left the rotor blade surface.

Figure IX-56 shows the experimental exit flow angle for the cooled rotor

blades compared to its predicted value. The flow angle is about 3° less than predicted, which is an indication of flow separation from the blade suction surface. This amount of underturning is about the amount that would result in the $2\frac{1}{2}$ percent less than design efficiency referred to earlier. Additional testing of this turbine will be done to determine whether the cause of flow separation from the blade surface was the poor flow pattern from the vane (fig. IX-55), the coolant from the blade itself, or both. Several combinations of solid and cooled vanes and blades will be tested to isolate the cause of separation.

The effect of each coolant flow on turbine efficiency was determined by varying the coolant flow individually in each of the five coolant circuits. It was found that performance was most sensitive to blade coolant. The effect of varying blade coolant on turbine efficiency is shown as figure IX-57. The circle on the figure represents the results when design conditions were imposed across the turbine. The curve represents the fractional change in efficiency as a function of blade coolant change. For example, if the blade coolant were reduced to only 60 percent of that required, turbine efficiency would increase by 2 percent. This concept, of course, is true for all of the cooling circuits. It is always desirable to minimize the required amount of cooling air.

Effect of temperature ratio on turbine efficiency. - So far, the data for this turbine has been for a fixed mainstream-to-coolant temperature ratio of about 3. This corresponds to that for a hot engine condition. Cold testing, where this temperature ratio is 1, is often used because it is cheaper, quicker, and can cover many more different configurations. To see how cold test results compare to those for actual engine temperature ratio, additional turbine tests were made at varying mainstream-to-coolant temperature ratio. The results are shown in figure IX-58 for both overall turbine tests and vane tests. Values of temperature ratio from 1 to about 3 were obtained by heating or cooling the mainstream inlet air relative to the coolant. Overall turbine efficiency varied about 1 percent over the range of temperature ratios tested. However the vane test indicated about a 3 percent difference in efficiency. Comparable inhouse tests for two-dimensional core vanes resulted in a constant vane efficiency over this same temperature ratio. Apparently, the radial pressure gradient and end-wall cooling effects of these three-dimensional tests, plus the large amounts of

secondary flows involved, had a significant influence on the overall losses associated with this vane. The net effect, then, is that care must be taken in translating the results of cold two-dimensional tests to actual engine conditions.

Direct Drive Fan Turbines

The main factors that complicate the direct drive fan turbine are the low noise requirements and the use of high bypass ratios. Both of these fan requirements impose low speed limits on the turbine, and low blade speed means using either many stages for high efficiency, or fewer stages with reduced efficiency. This is illustrated in figure IX-59, which shows the variation in turbine efficiency as a function of stage work factor. Conventional turbines are designed at low values of this stage work factor (values of two or less) in order to have high efficiency. At low blade speed U, this means extracting very low values of stage work ∆H. This, then, requires many stages to produce the required overall turbine work. Studies have shown nine or more stages may be required which would add to weight, size, and cost of the engine. Stage number can be reduced by increasing the work extracted by each stage but, as shown by the curve in figure IX-59, this results in a decrease in expected efficiency. The dashed efficiency curve shown was obtained by applying the same loss theory developed for conventional turbines (solid curve) to turbines with much higher work factors. This assumed that there were no additional loss mechanisms that apply at the higher work factors. In this respect the dashed curve was considered optimistic. As a matter of fact, there are published predictions, unsubstantiated by data over a work factor of 2, that fall well below the curve. Because the validity of the dashed curve was not known, a number of turbines were designed and tested that had average stage work factors between 2 and 5. Figure IX-60 is a photograph of a four-stage turbine designed and tested by General Electric as part of this program. It had an average stage work factor of five.

The results of the turbines tested thus far are shown in figure IX-61. The efficiency of the four-stage turbine (fig. IX-60) is seen to be 0.853 at an average stage work factor of 5. It is noted that all five turbines tested

had efficiencies within 1 percent of that predicted, which is considered very good. Other turbines in this area are being studied to determine the effect of higher Mach numbers and stage pressure ratios.

The same loss mechanisms that control conventional turbine efficiencies also hold true for the high work factor turbines. How high up the turbine designer can go in work factor depends on a balance between using an efficient, many stage turbine with weight, size and cost penalties, or a turbine with fewer stages with the penalties that go with the reduced efficiency. Fortunately, this curve (fig. IX-61) does not drop off very fast. For example, if stage work factor were doubled from 1.5 to 3, which would require only half as many stages, the curve indicates an expected turbine efficiency of 90 percent.

SUMMARY

It was shown that high fan efficiencies are obtainable at tip speeds up to about 1500 feet per second. Some of the new experimental techniques used in fan and compressor research were illustrated. These together with new analytical methods give the detailed knowledge of blade flow conditions that is required for improved design. Successful matching of efficient high bypass ratio fans with near-sonic inlets has been demonstrated in static tests. However, the use of design features to reduce the generation of noise within the fan must be carefully balanced against potential losses in fan performance. In the quest for higher pressure ratio cores, high pressure ratio, low aspect ratio stages in the compressor, and effective film cooling in the turbine are desired. High turbine efficiency becomes dear in the core turbine because of the mixing effects of the coolant and in the fan turbine because of the low blade speed. These are the challenges. However, past experience gives confidence that well-planned research programs will continue to produce the improved turbomachinery that is needed for more quiet, efficient, and more economical turbofan engines.

REFERENCES

1. Morris, A. L.; and Sulam, D. H.: High Loading, 1800 Ft/Sec Tip Speed, Transonic Compressor Fan Stage. 2: Final Report (PWA-4463, Pratt & Whitney Aircraft; NAS3-13493.), NASA CR-120991, 1972.

2. Messenger, H. E.; and Kennedy, E. E.: Two Stage Fan. 1: Aerodynamic and Mechanical Design. (PWA-4148, Pratt and Whitney Aircraft; NAS3-13493.), NASA CR-120859, 1972.

3. Messenger, H. E.; and Keenan, M. J.: Two-Stage Fan. 2: Data and Performance with Redesigned Second Stage Rotor Uniform and Distorted Inlet Flows. (PWA-5087, Pratt & Whitney Aircraft; NAS3-13493.), NASA CR-134710, 1974.

4. Bilwakesh, K. R.; Koch, C. C.; and Prince, D. C.: Evaluation of Range and Distortion Tolerance for High Mach Number Transonic Fan Stages. Task 2: Performance of a 1500-Feet-Per-Second Tip Speed Transonic Fan Stage with Variable Geometry Inlet Guide Vanes and Stator. (R71AEG195, General Electric Co.; NAS3-11157.), NASA CR-72880, 1972.

5. Wuerker, R. F.; Lobayashi, R. J.; Heflinger, L. O.; and Ware, T. C.: Application of Holography to Flow Visualization within Rotating Compressor Blade Row. (AiResearch-73-9889, AiResearch Manufacturing Co.; NAS3-15336.), NASA CR-121264, 1974.

6. Ware, T. C.; Lobayashi, R. J.; and Jackson, R. J.: High-Tip Speed Low-Loading Transonic Fan Stage. Part 3: Final Report (AiResearch-73-9488, AiResearch Manufacturing Co.; NAS3-13498.), NASA CR-121263, 1974.

7. Messenger, H. E.; Ruschak, J. T.; and Sofrin, T. G.: Two Stage Low Noise Advanced Technology Fan. 1: Aerodynamic Structural, and Acoustic Design. (PWA-5069, Pratt and Whitney Aircraft; NAS3-16811.), NASA CR-134662, 1974.

8. Brent, J. A.; Cheatham, J. G.; and Nilsen, A. W.: Single-Stage Experimental Evaluation of Tandem-Airfoil Rotor and Stator Blading for Compressors. Part 1: Analysis and Design of Stages A, B, and C. (PWA FR-4667, Pratt and Whitney Aircraft, NAS3-11158.), NASA CR-120803, 1972.

256

9. Brent, J. A.; Cheatham, J. G.; and Clemmons, D. R.: Single-Stage Experimental Evaluation of Tandem-Airfoil Rotor and Stator Blading for Compressors. Part 5: Analysis and Design of Stages D and E. (PWA FR-5212, Pratt & Whitney Aircraft; NAS3-11158.), NASA CR-121008, 1972.

10. Brent, J. A.: Single-Stage Experimental Evaluation of Tandem-Airfoil Rotor and Stator Blading for Compressors. Part 2: Data and Performance for Stage A. (PWA FR-4719, Pratt and Whitney Aircraft; NAS3-11158.), NASA CR-120804, 1972.

11. Clemmons, D. R.: Single-Stage Experimental Evaluation of Tandem-Airfoil Rotor and Stator Blading for Compressors. Part 6: Data and Performance for Stage D. (PWA FR-5852, Pratt and Whitney Aircraft; NAS3-11158.), NASA CR-134511, 1973.

12. Jones, B. A.: Single Stage Experimental Evaluation of Variable Geometry Inlet Guide Vanes and Stator Blading. Part 6: Final Report. (PWA-FR-2641, Pratt and Whitney Aircraft; NAS3-7604.), NASA CR-54559, 1970.

13. Bilwakesh, K. R.: Undistorted Inlet Flow Testing. Evaluation of Range and Distortion Tolerance From High Mach Number Transonic Fan Stages, Volume 1. Task 2: Stage Data and Performance. (GE-R70-AEG-427-Vol-1; General Electric Co.; NAS3-11157.), NASA CR-72787-Vol-1, 1971.

14. Crawford, M. E.; Choe, H.; Kays, W. M.; and Moffat, R. J.: Full Coverage Film Cooling Heat Transfer Studies - A Summary of the Data for Normal-Hole Injection and 30° Slant-Hole Injection. Rept. HMT-19, Stanford University, 1975.
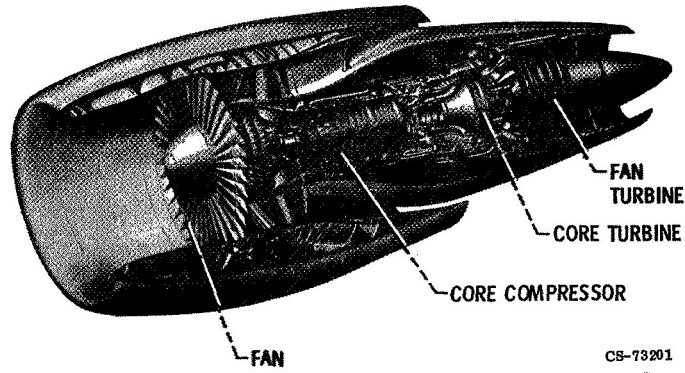
Figure IX-1. - Turbofan engine.
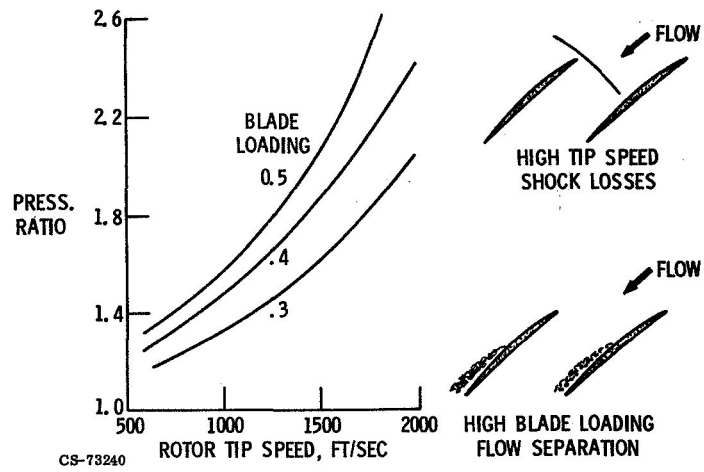
Figure IX-2. - Factors affecting stage pressure ratio.
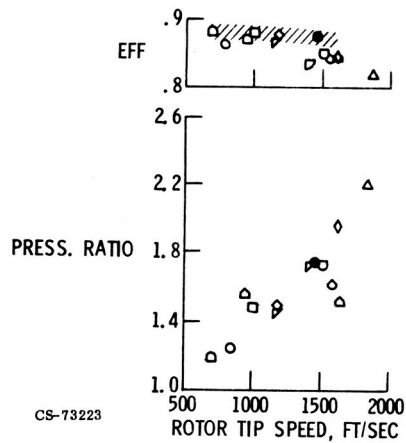
Figure IX-3. - Stage performance trends.
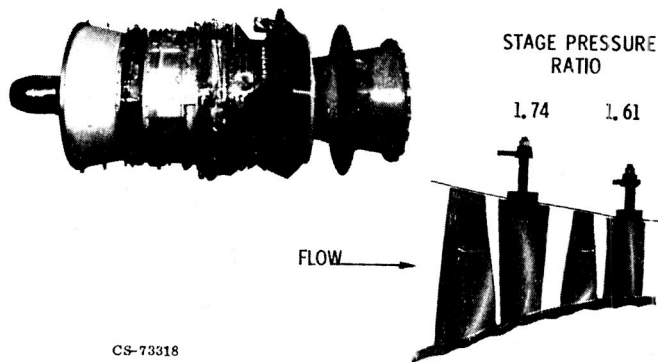
Figure IX-4. - High pressure ratio two-stage fan. (Tip speed, 1450 ft/sec; pressure ratio, 2.8.)
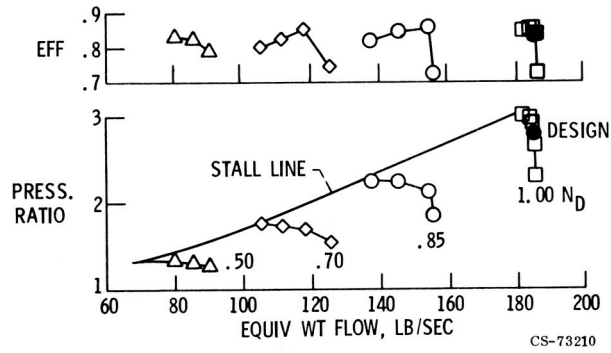
Figure IX-5. - High pressure ratio two-stage fan performance.
(Design tip speed, 1450 ft/sec.)
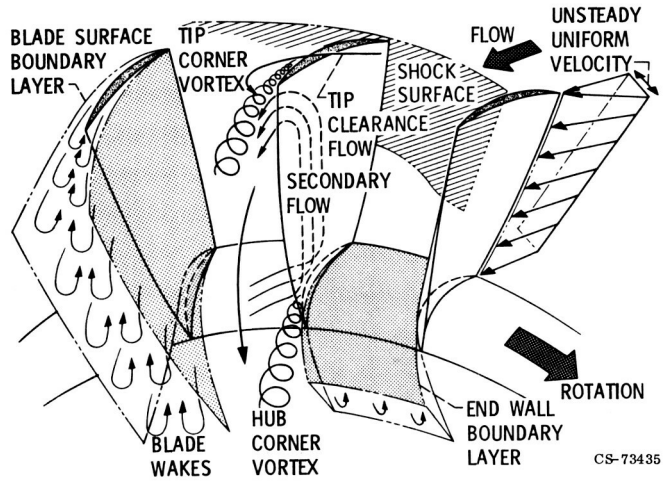
Figure IX-6. - Rotor blade row flow phenomena.
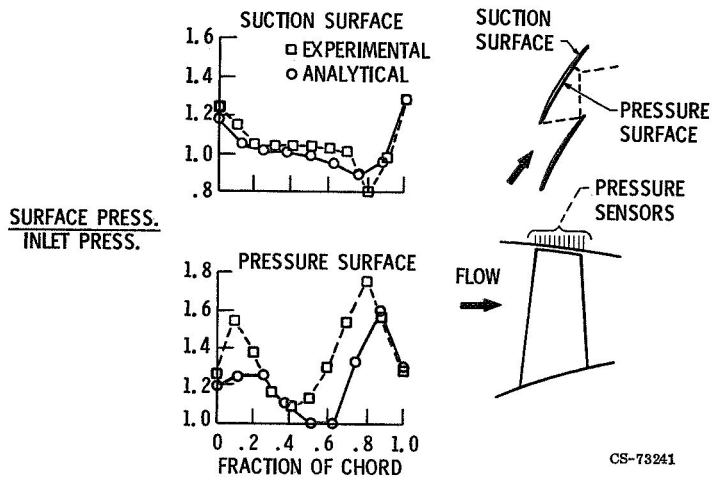
Figure IX-7. – Transonic rotor tip static pressures. (Design tip speed, 1500 ft/sec.)
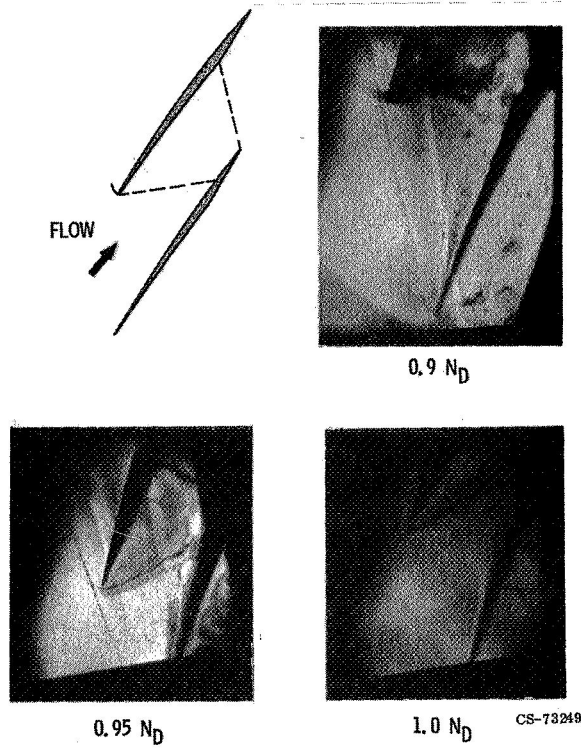
Figure IX-8. – Holographic view of rotor blade shocks. (Design tip speed, 1600 ft/sec.)

261
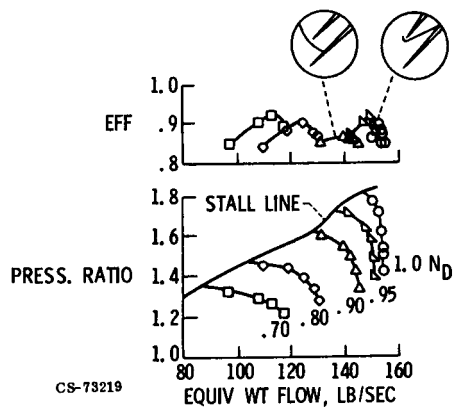
Figure IX-9. - Rotor performance. (Design tip speed, 1600 ft/sec.)
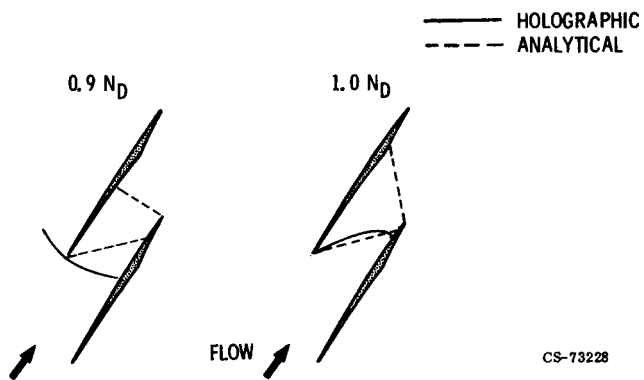
Figure IX-10. - Rotor tip shock patterns. (Design tip speed, 1600 ft/sec.)

HIGH TIP SPEED
SINGLE STAGE FAN

LOW TIP SPEED
TWO STAGE FAN

PRESS. RATIO	1.8	
TIP SPEED	1650 FT/SEC	
SPECIFIC FLOW	44.0 LB/SEC/FT^2	

PRESS. RATIO	1.9	
TIP SPEED	1200 FT/SEC	
SPECIFIC FLOW	42.9 LB/SEC/FT^2	

FLOW →

CS-73225
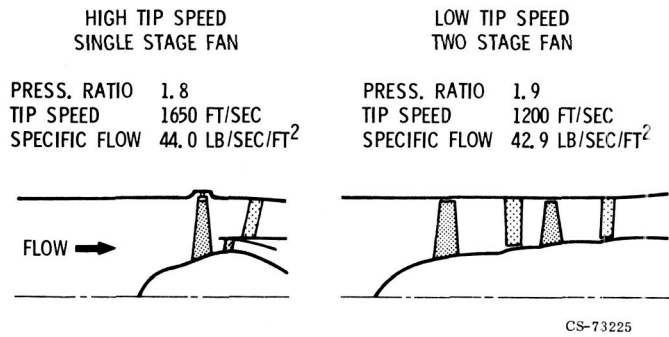
Figure IX-11. - Fans for low noise.

FLOW
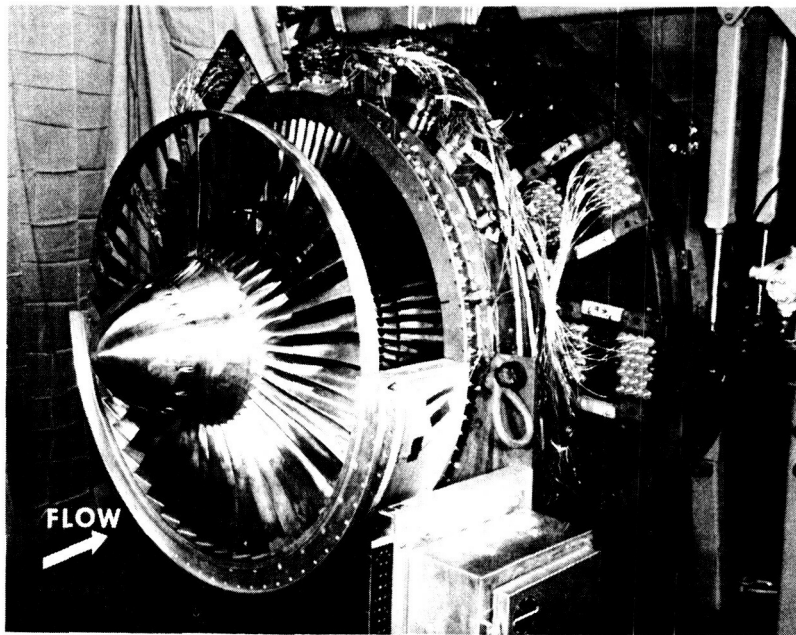
Figure IX-12. - Single-stage fan.

263
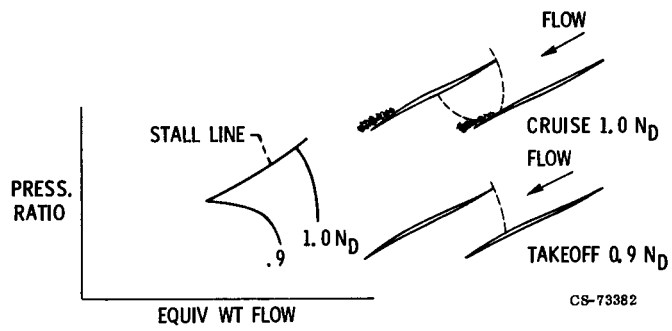
Figure IX-13. – Effect of rotor blade throat area.
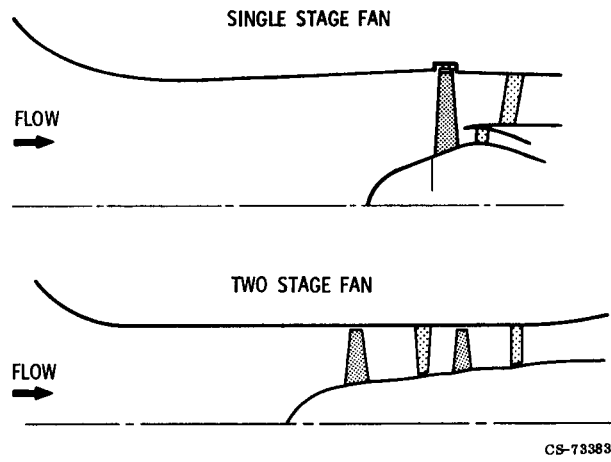
Figure IX-14. – Low noise fans (bellmouth inlet).

264
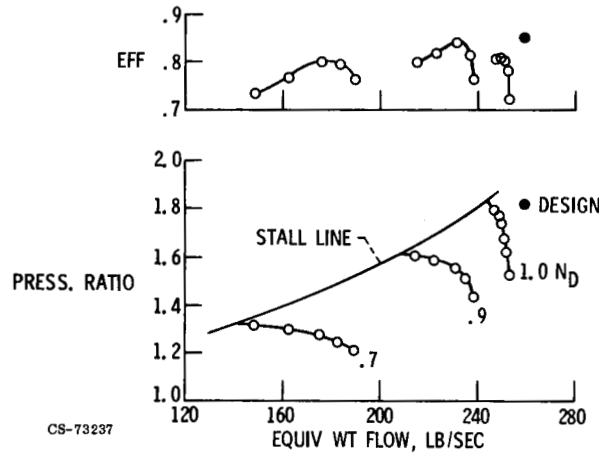
Figure IX-15. - Single-stage fan performance. (Design tip speed, 1650 ft/sec.)
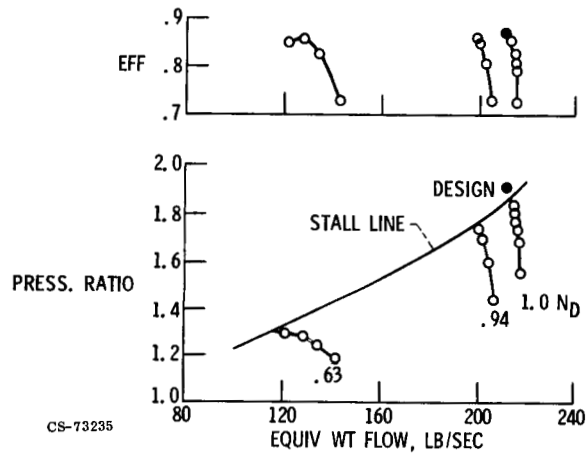
Figure IX-16. - Two-stage fan performance. (Design tip speed, 1200 ft/sec.)

265
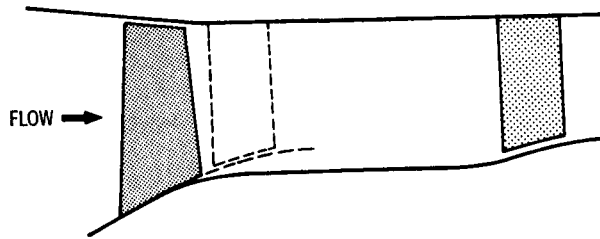
CS-73205

Figure IX-17. - Flow path geometry.
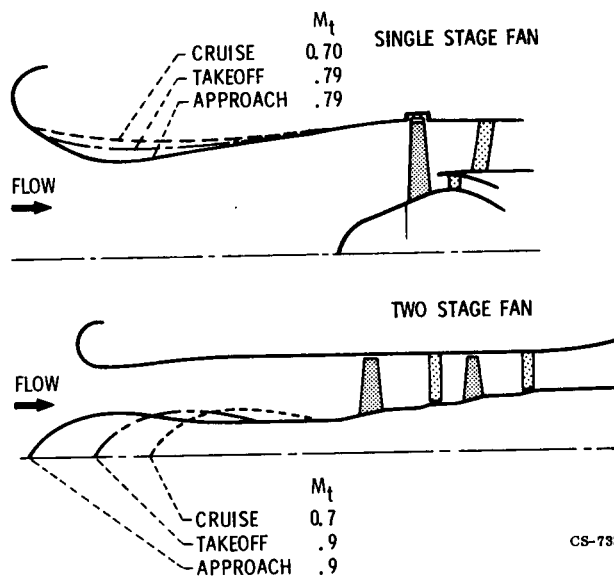
Figure IX-18. - Low noise fans (sonic inlet).
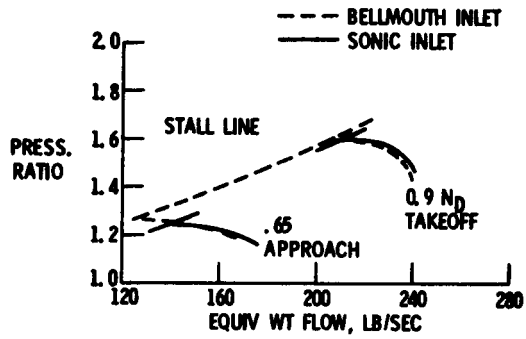
Figure IX-19. - Single-stage fan performance.
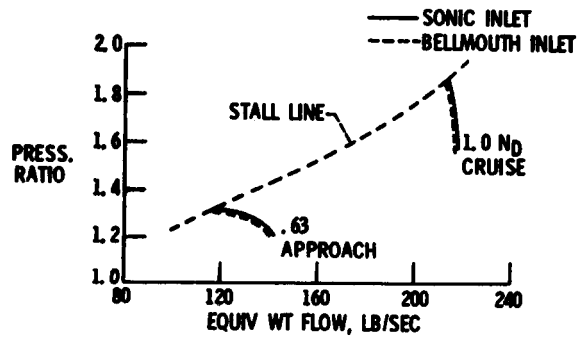
Figure IX-20. - Two-stage fan performance.
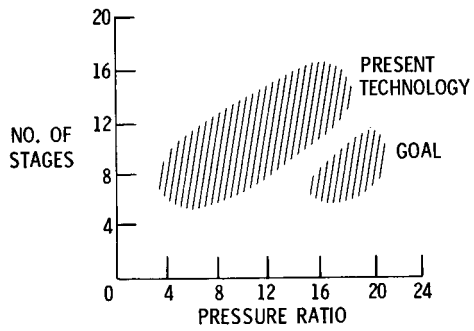
Figure IX-21. – Number of stages for core compressors.
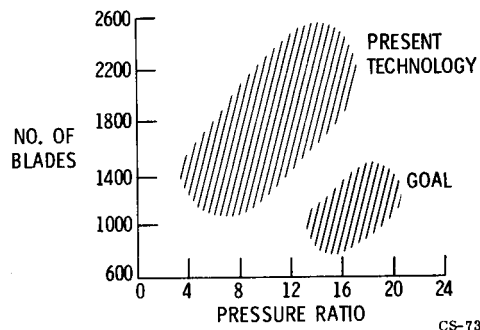
Figure IX-22. – Number of blades for core compressors.

PRESSURE RATIO   20
NO. OF STAGES   8
TIP SPEED   1500 FT/SEC
HUB TIP RATIO   0.70 TO 0.95

STAGE
PRESSURE
RATIO

1.82   1.66   1.53   1.43 1.37 1.32 1.29 1.25

FLOW

CS-73380
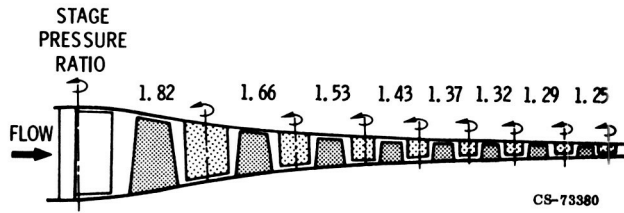
Figure IX-23. - Example advanced core compressor.

CONVENTIONAL   END WALL

CS-73748
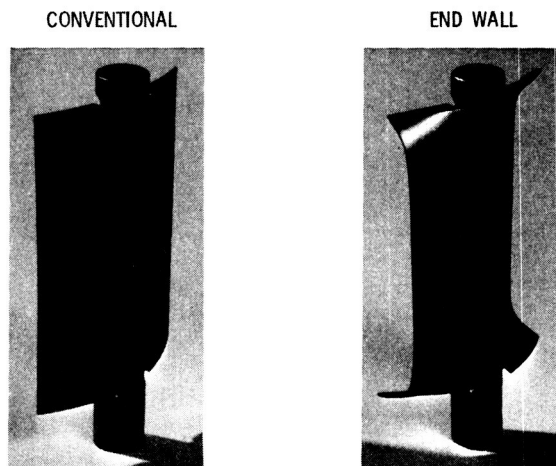
Figure IX-24. - Blade designs.
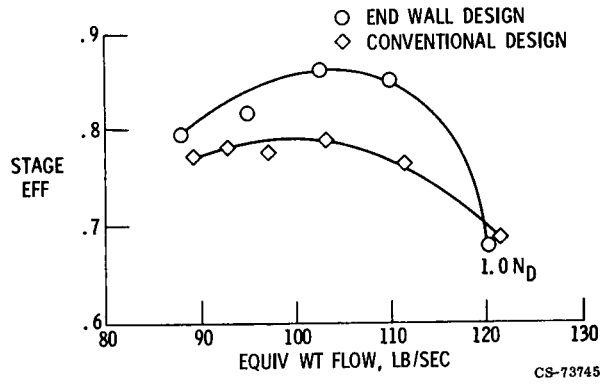
Figure IX-25. - Performance comparison.
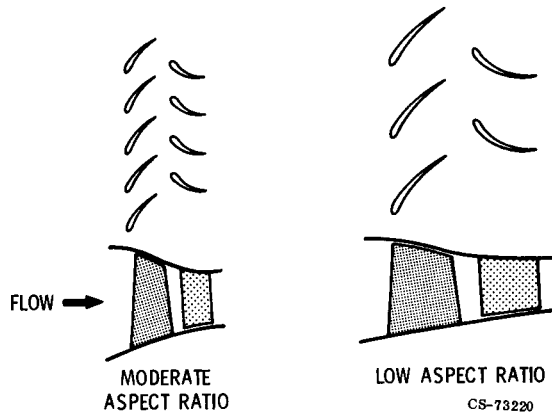
Figure IX-26. - Effect of reduced aspect ratio.
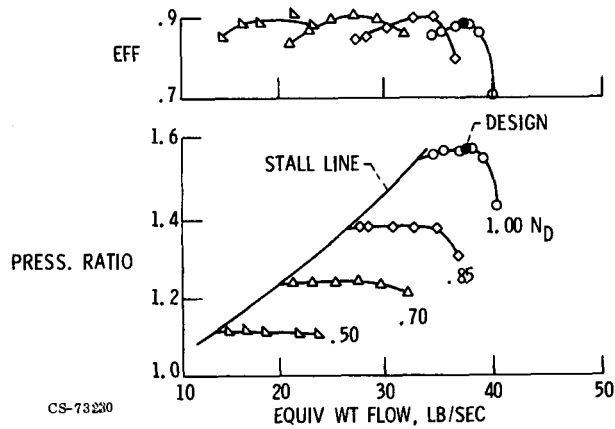
Figure IX-27. - Low aspect ratio highly loaded compressor stage.
(Design tip speed, 933 ft/sec.)
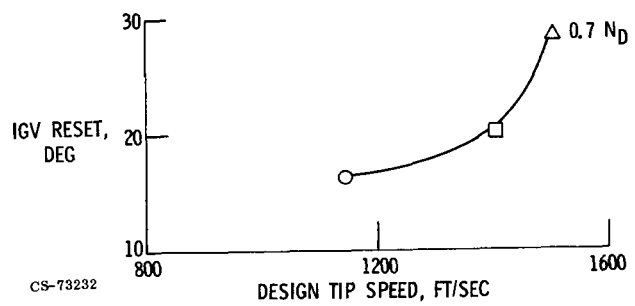
Figure IX-28. - Effect of tip speed on required inlet guide vane (IGV)
reset. (Outlet volume flow reduction, 10 percent.)
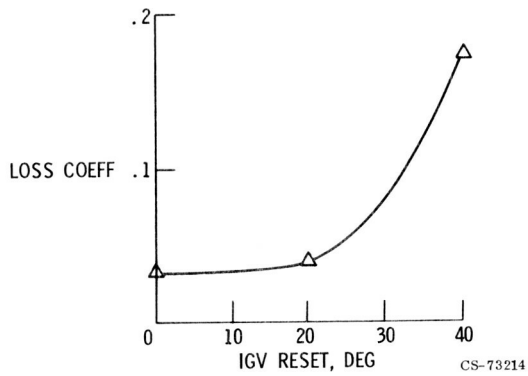
Figure IX-29. - Effect of reset on inlet guide vane loss.
(Relative inlet Mach no., 0. 3; 70 percent
immersion from tip.)
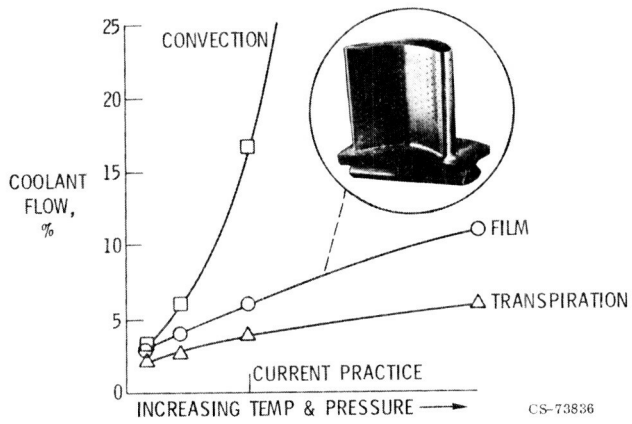
Figure IX-30. - Turbine cooling requirements.
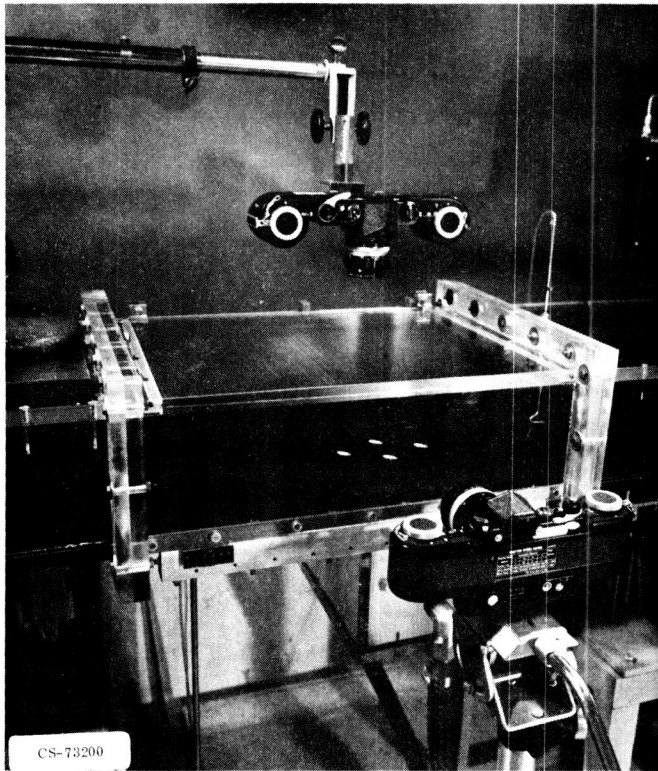
Figure IX-31. - Flow visualization test section.
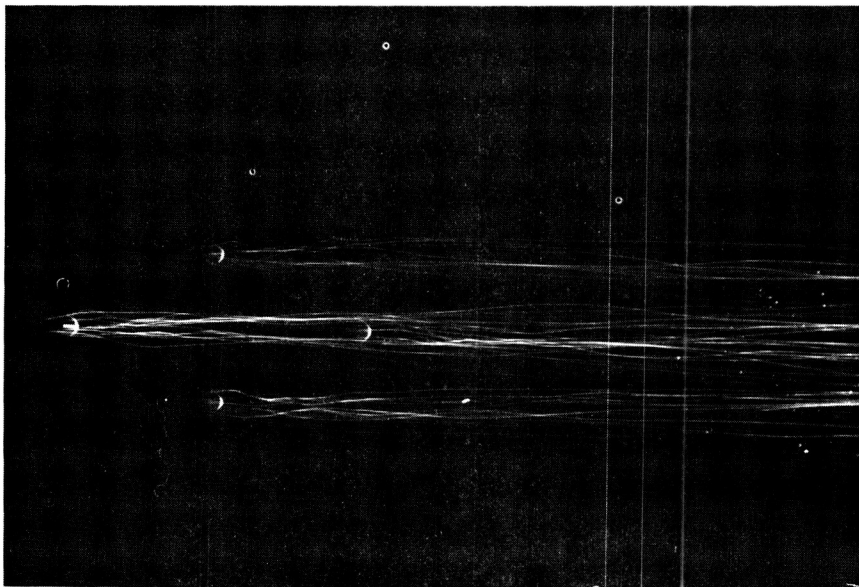
Figure IX-32. - Top view of film streaklines from four-hole staggered array; low blowing rate.
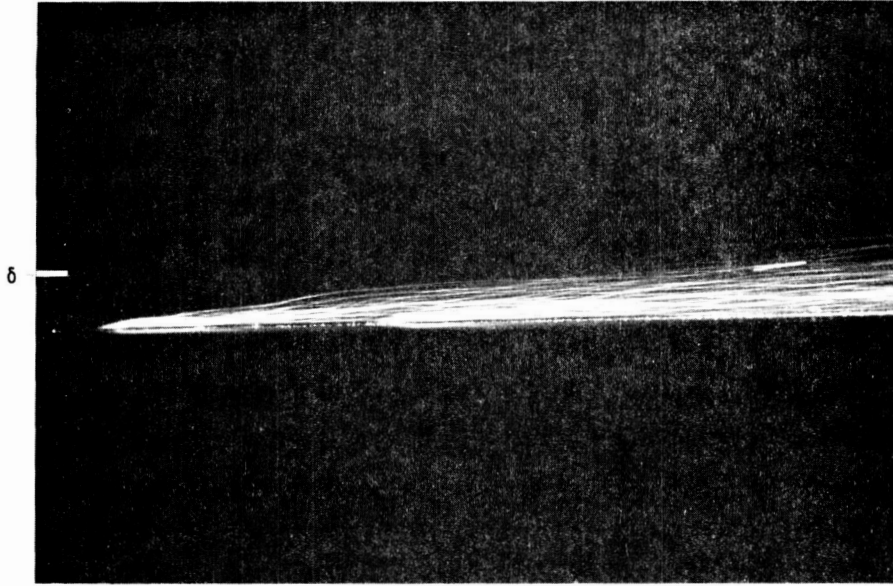
Figure IX-33. - Side view of film streaklines showing path of film relative to boundary layer thickness and surface; low blowing rate.
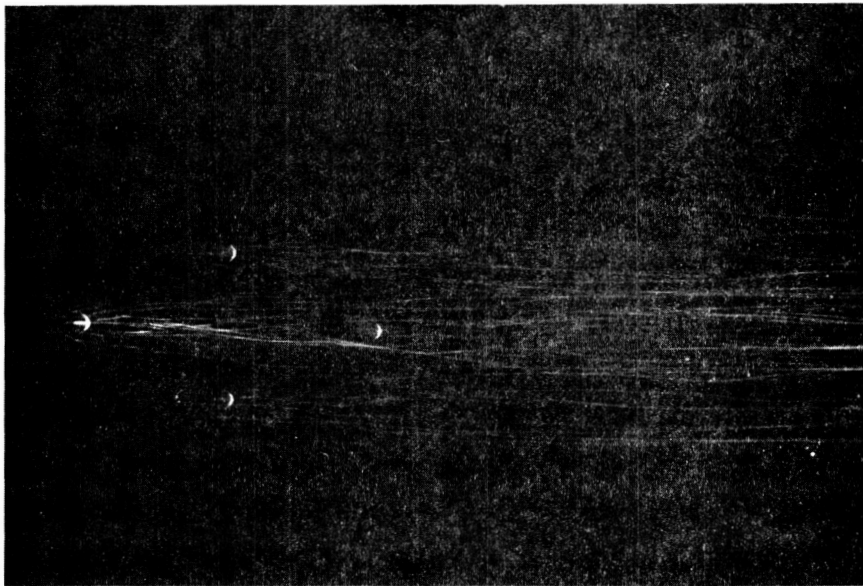
Figure IX-34. - Top view of high blowing rate case.

ORIGINAL PAGE
BLACK AND WHITE PHOTOGRAPH

274

δ
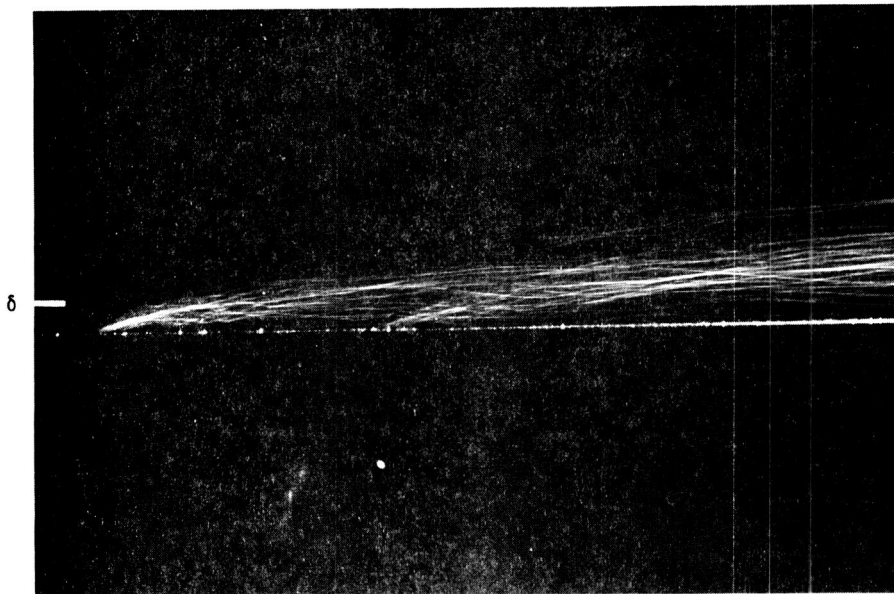
Figure IX-35. - Side view of high blowing rate case.
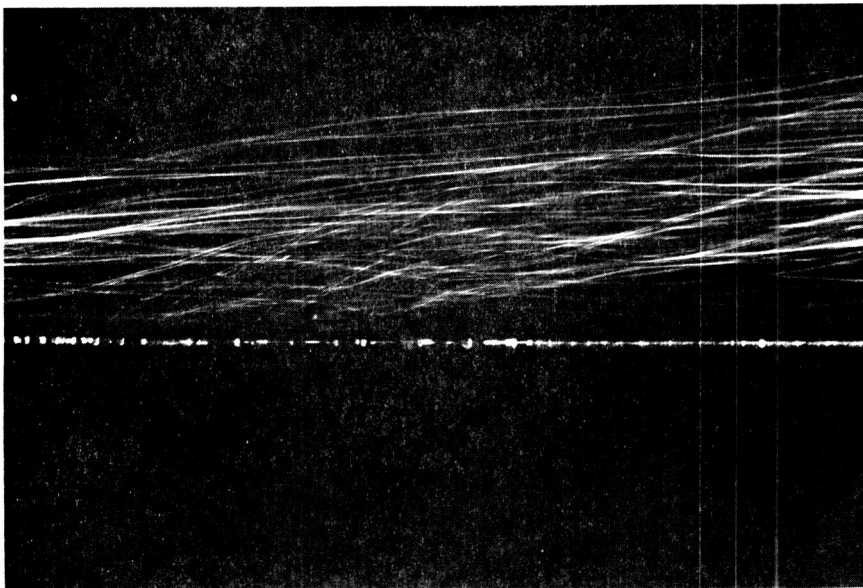
Figure IX-36. - Closeup view of downstream hole showing jet passing through upstream film.

ORIGINAL PAGE
BLACK AND WHITE PHOTOGRAPH
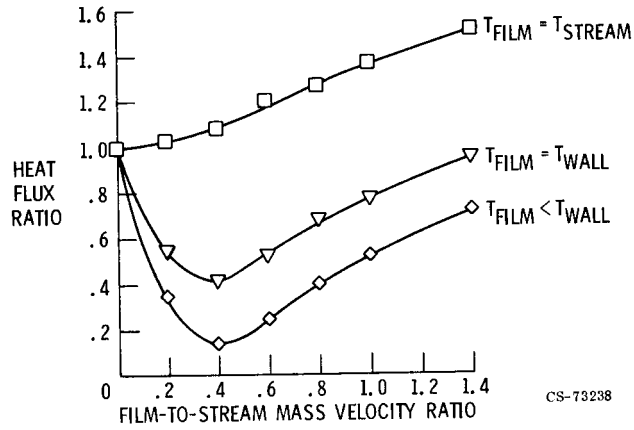
Figure IX-37. - Effect of blowing rate on film cooling heat transfer.
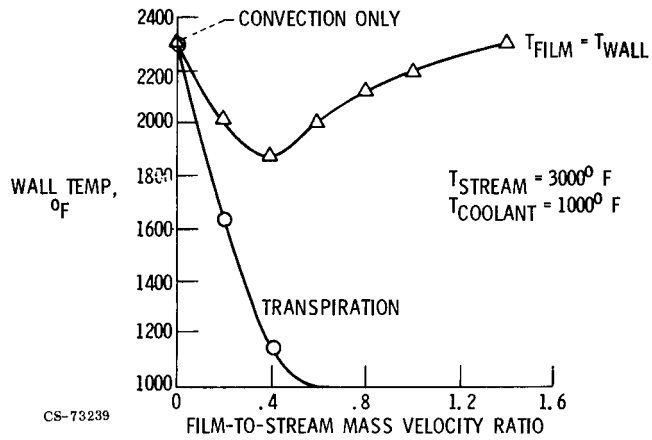
Figure IX-38. - Effect of film cooling on wall temperature.
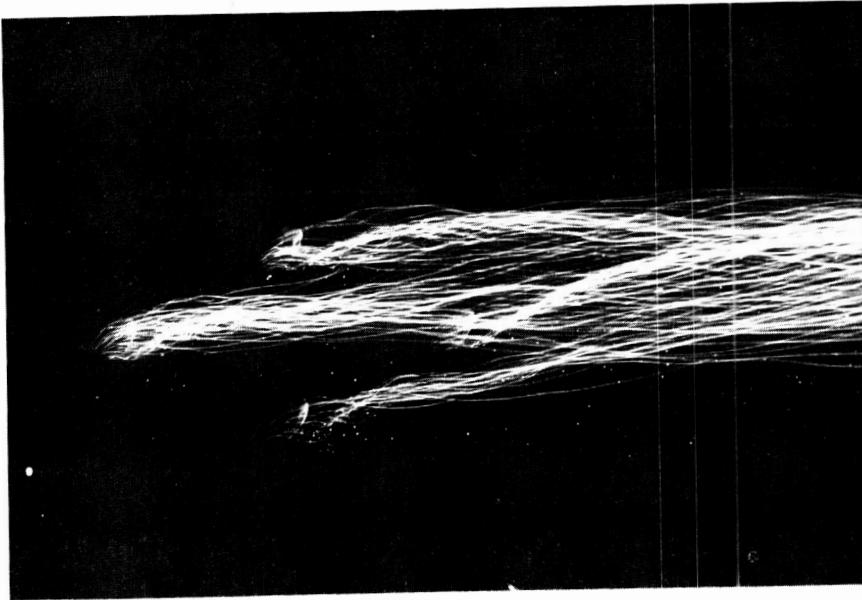
Figure IX-39. - Four-hole staggered array; compound angle injection.
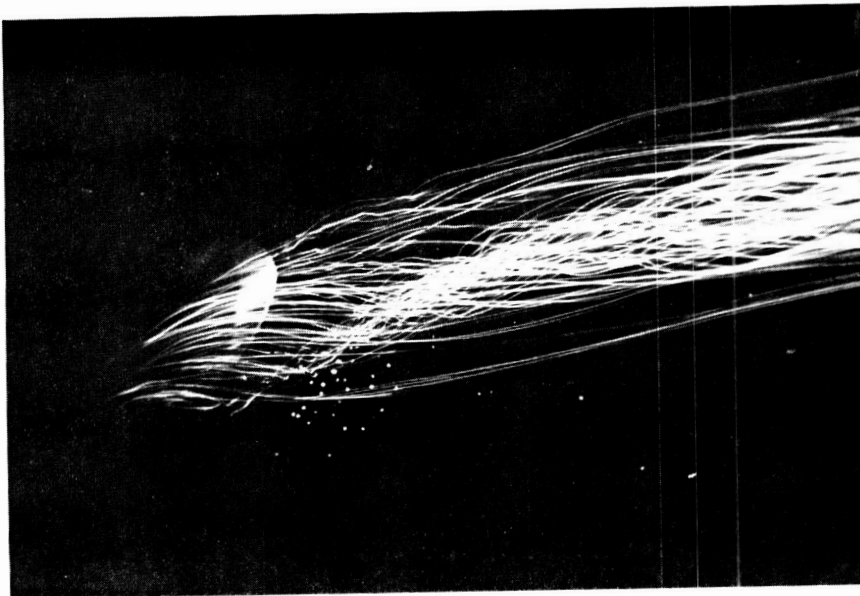
Figure IX-40. - Closeup top view of upstream hole; compound angle injection.
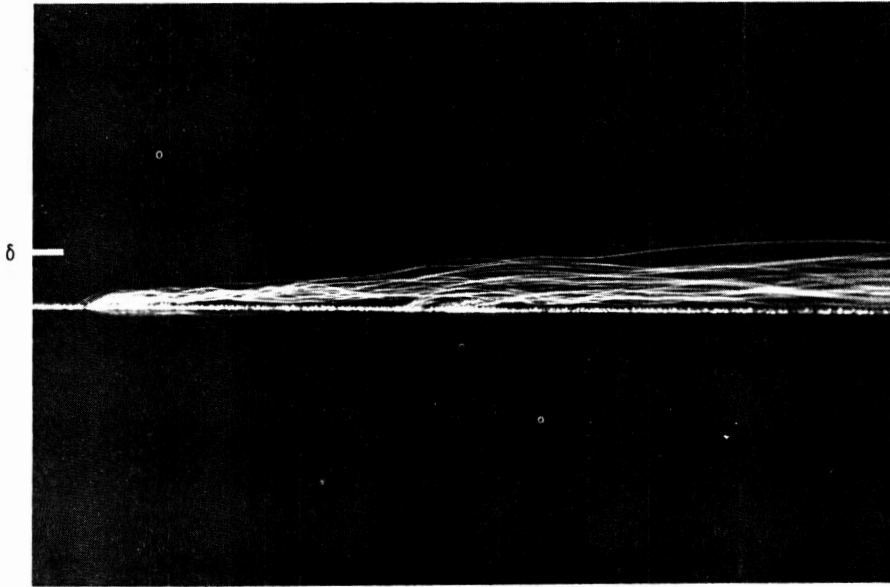
Figure IX-41. - Side view of compound angle injection; high blowing rate.

TEMP DISTRIBUTION

CS-73202
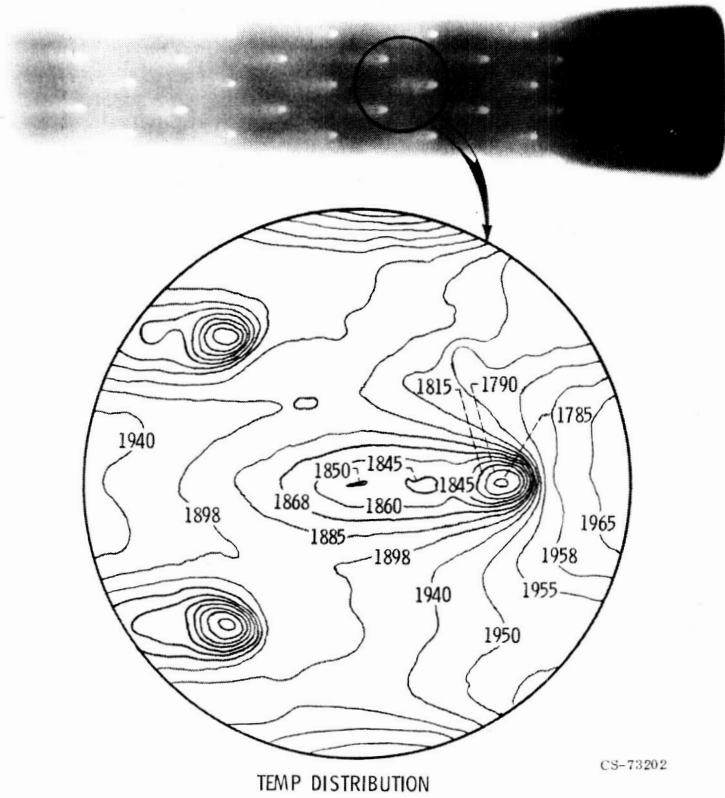
Figure IX-42. - Infrared image of film cooled wall.

278
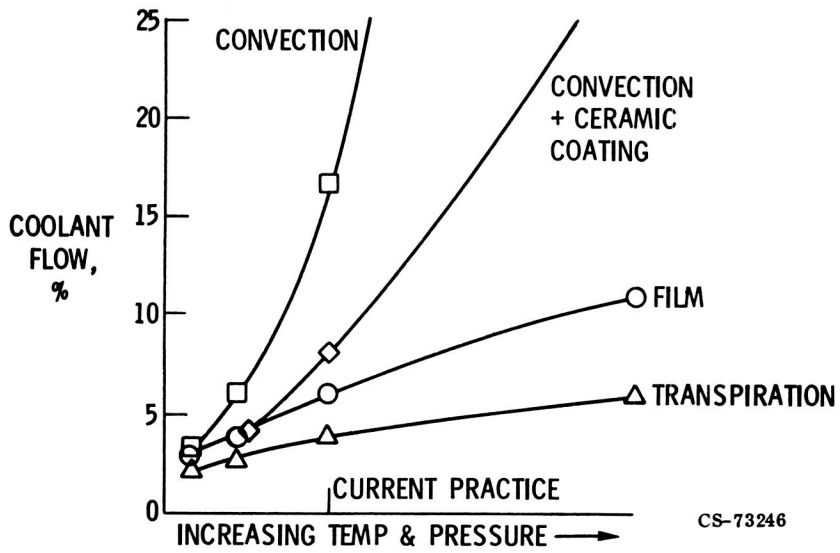
Figure IX-43. - Turbine cooling requirements.
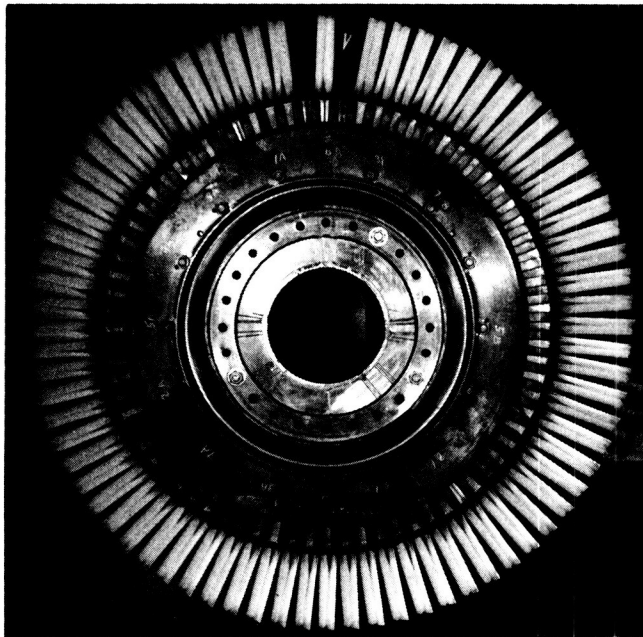
Figure IX-44. - Ceramic coated turbine blades.
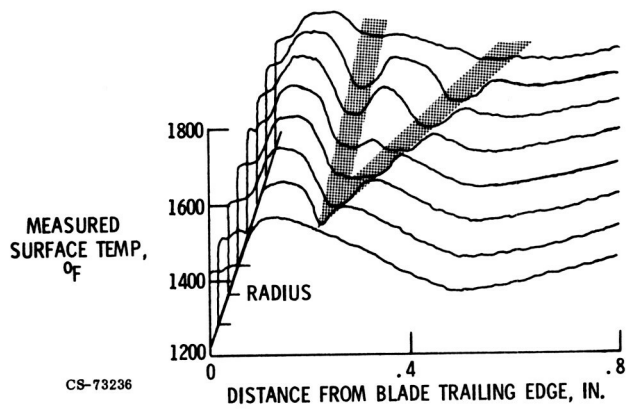
Figure IX-45. - Radiation pyrometer scans.

MEASURED SURFACE TEMP, °F

RADIUS

CS-73236

DISTANCE FROM BLADE TRAILING EDGE, IN.

HIGH PRESSURE AIR SYSTEM

PREHEATER

TURBINE RIG

COMBUSTOR RIG
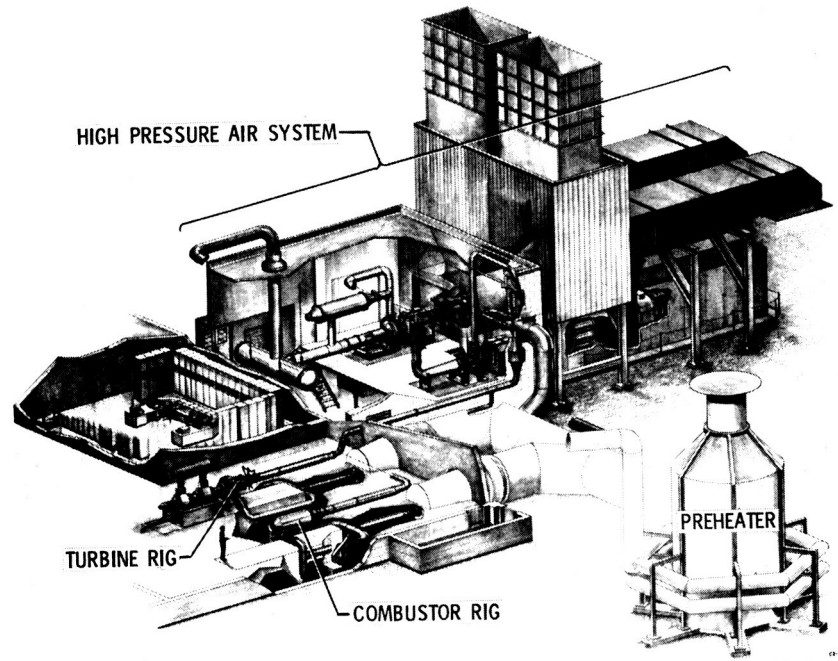
CS-73557

Figure IX-46. - High pressure, high temperature turbine facility.
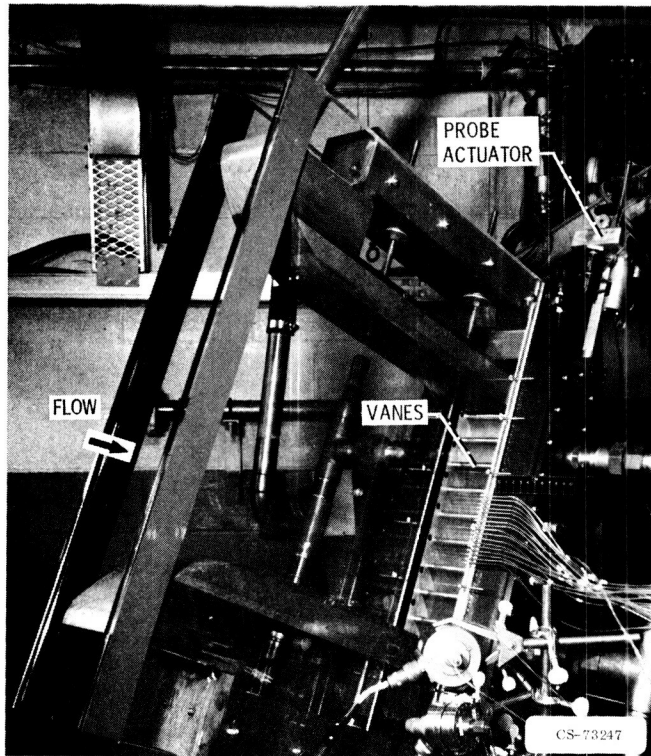
Figure IX-47. – Core turbine vane two-dimensional cascade.
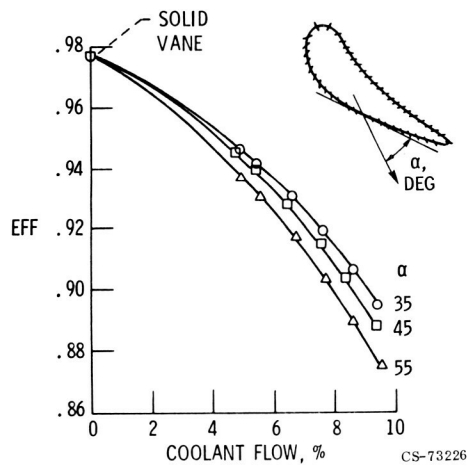
Figure IX-48. – Effect of inline ejection angle on
vane efficiency.

C-4
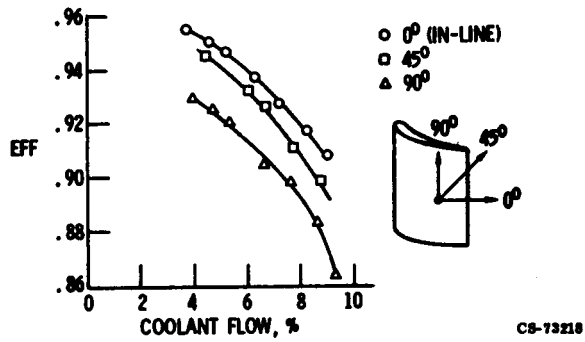
Figure IX-49. - Effect of compound ejection angle on vane efficiency. (All holes oriented 35° to local surface.)
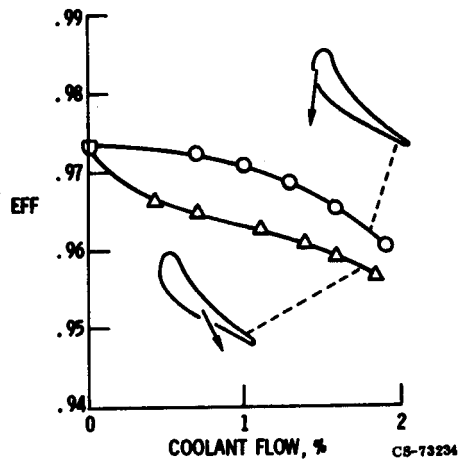
Figure IX-50. - Effect of hole location on vane efficiency. (Inline ejection angle, 35°.)
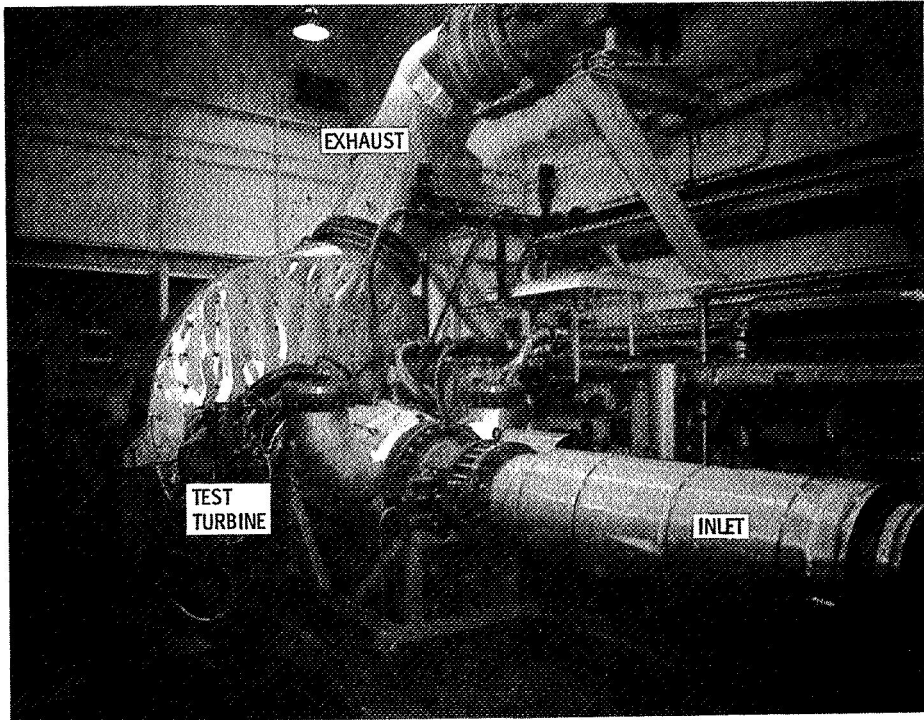
CS-73430

Figure IX-51. - Core turbine test facility.
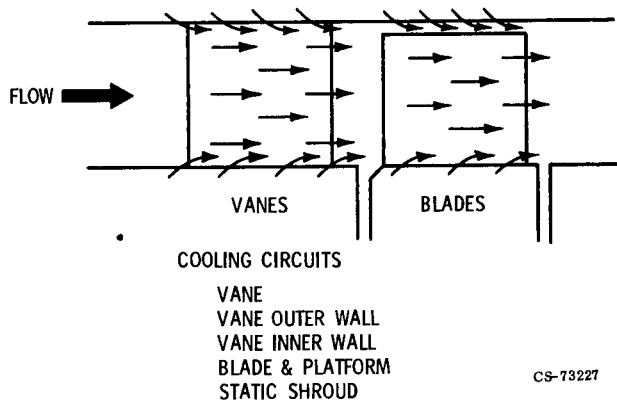

1.5 IN.
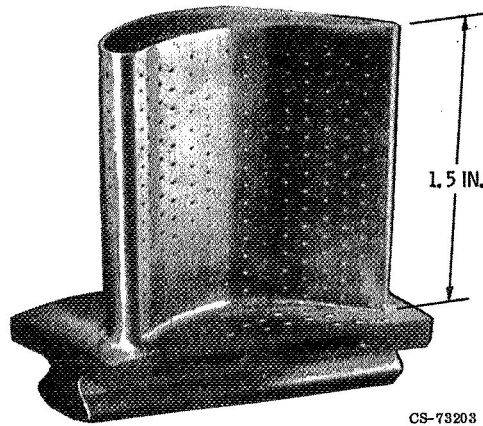
CS-73203

Figure IX-52. - Core turbine blade.

FLOW

VANES   BLADES

COOLING CIRCUITS
    VANE
    VANE OUTER WALL
    VANE INNER WALL
    BLADE & PLATFORM
    STATIC SHROUD

CS-73227

Figure IX-53. - 20-Inch core turbine cooling circuits.

$\dfrac{EFF}{EFF_{SOLID}}$

CS-73229

SOLID   PREDICTED   EXPERIMENTAL
               COOLED   COOLED
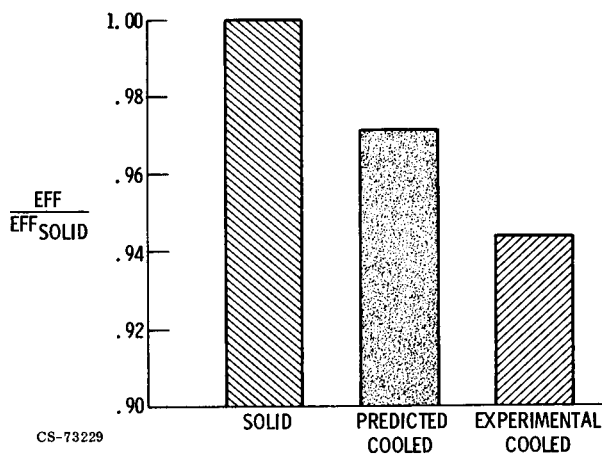
Figure IX-54. - Core turbine performance.

SOLID VANE COOLED VANE

TRAILING EDGE
PROJECTION

PRESSURE LOSS

☐ 0-0.02   ▥ 0.05-0.08
▨ 0.02-0.05   ■ 0.08+

CS-72439
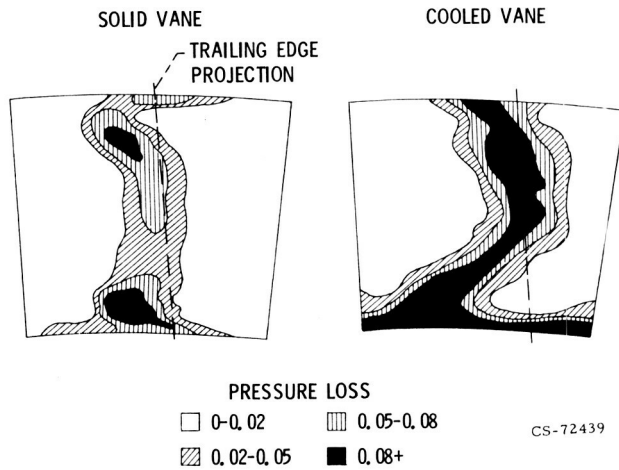
Figure IX-55. - Vane exit surveys.
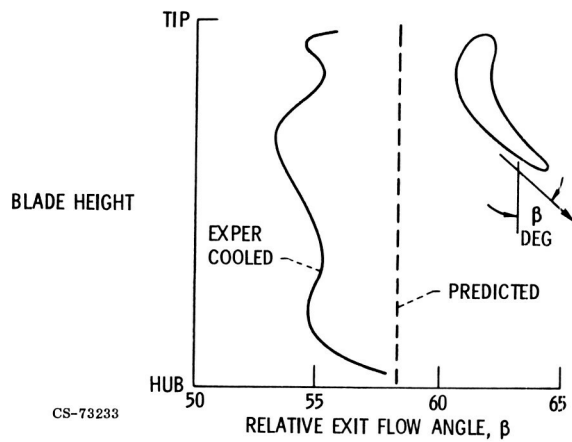
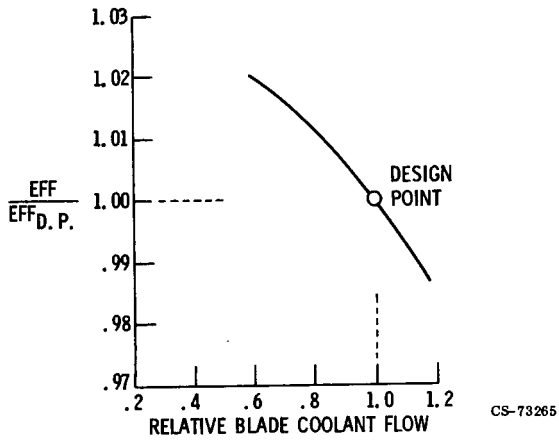Figure IX-56. - Core blade underturning.

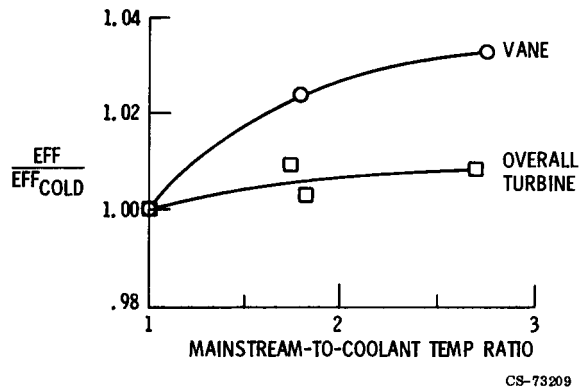Figure IX-57. – Effect of blade coolant on turbine efficiency.

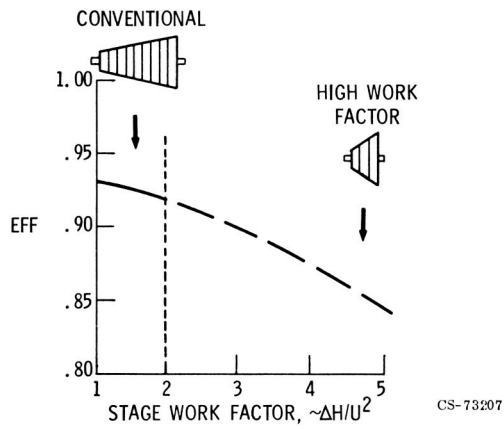Figure IX-58. – Effect of temperature ratio on turbine efficiency.

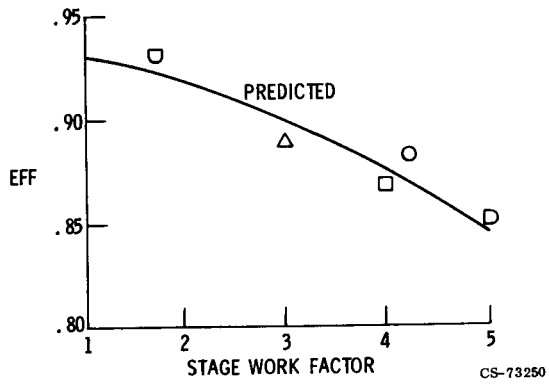Figure IX-59. - Predicted turbine efficiency.

Figure IX-60. - Fan turbine rotor.

Figure IX-61. – Performance of fan turbines.

X. BEARINGS AND GEARS FOR ADVANCED TURBINE ENGINES AND TRANSMISSIONS

Richard J. Parker

Advancements in turbine engine technology will require improved performance of many of the bearings on which engine shafts rotate and of gears which may transmit the power to a fan, rotor, or propeller. This paper discusses improved technology of engine main-shaft ball bearings (fig. X-1(a)) and of spur gears in power transmission drive trains (fig. X-1(b)). Much of the technology can be applied to other ball and roller bearings and to other spur and bevel gears throughout the engine, drive train, and accessory systems.

ROLLING-ELEMENT BEARINGS

A major area requiring improved technology for advanced turbine engines and transmissions is high-speed rolling-element bearings. Engine main-shaft speeds are expected to require ball and roller bearings that can operate at speeds up to 3 million DN (DN is a speed parameter equal to the bearing bore diameter in millimeters multiplied by the shaft speed in rpm). For example, a 120-millimeter-bore bearing running at 25 000 rpm would be operating at 3 million DN. Main-shaft bearings on current engines operate at DN values as high as 2.4 million.

High-speed bearings are discussed with particular reference to ball bearings. Figure X-2 illustrates a typical ball bearing. The inner race is fastened to and rotates with the shaft, while the outer race is usually encased in a fixed housing. The balls, in the annular space between the inner and outer races, are equally spaced by a cage. All contacts of the various components must be lubricated. In turbine engines, main-shaft ball bearings are lubricated with liquid lubricant.

Operation of ball bearings at shaft speeds approaching 3 million DN introduces problems caused by centrifugal effects and by the higher cycling rate. The effects are threefold. First, lubrication is more difficult since centrifugal force throws the lubricant outward, away from contacts at the inner race. Second, the rate of heat generation is greater because of the higher cycling rate, and thus more cooling is required. Third, fatigue life is reduced by both the higher cycling rate and the increased centrifugal force. At high speeds, centrifugal effects increase the load of the balls on the outer race. The increased load causes a drastic reduction in fatigue life. Figure X-3 shows relative fatigue life as a function of shaft speed. If the speed is doubled, the reduction in life is more than 50 percent because of the combined effects of increased centrifugal force and higher cycling rate.

Our approach to these high-speed problems includes new lubrication techniques, improved materials, and improved bearing design.

Underrace Lubrication

In order to cope with the more difficult lubrication and cooling requirements at high speeds, new techniques of lubricant supply are used. Commonly used for lower or moderate speed main-shaft bearings is jet lubrication, in which one or more jets of lubricant are directed toward the gap between the race and the cage (fig. X-4(a)). At higher speeds, above 2 to 2.5 million DN, lubrication by jets is not effective since the lubricant is centrifugally thrown away from the inner-race - ball contacts. These areas become starved for lubricant, and rapid wear and deterioration of the surfaces results.

Introducing the lubricant under the race (fig. X-4(b)) takes advantage of the centrifugal effects to supply lubricant directly to the inner-race contact areas. Also, for increased cooling effect, some lubricant may be directed through axial slots under the race. To maintain the desired temperature equilibrium between the inner and outer races, outer-race cooling may also be employed.

Improved Materials for Longer Fatigue Life

The third effect of high speeds, mentioned previously, is reduced rolling-element fatigue life. Rolling-element fatigue life is the life on which manufacturers base their catalog ratings.

What is rolling-element fatigue life, and what has been done to improve it? It must be assumed that the rolling surfaces are properly separated by a thin liquid lubricant film so that wear and excessive heat generation are not a concern. Some details about the characteristics of this thin lubricant film are given in paper XI. If there is sufficient lubrication, the fatigue of the rolling-element surfaces of the balls or rollers or of the races will, in fact, be the life limiting criterion.

Figure X-5 shows a typical fatigue spall on an inner-race groove of a ball bearing. Fatigue occurs as a result of cyclic stressing such as balls rolling over a point on a race. There is a discussion of fatigue of materials, in particular low-cycle fatigue, in paper VIII. Rolling-element fatigue is high-cycle fatigue, where the cycling rate is typically in the millions of cycles per hour, so that the total number of cycles that the material must withstand is in the billions.

As stress cycles accumulate, fatigue cracks begin to form at a weak point in either a ball or a race and propagate until a piece of material breaks out and forms a fatigue spall. The spall is relatively shallow in depth and localized in area. These characteristics are in contrast with those of low-cycle fatigue, which generally results in failure of an entire section. Surfaces away from the fatigue spall typically show no distress at all.

The weak points where fatigue cracks originate are typically subsurface in a zone where shear stresses in the material are highest. A flaw or inclusion in this subsurface zone can be a stress concentration where a fatigue crack originates. The micrograph in figure X-6 shows a subsurface crack that formed at an inclusion. A fatigue crack such as this would propagate to the surface with continued cycling and eventually would branch out until a fatigue spall would occur.

With improvements in vacuum processing of bearing steels, cleaner more homogeneous materials with fewer flaws and inclusions are possible.

The major and most recent improvement is a double-vacuum-melting process, referred to as VIMVAR, for vacuum induction melted, vacuum arc remelted.

Additionally, better control of material composition and heat treatment and new forging techniques for bearing races have resulted in very significant improvements in rolling-element fatigue life.

Optimized Design

With underrace lubrication and cooling to allow bearing operation at high speeds and improved materials for longer fatigue life, how do we improve the design or determine the best internal geometry of a bearing for a given application? What ball size, internal clearance, and curvatures are optimum? The prediction of performance limits, stresses, and fatigue life of bearings is aided by the use of computer analysis.

Computer programs are now available for analysis of ball and roller bearings, both single bearings and bearings in systems containing many bearings. The programs in use at the Lewis Research Center were developed and modified for improved prediction capabilities by an NASA contractor. These programs predict the performance and fatigue life of ball and roller bearings by taking into account the applied loads, including thrust, radial, and moment loads; the high-speed effects, specifically centrifugal force; and the temperature effects on the lubricant. The analyses determine stresses and lubricant film thickness in the contacts of balls or rollers and races. Ball or roller motion as affected by centrifugal forces and applied loads is determined. Fatigue life as affected by the material, the lubricant, and the loads is calculated. Temperatures of the bearing components are predicted by taking into account the lubricant, flow rates, and lubrication scheme. The value of these computer programs is their capability of optimizing a bearing design for a specific application.

Experimental Fatigue Results at 3 Million DN

A 120-millimeter-bore ball bearing was designed by using computer op-
timization; the bearing was made from the latest heat treated and forged
materials, had improved surface finishes, and had provision for underrace
lubrication and cooling. Two such bearings are shown in figure X-7. On
the inner race, which is manufactured in two split halves, can be seen the
lubrication grooves at the split line and the holes through which the lubri-
cant is centrifugally fed to the critical inner-race contacts.

These bearings were optimized to run at the following test conditions:
a shaft speed of 25 000 rpm or 3 million DN, a thrust load of 5000 pounds,
and a bearing temperature of 425° F. The lubricant was a type II ester
lubricant, like those currently used in commercial and military turbine en-
gines. The ball and race material was the new improved double-vacuum-
processed AISI M-50 steel, produced with very closely controlled composi-
tion and heat treatment.

Fatigue tests were begun on a group of 30 of these bearings, and al-
though the tests are not complete, the results to date are very encouraging.
These tests are being run under NASA contract.

Figure X-8 is a comparison of the experimental fatigue life results with
the life prediction of the Anti-Friction Bearing Manufacturers Association
(AFBMA). This life prediction is given a relative life of 1, and it is the
life that one would find in a manufacturer's catalog for the load and speed
conditions given previously. With multiplication factors, this life predic-
tion is the baseline commonly used today. Current turbine engine bearing
design practice uses the AFBMA life multiplied by a factor of 5. The re-
sults of the present tests, with over 65 000 hours of testing of the 30 bear-
ings, show an experimental life of about 100 times the AFBMA life, or
about 20 times the factor used in current design practice.

It should be recalled that these bearings are running at 3 million DN,
where centrifugal loads are significant. From centrifugal effects alone, the
load of each ball on the outer race is over 1000 pounds. The real signifi-
cance of these test results is that the life increase due to improved mater-
ials and design can more than make up for the expected life decrease due to
centrifugal effects at high speeds.

GEARS

Although the gear technology to be discussed relates to spur gears, such as in the planetary arrangement shown in figure X-1(b), much of it can be applied to bevel gears, such as the input bevel pinion and gear which allow a right angle bend in this transmission.

Advancements in gear technology are being sought in two major areas. They are longer fatigue life (or greater reliability) and higher temperature capability. To accomplish these advancements requires improvements in gear materials, gear design, and gear lubrication.

Forged Gear Teeth

Improved gear materials are needed to extend fatigue life and to raise upper temperature limits. An experimental fatigue test program was conducted with 3.5-inch-pitch-diameter spur gears. They were made of AISI M-50 steel, and a forging technique was used to form the gear teeth. This material was the same as the improved AISI M-50 material with which the improvements in ball bearing life discussed previously were attained.

The etched cross section of forged gear teeth in figure X-9 shows desirable grain flow, parallel to the surfaces, extending from the tooth root up along the tooth contacting surfaces. This parallel flow provides resistance to both tooth bending fatigue and rolling-element fatigue of the tooth surfaces. The use of AISI M-50 steel also provides higher temperature capability than that of the currently used gear materials.

The results of fatigue tests at a 170° F gear temperature comparing these forged AISI M-50 gears with gears of a standard AISI 9310 material are shown in figure X-10. The mode of failure in these tests was rolling-element fatigue spalling similar to that described for bearings. The fatigue life of the forged AISI M-50 gears improved by a factor greater than 5. Thus, the improved material can give longer fatigue life as well as higher temperature capability. Some caution must be exercised, however, in very-high-load applications with through-hardened AISI M-50 gears. This material possesses less tolerance to tooth breakage than the conventional surface-hardened gear materials.

Gear Design

In the area of gear design, the accuracy of life prediction has an effect on system reliability. With better means of gear life prediction, more reliable estimates of gear system life could be made. If a gear system is properly lubricated and cooled so that a sufficient lubricating film exists in the gear tooth contacts, the life of the gears will eventually be limited by rolling-element fatigue, as is the life of ball and roller bearings.

A method of fatigue life prediction is being developed for gear contacts which is similar to that currently used for rolling-element bearing contacts. The method determines the capacity of a tooth mesh based on gear tooth geometry, size, and number. The tooth mesh capacity is the load which a tooth mesh can transmit for one million cycles with a 90 percent survival probability. The fatigue life, in millions of cycles, is then determined by the ratio of this tooth mesh capacity to the actual transmitted load raised to an empirically determined power of 1.6. Material constants are then applied, as is done in bearing life predictions. For gear materials, these material factors have not yet been established.

This recent accomplishment provides a new tool which will allow life predictions for entire systems of rotating machinery, including gears as well as rolling-element bearings.

Gear Lubrication

The third approach to advancement of gear technology, mentioned previously, concerns lubrication. The functions of a liquid lubricant in a gear system, as well as in rolling-element bearings, are twofold: to provide a lubricating film and to provide cooling. In gears the effectiveness of a lubricant in providing these functions is related to the depth of penetration of the jet of lubricant between the gear teeth.

High-speed motion picture photography and stroboscopic lighting were used to observe this lubricant jet penetration in spur gears. The upper photograph in figure X-11 shows the jet of lubricant penetrating between gear teeth. Impingement on an advancing gear tooth is shown in the lower photograph in figure X-11. The depth of penetration and impingement below

the tooth tip was measured from these films for various rotational speeds and lubricant supply pressures. An analytical model was then developed, and the impingement depth was calculated from gear tooth geometry, rotational speed, and lubricant supply pressure. This model also accounts for windage effects.

Figure X-12 shows impingement depth in percent of tooth height as a function of lubricant supply pressure for two rotational speeds. Penetrations near 100 percent are desired for adequate cooling, especially for the very high speed gears in advanced aircraft transmissions, which could operate at speeds several times those of figure X-12. The higher supply pressures are required for penetrations near 100 percent. Good agreement between the experimental impingement depth, as measured from the films, and the analytical impingement depth was obtained at these higher supply pressures.

At lower pressures, the deviation from the analytical values is believed to be due to viscous losses in the oil nozzles.

From this new model a lubricant supply system can be tailored to provide the desired penetration of the lubricant jet, and thus adequate cooling and lubrication of the gear system can be assured.

CONCLUDING REMARKS

In addition to the areas of advancement in bearing and gear technology that were discussed, there are other areas that were not discussed where work is progressing. For example, a program to improve the life of high-speed tapered roller bearings is under way. These bearings are of interest for large helicopter transmissions such as used in the Army's Heavy Lift Helicopter. Specifically, the use of tapered-roller bearings is desired in the high-speed input pinion. Here the tapered-roller bearing offers better load capacity in less space and with less weight than a stack of ball bearings, as shown in figure X-1(b). Also, an experimental program studying the life, lubrication, and design of bevel gears such as the high-speed input pinion has been initiated. In the area of improved gear design, high-contact-ratio spur gears are being studied wherein the tooth mesh load is shared by more teeth in simultaneous contact. Improvements in gear system life and weight

are anticipated to result from the use of high-contact-ratio gears. In another program now in progress cylindrical roller bearings are being studied, specifically, the roller dynamics problems that are common to roller bearings on high-speed gas generator shafts. Traction drives, which use rollers rather than gears for power transmissions, are being designed and tested. These traction drives show promise for high reductions in speed from very high input speeds. In the area of shaft and rotor dynamics, significant improvements in multiplane balancing techniques now allow more reliable supercritical shafting.

The following advancements in bearing and gear technology were discussed: Improved double-vacuum-melted AISI M-50 bearing material and improved design can provide life improvements up to 100 times catalog life, or 20 times the factor used in current design practice. Underrace lubrication and cooling allow operation at bearing shaft speeds up to 3 million DN, where centrifugal effects can be detrimental. Improvements in gear technology include forged AISI M-50 steel gear teeth for significantly longer fatigue life and optimized lubricant jet penetration for more efficient lubrication and cooling. Greater gear system reliability and higher temperature capability will result from these improvements.

TURBINE ENGINE

(a) Turbine engine main-shaft bearings.

TRANSMISSION GEARS

(b) Transmission gears.
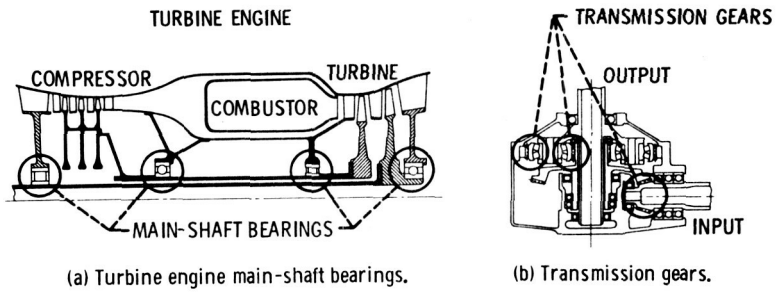
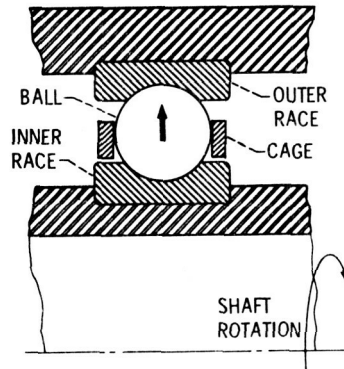Figure X-1. - Bearing and gear locations.
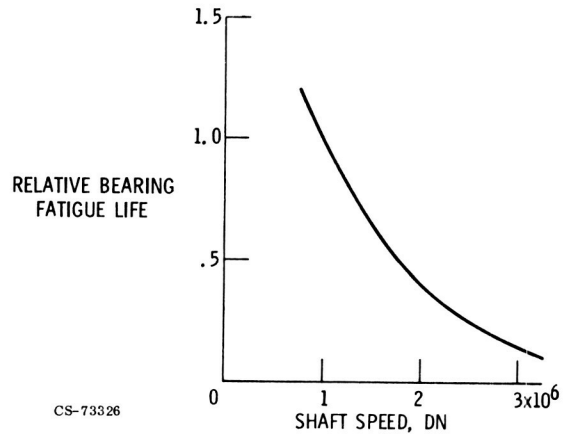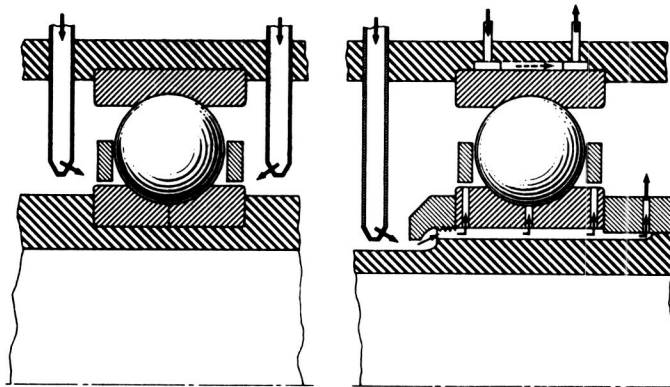

Figure X-2. - Typical ball bearing.

CS-73324

298

Figure X-3. - Effect of speed on fatigue life.

(a) Jet lubrication.

(b) Underrace lubrication.

Figure X-4. - Lubrication at high speeds.

299

INNER RACE
BALL GROOVE

SPALL
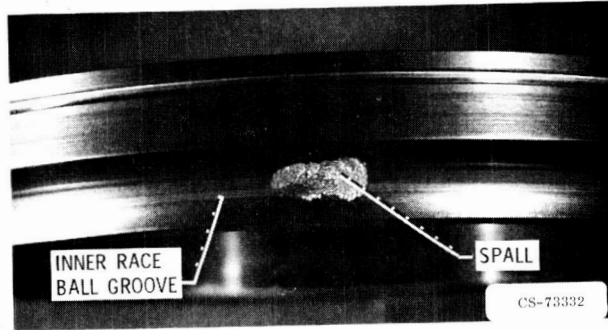
CS-73332

Figure X-5. - Typical fatigue spall.

SURFACE

0.015"

INCLUSION

CS-37915
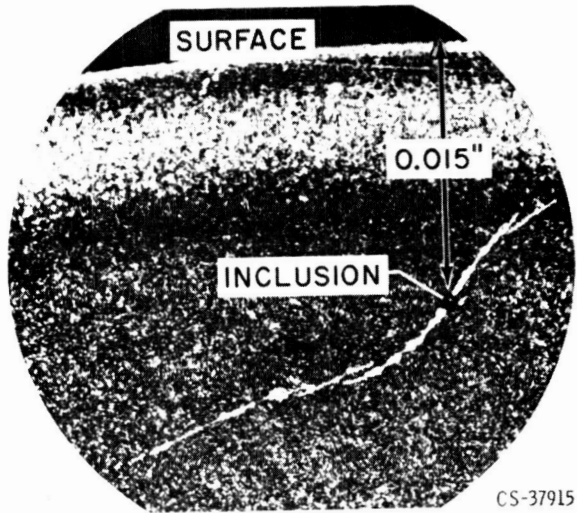
Figure X-6. - Fatigue crack originating at inclusion.

CS-73331

LUBRICATION
GROOVE

LUBRICATION
HOLE

SPLIT INNER RACE
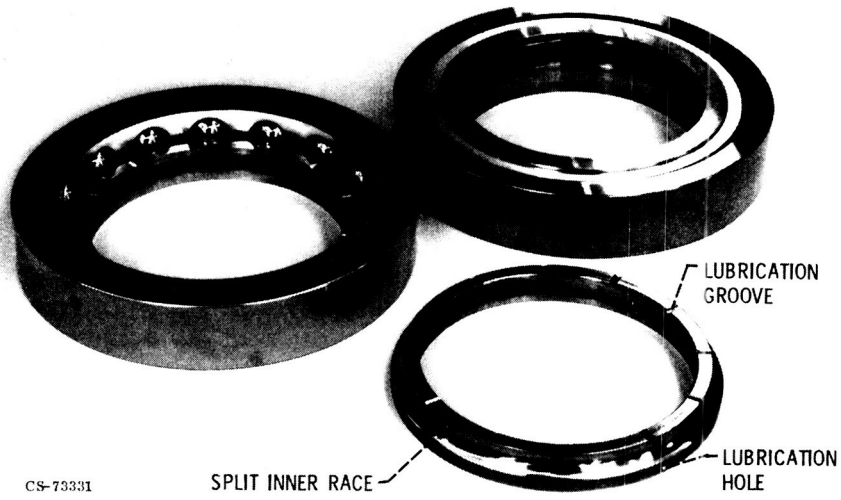
Figure X-7. - 120-Millimeter-bore high-speed ball bearings.

RELATIVE
FATIGUE LIFE

AFBMA
PREDICTION
(CATALOG
RATING)

PREDICTION
USING
CURRENT
DESIGN
PRACTICE

EXPERI-
MENTAL
RESULTS

CS-73329
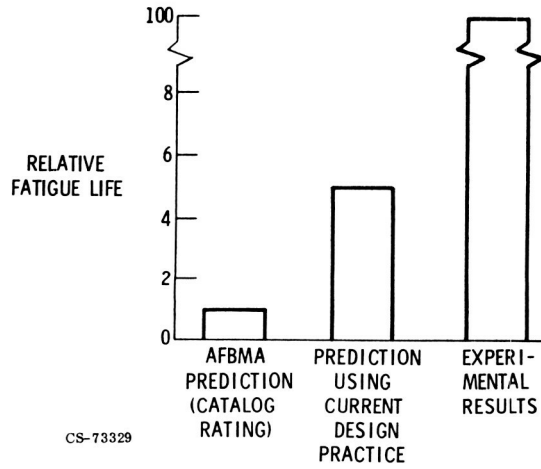
Figure X-8. - Fatigue life at 3 million DN.
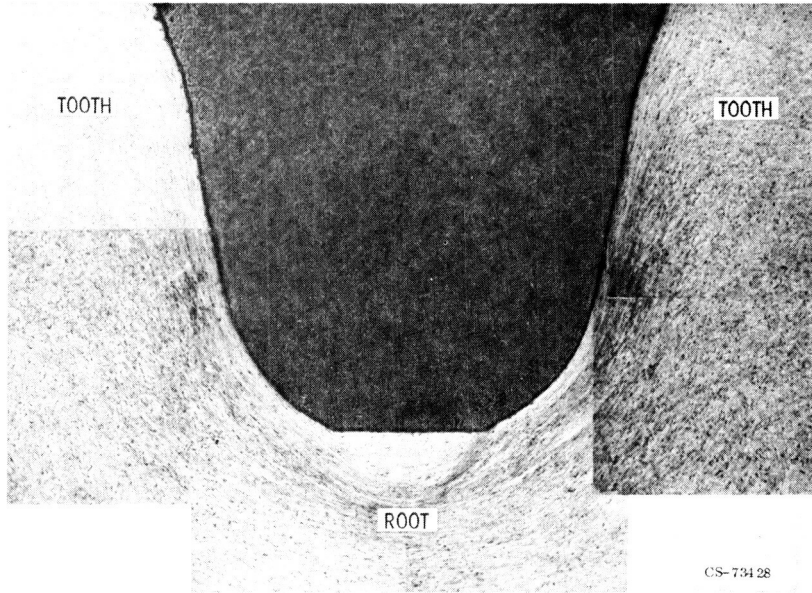
Figure X-9. - Cross section of forged AISI M-50 gear teeth.
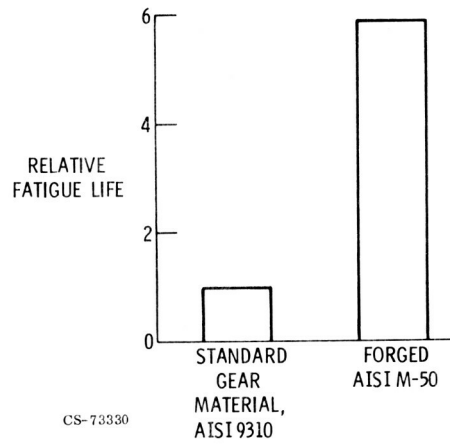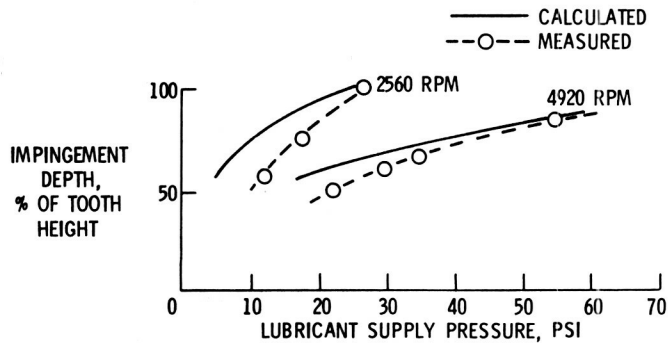

Figure X-10. - Experimental fatigue life of 3.5-inch spur gears.
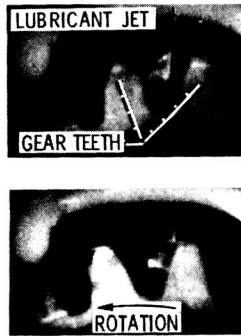
CS-73333

Figure X-11. - Lubricant jet penetration
and impingement.

Figure X-12. - Lubricant impingement depth.

CS-73327

Page intentionally left blank

XI. ENGINE SEALING AND LUBRICATION SYSTEMS

John Zuk

Advanced engines will require improved sealing and lubrication. Engine
sealing programs are directed toward the two major classes of engine seals:
engine shaft seals and primary gas path seals. In addition, some concepts
and results from fundamental lubrication research, as it pertains to the
lubrication of bearings, are presented.

Many seals are used in gas turbines. A large gas turbine engine, as
shown in figure XI-1, can have about 100 major seals and hundreds of minor
seals. Seals restrict gas leakage, provide thrust balancing, meter cooling
gas flow, and protect bearings and other mechanical components. The
cumulative effect of sealing practice on engine performance, maintenance,
and safety is appreciable. Energy conservation, improved performance,
performance retention, and safer engines can be achieved through better
seals.

SHAFT SEALS

The engine schematic in figure XI-2 shows two shaft seal locations.
These compartment seals are located adjacent to the engine mainshaft bear-
ings and are the compressor bearing compartment and the turbine bearing
compartment seals. The turbine bearing compartment shaft seal presents
a particularly critical sealing problem. The purpose of this seal is to mini-
mize high-pressure-air leakage into the compartment. This high-pressure
air is typically compressor discharge air and is used to cool the turbine and
also to isolate the bearing compartment from the hot environment.

Many engines use labyrinth seals at this location, as shown in figure
XI-3. A labyrinth seal is comprised of one or more stages of rotating knife
edges that act as flow restrictors and a rigid stationary surface. The trend

to higher pressures and temperatures at this location in high-performance engines results in very high leakage. The gap between the knife edge and the stationary surface must be large enough to accommodate large dynamic motions and distortions of the shaft. In addition to high leakage, there is high oil consumption. Oil is entrained as the leakage vents out of the engine.

In order to overcome these limitations, face contact seals are sometimes used at this location, as shown in figure XI-4.

In a face contact seal, a seal ring assembly, with a carbon sealing surface, is held against a rotating seal seat that is attached to the shaft. The nonrotating seal ring assembly can move axially to accommodate motions of the seal seat. However, the face contact seal is pressure and speed limited by the high heat generation and subsequent wear or other surface failures that can result from the rubbing contact.

The NASA self-acting lift pad seal, which was introduced during the 1970 Aeronautical Propulsion Conference, offers a solution to the shortcomings of both labyrinth and face contact seals. This seal has much greater pressure and speed capability than face contact seals and gives lower leakage than either labyrinth or face contact seals. It is similar to a face contact seal, with one very significant addition. A self-acting lift pad geometry has been added to the primary sealing surface (fig. XI-5). The self-acting lift pad geometry enables positive separation of the sealing surfaces during rotation by a very thin gas film.

A view of the self-acting lift pad seal ring showing details of the primary sealing surface is given in figure XI-6. This ring has 20 lift pads. The geometric details of this surface are shown in figure XI-7. The primary sealing surface is characterized by the following geometry:

(1) The recessed pad area, which is approximately 0.001 inch deep

(2) The shrouds surrounding the pad

(3) The radial feed grooves

(4) A circumferential groove

(5) The sealing dam, where the pressure drop and leakage occur

During rotation of the seat, the high-pressure gas is dragged into the pad and compressed as it passes over the step at the end of the pad (fig. XI-5). The resulting lifting action or force separates the primary seal ring and the rotating seat. Pressure balancing allows this small self-generated lift force to maintain positive separation. During shutdown or periods of non-

rotation, the primary ring is held in contact with the seat by compression springs (fig. XI-5). Thus, positive sealing is maintained.

Seals of this type are designed to operate at a clearance of about 0.0002 inch. This clearance is less than 1/10th to 1/100th that associated with labyrinth seals. Because clearance determines the amount of leakage, self-acting lift pad seals perform much more effectively than currently used seals. As shown in figure XI-8, the range of measured leakages is substantially higher for the conventional seals than for the self-acting lift pad seal. The higher leakage of the face contact seal is attributed to intermittent face separation caused by distortion and seal dynamics. These results were obtained with a $2\frac{1}{2}$-inch-diameter lift-pad seal operating at a rotating speed of 600 ft/sec and a sealed air temperature of 575° F. The wear of the sealing faces was negligible. The seal size and conditions are relevant to advanced small gas turbine engine operation. Additional testing indicated successful operation both in a high dust environment and during excessive shaft excursions. These conditions were more severe than are expected in normal aircraft engine operation.

Conventional face contact seals are generally limited to sealing pressures less than 200 psi at surface speeds below 400 ft/sec (fig. XI-9). A $6\frac{1}{2}$-inch-diameter self-acting lift pad seal, representative of larger engine shaft seals, has demonstrated successful operation at surface speeds to 500 ft/sec and pressure differentials to 500 psi. The sealed air temperatures ranged from room temperature to 1000° F. Actually, the maximum speed and pressure capability are unknown because tests to date have been limited by the test facility.

The lift pad seal concept is now being incorporated in some advanced engines and is being tested for use in high-pressure industrial applications.

PRIMARY GAS PATH SEALS

The main function of primary gas path seals is to keep the working fluid in the designed flow path. Thus, the working fluid can contribute to the useful work energy of the engine rather than be added to the wasted energy of leakage. Primary gas path seals, shown in figure XI-10, can be classified in two ways - outer and inner air seals. The inner air seals are usually

labyrinth seals and are the interstage or end seals. These seals are composed of rotating knife edges interfacing with a stationary sleeve composed of a rub-tolerant and erosion-resistant material. The outer air seals are blade-tip seals. They are located in the gaps between the blade tips and the casing shroud. The casing shroud also is composed of a rub-tolerant and erosion-resistant material. Of all the seals, the primary gas path seals have the greatest impact on performance, including fuel economy. For example, turbine efficiency, one measure of performance, is greatly affected by blade-tip clearance. The decrease in turbine efficiency variation with blade-tip clearance to blade-height ratio is shown in figure XI-11. These data are for a 5-inch reaction turbine. An increase of 1 percent in blade-tip clearance to blade-height ratio reduces the turbine efficiency variation by about 3 percent. Generally, the gas path sealing clearances change with each engine condition such as idle, takeoff, and cruise. The dimensional changes in the seal support structure are large relative to the seal clearances. The trend toward higher engine pressures and temperatures will tend to increase both seal displacements and erosion.

Although nominally rub-tolerant materials are presently used, problems arise during close-clearance operation when severe rubbing situations are encountered. In these situations, the blade tips can wear severely. Severe rubbing may be due to "hard landing" or to sudden changes in engine operation (such as an "aborted landing"). The surface of a conventional shroud seal material after severe rubbing is shown in figure XI-12. There are two distinct regions in the wear pattern. The rub tolerance shown on the right is acceptable. On the left, unacceptable "smearing," or transfer of the blade-tip material, has occurred. The blade-tip wear results in a larger leakage path. Similar but even more complex problems exist with knife-edge seals.

A program to develop improved turbine outer and inner air seals is being conducted by the NASA Lewis Research Center. Part of the program goal is to develop a material that has both good rub tolerance and good resistance to hot-gas erosion. Present shroud seal materials have either poor rub tolerance or poor gas erosion resistance, as shown in figure XI-13. An experimental material being developed by NASA is compared with two conventional shroud seal materials - porous metal and porous cermet. The porous metal shows very low friction, which indicates rub tolerance, but is badly eroded by hot gas. This loss of shroud material by erosion is, of

course, detrimental to performance. On the other hand, the porous cermet has good erosion resistance but poor rub tolerance. Accompanying the high friction, blade-tip material was transferred to the shroud, which is also detrimental to performance. With the shroud seal materials presently used, a trade-off must be made between rub tolerance and erosion resistance. The NASA experimental material, however, shows reasonable rub tolerance (friction) and excellent erosion resistance. Friction and erosion problems are overcome by using a plasma-sprayed solid lubricant coating on the conventional porous metal material. In addition, this lubricant coating is formulated to provide oxidation resistance; and further, it will reduce leakage flow through the porous structure.

Figure XI-14 is a magnified cross-sectional view of the shroud seal material. The plasma-sprayed solid lubricant surface coating and the porous metal substrate can be seen. Figure XI-15 is the same view after a knife-edge rub. The groove indicates a clean rub. No metal transfer from or to the knife edge was observed. The knife edge showed no measurable wear. The coating provided a glassy phase on the rub surface. This glassy phase acted as a high-temperature solid lubricant. Preliminary results with this lubricant coating material are promising. However, further studies and additional testing, simulating a complete engine environment and operating cycle, are necessary before this material concept can be used in an engine.

In addition to better seal materials to enable close clearance operation, clearance control of some type during engine operation will be required. Such design concepts are now being investigated.

THIN-FILM LUBRICATION

In gas turbine bearings, thin-film lubrication occurs in the loaded region between the ball and race, where pressures are typically 200 000 psi (fig. XI-16). Here the lubricant becomes wedged into and trapped between the surfaces so that they actually become separated by a very thin film of lubricant. This lubricant film is important because it prevents wear of the surfaces. The objective of our research is first to understand how thin-

film lubrication works so that it can be fully utilized and second to formulate better lubricants.

In the laboratory the ball-race contact is simulated with a ball loaded against a transparent disk (fig. XI-17). Optical interferometry is used to measure the very thin lubricating films. Hence, the wavelength of light is the unit of measure. Interference colors obtained from light reflected between the surfaces give a direct measure of the film thickness. A microscope is used to observe the fringes because the region of interest is very small - 0.030 inch or less in diameter.

A static contact, as viewed through the microscope, is shown in figure XI-18. The dark circular area is the region of elastic deformation, where the surfaces are touching each other. Colored interference fringes form around this region, where the surfaces are separated. Each color corresponds to a certain separation between the surfaces. Figure XI-19 shows the lubricated surfaces under dynamic conditions. The motion of the surfaces draws the fluid between them in a direction from left to right. The interference colors in the center indicate that the surfaces are separated by a thin oil film.

It is convenient to consider the lubrication process in terms of three functional zones:

(1) An inlet zone

(2) A load zone

(2) An exit zone

These zones and the cavitation regions are shown in figure XI-19. Each of these zones plays an important role in lubrication.

The performance of the lubricant is very much influenced by the pressure between the surfaces. The calculated pressure contours are shown in figure XI-20. In the inlet zone the pressure rises gradually to about 20 000 psi. In the load zone the pressure rises very rapidly to about 200 000 psi at the center of the load zone and then drops very rapidly in the exit zone, where the oil film ruptures. An important feature of thin-film lubrication is how these extremely high pressures influence the viscosity of the fluid.

The effect of pressure on the viscosity of a typical lubricant, synthetic paraffinic oil, is presented in figure XI-21. At atmospheric pressure the viscosity of this oil is like that of ordinary motor oil. As the pressure rises to

typical inlet pressures of 20 000 psi, the viscosity increases so that its consistency becomes like that of butter. When the lubricant pressure rises to 200 000 psi, as in the load zone, its consistency approaches that of asphalt.

These three zones are important in connection with lubrication. The inlet zone is perhaps the most important. The inlet determines the film thickness in the load zone. The fluid that is wedged into the inlet zone causes the surfaces to become separated. The thickness of the film in the load zone must be sufficient to separate the surfaces in order to prevent wear. This load zone is characterized by extremely high viscosity, which allows traction forces to be transmitted from one surface to another. If sufficient traction forces are not transmitted, the balls will tend to skid rather than roll within the bearing, and the rolling elements will experience abnormal wear. This can be a problem with high-speed bearings.

The behavior of the fluid and its environment within the load zone are being investigated by using infrared techniques. The energy emitted by the load zone is collected and analyzed. From this analysis the temperature distribution shown in figure XI-22 was found. The fluid temperature was about 70° F initially; it was 85° F in the inlet zone. Very high temperatures were observed in the load zone because the fluid is sheared when sliding is present. The maximum temperature of 680° F occurred at the locations of minimum film thickness and maximum shear. The effect of these high temperatures on thermal breakdown is being considered. In addition, a computer analysis of the emitted radiation is being undertaken to detect structural changes and solidification of the fluid in the actual load zone. This technique holds great promise for increasing our understanding of lubricated contacts.

The exit zone is characterized by cavitation of the fluid that is discharged from the load zone. A small quantity of fluid is left on the track for cooling and for reforming sufficient lubricant for the next ball's inlet region. Consequently, the inlet region of the next ball may not always be completely filled.

Studies on starvation (or lubricant supply conditions) have shown that the inlet region must be filled to a thickness at the boundary that is at least 10 times the thickness in the load zone. If this thickness is not maintained, the film in the load zone will become starved. In other words, as this boundary comes progressively closer to the leading edge of the load zone,

the film in the load zone will become thinner. On the other hand, excess lu-
bricant in the inlet region adds nothing to lubrication but contributes to churn-
ing losses within the bearing, which are reflected in higher torque and heat
generation. There is thus an optimum quantity and distribution of fluid.

GENERAL COMMENTS

Other programs include two lubrication systems studies. One is a mist
with supplemental air cooling that can be especially useful as an emergency
system when military helicopters lose their regular lubrication. The other
is a bearing-compartment fire prevention program. Seals for high-
temperature, high-pressure hydraulic systems and high-speed transmis-
sions are also being developed.

Friction and wear processes are being investigated from a fundamental
point of view on an atomic basis by using advanced techniques for examining
the surfaces.

A significant amount of the sealing and lubrication contractual efforts of
this Center is funded by the Army Air Mobility Research and Development
Laboratory. Further, all programs on sealing and lubrication are integrated
with those of corresponding organizations at Wright Technical Center of the
Air Force to maximize the efficiency and impact of our research efforts.
Several contractors, identified in the bibliography, have provided critical
efforts leading to the results reported in this paper.

CONCLUDING REMARKS

The NASA self-acting lift pad seal provides close-clearance, noncon-
tacting operation. The leakages are 1/10th to 1/100th those of labyrinth
seals, sealing 500-psi air at conditions such as 1000° F at speeds to
500 ft/sec. Operation of the lift pad seal is not speed or pressure limited,
and the severe environments of advanced engines can be effectively sealed.

A promising concept for a gas path seal material is being developed. A
lubricating surface coating on a porous metal shows excellent rub tolerance

and erosion resistance. Closer seal clearance operation will have a very significant impact on engine economy.

Research in the mechanisms of thin-film lubrication for mechanical components, such as ball bearings, will enable more reliable operation through more effective use and formulation of lubricants.

BIBLIOGRAPHY

Shaft Seals

Dobek, L. J.: Development of Mainshaft Seals for Advanced Air Breathing Propulsion Systems. (PWA-TM-4683, Pratt & Whitney Aircraft, NAS3-15346.) NASA CR-121177, 1973.

Hady, William F.; and Ludwig, Lawrence P.: New Circumferential Seal Design Concept Using Self-Acting Lift Geometries. NASA TN D-6805, 1972.

Hayden, T. S.; and Keller, C. H., Jr.: Design Guide for Helicopter Transmission Seals. (SER-50791, United Aircraft Corp.; NAS3-15684.) NASA CR-120997, 1974.

Hayden, T. S.; and Keller, C. H., Jr.: Development of Helicopter Transmission Seals. (SER-50776, United Aircraft Corp.; NAS3-15684.) NASA CR-120983, 1973.

Ludwig, Lawrence P.; and Johnson, Robert L.: Design Study of Shaft Face Seal with Self-Acting Lift Augmentation. III - Mechanical Components. NASA TN D-6164, 1971.

Ludwig, Lawrence P.; and Strom, Thomas N.: Improved Circumferential Shaft Seal for Aircraft Gear Transmissions. NASA TN D-7130, 1973.

Ludwig, Lawrence P.; Zuk, John; and Johnson, Robert L.: Design Study of Shaft Face Seal with Self-Acting Lift Augmentation. IV - Force Balance. NASA TN D-6568, 1972.

Lynwander, Peter: Development of Helicopter Engine Seals. (LYC-73-48, Avco Lycoming Div.; NAS3-16720.) NASA CR-134647, 1973.

Parks, A. J.; McKibbin, A. H.; Ng, C. C. W.; and Slayton, R. M.:
Development of Mainshaft Seals for Advanced Air Breathing Propulsion
Systems. (PWA-3161, Pratt & Whitney Aircraft; NAS3-7609.) NASA
CR-72338, 1967.

Povinelli, V. P.; and McKibbin, A. H.: Development of Mainshaft Seals
for Advanced Air Breathing Propulsion Systems, Phase 2. (PWA-3933,
Pratt & Whitney Aircraft; NAS3-7609.) NASA CR-72737, 1970.

Povinelli, V. P.; and McKibbin, A. H.: Development of Mainshaft Seals
for Advanced Air Breathing Propulsion Systems, Phase 3. (PWA-4263,
Pratt & Whitney Aircraft; NAS3-7609.) NASA CR-72987, 1971.

Waterman, A. W.; Gray, B. F.; Robinson, E. D.; Srinath, S. K.; and
Nelson, W. G.: Application of Polyimide Rod Seals. (D6-54351,
Boeing Co.; NAS3-14317.) NASA CR-120878, 1972.

Zuk, John: Analytical Study of Pressure Balancing in Gas Film Seals.
NASA TM X-68227, 1973.

Zuk, John; Ludwig, Lawrence P.; and Johnson, Robert L.: Design Study
of Shaft Face Seal with Self-Acting Lift Augmentation. I - Self-Acting
Pad Geometry. NASA TN D-5744, 1970.

Zuk, John; Ludwig, Lawrence P.; and Johnson, Robert L.; Design Study of
Shaft Face Seal with Self-Acting Lift Augmentation. II - Sealing Dam.
NASA TN D-7006, 1970.

Zuk, John; Ludwig, Lawrence P.; and Johnson, Robert L.: Quasi-One-
Dimensional Compressible Flow Across Face Seals and Narrow Slots.
I - Analysis. NASA TN D-6668, 1972.

Zuk, John; and Smith, Patricia J.: Quasi-One-Dimensional Compressible
Flow Across Face Seals and Narrow Slots. II - Computer Program.
NASA TN D-6787, 1972.

Zuk, John; and Smith, Patricia J.: Computer Program for Quasi-One-
Dimensional Compressible Flow with Area Change and Friction - Appli-
cation to Seals. NASA TN D-7481, 1974.

Gas Path Seals

Holeski, Donald E.; and Futral, Samuel M., Jr.: Effect of Rotor Tip Clearance on the Performance of a 5-Inch Single Stage Axial Flow Turbine. NASA TM X-1757, 1969.

Ludwig, L. P.; and Johnson, R. L.: Sealing Technology for Aircraft Gas Turbine Engines. AIAA Paper 74-1188, Oct. 1974.

Mahler, Frederic H.: Advanced Seal Technology. PWA-4372, Pratt & Whitney Aircraft (AD-739922; AFAPL-TR-72-8), 1972.

Shiembob, L. T.: Development of Abradable Gas Path Seals. (PWA-TM-5081, Pratt & Whitney Aircraft; NAS3-18023.) NASA CR-134689, 1974.

Lubrication

Beerbower, A.; and Overhoff, R. F.: Microfog Lubrication for Helicopter Gearing. (Exxon Research and Engineering Co.; NAS3-16825.) NASA CR-134741, 1974.

Carlson, S.; Jakobsen, J.; Nagaraj, H. S.; Molina, M. A.; Sanborn, D. M. D. M.; and Winer, W. O.: Investigations of Lubricant Rheology as Applied to Elastohydrodynamic Lubrication. (Georgia Institute of Technology.) NASA CR-134730, 1974.

Clark, F. S.; Green, R. L.; and Miller, D. R.: Synthesis and Evaluation of C-Ether Formulations for Use as High Temperature Lubricants and Hydraulic Fluids. (MRC-SL-460, Monsanto Research Corp.; NAS3-15333.) NASA CR-134643, 1974.

Johnson, Robert L.; and Ludwig, Lawrence P.: Lubrication, Friction, and Wear in Aircraft. Presented at 32nd Meeting of Structures and Materials, London, Mar. 2 - Apr. 2, 1971.

Jones, William R., Jr.; Johnson, Robert L.; Winer, Ward O.; and Sanborn, David M.: Pressure-Viscosity Measurements for Several Lubricants to 5.5×10^8 Newtons Per Square Meter (8×10^4 psi), and 149° C (300° F). NASA TN D-7736, 1974.

Lauer, James L.: Study to Define Behavior of Liquid Lubricants in an Elastohydrodynamic Contact. (Sun Oil Co.; NAS3-17593.) NASA CR-134671, 1974.

Rosenlieb, J. W.: Aircraft Engine Sump Fire Mitigation. (AL73T007, SKF Industries, Inc.; NAS3-14310.) NASA CR-121158, 1973.

Wedeven, L. D.; Evans, D.; and Cameron, A.: Optical Analysis of Ball Bearing Starvation. J. Lubrication Tech., ASME Trans., series F, vol. 93, no. 3, July 1971, pp. 349-363.

Wedeven, L. D.: Traction and Film Thickness Measurements Under Starved Elastohydrodynamic Conditions. J. Lubrication Tech., Trans. ASME, series F, vol. 97, no. 2, April 1975, pp. 321-329
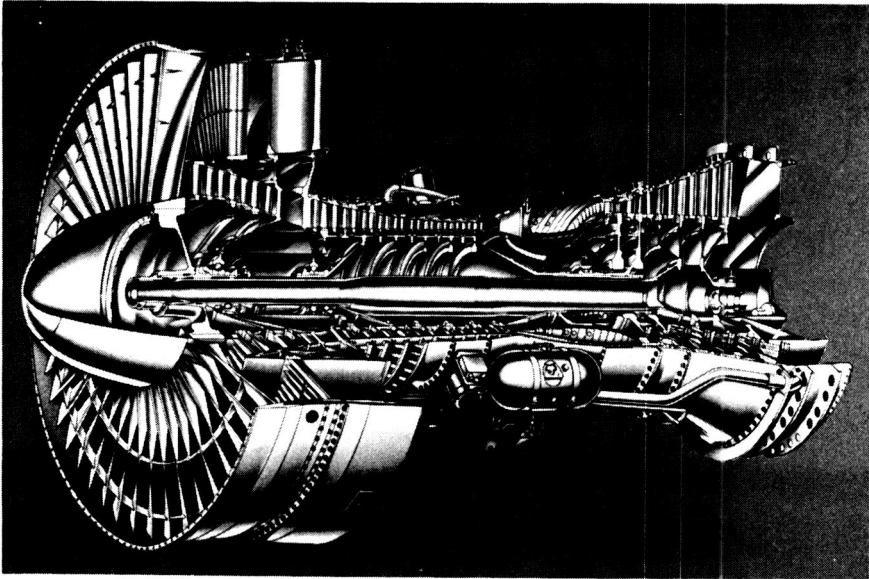
Figure XI-1. - Typical gas turbine engine.

CS-72962
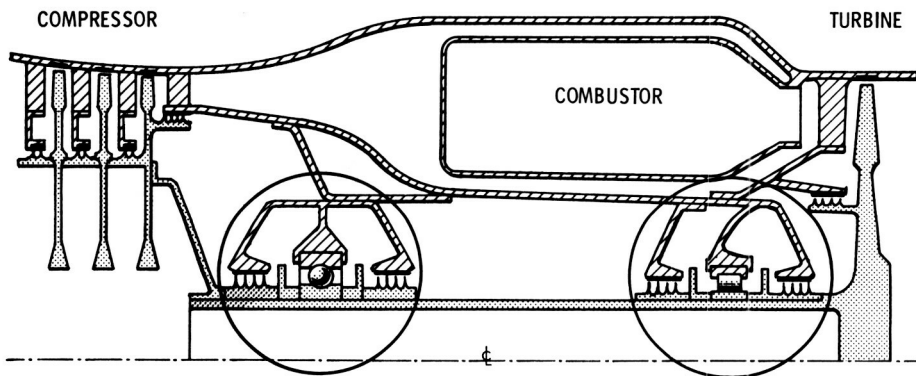
Figure XI-2. - Shaft seal locations.

CS-73420
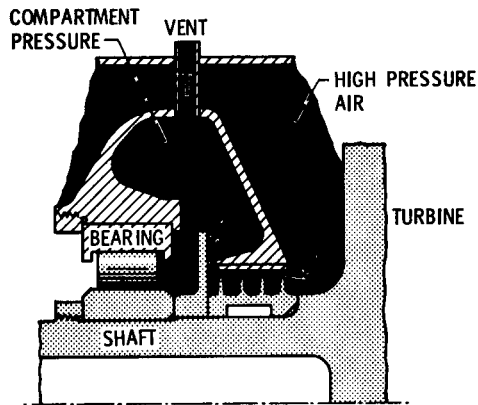
Figure XI-3. - Use of labyrinth seal as tur-
bine bearing compartment shaft seal.
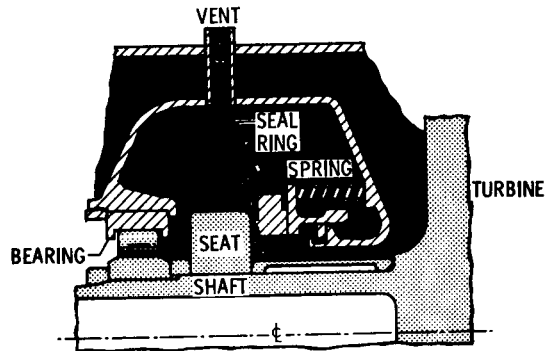
Figure XI-4. - Use of face contact seal as turbine bearing
compartment shaft seal.
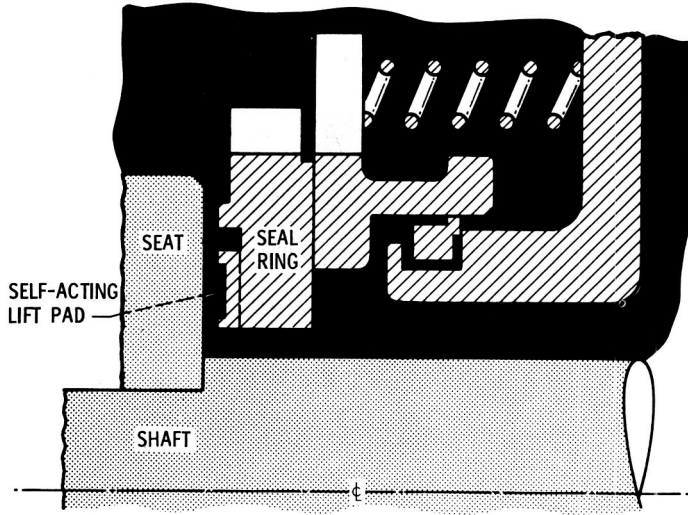
Figure XI-5. - Self-acting lift pad seal.

CS-73415
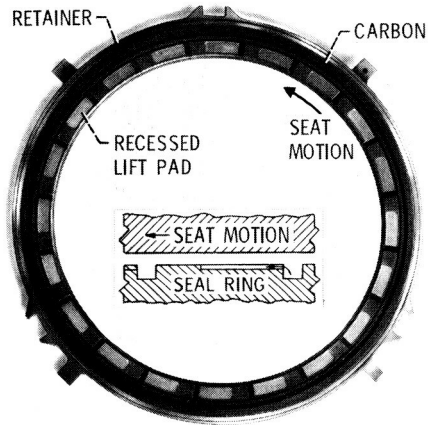
CS-73516

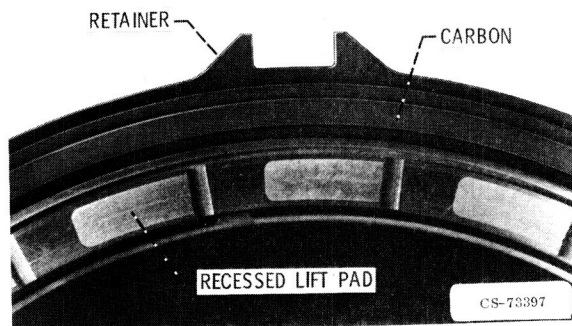Figure XI-6. - Details of self-acting lift pad
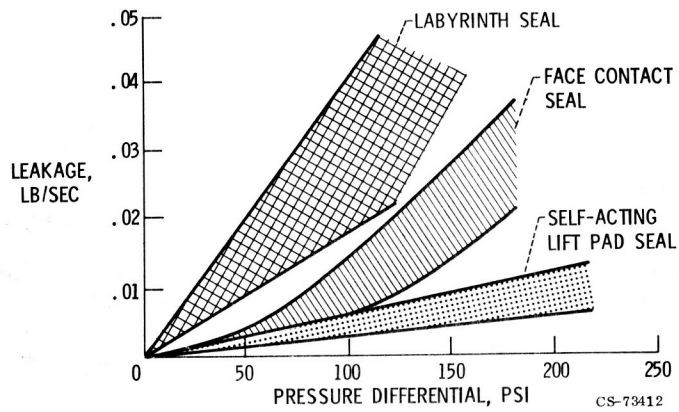seal ring.

Figure XI-7. - Section of seal ring.

Figure XI-8. - Comparison of seal leakage between conventional and self-acting lift pad seals.
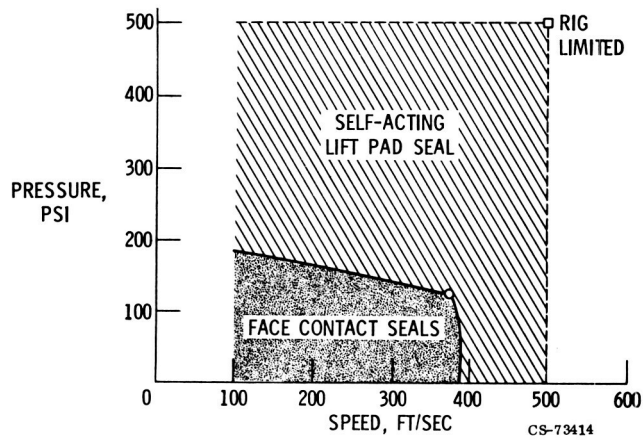
Figure XI-9. - Comparison of performance between face contact seals and self-acting lift pad seals.
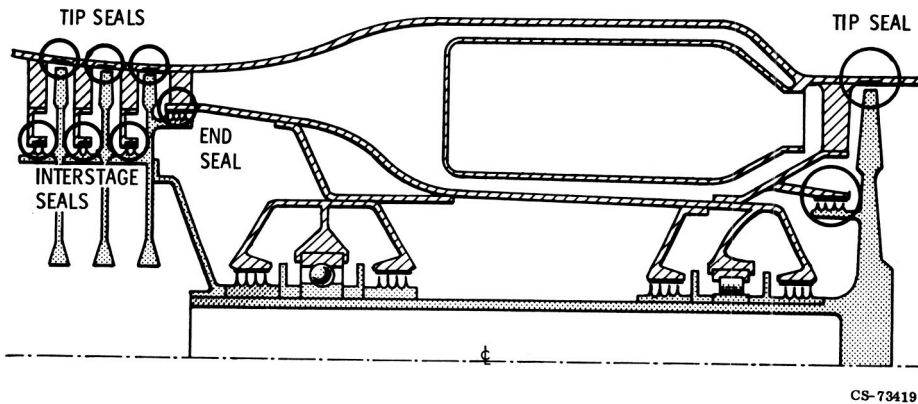
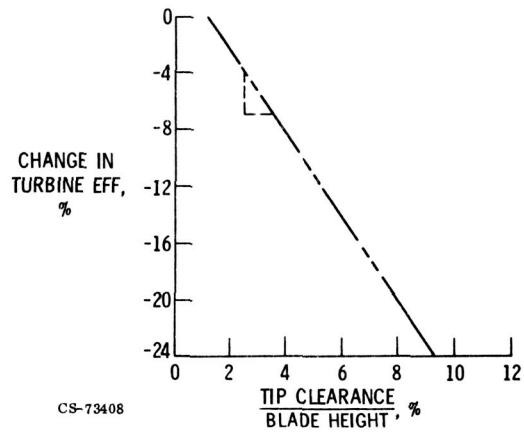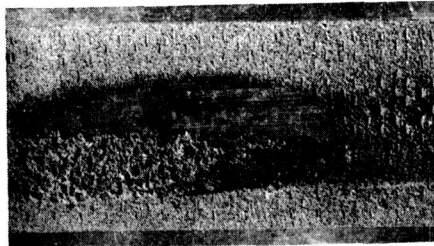Figure XI-10. - Primary gas path seal locations.

CS-73408

Figure XI-11. - Effect of blade-tip clearance on turbine performance.

CS-73399

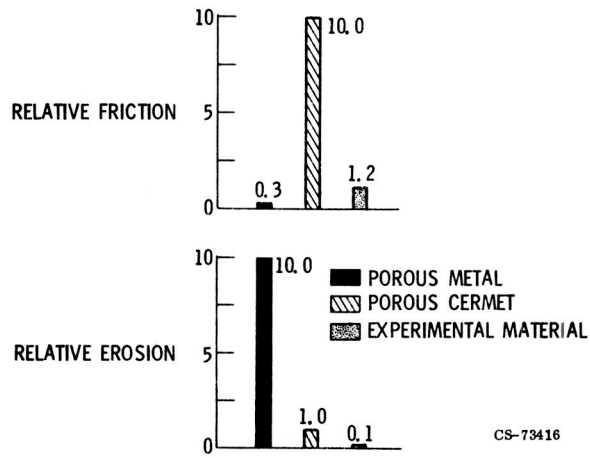Figure XI-12. - Surface of conventional shroud seal material after severe rubbing.

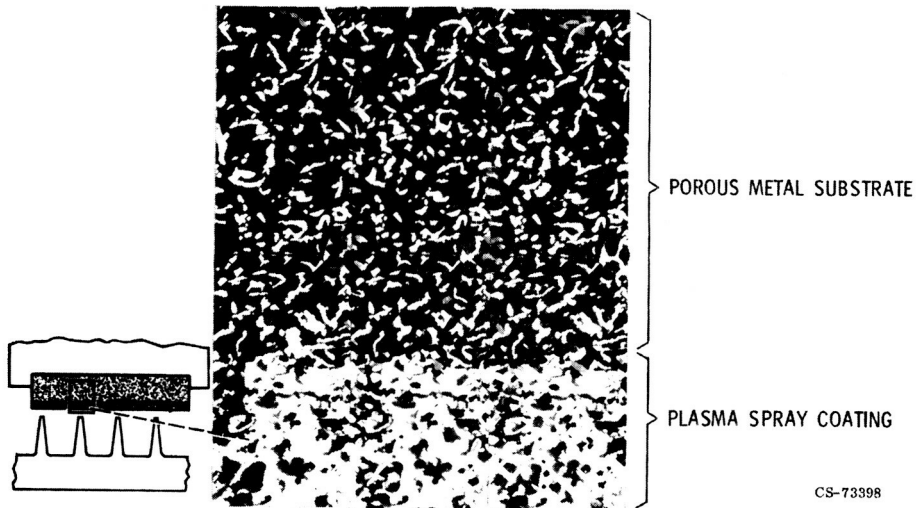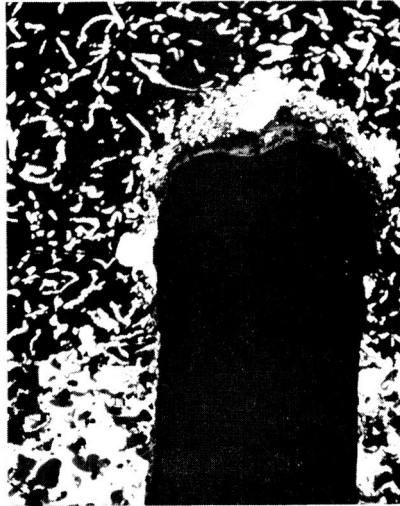Figure XI-13. - Comparison of friction and erosion of shroud seal materials.

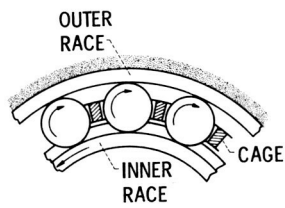Figure XI-14. - Cross-sectional photomicrograph of experimental shroud seal material.

CS-73455

Figure XI-15. - Photomicrograph of rub groove.

CS-73403

Figure XI-16. - Section of ball bearing.

324
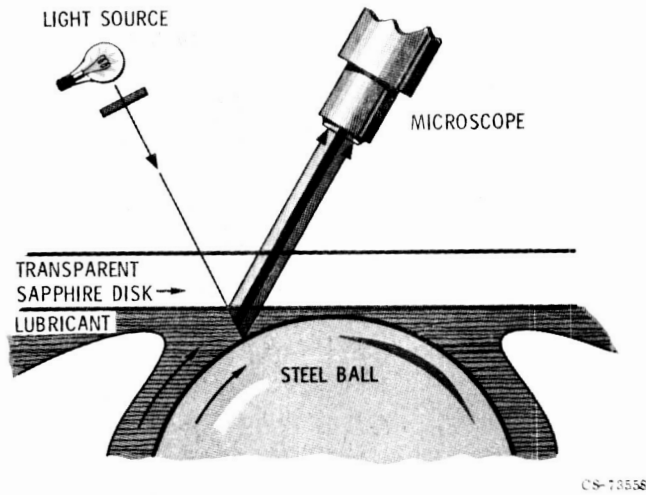
Figure XI-17. - Simulated ball-race contact.
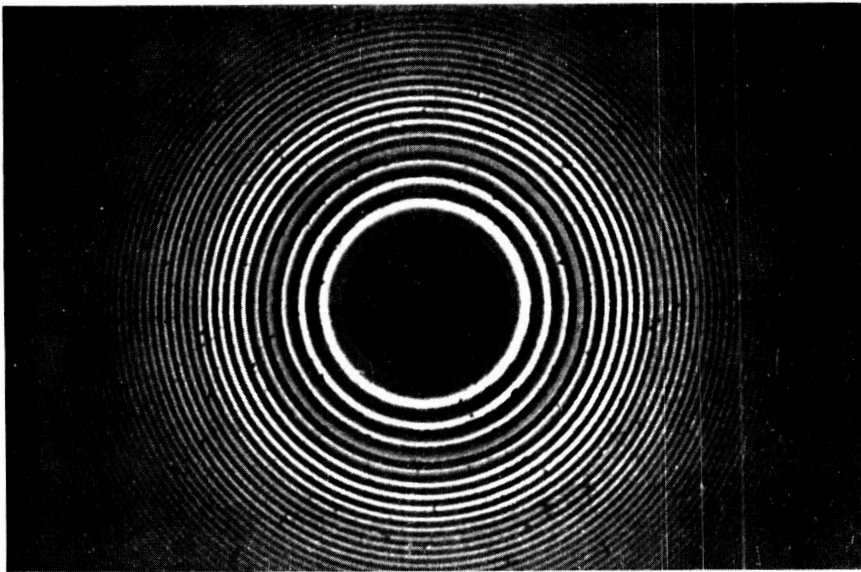
Figure XI-18. - Photomicrograph of load-zone static contact.

CS-73591

Figure XI-19. - Photomicrograph of dynamic lubricated surface. CS-73590

Figure XI-20. - Calculated pressure contours in load zone.

CS-73410

326

Figure XI-21. – Effect of pressure on viscosity of synthetic paraffinic lubricant at 100° F.

Figure XI-22. – Calculated temperature contours in load zone.

Page intentionally left blank

XII. ENGINE SYSTEMS TECHNOLOGY

Ross Willoh, Edwin J. Graber, Fred Teren, and Robert E. Coltrin

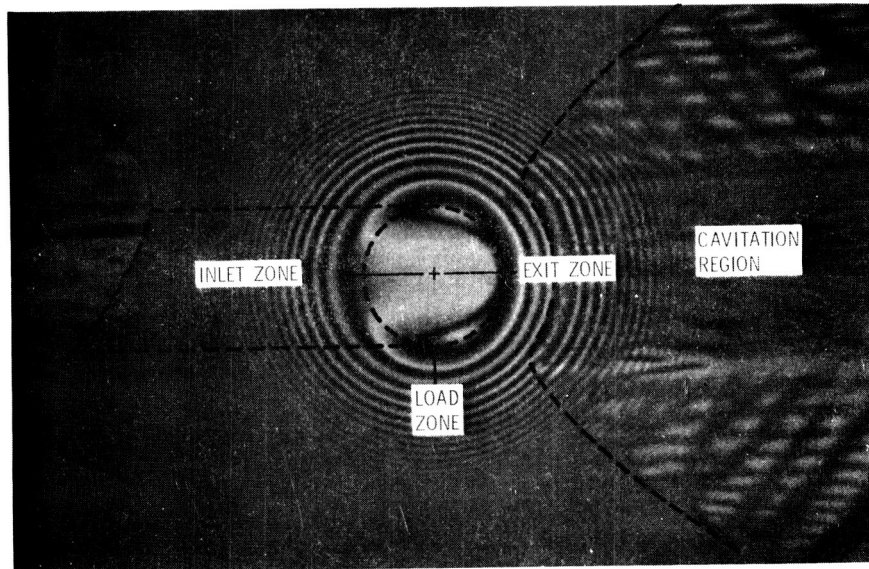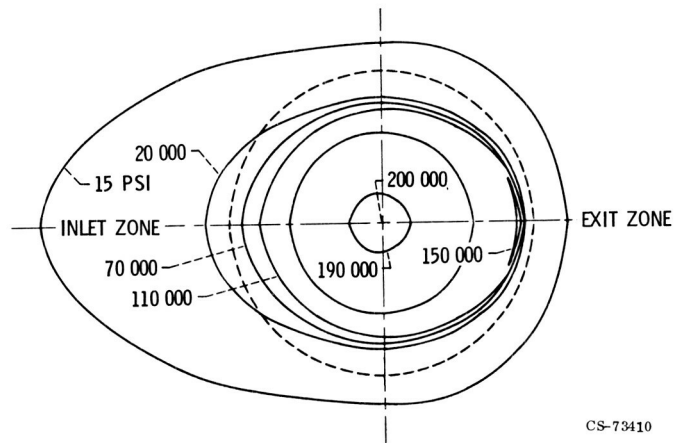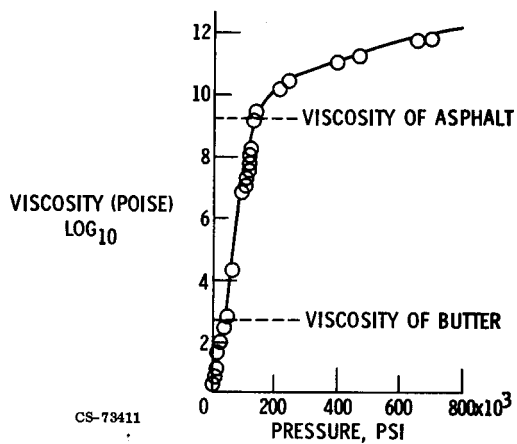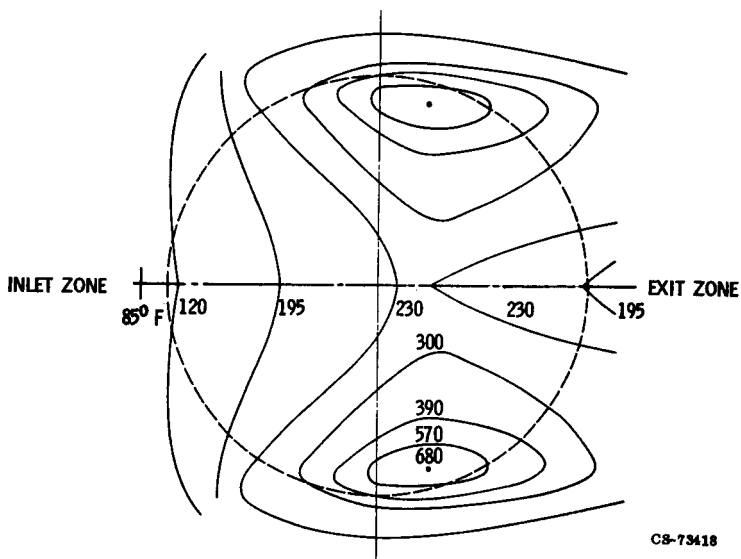Advanced airbreathing engines are required to accommodate a number of conflicting design criteria. They must meet desired performance and at the same time be dependable, quiet, and distortion insensitive; exhibit low emissions and low specific fuel consumption; and still remain at a reasonable cost. In order to establish the design for a new engine, advanced and existing component designs are combined to form an initial engine system design. After the initial design, engine development tends to be largely an empirical process in which the engine must be rebuilt and tested many times to achieve a satisfactory engine system.

Figure XII-1 presents a typical engine development history. The vertical line in the center represents the initiation of negotiations for a formal development contract and serves to separate the continuing research and development work carried out by industry and government from actual engine development.

The predevelopment phase supplies the advanced concepts that eventually appear in operational systems. This phase can be divided into exploratory development, which includes government and internally funded research, and advanced development such as the core engine programs sponsored by the Department of Defense.

During the system development phase of an engine program, much effort is spent on the experimental cycles that establish an operational system. In this phase, unexpected component interactions and problems not apparent during component testing are found and corrected.

FULL-SCALE PROGRAMS

Full-scale engine research at the Lewis Research Center is primarily in

support of future propulsion system development. Full-scale programs, however, are conducted for a variety of reasons, including the support of other NASA efforts such as the Refan and QCSEE Programs. Component research is performed in full-scale engine testing when such research is best done in the engine environment. In addition to these efforts, there is a continuing long-range objective to acquire basic data and understanding for the support of future engine development programs. The principal purpose of such full-scale research at Lewis is to provide a technology base for future programs. It is only through improved understanding and analytical techniques that the extensive experimentation associated with engine development can be reduced in future programs.

In this paper, current full-scale programs are discussed, and efforts to improve the available technology base are presented. The Lewis full-scale engine test facilities are briefly described, and several typical engine programs and plans for research in aeromechanical instability or flutter are summarized. Finally, an overview of Lewis studies of flow distortion and its effects on engine stability is presented. The origins and nature of the distortion problem are summarized, and some of the results and methods for both steady and time-varying distortion are discussed. Analytical techniques have been applied to the time-varying distortion problem to guide future work, and some of the more interesting results are reviewed.

Full-Scale Facilities

Figure XII-2 shows a TF30 engine with a flight-type inlet installed in the Lewis 10- by 10-Foot Supersonic Wind Tunnel. During this program, inlet-engine compatibility was investigated. Some of the results obtained are presented in this paper. In addition, integrated engine-inlet control was investigated. Combined inlet-engine research is conducted in this facility. The compressor face conditions that are encountered in flight can be closely duplicated during combined inlet-engine testing in the wind tunnel.

Inlet-engine interface conditions, however, are simulated in the Propulsion Systems Laboratory (PSL) shown conceptually in figure XII-3. This facility consists of four cells, all supplied by a central air system. For simplicity, a single cell is shown in the figure. Atmospheric air is com-

pressed, dried, and supplied to the engine through throttling valves. The desired temperature is achieved by mixing hot and cold air in the necessary proportions. The engine exhaust, which is isolated from the inlet flow by the bulkhead through which the engine is mounted, is cooled and exhausted to the atmosphere. With this arrangement, engine inlet and exhaust conditions can be controlled to simulate a wide range of flight conditions. In addition, various methods are used to perturb the engine system for performance studies at off-design and transient conditions (ref. 1).

During studies of the effects of nonuniform or distorted flow on compressor and fan performance, it is necessary to generate nonuniform compressor face conditions. Steady (or time invariant) spatially distorted patterns have traditionally been generated with screens of varying porosity and extent, such as the one shown in figure XII-4. This particular screen duplicated a complex pattern encountered during the F-111 flight program. Such screens are placed in the inlet ducting upstream of the compressor face. Screens, however, are very time consuming to use, and it is difficult to establish a desired pattern with them. Distorted compressor face conditions are also generated by the injection of secondary airflow directed counter to the primary flow. The system used is shown schematically in figure XII-5 and discussed in reference 2. The secondary flow nozzles are equally spaced to cover the entire inlet duct and have individual flow control for each 60° sector. Although it lacks the spatial resolution of screens, this system allows rapid change of patterns and can be used to generate dynamic (or time varying) distortion in the moderate frequency ranges.

A similar concept has been developed and applied to the generation of temperature distortion (refs. 3 to 5). As shown in figure XII-6, a gaseous-hydrogen-fueled temperature distortion generator (burner), located just upstream of the bellmouth, is used to produce both steady and time-varying temperature distortions. Distortion jets and a burner, together with screens, are used to generate combined temperature and pressure distortions.

Support Programs

Much of the full-scale engine research at Lewis is carried out in the 10- by 10-Foot Supersonic Wind Tunnel and the PSL. Two programs recently

completed in the PSL are typical support programs. Figure XII-7 shows the NASA Quiet Engine with an acoustically treated inlet mounted in one of the PSL cells. In this program, a series of tests were run to evaluate, at altitude, the effects of inlet flow distortion and a treated nacelle on fan performance and stall margin. The fan was designed to operate more quietly than those in current use; and the acoustic inlet included not only wall treatment, but, in addition, had three treated splitter rings. In this program, distortion was generated with screens upstream of the engine face, while fan stall was induced by back-pressuring the fan with air injected near the fan nozzle exit.

Altitude testing was also conducted to support the JT8D Refan Program. Figure XII-8 shows this engine installed in the PSL facility. During this program, basic engine steady-state altitude performance and starting data were obtained. In addition, engine transient characteristics at altitude and with distorted inlet conditions were studied. The distortion patterns used were the S-duct patterns typical of the center Boeing 727 engine installation. Extensive nozzle profile data were obtained on the engine's mixed-flow nozzle, along with a limited amount of emission data.

The full-scale testing for these programs is typical of the support provided for other Lewis programs. These efforts, however, are not representative of the more research-oriented programs. The work just beginning in the flutter area, however, does provide an example of a more fundamental program.

Aeromechanical Instability Program

The Air Force and NASA have agreed on joint full-scale engine research programs to investigate areas of technical uncertainty. These programs will emphasize basic research needs and not attempt to directly support current development programs. Planning areas include controls, component interactions, and flutter.

Aeroelastic instability problems have been encountered in the development of various advanced commercial and military engines. The experimental resolution of such problems can lengthen the development phase of an engine program. Large expenditures of both time and money may be required to establish flutter-free engine operation over the engine operating envelope.

The basis of flutter is reasonably well understood. As shown very schematically in figure XII-9, the incoming fluid stream and the blade orientation (or angle of attack) are inputs to the aerodynamic system which generate aerodynamic forces on the blade. These forces, in turn, act on the blade structural system to alter the angle of attack. If the phasing between the aerodynamic and structural systems is right, self-sustained oscillations can result. In this way, energy is fed into the oscillating blade from the airstream through dynamic coupling of the aerodynamic forces and the blade structure. Flutter can occur in a stage even though the flow field is steady prior to entering the blade row. The aeroelastic instabilities associated with blading can occur in a number of ways because of differences in the generation of the unsteady flow.

Flutter regions are superimposed on a typical compressor performance map in figure XII-10. The flutter regions occur in various areas of the map. Subsonic and supersonic stalled flutter occur near the surge boundary, while choke flutter and supersonic unstalled flutter occur well away from the surge line. In addition to the usual flutter regions indicated in figure XII-10, flutter has also been encountered in the central regions of a compressor map along the normal operating line.

All the parameters which govern flutter are not known for many of these regions. There are parameters in addition to those shown on a compressor map (pressure ratio, corrected flow, and speed) which affect flutter. The conventional compressor map thus cannot be used for flutter correlation as it is for the correlation of compressor aerodynamic performance. Flutter-free operation of a compressor over its entire map in sea-level static testing does not assure freedom at high Mach number or high dynamic pressure conditions.

The joint NASA/AF program in flutter (ref. 6) will work toward establishing compressor blading design that will avoid or minimize aeroelastic instability. The short-range objective of the program is to establish improved empirical methods for flutter prediction and correlation. The longer range objective is to develop a sound scientific basis for design. The overall program will include interacting analytical and experimental efforts. The experimental programs will include cascade tests and rotating rig tests as well as the full-scale engine tests discussed in this paper.

Much of the available experimental flutter data has come from develop-

ment program efforts to establish flutter-free engine operation over the regions of normal engine operation. The F100 engine, shown in the PSL facility in figure XII-11, is now being used for fan flutter testing. Preparations are underway for a program with the J85-21 compressor. In these programs, fan and compressor flutter boundaries will be systematically mapped, and the effects of various factors such as pressure and temperature on the flutter boundaries will be established. In addition to strain-gage instrumentation, extensive aerodynamic instrumentation is also included to permit study of the two systems, aerodynamic and structural, that couple to cause flutter.

Distortion Effects on Engine Performance

The effects of distorted flow on fan and compressor stability and performance have been investigated in a number of Lewis programs. Full-scale research programs have been conducted on both turbofan and turbojet engines in the PSL and on engines coupled with inlets in the 10- by 10-Foot Supersonic Wind Tunnel. An overview of the results obtained from these studies is presented herein.

FUNDAMENTALS OF INLET DISTORTION

Before progressing to the more detailed aspects of inlet distortion, we will review some of the fundamentals. This material will be very familiar to the distortion expert and is presented primarily to introduce the uninitiated to the basics of distortion. For additional information about the distortion problem, see references 7 to 38.

Definition of Inlet Distortion

Figure XII-12 illustrates what is meant by the term inlet distortion. Shown in this figure is a cutaway view of a typical propulsion system consisting of an inlet and an engine. It is at the interface plane between inlet and engine - indicated here as station 2 - that inlet distortion is defined. Any

flow nonuniformity across this plane is referred to as an inlet distortion. As mentioned in the section Full-Scale Facilities, pressure and temperature distortions can be simulated in the PSL altitude test facility by using screens, airjets, or burners located upstream of the engine. Since pressure distortions have been the more commonly encountered distortions during actual flight conditions, they have received the greatest attention to date and accordingly are emphasized in this paper. A typical example of the instrumentation used to measure pressure distortions is shown on the left of this figure as eight equally spaced rakes of five pressure measurements per rake - a total of 40 measurements. These transducers are generally located in the center of equal-area segments. By using these measurements, it is possible to generate a contour map - consisting of lines of constant pressure - to produce a picture of the distortion pattern as shown on the right in figure XII-12.

Sources of Inlet Distortion

Some of the flight situations which lead to inlet distortions are shown in figure XII-13. Flight conditions which result in either pressure, temperature, or combined pressure and temperature distortions are illustrated. Pressure distortions are created at supersonic flight speeds by a shockwave - boundary-layer interaction in the inlet. They are also produced when gusts, strong crosswinds, or operation at high angles of attack or yaw produce separated flow regions in the inlet. For fuselage-mounted inlets, pressure distortions occur when low-energy air from the fuselage enters the engine during certain operating conditions. Temperature distortions are encountered when military aircraft ingest steam from aircraft carrier catapult systems. Finally, wakes from nearby aircraft engines can produce a combination of pressure and temperature distortions.

Effect of Inlet Distortion

Once produced, what is the effect of these distorted flow patterns on the engine? Figure XII-14 will help answer this question. Shown here is a typical compressor performance map, including lines of constant compressor

efficiency. As can be seen, the point of highest compressor efficiency is located above the operating line. Thus, if the operating line shown here were to be moved up, operation at higher compressor efficiencies would result. Unfortunately, the operating line is restricted in this upward movement by many factors which can degrade or lower the surge line and prevent surge-free engine operation at the higher compressor efficiencies. One of the factors causing such a lowering of the surge line is inlet distortion. The more severe the distortion, the further down the degraded surge line moves. Thus, the effect of inlet distortion must be considered when locating the operating line.

Distortion Indices

Many distortion patterns may be encountered during flight. Distortion descriptors (or indices) are used to evaluate which patterns are the most severe. Basically, indices reduce each distortion pattern to a number which is proportional to the resulting surge-line drop. This surge-line drop is called the loss of surge pressure ratio - shown in figure XII-14 as the gap between the clean-inlet surge line and the degraded (or distorted) inlet surge line. Distortion test data are then presented typically in the form illustrated in figure XII-15. In this figure, the experimentally determined loss of surge pressure ratio because of distortion is shown as a function of some distortion index for a variety of distortion patterns. If the index used is a good one, all data will fall within some expected scatter band about a correlation curve, as shown.

In order to illustrate how a typical distortion index is calculated, consider the example of circumferential pressure distortion as a function of circumferential position shown in figure XII-16. Here the index is calculated as simply $\Delta P/P_{AVG}$, where ΔP is simply the difference between the average pressure and the minimum pressure at the compressor inlet. Unfortunately, however, not all indices or distortion patterns are as simple as the ones used in this example. Actual distortion patterns encountered during flight situations often vary both radially and circumferentially to produce some very complex patterns.

Figure XII-17 shows how these complex patterns have been traditionally

evaluated. Indices are first developed for two basic pattern types - pure circumferential and pure radial. Complex patterns such as the one shown on the left are then reduced to their circumferential and radial components as indicated. The index used for this complex pattern is finally calculated by using a simple linear combination of the individual indices for the component circumferential and radial patterns. Thus, most distortion testing uses primarily circumferential and radial patterns with only a few complex patterns added to establish the weighting factor B.

Once developed, an index can be used in many ways. It can be used to compare the distortion sensitivity of several engine designs, or it can be used to evaluate the distortion levels of several inlet designs. Perhaps the most important use of an index is made by prime contractors to establish a distortion interface agreement between engine and airframe manufacturers during the aircraft development cycle.

Figure XII-18 illustrates how an index would be used in establishing such a propulsion system interface agreement. Here the distortion index limits for both the engine and inlet are given as a function of the equivalent weight flow. The upper curve (engine goal) is the maximum distortion level which the engine must be capable of tolerating, and the lower curve (inlet goal) is the maximum distortion level which the inlet would be permitted to pass on to the engine. These goals are not easily agreed upon. Engines designed to tolerate high distortion levels generally suffer penalties in weight, complexity, and/or performance. Likewise, inlets which are restricted to low distortion levels suffer similar penalties. Thus, both the engine and inlet manufacturers are deeply concerned about the established goals. However, if the propulsion system efficiency is to be maximized, the safety zone shown in figure XII-18 must be kept as small as possible without jeopardizing system stability.

The size of the safety zone depends primarily upon the index, or distortion descriptor, used. If the index and measurements are perfect, the zone size could be considerably reduced. Unfortunately, because of imperfections in the index, variations in the pressure or temperature measurements, and other factors such as engine-to-engine variation and engine deterioration, some gap is usually required. The problem of establishing these goals is further complicated by the fact that no one index has been developed which adequately describes the distortion sensitivity of all engines. Many indices

337

have been developed, one for each engine and sometimes even more than one per engine, most of which are based on extensive distortion testing. Thus, the strictly empirical methods used in the past require an extensive amount of testing to adequately define a proper index. In addition, direct comparison of the results of different investigators is complicated by the resulting abundance of indices.

SIMPLE PARALLEL COMPRESSOR MODEL

A simple compressor model can be developed which provides a "feel" for what is actually happening when compressor inlet conditions are not uniform.

Circumferential Pressure Distortion

First, consider the simple case of a circumferential pressure distortion as shown in figure XII-19. The compressor is assumed to be composed of two (as shown) or more parallel pie-shaped segments, which are referred to as subcompressors. Each of these subcompressors is assumed to be operating independently of the others and to be operating on the same clean-inlet compressor map (shown on the right). The entire compressor is then assumed to surge when any one of these subcompressors reaches a surge-line operating condition. This model has been in existence for some time and is aptly called the parallel compressor model. In this example, the compressor is divided into two parallel subcompressors, one with a low inlet pressure and the other with a higher inlet pressure. Since no temperature distortion has been assumed, the entering temperature is uniform, and both subcompressors operate on the same equivalent speed line. Equivalent speed is the ratio of compressor speed N to the square root of the normalized inlet temperature $\sqrt{T_{IN}/T_{REF}}$. The additional simplifying assumption of a uniform exit total pressure was based on experimental J85 data. With this assumption, it became obvious that the subcompressor with the lowest inlet pressure would reach the surge line first, as shown in figure XII-19. Thus, it is only necessary to know the compressor equivalent speed, the com-

pressor exit pressure, and the lowest compressor inlet pressure to determine whether the distortion is severe enough to cause compressor surge. A pressure distortion is, therefore, a low-pressure region, and the extent of the distortion is defined as that portion of the compressor at this low inlet pressure.

Recall, however, that in the section FUNDAMENTALS OF INLET DISTORTION, it was stated that distortion data must be reduced to a distortion index which is based entirely upon compressor inlet conditions and that this index must be proportional to the loss of surge pressure ratio. By using this simple parallel compressor model, an index of this type was developed in reference 36 and is given here as simply 100 times the difference between the average and low pressure divided by the average pressure at the compressor inlet. This index turns out to be identical to the percentage loss of surge pressure ratio.

Shown in figure XII-20 is a comparison of the model with experimental J85 results for circumferential distortion patterns of several different extents. Here, the experimental loss of surge pressure ratio, in percent, is plotted as a function of the parallel compressor index just developed. The predicted relation from the parallel compressor model is shown as the solid line, and the acceptable scatter band about this predicted line is indicated by dashed lines. This acceptable scatter band was based on the repeatability of the surge pressure ratio measurement. Good agreement has been achieved with this model for patterns of extent greater than 30°. However, the 30° patterns did not correlate as well. As is shown in the next section, it was found that even this data could be accounted for by refining the parallel compressor model. A critical-extent argument is used which places a lower limit on the extent of any of the parallel subcompressors.

Radial Pressure Distortions

As illustrated in figure XII-21, the parallel compressor concepts developed for circumferential pressure distortions were next applied to hub and tip radial pressure distortions (ref. 38). In order to do this, the ratio of the compressor exit pressure P_{OUT} to the lowest compressor inlet pressure P_{LOW} was calculated and plotted as a function of the compressor equivalent

flow for surge-inducing distortions. As a reference, the previously present-ed critical pressure ratios for circumferential distortions are given by the solid line. The dashed lines represent the results of experimental J85 testing using hub and tip radial patterns such as those shown in this figure. As can be seen, the radial patterns produced two new and distinct curves, one for hub radial patterns and one for tip radial patterns. The significance of the new curves is not completely understood at this time and to aid in their under-standing, further testing is needed. The objectives of such tests would be first to verify the existence of these curves for other engine designs and sec-ond to relate them to the appropriate engine characteristics. One explanation for the curves could be a radial redistribution of the flow, which rapidly at-tenuated the distortion as it passed through the compressor. Whatever the reason for their existence, these new curves permitted the development of the radial distortion index shown by a technique similar to that used for the circumferential distortion index. The multiplying factor K is a function of the position of the newly established curves relative to the circumferential curve. For the example shown here, K is greater than 1 for both dashed curves, since they are above the circumferential curve. As these curves ap-proach the circumferential curve, K approaches unity.

The resulting correlation of the J85 data is shown in figure XII-22 for a wide variety of distortion patterns, including complex patterns combining both radial and circumferential distortions. The previously presented cir-cumferential distortions are also included here. Again, the loss of surge pressure ratio is plotted as a function of the distortion index. This index uses the largest of the three individual indices just developed for the hub ra-dial, tip radial, and circumferential components of the distortion pattern. In addition, the critical-extent modification mentioned previously was included in the circumferential index to improve the correlation of narrow-extent data. Obviously, the index developed here works very well for the J85 engine.

Circumferential Temperature Distortions

The parallel compressor model was next applied to circumferential tem-perature distortions, a type of distortion for which very little data or empiri-cal results have been generated. This model, as illustrated in figure XII-23,

uses the same parallel compressor assumptions as previously described. As for the pressure-distortion case, two subcompressors are used in this example. One has a high inlet temperature, and the other has a lower inlet temperature. Since it is assumed here that there is no inlet pressure distortion, both subcompressors operate at the compressor pressure ratio indicated by the dashed line. The compressor rotor speed N is obviously the same for both subcompressors. It follows, then, that the high-temperature subcompressor operates on the lowest equivalent speed line since equivalent speed varies inversely with the square root of temperature, as shown. Thus, the high-temperature subcompressor will be the first to reach the surge line. Accordingly, a temperature distortion is referred to in terms of the high-temperature region. The distortion extent is then defined as that portion of the compressor face at this higher temperature level.

In an effort to develop a simple distortion index based on interface measurements, as for the pressure-distortion case, one additional assumption was added to the model based on experimental results. This assumption was that the surge pressure ratio varies linearly with the compressor equivalent speed. The resulting index, developed in reference 37 and shown in figure XII-23, is a multiple of a known compressor speed function and ΔT over T_{AVG}, where ΔT is the difference between the high and average temperatures at the compressor inlet. The model results are compared with experimental J85 data in figure XII-24. The loss of surge pressure ratio as a function of the parallel compressor index just developed is plotted for temperature distortion extents of 90°, 180°, and 270°. Here, good agreement was achieved for distortion extents greater than 90°, but the 90° extent data do not correlate as well. The disagreement for the 90° extent patterns is possibly due to critical-extent effects similar to those encountered with the pressure-distortion data.

Combined Circumferential Pressure and Temperature Distortions

As a final test, the parallel compressor model was applied to combined pressure and temperature distortions, with the same assumptions as for the previous models. The development of this model is described in reference 37. As before, this model was used to develop a parallel compressor

index which is equal to the percentage loss of surge pressure ratio. Figure XII-25 shows the agreement with J85 test data achieved for various arrangements of combined 180° extent pressure and 180° extent temperature distortions. The index used here is basically a sum of the already developed pressure and temperature indices. However, the relative positioning of the low-pressure region to the high-temperature region is very important in the summing procedure. Observe in this figure that the loss in surge pressure ratio for opposed distortions of pressure and temperature is much less than for overlapping distortions, although both situations experienced similar distortion amplitudes of pressure and temperature. The parallel compressor model had revealed this trend prior to data reduction, an unusual situation in the area of distortion. Also, note that for the completely overlapping patterns and the completely opposed patterns, a good correlation was achieved. However, agreement was not as good for the 90° overlapping patterns. As with the temperature and pressure distortion cases, this deviation may be attributable to narrow-extent effects.

The empirical distortion approach using indices has been presented. It was noted that considerable testing was required to adequately define such an index. As an alternative, a simple parallel compressor model was presented which provided an adequate prediction of the loss in surge pressure ratio for pressure distortions, temperature distortions, and combined pressure and temperature distortions based on a minimum of distortion testing. However, for both the narrow-extent circumferential pressure and temperature distortions and for the radial distortion patterns, the parallel compressor model required modifications based on the results of additional distortion testing. In addition, since it includes no internal compressor characteristics, it cannot be used by compressor designers to improve the distortion tolerance of their compressors. In order to accomplish this task and to further reduce the testing requirements, a more detailed stage-by-stage compressor model such as that presented in the next section is required.

ANALYTICAL SURGE AND PERFORMANCE PREDICTION

Because of the limitations of the simple version of parallel compressor theory, the need for an analytical approach to the prediction of compressor

performance and stability for all forms of distorted flow is evident. An analytical approach should provide a more basic understanding of the distorted flow process, which can lead to compressors that can be operated more efficiently.

The starting point for development of the analytical compressor model for distorted flow was a model developed several years ago at Lewis (ref. 39) for predicting compressor stability for undistorted inlet flow.

The features of the analytical distorted flow model are shown in figure XII-26. The model is similar to the parallel compressor model previously described. Parallel and separate calculations are made for the high- and low-pressure sectors. There are also some differences. Compressor performance is calculated on a stage-by-stage basis, rather than by using an overall compressor map. Dynamic calculations are also included for each stage. The model is terminated by a common burner volume and a choked turbine area. Static pressures are matched in the burner volume.

The simple version of parallel compressor theory could not accurately predict surge for small circumferential extents. For this reason, circumferential crossflow was included between the high- and low-pressure sectors in the stage-by-stage model as an effort to improve the ability to predict surge for small extents. There are other approaches to this problem which do not make use of circumferential crossflow. Other investigators are pursuing these approaches.

An advantage of the stage-by-stage model is that an experimental surge line is not required. Instead, the model predicts surge in the same way it is observed in the engine - as a breakdown in the flow process. A disadvantage of the model is that performance maps are required for each stage, and these maps must be obtained experimentally. As a final comment on the analytical model, it should be noted that the model has been implemented on a digital computer, and a highly efficient digital computation technique has been developed which allows surge predictions to be made about 100 times faster than by conventional digital computation techniques.

Results obtained for the J85 engine are shown in figure XII-27. These results are reported in more detail in references 40 and 41. Overall compressor pressure ratio is shown as a function of equivalent weight flow for the 87 and 100 percent speed lines. The curves are the analytical speed lines and the analytical surge line. The open circles are experimental

points, and the solid circles are experimental surge points. These results are for a 180° circumferential pressure distortion pattern. Good agreement was achieved between the analytical and experimental results, for both speed lines and surge points. For this case, crossflow was not included in the model. However, when crossflow was included, the results changed very little. For this large-extent distortion pattern, the simple parallel compressor theory described previously does just as well in predicting the surge points.

Figure XII-28 presents results for a 30° extent distortion pattern. As in figure XII-27 the analytical speed lines and the analytical surge line are shown, along with the experimental data points, and there is no crossflow in the model. For this case, there is good agreement between the analytical and experimental speed lines, up to the analytical surge point. However, for both speeds shown, the predicted surge points are overly conservative compared with the true engine surge points.

Figure XII-29 presents results for the same 30° distortion pattern but with crossflow included in the model. In this case, the predicted speed lines and surge points are in very good agreement with the experimental results. In order to get this agreement, however, a different amount of crossflow was used for each of these two speed lines. Good agreement was achieved for other distortion extents and intensities as well. But for each case, a different amount of crossflow was required. So far, an adequate correlation relating the amount of crossflow to the physical variables has not been found. Therefore, the results must be considered inconclusive. The search for the proper correlation is continuing.

DYNAMIC DISTORTION MEASUREMENT AND VISUALIZATION

The time-honored method to measure total pressure distortion has been to install a large number of probes at the compressor face, each with a long transmission line to a remote sensor. These long lines time-average the data. A typical constant-pressure contour map constructed from these steady-state pressures is shown in figure XII-12 on the lower right. Steady-state pressure measurements such as these, along with steady-state distortion indices, were used to describe distortion from the inception of the

turbojet engine up until the wind tunnel tests of the B-70 propulsion system and flight tests of the F-111 aircraft.

Figure XII-30 shows data recorded during the F-111 flight tests. The steady-state index is plotted against engine equivalent weight flow. The crosshatched band shows the area where surges were encountered on the test stand when screens were used to produce distortion. It was then expected that the in-flight surges, which are shown by the circles, would be encountered in the same band. As can be seen, many of the surge data points fell well below the expected surge band. The cause for this lack of agreement became apparent when the long transmission lines were replaced by high-response subminiature pressure sensors.

Figure XII-31 shows that these sensors detect a fluctuating or dynamic component of total pressure superimposed on top of the steady-state value. The instantaneous pressure P measured by each sensor is then the sum of the steady-state pressure $\overline{P}$ and the dynamic component ΔP. These fluctuations can result from the same sources that produce steady-state distortion (fig. XII-13). Whatever the cause, these fluctuations do exist, and they combine with the steady-state pressure to produce a different distortion pattern at each instant of time.

Shown in figure XII-32 are typical pressure histories for four selected probes at the compressor face. There are, of course, similar pressure histories for each of the probes. At any given instant of time, an instantaneous pressure contour map can be constructed by placing a vertical line through the pressure histories and using the value of each pressure where the trace intersects this line. In the contour map representation shown here, shading has been used to indicate low-pressure-recovery areas. Contour maps can be made in this way at several instants of time. The series of maps created in this fashion can then be made into a motion picture by using cartoon methods. These motion pictures are a good way to get a feel for what is actually going on at the compressor face.

Such motion pictures have been made from data recorded during inlet-engine compatibility investigations in the Lewis 10- by 10-Foot Supersonic Wind Tunnel. Figure XII-33 shows selected frames from one such motion picture. It was recorded with the J85 turbojet engine operating behind a supersonic inlet at Mach 2.6 and 5° angle of attack. The pressure contour in the upper left is the steady-state pattern. The portrayal used here is

more detailed than that shown in the last figure. Here, each shade represents a 6 percent pressure recovery range, with the darkest area being the lowest recovery (64 percent and below), and the lightest area the highest recovery (94 to 100 percent). The circumferential pattern is typical of that produced by an inlet at angle of attack, with high pressure in the top portion of the inlet and low pressure in the bottom portion.

The motion picture shows that the overall motion is due to the expansion and contraction of the large high- and low-pressure regions at the top and bottom of the inlet. Also, as shown in figure XII-33, the instantaneous patterns are a variation of the basic steady-state pattern. This is typical for angle-of-attack operation.

Figure XII-34 shows selected frames from a motion picture made from data recorded with the same inlet-engine combination but with the propulsion system operating at Mach 2.5 and 0° angle of attack. Here the basic radial nature of the steady-state pattern, which is typical for 0° angle-of-attack operation, is shown. In this instance, each shade represents a 5 percent pressure recovery range, with the darkest area being the lowest recovery (65 percent and below) and the lightest area the highest recovery (90 to 95 percent). The motion picture for this operating condition shows that the dynamic motions take the form of low-pressure holes appearing and disappearing randomly around the inlet. Thus, as can also be seen from the figure, the instantaneous distortion is circumferential in nature, completely different from the steady-state radial pattern. For this condition, then, the engine never really sees the steady-state radial pattern. What it does see is a time-varying circumferential pattern.

From the motion pictures, it is obvious that the engine sees hundreds, if not thousands, of different pressure contour patterns each second and that none of them may resemble the steady-state pattern. The question is then, how is the steady-state distortion methodology used to account for these time variations. The answer, of course, is that there are several approaches in use today. Most of them are variations of either statistical or instantaneous methods. Two approaches are discussed herein, namely, a simple rms statistical approach and an instantaneous approach employing the parallel compressor concept.

STATISTICAL (RMS) DISTORTION INDEX

The simplest approach for handling time-varying distortion involves measurement of a single variable, which is a measure of the amplitude of the dynamic component. Even this simple method, however, does require dynamic pressure measurements. Figure XII-35 illustrates a common way in which the dynamic component is measured, that is, by using the root-mean-square (rms) level. On the right is a typical steady-state pressure contour map. On the left, pressure is shown as a function of time for one of the pressure sensors. The steady-state level is shown and is equal to the corresponding value from the contour map. As shown, pressure fluctuations are superimposed on the steady-state level. The rms level is a single number, which is a measure of both the amplitude and duration of these fluctuations averaged over a long time period. Qualitatively, the rms level is small if the fluctuations are small, and large if the fluctuations are large. Quantitatively, the largest peak-to-peak level of the fluctuations is usually about six times the rms level for normal random data.

When the rms level is used in a distortion index, the resulting index is statistical in nature. The reason is that compressor surge is correlated with the average level of dynamic activity, rather than with a distortion pattern occurring at a particular instant of time.

Figure XII-36 shows typical steady-state and dynamic (rms) contours measured during an experimental program conducted at Lewis. These data were obtained as part of a wind tunnel program, mentioned previously, which involved the TF30 engine and a supersonic inlet. The TF30 is a two-spool turbofan engine. In this case, the propulsion system was operating at 0° angle of attack. The steady-state and rms levels were ratioed to the average compressor face pressure, and the resulting values were used to construct the contour maps shown. For the steady-state contour map, the light areas represent regions of high-pressure recovery, and the dark areas are regions of low recovery. For the rms map, the dark regions indicate high dynamic levels, while the light regions indicate low dynamic levels. There are several points to be made from this figure. First, there is significant dynamic activity, in addition to the steady-state distortion. Second, the amount of dynamic activity varies over the compressor face. Third, the regions of high dynamic activity do not coincide with the regions of low steady-state

pressure recovery. Instead, the high dynamic activity is found in the region located between the high- and low-pressure areas.

The question, then, is how to include both dynamic activity and steady-state distortion in a distortion index in such a way that a good indicator of surge is achieved. This problem was investigated, and the results are reported in reference 42. The procedure was to first identify the low-pressure sector from a steady-state standpoint. Then, the rms levels measured over the same sector were averaged and added to the steady-state index. The results obtained with a steady-state index are examined first.

Figure XII-37 shows the results obtained when a steady-state index was used. The open circles are values of the index observed at nonsurge points, and the solid circles are the values observed when the engine surged. The distortion index used was the parallel compressor index described previously. The results are plotted as a function of engine exhaust nozzle area. The engine was operated at nearly constant speed for all cases. All the data points on a fixed vertical line represent essentially a fixed engine operating condition. If the distortion index is a good indicator of surge, there should be complete separation between the surge and nonsurge points. That is, all the surge points should lie above all the nonsurge points for each engine operating point. For this steady-state index, there is not a good separation. This is not surprising. It is simply another illustration of the fact that dynamic distortion must be accounted for in the distortion index.

Figure XII-38 shows similar results but for a different distortion index. In this case, the same steady-state parallel compressor index was used, but the rms level of dynamic distortion observed over the low-pressure region was added to the steady-state index. For this index, there is good separation between the surge and nonsurge points. The surge boundary determined from the data is shown by the curve.

As was mentioned previously, the steady-state-plus-rms index is statistical in nature, in that surge is correlated with the average level of dynamic activity. There is also a substantial effort at Lewis aimed at finding an instantaneous distortion index which will allow correlation of compressor surge with a specific instantaneous distortion pattern.

INSTANTANEOUS DISTORTION

The instantaneous distortion method is the most exacting method for handling time-varying distortion. This method is depicted in figure XII-39. This figure is similar in concept to figure XII-32, except that at each instant the value of the distortion index is computed, rather than a pressure contour. These instantaneous values of the distortion index are then plotted as a function of time. This, then, results in a quantitative measure of the distortion at each instant of time, whereas the motion picture resulted in a qualitative measure.

Figure XII-40 examines conceptually engine response to instantaneous distortion. These data were recorded with the J85 engine operating behind a supersonic inlet at Mach 2.6. The compressor face instrumentation for these data was a six-rake by five-probe (30 total probes) configuration. The data were processed by a digital computer at a sampling rate of 8000 samples per second per probe. (A more detailed explanation of the data reduction system is given in ref. 43. This reference also describes an instantaneous concept which uses an empirical index.) The index used in figure XII-40 is the parallel compressor index defined in figure XII-21. For the instantaneous implementation used here, P_{AVG} was set equal to the steady-state value, and the P_{LOW} was permitted to vary with time.

The upper trace in figure XII-40 shows the distortion produced by the inlet as a function of time in milliseconds. The critical level is the surge-producing level as determined from screen tests. Here the steady-state distortion level was below the critical level and thus was not large enough to cause surge. But as can be seen, several distortion peaks did exceed the critical level. However, the engine was affected only by the peak labeled "surge origin," which was the peak that finally did cause surge. The reason the previous peaks did not cause surge is that an engine will respond only to disturbances which persist for a given period of time. This persistence time is referred to as the engine "critical time" and is usually expressed in units of the time it takes for the engine rotor to make one revolution. It is generally assumed that the proper value for this engine critical time is of the order of 1/2 to 1 rotor revolution.

The bottom trace, in concept, is the "distortion the engine responds to." In this instance, a 1/2-rotor-revolution critical time has been assumed. In

essence, the bottom trace contains the information from the upper trace to which the engine will respond if 1/2 rotor revolution is the proper critical time. The bottom trace has a lower frequency content than does the upper trace, and now only the surge-origin peak exceeds the critical level. In effect, the engine ignores the high-frequency content and responds only to the lower frequency content. Thus, the critical-time concept is equivalent to removing the high-frequency portion of the signal.

Thus, in order to make sense out of the instantaneous index, the high-frequency content to which the engine will not respond must be removed. Figure XII-41 outlines the data reduction process which achieves this end. The pressure at each probe is measured by the sensor and recorded on frequency-modulated (FM) tape. On playback, the pressure signals are input to a device called a filter. This filter removes the high-frequency content to which the engine will not respond and transmits the low-frequency content. The low-frequency output of the filter is then input to an analog or digital computer which computes the time-varying distortion index.

In this context then, the engine is really acting like a filter. This analogy can be seen by comparing figure XII-40, which shows the engine effect, with figure XII-42, which shows the filter effect. The traces on both figures are identical. In fact, the traces on both figures were produced by the data reduction process of figure XII-41. For the upper traces (figs. XII-40 and XII-42) the filter was not used. The "unfiltered distortion" of figure XII-42 is thus equivalent to the "distortion produced by the inlet" of figure XII-40. For the bottom traces, a filter equivalent to 1/2-rotor-revolution critical time was used. The "filtered distortion" of figure XII-42 is thus equivalent, in concept, to the "distortion the engine responds to" of figure XII-40.

These filters usually take the form of either digital time averagers or analog filters, depending on the type of computer used. Either method will work satisfactorily if care is taken in sizing the filters to assure that the desired engine critical time is achieved. The determination of engine critical time is very important. Both experimental and analytical methods have been used in attempts to get a handle on the proper critical time for engines. Experimentally, devices which produce either discrete or random frequencies can be used in front of engines in altitude cells. Lewis is in the preliminary planning stages for such a test in PSL, which will use a siren-type device in

front of a J85 engine. The siren will produce higher frequencies than do the distortion jets described previously. Other experimenters, in other facilities, with other engines, have usually found critical times to be of the order of 1/2 to 1 rotor revolution, as has generally been assumed. Typical results are discussed in references 44 and 45.

Another experimental approach to determining engine critical time is to use an inlet-engine data set. This approach consists of applying several different critical-time filters to each inlet-engine surge data point and determining which critical time best fits the instantaneous distortion concept. This concept states that, with a valid index and the proper filter, only the peak distortion which caused surge will exceed the critical level. The bottom trace fulfills this requirement in that the surge-inducing peak exceeds the critical level and the prior peaks do not (at least for this time period near surge). In practice, this ideal condition is not always achieved with a filter. For some data points, some prior peaks may exceed the surge-inducing peak. This, however, is not surprising in that the index has the scatter band associated with it, as indicated by the dashed lines in figure XII-42.

This approach was applied to the data set obtained with the J85 engine operating behind a supersonic inlet at Mach numbers in the 2.5 to 2.7 range. For this study, the filter took the form of a digital time averager. The result for a selected data point is shown in figure XII-43. This is the standard plot of loss of surge pressure ratio against parallel compressor index, except that in this case the peak level of the distortion index is plotted. The value of the loss of surge pressure ratio is the critical level from figure XII-42 which locates a given horizontal line in figure XII-43. The peak value of the distortion index varies along this horizontal line with averaging time, with the longer averaging times to the left. The distortion index level at the left end of this horizontal line is then the steady-state distortion level taken from figure XII-42. The distortion index level at the right end of the horizontal line is the level of the tallest peak in the unfiltered upper trace of figure XII-42. These unfiltered data correspond to an averaging time of 0.07 rotor revolution, which is the smallest average time available for this data set. As a midpoint for reference, the distortion index level denoted by the x in figure XII-43 is the level of the tallest peak for 1/2-rotor-revolution averaging time taken from the bottom trace in figure XII-42. The proper critical time to satisfy the instantaneous distortion concept is at the

intersection of the prediction line and the horizontal line in figure XII-43. For this data point, the proper critical time is just slightly greater than that for the 1/2-rotor-revolution point.

Figure XII-44 shows the results for the full J85 data set. Here, each horizontal line represents a given data point. For most of the data points, the steady-state level was not large enough to cause surge, as the left ends of the horizontal lines fell to the left of the acceptable scatter band. Also, for most of the data points, the unfiltered peaks were too large, as the right ends of the horizontal lines fell to the right of the scatter band. In general, an averaging time between these two extremes could be found which would make each specific data point fit the instantaneous distortion concept. Again, this would be the averaging time at the intersection of the prediction line and the horizontal line for each data point. However, a universal averaging time, which would make all data points fall within the scatter band, could not be found. The angle-of-attack points tended to require less averaging time than did the 0° points. The "best" averaging time for the angle-of-attack points would be near the unfiltered right end of the horizontal lines. The "best" averaging time for the 0° points would be on the left side of the 1/2-rotor-revolution point at about 3/4 rotor revolution. The "best" universal averaging time for the entire data set would be about 1/2 rotor revolution. But as can be seen, some points fall outside the acceptable scatter band.

This variation in averaging time may be explained in part by basic differences in distortion types. The compressor may respond in a completely different manner to a steady-state radial distortion pattern in which "holes" of low-pressure air appear instantaneously than to a circumferential steady-state distortion pattern which maintains its basic shape instantaneously. Whatever the cause, the results of this data set indicate that a simple universal time-average concept may not be adequate to account for engine response where an infinite number of different pressure patterns can be seen by the engine.

As mentioned previously, analytical approaches are also used in attempts to get a handle on engine critical time. One such approach, which may shed some light on this most important area, is analytical modeling of dynamic distortion.

ANALYTICAL MODELING OF DYNAMIC DISTORTION

The analytical model developed for predicting the effect of steady-state distortion on compressor performance and stability is also useful for predicting the effect of dynamic distortion on compressor stability. The ability to predict the effect of dynamic distortion is important. It can help in the development of methodology for an instantaneous distortion index. Ultimately, this can lead to compressors which can be operated more efficiently. The features of the model are essentially the same as those which were described previously (fig. XII-26) and are reviewed in figure XII-45. Compressor performance is calculated on a stage-by-stage basis. Dynamic calculations are also included for each stage. As in simple parallel compressor theory, parallel and separate calculations are made for the high- and low-pressure sectors. The model is terminated by a common burner volume and a choked turbine area. Static pressures are matched in the burner volume. The model predicts surge to occur when a breakdown in the flow process is observed, just as it occurs in the real engine.

Figure XII-46 defines the pressure inputs, as a function of time, which are imposed on the high- and low-pressure sectors of the model. The model is subjected systematically to relatively simple combinations of steady-state and dynamic distortion. The high-pressure sector is denoted by the open semicircle. The pressure input to the high-pressure sector is constant; that is, it does not vary with time. The low-pressure sector is shown as the crosshatched semicircle. Its pressure input is also constant, except for a pulse which acts for a certain duration. The pulse duration and amplitude are defined in the figure. The difference between the high-pressure level and the steady, low-pressure level is called the steady distortion. By studying the effect of relatively simple patterns such as these, an understanding of the effect of more complex dynamic distortion patterns can be developed as well.

For each combined steady-state-plus-dynamic distortion pattern, the model simulates time histories of pressures, temperatures, and flows. The variables undergo oscillations in response to the pulse input. If the pulse amplitude is small, the oscillations die out after the pulse is gone. On the other hand, if the pulse amplitude is sufficiently large, the oscillations continue to grow even after the pulse is gone. The occurrence of surge in the

model is defined as the point at which the oscillations become so large that the flow direction reverses in the compressor.

Some typical results obtained from the model are shown in figure XII-47. The pulse amplitude required to initiate surge is shown as a function of pulse duration. The results shown are for a steady distortion of 1 psi and a circumferential extent of 180°. On the left, the pulse durations are short and the amplitudes are large. This is illustrated qualitatively by the tall, narrow pulse. On the right, the amplitudes are lower and the durations are longer, as illustrated by the short, wide pulse. For very short pulse durations, the amplitude required for compressor surge becomes large. In effect, the compressor responds too slowly to be affected by these short-duration pulses. For medium-to-long pulse durations, the pulse amplitude required for compressor surge stays relatively constant. Qualitatively, these results are in agreement with the experimental results presented previously.

Results of this kind have been obtained for different speeds, extents, and pulse shapes. Use is being made of these results in developing methodology for describing the effect of dynamic distortion on compressor performance and stability.

Another result obtained by using the model is displayed in figure XII-48. Here, triangular pressure pulses are imposed over the full compressor face. Here, there are no high- and low-pressure sectors. Instead, the pressure pulse is imposed over the whole compressor face. A typical pressure input profile is shown in figure XII-49. The value of pulse amplitude required to initiate surge is presented as a function of pulse duration. As before, for short pulse durations, the pulse amplitude required to surge is large. For this case, the pulse amplitude required to surge for long pulse durations is also large. This is because the long pulse durations are equivalent to slow changes in flight altitude. Pressures throughout the compressor are able to follow the slowly changing inlet pressure. In this way, compressor pressure ratio changes very little even for large pulse amplitudes. However, there is a range of pulse durations for which the pulse amplitude required to surge is not large.

Full-face pressure pulses like those shown in figure XII-49 have been observed in tests of real propulsion systems. The results presented show that the effect of such disturbances is important and should be accounted for in an instantaneous distortion index. This effect was not included in the

instantaneous distortion index presented previously. The way in which this effect should be included in the index is not yet clear, and work is continuing in this area.

The results presented appear to give a good qualitative estimate of the effect of dynamic distortion on compressor stability. There are insufficient experimental data at the present time to verify the dynamic compressor model used to obtain these results, especially for the shorter pulse durations. As was mentioned, an experimental program is currently being planned which will provide the data required for improving the model. Once the validity of the model is established, it should be quite useful for both qualitative and quantitative understanding of the effect of dynamic distortion on compressor performance and stability. This understanding should lead to design techniques which allow compressors to be operated more efficiently.

CONCLUDING REMARKS

Experimentally based distortion indices and more analytical approaches to the distortion problem have been investigated in our programs. Distortion descriptors or indices can be of significant value in the resolution of the inlet-engine interface problem. They are useful in providing a contractual interface in development programs and for component evaluation. Indices based on purely empirical methods are conceptually simple but require extensive testing to establish the necessary coefficients.

Indices and techniques based on more analytical approaches, such as the simplified parallel compressor technique, can reduce testing requirements. In addition, the various analytical approaches can provide improved understanding of the phenomena involved. Dynamic simulations based on the parallel compressor concept and its various offshoots are beginning to provide an analytical basis for the experimental programs. The possibility of establishing filter requirements for distortion data analysis through the use of engine simulations should be pursued.

Further work is also required to establish more understanding of the effects of distortion on compressor internal flow. Experimental work is also needed to validate the system dynamics postulated in current modeling approaches. Much, although not all, of our current work has been applied to

turbojet engines. This work needs to be extended to the more complex fan engines.

REFERENCES

1. Biesiadny, Thomas J.: Test Techniques for Obtaining Off-Nominal Compressor Data During Engine Tests. Presented at the Aerospace Engineering and Manufacturing Meeting, San Diego, Calif., Sept. 30-Oct. 3, 1974.

2. Meyer, Carl L.; McAulay, John E.; and Biesiadny, Thomas J.: Technique for Inducing Controlled Steady-State and Dynamic Inlet Pressure Disturbances for Jet Engine Tests. NASA TM X-1946, 1970.

3. Rudey, Richard A.; and Antl, Robert J.: The Effect of Inlet Temperature Distortion on the Performance of a Turbo-Fan Engine Compressor System. AIAA Paper 70-625, June 1970.

4. Braithwaite, Willis M.: Experimental Evaluation of a TF30-P-3 Turbofan Engine in an Altitude Facility: Effect of Steady-State Temperature Distortion. NASA TM X-2921, 1973.

5. Mehalic, Charles M.; and Lottig, Roy A.: Steady-State Inlet Temperature Distortion Effects on the Stall Limits of a J85-GE-13 Turbojet Engine. NASA TM X-2990, 1974.

6. Kerrebrock, J. S.: Assessment, Program Definition and Research in Turbomachine Aeroelasticity. Massachusetts Institute of Technology, Apr. 1-Dec. 31, 1974.

7. Baumbick, Robert J.: Device for Producing Dynamic Distortion Patterns at Inlets of Air-Breathing Engines. NASA TM X-2026, 1970.

8. Bellman, Donald R.; and Hughes, Donald L.: The Flight Investigation of Pressure Phenomena in the Air Intake of an F-111A Airplane. AIAA Paper 69-488, June 1969.

9. Braithwaite, Willis M.; Dicus, John H.; and Moss, John E.: Evaluation with a Turbofan Engine of Air Jets as Steady-State Inlet Flow Distortion Device. NASA TM X-1955, 1970.

10. Braithwaite, Willis M.; and Vollmar, William R.: Performance and Stall Limits of a YTF30-P-1 Turbofan Engine with Uniform Inlet Flow. NASA TM X-1803, 1969.

11. Burcham, Frank W., Jr.; and Hughes, Donald L.: Analysis of In-Flight Pressure Fluctuations Leading to Engine Compressor Surge in a F-111A Airplane for Mach Numbers to 2.17. AIAA, Paper 70-624, June 1970.

12. Calvert, Howard F.; Braithwaite, Willis M.; and Medeiros, Arthur A.: Rotating-Stall and Rotor-Blade-Vibration Survey of a 13-Stage Axial-Flow Compressor in a Turbojet Engine. NACA RM E54J18, 1955.

13. Harry, David P., III; and Lubick, Robert J.: Inlet-Air Distortion Effects of Stall, Surge, and Acceleration Margin of a Turbojet Engine Equipped with Variable Compressor Inlet Guide Vanes. NACA RM E54K26, 1955.

14. Huntley, S. C.; Sivo, Joseph N.; and Walker, Curtis L.: Effect of Circumferential Total-Pressure Gradients Typical of Single-Inlet Duct Installations on Performance of an Axial-Flow Turbojet Engine. NACA RM E54K26a, 1955.

15. Langston, C. E.: Distortion Tolerance - By Design Instead of by Accident. ASME, Paper 69-GT-115, Mar. 1969.

16. Lubick, Robert J.; and Wallner, Lewis E.: Stall Prediction in Gas-Turbine Engines. J. Basic Eng., vol. 81, no. 3, Sept. 1959, pp. 401-408.

17. Russey, Robert E.; and Lubick, Robert J.: Some Effects of Rapid Inlet Pressure Oscillations on the Operation of a Turbojet Engine. NACA RM E58A03, 1958.

18. Smith, Ivan D.; Braithwaite, Willis M.; and Calvert, Howard F.: Effect of Inlet-Air-Flow Distortions on Steady-State Performance of J65-B-3 Turbojet Engine. NACA RM E55I09, 1956.

19. Wenzel, Leon M.: Experimental Investigation of the Effects of Pulse Pressure Distortions Imposed on the Inlet of a Turbofan Engine. NASA TM X-1928, 1969.

20. Werner, Roger A.; Abdelwahab, Mahmood, and Braithwaite, Willis M.: Performance and Stall Limits of an Afterburner-Equipped Turbofan Engine with and without Inlet Flow Distortion. NASA TM X-1947, 1970.

21. Winslow, Larry J.; Wendland, Daniel W.; Smith, Brian D.; and Welliver, Albertus D.: Inlet Distortion Investigation, Upstream Engine Influence and Screen Simulation. Boeing Co. (AFAPL-TR-140; AD-847095), Jan. 1969.

22. Braithwaite, W. M.; Graber, E. J., Jr.; and Mehalic, C. M.: The Effects of Inlet Temperature and Pressure Distortion on Turbojet Performance. AIAA Paper 73-1316, Nov. 1973.

23. Calogeras, James E.; Mehalic, Charles M.; and Burstadt, Paul L.: Experimental Investigation of the Effect of Screen-Induced Total Pressure Distortion on Turbojet Stall Margin. NASA TM X-2239, 1971.

24. McAulay, John E.; and Abdelwahab, Mahmood: Experimental Evaluation of a TF30-P-3 Turbofan Engine in an Altitude Facility: Afterburner Performance and Engine-Afterburner Operating Limits. NASA TN D-6839, 1972.

25. Povolny, J. H.: Stall and Distortion Investigation of a YTF30-P-1 Turbofan Engine. Presented at Airframe-Propulsion Compatibility Symp., Miami Beach, Fla., June 24-26, 1969.

26. Straight, David M.; and Mehalic, Charles M.: Performance and Stall Characteristics of an Afterburning Turbofan Engine with Steady-State Inlet-Flow Distortion. NASA TM X-1898, 1970.

27. McAulay, John E.: Effect of Dynamic Variations in Engine-Inlet Pressure on the Compressor System of a Twin-Spool Turbofan Engine. NASA TM X-2081, 1970.

28. Antl, Robert J.; Smith, John M.; and Riddlebaugh, Stephen M.: The Effect of Screen-Induced Inlet-Flow Distortions on the Performance and Stall Characteristics of an Afterburner Equipped Turbofan Engine. NASA TM X-2242, 1971.

29. Moore, Michael T.: Distortion Data Analysis. General Electric Co. (AD-756481; AFAPL-TR-72-111), 1973.

30. Williams, D. D.: Some Aspects of Inlet/Engine Compatibility. ICAS Paper 72-19, International Council of the Aeronautical Sciences, Netherlands, 1972.

31. Reid, C.: The Response of Axial Flow Compressors to Intake Flow Distortion. ASME, Paper 69-GT-29, March 1969.

32. Calogeras, James E.; Burstadt, Paul L.; and Coltrin, Robert E.: Instantaneous and Dynamic Analysis of Inlet-Engine Compatibility. AIAA Paper 71-667, June 1971.

33. Calogeras, James E.: Instantaneous Distortion Investigation. Presented at the Tech. Interchange Meeting of Air Inlets and Diffusers Panel, Naval Aeroballistic Comm., Dahlgen, Va., Sept. 19, 1972.

34. Calogeras, James E.; Johnsen, Roy L.; and Burstadt, Paul L.: The Effect of Screen-Induced Total-Pressure Distortion on Axial-Flow Compressor Stability. NASA TM X-3017, 1974.

35. Pearson, H.; and McKenzie, A. B.: Wakes in Axial Compressors. J. Roy. Aeron. Soc., vol. 63, no. 583, July 1959, pp. 415-416.

36. Williams, D. D.; and Yost, J. O.: Some Aspects of Inlet/Engine Flow Compatibility. Aeron. J., vol. 77, no. 753, Sept. 1973, pp. 483-492.

37. Graber, E. J., Jr.; and Braithwaite, W. M.: Summary of Recent Investigations of Inlet Flow Distortion Effect on Engine Stability. AIAA Paper 74-236, Jan.-Feb. 1974.

38. Calogeras, J. E.; and Burstadt, P. L.: Formulation of a Distortion Index Based on Peak Compressor Pressure Ratios. Presented at the National Conf. on Environmental Effects on Aircraft and Propulsion Systems, 11th, Trenton, N. J., May 21-23, 1974.

39. Willoh, Ross G.; and Seldner, Kurt: Multistage Compressor Simulation Applied to the Prediction of Axial Flow Instabilities. NASA TM X-1880, 1969.

40. Daniele, Carl J.; Blaha, Ronald J.; and Seldner, Kurt: Prediction of Axial-Flow Instabilities in a Turbojet Engine by Use of a Multistage Compressor Simulation on the Digital Computer. NASA TM X-3134, 1975.

41. Daniele, Carl J.; and Teren, Fred: Prediction of Compressor Stall for Distorted and Undistorted Flow by Use of a Multistage Compressor Simulation on the Digital Computer. AIAA Paper 75-28, Jan. 1975.

42. Costakis, William G.: Experimental Investigation of a Simple Distortion Index Utilizing Steady-State and Dynamic Distortions in a Mach 2.5 Mixed-Compression Inlet and Turbofan Engine. NASA TM X-3169, 1975.

43. Burstadt, Paul L.; and Calogeras, James E.: Instantaneous Distortion in a Mach 2.5, 40-Percent-Internal-Contraction Inlet and Its Effect on Turbojet Stall Margin. NASA TM X-3002, 1974.

44. Reynolds, G. G.; Vier, W. F.; and Collins, T. P.: An Experimental Evaluation of Unsteady Flow Effects on an Axial Compressor - P3 Generator Program. R73AE6309, General Electric Co. (AFAPL-TR-73-43), 1973.

45. Brimelow, B.; Collins, T. P.; and Pfefferkorn, G. A.: Engine Testing in a Dynamic Environment. AIAA Paper 74-1198, Oct. 1974.
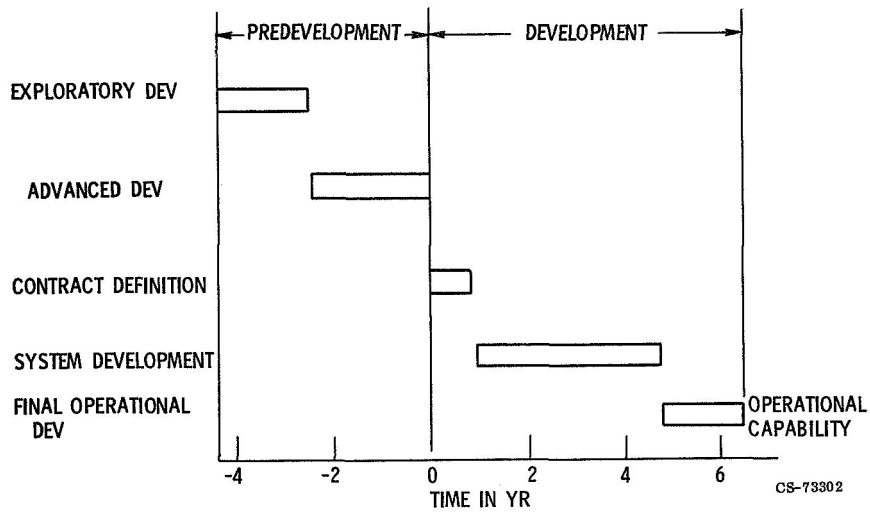
Figure XII-1. - Typical engine development history.
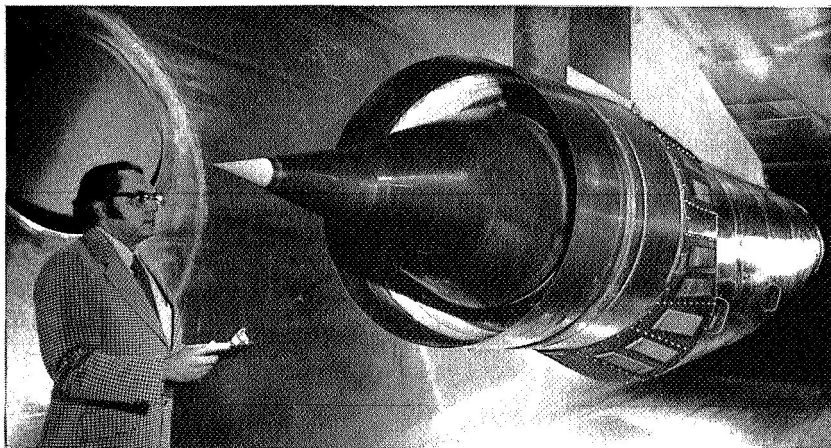
CS-73305

Figure XII-2. - Inlet and TF 30 turbofan in wind tunnel.

361
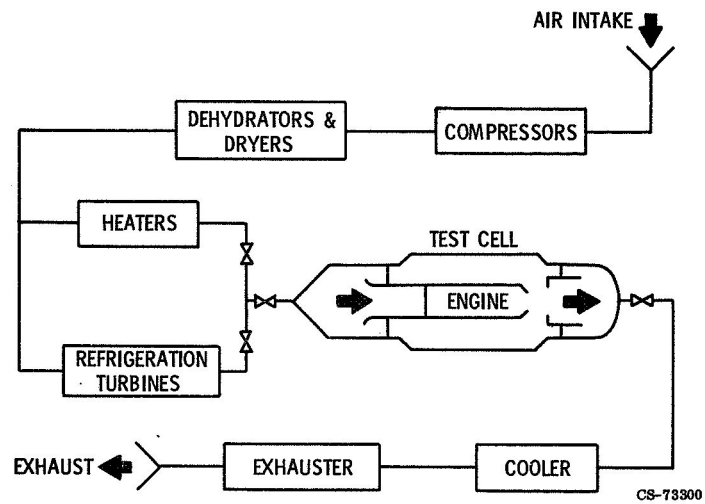
Figure XII-3. – Schematic of Propulsion Systems Laboratory (PSL).
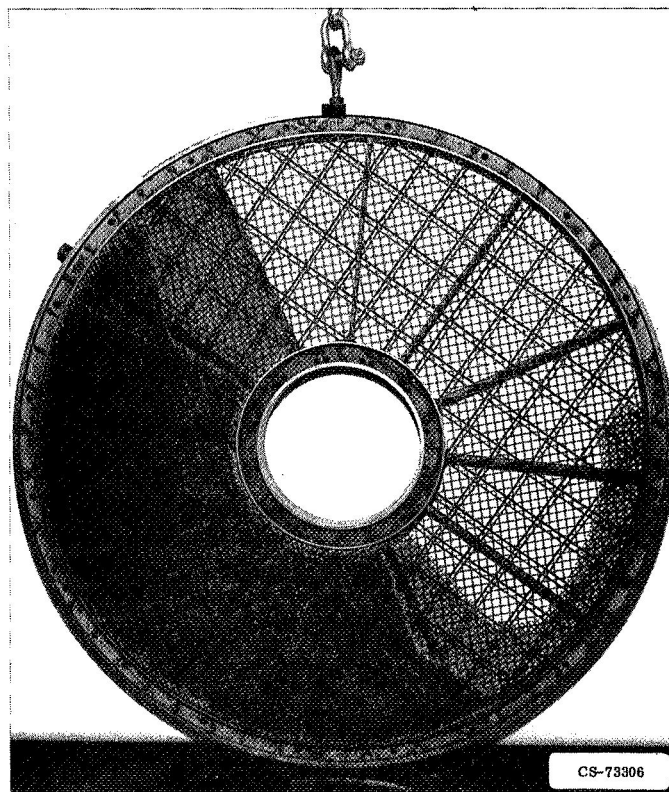
Figure XII-4. – Typical distortion screen.
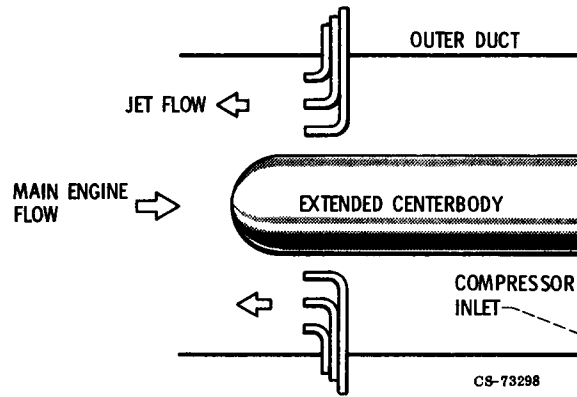
Figure XⅡ-5. - Schematic of pressure-jet distortion and pulse
generator.
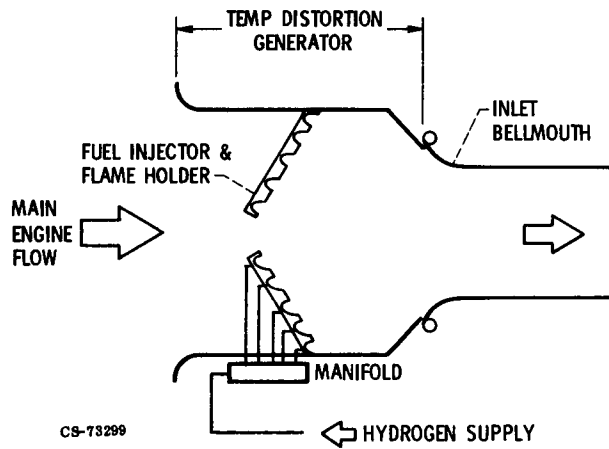
Figure XⅡ-6. - Schematic of hydrogen-fueled temperature distortion
generator.
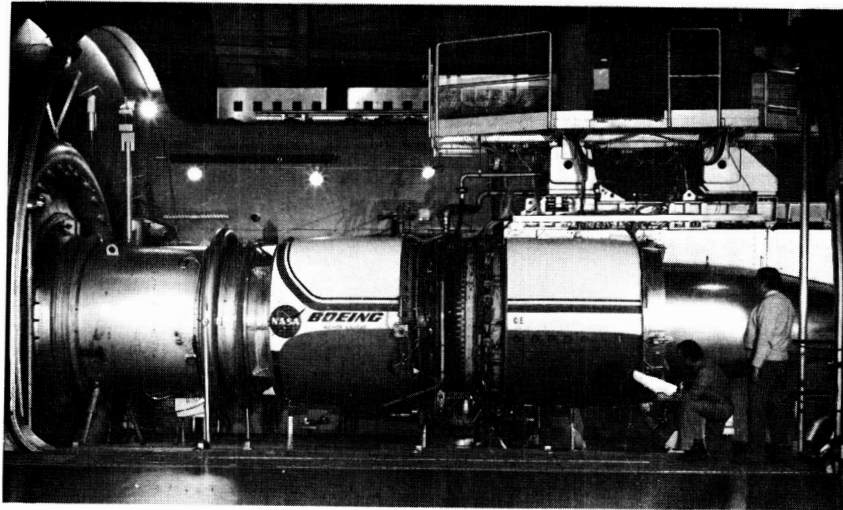
CS-73304

Figure XII-7. - Quiet Engine installed in PSL.
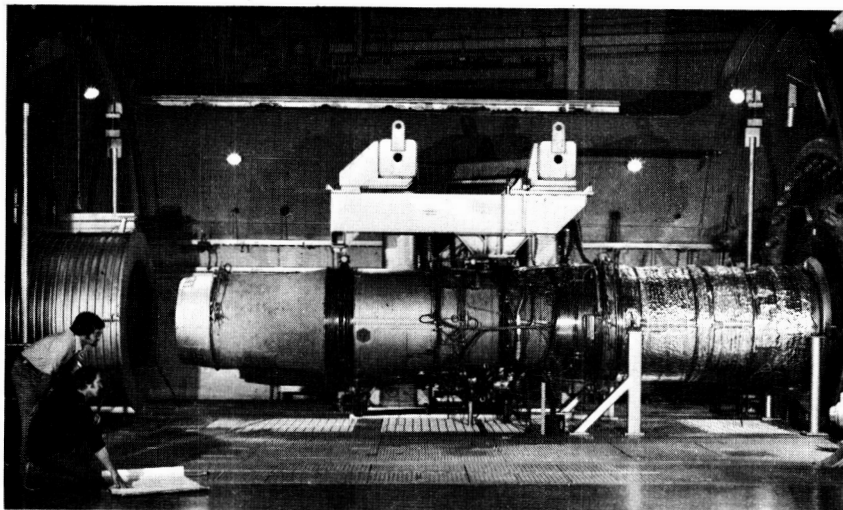
CS-73546

Figure XII-8. - Refanned JT8D installed in PSL.

364
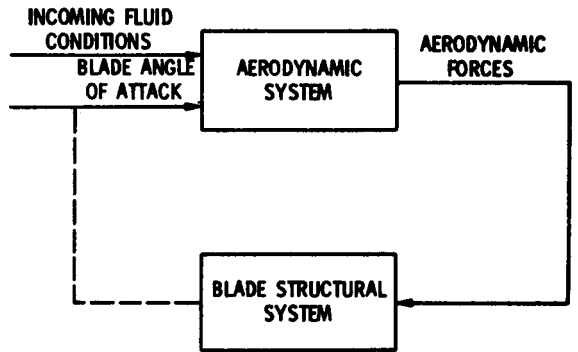
Figure XII-9. - Schematic diagram of aeromechanical instability (flutter) mechanism.
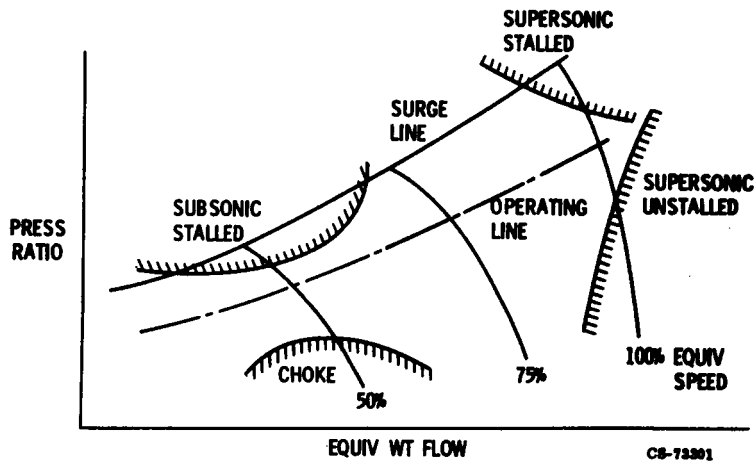
Figure XII-10. - Flutter regions.
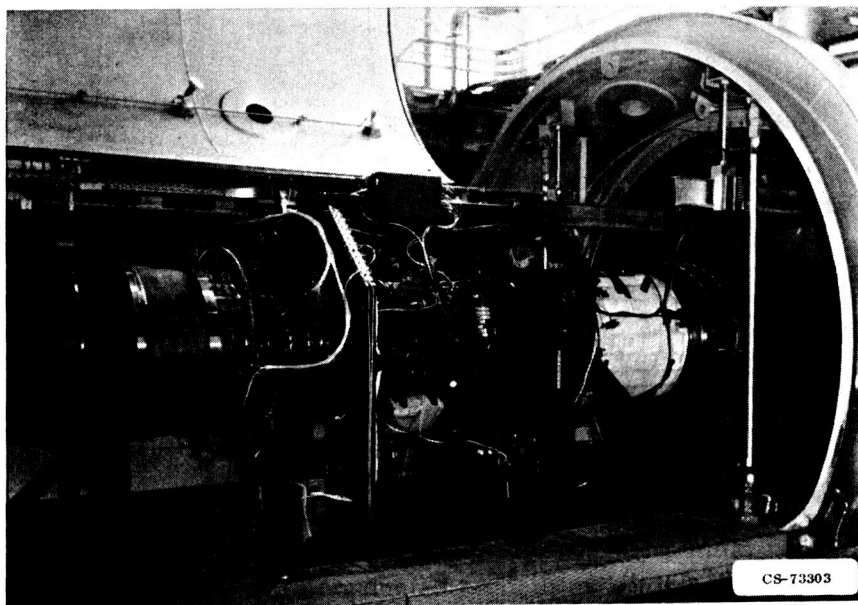
Figure XII-11. - F100 engine installed in PSL.
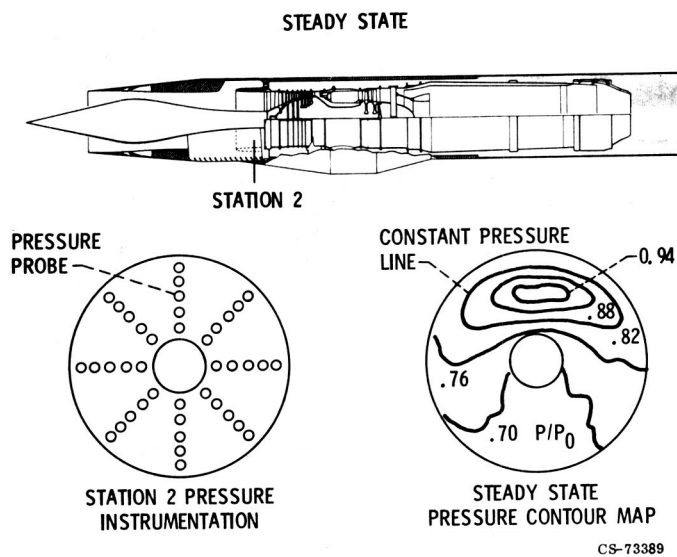
Figure XII-12. - Illustration of inlet distortion.

SHOCKS IN INLET   GUSTS, CROSSWINDS,   FUSELAGE EFFECTS
                     HIGH ANGLES OF
                    ATTACK &/OR YAW

PRESSURE DISTORTION

STEAM INGESTION FROM CATAPULTS   WAKES FROM NEARBY AIRCRAFT
        TEMP DISTORTION   PRESS & TEMP DISTORTION

CS-73425
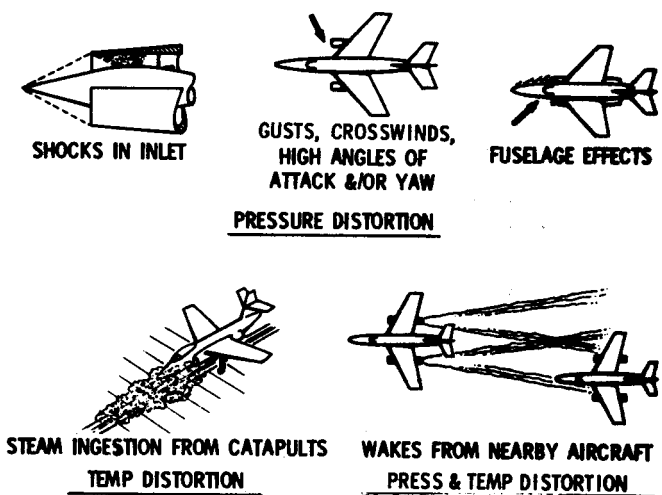
Figure XII-13. - Sources of inlet distortion.
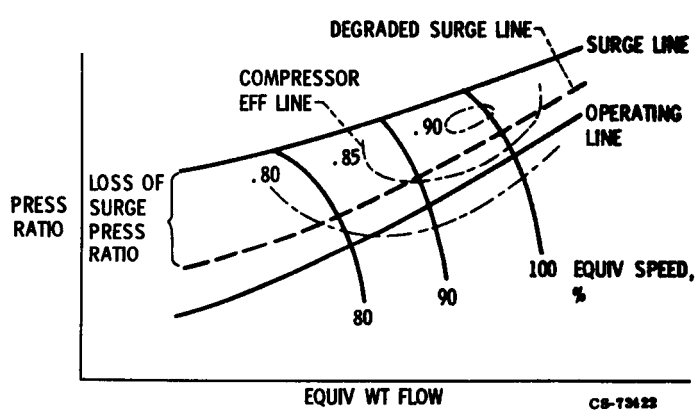
Figure XII-14. - Typical compressor performance map.

LOSS OF
SURGE
PRESS
RATIO

ACCEPTABLE
SCATTER BAND

DISTORTION INDEX

CS-73309
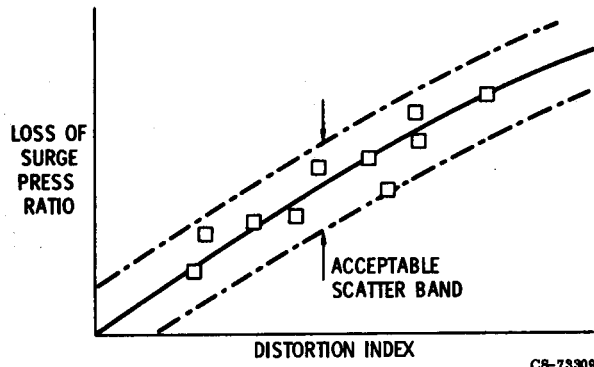
Figure XII-15. - Typical empirical distortion correlation.

$$\text{INDEX} = \frac{\Delta P}{P_{AVG}}$$

PRESSURE

AVG PRESS, P_{AVG}

ΔP

MIN. PRESS

CIRCUMFERENTIAL LOCATION

CS-73310
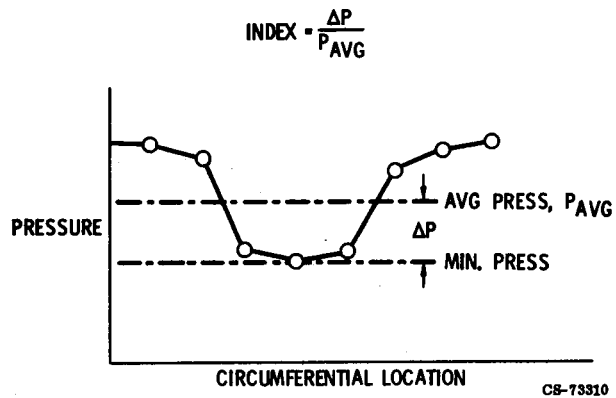
Figure XII-16. - Simple distortion index.

$$\begin{bmatrix} COMPLEX \\ INDEX \end{bmatrix} = \begin{bmatrix} CIRCUMFERENTIAL \\ INDEX \end{bmatrix} + B \begin{bmatrix} RADIAL \\ INDEX \end{bmatrix}$$

CS-73421
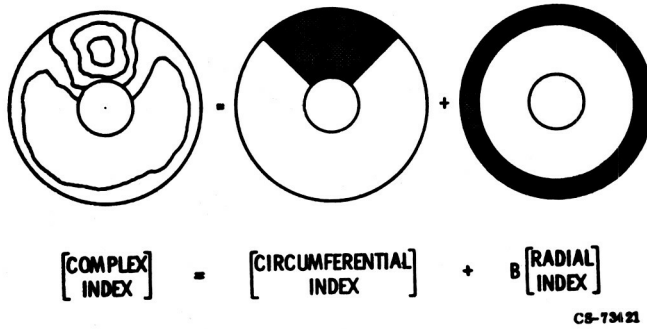
Figure XII-17. - Distortion pattern components.

CS-73311
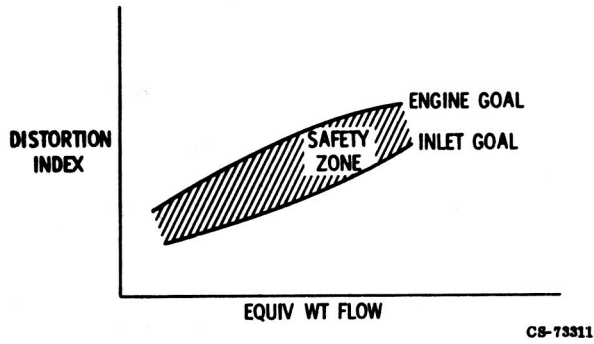
Figure XII-18. - Use of distortion index to achieve propulsion
system interface agreement.

$$\text{PARALLEL COMPRESSOR INDEX} = \frac{P_{AVG} - P_{LOW}}{P_{AVG}} \times 100$$

CS-73427
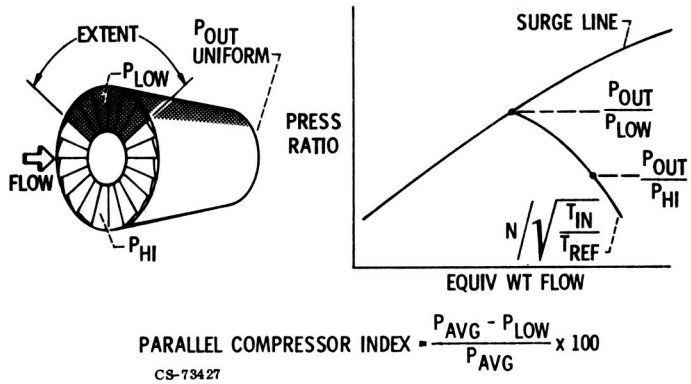
Figure XII-19. - Parallel compressor model of circumferential pressure distortion.

CS-73314
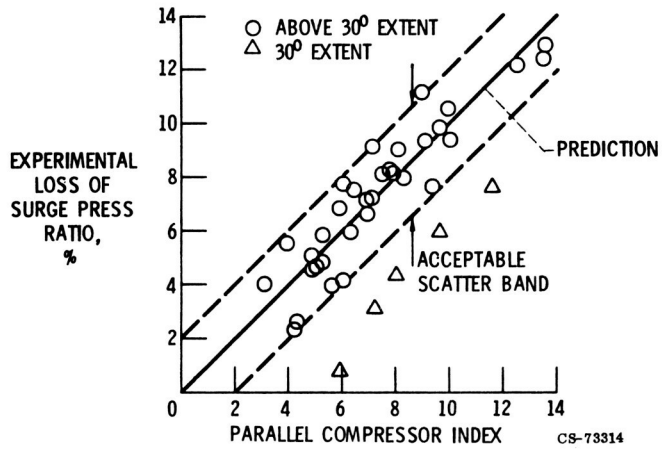
Figure XII-20. - Correlation of J85 circumferential pressure distortion data using parallel compressor index.
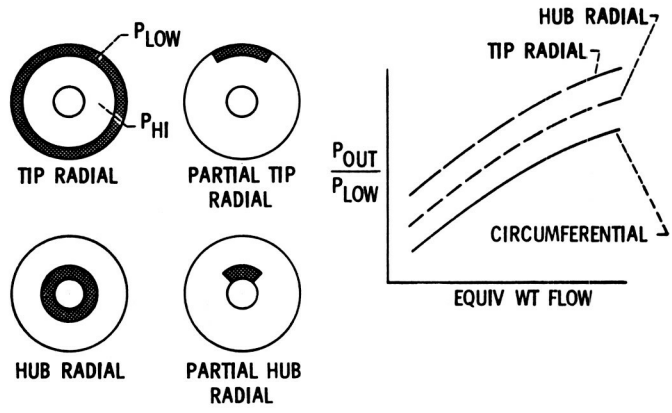
$$\text{PARALLEL COMPRESSOR INDEX} = \frac{P_{AVG} - KP_{LOW}}{P_{AVG}} \times 100 \qquad \text{CS-73426}$$

Figure XII-21. – Parallel compressor model applied to radial pressure distortions.
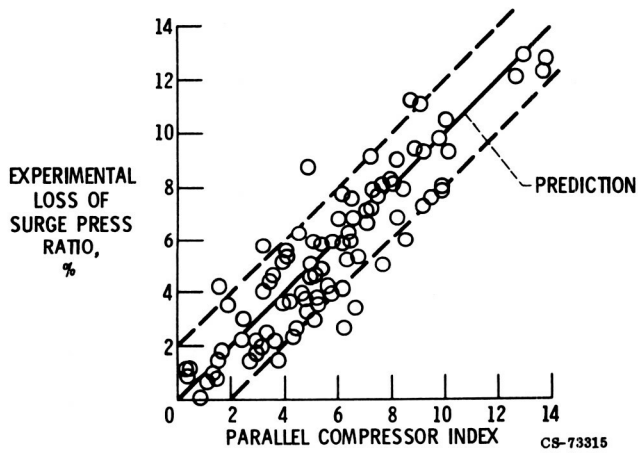
Figure XII-22. – Correlation of J85 complex pressure distortion data by using parallel compressor index.
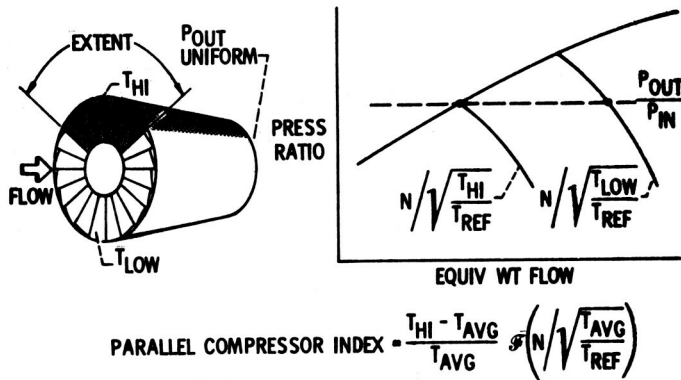
Figure XII-23. – Parallel compressor model applied to circumferential temperature distortions.

CS-73424
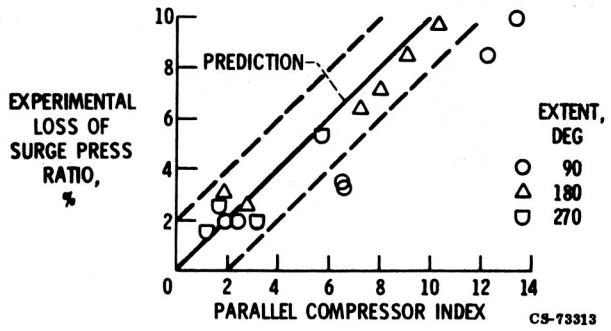
Figure XII-24. – Correlation of J85 circumferential temperature distortion data by using parallel compressor index.
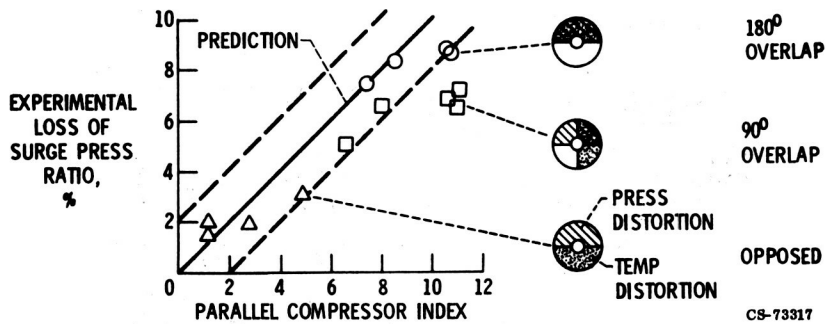
Figure XII-25. - Correlation of J85 combined pressure and temperature data by using parallel compressor index.

- PARALLEL CALCULATIONS FOR HIGH AND LOW PRESSURE SECTORS
- STAGE-BY-STAGE PERFORMANCE & DYNAMICS
- CIRCUMFERENTIAL CROSSFLOW
- DYNAMIC SURGE PREDICTION
- EFFICIENT DIGITAL CALCULATION

CS-73448
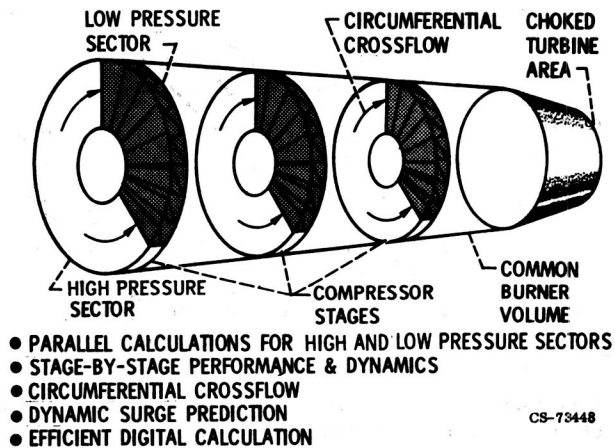
Figure XII-26. - Analytical steady-state distortion model.
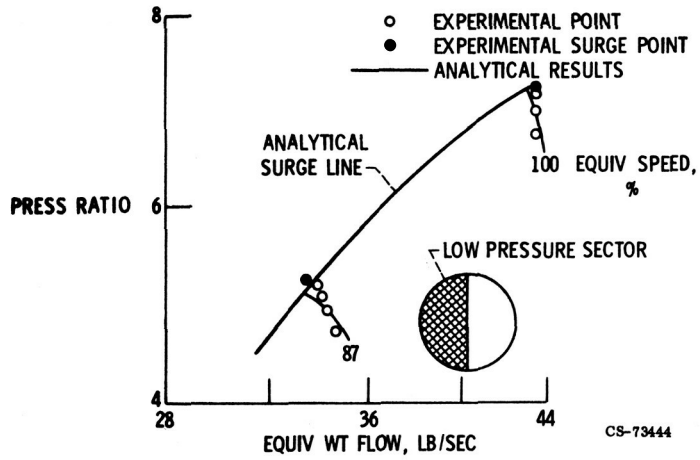
Figure XII-27. - Results of using analytical model with no crossflow to predict effect of 180° extent circumferential distortion.
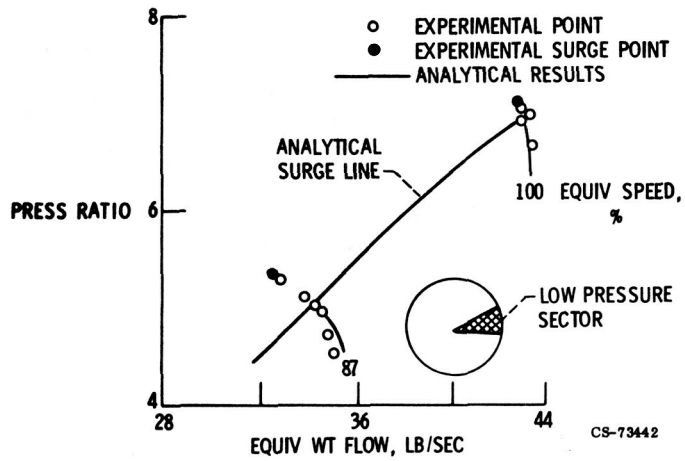
Figure XII-28. - Results of using analytical model with no crossflow to predict effect of 30° extent circumferential distortion.
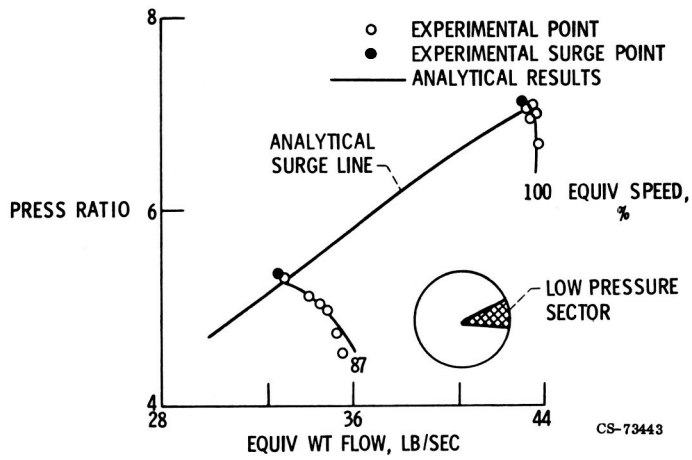
Figure XII-29. - Results of using analytical model with crossflow to predict effect of 30° extent circumferential distortion.
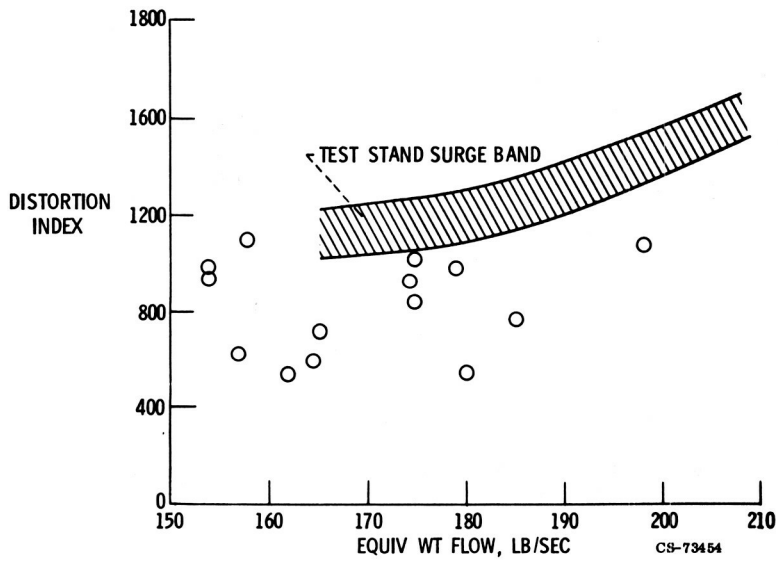
Figure XII-30. - Steady-state distortion index for F-111 flight tests.

375
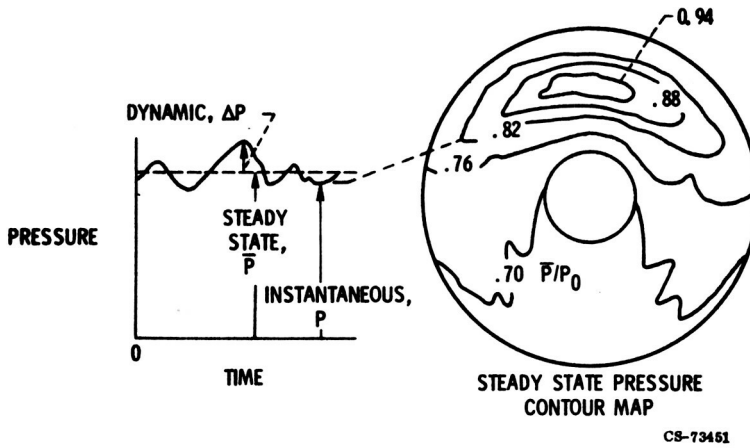
Figure XII-31. - Instantaneous inlet distortion.
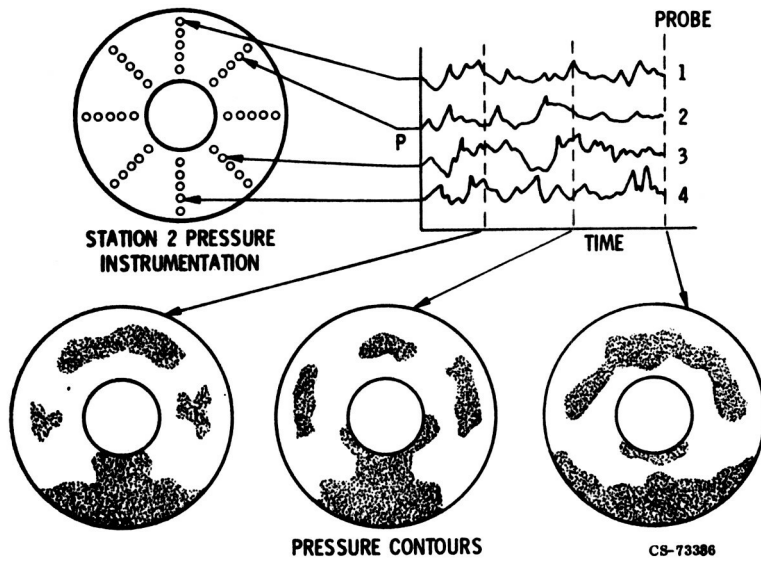
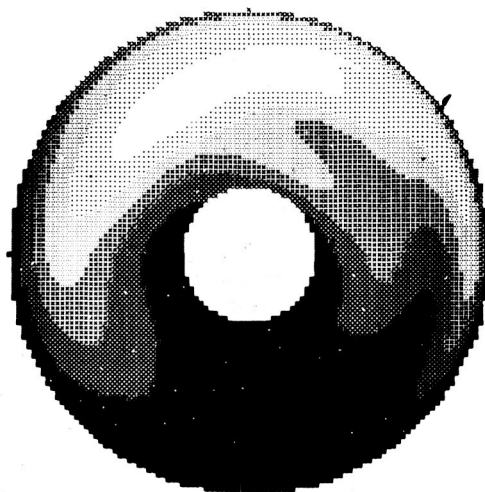

Figure XII-32. - Instantaneous pressure contours.
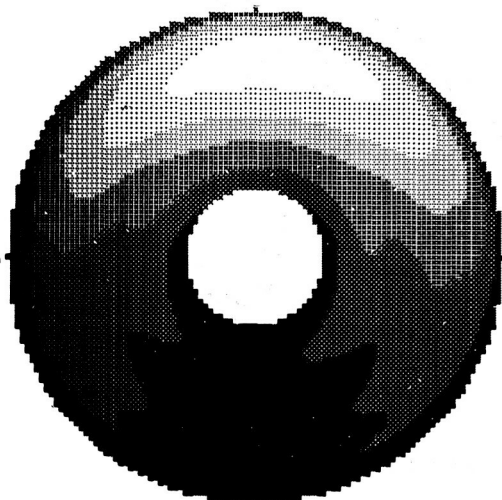
Steady state
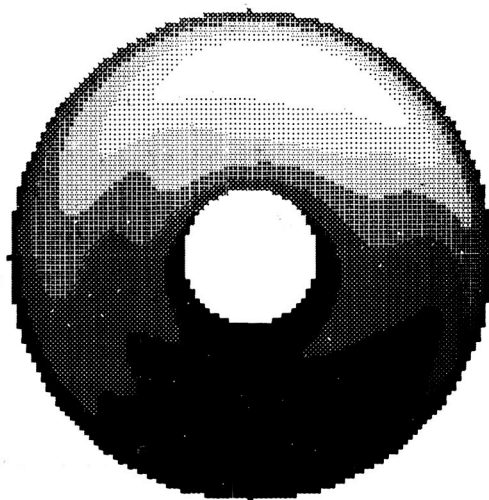
Instant 1
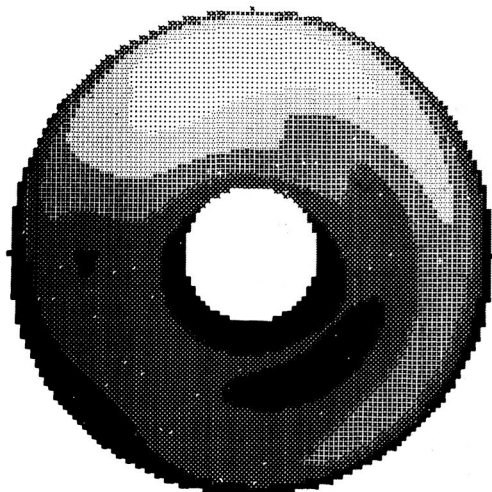
Instant 2

Instant 3

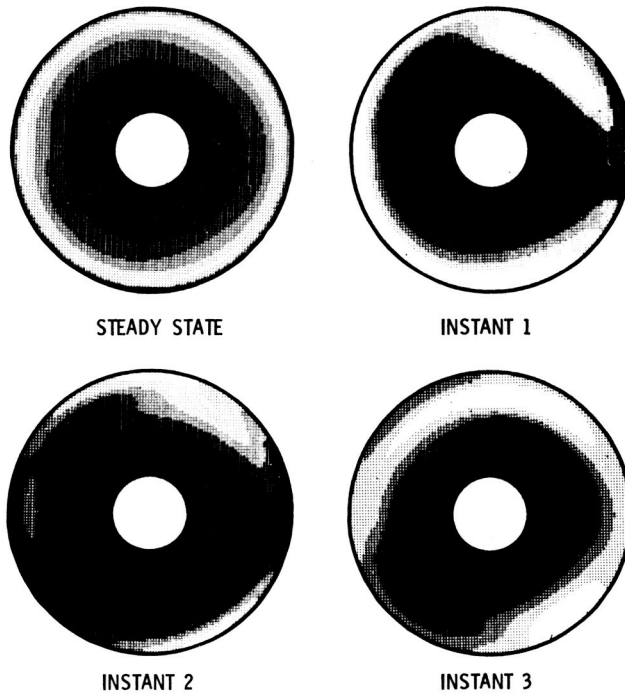Figure XII-33. – Instantaneous distortion contours at 5° angle of attack.

C-5

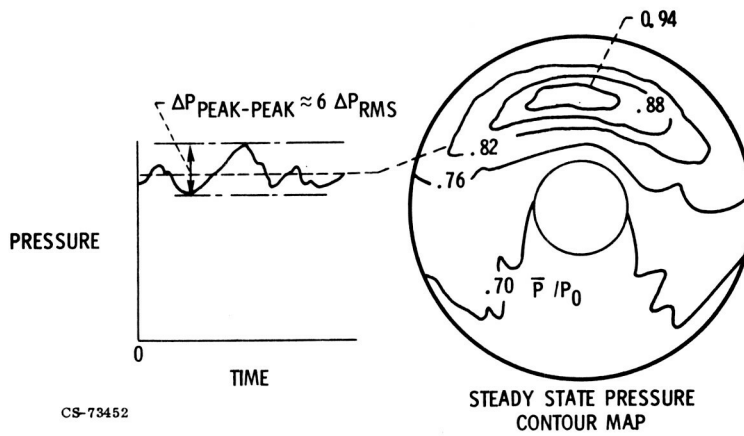Figure XII-34. – Instantaneous distortion contours at 0° angle of attack.

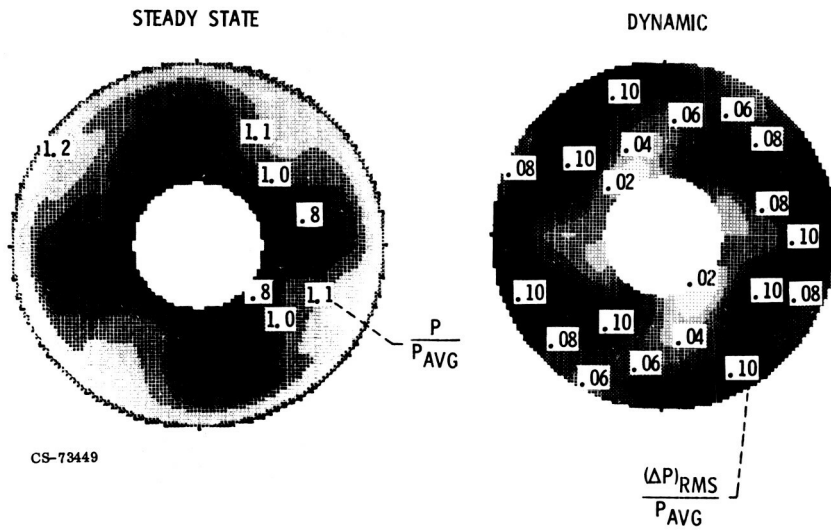Figure XII-35. – Statistical root-mean-square model of inlet distortion.

STEADY STATE   DYNAMIC

$$\frac{P}{P_{AVG}}$$

$$\frac{(\Delta P)_{RMS}}{P_{AVG}}$$

CS-73449

Figure XII-36. – Steady-state and dynamic pressure contours for TF30-P-3 engine at 0^0 angle of attack.
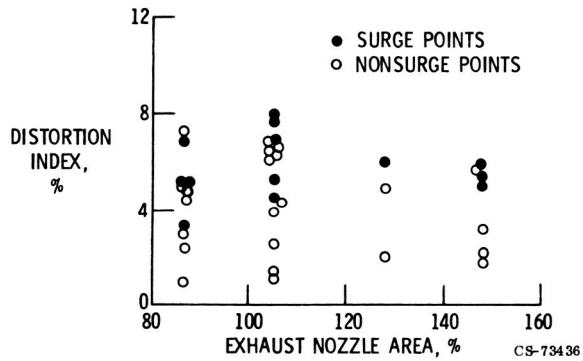

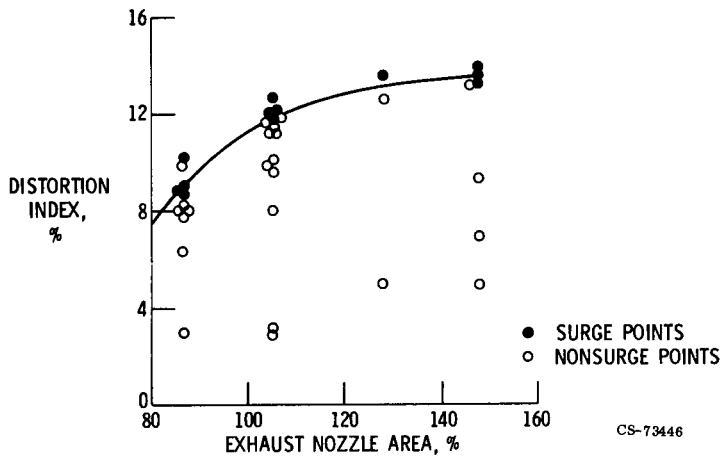Figure XII-37. – Surge correlation obtained using steady-state index.

379

Figure XII-38. - Surge correlation obtained using steady-state and low-pressure-sector rms index.
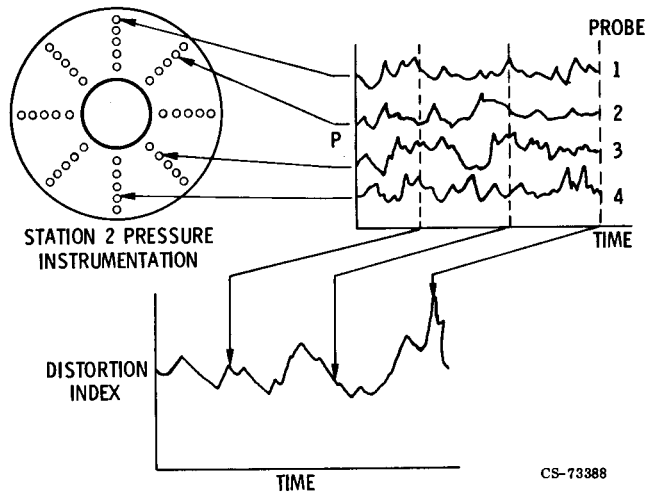
Figure XII-39. - Instantaneous distortion index.
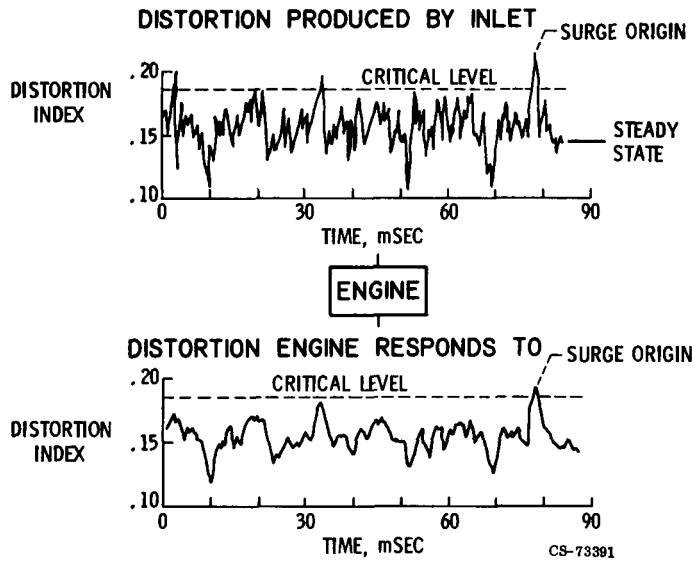
DISTORTION PRODUCED BY INLET

Figure XII-40. - Engine response to instantaneous distortion.
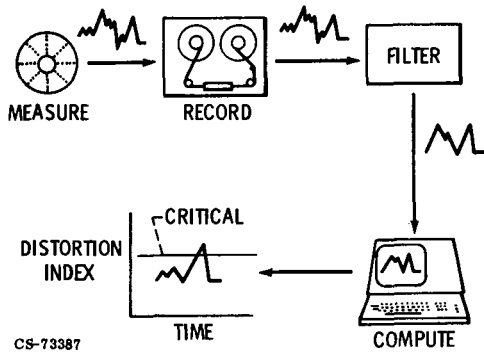
Figure XII-41. - Data reduction process for instantaneous distortion index.
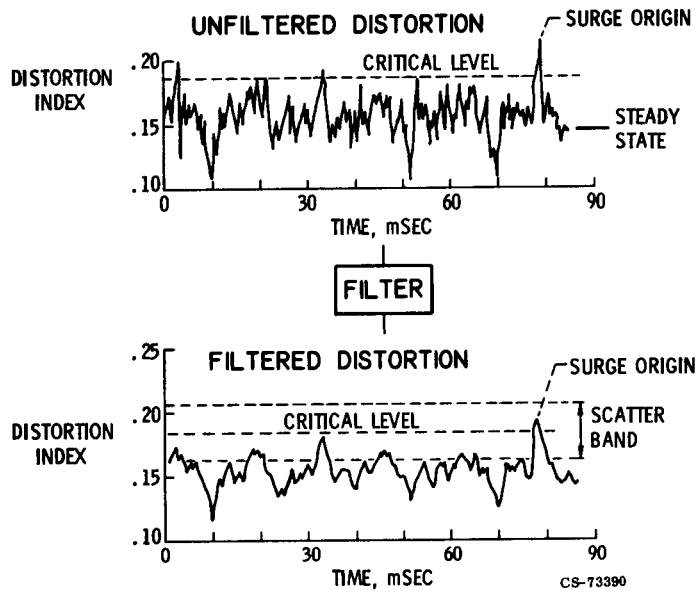
Figure XII-42. - Filter effect on instantaneous distortion.
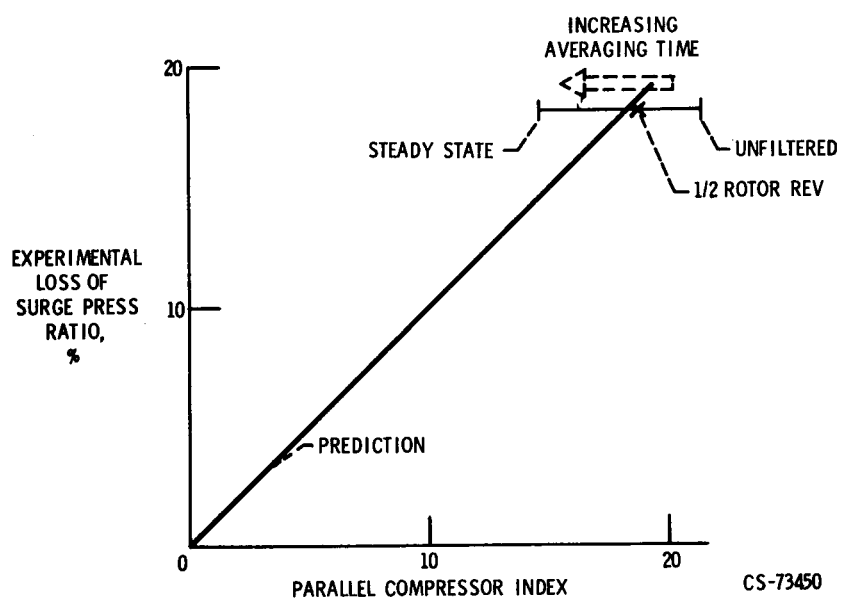
Figure XII-43. - Filter effect on peak distortion.
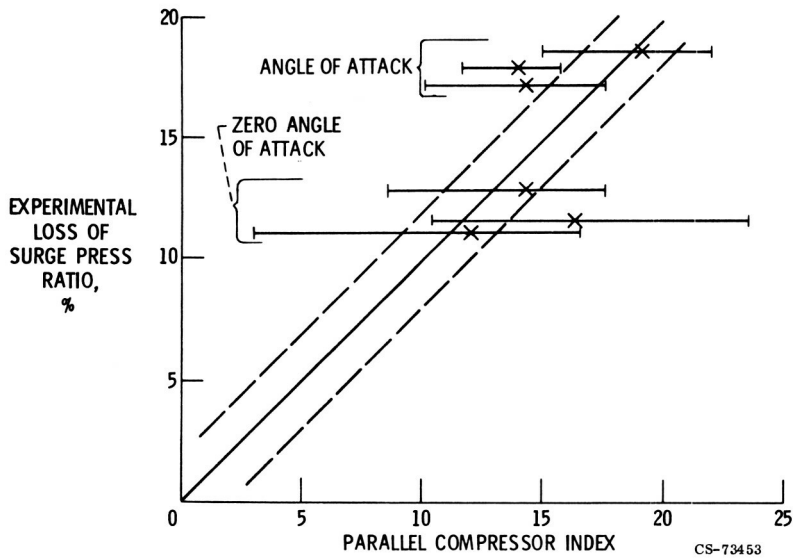
Figure XII-44. - Filter effect on peak distortion for J85 data set.

- STAGE BY STAGE PERFORMANCE & DYNAMICS
- PARALLEL CALCULATIONS FOR HIGH AND LOW PRESSURE SECTORS
- DYNAMIC SURGE PREDICTION

CS-73447

Figure XII-45. - Analytical dynamic distortion model.

Figure XII-46. - Inlet pressure for combined steady and dynamic pressure distortions.
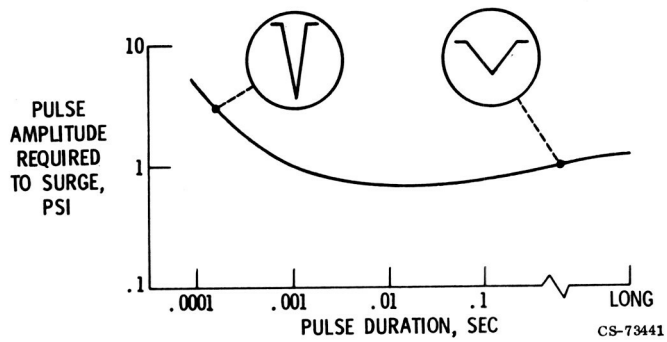
Figure XII-47. - Effect of combined steady and dynamic distortion. Steady distortion, 1 psi; extent of distortion, 180°.
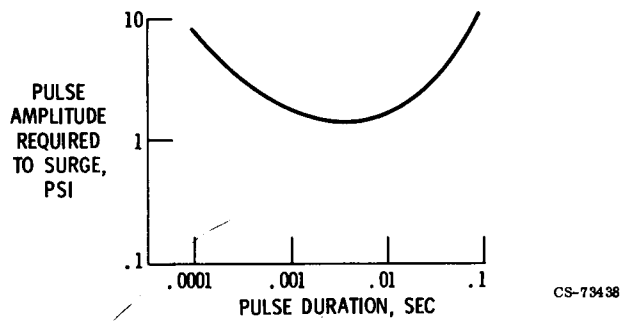
Figure XII-48. – Effect of full-compressor-face pressure pulse.
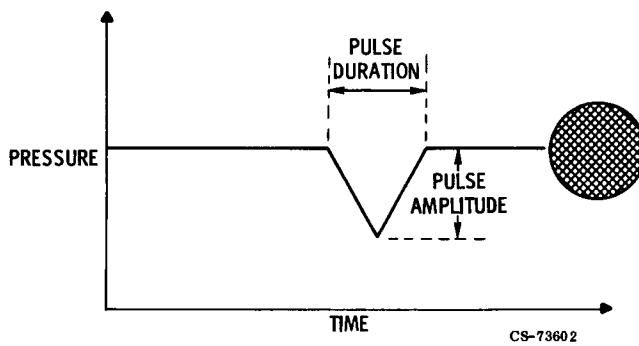
Figure XII-49. – Full-compressor-face pressure pulse.

385

Page intentionally left blank

XIII. PROPULSION SYSTEMS TECHNOLOGY

Kirby W. Hiller, Peter G. Batterton, Paul L. Burstadt,
and John R. Szuch

Usually, a new propulsion system is developed in order to achieve better performance. In order to do this, it has to stretch the technology. It is important to know what to expect when the new inlet and engine are assembled in an airframe and subjected to maneuvers, thrust changes, and atmospheric disturbances. In order to solve this systems problem, the following steps must be taken:
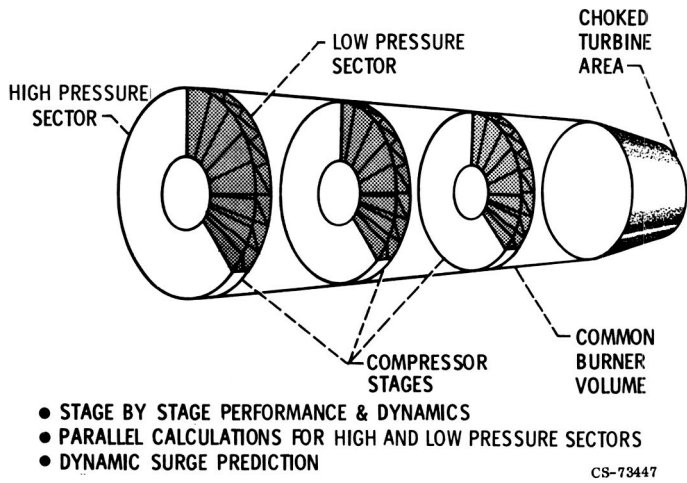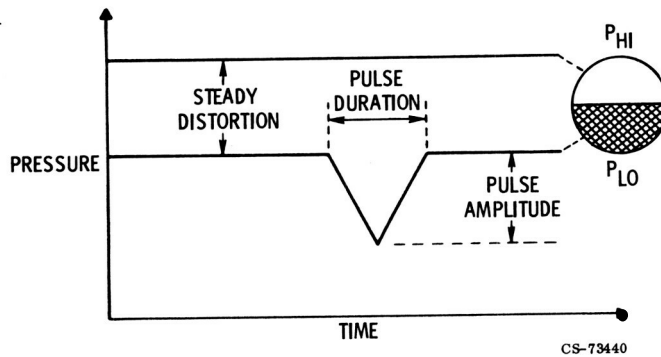
(1) The inlet and engine types must be selected to be compatible with each other and with the mission and to achieve improved performance. Inlet-engine compatability in this context refers to the ability of the controlled inlet-engine system to tolerate large transient disturbances.

(2) A control must be designed to ensure efficiency and tolerate the transients, but not to be so complex that it is unreliable.

(3) The system must be understood before it is assembled. This understanding is achieved by realistic simulation and testing, both static and dynamic.

This paper is structured along the lines of selecting components, designing controls, and simulation and testing. It deals primarily with the supersonic propulsion system because the systems problems are the most severe in this case.

Two inlet-engine combinations are shown in figures XIII-1 and XIII-2. These are research models that were investigated in the NASA Lewis 10- by 10-Foot Supersonic Wind Tunnel. Both were under electronic control, that is, the standard controls were bypassed, and these models were run from electronic computers. Both used high-performance inlets suitable for supersonic cruise. The model in figure XIII-1 used a turbojet engine. Early experiments with integrated control were made with that system (refs. 1 to 3). The model in figure XIII-2 used an afterburning turbofan engine. This

was the first time an afterburning turbofan and supersonic cruise inlet had been tested together. The design and test results from the integrated control for that system are presented in this paper. The inlet in that case, which was designed for low bleed drag, is also explained in this paper.

INLET DESIGN

A supersonic inlet is used to illustrate the selection of components. The inlet was chosen for this because it is very important at supersonic speeds. At Mach 2.5, the inlet generates half of the thrust, the engine supplying the remainder.

Within the last 10 years, a considerable number of supersonic cruise inlets have been tested within industry and government. Each inlet research group seems to prefer a given type of inlet, some of which are shown in figure XIII-3. Both axisymmetric and two-dimensional inlets have variable centerbodies to change the geometry for off-design operation. Each type has advantages from an aerodynamic or mechanical standpoint. These advantages make a particular inlet more adaptable to one aircraft configuration than another. Therefore, it is necessary to evaluate the effect of each inlet type on aircraft range, so its aerodynamic characteristics can be traded against other characteristics of the configuration.

The three inlet performance characteristics which have the largest effect on aircraft range are total pressure recovery, boundary layer bleed, and cowl drag. NASA has completed tests on a series of inlets to define these performance characteristics. Some of the inlets are shown in figure XIII-3. Both axisymmetric and two-dimensional inlets, with various amounts of internal compression, have been tested. The cone compresses the flow in the axisymmetric inlet; two-dimensional inlets use double or single ramp designs.

Supersonic inlets are often described by their percentage of internal compression; figure XIII-4 shows what that term means. The total supersonic area change is the difference between the capture area out front and the throat, or minimum, area. The area change that occurs in front of the cowl lip is called external compression. Aircraft which are designed to cruise long distances at supersonic speeds use inlets with all-external com-

pression for design Mach numbers up to about 2 or 2.2. The same is true for fighter-type aircraft, which may attain speeds of Mach 2.5 for short distances.

The amount of supersonic area change that takes place between the cowl lip and the throat is called internal compression. It usually is referred to as a percentage of the total supersonic area change. An inlet which uses a combination of external and internal compression is called a mixed-compression inlet. Designs of this type are used for long-range cruise above Mach 2 or 2.2.

Figure XIII-5 shows inlets that have different percentages of internal compression. Oblique shock waves are shown as dashed lines, and normal shocks are shown as jagged lines. The all-external-compression inlet is a limiting case. The throat, and the normal shock which changes the flow from supersonic to subsonic, are located at the cowl lip. Inlets compress supersonic flow by changing its direction. The centerbody turns the flow outward, and then the cowl catches it and turns it back toward the engine. All-external compression turns the flow to a very high angle, and thus a high cowl-lip angle is needed to capture the flow. A high cowl-lip angle causes high drag. With internal compression, the inlet starts turning the flow back toward the engine while it is still supersonic. Thus, the cowl angle, and therefore drag, can be kept low.

Cowl Drag and Total Pressure Recovery

When the cowl turns the flow back toward the engine, a shock wave is generated. Shock waves are formed when a supersonic flow is turned suddently, and they decrease the total pressure of the flow. Besides determining cowl drag, the cowl angle also determines the strength of this shock, which affects the total pressure that is recovered from the free stream. Since drag and pressure recovery both affect aircraft range, it is necessary to select an optimum cowl angle which provides the best range.

For small amounts of internal compression, most of the flow turning is done externally, and the optimum cowl angle must be relatively high. As a result, inlets with low percentages of internal compression have high cowl drag and low total pressure recovery, as shown in figure XIII-6. Total

pressure recovery and cowl drag are plotted against internal compression. The total pressure recovery and cowl drag were determined for the optimum cowl angle at each percentage of internal compression by using simple theoretical calculations which neglect viscosity. The curves represent axisymmetric inlets designed for a cruise Mach number of 2.5. Both high recovery and low cowl drag are advantages of high percentages of internal compression, but there are compensating disadvantages.

Boundary Layer Bleed

Figure XIII-7 shows a mixed-compression inlet with boundary layer bleed. At a flight Mach number of 2.5, the static pressure ratio across the supersonic section of an inlet is about 11. This pressure gradient acts against the flow and can cause it to separate from the walls. If this happens, the inlet's performance will suffer. This problem is controlled by removing some of the low-energy air near the walls at the points where the shock waves reflect. The flow faces an additional pressure rise in the subsonic section of the inlet; so enough low-energy air is removed forward of the subsonic section to help the flow through this section too. The airflow removed is called bleed or boundary layer bleed.

Boundary layer bleed flow is needed to avoid separation and to provide good performance. Figure XIII-8 shows a correlation between the bleed flow, which is expressed as a fraction of the flow captured by the inlet, and the ratio of wetted area to throat area. The wetted area is the wall area inside the inlet (fig. XIII-7). The data points represent a series of two-dimensional and axisymmetric inlets which are designed for flight Mach numbers between 2.5 and 3.5 and which use various amounts of internal compression (ref. 4). When the wetted area (or wall area inside the inlet) increases, more bleed is needed. The solid circular data point represents a Lewis inlet design that has less bleed and is an exception to the general trend. It is discussed later in this paper.

The variation of bleed flow with wetted area has been shown; but since inlets are often classified in terms of percentage of internal compression, it is useful to have a correlation in terms of this variable. A correlation of this type is given in figure XIII-9, which shows the relation between the

ratio of wetted area to capture area and the percentage of internal compression. In figure XIII-8 wetted area was divided by throat area, but in figure XIII-9 it was divided by capture area to get the correlation with internal compression to cover inlets with different design Mach numbers. The data points represent the same wide range of two-dimensional and axisymmetric inlets. However, a geometric relation was used to adjust all two-dimensional inlets to the same width-height ratio for the purposes of this correlation. The solid circular data point below the line in figure XIII-8 also appears in figure XIII-9. It represents an inlet with less wetted area than the correlation would predict. That design concept is discussed later in this paper. It is clear from figure XIII-9 that a two-dimensional inlet has about 70 percent more wetted area than an axisymmetric inlet with the same internal compression. So the two-dimensional inlet would need a similar increase in bleed. Also, the figure shows that when internal compression increases, the wetted area, and therefore the amount of bleed needed, is also increased.

Range

It has been shown how bleed, total pressure recovery, and cowl drag change with internal compression. In order to get the best aircraft range, it is necessary to have low bleed and low cowl drag with high recovery. Figure XIII-10 shows how all these factors combine to affect aircraft range. Range is shown as a reduction from a reference value, and it is plotted against internal compression. The results are for a supersonic cruise aircraft with a design Mach number of 2.5. Appropriate range decrements were determined for recovery, cowl drag, and bleed from mission analysis studies. This allowed the three factors to be combined to show the total effect of internal compression on range for axisymmetric inlets. The three variables trade off to provide almost constant range between 45 and 80 percent internal compression. It was mentioned previously that an all-external-compression inlet would have high drag and low recovery. For cruise at Mach 2.5, the range decrement for an axisymmetric inlet with no internal compression is more than 1300 miles, which is way off the plot. Two-dimensional inlets with a high percentage of internal compression are

represented in figure XIII-10 by a dashed line. The cowl drag and total pressure recovery were assumed to be the same as for the axisymmetric inlets, so the extra range penalty of about 200 miles is due only to the extra bleed required for the two-dimensional inlets. However, there may be mechanical advantages and configuration characteristics which would lead to the selection of a two-dimensional design.

Inlet Unstart

Factors besides aircraft range must also be considered when selecting an inlet design, and figure XIII-11 illustrates one of these factors. The top sketch shows an inlet with internal compression. The normal shock is located inside the inlet and is stable when it is located downstream of the throat, where the walls diverge. However, the highest total pressure recovery occurs when the shock is at the throat. If the shock is moved ahead of the throat, perhaps by some disturbance, it becomes unstable and pops out ahead of the cowl lip. This condition is known as an unstart and is shown in the bottom sketch in figure XIII-11. When unstart happens, the pressure recovery drops and flow is spilled over the cowl, producing high drag. An unstart occurs as rapidly as an explosion, and it can cause aircraft control problems. As internal compression is increased, the disturbance caused by the unstart becomes more severe. Because of this unstart problem, mixed-compression inlets are not used when an all-external-compression design will provide the necessary performance.

Angle-of-Attack Limits

Unstart can also occur when the throat area is reduced. When this happens, the flow chokes. In other words, it cannot fit through the space available and the shock pops out ahead of the cowl lip. A similar choking effect occurs locally on the downwind, or leeward, side of an inlet at angle of attack. This condition is shown in figure XIII-12. The top sketch shows the position of the internal shock waves when the inlet is at zero angle of attack. When the flow approaches the inlet at angle of attack, the shock structure on

the leeward side moves forward. In the bottom sketch, the flow is shown approaching the inlet at an angle, rather than the inlet being tilted. This allows an easier comparison of the shock structures for the two cases. If the angle of attack gets too large, the flow will choke in a region near the cowl, and the inlet will unstart.

Figure XIII-13 shows how the angle of attack which causes unstart changes with internal compression. A portion of the data shown in figure XIII-13 were presented in reference 5. When internal compression is increased, a smaller angle of attack will cause unstart. The data points represent some of the inlet designs shown in the preceding figures. The two-dimensional inlets tend to have less angle-of-attack capability than the axisymmetric inlets, but there is a significant area where they overlap. Note that at about 50 percent internal compression, different inlet designs can obtain a wide range of unstart angles of attack. This variation is achieved by adding extra boundary layer bleed along the cowl to delay the local choking of the flow. This method, however, is not very effective for high-internal-compression inlets.

A supersonic cruise aircraft would need to tolerate at least a 2^O to 3° angle of attack. But this does not give much of a safety margin and more would be better. Highly maneuverable aircraft need much more angle-of-attack capability.

The results of experimental programs have been discussed, and the effects of various designs on inlet performance have been shown. The discussion now centers on a particular low-bleed inlet design.

Low-Bleed Inlet

Figure XIII-14 shows an axisymmetric inlet that was designed at the Lewis Research Center. It was designed to have low bleed and 45 percent internal compression. More detailed information about the design and operation of this inlet is given in references 6 to 8.

Methods are available that allow calculation of the shock structure and the amount of bleed required for the supersonic section of the inlet. Results have shown that bleed is normally needed only in the areas where the shocks strike the wall. The internal shock structure of the low-bleed inlet is a little

different from other inlet shock structures, such as the one shown in figure XIII-15. The low-bleed inlet was designed to focus all the internal compression at one location on the centerbody, instead of reflecting the shocks inside the inlet. This reduces the internal wetted area for a given amount of internal compression, which as shown earlier means that less bleed flow is needed. The solid symbol that fell below the correlation lines in figures XIII-8 and XIII-9 represented this design.

An added feature of this focused-compression design is that only one bleed slot is needed because the focused shock strikes the centerbody at only one location. Bleed is not needed on the cowl surface, because the compression is distributed across a series of weak shock waves. The focused-compression concept is not new and was discussed in reference 5. However, this new design modified the concept slightly. Instead of the shocks being focused at one point, they were focused to span the bleed slot. As a result, this design obtained good performance with very low bleed flow.

Discussion has centered on the supersonic section of the inlet, but the subsonic diffuser section must be considered too. The velocity profile entering the subsonic diffuser is reasonably uniform when the normal shock is at its design location. But if the shock is moved downstream, the profile entering the diffuser is distorted.

Figure XIII-16 is an enlarged view of this subsonic diffuser. The flow in the subsonic diffuser is analyzed by using a fully viscous axisymmetric flow program. With this program, the performance of various diffuser designs can be evaluated. Flow separation can also occur in the subsonic diffuser, depending on the entrance conditions and the diffuser shape. The figure shows the velocity profile midway down the diffuser for a typical operating condition where the flow separates from the centerbody. It can be seen that the theoretical calculations agree quite well with the experimental results. Since this flow separation occurs well downstream of the throat, there is adequate length to make use of the mixing action produced by vortex generators to prevent separation. The low-bleed inlet design shown in figure XIII-15 has these generators installed just downstream of the throat. The result is a subsonic diffuser design that provides good recovery and is tolerant to distorted velocity profiles which result from changes in shock position and small amounts of boundary layer bleed.

Figure XIII-17 shows the overall performance of this low-bleed inlet design that was measured during a wind tunnel test. Total pressure recovery is measured at the diffuser exit. It is plotted against inlet mass flow, which is expressed as a fraction of the inlet capture flow. A mass flow ratio less than 1 means that bleed flow has been extracted from the inlet. The plot shows that the inlet requires only about 2 percent bleed. The peak recovery of about 90 percent is very good for this low bleed flow. Moving down the curve corresponds to moving the normal shock back. As the shock moves off the bleed slot, the bleed flow decreases. The shock cannot go too far forward, because the inlet will unstart.

The low-bleed inlet with a collapsed centerbody is shown installed in the Lewis 10- by 10-Foot Supersonic Wind Tunnel in figure XIII-18. The close-up view down inside the inlet shows the bleed slot and also some of the vortex generators on the cowl and centerbody. This inlet design provides high total pressure recovery with a very small amount of bleed. It has 45 percent internal compression; so the cowl angle and drag are not large. All these factors favor good supersonic cruise range. This inlet also has a subsonic diffuser that is tolerant to rearward movement of the normal shock. But in order to operate this low-bleed inlet at a high-performance point, a good inlet control is needed.

INLET CONTROL

Inlet Control Problem

The next consideration is that of inlet control. Figure XIII-17 indicates a control requirement. The inlet must be operated at a point well up on the pressure recovery curve. If, however, the flow increases, the shock will move downstream, reducing the total pressure recovery. This is undesirable. If the flow decreases, the shock will move forward and the inlet will unstart. This must be avoided. Thus, the inlet is seen to be nearly a constant-airflow device.

The general inlet control problem can be described better with the aid of figure XIII-19. A mixed-compression inlet is shown coupled to an engine. The solid arrows indicate disturbances to the inlet. They can originate from

the atmosphere (an external disturbance) or from the engine (an internal dis-turbance). In an engine disturbance, the phenomenon is that too much flow will pull the shock back and deteriorate performance; too little flow will cause the shock to move forward and the inlet to unstart. Thus, distur-bances from either external or internal causes have to be controlled. One way to control the inlet is by using a bypass door. If engine airflow de-creases, the bypass door is opened to increase bypass flow. This keeps the inlet airflow constant, as the curve in figure XIII-17 indicates.

Inlet Dynamics

A dynamic process is frequently studied with sine wave testing. By ap-plying sinusoidal disturbances of all frequencies and measuring the output sine waves, it is possible, through analysis, to determine the inlet's re-sponse to a particular waveform. For a downstream disturbance, engine airflow is the forcing function and shock position is the response. Figure XIII-20 shows the frequency response of the shock position of the low-bleed inlet for constant-amplitude disturbance airflow. The attenuation of shock position amplitude at the higher frequencies is due to the volume dynamics of the inlet. What happens physically is that the volume of air in the inlet absorbs a rapid airflow change. This represents the behavior of the uncon-trolled inlet. The inlet's natural dynamics absorb the disturbance above 10 Hz. In the lower frequency region, a control device is needed to stabilize shock position.

Bypass-Door Control

Figure XIII-21 shows a closed-loop, bypass door control for the inlet. A signal that represents measured shock position is fed to the control. This measurement is compared with requested shock position. The difference causes the control action, positioning the bypass door. If the shock is too far forward, the control commands the door to open, which returns the shock. Thus, in steady state, the bypass door keeps the shock at its "requested" position. The requested position corresponds to the operating

point on the pressure recovery - mass flow curve in figure XIII-17.

The dynamic behavior of the controlled inlet for constant-amplitude dis-
turbance airflow is displayed in figure XIII-22. The shock amplitude is
greatly attenuated at low frequencies. But, at higher disturbance frequen-
cies, the shock starts to respond. It reaches a maximum amplitude at about
6 Hz. Above this frequency, the volume dynamics of the inlet attenuate the
disturbance. This characteristic is typical of the dynamic response of an
inlet under bypass door control: good attenuation at low and high frequen-
cies, but some shock motion at intermediate frequencies. Results of dynam-
ics and controls investigations of a number of inlets, together with inlet dy-
namic analyses, analytical inlet control design results, and results of an in-
let sensor design effort are presented in references 9 to 30.

Downstream Disturbances

In order to study downstream disturbances, the low-bleed inlet coupled
to a TF30 turbofan engine was tested in a supersonic wind tunnel. The en-
gine's rotor speed could change and thus change airflow. These were slow
changes so that the bypass door could compensate. But this was a turbofan
engine with an unchoked fan. Thus, downstream variations such as after-
burner changes or exhaust nozzle changes, could feed up into the inlet. Of
concern was a sudden decrease in engine airflow, which could unstart the
inlet. An afterburner lightoff is this kind of disturbance. Figure XIII-23
shows the result of lighting off the TF30 afterburner. Engine airflow is
shown as a function of time. On lightoff, a decrease of approximately 5 per-
cent of total engine airflow occurred. Also, it occurred at a rate of approx-
imately 50 percent per second. High-response bypass doors were used in
this inlet, but they could not prevent unstart with the shock at its normal op-
erating point. Thus, other ways to control the inlet are needed.

Disturbance Simulation

In order to test a control scheme, it is desirable to be able to simulate
a disturbance such as afterburner lightoff. Such tests are a part of engi-

neering the system. In order to test the inlet to such a disturbance before the engine was available, a lightoff characteristic could be postulated, based on results from similar engines, and simulated with a fast-acting valve. Figure XIII-24 represents a set of fast-acting valves located on plates. The plates fold up like an umbrella. Folding the umbrella down was necessary to permit starting the supersonic wind tunnel; it reduced the blockage of the inlet. With the umbrella open, the valves could simulate the airflow variations produced by an engine.

A photograph of the umbrella assembly is shown in figure XIII-25. Each of the valves was a multiple-slot valve, which permitted it to obtain full-open area with a shorter stroke. It could achieve full-stroke operation to a frequency of 35 Hz. A closer view of a valve is provided in figure XIII-26. These valves were also used as bypass doors for the low-bleed inlet. The servosystem and mechanical design techniques for these fast valves are described in references 31 to 35.

Inlet Control Using Valved Throat Bleed

The inlet's role is extremely important with a supersonic cruise aircraft. At Mach 3, the inlet generates about 70 percent of the thrust. If the inlet unstarts, its pressure recovery drops drastically, which can upset the flight stability of an aircraft. Solving this problem has led to consideration of other methods of inlet control.

In figure XIII-27, a method of inlet control is shown which relies on a special kind of bleed from the inlet throat. This bleed can be done on either the cowl or the centerbody. Cowl bleed is considered first. A section of the inlet in the throat region is shown in figure XIII-28. A porous skin is installed in the throat region. There is a rise in static pressure across the normal shock. If the shock moves forward, more of the bleed area is exposed to the higher pressure. This increases the bleed flow from the inlet and stabilizes the shock. In the figure, the shock is shown well ahead of the throat. The valves shown are used to prevent excessive bleed at design conditions, when the shock is aft of the throat. Without them, there would be too much supersonic bleed, causing too much drag. The valves are self-acting. They trap their own reference pressure through the orifice shown

in the piston when the shock is aft of the throat. When the shock moves for-
ward as shown in figure XIII-28, the pressure behind the porous bleed in-
creases and forces the valves open. Thus, figure XIII-28 represents the
case of increased throat bleed causing the inlet to operate stably with the
normal shock ahead of the throat. When the disturbance is removed or the
bypass doors readjust, the shock will move back and the relief valves will
close causing the inlet to return to operation with very low throat bleed. A
similar thing happens to the front row of valves when upstream conditions
change. The cowl pressure increases and forces those valves open. This
scheme requires no electronics and no hydraulics, which is an advantage
since supersonic cruise inlets operate at high temperatures.

The operating principle with centerbody bleed shown in figure XIII-27
is quite similar. Again, a valve is required to prevent bleed at design con-
ditions. In the figure, a pipe is shown through the centerbody to a strut and
then overboard through the valve. This is rather schematic. The inside of
the entire centerbody can be used for the flow duct. This has the advantage
that the volume absorbs the sudden change in flow when the shock moves
forward. Thus, the strut valve can be slow acting. The cowl valves, on
the other hand, have to be fast acting. But this can be achieved by proper
design.

Both kinds of throat bleed systems have been tested at the NASA Lewis
Research Center and both show promise. Results are given in references
36 to 40. Centerbody bleed was used on the low-bleed inlet. It improved
the inlet's stability considerably - even with slow-acting strut valves
(ref. 41).

The last inlet experiment used a set of cowl valves. The design of these
valves is described in reference 42. A dynamic analysis of these valves is
given in reference 43. The ability of a modified YF-12 inlet to tolerate a
reduction in engine airflow is shown in figure XIII-29. The upper portion of
this figure is a plot of the change in engine airflow as a function of time. The
tickmarks on the horizontal axis are 1-second lines. The engine airflow was
ramped down and then back again. Increasingly larger ramps were used un-
til the inlet unstarted. The solid line represents the inlet with cowl valves
locked closed. The dashed line shows the largest ramp the inlet would
tolerate with the cowl valves free to move.

The lower portion of the figure is a summary of the results with a

variety of ramps of various durations. The horizontal axis represents the duration of the ramp. Long-duration (slow) ramps are plotted on the left and short-duration (fast) ones on the right, because the frequency content of a fast ramp is higher. The "no control" curve consists of data points for the inlet with the cowl valves locked closed. Below this line, the uncontrolled inlet would always unstart. Above this line, it would never unstart. For slow ramps, the inlet could tolerate a 4 percent reduction in engine airflow. Larger reductions are tolerated for the faster ramps because of the volume dynamics of the inlet.

The "cowl bleed" curve in figure XIII-29 represents the behavior of the inlet with the cowl valves free to move. Using the valves made a threefold improvement in the intermediate range. Also, it helped even with the fastest ramps. For the slow ramps the "cowl bleed" and "no control" curves join because of the action of the orifice - volume chamber method of obtaining the reference pressure for the relief valves; the reference pressure bleeds off through the orifices in the valve pistons. Use of a smaller orifice would permit the valves to be effective for slower ramps.

The "bypass door and cowl bleed" curve in figure XIII-29 shows the behavior of the system with the bypass doors also active. Bypass doors are very effective for slow ramps. But they become ineffective for faster ramps.

Thus, the cowl bleed and bypass door systems complement each other. Three regions of operation are noted: the region of slow ramps where the bypass doors are active, an intermediate region where the cowl valves are active, and a region of fast ramps where the volume dynamics of the inlet stabilize the shock position. Overall, the inlet can always tolerate a 10 percent reduction in airflow. This reduction is twice as great as the afterburner lightoff for the TF30 engine shown in figure XIII-23, recognizing that the different waveforms do not make the two results directly comparable.

The "no control" line in figure XIII-29 is different from the characteristic of the unmodified YF-12 inlet. It is the characteristic of the inlet after the porous skin had been installed. Thus, the improvement shown in figure XIII-29 represents the comparison of a passive bleed system and a valved bleed system. The advantage of the valved bleed system is obvious.

INTEGRATED INLET-ENGINE CONTROL

The controllability of a mixed-compression inlet can be improved by integration of the inlet and engine control systems. Integration of the controls provides other advantages also. Historically, inlet and engine control systems have been designed by separate people. As a result, the inlet and engine controls were usually kept separate. Each control, however, contains information which would be helpful to the other. So by tying the controls together, they can be improved. Such a control can be labeled an "Integrated Control" (ref. 41). As shown by the horizontal arrow in figure XIII-30, the inlet control and the engine, afterburner, and exhaust nozzle controls can now communicate. This was done easily, since these two controls were programs on an electronic digital computer. This Integrated Control provides an alternate approach for handling the afterburner lightoff problem discussed previously. However, this control method will work only for disturbances which can be predicted, or anticipated.

TF30 Program

Test results in figure XIII-31 show how the Integrated Control handles afterburner lightoff and avoids inlet unstart. In the top trace, the sudden drop in engine airflow results from the afterburner lightoff. The afterburner control knows this is coming, so it sends the inlet control an anticipation signal before the lightoff. The inlet control then uses this signal to relocate the shock further away from the unstart. At the lightoff, the inlet shock is pushed toward its unstart value, shown in the figure by the dashed line. Now compare the amount the shock moved at lightoff with the amount the shock was relocated. The shock would have crossed the unstart line had it not been relocated in anticipation of the lightoff. Once the lightoff is over, the control returns the shock to its normal position.

The loss in inlet performance, for the few seconds the shock is relocated, is not important when compared to the effect of an unstart. Thus, the inlet bypass doors and the inlet control system no longer need to handle the initial rapid drop in engine airflow following lightoff. Bypass doors of limited capability were actually used for this test.

During normal operation for this Integrated Control, the inlet control provides a signal to the engine and exhaust nozzle controls. These controls then trim engine airflow to close the inlet bypass doors and to position the shock where it is wanted.

A digital computer was used for the Integrated Control. Other wind tunnel and sea-level testing of digital controls has shown the feasibility for the flight testing of a digital integrated propulsion system control.

Integrated Propulsion Control System (IPCS) Program

The Integrated Propulsion Control System Program (IPCS) is described in reference 44. IPCS is a contract effort, with Boeing as the prime contractor and Pratt & Whitney and Honeywell as the principal subcontractors. This effort is being led by the Air Force Aero Propulsion Laboratory. It is being closely supported by NASA Lewis Research Center and NASA Flight Research Center. These tests will be performed on the left engine and inlet of the F-111E aircraft shown in figure XIII-32. Even though this program will try to show improved inlet-engine matching, most of the new developments are in the engine control. A reduction in compressor surges remains as a principal objective of IPCS.

One of the IPCS engines is being tested in the Lewis Propulsion Systems Laboratory (PSL) altitude test facility. The engine has been successfully run at several simulated flight conditions under digital computer control.

The Integrated Propulsion Control System Program has many new features. The control is designed to provide more stable propulsion system operation by providing a better overall inlet and engine match. A digital computer is used to accomplish this match. The IPCS engine control will include several new control inputs not found on production engine systems. Turbine inlet temperature will be used to limit maximum and minimum fuel flow. Compressor discharge Mach number, which is related to compressor surge margin, will also limit maximum and minimum fuel flow. Inlet buzz, an unstable external compression inlet shock pattern, will cause the control to increase engine airflow and stabilize the inlet. Distortion level will tell the control to open engine bleeds to improve engine surge margin. And, finally, afterburner rumble, or combustion instability, will cause the control

to adjust afterburner fuel-air ratios and thus stabilize combustion.

Some of these control features will be very necessary for future advanced turbofan engines. The IPCS program is providing good fundamental digital control experience.

Advanced Control Hardware

Advanced control systems, of which IPCS is an example, will be quite complex. These controls use more propulsion system information to achieve better performance, greater stability, and greater efficiency. As a result, the hydromechanical control system will no longer do the job. Figure XIII-33 is an example of a hydromechanical control. It shows a closeup of the TF30 main fuel control with its cover removed. The entire control for the TF30, including the afterburner and exhaust nozzle controls, contains over 8000 parts.

Figure XIII-34 is a projection, based on anticipated control system requirements, of how engine control system mechanizations will probably evolve over the near future. The second block indicates hydromechanical controls with electronic supervision or trim. An example of one of these control systems, including the afterburner and exhaust nozzle functions, is shown in figure XIII-35. In this type of control, the hydromechanical part produces most of the control output, while the electronic part trims the outputs so that the engine achieves the desired performance. Because of the electronic part, performance can be maintained over a greater portion of the flight envelope. Finally, electronic failures result only in the loss of trim capability.

Increased control complexity, however, requires full-authority digital control. The hydromechanical part of such a control will provide only backup capability. Advanced engines with variable-pitch fans, such as QCSEE, or engines with variable-pitch turbine stators will use this type of control mechanization. The packaging of such controls appears to be essentially the same as that shown in figure XIII-35.

Lastly, figure XIII-36 is an example of a full-authority, all-electronic digital control. This is the Bendix control for a B-1 prototype engine. The all-electronic digital control system will become a reality when the engine

cannot be operated satisfactorily with a reasonable-cost hydromechanical backup control. Then computer programming techniques and additional electronics will be used for backup control. An example of one of these computer programming techniques is provided in the section Fail-operational control. This particular technique can be used for engine sensor failures.

Before full-authority electronic digital controllers such as that shown in figure XIII-36 can be used, practical experience with them needs to be gained. Their reliability and maintainability must be improved. This includes the sensors, connectors, power supplies, cooling, and actuators, as well as the computer itself and its memory. The advantages of digital propulsion system control are enormous. The digital computer provides greater flexibility in the choice of control modes. Digital control will also be capable of propulsion system condition monitoring. In addition, digital control has the capability for handling some of the latest control theory developments. An example of this is also provided (see section ADVANCED CONTROL THEORY APPLICATION).

PROPULSION SYSTEM SIMULATION

An important aspect of developing an airbreathing propulsion system is to acquire an in-depth understanding of the complete, interrelated system through realistic simulation and testing. Thus, the field of simulation is assuming increased importance. Simulating a propulsion system dynamically with its control becomes more realistic if the simulation can include everything of importance: velocity limits of the actuators, time lags of the sensors, or even changing tip clearances in the compressors. Sometimes real hardware is interconnected as part of the simulation. This can become very complex, but it can pay off if the model displays real problems. Significant progress is being made in the simulation field. Some recent accomplishments are described in this section.

Simulations or propulsion systems and their controls provide a means of analyzing the behavior and interactions of these increasingly complex systems. Simulations can be very useful during system development and

also serve as aids in solving problems that arise after the development phase is completed.

The usual approach to simulating a complex system, such as a turbofan engine, is illustrated in figure XIII-37. The problem is reduced to one of combining mathematical models of a number of well-understood components such as fans, compressors, and turbines into one larger, more complicated model, namely the simulation. These individual component models relate a number of input variables, such as flows and rotor speeds, to a number of output variables, such as pressures and temperatures. In order to ensure accuracy in the simulation, the component models, if possible, incorporate actual performance data.

Simulations can generally be divided into the two categories (fig. XIII-38): (1) simulations having only steady-state computing capability and (2) those having transient capability. Steady-state simulations (refs. 45 to 48) provide information about system performance for fixed flight conditions, pilot commands, and system parameters. By performing a series of steady-state calculations, we could determine, for example, a compressor steady-state operating line. In transient simulations (refs. 49 to 52), each individual component model must account for dynamic factors such as rotor inertias and mass and energy storage. Including these effects requires the solution of differential equations which describe the dynamics of the system. By solving these equations at various points in time, we obtain a time-history of the response of a variable such as the compressor pressure ratio to changes in flight conditions, pilot commands, or system parameters.

Figure XIII-39 compares some of the capabilities of the three types of computers currently being used for propulsion system simulation. These are digital computers, analog computers, and hybrid computers which can perform varying amounts of both digital and analog calculations. Factors to be considered when selecting a computer include computer accuracy, computer speed, and available computer interface. Digital computers are powerful tools for most simulation applications primarily because they are very accurate. They are also very flexible and convenient to use. However, digital computers are limited in speed because they must perform calculations sequentially. Thus, digital simulations consume much expensive computer time, particularly when they are used to get transient solutions. Some recent advances in digital simulation techniques have reduced

digital computing times to the point where it is now possible to perform both steady-state and transient simulations of a wide-range of gas turbine engines with a single digital program. Such a program (ref. 53) has been developed at the Lewis Research Center and is available for general use.

Real-Time Simulations

The digital computer is not suited for a real-time simulation. An example of a real-time simulation is shown in figure XIII-40. It may be desirable to have an engine simulation that can be controlled by actual control system hardware. If the engine simulation can provide realistic inputs to the control while reacting properly to the control action, it can be a useful tool for evaluating control design and hardware prior to their being tested on the actual engine. This pretesting can significantly reduce the amount of required engine testing. The simulation could also be used to evaluate both research digital controls (ref. 54) and simulated hydromechanical controls.

In order to provide these realistic inputs to the control, the simulation must run in real time and must provide continuous signals at the control interface. General-purpose digital computers (fig. XIII-39) cannot satisfy these simulation requirements. Analog computers can, but they cannot match digital computers in accuracy and they do require considerable computing equipment for large system simulations.

The hybrid computer, because it combines the features of both the analog and digital computers, is an excellent tool for simulating propulsion systems in real time. The analog portion of the hybrid computer provides the required computing speed and interface, while the hybrid's digital computer provides computing accuracies not possible with all-analog simulations. Figure XIII-41 shows that there are limits on the digital work load in a hybrid simulation. Because of the sequential calculations in the digital computer, the more calculations that the digital computer performs, the longer it takes to get a solution. This digital solution time, in a hybrid environment, appears as a time delay to the analog computer and, if large enough, can cause dynamic errors and even instabilities in the simulation. For this reason, the digital work load must be limited, or the simulation must be run slower than real time. In the real-time, hybrid simulations

of the Pratt & Whitney TF30 and F100 engines developed at Lewis (refs. 51 and 52), the digital computer has been limited to performing function generation associated with modeling the fans, compressors, and turbines. Even with this limitation, however, computing accuracies that were unattainable with similar analog simulations have been achieved.

Simulation Applications

Compressor dynamics. - One of the problems is controlling gas turbine engines is to maintain compressor stability during all phases of engine operation. Figure XIII-42 shows a typical compressor map with pressure ratio plotted against equivalent airflow for a range of equivalent rotor speeds. Also shown is a surge line which defines the maximum allowable pressure ratio for stable operation. A given control design might be able to provide adequate surge margin and good performance along a steady-state operating line. However it might not be able to keep the compressor from surging during a "slam" of the power level, for example, from idle to the military power setting. The term "military power" refers to the maximum thrust the engine can deliver without afterburning. The rapid increase in fuel flow to the combustor results in an increase in the compressor pressure ratio. The rotor speed response, however, lags behind the increase in pressure ratio because of the inertia of the rotor. The operating point, therefore, moves toward the surge line until the rotor speed increases. The control must somehow limit the rise in pressure ratio during this transient.

A real-time simulation provides the control designer with an opportunity to observe, on line, the effects of changes in the control design on the compressor's transient performance. For example, figure XIII-43 shows the movement of a simulated compressor's operating point for a series of idle-to-military power level slams. Trace A was obtained with a conventional, schedule-type control. This control did limit the rise in pressure ratio although there was some overshooting of the final value. The dip in the trace was caused by a turbine-temperature-limiting feature in this control. Trace B was obtained with a speed-regulating control. This type of control can provide more rapid speed and thrust responses. Obviously, this particular control design did not provide any surge margin

and would not be tried on a real engine. It should be noted that the actual surge phenomenon was not modeled. The simulation was designed to allow stable operation above the surge line. Trace C was obtained with the same speed-regulating control but with a modified compressor blade schedule. The operating point initially moved toward the military power point, then just skirted the surge line, overshooting in equivalent speed. Further control modifications would be needed to provide sufficient surge margin and satisfactory speed response.

Fail-operational control. - Another control concept currently being investigated at Lewis with the aid of real-time, hybrid simulations is what is referred to as fail-operational control (ref. 55). Figure XIII-44 shows how this control works. As previously indicated, the power of a full-authority digital control could be used to compensate for engine sensor failures. In the fail-operational control, the digital control computer is used to store engine data during normal operation. These data are then used to construct tables or schedules relating each measured engine variable to the other measured variables. The schedules then provide estimates of each measured engine variable. In the example shown in figure XIII-44, an engine pressure is estimated from a measured rotor speed. In the event of a detected pressure sensor failure, the computer would switch from the sensor output to the estimated pressure with, hopefully, no loss in control performance.

Figure XIII-45 demonstrates the potential of this technique. Trace A shows what happens to the simulated compressor operating point when a pressure sensor fails during the idle-to-military power transient. In this case, the sensor was assumed to work properly only at the lower pressures, resulting in the cycling of the pressure ratio and the corresponding sensor output. This would be catastrophic without some form of backup control. Trace B resulted when fail-operational capability was added to this control. There is virtually no difference between this trace and the one obtained with no sensor failure (trace C).

ADVANCED CONTROL THEORY APPLICATION

In the integrated control discussion, it was indicated that some new control hardware will evolve. At the same time, design techniques for

automatic controls have been changing. This is partly due to the availability of on-line digital control. The process control industry, where the number of inputs and outputs is very large, has led these developments. The need to look at the application of these advanced design techniques to the propulsion system is very real.

Figure XIII-46 represents the results of using some Modern Control Theories to design an advanced control. These theories treat the inlet and engine as a whole rather than separately, and the control that results has been labeled a Modern Control. In the Integrated Control (fig. XIII-30), the inlet controls and the engine controls were pretty much designed separately and then tied together. This is denoted by the horizontal arrow. However, this integrated approach may not work for more complex engines. More on these variable cycle concepts appears in conference paper XIV.

In the supersonic propulsion system example, the control inputs include shock position, engine rotor speeds, and other appropriate propulsion system pressures and temperatures. The control outputs are inlet bypass door position, spike position, fuel flows (both main and afterburner), compressor stators or bleeds, and exhaust nozzle area. In the Modern Control, each of these control inputs directly affects each of the control outputs. This allows any control input to be used in the best way. Instead of many controls all tied together, there is now only one control, as in figure XIII-46.

The problem is in designing such a control. How much of an effect should each input have on each output? Modern Control Theory addresses this control design problem. The Lewis Research Center, both in house (refs. 24 to 26 and 56) and through grants and contracts, is looking at these control theories to see if they are applicable to the propulsion control problem. Because Modern Control Theories are mathematically complex, these controls are designed on digital computers for all but the most simple cases.

One design approach is called optimization. First, a performance index must be picked. A performance index is a relative figure of merit which allows the comparison of one control design to another. A simple inlet control was chosen for this example. It has two adjustable control parameters called A and B. The performance index for this control is shown in figure XIII-47. The concave surface is the solution of the performance index for a range of A and B values. In this example, the performance index is related to shock position error and motion; so the best control is at the bottom

of the valley. The best control can be found by evaluating all combinations of A and B, but this is inefficient. Optimization techniques provide systematic schemes for choosing the next control to evaluate, and the best control can be searched out without solving the entire surface.

In figure XIII-47, the starting control design given the computer is at the upper right on the surface. The figure shows the path taken by the computer. The control designs evaluated by the computer are connected by the straight lines. The computer takes smaller steps as it gets closer to the minimum point, or best control. This example used the Conjugate Gradient Search Method and was taken from reference 26. This procedure works for more complex controls, but it is difficult to show what happens for more than two control parameters at a time. It is only one of many such procedures which can be used for designing controls.

Hopefully, advanced control theories will provide powerful control design techniques. The use of computers should allow some of the cut-and-try design methods to be abandoned. Finally, advanced control theories should enable full advantage to be made of the digital computer for propulsion system control.

CONCLUDING REMARKS

Airbreathing propulsion is now faced and will continue to be faced with interesting and important systems problems. For supersonic cruise, inlet design improvements can have an important effect on aircraft range. Propulsion controls are evolving toward greater reliance on electronic digital control, thus permitting better and more complex control schemes. At the same time, simple control mechanizations, like the valved throat bleed, can complement the more complex control schemes. Integration to make inlet and engine controls work together can ease the requirements on individual control loops and increase overall efficiency. Digital controls can automatically compensate for component failures, thus partially overcoming the lower reliability of electronics. Propulsion simulation with a computer that gives accurate real-time results is now possible. And Modern Control Theory that uniformly treats a multivariable system will probably improve propulsion control.

REFERENCES

1. Cole, Gary L.; Neiner, George H.; and Wallhagen, Robert E.: Coupled Supersonic Inlet-Engine Control Using Overboard Bypass Doors and Engine Speed to Control Normal Shock Position. NASA TN D-6019, 1970.

2. Paulovich, Francis J.; Neiner, George H.; and Hagedorn, Ralph E.: A Supersonic Inlet-Engine Control Using Engine Speed as a Primary Variable for Controlling Normal Shock Position. NASA TN D-6021, 1971.

3. Wallhagen, Robert E.; Paulovich, Francis J.; and Geyser, Lucille C.: Dynamics of a Supersonic Inlet-Engine Combination Subjected to Disturbances in Fuel Flow and Inlet Overboard Bypass Airflow. NASA TM X-2558, 1972.

4. Bowditch, David N.: Some Design Considerations for Supersonic Cruise Mixed-Compression Inlets. AIAA Paper 73-1269, Nov. 1973.

5. Aircraft Propulsion. NASA SP-259, 1971.

6. Wasserbauer, Joseph F.; Shaw, Robert J.; and Neumann, Harvey E.: Design of a Very-Low-Bleed Mach 2.5 Mixed-Compression Inlet with 45 Percent Internal Contraction. NASA TM X-3135, 1975.

7. Neumann, Harvey E.; Wasserbauer, Joseph F.; and Shaw, Robert J.: Performance of Vortex Generators in a Mach 2.5 Low-Bleed Full-Scale 45 Percent Internal Contraction Axisymmetric Inlet. NASA TM X-3195, 1975.

8. Wasserbauer, Joseph F.: Neumann, Harvey E.; and Shaw, Robert J.: Distortion in a Full-Scale Bicone Inlet with Internal Focused Compression and 45 Percent Internal Contraction. NASA TM X-3133, 1974.

9. Wasserbauer, Joseph F.; and Willoh, Ross G.: Experimental and Analytical Investigation of the Dynamic Response of a Supersonic Mixed-Compression Inlet. AIAA Paper 68-651, June 1968.

10. Crosby, Michael J.; Neiner, George H.; and Cole, Gary L.: Restart and High Response Terminal Shock Control for an Axisymmetric Mixed-Compression Inlet with 60 Percent Internal Contraction. NASA TM X-1792, 1969.

11. Cole, Gary L.; Neiner, George H.; and Crosby, Michael J.: An Automatic Restart Control System for an Axisymmetric Mixed-Compression Inlet. NASA TN D-5590, 1969.

12. Neiner, George H.; Crosby, Michael J.; and Cole, Gary L.: Experimental and Analytical Investigation of Fast Normal Shock Position Controls for a Mach 2.5 Mixed-Compression Inlet. NASA TN D-6382, 1971.

13. Neiner, George H.; Cole, Gary L.; and Arpasi, Dale J.: Digital-Computer Normal-Shock-Position and Restart Control of a Mach 2.5 Axisymmetric Mixed-Compression Inlet. NASA TN D-6880, 1972.

14. Baumbick, Robert J.; Neiner, George H.; and Cole, Gary L.: Experimental Dynamic Response of a Two-Dimensional, Mach 2.7, Mixed-Compression Inlet. NASA TN D-6957, 1972.

15. Cole, Gary L.; Neiner, George H.; and Baumbick, Robert J.: Terminal Shock Position and Restart Control of a Mach 2.7, Two-Dimensional, Twin-Duct Mixed-Compression Inlet. NASA TM X-2818, 1973.

16. Baumbick, Robert J.; Wallhagen, Robert E.; Neiner, George H.; and Batterton, Peter G.: Dynamic Response of Mach 2.5 Axisymmetric Inlet with 40 Percent Supersonic Internal Area Contraction. NASA TM X-2833, 1973.

17. Baumbick, Robert J.; Wallhagen, Robert E.; and Seidel, Robert C.: Terminal-Shock and Restart Control for a Mach 2.5, Axisymmetric, Mixed-Compression Inlet with 40 Percent Internal Contraction. NASA TM X-2992, 1974.

18. Wind-Tunnel Installation of Full-Scale Flight Inlet of YF-12 Aircraft for Steady-State and Dynamic Evaluation. NASA TM X-3138, 1974.

19. Cole, Gary L.; Cwynar, David S.; and Geyser, Lucille C.: Wind-Tunnel Evaluation of the Response of a YF-12 Aircraft Flight Inlet to Internal Airflow Perturbations by Frequency-Response Testing. NASA TM X-3141, 1974.

20. Neiner, George H.; Arpasi, Dale J.; and Dustin, Miles O.: Wind-Tunnel Evaluation of YF-12 Aircraft Inlet Control System by Frequency-Response and Transient Testing. NASA TM X-3142, 1974.

21. Neiner, George H.; Seidel, Robert C.; and Arpasi, Dale J.: Wind-Tunnel Evaluation of Experimental Controls on YF-12 Aircraft Inlet by Frequency-Response and Transient Testing. NASA TM X-3143, 1974.

22. Willoh, Ross G.: A Mathematical Analysis of Supersonic Inlet Dynamics. NASA TN D-4969, 1968.

23. Cole, Gary L.; and Willoh, Ross G., Jr.: Analysis of the Dynamic Response of a Supersoinc Inlet to Flow-Field Perturbations Upstream of the Normal Shock. NASA TN D-7839, 1975.

24. Lehtinen, Bruce; Zeller, John R.; and Geyser, Lucille C.: Optimal Control of Supersonic Inlets to Minimize Unstarts. NASA TN D-6408, 1971.

25. Zeller, John R.; Lehtinen, Bruce; Geyser, Lucille C.; and Batterton, Peter G.: Analytical and Experimental Performance of Optimal Controller Designs for a Supersonic Inlet. NASA TN D-7188, 1973.

26. Seidel, Robert C.; and Lehtinen, Bruce: Control System Design Using Frequency Domain Models and Parameter Optimization, with Application to Supersonic Inlet Controls. NASA TM X-3108, 1974.

27. Cole, Gary L.; Neiner, George H.; and Crosby, Michael J.: Design and Performance of a Digital Electronic Normal Shock Position Sensor for Mixed-Compression Inlet. NASA TN D-5606, 1969.

28. Dustin, Miles O.; Cole, Gary L.; and Wallhagen, Robert E.: Determination of Normal-Shock Position in a Mixed-Compression Supersonic Inlet. NASA TM X-2397, 1971.

29. Dustin, Miles O.; and Cole, Gary L.: Performance Comparison of Three Normal-Shock Position Sensors for Mixed-Compression Inlets. NASA TM X-2739, 1973.

30. Dustin, Miles O.; Cole, Gary L.; and Neiner, George H.: Continuous-Output Terminal-Shock-Position Sensor for Mixed-Compression Inlets Evaluated in Wind-Tunnel Tests of YF-12 Aircraft Inlet. NASA TM X-3144, 1974.

31. Zeller, John R.: Design and Analysis of a Modular Servoamplifier for Fast-Response Electrohydraulic Control Systems. NASA TN D-4898, 1968.

32. Batterton, Peter G.; and Zeller, John R.: Performance Characteristics of Improved Servoamplifier for Electrohydraulic Control Systems. NASA TM X-2167, 1971.

33. Zeller, John R.: Analysis of Dynamic Performance Limitations of Fast Response (150 to 200 Hz) Electrohydraulic Servos. NASA TN D-5388, 1969.

34. Zeller, John R.; and Webb, John A., Jr.: Determination and Evaluation of Performance Limit Criteria of Fast-Response Electohydraulic Servosystems. NASA TM X-2736, 1973.

35. Webb, John A., Jr.; Mehmed, Oral; and Hiller, Kirby W.: Improved Design of a High-Response Slotted-Plate Overboard Bypass Valve for Supersonic Inlets. NASA TM X-2812, 1973.

36. Gebben, Vernon D.: High Capacity, Compact Vortex Valve for Increasing Stability of Supersonic Mixed-Compression Inlets. NASA TN D-6662, 1972.

37. Sanders, Bobby W.; and Mitchell, Glenn A.: Throat-Bypass Bleed Systems for Increasing the Stable Airflow Range of a Mach 2.5 Axisymmetric Inlet with 40 Percent Internal Contraction. NASA TM X-2779, 1973.

38. Mitchell, Glenn A.; and Sanders, Bobby W.: Pressure-Actuated Stability-Bypass-Control Valves to Increase the Stable Airflow Range of a Mach 2.5 Inlet with 40 Percent Internal Contraction. NASA TM X-2972, 1974.

39. Sanders, Bobby W.; and Mitchell, Glenn A.: Increasing the Stable Operating Range of a Mach 2.5 Inlet. AIAA Paper 70-686, June 1970.

40. Mitchell, Glenn A.; and Sanders, Bobby W.: Airflow Control System for Supersonic Inlets. U.S. Patent 3,799,475, March 26, 1974.

41. Batterton, Peter G.; Arpasi, Dale J.; and Baumbick, Robert J.: Digital Integrated Control of a Mach 2.5 Mixed-Compression Supersonic Inlet and an Augmented Mixed-Flow Turbofan Engine. NASA TM X-3075, 1974.

42. Dustin, Miles O.; and Neiner, George H.: Evaluation by Step Response Tests of Prototype Relief Valves Designed for YF-12 Inlet Stability Bleed System. NASA TM X-3262, 1975.

43. Webb, John A., Jr.; and Dustin, Miles O.: Analysis of a Stability Valve System for Extending the Dynamic Range of a Supersonic Inlet. NASA TM X-3219, 1975.

44. Beatz, Charles E.; and Zeller, John R.: Integrated Propulsion Control System Program. SAE Paper 730359, Apr. 1973.

45. McKinney, John S.: Simulation of Turbofan Engine, Part 1: Description of Method and Balancing Technique. AFAPL-TR-67-125, Air Force Aero Propulsion Laboratory, Air Force Systems Command (AD-825197), 1967.

46. McKinney, John S.: Simulation of Turbofan Engine. Part 2: User's Manual and Computer Program Listing. AFAPL-TR-67-125, Air Force Aero Propulsion Laboratory, Air Force Systems Command (AD-825198), 1967.

47. Koenig, Robert W.; and Fishbach, Laurence H.: GENENG - A Program for Calculating Design Performance for Turbojet and Turbofan Engines. NASA TN D-6552, 1972.

48. Fishbach, Laurence H.; and Koenig, Robert W.: GENENG II - A Program for Calculating Design and Off-Design Performance of Two- and Three-Spool Turbofans with as Many as Three Nozzles. NASA TN D-6553, 1972.

49. Seldner, Kurt; Mihaloew, James R.; and Blaha, Ronald J.: Generalized Simulation Technique for Turbojet Engine System Analysis. NASA TN D-6610, 1972.

50. Szuch, John R.: HYDES: A Generalized Hybrid Computer Program for Studying Turbojet or Turbofan Engine Dynamics. NASA TM X-3014, 1974.

51. Szuch, John R.; and Bruton, William M.: Real-Time Simulation of the TF30-P-3 Turbofan Engine Using a Hybrid Computer. NASA TM X-3106, 1974.

52. Szuch, John R.; and Seldner, Kurt: Real-Time Simulation of F100-PW-100 Turbofan Engine Using the Hybrid Computer. NASA TM X-3261, 1975.

53. Sellers, James F.; and Daniele, Carl J.: DYNGEN - A Program for Calculating Steady-State and Transient Performance of Turbojet and Turbofan Engines. NASA TN D-7901, 1975.

54. Cwynar, David S.; and Batterton, Peter G.: Digital Implementation of the TF30-P-3 Turbofan Engine Control. NASA TM X-3105, 1974.

55. Hrach, Frank J.; Arpasi, Dale J.; and Bruton, William M.: Design and Evaluation of a Sensor Fail-Operational Control System for a Digitally Controlled Turbofan Engine. NASA TM X-3260, 1975.

56. Geyser, Lucille C.; and Lehtinen, Bruce: Digital Program for Solving the Linear Stochastic Optimal Control and Estimation Problem. NASA TN D-7820, 1975.
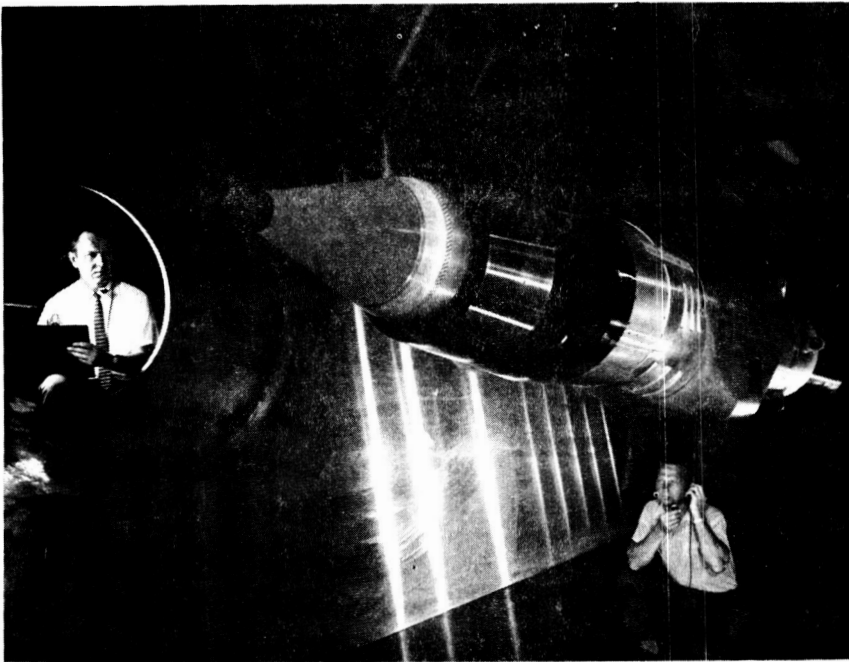
CS-73362

Figure XIII-1. - Supersonic cruise propulsion system - turbojet.
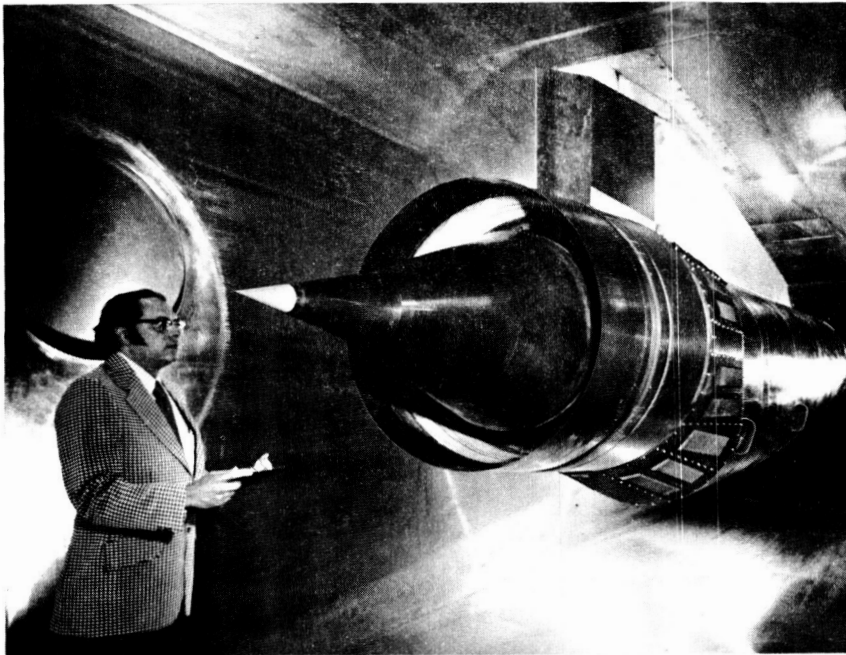
CS-73361

Figure XIII-2. - Supersonic cruise propulsion system - turbofan.

417

AXISYMMETRIC   TWO-DIMENSIONAL DOUBLE WEDGE   TWO-DIMENSIONAL SINGLE WEDGE
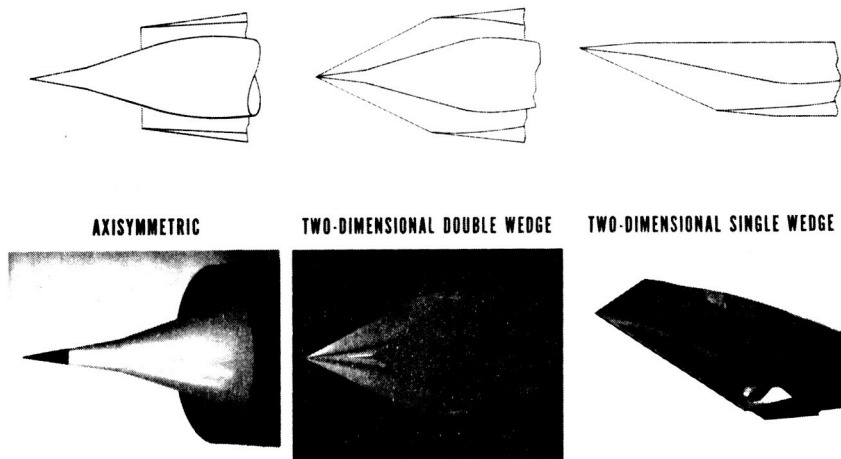
Figure XIII-3. - Inlet concepts.
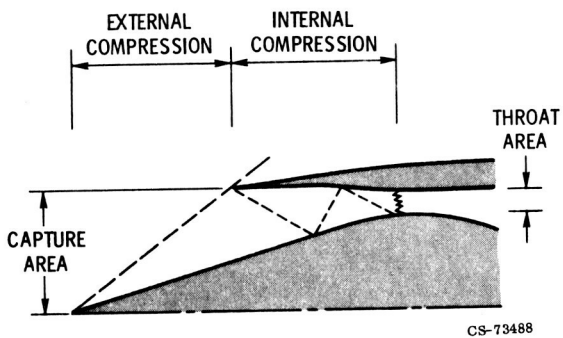
Figure XIII-4. - Definition of internal compression.
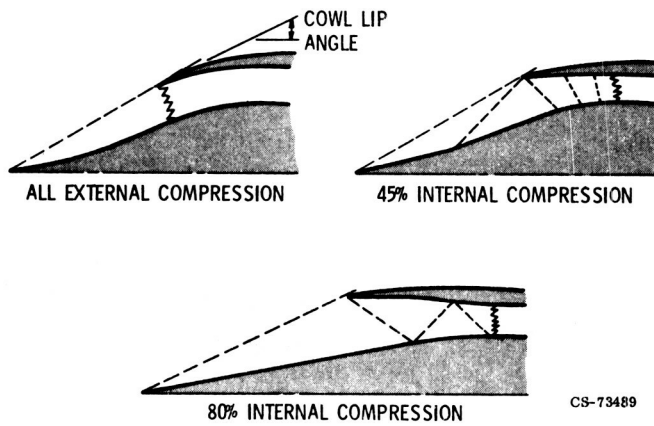
Figure XIII-5. - Inlet designs using different percentages of internal compression.
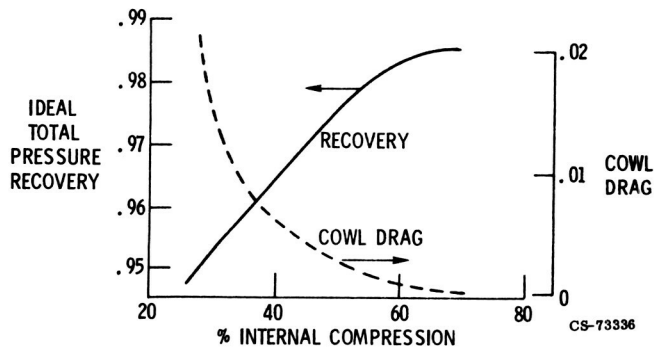
Figure XIII-6. - Effect of internal compression on total pressure recovery and cowl drag. Mach number, 2.5.
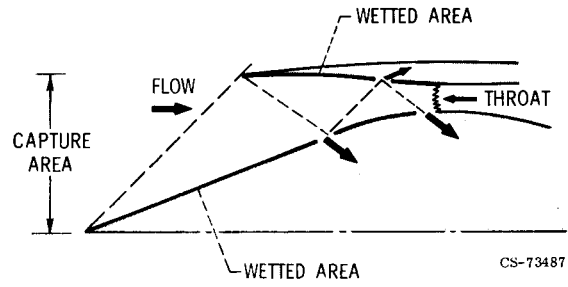
Figure XIII-7. - Mixed-compression supersonic inlet with
boundary layer bleed.
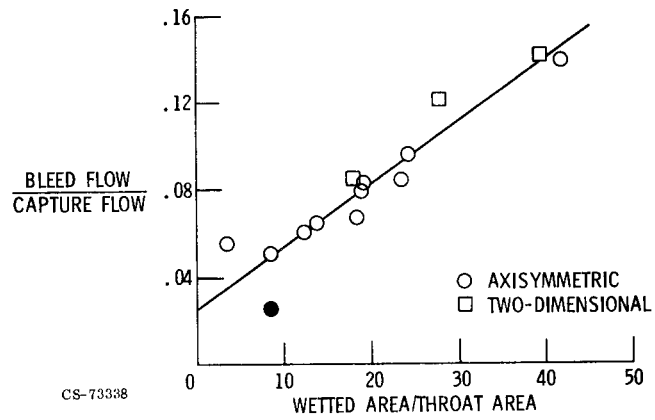
Figure XIII-8. - Correlation of bleed flow with wetted area. Mach
number, 2.5 to 3.5.
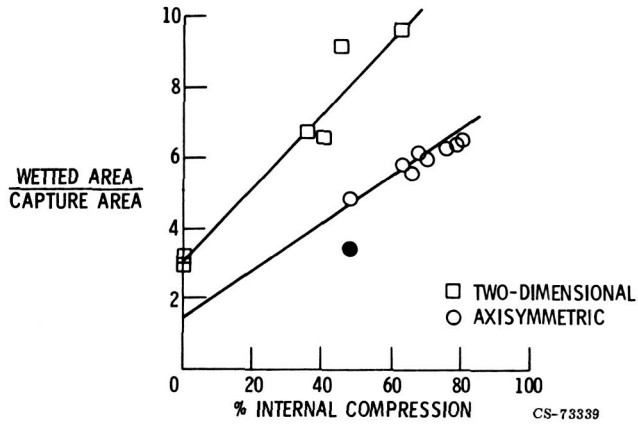
Figure XIII-9. - Correlation of wetted area with internal compression. Mach number, 2.5 to 3.5.
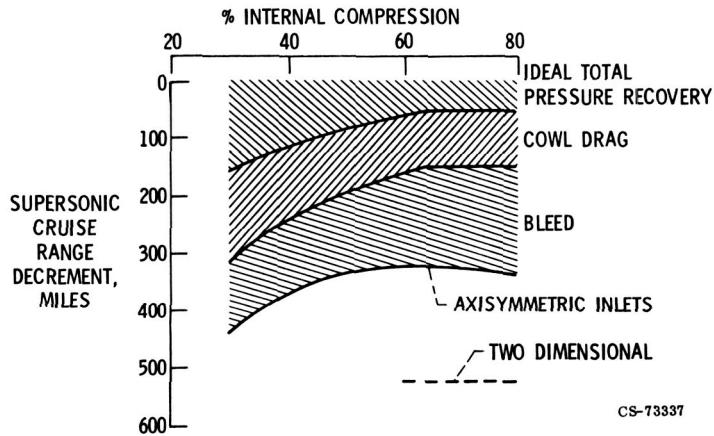
Figure XIII-10. - Effect of internal compression on aircraft range. Mach number, 2.5.

421

STARTED

FLOW

UNSTARTED　　CS-73490
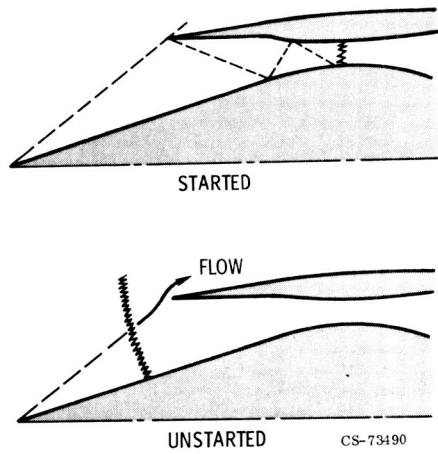
Figure XIII-11. - Definition of inlet unstart.

M_0

ZERO DEG
ANGLE OF ATTACK

M_0

ANGLE OF ATTACK
OPERATION

CS-73486
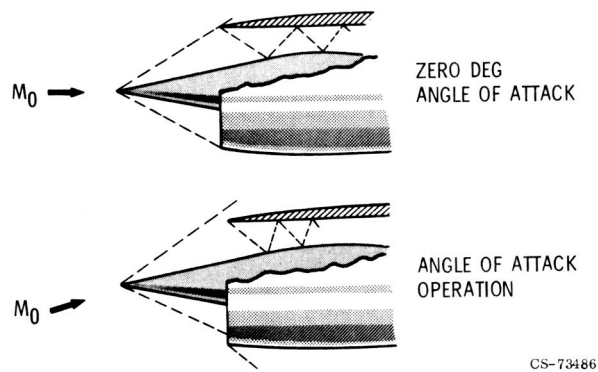
Figure XIII-12. - Modification of inlet shock structure at angle
of attack.
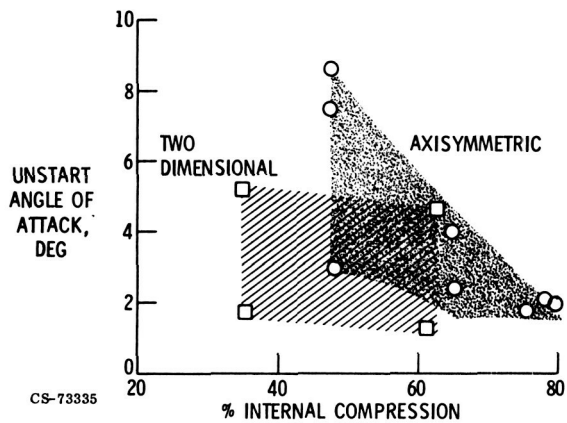
Figure XIII-13. - Effect of internal compression on unstart angle of attack. Mach number, 2.5 to 3.5.
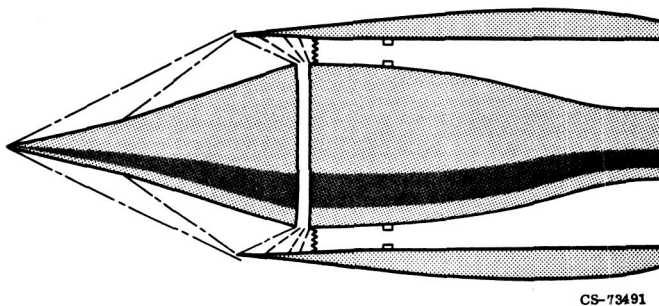
Figure XIII-14. - Low-bleed inlet. Percentage of internal compression, 45; Mach number, 2.5; inlet type, axisymmetric.
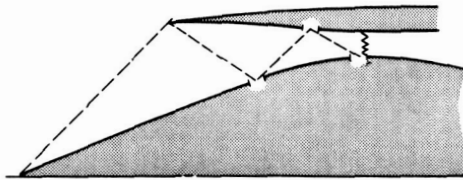
Figure XIII-15. - Typical internal shock structure.   CS-73800
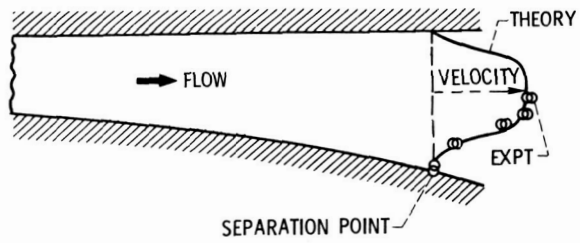
Figure XIII-16. - Flow separation in a subsonic diffuser.
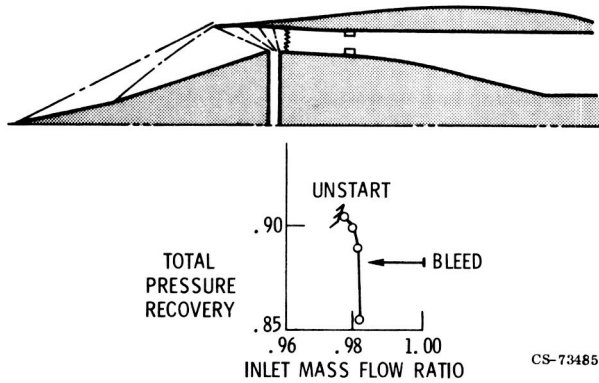
Figure XIII-17. - Overall performance of low-bleed inlet.

CS-73524
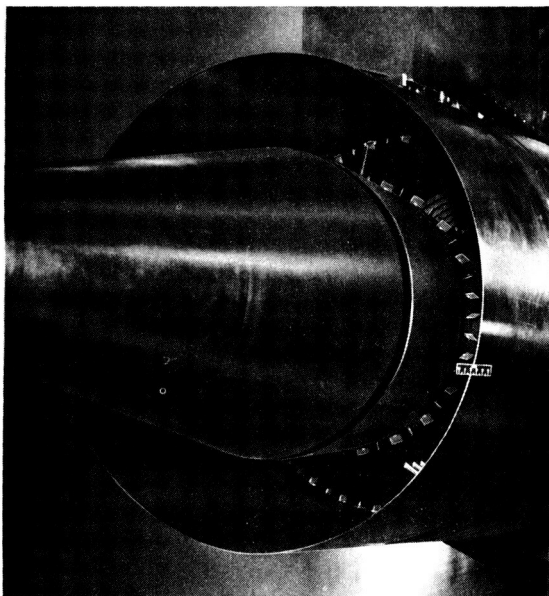
Figure XIII-18. - Low-bleed inlet installed in wind tunnel.

ORIGINAL PAGE
BLACK AND WHITE PHOTOGRAPH
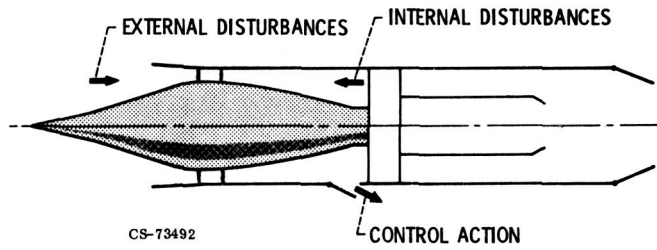
Figure XIII-19. – General inlet control problem.
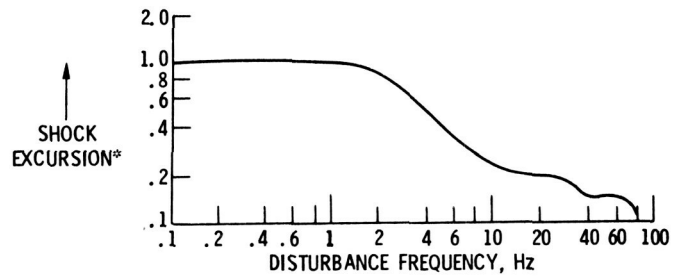
*INFERRED FROM THROAT STATIC PRESSURE EXCURSION.

Figure XIII-20. – Frequency response of low-bleed-inlet shock position.
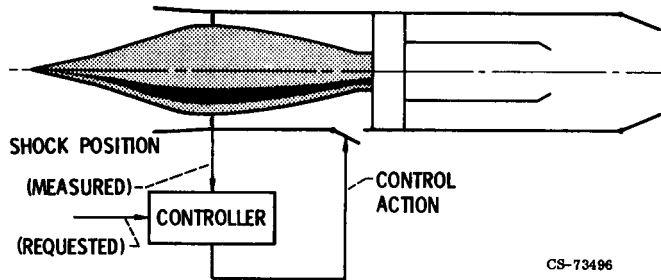
Figure XIII-21. - Inlet control with bypass doors.
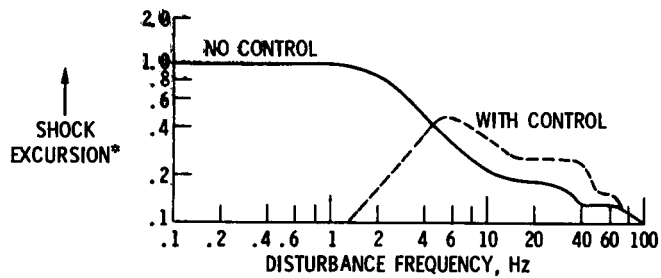
*INFERRED FROM THROAT EXIT STATIC PRESSURE MEASUREMENT.

CS-73370

Figure XIII-22. - Dynamic behavior of bypass-door controlled inlet.

427

% CHANGE
IN ENGINE
AIRFLOW

TIME, SEC

CS-73363
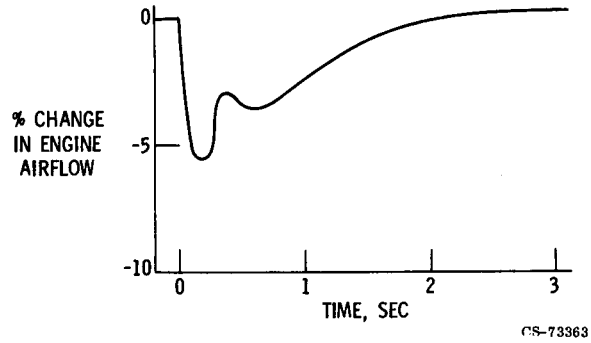
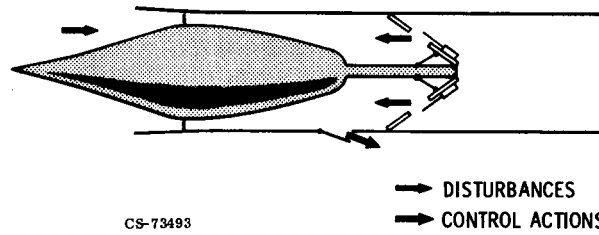Figure XIII-23. - Airflow disturbance induced by afterburner lightoff.

CS-73493

➡ DISTURBANCES
➡ CONTROL ACTIONS

Figure XIII-24. - Engine airflow simulator - schematic representation.
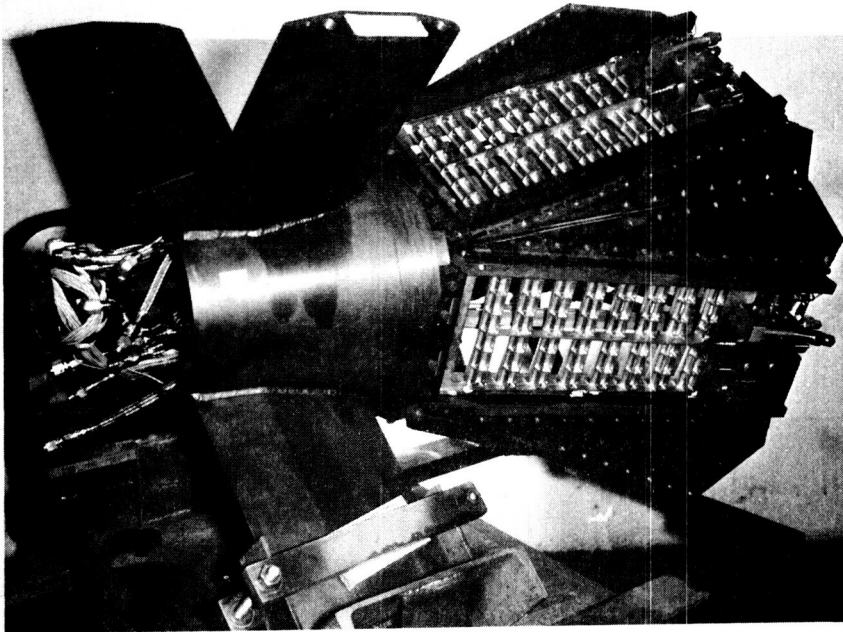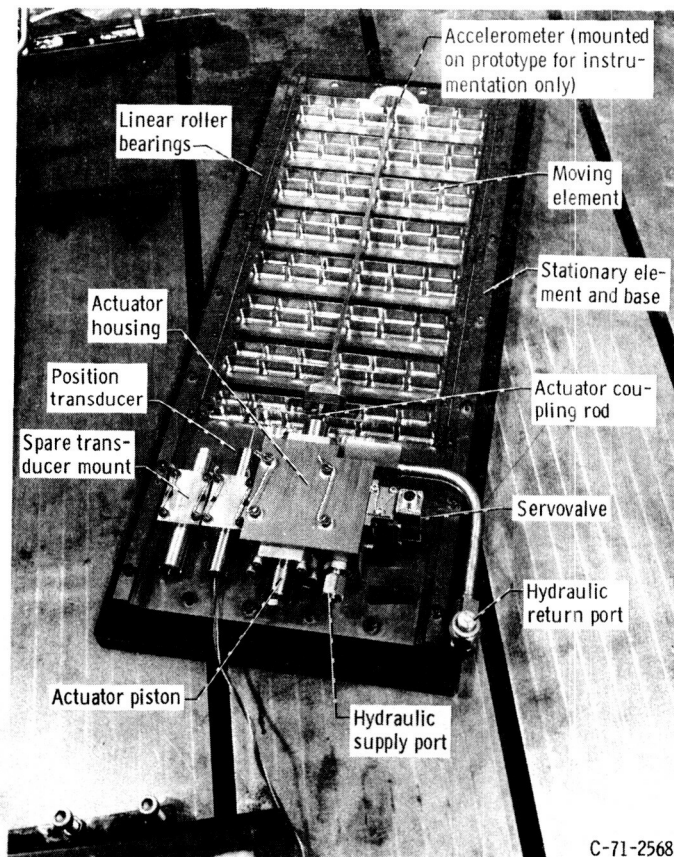
Figure XIII-25. - Engine airflow simulator - photograph.
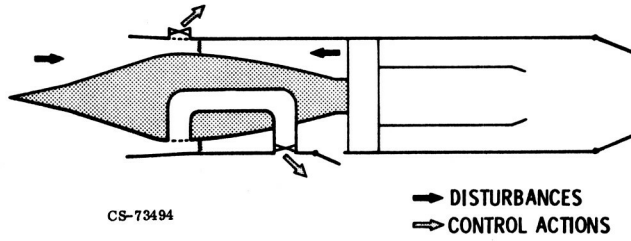

Figure XIII-26. - Closeup of fast-acting valve.

C-71-2568

429

CS-73494

➡ DISTURBANCES
⇨ CONTROL ACTIONS

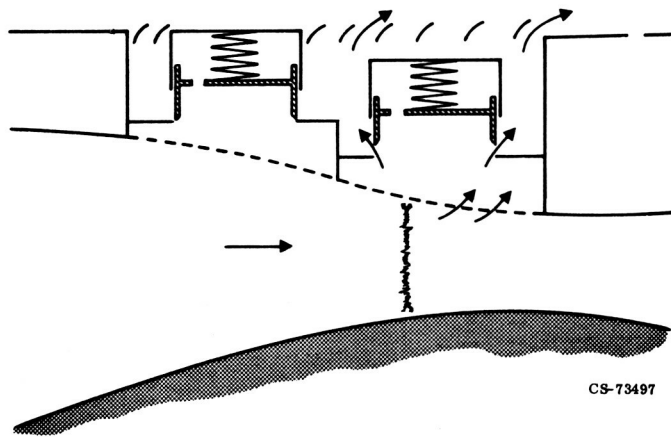Figure XIII-27. - Inlet control with throat bypass bleed.

CS-73497

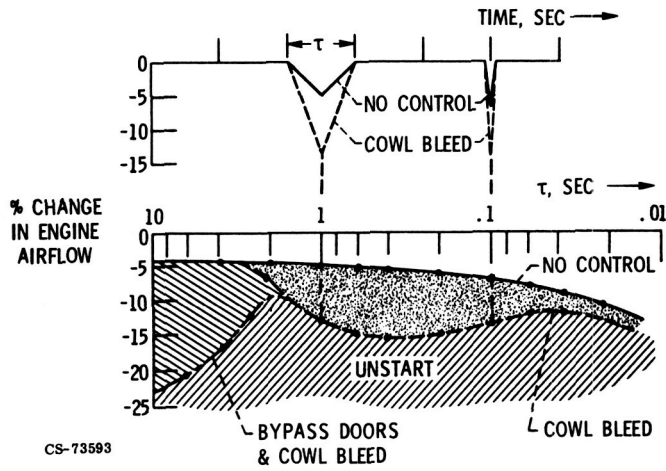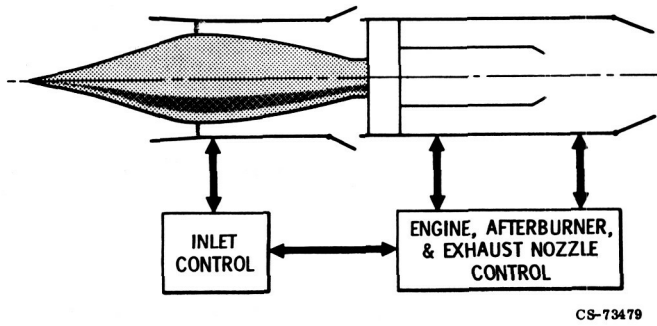Figure XIII-28. - Inlet throat showing stability valves for cowl bleed.

Figure XIII-29. - Effectiveness of cowl bleed system - YF-12 at Mach 2.5.

Figure XIII-30. - Integrated control.
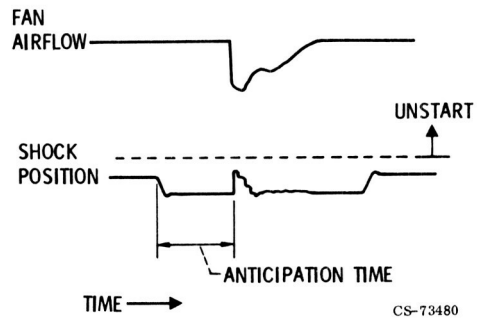
Figure XIII-31. - Integrated control with anticipation for afterburner lightoff.
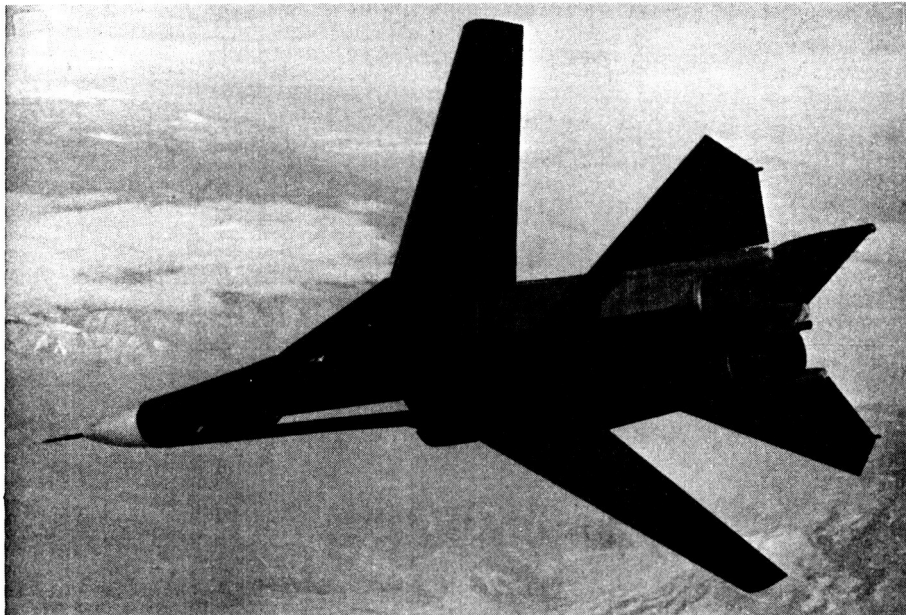
CS-73348

Figure XIII-32. - F-111E aircraft modified for Integrated Propulsion Control System tests.
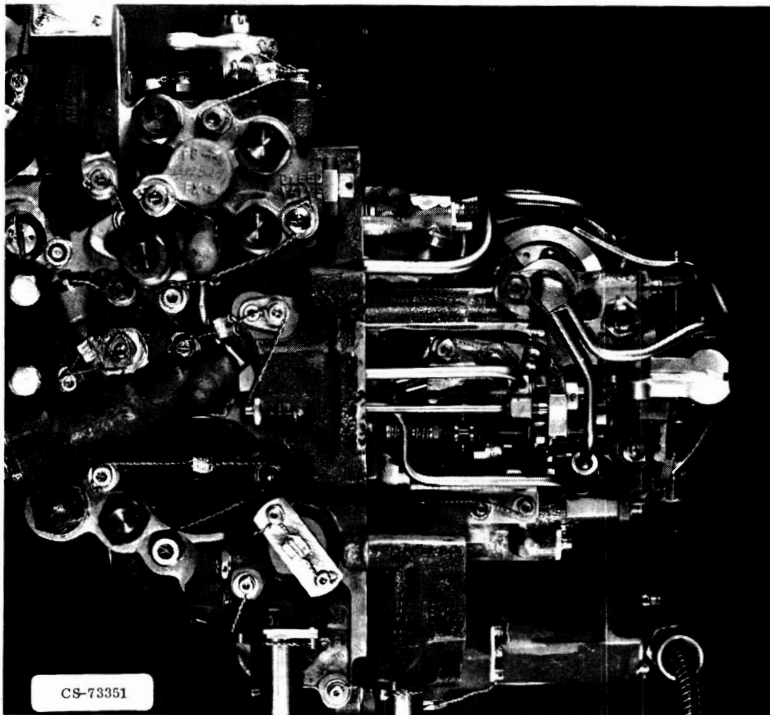
CS-73351

Figure XIII-33. - Hydromechanical fuel control for TF30 turbofan engine.

CONTROL
REQUIREMENTS

ALL ELECTRONIC
DIGITAL

ELECT. DIGITAL
HYDROMECH
BACKUP

HYDROMECH
ELECT. TRIM

HYDROMECH

1970   1975   1980
TIME
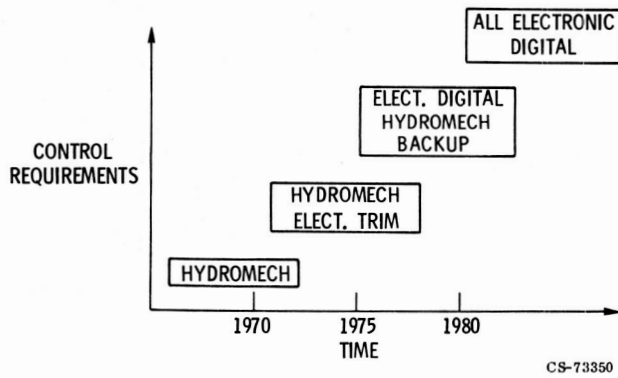
CS-73350

Figure XIII-34. - Probable evolution of control system mechanization.
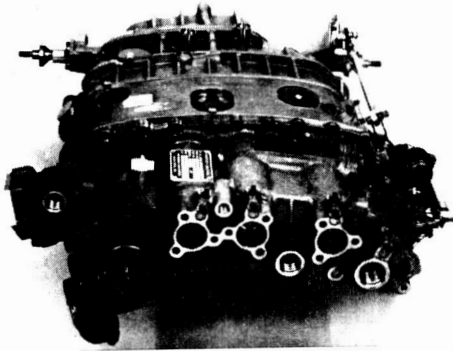
HYDROMECHANICAL   ELECTRONIC TRIM COMPUTER
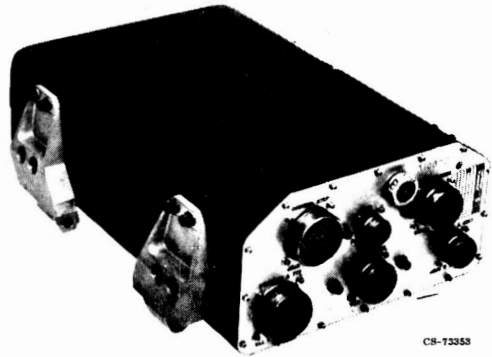
CS-73353

Figure XIII-35. - Hydromechanical engine control with electronic trim, for F100 turbofan engine.
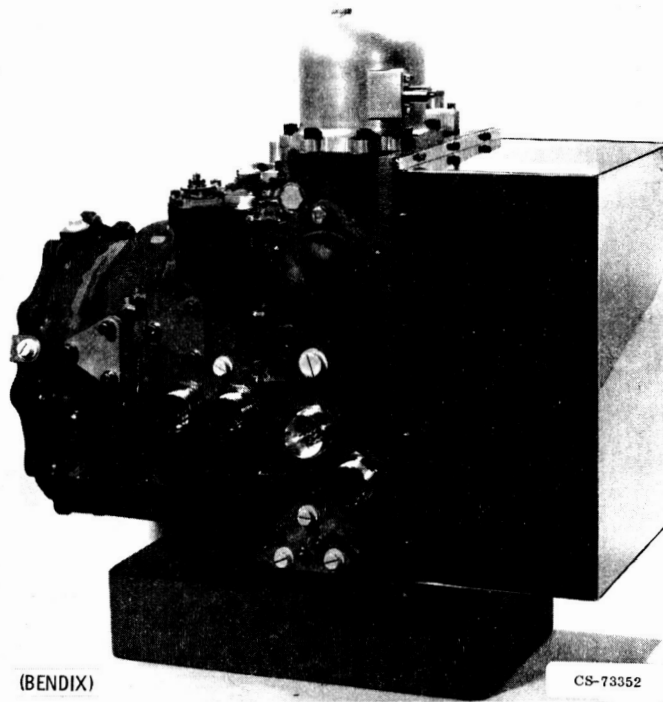
(BENDIX)   CS-73352

Figure XIII-36. - Full-authority, all-electronic digital control.

ORIGINAL PAGE
BLACK AND WHITE PHOTOGRAPH
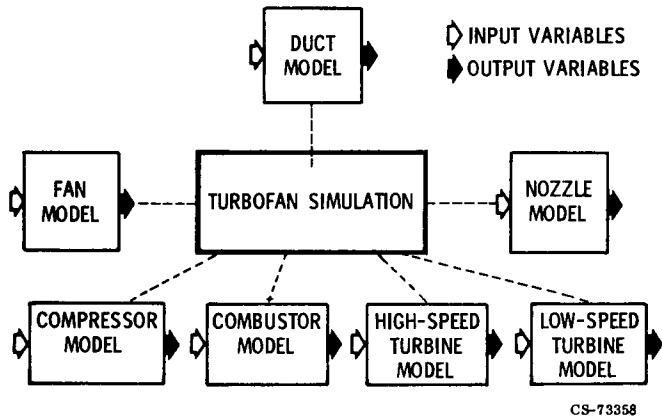
Figure XIII-37. - Approach to simulating complex systems.

STEADY-STATE
    SOLUTION WITH FIXED
        FLIGHT CONDITION
        PILOT COMMANDS
        SYSTEM PARAMETERS
TRANSIENT
    RESPONSE TO CHANGES IN
        FLIGHT CONDITION
        PILOT COMMANDS
        SYSTEM PARAMETERS

COMPRESSOR
PRESSURE
RATIO

COMPRESSOR AIRFLOW

TIME

CS-73359
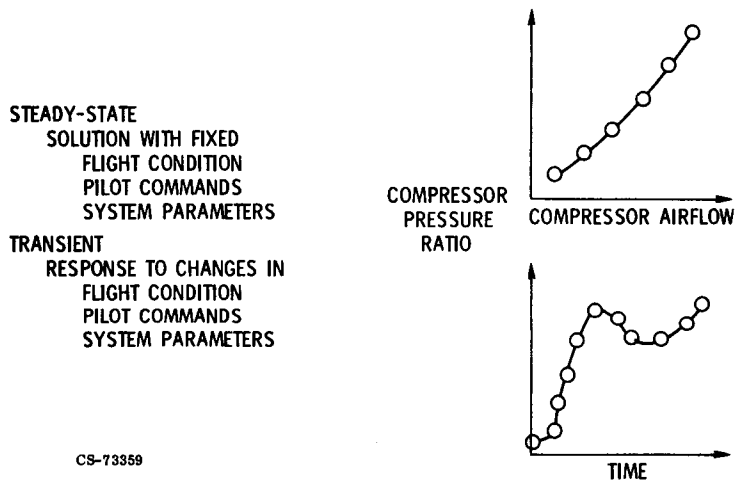
Figure XIII-38. - Categories of propulsion system simulations.
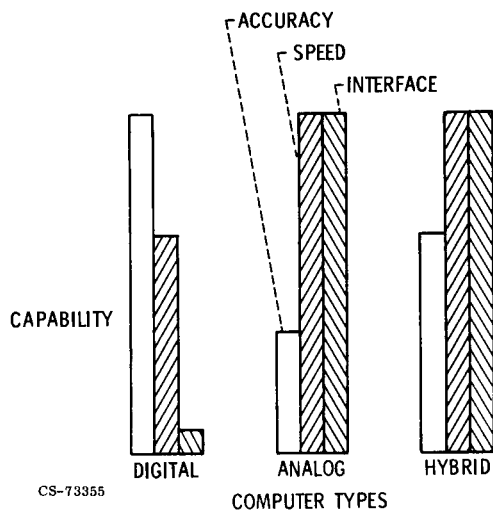
Figure III-39. - Comparison of computers used for simulation.
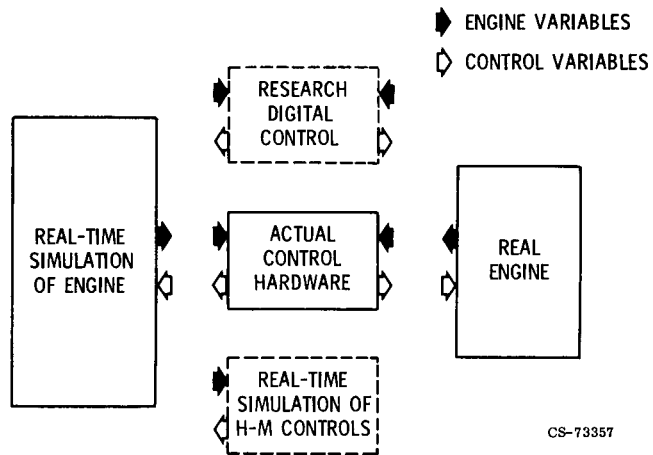
Figure XIII-40. - Evaluation of control system using real-time computer simulation.

REAL-TIME
CAPABILITY

SLOW-TIME
REQUIRED

DIGITAL
SOLUTION TIME

0

100

DIGITAL WORK LOAD, %

CS-73356

(ALL ANALOG)

(ALL DIGITAL)
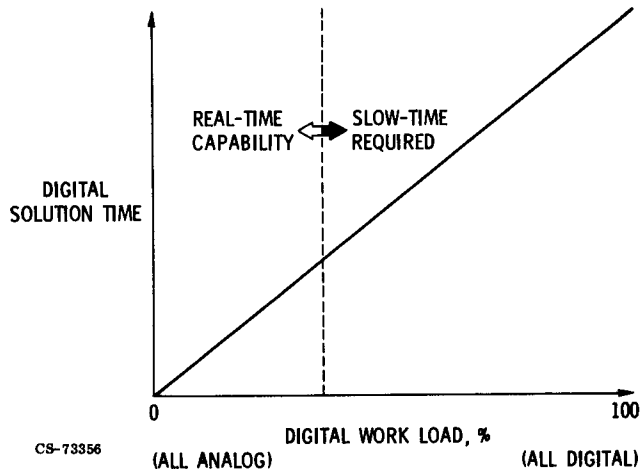
Figure XIII-41. - Limits on digital workload in hybrid simulation.

SURGE LINE

TRANSIENT

COMPRESSOR
PRESSURE
RATIO

MILITARY

IDLE

COMPRESSOR
EQUIV
SPEED,
%

110

STEADY-
STATE

100

90

80

70

IDLE

MILITARY

COMPRESSOR EQUIV AIRFLOW

CS-73360
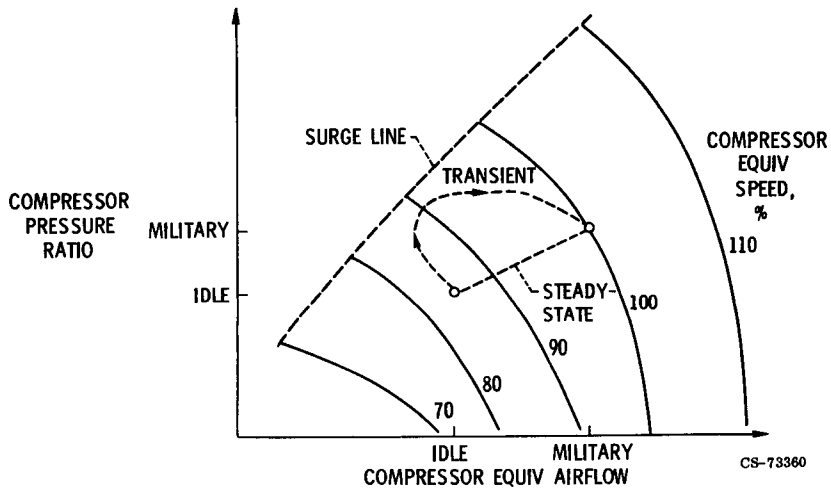
Figure XIII-42. - Compressor transient performance.

437

COMPRESSOR
PRESSURE
RATIO

MILITARY ———

IDLE ———

A SCHEDULED CONTROL
B SPEED-REGULATING CONTROL
C MODIFIED BLEED SCHEDULE

SURGE LINE

IDLE   MILITARY
COMPRESSOR EQUIV AIRFLOW
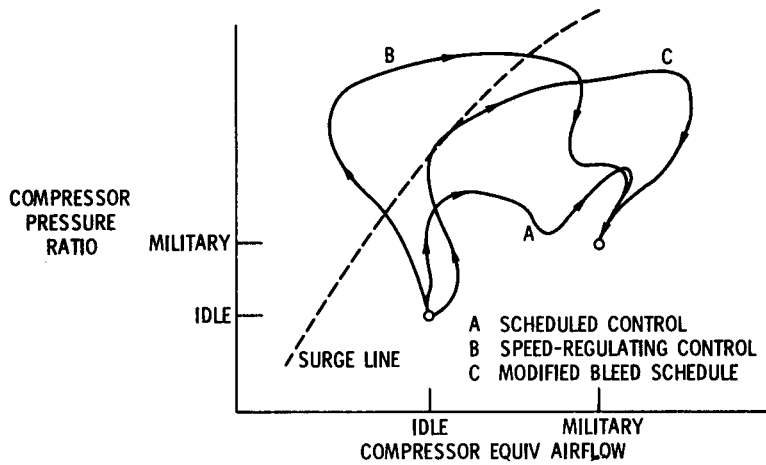
Figure XIII-43. - Movement of compressor operating point for series of power lever slams.

MEASURED SPEED

FAIL-OP SCHEDULE

ESTIMATED PRESSURE

SWITCH

BASIC CONTROL FUNCTIONS

CONTROL VARIABLES TO ENGINE

MEASURED PRESSURE

DIGITAL CONTROL COMPUTER

CS-73354

Figure XIII-44. - Fail-operational control.

Figure XIII-45. - Example of fail-operational control.
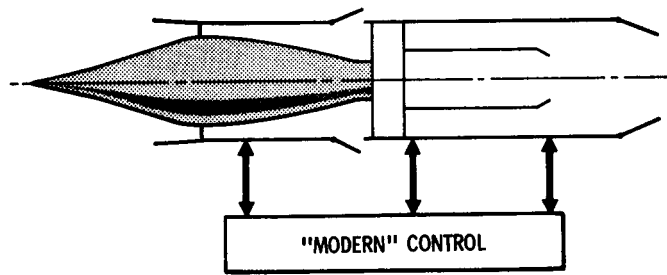
Figure XIII-46. - Advanced control theory.
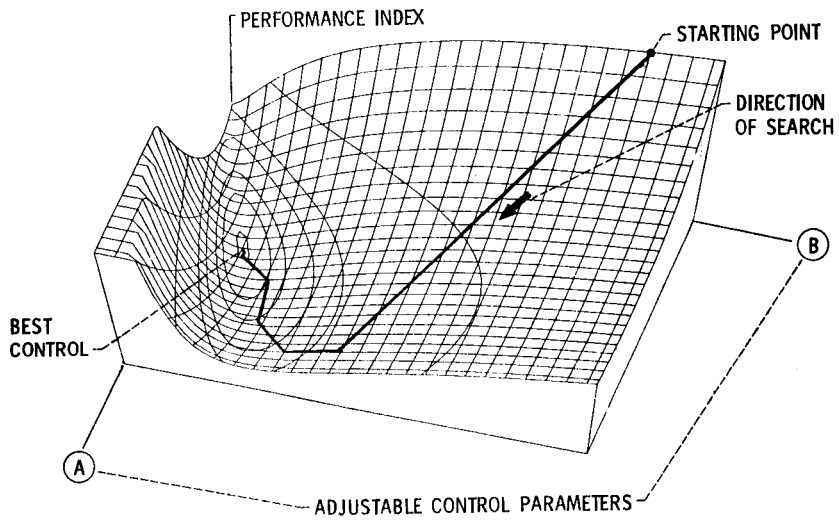
Figure XIII-47. - Control optimization.

XIV. SUPERSONIC PROPULSION

John B. Whitlow, Jr.

NASA has been engaged in a Supersonic Cruise Airplane Research (SCAR) technology program since October 1972. Unlike the SST program, which was canceled in 1971 because of technological, environmental, and financial problems, SCAR is not a program to design and build a supersonic transport. It is aimed instead at advancing the technologies needed for the successful development of any future supersonic airplane, such as the one shown in figure XIV-1. This airplane is a modified arrow-wing concept. It has excellent supersonic-cruise aerodynamics, but the more complicated structure may be heavier than that of the simpler delta-wing concept. Technological advances which lighten the airframe could considerably benefit airplanes such as this. The use of composite structure in such an airframe could result in considerable weight reduction once composite technology is better developed. Active controls, also, could lighten the structure and at the same time improve the aerodynamics.

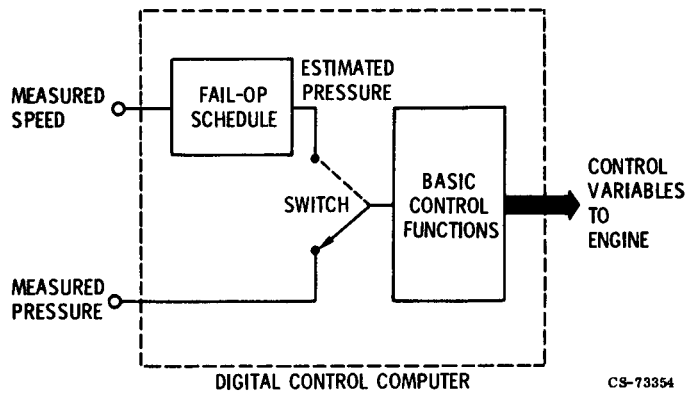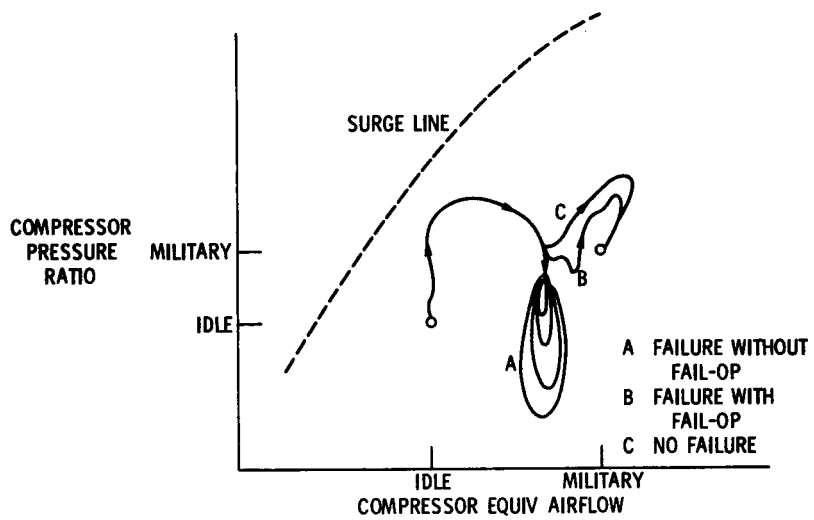A major part of the SCAR program involves seeking advances in such technologies. These activities are being performed by other NASA research centers - both in house and under contract. The interest at NASA Lewis Research Center is primarily in the improvement of the needed propulsion system technology. An advanced propulsion system is needed to supply high thrust at supersonic conditions while retaining good fuel economy both supersonically and subsonically. An engine with low takeoff noise characteristics is also needed. It is difficult for a conventional engine to meet all these requirements simultaneously.

MISSION REQUIREMENTS

One of the most important mission choices to be made is that of supersonic-cruise Mach number. In figure XIV-2, the relative operating

441

cost on a seat-mile basis is shown as a function of cruise Mach number for a variety of airplanes. These operating costs are normalized to that of a current wide-body jet. The figure shows that the current SST's operate at about Mach 2 and have operating costs about three times that of the reference wide-body jet. Some of the initial SCAR study results from 1973 (top curve, fig. XIV-2) show that very high Mach numbers increase the operating cost. According to these results, even at Mach 2.7 there would be an operating cost penalty of more than 40 percent relative to the current wide-body jets. On the other hand, productivity considerations argue strongly for a Mach number of 2 or more. The initial SCAR study effort, therefore, concentrated on the range from 2.2 to 2.7. The goal, as shown by the lower curve, is to reduce the SCAR operating cost to a level comparable to that of the current wide-body jets.

Once a Mach number band of interest has been chosen, mission range can be considered. The traffic projections in figure XIV-3 show how passenger-miles are distributed according to the distances traveled. A total of 5046 international city-pairs were considered in this traffic survey. The bumpy shape of these curves is related to the inclusion of certain large segments of the total market within discrete range bands - for example, virtually all the transatlantic market can be included within a 4000-nautical-mile range. As a minimum for transatlantic operation, a 3200-mile range is needed. Major parts of the transpacific market are included at the 5000-mile range.

Low-level traffic growth projections were used in arriving at the traffic estimates for the years 1980 and 2000 shown in figure XIV-3. They were based on an annual growth rate which decreases to 2 percent in the year 2000. (Total free-world traffic grew at an annual rate of about 14 percent between 1958 and 1968.) By the year 2000, a smaller percentage of the available traffic will be carried by intermediate-range aircraft. Since the growth rate for long-range missions is expected to be higher, the market share for the shorter-range missions will be smaller. As an example, the share of the market for ranges of 3200 nautical miles and less will decrease from 60 percent in 1980 to 30 percent in the year 2000. A significantly larger part of the market is included at ranges of 4000 miles and less - especially by the year 2000. Other SCAR study results indicate that airplane size and gross weight will increase significantly if a design range of more than 4000 nautical

miles is selected. A 4000-mile basic mission was, therefore, chosen for the engine evaluation.

A typical SCAR mission is illustrated in figure XIV-4. Eighty to 90 percent of the total 4000-mile range is flown at supersonic cruise. It is essential, therefore, to have outstanding supersonic-cruise performance. Good subsonic-cruise performance is also needed. As a minimum, it enters into the reserve fuel calculation for the cruise-to-alternate and 30-minute-hold requirements. There may also be a subsonic cruise leg of several hundred miles in the basic mission to allow the airplane to fly out of some inland cities without sonic boom. There is also a need, as indicated on the figure, to control jet noise at takeoff.

The airframe and mission characteristics chosen for this analysis provide a common ground for evaluating the various propulsion system concepts and their related technologies. The following discussion shows how some of the conflicting requirements of the typical SCAR mission influence engine cycle selection. Some of these cycle concepts and technologies may have a military as well as a civil application. Coordination with the Air Force is, therefore, being maintained. Militarized versions of some of the better engine concepts are being evaluated for military missions as part of the SCAR program.

CYCLE CONSIDERATIONS

All the better SCAR engine concepts currently under consideration have some bypass airflow, primarily in order to reduce engine weight. The airflow requirements are largely dictated by the takeoff noise and thrust requirements, as well as by the suppression characteristics of any given engine. As the bypass ratio is increased with the total airflow held constant, the engine weight decreases because the heavy part of the engine - the core turbomachinery - represents a smaller part of the total engine cross section. This fact is illustrated by the top curve in figure XIV-5, which is a band incorporating data supplied by the SCAR engine contractors for both mixed-flow and separate-flow turbofan engines. The exhaust systems, together with multielement mechanical suppressors for the mixed-flow engines,

were included in this data band. The curve shows that considerable weight reductions are possible up to a bypass ratio (BPR) of about 1.5. Little further weight reduction occurs as the BPR is increased above this value.

The effect of BPR on specific fuel consumption (SFC) at supersonic cruise (middle curve in fig. XIV-5) is of prime importance because by far the most range in our typical SCAR mission is flown at the supersonic-cruise condition. This curve, as well as the one for subsonic cruise, are for separate-flow, duct-burning turbofans in which the fan pressure ratio has been reoptimized at each different BPR. At supersonic cruise, low bypass ratios are best. The throttle setting needed for a constant cruise thrust is different at each BPR. For a BPR of 0.5, for example, maximum dry thrust is required at Mach 2.4 cruise. Much of the SFC increase which occurs as BPR is increased above 0.5 is the result of the need for more duct burning in order to obtain the required thrust.

For Mach 0.9 cruise, much less thrust is needed than for supersonic cruise, and the engine operates in a part-throttle mode. Less throttling back is needed as the bypass ratio is increased to meet the cruise thrust requirement, and the SFC improves (bottom curve in fig. XIV-5). The Mach 0.9 cruise thrust used here is the one required for the reserve cruise-to-alternate flight condition. At subsonic cruise, higher bypass ratios are best.

The point to be made from figure XIV-5 is that the optimum bypass ratio is different for the Mach 2.4 and the Mach 0.9 cruise conditions. The optimum BPR for engine weight, however, is similar to that for minimum Mach 0.9 SFC. For a conventional engine, then, some compromises must be made between the BPR for best supersonic-cruise performance and that for the lowest engine weight and best subsonic-cruise performance. A likely compromise appears to be in the vicinity of a BPR of 1.0, but the final determination would be made through simulated-flight mission computations.

Figure XIV-5 shows the effect bypass ratio has an engine weight and cruise performance for a constant takeoff airflow and, hence, constant sideline jet noise. Figure XIV-6 shows how both the takeoff airflow and gross weight go up as the sideline jet noise is reduced. If jet noise is to be reduced, jet exhaust velocity, which is the primary variable in the noise calculation procedure, must go down. Airflow must, therefore, be increased to produce the required takeoff thrust. For a given cycle, larger airflow requirements lead to heavier engines and the takeoff gross weight increases rapidly.

ENGINE EVALUATION

As we have seen, mission characteristics influence the cycle selection process for conventional turbofan engines. There is an apparent need for an engine with high-BPR weight and subsonic-cruise performance characteristics but with the supersonic-cruise performance characteristics of a lower-BPR engine. Such an unconventional engine concept is referred to as a variable cycle engine (VCE). A VCE, then, has the ability to tailor its BPR, and perhaps also its fan pressure ratio, to whatever values are optimum at any particular flight condition.

Many types of engines, both conventional and unconventional, have been suggested at one time or another in the SCAR program. The SCAR philosophy has been to start with a broad matrix of concepts and then to systematically sort out the best engines for further study. Both conventional and variable cycle engines have been considered in the SCAR program. The conventional engines considered were the afterburning turbojet, the dry turbojet, the duct-burning turbofan, the mixed-flow turbofan, and the mini-bypass turbojet. Only the duct-burning turbofan and the mini-bypass turbojet have survived the screening process to date. Many variable cycle engines have been considered: the auxiliary engine; the fan-in-wing; the augmentor wing; the turbofan-ramjet; the turbo-augmented cycle; the flex cycle; the triple-rotor, modulating airflow turbofan; the front-valve, series-parallel fan; the dual-valve, series-parallel fan; the rear-valve turbofan/turbojet; the variable-bypass supersonic fan; the multimode integrated propulsion system (MMIPS); and the dual-cycle/double bypass engine. Only three have survived the screening process: the rear-valve turbofan/turbojet, the variable-bypass supersonic fan, and dual-cycle/double bypass.

The mini-bypass turbojet is the surviving conventional engine which is most similar to the afterburning turbojet used in the canceled SST program. The mini-bypass turbojet, however, has a bypass ratio of up to 0.5 and a turbine inlet temperature several hundred degrees higher than the earlier turbojet. The mini-bypass turbojet mission results are compared with those of that afterburning turbojet in figure XIV-7. In this figure, both engines are being flown in an advanced airframe. The takeoff gross weights (TOGW) are shown as a function of sideline jet noise for airplanes scaled to fly a constant range. Sideline noise is used as the abscissa here because it is

usually the most difficult of the three FAR noise criteria to meet with engines designed for supersonic cruise. The older-technology afterburning turbojet, denoted by curve 1 in figure XIV-7, is much noisier than the present FAR 36 allowable sideline noise of 108 EPNdB. The higher turbine inlet temperature and lighter weight of the mini-bypass turbojet, identified as curve 2 in figure XIV-7, produce a significant gross weight reduction; but the noise is still too high. The mini-bypass engine jet noise can be reduced to the FAR 36 level by the addition of an advanced-technology multielement suppressor in the exhaust stream. This noise reduction can be accomplished with only a slight gross weight penalty, as shown by curve 3 in figure XIV-7.

Among the other engines still under consideration, the variable-bypass supersonic fan is the most poorly defined and is difficult to evaluate with any degree of certainty at this time. Three promising engines which are better defined and are receiving more in-depth study are the duct-burning turbofan in the conventional category and both the rear-valve and the double-bypass engines in the variable-cycle category.

The duct-burning turbofan, shown schematically in figure XIV-8, is representative of modern conventional engine technology which may be apropos for an early- to mid-1980's design. One major advantage it has, compared to the turbojet, is the noise reduction it receives from the coannular flow suppression effect, which is referred to in paper I. Another advantage of the duct-burning turbofan which is common to all better SCAR engines to some extent is the bypass flow steam. With bypass flow, less engine weight is required for a given total airflow. Turbofan engines also have superior subsonic-cruise fuel economy.

SCAR advanced technology engines can attain supersonic-cruise turbine inlet temperatures about 500° F higher than those possible with the 1965-era turbojet design. These higher temperatures are possible because of improved turbine materials and cooling technology. The higher temperatures permit the use of moderate bypass ratios for lower weight and better subsonic fuel economy without much penalty to supersonic-cruise fuel consumption. If bypass ratio is increased with a fixed turbine inlet temperature, the unaugmented cruise thrust will decrease for a fixed sea-level-static airflow. But if the turbine inlet temperature is increased simultaneously with the bypass ratio, this short-fall in cruise thrust (unaugmented) can be minimized, leaving very little difference to be made up with augmentation. Min-

imizing the augmentation requirement for supersonic cruise is a big factor in obtaining low supersonic-cruise SFC with a turbofan engine.

As also indicated in figure XIV-8, further weight improvements from advanced technology are due to higher turbomachinery stage loadings and increased use of composite materials. In addition, the duct-burning turbofan engine must have several variable geometry features to satisfactorily perform the SCAR mission. In fact, so much variable geometry is either essential, or at least desirable, that this engine might also be referred to as a VCE. The bypass stream nozzle must have a variable throat area to adjust to changes in the duct-burner temperature, which is modulated throughout the flight to meet the varying thrust needs. The core nozzle throat area may also need to be variable to better match the engine airflow demand to the airflow supplied by the inlet for reduced spillage drag. Constant airflow throttling could be obtained, for example, by opening the primary nozzle throat area. This would minimize both the inlet spillage and the nozzle boattail drag in part-throttle subsonic cruise. The nozzle exit area also must be variable to accommodate the wide range of expansion ratios commensurate with the flight spectrum of the SCAR mission.

Some of the other components of this particular turbofan engine (e.g., the fan and compressor) will probably need variable geometry. The benefits and costs of a variable turbine are still being studied. It is essential, however, for an engine such as this to have a special turbine inlet temperature schedule to keep the takeoff jet noise low. The supersonic-cruise temperature must be high, as mentioned previously, for good fuel economy at this condition. But the turbine inlet temperature at takeoff must be lower to reduce the exit velocity of the core stream to a value considerably below that of the augmented bypass stream to take full advantage of the coannular suppression effect. This situation is opposite from that usually found with subsonic engines, where takeoff temperatures may be several hundred degrees hotter than those used at cruise. Knowing in advance that an inverted temperature schedule is to be used, the designer can take advantage of this fact in the component mechanical design (for minimum weight and better matching).

A variable-cycle concept which was derived from the duct-burning turbofan is the rear-valve VCE, as shown schematically in figure XIV-9. It differs from the conventional turbofan engine in that a rear diverter valve and a second low-pressure turbine have been added. In takeoff and supersonic op-

eration - in fact, at all conditions except for subsonic cruise - this engine simulates the operation of two parallel turbojets. In this mode, the duct burner is on. The rear valve, in the crossover position, diverts this flow into the second low-pressure turbine. There work is extracted, as shown in the top flow-path sketch of figure XIV-9. The other flow stream from the engine core is diverted around the second low-pressure turbine by the valve so that it becomes the outer annulus flow in the nozzle. This simulated turbojet operation should produce good supersonic-cruise SFC. The curve of supersonic-cruise SFC as a function of bypass ratio (fig. XIV-5) indicates that low bypass ratios are best for this condition. During takeoff, the duct burner would still be on and the parallel-turbojet operating mode would be retained. The burner temperatures at takeoff would be readjusted to fully use the coannular suppression effect in meeting the noise goal.

In subsonic cruise, the thrust requirement is such that the duct burner must be turned off. As a result of the temperature reduction of this stream, its corrected flow is reduced. But the second low-pressure turbine, to which this flow is directed, is essentially a constant-corrected-flow machine. In order to maintain the flow at the turbine's design value, the diverter valve must be repositioned so that both flow streams go into the turbine, as shown by the bottom flow-path sketch of figure XIV-9. Rear-valve VCE operation during subsonic cruise thus simulates that of a mixed-flow turbofan of moderately high BPR. The SFC data in figure XIV-5 indicated that for subsonic cruise moderately high bypass ratios were desirable.

The relatively large bypass duct of the rear-valve VCE gives it some of the weight advantage of a higher-BPR turbofan, as would be expected from the weight-against-BPR trend shown in the top curve of figure XIV-5. There is, however, a weight penalty for the introduction of the diverter valve and the second low-pressure turbine, which neutralizes some of beneficial effect of the larger bypass duct. There is also some performance penalty due to additional pressure drops for flow through the diverter valve and for the greater lengths of the flow paths. Some additional external drag will also be introduced because of the greater length of the engine relative to the duct-burning turbofan.

The double-bypass engine is another promising VCE currently receiving more in-depth study in the SCAR program. It is essentially a turbofan engine which can operate in a high-BPR mode at takeoff but cruise superson-

ically in a low-BPR mode. The high-BPR takeoff capability allows the airflow requirement for low noise and high thrust to be met without excessive engine weight. The low-BPR supersonic-cruise mode allows that relatively high thrust requirement to be met with a minimum of augmentation for good fuel economy. This VCE requires extensive amounts of variable component geometry but does not require a hot rear valve like the previously discussed VCE derived from the duct-burning turbofan.

SCAR STUDY RESULTS

The advanced duct-burning turbofan and the two VCE's just discussed produce more favorable mission results than the mini-bypass and 1965-era turbojets (fig. XIV-7). These results are repeated for reference in figure XIV-10, where relative takeoff gross weight is plotted as a function of sideline jet noise. The turbojet is denoted as curve 1 and the unsuppressed mini-bypass turbojet as curve 2. The suppressed mini-bypass turbojet (curve 3) is represented by a crosshatched band in figure XIV-10 to show that it has the potential to meet the FAR 36 noise rules. Some of the early VCE concepts, represented by crosshatched band 4 in figure XIV-10, seemed attractive when first studied in 1973. However, these series-parallel fan VCE's had an unfortunate tendency toward greater weight and degraded performance when studied in more depth. The upper bound of band 4 represents the dual-valve (front and rear), series-parallel fan VCE's. The lower bound represents the front-valve, series-parallel VCE's. The duct-burning turbofan and both the rear-valve and double-bypass VCE's are included in band 5. The results for these engines are better than those for either the early VCE's or the suppressed mini-bypass turbojet. The results for all three engine concepts in band 5 are very similar, and the choice among them would depend on airframe and mission details.

These encouraging results for the three prime engine concepts depend heavily on continuing advances in the technology programs shown in table XIV-1. The base technologies in the various disciplines are as helpful to SCAR engines as to any others. Some technologies are specifically related to supersonic cruise aircraft. For example, coannular noise suppression will continue to be important; some preliminary results are included in

paper I. Forward-velocity flight effects on jet noise and suppressor characteristics, including coannular suppression, are very important to the SCAR results and are continuing to be studied under contract. Low NO_x emission is especially important in high-altitude cruise to avoid any significant stratospheric ozone reduction. Virtually all engines require some augmentation at supersonic cruise. The augmentors as well as the primary combustors must be low polluting.

Highly variable-flow components are critical to some of the VCE concepts just discussed. Composite materials such as large-fiber, boron-aluminum appear to be attractive for lighter fans. Some of the inlet stability problems are included in paper XIII. Further study of coannular exhaust system aerodynamics is needed to optimize the performance of both the duct-burning turbofan and the rear-valve VCE. Silicon carbide composite sheet could provide much lighter weight for any of the exhaust systems, but it needs further development and testing. A need has been found for such unique components as flow control valves and, perhaps, a supersonic throughflow fan. Technology programs are underway in many of these areas, but there are still some gaps to be filled.

Table XIV-2 shows how technology advances of the type just described can pay off in a supersonic airplane. Some major characteristics of a current subsonic wide-body jet are compared with those of the Concorde. This first-generation supersonic transport has a transatlantic range at a speed more than twice that of the wide-body jet. However, this major advance has been achieved at the expense of greater noise exposure and a significantly higher total operating cost. (A fuel cost of 40 ¢/gal was used in the operating cost estimates.)

The second-generation supersonic transport (third column, table XIV-2) combines an advanced propulsion system with an advanced airframe. Improved technologies appear capable of providing this airplane with larger payload, longer range, lower noise, and lower operating cost. However, a long-term research goal is to do even better than this, for example, to achieve a still more advanced airplane with noise and total operating cost goals about equivalent to those of the subsonic wide-body jet. In order to achieve these levels, the SCAR program will have to make further major advances in both propulsion and airframe technologies.

CONCLUDING REMARKS

Improved aerodynamics and structures, greater use of composites, and more-refined active controls are needed in the airframe area. In the engine area, the need is to concentrate on optimizing the cycle to a greater extent for supersonic cruise since 80 to 90 percent of the total range is flown at this condition. For lower noise, the takeoff airflow capacity must be increased without increasing engine weight or compromising supersonic-cruise performance. Hopefully, the results of all these propulsion activities, when combined with the airframe improvements also being sought in the NASA SCAR program, will provide the technology for an economically viable, environmentally acceptable supersonic aircraft.

TABLE XIV-1. - BASE AND SPECIFIC TECHNOLOGIES APPLICABLE TO SCAR ENGINES

DISCIPLINE	BASE	SPECIFIC
ACOUSTICS	NOISE SOURCES SUPPRESSION	COANNULAR SUPPRESSION FLIGHT EFFECTS
COMBUSTORS	CLEAN PRIMARY COMBUSTORS	LOW CRUISE NOX CLEAN AUGMENTORS
CONTROLS	FULL-AUTHORITY ELECTRONIC	
FANS, COMPRESSORS, & TURBINES	HIGH AERO LOADING ADVANCED COOLING MATERIALS	HIGHLY VARIABLE FLOW LARGE FIBER BAI COMPOSITES
INLETS & NOZZLES	MIXED COMPRESSION INLETS EXHAUST SYSTEM AERO	INLET STABILIZATION COANNULAR NOZZLE AERO SiC COMPOSITES
UNIQUE COMPONENTS		FLOW CONTROL VALVES SUPERSONIC FAN

CS-73820

451

TABLE XIV-2 - SCAR PROGRAM RESULTS AND OBJECTIVES COMPARED WITH CURRENT AIRCRAFT

	CURRENT AIRCRAFT		SCAR STUDIES	
	WIDE-BODY	CONCORDE	PRESENT	GOAL
TOGW, LB	~750 000	~400 000	760 000	600 000
PAX	~390	~135	290	290
RANGE, N MI	~5000	~3200	~4000	3800-4000
M_{CRUISE}	0.8	~2.0	2.2-2.7	2.2-2.5
90 dB FOOTPRINT, MI^2	~10	~70	~20	10-20
REL OPER COST/ SEAT-MI	1.0	~3.2	~1.4	1.0

CS-73818
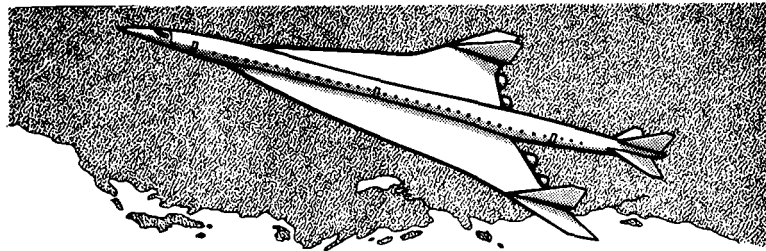
ARROW WING AERODYNAMICS & STRUCTURE
COMPOSITE STRUCTURAL MATERIALS
ACTIVE CONTROLS
ADVANCED PROPULSION SYSTEM   CS-73821

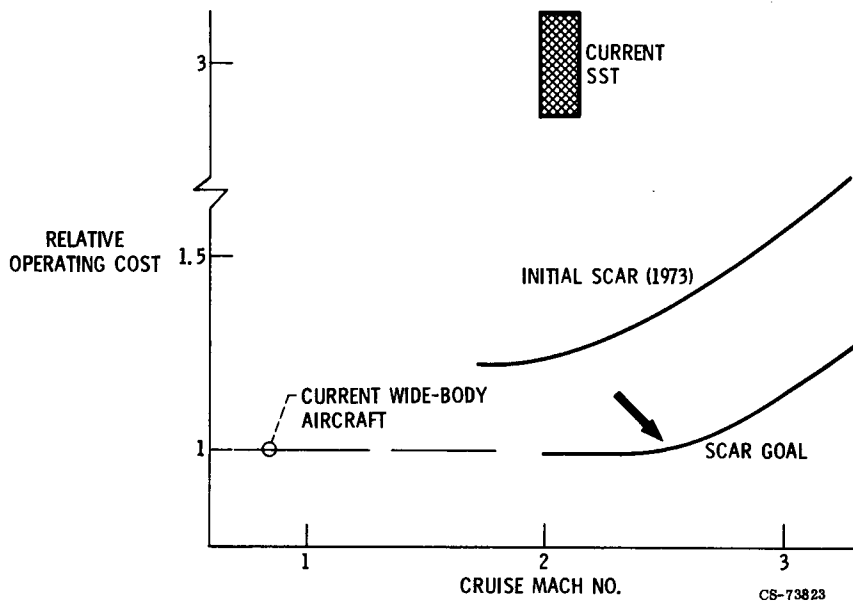Figure XIV-1. - Supersonic cruise airplane concept and related technologies.

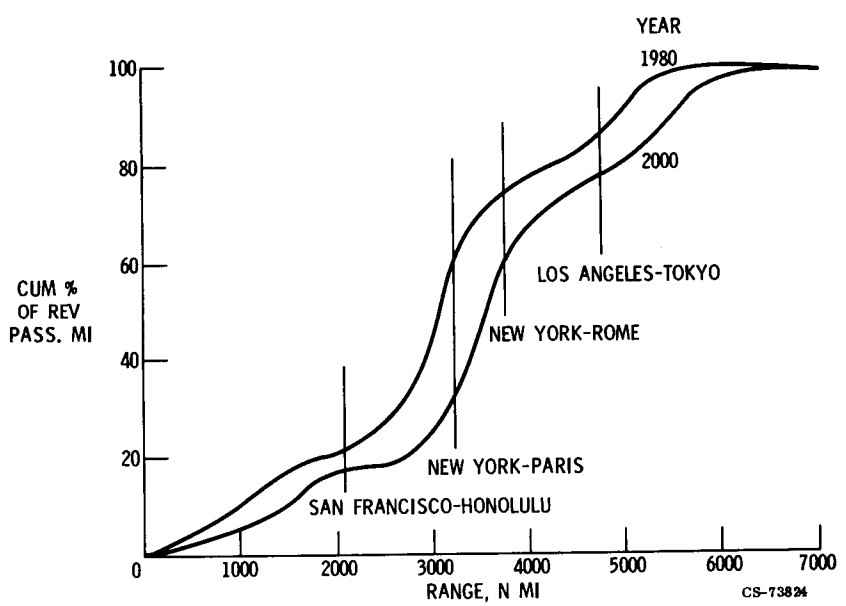Figure XIV-2. - Relative operating cost as function of cruise Mach number.
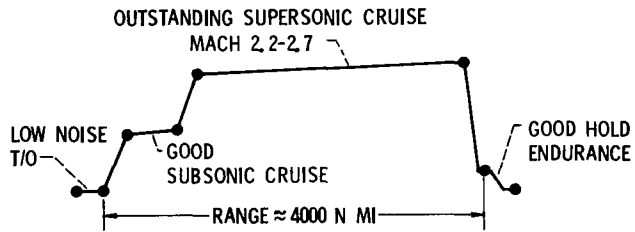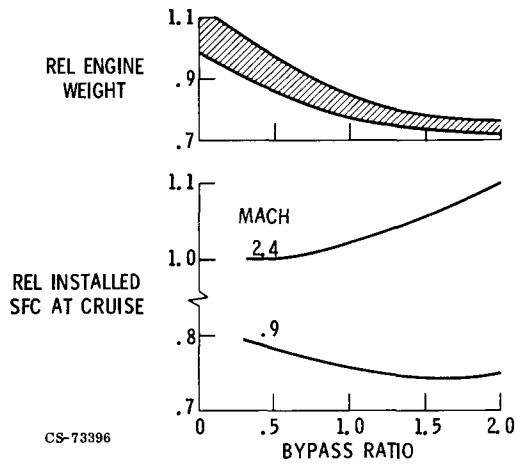

Figure XIV-3. - Distribution of revenue passenger-miles.

453

Figure XIV-4. - Typical SCAR mission.

Figure XIV-5. - Factors to consider in cycle selection - relative engine weight and specific fuel consumption trends at cruise. Duct-burning turbofan; constant sideline noise.
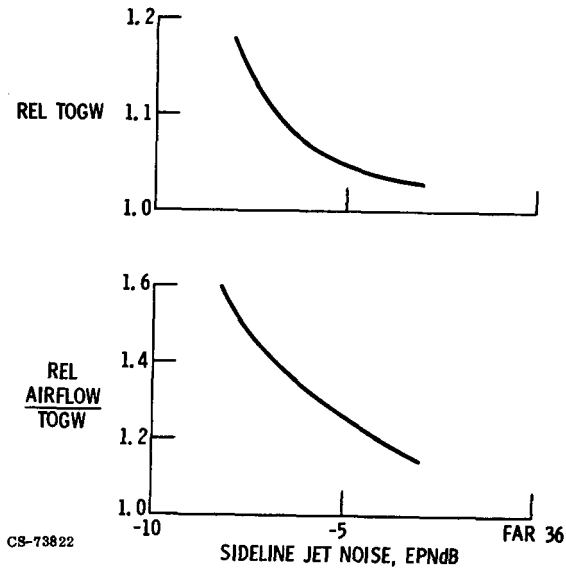
Figure XIV-6. – Additional factors in cycle selection – relative takeoff gross weight and relative airflow. SCAR engines with suppression.
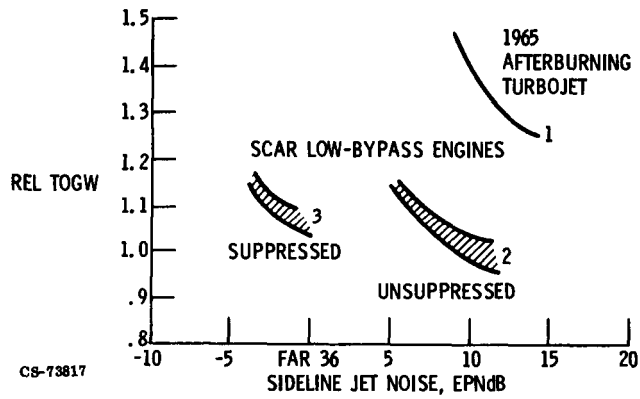
Figure XIV-7. – Comparison of SCAR mini-bypass engines (suppressed and unsuppressed) with 1965-era turbojet on basis of relative takeoff gross weight as function of sideline jet noise.

IMPROVED COMPONENT
WEIGHT & PERFORMANCE⌐

⌐BYPASS FLOW

⌐HIGHER CRUISE T_4

COANNULAR
SUPPRESSION
EFFECT⌐

CS-73394
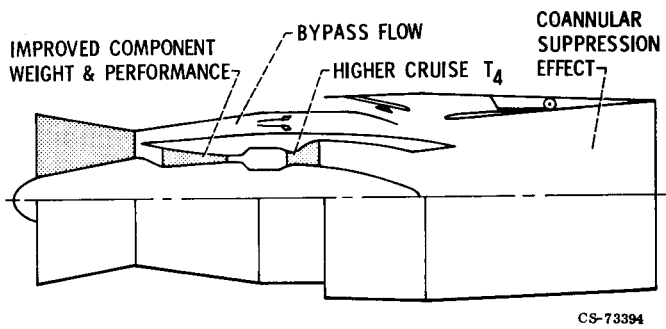
Figure XIV-8. - SCAR engine improvements to duct-burning turbofan
relative to 1965-era turbojet.

TAKEOFF & SUPERSONIC CRUISE - 2 PARALLEL TURBOJETS

DIVERTER VALVE⌐   ⌐2ND L. P. TURBINE

SUBSONIC CRUISE - HI-BYPASS MIXED-FLOW TURBOFAN

DIVERTER VALVE⌐

CS-73826
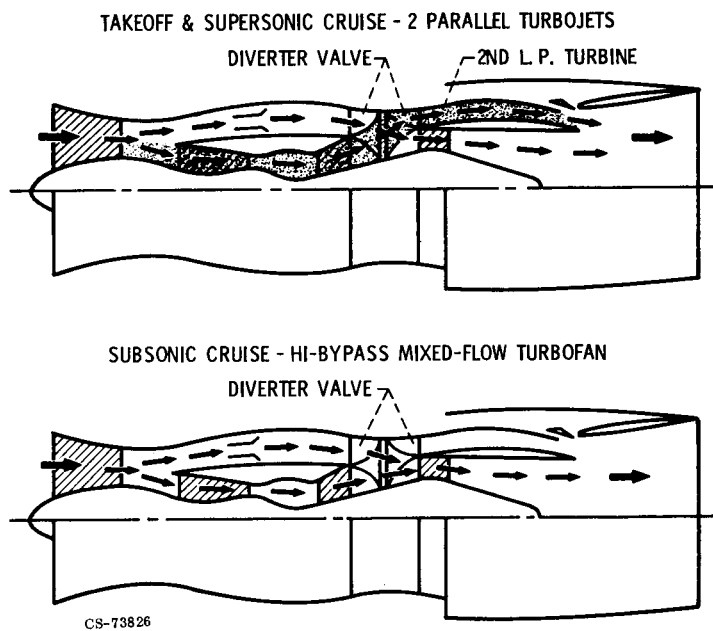
Figure XIV-9. - Rear-valve VCE concept.

REL TOGW

1.5 ┌ EARLY VCE'S
1.4
1.3   1
1.2   4
                5
1.1   3
1.0   └ DUCT BURNING TURBOFAN   2
         DOUBLE BYPASS VCE
.9   REAR VALVE VCE
.8
  -10   -5   FAR 36   5   10   15   20
CS-73816   SIDELINE JET NOISE, EPNdB
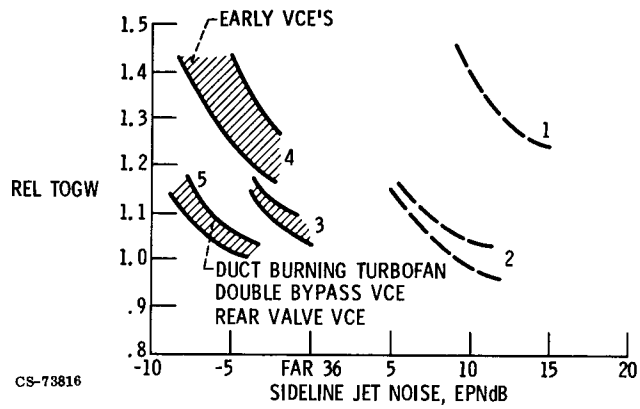
Figure XIV-10. – Comparison of most promising SCAR engines and early variable cycle engines with results of figure XIV-7.

457

Page intentionally left blank

XV. HYPERSONIC PROPULSION

Griffin Y. Anderson *

For aircraft speeds of Mach 5 to 10 and higher, new types of airbreath-ing engines will be required for efficient propulsion. At these speeds the compressor in conventional turbojets is no longer needed; inlet compres-sion alone produces sufficient pressure to drive a jet propulsion cycle. Without a compressor (and its driving turbine), at Mach 3 the engine be-comes a ramjet, and at higher speeds the engine becomes a supersonic combustion ramjet, or scramjet, employing supersonic combustion to re-duce internal pressure and heat flux in the engine.

For future systems like the airbreathing launch vehicle shown in figure XV-1, a combination of turbojets with some form of integrated ramjet-scramjet engine offers superior performance potential up to the required maximum speeds of Mach 10 to 12 (ref. 1). Scramjets are also attractive for high-speed transport vehicles at speeds of Mach 6 to 7 (ref. 2), where the reduced engine cooling requirement of the scramjet compared with that of conventional subsonic combustion ramjets provides an excess of fuel cool-ing capability which can be applied to active cooling of the airplane struc-ture (ref. 3). Various military applications for airbreathing propulsion in the Mach 5 to 12 speed range are also apparent (ref. 4).

This paper gives a status report covering NASA research on scramjet technology for future systems which require speeds above Mach 5. A brief overview of the NASA Hypersonic Research Engine project is presented which emphasizes the most significant contributions of the HRE to scramjet technology. Then the current research effort focused on high-performance airframe-integrated scramjet engines is described. Finally, progress in a joint NASA - Air Force effort to define a new versatile research airplane is discussed with emphasis on the propulsion aspect of this new program.

---

*NASA Langley Research Center.

459

NASA HYPERSONIC RESEARCH ENGINE PROJECT

During the 1960's, a considerable research effort on scramjet propulsion was mounted in industry with support from the Air Force, the Navy, and NASA. Basic research was conducted on combustion and engine components, and a number of small-scale complete scramjet engines were built and successfully ground tested (see ref. 5 for a summary of this work). In 1965, NASA undertook an ambitious program to advance scramjet technology, the Hypersonic Research Engine (HRE) project, which was to test a complete regeneratively cooled flight-weight scramjet engine on the X-15 research airplane. The chance for a flight test of the HRE was lost when the X-15 program was terminated in 1968, but significant advances in flight-weight engine structures and systems were accomplished by the HRE project because of the initial goal of a flight test on the X-15.

Flight-Weight Engine and Systems

The HRE structural assembly model (SAM), shown in figure XV-2, is a complete flight-weight regeneratively cooled scramjet; it was successfully ground tested in the Langley 8-Foot High Temperature Structures Tunnel (refs. 6 and 7). As shown in the detail in figure XV-2, aerodynamic surfaces of the engine consist of a Hastelloy skin backed by an integral offset-fin ring-stiffened heat exchanger through which the hydrogen fuel is circulated to provide cooling of the structure before injection in the combustor. The cowl leading edge, with a 0.030-inch radius, is cooled to survive a maximum heat flux of 1800 Btu per square foot per second by hydrogen flowing perpendicular to the leading edge from the outer to the inner surface. The tests of the SAM verified the structural and cooling design of the engine for conditions simulating Mach 7 flight and included operation with reduced cooling flow to achieve structure temperatures appropriate for even higher flight speeds.

Key components of the engine systems necessary for flight tests were also developed during the HRE project (ref. 8). These included hot fuel control valves, a fuel pump, a digital engine control system, and so on. Many of these components were built and bench tested before termination of

the X-15 program. The design of the SAM, the development of practical manufacturing techniques, and successful ground tests of the SAM plus the development of major flight system components represent a major advance in technology toward practical application of scramjet propulsion.

Thrust Performance of Hypersonic Research Engine

Thrust performance of the HRE concept was measured with a separate water-cooled heavy-walled engine called the aerothermodynamic integration model (AIM), shown in figure XV-3. The AIM engine was tested in the Hypersonic Tunnel Facility at the Plum Brook Station of the Lewis Research Center under conditions simulating flight at Mach 5, 6, and 7 (refs. 9 and 10). Fuel specific impulse based on internal thrust measured at the different Mach numbers in these tests for stoichiometric combustion is shown in figure XV-3 and compared with the performance goal for the HRE. At Mach 5 the performance is presented for subsonic combustion operation; at Mach 6 for both subsonic and supersonic combustion operation (the level is the same); and at Mach 7 for supersonic combustion operation. The measured performance is quite close to the performance goal. The upper edge of the shaded band indicates the level of performance that might be achieved by a series of different engines designed for operation at only one flight Mach number and without performance penalties for inlet, combustor, and nozzle losses. Measured AIM performance approaches 70 percent of this ideal level and constitutes an important demonstration of the feasibility of producing good thrust over a range of flight speed with both subsonic and supersonic combustion operation in a single engine.

AIRFRAME-INTEGRATED SCRAMJET RESEARCH

The successful AIM and SAM tests amply fulfill important parts of the original HRE program goals, that is, to demonstrate good internal thrust over a range of flight speed and to develop practical engine structures, regenerative cooling, and manufacturing techniques. The experience gained through the HRE project provides a firm basis for the current NASA effort

461

in hypersonic propulsion. While internal thrust performance was the principal consideration in selecting the HRE configuration, integration of the engine with the vehicle is also necessary to achieve high installed performance (internal thrust minus external drag), particularly as flight speed increases. The current NASA program is focused on defining practical airframe-integrated scramjet concepts. The next section describes engine-airframe integration for hypersonic flight and shows how integration can improve vehicle performance.

Scramjet Module Concept

The first fact apparent for an airbreathing vehicle at Mach 10 to 12 is that the engine needs to use nearly all the airflow between the undersurface of the vehicle and the vehicle shock wave. The requirement for maximum airflow means an inlet capture area with an annular shape, as shown in the cross section in figure XV-4. If this annular area is split into smaller rectangular units or modules, the engine becomes a number of identical pieces which are the right shape to fit in a ground facility. The whole engine is made by placing several of the modules side by side. When the engine is treated in this way, the vehicle forebody performs part of the engine inlet compression process, the aftbody takes over part of the nozzle expansion process, and the entire undersurface of the vehicle is integrated into the engine design. Two principal advantages of this approach are that (1) engine external surfaces can easily be shaped to minimize installation losses, and (2) the vehicle base region can be used to continue the nozzle expansion process.

A particular module concept which uses these advantages is shown in the lower part of figure XV-4. The module has a rectangular capture area. Since the vehicle compresses flow in the vertical direction, the module inlet has wedges to compress the flow horizontally; this design reduces the degree of change in the inlet flow field that occurs with changing flight speed and makes fixed geometry feasible. Sweep of the compression wedges and a cutback cowl provide spillage which allows the inlet to start at low flight speeds. The inlet compression process is completed by wedge-shaped struts located at the throat which block about 60 percent of the flow cross

section. The struts make the inlet shorter; they also provide multiple planes for fuel injection and thus shorten the combustor. The combustor is diverging and employs varying amounts of parallel and perpendicular fuel injection from the struts to control the distribution of heat released in the combustor as flight speed changes. These features combine to give good performance with a significant reduction in the cooling requirement and the internal pressure compared with those of a constant-area combustor with wall fuel injection.

The Langley Research Center is currently engaged in a program to establish the performance potential of this scramjet module concept. The program includes research on the module inlet and combustor to establish design criteria and operating characteristics. This effort provides the background for the design and testing of complete subscale scramjet engine modules in ground facilities. In the subscale engine work maximum advantage is taken of heat sink cooling, single purpose design, and other techniques to limit the cost and fabrication time for hardware. Analysis of the flight engine structure is under way in parallel with this effort to apply HRE technology to the integrated scramjet module configuration. The goal of the combined subscale engine testing and flight structure effort is to define an integrated scramjet module configuration with attractive performance potential which can be fabricated with a flight-weight regeneratively cooled structure and performance tested in ground facilities. This engine will have an 18- to 20-inch-high cowl to allow realistic flight structures and fabrication techniques and to represent an engine of appropriate size for flight demonstration on a research airplane. The next three sections present the status of the inlet, combustor, and subscale engine test efforts.

Inlet Research

The inlet concept has been refined to a high state of development (see refs. 11 and 12 for details). Figure XV-5 shows an aerodynamic test model of the scramjet module inlet. The flat plate and trips ahead of the inlet simulate the boundary layer on the underside of the vehicle. One sidewall of the inlet has been removed to show the struts and a rake to measure flow pro-

files at the throat. This model is the third in a series of models tested to establish the inlet performance.

Tests of this model have been completed with Mach numbers ahead of the inlet from 2.3 to 6; this range of flow field Mach number corresponds to a range of flight speeds from about Mach 3 to 8. Figure XV-6 presents four parameters deduced from these tests which give an overall measure of the inlet performance as a function of the flow field Mach number. The throat Mach number variation (upper left part in fig. XV-6) shows that the inlet is self-starting at the lowest Mach number tested. Sweep of the compression surfaces and the cutback cowl produce variations in inlet spillage (lower left part in fig. XV-6) and aerodynamic contraction (upper right part in fig. XV-6) that combine to give this fixed-geometry inlet characteristics which are similar to those of a variable-geometry inlet. Pressure recovery (lower right part in fig. XV-6) is adequate for good engine performance, and the inlet is able to ingest the large boundary layer without separation or other problems.

Combustor Research

Of course, fuel injector and combustor designs are high risk elements in the development of any new configuration. In recognition of this fact, considerable effort has been expended to assemble a combustion heated facility for supersonic combustor testing at Langley. The facility burns a mixture of hydrogen, oxygen, and air to produce a high-temperature test gas with the same unburned oxygen content as the atmosphere. A maximum stagnation pressure of about 500 pounds per square inch can be produced with stagnation temperatures up to 4700° R, values which simulate Mach 8 flight speed. Figure XV-7 presents results from one of the experiments conducted in this facility that is typical of the work under way to establish combustor performance. Imagine a cross section of the fuel injector struts in the plane of the engine cowl. This cross section is shown by the shaded shapes in the upper portion of figure XV-7. The combustion heater and a supersonic nozzle are used to simulate the flow between the center and outer struts of the engine. The upper wall of the combustor model is shaped to represent the engine centerline, and the lower wall is shaped to represent

the dividing streamline for the flow past the outer strut. The length of the combustor model is about one-third of the length of the engine combustor. Fuel is injected perpendicular to the flow from both walls downstream of small reward facing steps. The wall pressure distribution for conditions simulating Mach 7 flight and stoichiometric fuel injection is shown in the lower portion of figure XV-7. The increase in static pressure near the injector shows the effectiveness of the wall step and divergence downstream of the injectors in controlling combustion-generated pressure rise. Heat release maintains the static pressure nearly constant as the flow expands in the diverging duct downstream of the struts.

In addition to surveys of wall static pressure distribution, surveys of gas composition and pitot pressure are made at the combustor exit to provide a direct means of determining where the injected fuel goes and how much reacts. Fuel distribution contours constructed from the gas sample surveys are shown in figure XV-8. A rich region corresponding to each injector can be identified. The overall amount of fuel injected is stoichiometric, and integration of these composition contours with the local mass flux shows that at the exit of the combustor model about two-thirds of the injected fuel has reacted. In other words, two-thirds of the fuel reacts in a length corresponding to one-third of the engine combustor length. This amount of reaction indicates combustor efficiencies of 90 to 95 percent for the engine. The kind of fuel distribution map shown in figure XV-8 represents an important capability that will be applied to optimizing fuel injector design in tests which are now being prepared with more complete simulation of the combustor flow field.

Subscale Engine Tests

The work on the inlet and combustor components is intended to provide the information necessary for the design and testing of complete subscale scramjet engine modules. Figure XV-9 shows the facility and some of the hardware being prepared for this work. The upper photograph shows (from left to right) the new arc heater, the nozzle, and the test section with calibration probes. The arc uses a 20-megawatt direct-current power supply plus the air, water cooling, and exhaust systems of the Langley 4-Foot

Hypersonic Tunnel Facility. The engine model shown in the lower photograph in figure XV-9 has an 8-inch-high cowl and is constructed mostly of copper for heat sink cooling. Some water cooling is used in local areas in the combustor region to limit thermal stress due to temperature gradients. The arc heater has been run successfully at full power, and calibration runs with the test section and probe rake are in progress. The engine model is being installed in a separate test cabin which has a model insertion and thrust measuring capability; the first tests of the engine are scheduled to begin in June.

RESEARCH AIRPLANE

The goal of the current Langley program described in the preceding sections is to define and substantiate an integrated scramjet engine module concept with high performance potential. The final step of this program is to document the performance of a flight-weight regeneratively cooled version of the engine module in ground tests. The next logical step toward evolving practical applications of scramjet propulsion is to demonstrate the performance of a complete integrated scramjet engine system in flight on a research airplane. Once performance of the engine module has been proven on the ground, a flight demonstration is needed to provide validation of the vehicle forebody and aftbody integration with the engine and to prove the performance of a complete combination of vehicle and engine systems in a realistic dynamic environment. Neither of these areas can be investigated satisfactorily on the ground.

Some interesting activity related to a new research airplane is now in progress. A joint NASA - Air Force team has recently completed the definition of a vehicle that offers good potential for flight demonstration of the scramjet. Figure XV-10 shows a model of this new research airplane concept, the X-24C, with scramjets installed. The X-24C is a versatile research tool that can accommodate a number of major flight system demonstrations including scramjet propulsion. The strakes and fins are removable and can be replaced with a variety of actively cooled or hot structural test items. A 10-foot payload bay section is incorporated into the forward section of the fuselage aft of the pilot. This entire section is available for cryogenic hydrogen tankage, an integral tank, or other experiment payload.

466

The vehicle can reach speeds greater than Mach 6 with scramjets installed and has enough rocket fuel and thermal protection for 40 seconds of cruise at Mach 6. The forebody and aftbody of the vehicle are configured to accept an integrated scramjet engine system large enough to give the airplane the capability of cruising at Mach 6 on scramjet thrust alone. If pursued, this new research airplane could begin flights early in the 1980's and could provide the capability necessary for demonstration of a complete airframe-integrated scramjet propulsion system in flight before the end of the decade.

SUMMARY

The HRE project has been completed successfully with conclusion of the AIM test program at Plum Brook. The HRE project provided a practical regeneratively cooled structure for hypersonic airbreathing engines and defined the level of internal performance that could be achieved over a range of speed; the project now serves as the basis for our current hypersonic research.

A research program is under way at Langley to refine and substantiate integrated modular scramjet concepts. A fixed-geometry inlet configuration has been developed with attractive performance characteristics. A capability for supersonic combustion testing and the measurement techniques to allow injector optimization have been established. Preliminary results from tests simulating a part of the combustor flow field indicate adequate length has been provided in the engine design for good mixing. A new facility for complete subscale engine testing at Mach 7 flight conditions is operational. The overall goal of this program is to document the performance of a flight-weight regeneratively cooled scramjet engine module in ground tests.

The next logical step toward evolution of practical applications of scramjet propulsion is to demonstrate an integrated scramjet engine system in flight on a research airplane. A joint NASA - Air Force study team has defined a versatile new hypersonic research airplane with broad flight research capability. If pursued, this airplane could offer the opportunity for flight demonstration of a complete integrated scramjet propulsion system in the next decade, including Mach 6 cruise on scramjet thrust.

REFERENCES

1. Morris, R. E.; and Williams, N. B.: A Study of Advanced Air-Breathing Launch Vehicles with Cruise Capability. Vol. 1: Summary. (LR-21042, V.1; LAC-618274, Lockheed-California Co.; (NAS2-4084.), NASA CR-73194, 1968.

2. Jarlett, F. E.: Performance Potential of Hydrogen Fueled, Airbreathing Cruise Aircraft. Vol. 1: Summary. (GDC-DCB-66-00411, General Dynamics/Convair; NAS2-3180.), NASA CR-80499, 1966.

3. Becker, John V.: New Approaches to Hypersonic Aircraft. Paper ICAS-70-16, Intern. Council Aeron. Sci., Sept. 1970.

4. Stewart, J. T.: Evolving Strategic Airpower and B-1. Aeron. Astron., vol. 10, no. 6, June 1972, pp. 22-29.

5. Henry, J. R.; and McLellan, C. H.: Air-Breathing Launch Vehicle for Earth-Orbit Shuttle - New Technology and Development Approach. J. Aircraft, vol. 8, no. 5, May 1971, pp. 381-387.

6. Jilly, L. F., ed.: Hypersonic Research Engine Project. Phase 2: Structures Assembly Model (SAM) Test Report. (AP-71-7702, AiResearch Manufacturing Co.; NAS1-6666.) NASA CR-111993, 1971.

7. Wieting, Alan R.: Aerodynamic and Thermal Analysis of Results of Tests of a Hydrogen-Cooled Scramjet Engine (ARE-SAM) at Mach 6.3. NASA TM X-2767, 1973.

8. Hypersonic Research Engine Project Technological Status, 1971. NASA TM X-2572, 1972.

9. Hypersonic Research Engine Project - Phase II, Aerothermodynamic Integration Model Development - Final Technical Data Report. (AP-75-11133, AiResearch Manufacturing Company of California; NAS1-6666.) NASA CR-132654, 1975.

10. Andersen, W. L.; and Kado, L.: Hypersonic Research Engine Project - Phase II, Aerothermodynamic Integration Model (AIM) Test Report. (AP-74-10784, AiResearch Manufacturing Company of California; NAS1-6666.) NASA CR-132655, 1975.

11. Trexler, Carl A.: Performance of an Inlet for an Integrated Scramjet Concept. J. Aircraft, vol. 11, no. 9, Sept. 1974, pp. 589-591.

12. Trexler, Carl A.: Design and Performance at a Local Mach Number of 6 of an Inlet for an Integrated Scramjet Concept. NASA TN D-7944, 1975.

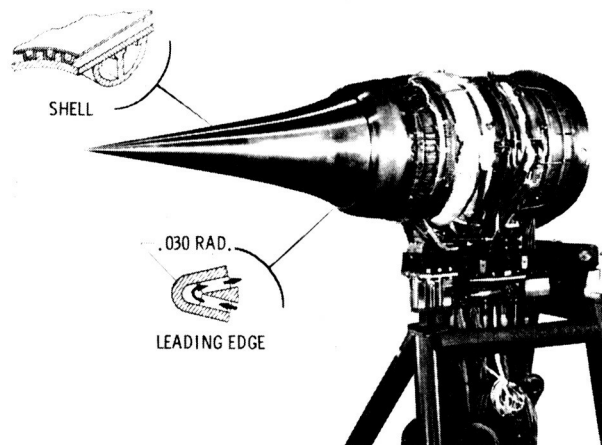Figure XV-1. - Airbreathing launch vehicle designed for hypersonic speeds.

Figure XV-2. - Structural assembly model (SAM) of hypersonic research engine.
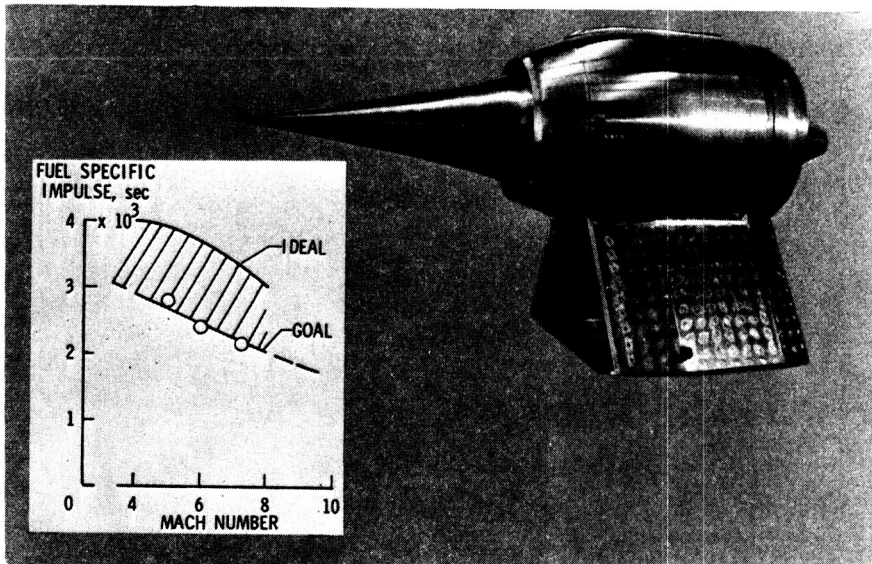
Figure XV-3. - Aerothermodynamic integration model (AIM) of hypersonic research engine and specific impulse based on internal thrust.
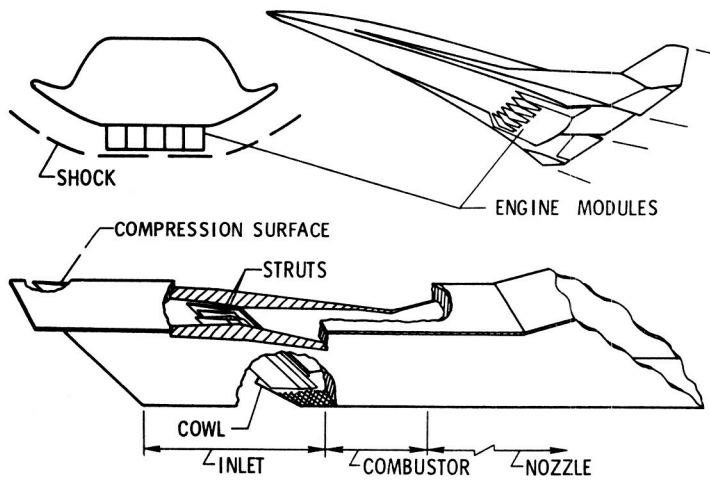
Figure XV-4. - Scramjet module concept. Fixed geometry; speeds of Mach 3 to 10.

471
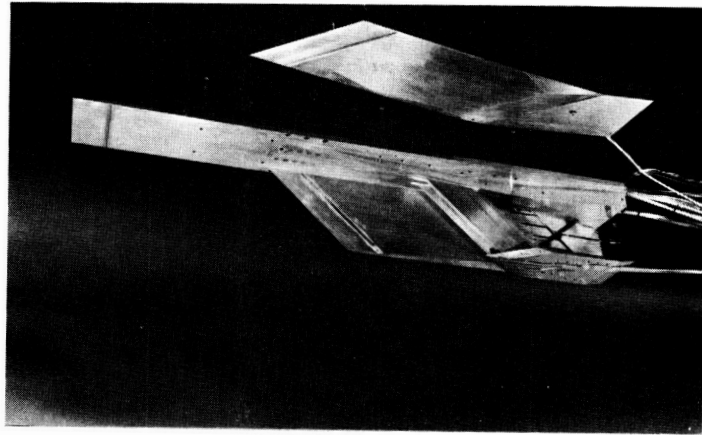
Figure XV-5. - Scramjet inlet model.
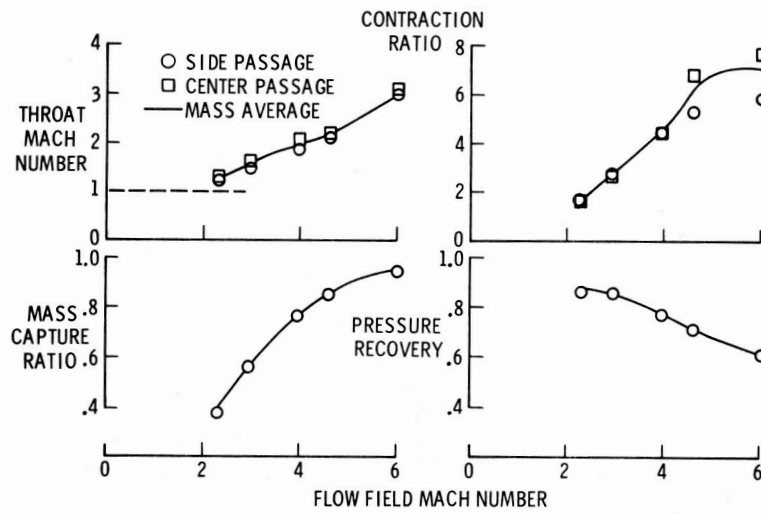
Figure XV-6. - Scramjet module inlet performance.
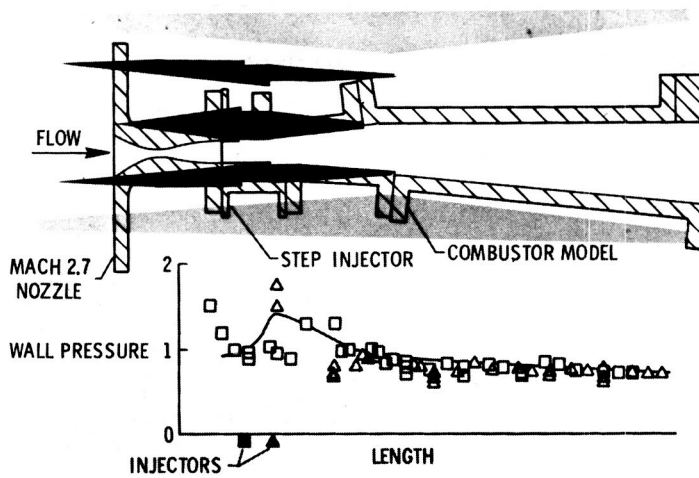
Figure XV-7. - Strut injector simulation in scramjet combustor model and wall pressure distribution.
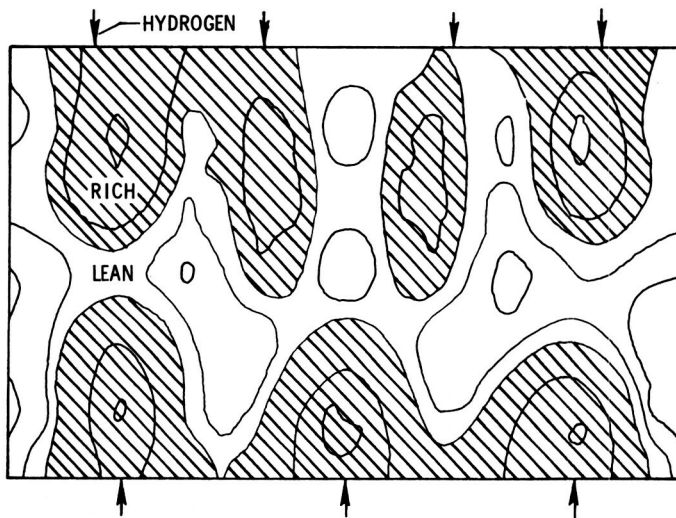

Figure XV-8. - Exit fuel distribution with stoichiometric injection.
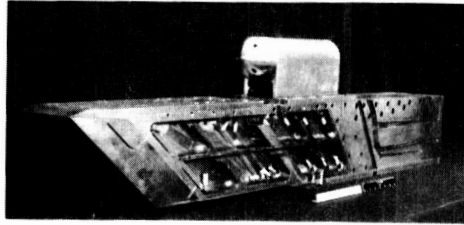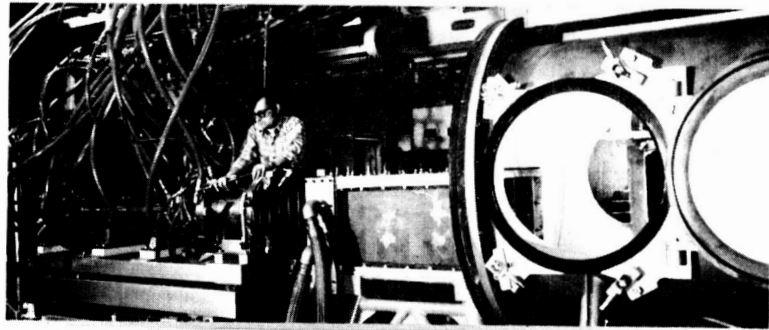
C-6

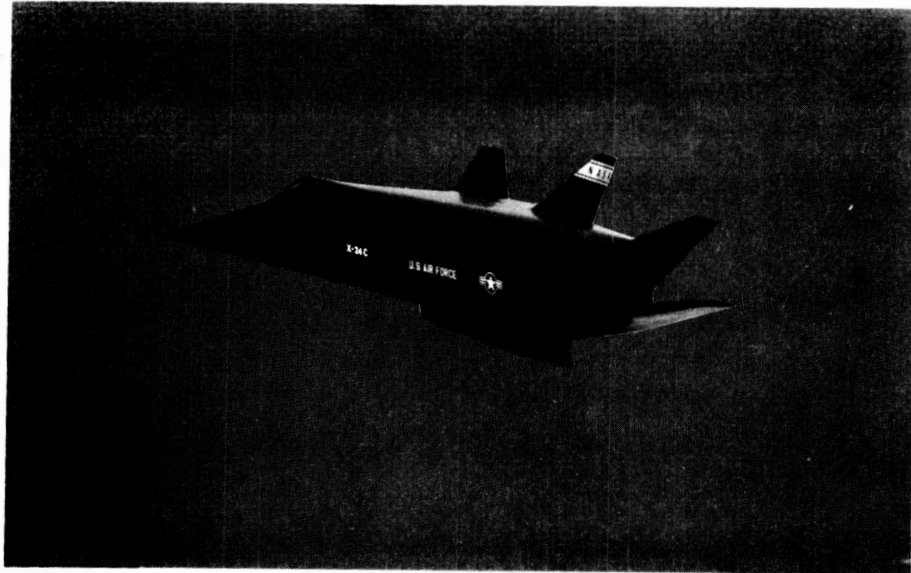Figure XV-9. - Mach 7 subscale engine test facility and engine model.

Figure XV-10. - Joint NASA - Air Force X-24C research airplane with capability for integrated scramjet system demonstration.

RESEARCH AND DEVELOPMENT CONTRACTORS AND GRANTEES

NASA relies heavily on the support and expertise of industry, universities, and research organizations in conducting its research and technology programs in aeronautical propulsion. The following is a list of contractors and grantees who are currently supplementing the in-house efforts of the NASA Lewis Research Center in this program area. In view of the large number of organizations involved, inadvertant omissions are possible, for which apology is duly expressed.

Companies

Accurton Toll & Instrument Co.
Advanced Technology Laboratories, Inc.
Aeroquip Corp.
AiResearch Manufacturing Co.
American Airlines, Inc.
Andros, Inc.
Applied Systems Corp.
Applied Technology Laboratories, Inc.
Avco Corp., Avco Lycoming Division
Bacharach Instrument Co.
Beckman Instruments, Inc.
Bela Machiné and Manufacturing, Inc.
Bell Aerospace Co.
The Bendix Corp.
The Boeing Co.
Bolt, Baranek, & Newman, Inc.
Ceramic Finishing Co.
Churchill Corp.
Creare, Inc.
Curtiss-Wright Corp.
Dasibi Corp.
Delaval Turbine, Inc., Special Products Division
Detroit Diesel Allison
Development Engineering, Inc.
Douglas Aircraft Co.
EG & G, Inc.
Electronic Associates, Inc.
Engelhard Industries, Inc.
Environment/One Corp.
Exxon Corp.
Federal-Mogul Corp.
Fiber Sciences, Inc.
Fluidyne Engineering Corp.
General Applied Science Laboratories, Inc.
General Electric Co.
General Motors Corp.
Gilmore Industries, Inc.
Goodyear Aerospace Corp.
Hamilton Standard
Hersh Acoustical Engineering
Hollingsead-Pryor Enterprises, Inc.

Honeywell, Inc.
Industrial Techtonics, Inc.
Arthur D. Little, Inc.
Lockheed Aircraft Corp.
Marlin-Rockwell Corp.
McDonnell Douglas Corp.
Mechanical Technology, Inc.
Metal Bellows Corp.
Monsanto Research Corp.
MRC Corp.
Norton Co.
Panametrics, Inc.
Pan American World Airways, Inc.
Pratt & Whitney Aircraft
Qantas Airways of Australia
REM Metals Corp.
Rocketdyne
Rockwell International Corp.
Rosemount Engineering Co.
Royco Instruments, Inc.
Sikorsky Aircraft
SKF Industries, Inc.
Solar, Division of International Harvester Co.
Spectrametrics, Inc.
The Standard Oil Co. (Ohio)
Sundstrand Corp.
Sun Oil Co.
Systems Engineering, Inc.
Tech Development, Inc.
Thermo Electron Corp.
Thermo Mechanical Systems Co.
Theta Sensors, Inc.
Transmission Research, Inc.
Trans World Airlines, Inc.
TRW, Inc.
United Techlogolies Corp.
United Technologies Research Laboratory
United Airlines, Inc.
Universal Cyclops
Wilkes Scientific Corp.

Educational and Research Institutions

Battelle Memorial Institute, Columbus Laboratory
California Institute of Technology
California State University at Chico
California State University at Northridge
Case Western Research University
Cleveland State University
Cornell University
Franklin Institute
Georgia Institute of Technology
Iowa State University of Science and Technology
Lehigh University
Massachusetts Institute of Technology
Mississippi State University
Pennsylvania State University
Princeton University
Purdue University
Rensselaer Polytechnic Institute
Rochester Institute of Technology

Stanford University
Syracuse University
Texas A & M University
University of California
University of Cincinnati
University of Illinois
University of Kentucky
University of Michigan
University of Notre Dame
University of Southern California
University of Tennessee
University of Tennessee Space Institute
University of Toledo
University of Virginia
Virginia Polytechnic Institute and State University
Wichita State University
York University